UPC - Universitat Politècnica de Catalunya
DECA - Departament d'Enginyeria Civil i Ambiental
Programa de Doctorat en Anàlisi Estructural

Mixed finite element formulations for strain localization and failure in plasticity

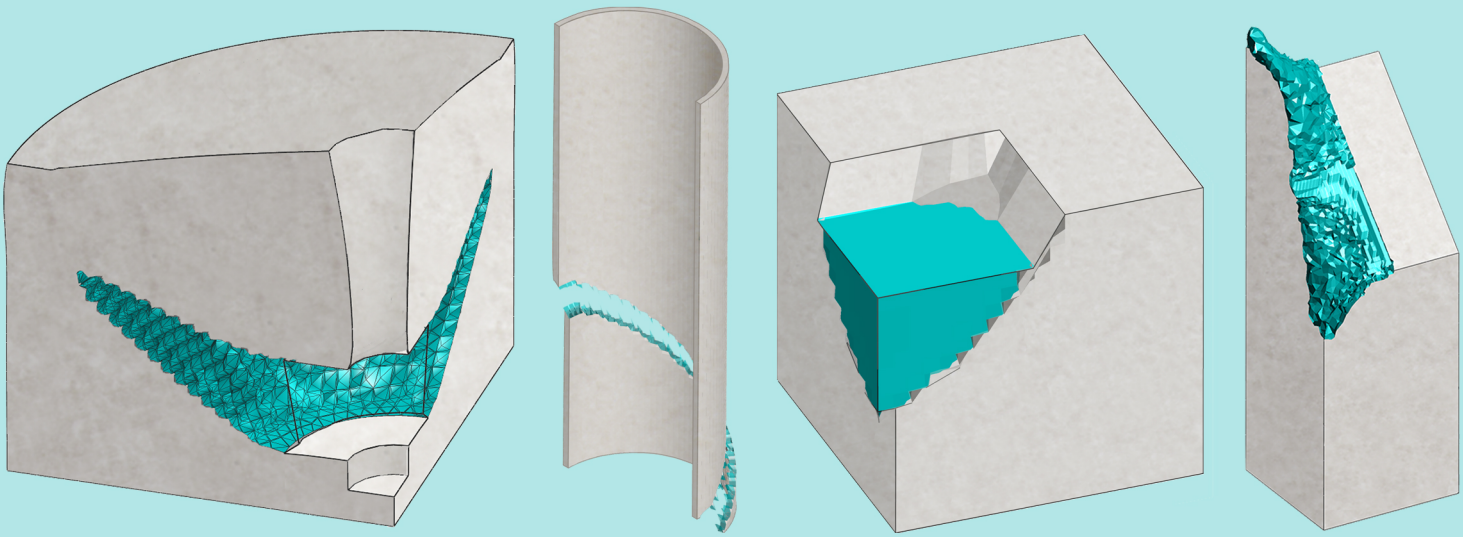

Candidate:
Lorenzo Benedetti

Supervisors:
Prof. Miguel Cervera
Prof. Michele Chiumenti

This page is left intentionally blank.

Universitat Politècnica de Catalunya

DECA - Departament d'Enginyeria Civil i Ambiental

Mixed finite element formulations for strain localization and failure in plasticity

Thesis submitted in fulfillment of the requirements for the degree of
Doctor of Philosophy in Structural Analysis

Candidate:
Lorenzo BENEDETTI

Supervisors:
Prof. Miguel CERVERA
Prof. Michele CHIUMENTI

This page is left intentionally blank.

UNIVERSITAT POLITÈCNICA DE CATALUNYA
BARCELONATECH
Escola de Doctorat

Acta de calificación de tesis doctoral

Curso académico:

Nombre y apellidos

Programa de doctorado

Unidad estructural responsable del programa

Resolución del Tribunal

Reunido el Tribunal designado a tal efecto, el doctorando / la doctoranda expone el tema de su tesis doctoral titulada_____

_____.

Acabada la lectura y después de dar respuesta a las cuestiones formuladas por los miembros titulares del tribunal, éste otorga la calificación:

☐ NO APTO ☐ APROBADO ☐ NOTABLE ☐ SOBRESALIENTE

(Nombre, apellidos y firma) Presidente/a		(Nombre, apellidos y firma) Secretario/a
(Nombre, apellidos y firma) Vocal	(Nombre, apellidos y firma) Vocal	(Nombre, apellidos y firma) Vocal

_____, _____ de _____ de _____

El resultado del escrutinio de los votos emitidos por los miembros titulares del tribunal, efectuado por la Comisión Permanente de la Escuela de Doctorado, otorga la MENCIÓ CUM LAUDE:

☐ SÍ ☐ NO

(Nombre, apellidos y firma) Presidente/a de la Comisión Permanente de la Escuela de Doctorado	(Nombre, apellidos y firma) Secretario/a de la Comisión Permanente de la Escuela de Doctorado

Barcelona, _____ de _____ de _____

Mención Internacional en el título de doctor o doctora

- Como secretario/a del tribunal hago constar que parte de la tesis doctoral, como mínimo el resumen y las conclusiones, se ha redactado y presentado en una de las lenguas habituales para la comunicación científica en su campo de conocimiento y diferente de las que son oficiales en España. Esta norma no se aplica si la estancia, los informes y los expertos provienen de un país de habla hispana.

(Nombre, apellidos y firma) Secretario/a del Tribunal

This page is left intentionally blank.

A ship in harbor is safe,
but that is not what ships are made for.

John Augustus Shedd

from *Salt from My Attic* (1928)

This page is left intentionally blank.

Acknowledgments

This thesis is the outcome of a journey that made the last 5 years a unique mix of emotions. When I arrived at UPC in Barcelona, I knew very few things on numerical methods and finite elements. I had the opportunity to follow the lectures of the master in computational mechanics and while I was feeling definitely overwhelmed, I realized my interest and affinity for the topic.

After one year of learning, it was time to embark in the world of strain localization and failure. I would like to thank my supervisors, Prof. Miguel Cervera and Prof. Michele Chiumenti, for introducing me in the solid mechanics group and allowing me to use the Comet software. Their continuous challenging of my ideas and my thinking has been quite intense but nevertheless it solidified the foundations of my knowledge and the validity of this work.

I also would like to thank Prof. Eugenio Oñate for accepting my application for the European project Mumolade which provided financial support. Finally, I would like to acknowledge Prof. Luca Pelá, being him the first contact in Barcelona and for suggesting me to come.

I am grateful to Dr. Jan-Thomas Fischer, Dr. Karl Kleemayr and the BFW institute for accepting me and providing not only the tools to continue my work but also a great environment to support it.

Completing a Ph.D. research is not an easy task. A roller coaster of expectations and fears, good and bad moments mix up continuously but time flies faster and faster, out of control. I am grateful to my roommates Savvas and Stefano for helping me see everything in a lighter way, day by day. Also, Alessandro and Lucia, for letting me stay at their house to allow me finishing this thesis.

My colleagues at CIMNE Jordi, Ilaria, Alex, Mabel, Mario, Nerea, Manuel, Lucia, Pablo, thank you for your words, your sincere critiques and your constant backing. The BFW “Schnee und Lawinen” group, starting from Antonia, Reini, Thomas and Simone, who helped me constantly through the year in Innsbruck. Andi (the two of you), Veronica, Marc, Mathias, it was really cool to learn from you basically anything about mountains, and schnitzel.. and knödel. Thank you also to those that I forgot right now... you know that you can blame me for this and I owe you a beer!

I would like to thank my parents and my family, for allowing me to study in

Barcelona and not restricting my horizons. Franco and Maria, I do not know what I could have done without you. You helped me to see the path to follow many times, even in the darkest of my hours.

Finally, I have to say thank you to Chiara. She has always been there, in the good moments and in the struggle. She gave me the motivation and the force to continue when I was ready to quit. She put me in the position to succeed by her unique leading by example and I know the love (and the patience!) that comes with it. Thank you from the deep of my hearth.

Abstract

Strain localization and quasi-brittle failure in frictional-cohesive materials is still an open and challenging problem in computational mechanics. Owing to its complexity and the significant implications on numerous engineering problems, a considerable effort has been devoted to the development of theories and techniques capable of dealing with this topic.

The introduction of numerical methods in the 70's provided a way to compute solutions, even if approximated. The Finite Element Method is able to describe efficiently a large number of geometries, engineering problems and various boundary conditions and the displacement-based irreducible formulation represents the preferred choice in the mechanical analysis of a solid body. Moreover, assuming the displacement jump created by a crack to be smeared across an element band, the calculation of the onset and evolution of a fracture can be readily performed.

However, standard finite elements are well-known to behave poorly in the case of strain localization of softening materials. Indeed, the irreducible formulation is strongly mesh-biased and the resulting fracture direction is frequently incorrect. Plasticity constitutive models are largely affected by this issue, being directional by nature. In addition, when dealing with isochoric conditions, locking of the stresses provokes spurious pressure oscillations, that inevitably spoil the numerical solution. Both problems can be shown not to be related to the mathematical statement of the continuous problem but, instead, to its discrete (FEM) counterpart.

In this work, a novel mixed $\boldsymbol{\varepsilon} - \boldsymbol{u}$ strain-displacement finite element method for strain localization and failure in plasticity is presented. Thanks to the independent interpolation of the strain and displacement fields, the proposed formulation is characterized by enhanced kinematic properties which result in a crucial improvement in the accuracy of stresses and deformations. Moreover, it is proved that the numerical quandaries typical of the irreducible formulation are alleviated with the introduction of this FE technology. The $\boldsymbol{\varepsilon} - \boldsymbol{u}$ FEM is applied to 2D and 3D problems aimed at benchmarking its numerical capabilities as well as proving high-fidelity predictions and simulations of experimental results.

Firstly, failure under Mode I (opening) loading is considered, using a Rankine failure criterion to describe the mechanical behavior of materials, such as concrete,

which exhibit cracking under tensile load. Secondly, failure under Mode II (shearing) loading is studied, employing the J2 von Mises and the Drucker-Prager failure criteria for incompressible and compressible plasticity cases. Thirdly, failure under Mode III (tearing) and Mixed Mode loading is discussed. To study the complex stress state arising in torsional and skew-symmetrical bending cases and its non-linear evolution, Rankine and Drucker-Prager failure criteria are developed in both plasticity and isotropic continuum damage models. Finally, the formulation is applied to crack propagation in weak snowpack layers, which is the main cause for the initiation of snow avalanches.

From the results, three main conclusions emerge:

(i) the mixed $\boldsymbol{\varepsilon} - \boldsymbol{u}$ finite element method proposed is capable of overcoming many of the challenges posed by strain localization in solids, providing reliable and accurate solutions;

(ii) the smeared crack approach is able to describe effectively the creation and propagation of fracture surfaces in Mode I, Mode II, Mode III and Mixed Mode loading;

(iii) the improvement of the kinematic description, with continuity of displacements and strains, is considered a key factor to empower the numerical solution.

The $\boldsymbol{\varepsilon} - \boldsymbol{u}$ finite elements share numerous aspects with the standard displacement-based ones, in terms of implementation of constitutive laws, initial set of data and geometrical discretization. However, the proposed mixed formulation is superior in predicting peak loads, strain localization patterns and failure mechanisms. Moreover, it demonstrates its generality and its possibilities in the engineering practice.

Resumen

La resolución de problemas de localización de deformaciones y fallos cuasi-frágiles en materiales friccional-cohesivos sigue siendo un tema abierto a discusión. Debido a su complejidad y a las implicaciones en numerosos problemas de ingeniería, se ha dedicado un considerable esfuerzo al desarrollo de teorías y técnicas capaces de manejar el comportamiento inelástico de los sólidos.

Respecto a esto, la introducción de los métodos numéricos en los años '70 proporcionó una técnica rápida de cálculo que permitía obtener una solución, aunque aproximada, del problema a tratar. El Método de Elementos Finitos (FEM) es capaz de describir de manera eficiente un gran número de geometrías, problemas de ingeniería y diversas condiciones de contorno, por lo que hace de la formulación irreducible la opción mayoritariamente escogida en el análisis mecánico de cuerpos sólidos. Asimismo, considerando la regularización del salto por el desplazamiento producido por una grieta a través de una banda de elementos, es posible calcular fácilmente la aparición y evolución de una fractura.

Sin embargo, los elementos finitos estándar se comportan de manera inadecuada en cálculos de localización de deformaciones y en materiales con ablandamiento. De hecho, la formulación irreducible está altamente influenciada por la malla empleada, y frecuentemente la dirección de fractura resultante es incorrecta. Consecuentemente, este fenómeno afecta de manera significativa los modelos constitutivos de plasticidad, siendo ortotrópicos por naturaleza propia. De igual manera, cuando se trata con modelos isocóricos, el bloqueo de las deformaciones provoca oscilaciones de presión espurias, que hacen inutilizable la solución numérica obtenida. Es posible demostrar que ambos problemas no están relacionados con la definición matemática del problema continuo, sino con su formulación discreta.

En este trabajo se presenta una nueva formulación mixta $\boldsymbol{\varepsilon} - \boldsymbol{u}$ de elementos finitos en desplazamientos y deformaciones para la localización de deformaciones y fallo en plasticidad. Gracias a la solución independiente de los campos de deformaciones y desplazamientos, la formulación propuesta se caracteriza por la mejora de las capacidades cinemáticas, que da como resultado una mejora crucial en la precisión del cálculo de tensiones y deformaciones. Además, se demuestra que los problemas numéricos comunes en la formulación irreducible se ven mitigados con el uso de la

técnica de los elementos finitos mixtos.

En primer lugar, se considera el fallo con carga en Modo I (apertura) a través de un criterio de fallo de Rankine para describir el comportamiento mecánico de materiales, como el hormigón, que presentan grietas bajo carga de tracción.

En segundo lugar, se estudia el fallo con carga en Modo II (cizallamiento), empleando los criterios de fallo de J2 von Mises y de Drucker-Prager para la plasticidad incompresible y compresible.

En tercer lugar, se discute el fallo en Modo III (rasgado) y en Modo Mixto. Se implementan los criterios de fallo Rankine y Drucker-Prager tanto en plasticidad como en modelos isótropo de daño continuo para realizar el estudio del estado de tensión (y su evolución no lineal) que aparece en casos de flexión desviada y de torsión.

A partir de los resultados, surgen tres conclusiones principales:

(i) el método de elementos finitos mixto $\boldsymbol{\varepsilon} - \boldsymbol{u}$ es capaz de superar muchos de los desafíos planteados por la localización de la deformación en sólidos, proporcionando soluciones confiables y precisas;

(ii) el modelo de fisura distribuida es capaz de describir efectivamente la creación y propagación de superficies de fractura por carga en Modo I, Modo II, Modo III y Modo Mixto;

(iii) la mejora de la descripción cinemática, con continuidad de desplazamientos y deformaciones, se considera un factor clave para mejorar la solución numérica.

Los elementos finitos de $\boldsymbol{\varepsilon} - \boldsymbol{u}$ comparten muchos detalles en términos de implementación de leyes constitutivas, conjunto inicial de datos y discretización geométrica con aquéllos del método estándar basado en desplazamientos. Sin embargo, la formulación mixta propuesta es superior en la predicción de las cargas máximas, patrones de localización de deformación y mecanismos de fallo. Además, demuestra su generalidad y sus posibilidades para un uso favorable en la práctica de la ingeniería.

Contents

This page is left intentionally blank.

Chapter 1

Introduction

1.1 Motivation

The last three decades have experienced the widespread use of computer methods for the prediction of complex physical phenomena. A broad range of research fields, such as industrial manufacturing, natural hazards, biomedical applications have been heavily benefiting from these technological advances.

Strength of materials is the discipline that deals with the mechanics of solids from initial stress-free state to failure. The problem of calculating the ultimate resistance of a structural component with respect to various load combinations attracted the interest of a large number of researchers, being crucial in many everyday applications. At the same time, the prediction of the inelastic processes carries a high degree of complexity and, as a consequence, it resulted in a broad adoption of numerical methods.

The Finite Element Method (FEM) represents a standard tool in computational mechanics, being able to deal with an extensive set of problems of different nature and geometry. In addition, thanks to the numerous proven theorems and properties, a solid mathematical foundation is available. Nevertheless, dealing with phenomena such as material and geometrical nonlinearities or incompressibility constraints has always been a daunting task for the standard displacement based FEM. In particular, numerically predicting the onset and propagation of fracture in Mode I (opening), Mode II (sliding), Mode III (tearing) or a combination of the previous modes is still an open and challenging subject in computational solid mechanics.

Over the years, a considerable number of methods have been developed in order to tackle localization and failure, but, unfortunately, there has not been a consistent yet general numerical tool available. Indeed, in the study of material nonlinearity, several theoretical and practical roadblocks are found. For example, a bifurcation condition is satisfied when moving from the elastic to the inelastic range which implies that, after said point, the strong form of the mechanical problem loses uniqueness of

solution. Numerous methods tried to address the creation and propagation of fracture surfaces by explicitly taking into account the jump in displacements or strains across the computational domain, but this has either caused further complexity to the numerical treatment of the problem or required the use of additional techniques such as tracking. The introduction of advanced computational methods such as Enhanced Assumed Strain, B-bar elements or X-FEM shows the large research interest in the topic as well as the need of finding an effective and general solution to the problem.

Lately, mixed finite element formulations have proved to be a reliable tool, both in fluid and structural mechanics. In particular, the mixed $\boldsymbol{u} - \boldsymbol{p}$ displacement-pressure formulation [1–4] has been capable of tackling mechanical problems in the framework of J2 softening plasticity. More recently, the foundations for a more general approach were introduced by using mixed finite elements in term of displacement and stress/strain variables [5–7]. Hence, starting from previous seminal works on the topic, this thesis aims to explore the unbeaten track which links the mixed finite element framework with the one of strain localization, propagation of cracks and failure in solids. The focus is put especially on plasticity constitutive law since the resulting orthotropic non-linear behavior is very challenging from both theoretical and numerical standpoint and it requires the development a very general computational approach.

Notwithstanding the theoretical contribution, this work addresses practical applications as well. Natural hazards represent one of the prevalent risks to human life. Earthquakes, landslides, debris flows, and avalanches are just some of the devastating events which threaten the population everyday and frequently result in substantial economical and social costs. The current increase in climatic changes and land use creates a widespread natural feedback phenomena mainly observable through the higher rate of disastrous events.

Even considering only the landslides occurrence, it accounts for the 25 percent of deaths due to natural hazards worldwide [8]. From an economical stand point, the European Community estimated the annual social costs of landslides damages up to 1.2 billion of euros, without taking into account collateral damages like contamination or erosion [9]. Similarly, the Alpine range is susceptible to snow avalanches, a seasonal threat frequently caused by poor mechanical conditions of the snowpack and mindless behavior of skiers, which causes about 100 fatalities per year [10] and five hundred thousand euros in constructions and infrastructures damages [11].

With regard to the occurrence of these events, the determination of the volume of detached soil or snow is vital for the forecast and the introduction of proper countermeasures. The mass of mobilized material is directly related with its momentum and, consequently, with the level of hazard. Likewise, the design of a protective structures capable of deviating or restraining the flowing mass not only requires a clear determination of their bearing capacity but also an accurate prediction of the

post-peak behavior in case of collapse. Then, it is clear that a profound understanding of the initiation of landslide and snow avalanches is required for an adequate characterization of the subsequent outcomes. Recreating a realistic setting with an experimental setup has significant limitations, especially with large size study cases and complex boundary conditions. Nevertheless, numerical analysis overcomes such restriction and any problem of interest can be studied with a high degree of accuracy.

1.2 Objective

The objective of this work is the design, development, assessment and application of a finite element technology in the framework of a mixed formulation for the numerical solution of localization of strain and failure in plasticity.

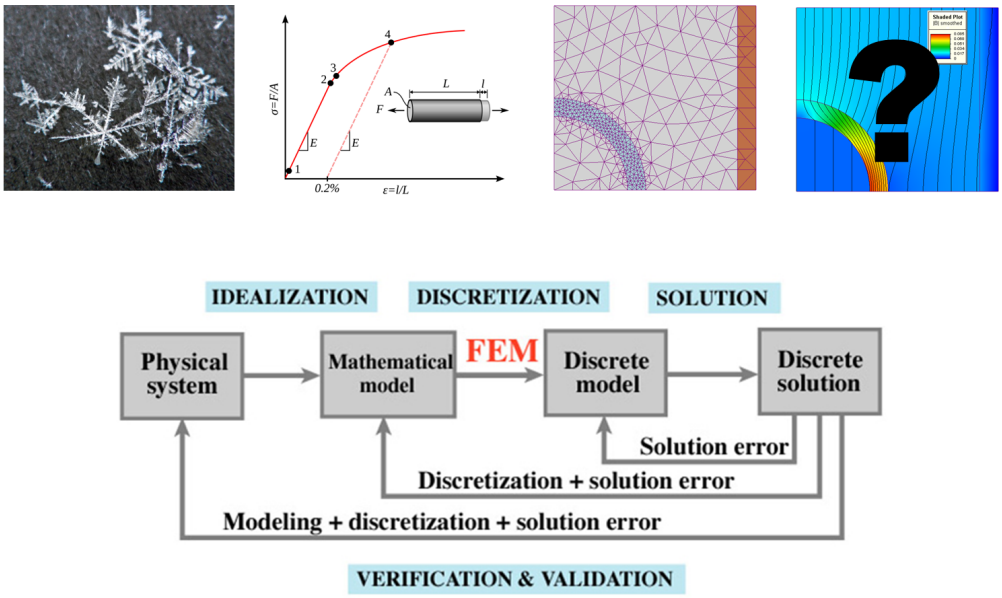

Figure 1.1: The conceptual sequence of numerical modeling: from the physical system to the discrete solution, the steps of idealization, discretization and solution, from Felippa [12].

When a numerical analysis is devised, there are four common steps in the conceptual road-map, as shown in Figure 1.1. The starting point is usually the delineation of the physical system and its boundaries. The materials to be studied, the scale of the analysis and mechanical constraint are decided at this moment. Then, the mathematical model is formulated. This first idealization allows to relate the physical behavior to a set of quantities and link them through, for example, governing partial differential equations, boundary and initial conditions.

Next, a discretization of the domain of interest is usually needed. This step is

strictly linked with the numerical method that will be used as, for finite elements and finite volumes, a mesh needs to be constructed whereas, for discrete elements or particle methods, this could not be required. Among the possible limitations and errors introduced in the discretization procedure, Strang and Fix [13] identified the following:

- interpolation of the original physical data;
- choice of a finite number of polynomial trial functions;
- simplification of the geometry of the domain;
- modification of the boundary conditions;
- numerical integration of the underlying functional in the variational principle;
- roundoff error in the solution of the discrete system.

The discretization procedure frequently introduces an inherent approximation error for the formulation used. When choosing a discrete space of interpolation, one is effectively excluding possible forms of the solution. In practice, there is the possibility that the discrete setting is not capable of capturing the basic characteristic phenomena of the analyzed problem.

This issue arises for instance in the local error committed evaluating quantities such as strains or stresses in a non-linear mechanical problem. If local convergence is not guaranteed, it may become impossible to reduce such error due to the limitations of the discretization and this may result in spurious numerical solution.

It is crucial to emphasize that, even if the phenomena of interest is extensively described by its continuous mathematical framework, the discrete model is capable of representing only an approximated numerical projection of the problem over the computational domain. Indeed, in this work, the focus is mainly pointed to the capabilities of the mixed finite element method when dealing with localization and failure in solids being capable of delivering high accuracy discrete solutions with a relative simple formulation.

Finally, a solver is introduced with the objective of inverting the system of algebraic equations. In this stage, it is possible to choose between direct or iterative solvers and, possibly, introduce an optimized solution procedure to take advantage of the characteristics of the global stiffness matrix. In finite elements, apart from the element assembly, the algebraic solution is the most computationally intensive process. While iterative solvers provide an approximated solution depending on the required tolerance, they may be more suitable than direct solvers, for a particular computer architecture and be, therefore, more efficient. However, the trade-off in computational resources is frequently determining which solver is the most suitable.

Once the numerical analysis has been performed, a validation of the results is crucial in the engineering practice. By comparing the computed solutions with analytical or experimental ones, it is possible to identify issues in the mathematical model, lack of accuracy in the discretization method or difficulties in the algebraic calculations. This step is indispensable to prove the usefulness and reliability of FE formulations.

The analysis of failure, whether it is represented by localization of strains, crack propagation or fracture, is studied in numerous ways. Within the framework of standard irreducible finite elements, the physical separation induced by the failure can be approximated with the smeared crack approach. By a smoothing procedure across a finite band width, the crack is treated as a zone where the field of displacements is continuous and the strains are discontinuous, but bounded. Unfortunately, this approximation is well-known to cause serious numerical drawbacks in the standard finite element technology. Solving problems that involve strain softening, spurious mesh dependence appears and the localization band direction is mesh biased. Moreover, when isochoric behavior is enforced (as in the case of Von Mises plasticity), locking of the stresses provokes unbounded pressure oscillations, with the consequent pollution of numerical calculations. Both problems are related to the mathematical aspects of the discrete (FEM) problem, rather than its continuous counterpart.

In fact, when the elements of the computational mesh are oriented in the direction of the localization band, the irreducible formulation provides a flawless solution. Moreover, as the characteristic size of discretization reduces, the solution of the continuous weak problem is recovered and the localization is calculated within the accuracy limitations of the formulation. However, except for a few cases, the localization of the crack is unknown a priori and the mesh cannot be pre-designed.

To alleviate the issues posed by the displacement based elements, mixed finite element formulations can be introduced. In the field of fluid mechanics, the use of mixed finite elements represents a well-known option for an accurate solution of incompressibility and advective-convective-diffusive problems [14–17]. Thanks to the similarity in the structure of the partial differential equations, the Stokes flow and the incompressible elasticity can be solved with the same mixed formulation. Solving displacements and pressure [1–4] as independent unknowns not only provides a propitious strategy to the problem of incompressibility, but also it possesses the needed robustness in the case of strain localization for J2 softening plasticity.

A natural extension of the $\boldsymbol{u} - \boldsymbol{p}$ formulation is to consider the stress or strain tensors as unknown. Consequently, starting from the contributions of Cervera et al. [5, 6, 7], the present work intends to extend, enhance and generalize these premises on mixed finite element methods in nonlinear solid mechanics. Moreover, the objective is to apply the proposed formulation to examples involving Mode I, Mode II, Mode III and Mixed Mode fracture, in order to ensure a high level of performance under all

loading conditions. To summarize, the mixed finite element formulation developed in this work has the following requirements:

- it tackles efficiently the problem of strain localization;
- it results in a general approach to be used with any constitutive law;
- it possesses the required robustness, consistency and (mesh) objectivity;
- it increases the accuracy and the fidelity of standard FEM results;
- it avoids the need of additional techniques as, for example, tracking.

The performance of the proposed formulation is assessed in a set of 2D and 3D numerical benchmarks and practical case studies using low order finite elements (P1P1 triangles or tetrahedra and Q1Q1 quadrilaterals, linear hexahedra and prisms elements with triangular base).

1.3 Outline of the thesis

This thesis is divided as follows. Chapter 2 is dedicated to the state of the art regarding the numerical analysis of localization and failure phenomena; it lays the foundation on which this work is based on. Chapter 3 presents the developed formulation and its mathematical basis. The stabilization procedure is included as well. Chapter 4 provides the implementation details of the proposed methodology in its algebraic version. Additionally, possible savings in resources and computational time are discussed.

Chapter 5 presents the first application, with the study of failure under Mode I loading. The 2D and 3D pullout tests of steel anchorages embedded in plain concrete structures are studied with a Rankine-based failure criterion in plasticity. The results of the numerical analysis are compared with published experimental tests. Chapter 6 discusses the description of failure under Mode II loading with isochoric (von Mises) and pressure dependent (Drucker-Prager) criteria. The proposed mixed formulation is used to describe problems of geotechnical nature and the method is benchmarked against the mixed $\boldsymbol{u} - \boldsymbol{p}$ formulation. Additionally, the energy dissipation from the nonlinear strain-softening constitutive law is addressed. In Chapter 7, failure under Mode III and Mixed Mode loading are analyzed with the study of skew notched beams under three point bending and torsion. The results are compared with experimental tests and a comparison between Rankine-based and pressure dependent criteria is drawn.

A further application of the method is presented in Chapter 8, with the integration of this work in the *Bundesforschungs - und Ausbildungszentrum für Wald, Naturgefahren und Landschaft (BFW)* Federal Institute in Innsbruck (Austria). Here

the focus has been placed on the propagation of cracks in weak layers in the snowpack, for the evaluation of the mechanical response of the snow, the description of the outcomes of in-situ testing and prediction of avalanche release.

Finally, Chapter 9 lays out the conclusions and provides a short discussion of the contributions of this thesis.

Mumolade Project Acknowledgment

This research work is carried out under the financial support of the MUMOLADE Project – *Multiscale Modeling of Landslides and Debris flows.* This project belongs to the EC 7^{th} Framework Programme within the framework of Marie Curie ITN (Initial Training Network). MUMOLADE deals with the numerical and physical simulation of landslide and debris flows. CIMNE is one of the research leaders in the project, supervising the work package 3, *Numerical simulation of debris flows, landslide and protection measures* and being the initial institution for the first 2 years. BFW is one of the industrial partners participating in the MUMOLADE Project and providing support for the third year of research.

Part of the work has been also realized for the EACY project-Enhanced accuracy computational and experimental framework for strain localization and failure mechanisms- within the "Excellency" Program for Knowledge Generation by the Spanish Ministry of Economy and Competitivity.

This page is left intentionally blank.

Chapter 2

State of the art

2.1 Introduction

The understanding of the mechanical strength of solids has an intrinsic sense of necessity in the human history. Predicting the behavior of materials and structures -not only in civil engineering- is fundamental to provide a safe environment for the population.

Many are the examples of structural failures and collapses that, even causing priceless losses, improved remarkably the knowledge in the field. The leaning tower of Pisa, completed in 1372, is one of the first examples of a soil-structure interaction related problem. The 5.5° tilt, which appeared during the construction, is the result of the uneven rigidity of the soil under the foundations of the tower. In the 1990's, this monument experienced a partial structural rehabilitation and the engineering challenge spurred the advancements in the topics of ground stabilization techniques. Even if the tower never collapsed, it remains a beautiful engineering failure.

In 1940, in the state of Washington (US), the Tacoma bridge was open to the traffic. Later that year, the bridge collapsed due to large oscillations caused by a 64 km/h wind. The aerodynamic properties of the narrow bridge played a key role in the amplification of the torsional movements caused by the vortices detaching from the deck structure. In the engineering practice, this collapse is a memento of the possible unexpected effects that every structure may sustain in the whole service life.

In 1963, during the initial filling of the Vajont Dam, a 260 million cubic meters landslide from Monte Toc entered in the basin creating a tsunami wave. While the structure of the dam was able to withstand the high dynamic pressures, 1917 deaths were recorded as several downstream villages and towns were wiped out by the force of 50 million cubic meters of water. The disaster proved the need of a better understanding of failure precursors in large structures, either natural or man-made, with particular regard to those characterized by a high risk factor.

Nowadays, mechanics of solids comprises numerous intertwined research fields.

Structural design is mainly based on the concepts developed in solid mechanics and, clearly, it can not be performed without a profound understanding of the properties of the materials. Similarly, numerous innovative fields of study (e.g. biomedical, manufacturing, environmental, nuclear and energy production engineering) benefit from the knowledge of linear and non-linear mechanical response for any given application. Numerical analysis and computer simulations play a crucial role in the research setting, being a multipurpose prototyping platform and bolstering a rapid scientific development.

Among the wide range of topics, material nonlinearity and, in particular, the mechanics of failure is one of the most tackled. The ultimate behavior of solids is a complex topic to be addressed, mainly due to the ephemeral and frequently sudden nature of such process. Failure is a rather general phenomenon which appears in numerous forms. By definition, when a structure is designed and built, the engineers have the objective of achieving a certain performance level with respect to a precise task. From a macroscopic point of view, the loss of carrying capability, structural integrity, serviceability or even cosmetic requirements can be considered failure.

In this work, failure is referred to as the ultimate state of a structure and of the material therein, when the residual strength is null and any further load cannot be supported. It is a common experience that a solid body subjected to increasing external load or straining shows different stages of response. Initially, for low level of stresses, the behavior of the material is elastic. In such case, the deformation caused by the external load can be recovered if this is removed [18–20]. For higher values of the external forces, it is possible to observe a modification of the mechanical response in some locations of the body, upon reaching the peak load. In most situations, a concentration of the stresses is found in the vicinity of preexistent cracks or material flaws, where the beginning of the inelastic behavior takes place and the proportionality between external load and internal response is lost. Locally, the subsequent nonlinear behavior can take place under various forms. The creation of residual strains due to microscopic dislocations [21–25], reduction of stiffness [26–31], nucleation of voids or opening of cracks [32–36] are few of the observed phenomena during inelastic processes.

Moreover, local failure is usually accompanied by the creation and growth of a fault zone. A typical phenomenon is the formation of localization bands in small regions of the solid where the strain increases while the neighborhood material unloads. There, energy is dissipated in the advancement and concentration of the inelastic zone. The amount of available energy required to mechanically separate a unit surface is generally defined as fracture energy and accepted as a material parameter. Localization and the subsequent fracture can be observed from a macroscopic point of view in various ways (Figure 2.1).

If the loading process produces the separation of the two newly created surfaces

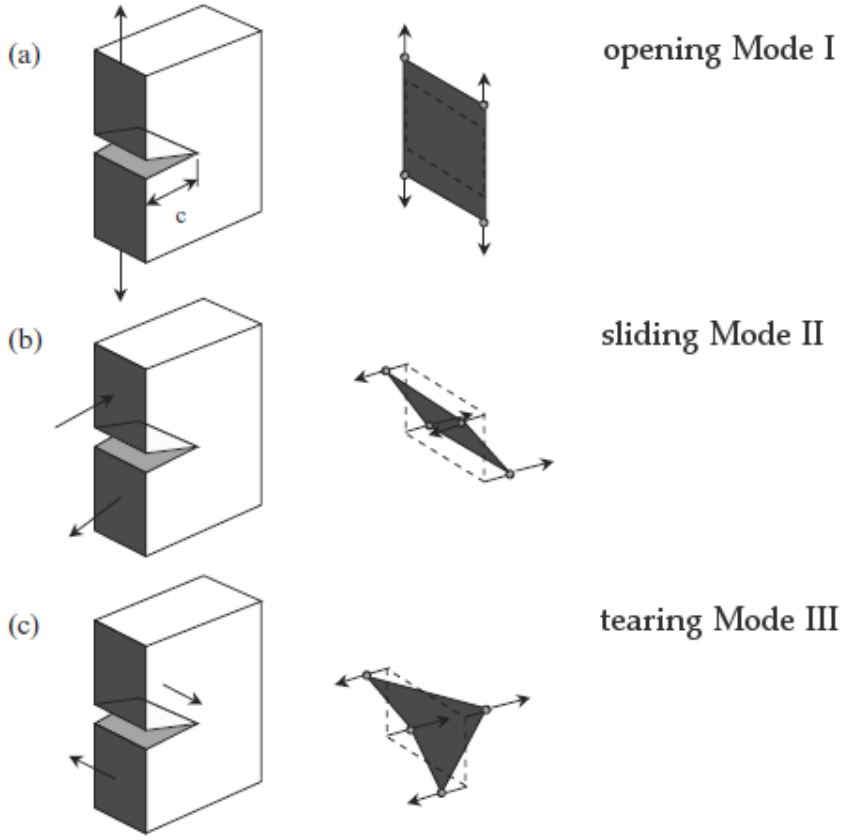

Figure 2.1: Representation of (a) Mode I, (b) Mode II and (c) Mode III loading from Fischer-Cripps [37]. On the right, it is indicated the given displacements of material points located on a plane which is normal to the crack in the vicinity of the tip.

in an orthogonal direction, this fracture type is called *Mode I* or *opening mode*. This mode is typical of materials like concrete, which are relatively weak with respect to tensile stresses and separate under sustained uniaxial traction. Historically, pure compressive failure is not considered to pertain to mode I. However, in the literature, it is possible to find references to collapse due to compression as in Carroll and Holt [38], Klein et al. [39] and Wong et al. [40]. Some very porous materials, such as snow [41], exhibit failure of the internal structure with a sudden reduction of volume due to closing (rather than opening) of the fracture surfaces.

Mode II or *sliding mode* considers the case in which two surfaces slide along the localization band. A typical example is steel, which generally shows pure isochoric plastic response and the creation of Luder's bands as indication of the incipient fracture. Frequently, soil and granular material present a similar non-linear behavior but with dependence between the volumetric pressure and the shear force through the friction angle.

Finally, *Mode III* or *tearing mode* represents the separation of two failure surfaces by relative rotation and it is found in torsion-like loading. This mode is less frequently

encountered in practice but, nevertheless, it is important in the analysis of skew symmetric structures.

In the field of Linear Elastic Fracture Mechanics (LEFM), Modes I, II and III are defined as *fracture* modes, as they refer to the motion of the newly created fracture surfaces in the vicinity of the crack tip. However, it is frequent in the literature to encounter Mode I, II and III *loading* as an extension of the previous concept.

The characterization of the material has to be distinguished from the applied loads. The former provides the mechanical response of the solid body in its equilibrium configuration. The latter depends on the set of external forces and boundary conditions that are externally imposed. The material can be characterized using LEFM, which establishes the conditions for the progression of the existing crack under a local fracture mode, or via a constitutive law, that links stresses and strains and describes the evolution of the admissible elastic space for the inelastic behavior.

For example, uniaxial tensile tests on steel specimens is defined as Mode I loading. Nonetheless, steel is characterized by failure in shear and, consequently, Mode II fracture. In fact, the appearance of diagonal localization bands during the test is typical of the inelastic response of the material and the precursor of fracture. Likewise, an applied torsional moment on a concrete beam creates a state of Mode III loading, but, given the low strength of concrete to tensile stress, a Mode I fracture is observed.

Moreover, some loading conditions result in a *mixed* distribution of stresses. Classical experiments of non-uniform bending on notched beams produce mixed tensile and shear loading at the tip of the notch. As the crack advances, it is visible how the fracture surface is the result of the mechanical characteristics of the material

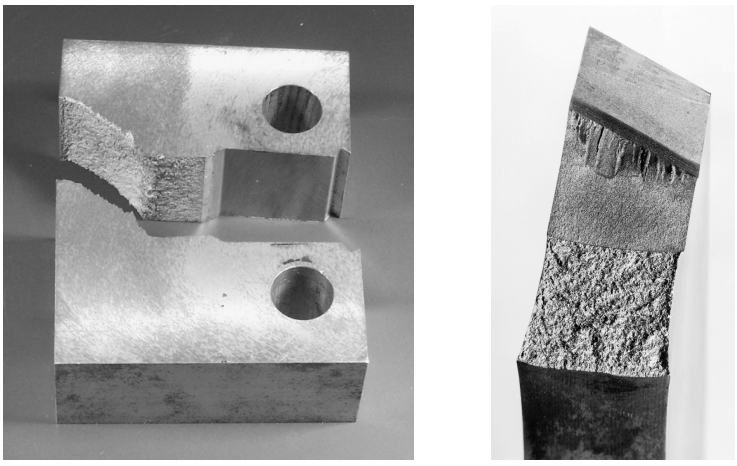

(a) (b)

Figure 2.2: Mixed mode fracture: (a) Mode I+II and (b) Mode I+III (from Pook [42])

(Figure 2.2). Likewise, in a triaxial test of a pressure sensitive material, even when the load is clearly orientated vertically, the specimen fails for an exact combination of volumetric and deviatoric components, resulting in a *mixed* mode fracture.

It is stressed that failure does not require the presence of a physical separation of the solid but rather the initiation of a unrestrained kinematic mechanism. The creation of fracture surfaces is definitely one of the visible effects of the failure process, but it is regarded as equivalent to the creation of a band of localized strains with null residual strength. Once again, this work investigates the numerical description of failure in a general sense, implying the loss of carrying capabilities which causes the subsequent collapse.

2.2 An historical perspective

In 1773, after returning from the military base of French Martinique where he was the chief engineer in charge of fortifications, Charles Augustine de Coulomb presented his original work on engineering structures to the *Académie des Sciences* in Paris [43]. Among the copious number of discoveries regarding retaining walls, structural elements and variational calculus, he introduced the very first yielding criterion for soil, characterized by a linear proportionality between tangential shear forces and normal pressure. Almost one century later, Henri Tresca [44] started the study on plastification of punctured and extruded metal tubes. In his experiments, he discovered that the overcoming of a threshold shear stress provoked the creation of residual strains. Simultaneously, William John Macquorn Rankine [45] published his thorough work on equilibrium and strength of solids, including the analysis of stability of ground works.

Adopting Saint-Venant's theory on ideally plastic materials, Lévy proposed in 1871 [46] a 3D relationship between stresses and rate of plastic strain. Apart from various applications of the proposed methods, this work was not further developed until the 1910's. In 1913, using only mathematical arguments, von Mises independently confirmed Lévy's formula for isochoric plastic strain [47], promoting the reappraisal of the topic of plasticity. In the following years, Ludwig Prandtl [48], Heinrich Hencky [49] and A. Reuss [50] defined the theoretical bases for the rate of inelastic strains based on general 3D plastic flow. Finally, much scattered information on plasticity of solids was gathered together in a self contained format in the essential works of Nadai [51] and Hill [52].

With similar mathematical basis as plasticity [53], in 1958 Kachanov identified the reduction of stiffness in concrete structures [26] as a failure mechanism. Continuum damage mechanics poses its foundation on the assumption that the unknown response of the real damage material is established by considering the behavior of an undamaged fictitious one. Mazars and Lemaitre [54], Lemaitre [27] and Chaboche [29, 30] assume

that the strains in the damaged and undamaged solids are equivalent whereas the evolution of the state of the material is dependent on the effective stress. Vice versa, Simo and Ju [55, 56] base their continuum damage constitutive model on the equivalence of stresses between the real and fictitious solids and the concept of effective strains. Finally, Cordebois and Sidoroff [57] introduce the energy equivalence between the damaged and undamaged states using both effective stress and effective strain. A comparison on the various possibilities to measure damage is presented by Lemaitre and Dufailly [28] and, more recently, by Voyiadjis and Kattan [58]. Finally, the continuum damage model has been expanded and generalized by the work of Chow and Wang [59, 60], as well as combined with plasticity, as, for instance, in Lubliner et al. [61].

In between to the early development of plasticity and the more recent one of damage, Linear Elastic Fracture Mechanics (LEFM) was proposed. The first steps in the field of LEFM coincide with the beginning of the XX century, when Kirsch [62] noticed the stress concentration in the vicinity of a circular hole in an infinite isotropic elastic plate under uniaxial tension. Fifteen years later, Inglis [63] provided a similar solution for the elliptic hole case and he highlighted that the stress values close to the sharper curvatures were several times higher than the mean stress. Hence, in 1921, Griffith [64] presented a novel understanding of the process of fracture when observing the rupture of glass. Firstly, he observed that the crack tip was developing from scratches and other material flaws. Secondly, he stated that, for the crack to progress, the available energy to be dissipated in the creation of the crack surface has to be less than the amount of stored elastic strain energy. The utmost significance of this step lays in the fact that, for the first time, it was possible to relate the development of the fracture of a material to an energy related quantity.

Nevertheless, this finding was only partially recognized. In fact, scientists in the field found difficulties in embracing a theory which provided infinite stresses at the tip of a crack. Almost 40 years later, Irwin [65], Banreblatt [66] and Dugdale [67] proposed the concept of plastic zone in the vicinity of the crack front, giving the theory more realistic prediction capabilities and the possibility of meeting again with the classical continuum mechanics.

At the turn of the 1960's, both plasticity, continuum damage and linear elastic fracture mechanics were based on firm theoretical foundations. On the one hand, the former two showed versatility in dealing with different failure criteria. On the other hand, the latter provided a way to evaluate the strength of quasi brittle structures. Nevertheless, their limitations were apparent. Linear elastic fracture mechanics provides the stress required for the crack opening but does not provide insight in the shape and propagation of the failure surface. In the case of plasticity, the reduction of the stresses and the direction of the flow are available, but the change in the structural configuration due to the creation of localization increases significantly the

solution complexity. Analytical solutions were not available for most of practical problems. A significant change in the way calculations were performed was needed.

2.3 Size effect

Linear Elastic Fracture Mechanics deals with perfectly brittle materials characterized by zero or negligible fracture energy. This fact implies that the elastic solution determines unambiguously the ultimate load and the fracture mode. Moreover, in this theory, the crack advances when the stored elastic energy at the tip is greater than the energy required to create new fracture surfaces [64].

However, many materials are not brittle and show a plasticization zone in the vicinity of the crack. For example, in the cohesive zone model [67, 68], the fracture process is gradual and it takes place in a non negligible extent of solid around the crack tip. This model describes the evolution of the forces that pull the material apart and, consequently, the redistribution of the stresses in the inelastic range. In such cases, the energy criterion previously presented is not efficient and a stress criterion is also pertinent.

Experimental studies show that specimens at different scales behave significantly differently. At the small scale limit, the structural response is characterized by ductile behavior whereas, a the large scale limit, the material presents a very brittle behavior. Bazant and Planas [69] and, later, Carpinteri [70] showed theoretically and experimentally that the nominal stress σ_N at failure for notched specimens of dimension L follows the law:

$$\sigma_N = \frac{c\,\sigma_R}{\sqrt{\left(1 + \frac{L}{L_R}\right)}} \tag{2.1}$$

where σ_R is the stress pertaining to a reference scale L_R and c is a constant. This formula describes the non-linear change in behavior between the scales for a given geometry of the specimen (Figure 2.3).

In the engineering practice, the structural mechanical response is rarely purely brittle or perfectly ductile. In reality, most of the study cases fall in the quasi-brittle failure case, where the size effect controls not only the peak load but also the energy dissipated in post-peak branch. Tests on smaller specimens, such as in laboratory experiments, are usually characterized by smaller peak loads but also a smooth reduction of stresses, closer to a ductile-like material. Bigger structures, such as long bridges and skyscrapers, have a high peak load followed by very steep reduction of carrying capability. When the scale of the solid is large enough, it is possible to observe a snap-back effect, where the unloading path has an inclination close to the loading one, as the dissipated energy during the inelastic process is closer to

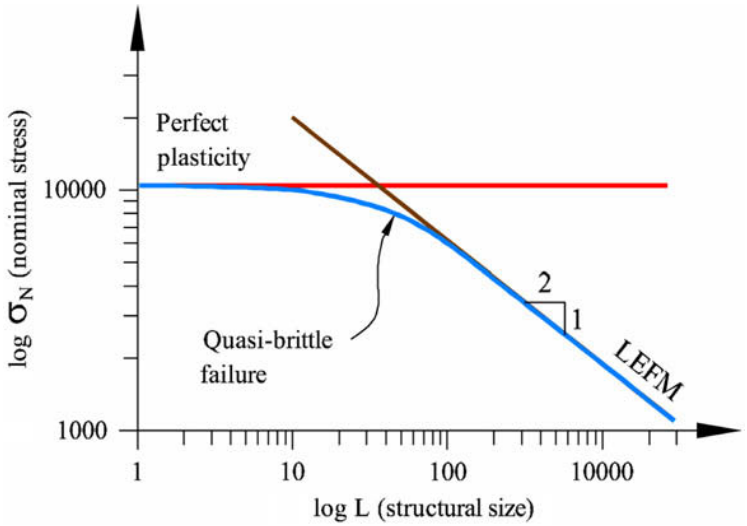

Figure 2.3: Nominal stress at failure with respect to the characteristic structural size, from Cervera and Chiumenti [71]

zero. Cervera and Chiumenti [71] show that it is possible to take into account the structural size effect in the quasi-brittle range with local constitutive models and accurate finite element formulations.

2.4 The introduction of FEM in computational failure mechanics

The advent of digital computers introduced the possibility of dealing with complex problems by discretizing space and time. Numerical methods represented a significant leap in the scientific research and engineering practice, thanks to the capability of providing approximate but convergent solutions.

In the community of structural mechanics, the method of finite elements emerged as the numerical tool of choice for the stress analysis in aerospace structures due to its tight connection with the matrix structural analysis. From the seminal works of Argyris [72], Turner [73–75], Clough [76, 77] and, later, the fundamental contributions of Melosh [78], Wilson [79] and Irons [80–82], the FEM rapidly got solid theoretical bases and attracted a broad interest from many engineering fields, being able to tackle with ease generic nonlinear structural problems [83]. Already in the 1970's, the method was well accepted and comprehensive books on the topic (such as Martin and Carey [84] and Zienkiewicz and Taylor [85]) were published. A far more detailed historical perspective is available in the article from Felippa [86].

The study of failure propagation in finite elements has always attracted a considerable interest with numerous alternative methods proposed over the years, due to the intrinsic difficulty of representing it numerically.

In the field of continuum mechanics, fracture may be mathematically modeled by a *discontinuity* in the displacement field. In this case, the fracture occurs at a line (in 2D) or a surface (in 3D) where the displacement field presents a jump, whereas the strains are unbounded and described by a Dirac's delta function. This representation is equivalent to separating the body in two parts Ω^+ and Ω^- and creating boundaries between them; Maxwell's compatibility conditions apply across the failure line $\boldsymbol{S}$ [87]. This approach is called *continuum strong discontinuity* and it is presented in Figure 2.4(a).

Dealing with discontinuities and Dirac's deltas is not straightforward and, from a practical point of view, not always necessary. For this reason, it is possible to regularize the strong discontinuity by assuming a finite band of width b, comprised between the curves $\boldsymbol{S}^+$ and $\boldsymbol{S}^-$, in which the displacement field is continuous and the strains are discontinuous but bounded. In particular, the displacement jump w is *smeared* across the localization band so that the strains in the band are the gradient of the smeared displacement field. This approach is called *continuum weak discontinuities* or, frequently, *continuum smeared approach*, and it is presented in Figure 2.4(b). It is noteworthy to stress that this procedure creates two weak discontinuities, two jumps in the strain field at $\boldsymbol{S}^+$ and $\boldsymbol{S}^-$, rather than a single displacement discontinuity at $\boldsymbol{S}$.

Moving from the continuum to the discrete setting, as when the finite element method is introduced, a computational grid composed of discrete subdomains is considered. In this grid, the displacement field is evaluated at the nodes whereas the derived variables, such as the strains, are computed at the sampling points.

The *discrete strong discontinuity* was initially proposed by Clough [88], Ngo and Scordelis [89], Nilson [90] and it consists of separating the elements in the computational mesh upon a certain failure criterion. The process assumes that the strong discontinuity is approximated with the boundary of the elements and the affected nodes are effectively doubled as shown in Figure 2.5a. Soon it was realized that this method is mesh dependent by construction as the set of available propagation directions is restricted to the ones of the element boundaries.

To overcome this limitation, *remeshed strong discontinuity* approaches were introduced by Shephard et al. [91], Wawrzynek and Ingraffea [92] and then extended by Bittencourt et al. [93], Trädegård et al. [94], Bouchard et al. [95]. A review on the topic is presented in Bouchard et al. [96]. This technique is devised in such a way that the mesh is refined in the vicinity of the propagating crack tip or, similarly, the affected elements are divided into smaller ones. This method appears more promising than the previous as shown in Figure 2.6a and Figure 2.6b. However, it requires additional computational resources since the remeshing procedure has direct effect on the topology of the mesh and on the structure of the global stiffness matrix. The remeshing of the computational grid requires to know the direction of the progressing

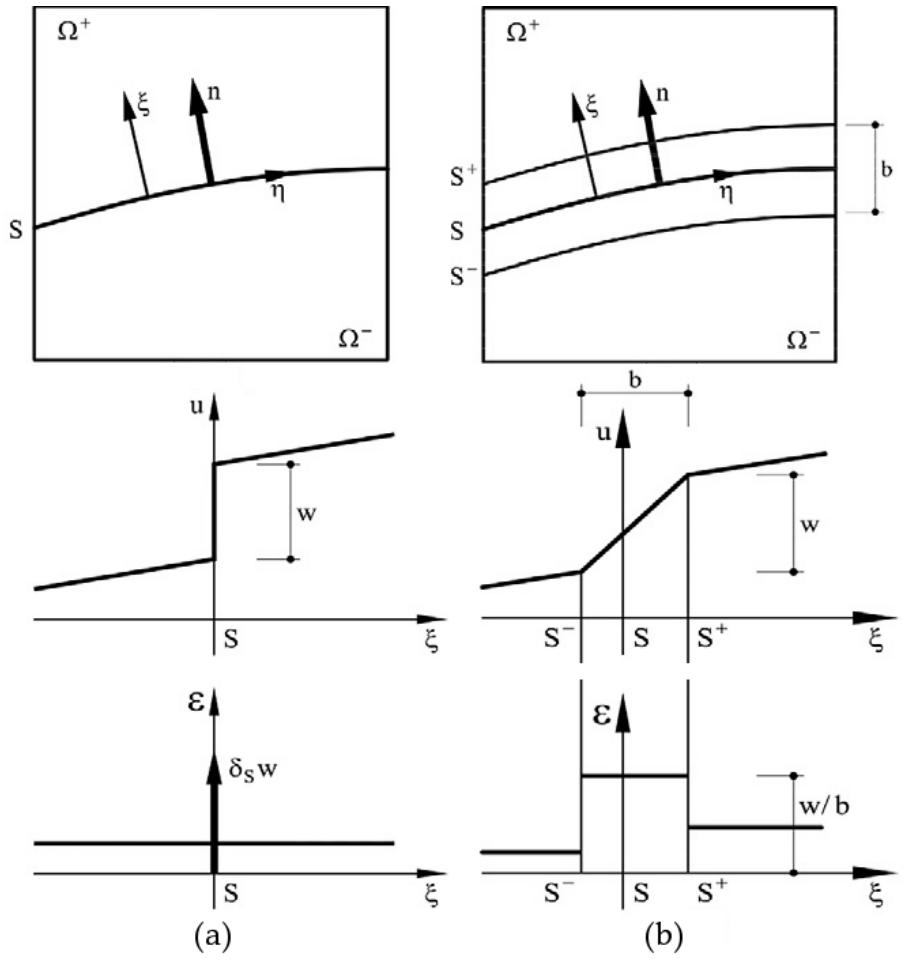

Figure 2.4: Graphical representation of modeling a localization in the continuum, using (a) strong and (b) weak discontinuity (or smeared) approach. Image from Cervera et al. [6].

crack but the standard displacement-based formulation cannot accurately predict it. Moreover, being this an explicit scheme, it incorporates an extrapolation error which is not recoverable.

After these experiences, a substantial number of researchers focused on the possibility of inserting the discontinuity directly in the elements, in order to avoid the limitations of the previous methods. The *embedded strong discontinuity* approaches have the objective of enhancing performance of the affected elements in order to provide accurate discontinuity orientation and avoiding the need of remeshing. Figure 2.6c depicts an example of enriched elements and an embedded strong discontinuity.

Ortiz et al. [98] introduced the displacement field caused by the strong discontinuity in the description of the deformation at nodes. The resulting additional modes were condensed at element level. Likewise, Belytschko et al. [99] developed a formulation that considers the jump in the displacement field while preserving traction continuity and compatibility within the element. This work resulted, some years

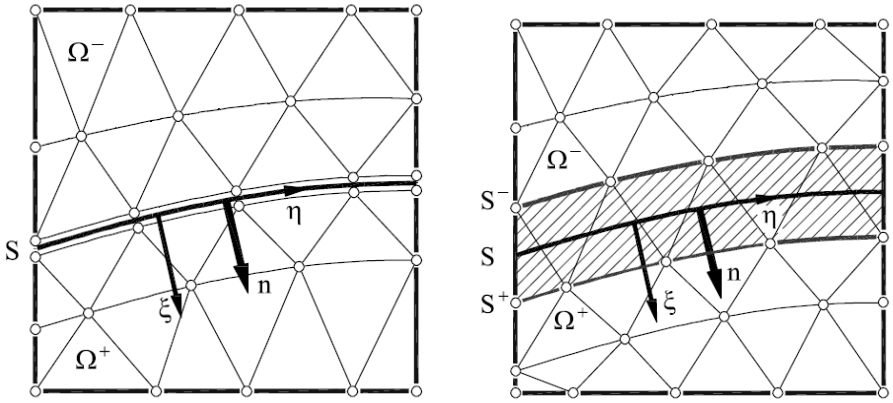

Figure 2.5: Modeling of a discontinuity in a discrete setting: (a) discrete strong and (b) discrete weak discontinuity. Image from Cervera [97]

later, in the Extended Finite Element Method (XFEM) [100–104], which assumes an enhanced set of shape functions to interpolate the displacement in the elements interested by the crack. The additional shape functions consist either of analytical linear elastic fracture mechanics solutions or Heaviside functions. The method requires additional degrees of freedom at each node, which cannot be condensed at the element level but solved at each time step. Similar approaches for the study of the propagation of localization by shape function enrichment are the Partition of Unit finite element method (PUFEM) [105, 106] and the Generalized finite element method (GFEM) [107, 108]. A review of the latter techniques with respect to the XFEM has been done by Fries and Belytschko [109].

In parallel, Simo et al. [110] and Oliver and coworkers [111–113] assumed non-conforming enrichments of the displacement field defined at the elemental level. This contribution inspired later works from Armero and coworkers [114–116] and Borja and coworkers [117–120].

Although the embedded strong discontinuity approach is appealing, it poses some significant limitations and computational quandaries. With regards to the constitutive model, a traction-separation law at the discontinuity location is required but, from the experimental standpoint, it is not always available. In fact, most of the models are based on the relationship between stresses and strains.

The embedding of a crack in the finite elements mesh, as mentioned before for the remeshing, requires to know the direction of the progressing crack and, unfortunately, this is not accurately predicted by the standard displacement-based formulation. Any error introduced in the process is irreversible, as the solution depends on the subsequent embedding.

Moreover, in the computational setting, the enriched elements require a particular

treatment. For example, in the case of XFEM, a set of different integration rules is required, to take into account the contribution of the split elements. The used integration methodology is crucial in this technique, since the stiffness matrix relative to the additional nodal degrees of freedom is frequently singular. In particular, the region between enriched and non-enriched domains is composed by the so-called blending elements, which often are source of numerical issues as reported by Chessa et al. [121], Fries [122], Tarancón et al. [123]. Moreover, the discontinuity orientation is an unknown of the problem and, often, an additional tracking technique is required in order to take into account which elements have to be enriched. For further references, see the works of Gasser and Holzapfel [124], Sancho et al. [125], Jäger et al. [126].

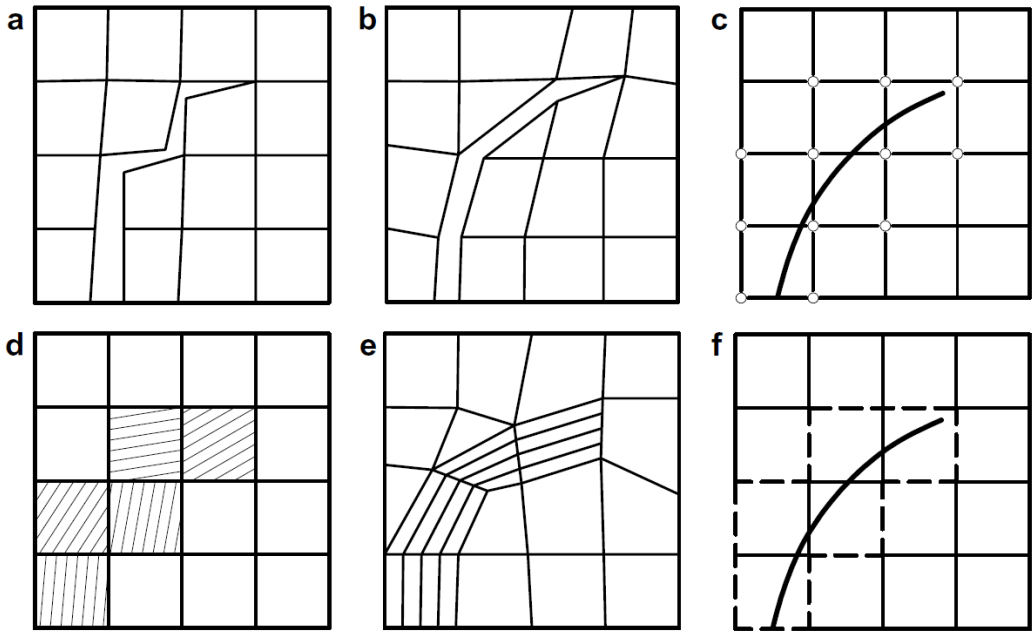

Figure 2.6: Modeling of a discontinuity in a discrete setting: (a) discrete, (b) remeshed and (c) embedded strong discontinuity; (d) discrete, (e) remeshed and (f) embedded weak discontinuity. Image from Cervera and Chiumenti [127]

Conversely, the FE counterpart of the continuum weak discontinuities model is represented by the *discrete weak discontinuities* or most commonly known as *smeared crack approach*. This model was firstly introduced in the article of Rashid [128] in the late 1960's and, in it, the crack is approximated by a band of elements which presents continuous displacements and discontinuous (although bounded) strains. Figure 2.5b shows the computational domain with the elements that are affected by the weak discontinuities. A comparison between this method and the discrete strong discontinuity one is depicted in Figure 2.6d. Abundant work has been done over the years thanks to its continuum mechanics basis and straightforward implementation in finite elements codes. The approach relies on constitutive laws based on the

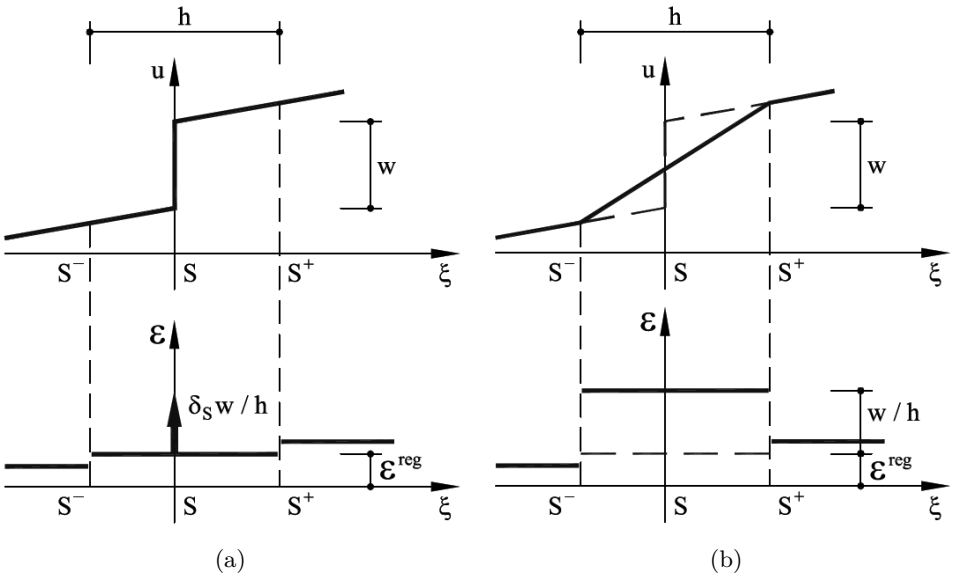

(a) (b)

Figure 2.7: Embedded approaches in the (a) strong and (b) discontinuous setting. Image from Cervera [97].

relationship between stress and strain and the strain localization is induced by strain-softening. Additionally, smeared crack models use the computational grid "as is", since, avoiding the insertion of discontinuities, the mesh topology needs not to be modified. Hence, it was possible to develop numerous constitutive models, as in the case of Bažant and Cedolin [129, 130], Rots et al. [131] or Lubliner et al. [61], Feenstra and De Borst [132], as well as increasingly larger structural analyses as done by Ingraffea and Panthaki [133], Bažant and Pfeiffer [134], Rots and De Borst [135], and Cervera et al. [136, 137].

Despite its wide adoption, the smeared crack approach is not free from numerical plights. Few years after its introduction, Pietruszczak and Mroz [138] and Bažant and Oh [139] noticed that, within the finite element setting, the creation of a failure surface is not only dependent on the available fracture energy but also on the characteristic size of the mesh resolution. Consequently, the global fracture energy appears to be not objective since it scales with the element size h. As it tends to zero upon refinement, the energy reduces as well and the model becomes more and more brittle, which is physically unacceptable.

This is because the energy dissipated by an element during the inelastic process is defined per unit volume whereas the fracture energy is measured per unit surface. The spurious mesh-size dependence is overcome by adjusting the softening parameters of the smeared approach in terms of the fracture energy and the width of localization band [113, 140], related to the resolution of the discrete mesh.

As an alternative to the previous numerical technique, numerous strategies have

been proposed with the objective of recovering the missing length scale at continuum level. Non-local constitutive laws [141–143] affirm that the behavior of a material and, in particular, the energy release rate are spatially averaged over a representative volume. Furthermore, they allege that the size of the "non-local" averaging zone is a material characteristic. In the Gradient Enhanced models [144–146], non-local effects are introduced via the consideration of higher-order deformation gradients, which allow to take into account non-local effects. In turn, the localization is regularized and the objectivity in the energy dissipation is recovered. Micro-polar or Cosserat generalized media models [147–149] introduce the rotational degrees of freedom in addition to the displacement ones to describe the material strain resulting in an alluring non-symmetric stress tensor. Recently, the Phase Field models have been introduced by Miehe et al. [150] and Kuhn and Müller [151], fanning out the crack with the definition of a regularized crack surface functional. The crack dissipation function and its topology are defined through the proposed functional. A review of the advances and implementation details of such constitutive model is presented in [152–154].

In all these approaches, the underlying continuum problem is altered and a characteristic length is inserted in it. The outcome is that strong discontinuities are precluded from the solution space of the continuum problem and, therefore, the corresponding discrete formulation is not disrupted by the need to approximate them. The entire physical concept of a crack is excluded from the setup of the problem. Additionally, these new trends carry over their own numerical gripes.

Notwithstanding the adoption of numerous and different strategies in the discrete weak discontinuities approach, the standard displacement-based formulation appears to be lacking of the required accuracy when dealing with the onset of localization band in softening problems. Indeed, the irreducible formulation fails to correctly predict stresses or strains whether it is at the tip of a notch or in the localization band during propagation. Moreover, the direction of the discontinuity depends only too often on the orientation of the elements in the mesh. However, when the computational grid is properly "designed" to be oriented in the direction of the crack propagation, the standard irreducible formulation appears to provide correct solutions [155]. Consequently, a *remeshed weak discontinuities* approach was suggested (Figure 2.6e) as in the case of the Adaptive Mesh Refinement by Zienkiewicz et al. [156, 157]. Nonetheless, remeshing requires additional solution procedures and computational resources and, if not properly devised, it can significantly slow down the calculation.

It is also possible to introduce enrichments in the definition of the strain tensor, rather than in the displacement field, and devise an *embedded weak discontinuities* approach. Figure 2.6f shows the elements that are subjected to the strain enrichment due to the embedding of the crack. In contrast with the standard smeared approach, in these procedures the inelastic part of the strain tensor is accounted for explicitly,

by means of extra incompatible deformation modes in the affected elements.

The Enhanced Assumed Strain method, proposed by Simo [158–160], is the precursor of these methods. In it the enhanced assumed strains are incompatible modes which are enforced to be orthogonal (in a L_2 sense) to the stress field. More recently, Cervera [97, 161] introduced a Mesh Corrected Crack Model, based on the split between elastic and inelastic stresses. For the latter, an orthotropic structure is assumed and this method can be considered an embedded version of the non-conforming enrichments of the displacement field, introduced also by Simo et al. [110].

With regard to enhancements in the finite element approximation space, either in the displacement or strain fields, two considerations are of paramount importance. Extending these techniques to 2D and, especially, 3D problems is not straightforward but rather cumbersome. While in the 1D case the value of the displacement jump divided by length of the element serves the purpose, in the multidimensional case consistent procedures are required to take into account the actual geometry of the affected elements. In addition, as in the case of embedded strong discontinuities, numerical instabilities and ill-conditioning frequently arise.

Secondly, the added enhancements are activated depending on the elastic strain or stress field computed at the previous time step to their introduction, almost always in a quasi-singular situation. Displacement-based finite element methods cannot guarantee local convergence of the stress values and, therefore, the decisions on how to introduce the enhancement are founded on quicksand. This is why techniques such as X-FEM and E-FEM require the use of auxiliary crack tracking techniques, which are not variationally consistent and lack of generality.

2.5 Mixed finite element formulations

The poor performance of the low order elements of the standard formulation was known since the initial years of the FEM. As discussed previously, a posteriori computation of stresses in displacement based elements is frequently unsatisfactory. For this reason, stress recovery techniques were studied by Hinton and Campbell [162] and Zienkiewicz and Zhu [163, 164] to retrieve improved a posteriori stress or strain fields. More recently, Payen and Bathe [165, 166] suggested a novel stress recovery method based on the element nodal point forces.

Over the years, other FE formulations were introduced to provide further computational enhancements such as hybrid formulations in terms of assumed stresses [167] or assumed strains [158, 168, 169], displacements and equilibrium models [170] and using the pressure as additional variable in incompressible elasticity [171, 172]. These methods can be easily implemented in a direct stiffness matrix fashion and their adoption showed various degrees of success.

The term *mixed* finite element was introduced in the 1960's to describe formulations which simultaneous resolve multiple field of interest. The mechanical description of a solid body with multiple variables can be provided with the use of variational formulations. By enforcing the minimum total potential energy, it is possible to find the equilibrium configuration in terms of the field unknowns. The Hu-Washizu variational principle describes a solid body in terms of displacements, strains and stresses using the equations of elasticity [173, 174]. By assuming the constitutive law that links strain and stress fields, the Hellinger-Reissner variational principle is recovered in terms of displacement and stress. Minimization of these leads to the weak mixed formulation of the mechanical problem.

Initial work on mixed FEM was done by Crouzeix and Raviart [175] for the stationary Stokes equations, Raviart and Thomas [176] for second order elliptic problems and Pian and Sumihara [177] for quadrilateral finite elements with assumed strain. An in-depth review of the method and its features can be found in the books by Boffi et al. [178] and Girault and Raviart [179].

In the field of computational analysis of fluids, mixed finite elements found fertile ground for large development, as most fluids are studied under the assumption of incompressibility. In fact, the incompressible Stokes problem cannot be written in an irreducible format but it requires a formulation in terms of both velocity and pressure field [180, 181].

Nevertheless, to consistently solve a mixed finite element problem, there are two important considerations to make. On the one hand, mixed formulations are computationally more expensive than standard ones, since they require the simultaneous solution of multiple unknowns. To overcome this additional cost, substantial work has been devoted through the years to fractional step methods [182–184], as a staggered technique for the efficient solution of $\boldsymbol{u} - \boldsymbol{p}$ mixed problems. On the other hand, the choice of elements to be used is not arbitrary as the discretization fields (velocity and pressure or displacements and stresses/strains) have to satisfy the so-called *Inf-Sup* condition [185–187] for the stability of the mixed formulations. This restriction is difficult to fulfill, and it leaded to the development of elements such as the Q1-P0 [188, 189], Q2-P0 [190], P1-P1 [191], Q2-Q1 Taylor-Hood [192, 193], cubic hexahedral elements [194] and the "mini" [195] elements.

Alternatively, to allow the use of arbitrary interpolations, a stabilization strategy is required as proposed by Franca and Hughes [196]. Initially, it was recognized that introducing a penalization method would alleviate the numerical troubles encountered in the solution of the mixed formulations [197]. Then, Hughes and co-workers were able to prove that the *Inf-Sup* condition can be circumvented with a Petrov-Galerkin stabilization technique [14, 198] to accommodate equal-order interpolation. These observations leaded to the introduction of the Variational Multiscale Stabilization (VMS) by Hughes [199], Hughes et al. [200]. In the following years this stabilization

framework was widely adopted, expanded and generalized by the work of Codina and co-workers [16, 201–205], among many others.

As the Stokes and the Darcy equations have the same mathematical structure than the ones of incompressible and compressible elasticity, respectively, it is possible to apply a large number of formulations that have been developed in the last two decades from the analysis of fluids to solid mechanics [206, 207].

For example, Bonet et al. [208, 209] constructed a linear tetrahedral element for incompressible and nearly incompressible elasticity in which either the pressure or the deformation gradient are averaged in the elements. Maniatty and coworkers [210, 211] developed a higher order stabilized finite element for hyperelasticity and viscoplastic flow. Djoko [212, 213] focused on the Hu-Washizu variational principle at the incompressible limit while Reddy [214, 215] used penalty function methods for mixed finite elements. De Souza [216, 217] designed low order enhanced strain elements for elastoplasticity and large deformation. Finally, Kasper and Taylor [218, 219] noted that the introduction of strain enhanced methods was beneficial for the analysis of bending dominated problems.

Pastor et al. [220, 221] provided a first mixed displacement pressure finite element for plasticity problems in the geotechnical setting. Likewise, Cervera et al. [1], Chiumenti et al. [2, 222] used a mixed $\boldsymbol{u} - p$ formulation for the modeling of incompressible solids in elasticity and plasticity. Their approach proved to be (i) easy to implement in 2D and 3D thanks to the equal low order interpolation, (ii) accurate for isochoric situations and (iii) consistent being the used variational multiscale stabilization residual-based. This finite element technology was benchmarked with problems involving both damage [3] and plasticity [4, 155].

As a natural extension of the mixed displacement-pressure formulation, in 2010, Cervera et al. [5, 6, 7] developed the mixed stress-displacement and strain-displacement finite elements. Using this novel technology, the order of convergence in the stress and strain fields is one order higher than the irreducible formulation, while maintaining the order of convergence in the displacement field. The enhancement in the accuracy of the solution is crucial to provide (almost) mesh independent numerical results and alleviate the stress-locking phenomena which pollutes the standard irreducible displacement-based formulation.

The contribution here presented is built on this previous work and it represents its continuation, in order to generalize and exploit the high computational accuracy of mixed finite elements in the prediction of the onset of crack propagation and localization of strains in plasticity.

This page is left intentionally blank.

Chapter 3

Mixed strain-displacement $\boldsymbol{\varepsilon} - \boldsymbol{u}$ formulation

3.1 Strong form

Consider a body occupying the space domain $\Omega \subset \mathbb{R}^{\dim}$ (where dim is the dimension of the space), its boundary being $\partial\Omega$ and being subjected to the body forces $\boldsymbol{f}$, the boundary tractions $\boldsymbol{t}$ and the imposed displacements $\boldsymbol{u}_0$. In a (quasi-)static mechanical problem, its configuration is properly described by three quantities: the displacement vector $\boldsymbol{u}$, the Cauchy stress tensor $\boldsymbol{\sigma}$ and the total strain tensor $\boldsymbol{\varepsilon}$. These variables and their spatial variations are linked through the field equations. The equilibrium of the body in a (quasi-)static mechanical problem is described by the balance equation and relates the source of stresses with respect to the external body forces:

$$\boldsymbol{\nabla} \cdot \boldsymbol{\sigma} + \boldsymbol{f} = \boldsymbol{0} \tag{3.1}$$

Likewise, for infinitesimal deformation, the variation in the displacement field has to be reflected in the strains as the kinematic compatibility equation reads:

$$-\boldsymbol{\varepsilon} + \boldsymbol{\nabla}^s \boldsymbol{u} = \boldsymbol{0} \tag{3.2}$$

The symbol $\boldsymbol{\nabla}^s(\cdot)$ is used to denote the symmetric gradient whereas $\boldsymbol{\nabla} \cdot (\cdot)$ refers to the divergence operator. Note that the latter is the adjoint operator of the former.

In order to complete the set of field equations, a constitutive equation connecting strain and stresses is required. In case of plasticity, the total strain tensor is decomposed additively owing to the assumption of small strains:

$$\boldsymbol{\varepsilon} = \boldsymbol{\varepsilon}_e + \boldsymbol{\varepsilon}_p \tag{3.3}$$

where $\boldsymbol{\varepsilon}_e$ is the elastic strain tensor and $\boldsymbol{\varepsilon}_p$ is the plastic strain tensor. Then, the

constitutive equation is written as:

$$\boldsymbol{\sigma} = \mathbb{C}_0 : \boldsymbol{\varepsilon}_e = \mathbb{C}_0 : (\boldsymbol{\varepsilon} - \boldsymbol{\varepsilon}_p) \tag{3.4}$$

where $\mathbb{C}_0$ is the fourth order elastic constitutive tensor. Note that being $\mathbb{C}_0$ positive definite, expression (3.4) can be inverted:

$$\boldsymbol{\varepsilon} = \mathbb{C}_0^{-1} : \boldsymbol{\sigma} + \boldsymbol{\varepsilon}_p \tag{3.5}$$

where $\mathbb{C}_0^{-1}$ is the fourth order elastic compliance tensor.

Now, two mixed strong forms are available. The first one, in terms of total strains and displacements is found by substituting (3.4) in (3.1), and the problem reads

$$\begin{aligned} -\boldsymbol{\varepsilon} + \boldsymbol{\nabla}^s \boldsymbol{u} &= \mathbf{0} \\ \boldsymbol{\nabla} \cdot [\mathbb{C}_0 : (\boldsymbol{\varepsilon} - \boldsymbol{\varepsilon}_p)] + \boldsymbol{f} &= \mathbf{0} \end{aligned} \tag{3.6}$$

Pre-multiplying the first equation by the elastic constitutive tensor $\mathbb{C}_0$:

$$\begin{aligned} -\mathbb{C}_0 : \boldsymbol{\varepsilon} + \mathbb{C}_0 : \boldsymbol{\nabla}^s \boldsymbol{u} &= \mathbf{0} \\ \boldsymbol{\nabla} \cdot [\mathbb{C}_0 : (\boldsymbol{\varepsilon} - \boldsymbol{\varepsilon}_p)] + \boldsymbol{f} &= \mathbf{0} \end{aligned} \tag{3.7}$$

provides a symmetric system only in the case of elasticity ($\boldsymbol{\varepsilon}_p = 0$). In fact, in the case of plasticity, the functional dependence of the plastic strains with respect to the field variables provide an asymmetric set of equations. Instead, considering the constitutive secant matrix $\mathbb{C}$ defined as:

$$\mathbb{C} : \boldsymbol{\varepsilon} = \mathbb{C}_0 : (\boldsymbol{\varepsilon} - \boldsymbol{\varepsilon}_p) \tag{3.8}$$

it is possible to write the system of equations in (3.7) as

$$\begin{aligned} -\mathbb{C} : \boldsymbol{\varepsilon} + \mathbb{C} : \boldsymbol{\nabla}^s \boldsymbol{u} &= \mathbf{0} \\ \boldsymbol{\nabla} \cdot [\mathbb{C} : \varepsilon] + \boldsymbol{f} &= \mathbf{0} \end{aligned} \tag{3.9}$$

Hence, (3.9) is the final system of partial differential equations in strong form in terms of the total strains $\boldsymbol{\varepsilon}$ and displacements $\boldsymbol{u}$ for the mechanical problem involving plasticity. In general, the secant matrix in (3.8) is not uniquely defined. Nevertheless, it can be easily built as:

$$\mathbb{C} = \mathbb{C}_0 - \frac{[\mathbb{C}_0 : \boldsymbol{\varepsilon}_p] \otimes [\mathbb{C}_0 : \boldsymbol{\varepsilon}_p]}{\boldsymbol{\varepsilon} : \mathbb{C}_0 : \boldsymbol{\varepsilon}_p} \tag{3.10}$$

Alternatively, in plasticity, the constitutive equation is expressed in rate form:

$$\dot{\boldsymbol{\sigma}} = \mathbb{C}_{ep} : \dot{\boldsymbol{\varepsilon}} \tag{3.11}$$

being $\mathbb{C}_{ep}$ the elasto-plastic constitutive tensor and $\dot{(\cdot)}$ the time derivative operator. The rate form of expression (3.6) becomes:

$$\begin{aligned} -\mathbb{C}_{ep} : \dot{\boldsymbol{\varepsilon}} + \mathbb{C}_{ep} : \boldsymbol{\nabla}^s \dot{\boldsymbol{u}} = \mathbf{0} \\ \boldsymbol{\nabla} \cdot [\mathbb{C}_{ep} : \dot{\boldsymbol{\varepsilon}}] + \dot{\boldsymbol{f}} = \mathbf{0} \end{aligned} \tag{3.12}$$

where $\dot{\boldsymbol{f}}$ is the rate counterpart of the volumetric external load $\boldsymbol{f}$.

Recalling the initial set of equations, it is possible to introduce the constitutive expression (3.5) in the compatibility one (3.2). Then, the strong form is expressed in terms of stresses $\boldsymbol{\sigma}$ and displacements $\boldsymbol{u}$ and it reads:

$$\begin{aligned} -\mathbb{C}_0^{-1} : \boldsymbol{\sigma} + \boldsymbol{\nabla}^s \boldsymbol{u} - \boldsymbol{\varepsilon}_p = \mathbf{0} \\ \boldsymbol{\nabla} \cdot \boldsymbol{\sigma} + \boldsymbol{f} = \mathbf{0} \end{aligned} \tag{3.13}$$

Similarly to the $\boldsymbol{\varepsilon} - \boldsymbol{u}$ case, the functional dependence of the plastic strains from the field variables makes the the final strong form of the mixed mechanical problem not symmetric.

Expressions (3.6), (3.7), (3.9) and (3.12) represent alternative of the mixed formulation in terms of total strains and displacement, whereas (3.13) is written in terms of the stresses an displacements. In this work, the mixed problem in the unknown fields $[\boldsymbol{\varepsilon}, \boldsymbol{u}]$ is used, starting from the strong form in equation (3.9), along with appropriate boundary conditions and evolution laws for the plastic strain field [223].

3.2 Weak form

Let us consider a set of test functions $\boldsymbol{\gamma} \in \mathbb{G}$ for the symmetric tensor field of strains and $\boldsymbol{v} \in \mathbb{V}$ for the vector field of displacements. Weighting the residual of the mixed strong form and integrating over the volume of the body Ω, the continuous weak form of the set of equations presented in (3.9) reads:

$$\begin{aligned} -\int_\Omega \boldsymbol{\gamma} : \mathbb{C} : \boldsymbol{\varepsilon} + \int_\Omega \boldsymbol{\gamma} : \mathbb{C} : \boldsymbol{\nabla}^s \boldsymbol{u} = 0 \quad \forall \boldsymbol{\gamma} \in \mathbb{G} \\ \int_\Omega \boldsymbol{v} : [\boldsymbol{\nabla} \cdot (\mathbb{C} : \boldsymbol{\varepsilon})] + \int_\Omega \boldsymbol{v} : \boldsymbol{f} = 0 \qquad \forall \boldsymbol{v} \in \mathbb{V} \end{aligned} \tag{3.14}$$

Integrating by parts the second equation, it is possible to write:

$$\begin{aligned} -\int_\Omega \boldsymbol{\gamma} : \mathbb{C} : \boldsymbol{\varepsilon} + \int_\Omega \boldsymbol{\gamma} : \mathbb{C} : \boldsymbol{\nabla}^s \boldsymbol{u} = 0 \quad & \forall \boldsymbol{\gamma} \in \mathbb{G} \\ \int_\Omega \boldsymbol{\nabla}^s v : \mathbb{C} : \boldsymbol{\varepsilon} = F(\boldsymbol{v}) \quad & \forall \boldsymbol{v} \in \mathbb{V} \end{aligned} \tag{3.15}$$

where the tractions $\bar{\boldsymbol{t}}$ on the boundary $\partial\Omega$ and body forces $\boldsymbol{f}$ are collected in the term representing the work of external forces

$$F(\boldsymbol{v}) = \int_{\partial\Omega} \boldsymbol{v} : \bar{\boldsymbol{t}} + \int_\Omega \boldsymbol{v} : \boldsymbol{f} \tag{3.16}$$

From the mathematical requirements of the problem in (3.15), $\mathbb{V}$ is in the space of square integrable functions $\boldsymbol{v}$ which are at least square integrable and have square integrable first derivative, that is $\mathbb{V} \subseteq \boldsymbol{H}^1(\Omega)^{\dim}$, whereas $\mathbb{G}$ belongs to the set of square integrable symmetric tensors $\boldsymbol{\gamma}$, that is $\mathbb{G} \subseteq \boldsymbol{L}^2(\Omega)^{\dim\times\dim}_{\text{sym}}$, where dim is the number of the dimensions of the domain of the problem.

Note that the weak form in expression (3.15) is symmetric and it can be derived from the Hellinger-Reissner principle. The functional Π_{HR} is written in terms of displacement $\boldsymbol{u}$ and stress $\boldsymbol{\sigma}$ variables and it reads:

$$\Pi_{HR} = \int_\Omega \left[\boldsymbol{\sigma} : (\boldsymbol{\nabla}^s \boldsymbol{u} - \boldsymbol{\varepsilon}_p) - \frac{1}{2} \boldsymbol{\sigma} : \mathbb{C}_0^{-1} : \boldsymbol{\sigma} - \boldsymbol{f} \cdot \boldsymbol{u} \right] - \int_{\partial\Omega} \boldsymbol{t} \cdot \boldsymbol{u} \tag{3.17}$$

The variation of this expression reads:

$$\delta\Pi_{HR} = \int_\Omega \left[\delta\boldsymbol{\sigma} : (\boldsymbol{\nabla}^s \boldsymbol{u} - \boldsymbol{\varepsilon}_p) + \boldsymbol{\sigma} : \delta\boldsymbol{\nabla}^s \boldsymbol{u} - \boldsymbol{\sigma} : \mathbb{C}_0^{-1} : \delta\boldsymbol{\sigma} - \boldsymbol{f} \cdot \delta\boldsymbol{u} \right] - \int_{\partial\Omega} \boldsymbol{t} \cdot \delta\boldsymbol{u} \tag{3.18}$$

Finally, plugging in the constitutive equation in (3.8), $\boldsymbol{\sigma} = \mathbb{C} : \boldsymbol{\varepsilon}$, and collecting the common variations, it reads:

$$\delta\Pi_{HR} = \int_\Omega \delta\boldsymbol{\varepsilon} : \mathbb{C} : (\boldsymbol{\nabla}^s \boldsymbol{u} - \boldsymbol{\varepsilon}) + \int_\Omega \delta\boldsymbol{\nabla}^s \boldsymbol{u} : \mathbb{C} : \boldsymbol{\varepsilon} - \int_\Omega \boldsymbol{f} \cdot \delta\boldsymbol{u} - \int_{\delta\Omega} \bar{\boldsymbol{t}} \cdot \delta\boldsymbol{u} \tag{3.19}$$

Hence, if the condition $\delta\Pi_{HR} = 0$ is enforced, this correspond exactly to the weak form presented in (3.15), with $\delta\boldsymbol{u} = \boldsymbol{v}$ and $\delta\boldsymbol{\varepsilon} = \boldsymbol{\gamma}$. A further extension of the Hellinger-Reissner principle which takes into accounts the variational foundation of plasticity and the inclusion of dissipation in the total free energy is presented in Simo and Hughes [223].

3.3 Discrete Galerkin formulation

The discretized version of the continuous weak form is obtained considering a finite set of interpolating functions for both the solution and the test function. For this reason the discrete functional spaces are a subset of their continuous version:

$$\mathbb{G}_h \subset \mathbb{G} \text{ and } \mathbb{V}_h \subset \mathbb{V} \tag{3.20}$$

Now, the strain tensor $\boldsymbol{\varepsilon}$ and the displacement field $\boldsymbol{u}$ are approximated as

$$\begin{aligned} \boldsymbol{\varepsilon} \to \boldsymbol{\varepsilon}_h &= \sum_{i=1}^{n_{pts}} \boldsymbol{\gamma}_h^{(i)} \boldsymbol{\varepsilon}_h^{(i)} \quad \boldsymbol{\gamma}_h \in \mathbb{G}_h \\ \boldsymbol{u} \to \boldsymbol{u}_h &= \sum_{i=1}^{n_{pts}} \boldsymbol{v}_h^{(i)} \boldsymbol{u}_h^{(i)} \quad \boldsymbol{v}_h \in \mathbb{V}_h \end{aligned} \tag{3.21}$$

The system of equations (3.15), in its discrete form, reads

$$\begin{aligned} &- \int_\Omega \boldsymbol{\gamma}_h : \mathbb{C} : \boldsymbol{\varepsilon}_h + \int_\Omega \boldsymbol{\gamma}_h : \mathbb{C} : \boldsymbol{\nabla}^s \boldsymbol{u}_h = 0 \quad \forall \boldsymbol{\gamma}_h \in \mathbb{G}_h \\ &\int_\Omega \boldsymbol{\nabla}^s \boldsymbol{v}_h : \mathbb{C} : \boldsymbol{\varepsilon}_h = F(\boldsymbol{v}_h) \quad \forall \boldsymbol{v}_h \in \mathbb{V}_h \end{aligned} \tag{3.22}$$

In the following, equal interpolation finite element spaces for displacements and strains is considered. Particularly interesting is the case of low order linear-linear (P1P1) triangular and bilinear-bilinear (Q1Q1) quadrilateral elements.

From the work of Ladyzhenskaya [185], Babuška [186] and Brezzi [187], it is well known that the *Inf-Sup* condition restricts severely the choice of solution spaces in a mixed problem. Indeed, an identical interpolation of $\mathbb{G}_h$ and $\mathbb{V}_h$ spaces does not provide the required numerical stability, which manifests in spurious oscillations in the unknowns. Consequently, a stabilization procedure is now introduced.

3.4 Variational Multiscale Stabilization

In order to stabilize the set of equations of the mixed problem, it is required to perform a modification of the discrete variational form, while maintaining consistency. Hence, providing the necessary numerical stability, the *Inf-Sup condition* is circumvented and the initial problem can be successfully resolved.

The Variational Multiscale Stabilization (VMS) was developed in first instance by Hughes et al. [200] and then generalized by Codina [16]. This technique assumes that the solution of the unknowns variables $\boldsymbol{\varepsilon}, \boldsymbol{u}$ is composed of two contributions. The first one is provided by the resolvable scale at the FEM mesh level, which gives $\boldsymbol{\varepsilon}_h, \boldsymbol{u}_h$. The second one is represented by a smaller scale, which cannot be computed on the FEM mesh. It is called subscale solution and it is denoted as $\tilde{\boldsymbol{\varepsilon}}, \tilde{\boldsymbol{u}}$. This

contribution can be thought as a high frequency solution that cannot be captured with the coarse FEM mesh. The Variational Multiscale Stabilization assumes that the solution fields are given by the sum of resolvable and irresolvable scales:

$$\begin{aligned} \boldsymbol{\varepsilon} &= \boldsymbol{\varepsilon}_h + \tilde{\boldsymbol{\varepsilon}} \\ \boldsymbol{u} &= \boldsymbol{u}_h + \tilde{\boldsymbol{u}} \end{aligned} \tag{3.23}$$

The subscale variables (and, later, their test functions) pertain to their respective functional spaces $\tilde{\mathbb{G}}$ for the strain tensor and $\tilde{\mathbb{V}}$ for the displacement vector. This hypothesis allows to effectively solve the unknowns in the extended solution spaces given by $\mathbb{G} \approx \mathbb{G}_h \oplus \tilde{\mathbb{G}}$ and $\mathbb{V} \approx \mathbb{V}_h \oplus \tilde{\mathbb{V}}$. Then, in the case of low order elements, the subscale variables are interpolated with continuous piecewise functions. Nevertheless, their contribution on the boundary $\partial\Omega$ is considered null, i.e. imposed displacements or external forces are exactly represented by the finite element space. In the eventuality that additional boundary terms appear, further contributions should be considered as in Badia and Codina [204], Codina et al. [224].

The plastic strains $\boldsymbol{\varepsilon}_p$ are computed by the return mapping algorithm, given the stress tensor $\boldsymbol{\sigma}$ as input data. In turn, $\boldsymbol{\sigma}$ is computed using the field variables, and, in particular, the total strain. Since $\boldsymbol{\varepsilon}$ presents both coarse and subscale contribution, then the plastic strain tensor $\boldsymbol{\varepsilon}_p$ could posses a corresponding subscale part. However, since the subscale contribution is assumed to be small, it is reasonable to assume that the plastic strain depends only on the finite element solution counterpart and, consequently, it does not posses a subscale:

$$\boldsymbol{\varepsilon}_p = \boldsymbol{\varepsilon}_p(\boldsymbol{\sigma}) \approx \boldsymbol{\varepsilon}_p(\boldsymbol{\sigma}_h) \tag{3.24}$$

with

$$\boldsymbol{\sigma}_h = \mathbb{C}_0 : [\boldsymbol{\varepsilon}_h - \boldsymbol{\varepsilon}_p(\boldsymbol{\sigma}_h)] = \mathbb{C} : \boldsymbol{\varepsilon}_h \tag{3.25}$$

Within this enhanced functional setting, the set of equations are split in the coarse and fine scales and they reads:

$$\begin{aligned} -\int_\Omega \boldsymbol{\gamma}_h : \mathbb{C} : (\boldsymbol{\varepsilon}_h + \tilde{\boldsymbol{\varepsilon}}) + \int_\Omega \boldsymbol{\gamma}_h : \mathbb{C} : \boldsymbol{\nabla}^s (\boldsymbol{u}_h + \tilde{\boldsymbol{u}}) &= 0 && \forall \boldsymbol{\gamma}_h \in \mathbb{G}_h \\ \int_\Omega \boldsymbol{\nabla}^s \boldsymbol{v}_h : [\mathbb{C} : (\boldsymbol{\varepsilon}_h + \tilde{\boldsymbol{\varepsilon}})] &= F(\boldsymbol{v}_h) && \forall \boldsymbol{v}_h \in \mathbb{V}_h \\ -\int_\Omega \tilde{\boldsymbol{\gamma}} : \mathbb{C} : (\boldsymbol{\varepsilon}_h + \tilde{\boldsymbol{\varepsilon}}) + \int_\Omega \tilde{\boldsymbol{\gamma}} : \mathbb{C} : \boldsymbol{\nabla}^s (\boldsymbol{u}_h + \tilde{\boldsymbol{u}}) &= 0 && \forall \tilde{\boldsymbol{\gamma}} \in \tilde{\mathbb{G}} \\ \int_\Omega \tilde{\boldsymbol{v}} : (\boldsymbol{\nabla} \cdot [\mathbb{C} : (\boldsymbol{\varepsilon}_h + \tilde{\boldsymbol{\varepsilon}})]) + \int_\Omega \tilde{\boldsymbol{v}} : \boldsymbol{f} &= 0 && \forall \tilde{\boldsymbol{v}} \in \tilde{\mathbb{V}} \end{aligned} \tag{3.26}$$

Owing to the fact that the subscale unknowns $(\tilde{\boldsymbol{\varepsilon}}, \tilde{\boldsymbol{u}})$ vanish on the boundary, it

follows that the second two equations are arranged as

$$\begin{aligned} -\int_\Omega \tilde{\boldsymbol{\gamma}} : \mathbb{C} : [\tilde{\boldsymbol{\varepsilon}} - \boldsymbol{\nabla}^s \tilde{\boldsymbol{u}}] &= \int_\Omega \tilde{\boldsymbol{\gamma}} : \mathbb{C} : [\boldsymbol{\varepsilon}_h - \boldsymbol{\nabla}^s \boldsymbol{u}_h] \quad \tilde{\boldsymbol{\gamma}} \in \tilde{\mathbb{G}} \\ \int_\Omega \boldsymbol{\nabla}^s \tilde{\boldsymbol{v}} : \mathbb{C} : \tilde{\boldsymbol{\varepsilon}} &= -\int_\Omega \tilde{\boldsymbol{v}} : [\boldsymbol{\nabla} \cdot (\mathbb{C} : \boldsymbol{\varepsilon}_h) + \boldsymbol{f}] \quad \tilde{\boldsymbol{v}} \in \tilde{\mathbb{V}} \end{aligned} \tag{3.27}$$

The last system of equations shows that the solution of the subscale variables depends on the residuals of the strong form of the problem upon substitution of the FEM solution. In particular, it is possible to see that the differential form is applied both to the coarse scale (right hand part) and the fine scale (left hand part). Defining the (FE scale) residuals of compatibility and equilibrium in their strong form as $\boldsymbol{R}_{1,h}$ and $\boldsymbol{R}_{2,h}$ respectively:

$$\begin{aligned} \boldsymbol{R}_{1,h} &= -\mathbb{C} : \boldsymbol{\varepsilon}_h + \mathbb{C} : \boldsymbol{\nabla}^s \boldsymbol{u}_h \\ \boldsymbol{R}_{2,h} &= \boldsymbol{\nabla} \cdot (\mathbb{C} : \boldsymbol{\varepsilon}_h) + \boldsymbol{f} \end{aligned} \tag{3.28}$$

equations (3.27) represent the projection through the operators $\tilde{P}_1$ and $\tilde{P}_2$ of the residuals on the subscale grid. They can be rewritten as:

$$\begin{aligned} \tilde{P}_1 \left(-\mathbb{C} : \tilde{\boldsymbol{\varepsilon}} + \mathbb{C} : \boldsymbol{\nabla}^s \tilde{\boldsymbol{u}}\right) &= \tilde{P}_1 \left(\mathbb{C} : \boldsymbol{\varepsilon}_h - \mathbb{C} : \boldsymbol{\nabla}^s \boldsymbol{u}_h\right) = -\tilde{P}_1 \left(\boldsymbol{R}_{1,h}\right) \\ \tilde{P}_2 \left(\boldsymbol{\nabla}^s \tilde{\boldsymbol{v}} : \mathbb{C} : \tilde{\boldsymbol{\varepsilon}}\right) &= -\tilde{P}_2 \left(\boldsymbol{\nabla} \cdot (\mathbb{C} : \boldsymbol{\varepsilon}_h) + \boldsymbol{f}\right) = -\tilde{P}_2 \left(\boldsymbol{R}_{2,h}\right) \end{aligned} \tag{3.29}$$

In order to determine the value of the subscale variables, it is required to solve the equivalence of projections. Codina [16] shows that the subscale cannot be resolved exactly but it has to be approximated. In turn, this implies that the projection operator has to be chosen. By linear Fourier analysis, it follows that it is possible to approximate the subscale variables within each element as:

$$\begin{aligned} \tilde{\boldsymbol{\varepsilon}} &= \tau_\varepsilon \, \mathbb{C}^{-1} : \tilde{P}_1 \left(\boldsymbol{R}_{1,h}\right) \\ \tilde{\boldsymbol{u}} &= \tau_u \, \tilde{P}_2 \left(\boldsymbol{R}_{2,h}\right) \end{aligned} \tag{3.30}$$

where τ_u and τ_ε are the stabilization parameters. From dimensional considerations, they are computed for the problem in analysis as:

$$\tau_u = c_u \frac{h L_0}{\mu_0} \quad \text{and} \quad \tau_\varepsilon = c_\varepsilon \frac{h}{L_0} \tag{3.31}$$

In the last expressions, c_u and c_ε are arbitrary positive numbers, h is the representative size of the finite element mesh and L_0 is a characteristic length of the problem. Finally, μ_0 is a mechanical parameter of the elastic problem, usually chosen as twice the shear modulus of the material G or Young's modulus E.

The stabilization contribution is then given by residuals $\boldsymbol{R}_{1,h}$ and $\boldsymbol{R}_{2,h}$ computed in an element by element manner. In the case of low order elements, the subscale is piecewise linear and interelemental discontinuous. However, it is not possible to condense its contribution at the element level since the field variable $\boldsymbol{\varepsilon}_h$ and $\boldsymbol{u}_h$ are continuous.

Upon mesh refinement, the coarse scale becomes finer and the contribution of the residuals reduces. For that reason it is reasonable to say that the subscale variables $[\tilde{\boldsymbol{\varepsilon}}, \tilde{\boldsymbol{u}}]$ are smaller than their coarse scale counterpart $[\boldsymbol{\varepsilon}_h, \boldsymbol{u}_h]$. Consequently, owing to the fact that the plastic strain $\boldsymbol{\varepsilon}_p$ is clearly smaller than total strain $\boldsymbol{\varepsilon}$ and that residual-based subscale vanishes upon convergence, the assumption of negligible plastic strain subscale $\tilde{\boldsymbol{\varepsilon}}_p$ holds.

To complete the stabilization method, an appropriate projection operator has to be selected in order to be able to compute explicitly the subscale variables and, hence, avoiding calculating the last two equations of system (3.26).

Algebraic Subgrid Scale Stabilization (ASGS)

In the Algebraic Subgrid Scale Stabilization method [204], the projection operator is taken as the identity, that is:

$$\tilde{P} = I \quad \Rightarrow \quad \begin{aligned} \tilde{\boldsymbol{\varepsilon}} &= \tau_{\varepsilon} \left(-\boldsymbol{\varepsilon}_h + \boldsymbol{\nabla}^s \boldsymbol{u}_h \right) \\ \tilde{\boldsymbol{u}} &= \tau_u \left(\boldsymbol{\nabla} \cdot \boldsymbol{\sigma}_h + \boldsymbol{f} \right) \end{aligned} \tag{3.32}$$

Back-substituting in the system of equations tested against the finite element functions and rearranging:

$$\begin{aligned} &- (1 - \tau_{\varepsilon}) \int_{\Omega} \boldsymbol{\gamma}_h : \mathbb{C} : \boldsymbol{\varepsilon}_h + (1 - \tau_{\varepsilon}) \int_{\Omega} \boldsymbol{\gamma}_h : \mathbb{C} : \boldsymbol{\nabla}^s \boldsymbol{u}_h \\ &\qquad + \tau_u \int_{\Omega} \boldsymbol{\gamma}_h : \mathbb{C} : \boldsymbol{\nabla}^s \left(\boldsymbol{\nabla} \cdot \boldsymbol{\sigma}_h + \boldsymbol{f} \right) = 0 \quad \forall \boldsymbol{\gamma}_h \in \mathbb{G}_h \\ &\int_{\Omega} \boldsymbol{\nabla}^s \boldsymbol{v}_h : \left[\mathbb{C} : \left(\left(1 - \tau_{\varepsilon} \right) \boldsymbol{\varepsilon}_h + \tau_{\varepsilon} \boldsymbol{\nabla}^s \boldsymbol{u}_h \right) \right] = F(\boldsymbol{v}_h) \quad \forall \boldsymbol{v}_h \in \mathbb{V}_h \end{aligned} \tag{3.33}$$

Now, integrating again by parts in the first equation and taking $\boldsymbol{\gamma}_h = 0$ on $\partial\Omega$, the final system of equations reads:

$$\begin{aligned} &- (1 - \tau_{\varepsilon}) \int_{\Omega} \boldsymbol{\gamma}_h : \mathbb{C} : \left(\boldsymbol{\varepsilon}_h - \boldsymbol{\nabla}^s \boldsymbol{u}_h \right) \\ &\qquad - \tau_u \int_{\Omega} \left[\boldsymbol{\nabla} \cdot \left(\mathbb{C} : \boldsymbol{\gamma}_h \right) \right] \cdot \left[\boldsymbol{\nabla} \cdot \boldsymbol{\sigma}_h + f \right] = 0 \quad \forall \boldsymbol{\gamma}_h \in \mathbb{G}_h \\ &\int_{\Omega} \boldsymbol{\nabla}^s \boldsymbol{v}_h : \mathbb{C} : \left[\left(1 - \tau_{\varepsilon} \right) \boldsymbol{\varepsilon}_h + \tau_{\varepsilon} \boldsymbol{\nabla}^s \boldsymbol{u}_h \right] = F(v_h) \quad \forall v_h \in \mathbb{V}_h \end{aligned} \tag{3.34}$$

The first term in the first equation represents a projection (or smoothing) of the discontinuous strain given by the discrete displacement field over the continuous nodal strain field. The second additional term is given by the displacement subscale which has a crucial role in the stabilization of problems involving incompressibility. This contribution depends on the residual of the strong form of the equilibrium equation. The second equation is related to the balance of momentum. Defining the stabilized total strain field as:

$$\boldsymbol{\varepsilon}_{stab,h} = (1 - \tau_{\varepsilon})\, \boldsymbol{\varepsilon}_h + \tau_{\varepsilon} \boldsymbol{\nabla}^s \boldsymbol{u}_h \tag{3.35}$$

as a blending of the continuous and discontinuous strain fields through the stabilization parameter τ_{ε}, the system of equations (3.36) reads:

$$\begin{aligned} &-(1 - \tau_{\varepsilon}) \int_{\Omega} \boldsymbol{\gamma}_h : \mathbb{C} : (\boldsymbol{\varepsilon}_h - \boldsymbol{\nabla}^s \boldsymbol{u}_h) \\ &\qquad -\tau_u \int_{\Omega} [\boldsymbol{\nabla} \cdot (\mathbb{C} : \boldsymbol{\gamma}_h)] \cdot [\boldsymbol{\nabla} \cdot \boldsymbol{\sigma}_h + \boldsymbol{f}] = \mathbf{0} \quad \forall \boldsymbol{\gamma}_h \in \mathbb{G}_h \\ &\int_{\Omega} \boldsymbol{\nabla}^s \boldsymbol{v}_h : \mathbb{C} : \boldsymbol{\varepsilon}_{stab,h} = F(\boldsymbol{v}_h) \quad \forall \boldsymbol{v}_h \in \mathbb{V}_h \end{aligned} \tag{3.36}$$

Orthogonal Subgrid Stabilization Scale (OSGS)

In the Orthogonal Subgrid Scale Stabilization [204], the projection operator selected to solve the unresolvable scale variables is the orthogonal projector

$$\tilde{P}_h^{\perp}(\boldsymbol{X}) = I(\boldsymbol{X}) - P_h(\boldsymbol{X}) \tag{3.37}$$

where P_h represents the projection over the finite element mesh. It represents the L^2 projection of a generic variable $\boldsymbol{X}$, or *least square fitting*, on the finite element space [1]. It is performed taking advantage of the orthogonality condition

$$\int_{\Omega} (\boldsymbol{X}_{\Pi} - \boldsymbol{X}) : \eta_h = 0 \quad \forall \eta_h \in \mathbb{V}_h \text{ or } \mathbb{G}_h \tag{3.38}$$

where $\boldsymbol{X}_{\Pi}$ is the projected value of $\boldsymbol{X}$ on the mesh nodes. In practice, the stabilization given by the OSGS method adds a contribution that is located in a space which is orthogonal to the FE one. Both ASGS and OSGS are residual based methods which disappear when the discrete solution is converged. However, the orthogonality between spaces of the latter method ensures less numerical dissipation in the calculation and maximizes accuracy for a given mesh.

Substituting in (3.30), the subscale variables $\tilde{\boldsymbol{u}}$ and $\tilde{\boldsymbol{\varepsilon}}$ can be approximated as:

$$\begin{aligned}\tilde{\boldsymbol{\varepsilon}} &= \tau_{\boldsymbol{\varepsilon}}\, \mathbb{C}^{-1} : [\boldsymbol{R}_{1,h} - P_h\left(\boldsymbol{R}_{1,h}\right)] \\ \tilde{\boldsymbol{u}} &= \tau_{\boldsymbol{u}}\ [\boldsymbol{R}_{2,h} - P_h\left(\boldsymbol{R}_{2,h}\right)]\end{aligned} \tag{3.39}$$

with the residuals $\boldsymbol{R}_{1,h}, \boldsymbol{R}_{2,h}$ defined in (3.28). First of all, as the nodal projection of a nodal variable is an identity operation i.e. $P_h\left(\boldsymbol{\varepsilon}_h\right) = \boldsymbol{\varepsilon}_h$, the strain subscale is given by

$$\tilde{\boldsymbol{\varepsilon}} = \tau_{\boldsymbol{\varepsilon}}\left[(-\boldsymbol{\varepsilon}_h + \boldsymbol{\nabla}^s \boldsymbol{u}_h) - P_h\left(-\boldsymbol{\varepsilon}_h + \boldsymbol{\nabla}^s \boldsymbol{u}_h\right)\right] = \tau_{\boldsymbol{\varepsilon}}\left[\boldsymbol{\nabla}^s \boldsymbol{u}_h - P_h\left(\boldsymbol{\nabla}^s \boldsymbol{u}_h\right)\right] \tag{3.40}$$

Now, comparing the equations (3.22) and (3.38), the weighted projection of the discontinuous strains over the finite element mesh corresponds to the nodal continuous strain field:

$$\int_\Omega \boldsymbol{\gamma}_h : \mathbb{C} : P_h\left(\boldsymbol{\nabla}^s \boldsymbol{u}_h\right) = \int_\Omega \boldsymbol{\gamma}_h : \mathbb{C} : \boldsymbol{\varepsilon}_h \tag{3.41}$$

For the displacement subscale, assuming that the body force $\boldsymbol{f}$ pertains to the FE space i.e. $P_h\left(\boldsymbol{f}\right) = \boldsymbol{f}$, it can be written:

$$\tilde{\boldsymbol{u}} = \tau_u\left[\boldsymbol{\nabla} \cdot \boldsymbol{\sigma}_h - P_h\left(\boldsymbol{\nabla} \cdot \boldsymbol{\sigma}_h\right)\right] \tag{3.42}$$

Back-substituting in the set of equations of the problem, it reads:

$$\begin{aligned}&-\left(1-\tau_{\boldsymbol{\varepsilon}}\right)\int_\Omega \boldsymbol{\gamma}_h : \mathbb{C} : \left(\boldsymbol{\varepsilon}_h - \boldsymbol{\nabla}^s \boldsymbol{u}_h\right) + \\ &\qquad +\tau_u \int_\Omega \boldsymbol{\gamma}_h : \mathbb{C} : \nabla^s\left[\boldsymbol{\nabla} \cdot \boldsymbol{\sigma}_h - P_h\left(\boldsymbol{\nabla} \cdot \boldsymbol{\sigma}_h\right)\right] = \boldsymbol{0} \quad \forall \boldsymbol{\gamma}_h \in \mathbb{G}_h \\ &\int_\Omega \boldsymbol{\nabla}^s \boldsymbol{v}_h : \mathbb{C} : \left[\left(1-\tau_{\boldsymbol{\varepsilon}}\right)\boldsymbol{\varepsilon}_h + \tau_{\boldsymbol{\varepsilon}} \boldsymbol{\nabla}^s \boldsymbol{u}_h\right] = F(\boldsymbol{v}_h) \quad \forall \boldsymbol{v}_h \in \mathbb{V}_h\end{aligned} \tag{3.43}$$

Integrating by parts the second equation and rearranging, the final set of equations is:

$$\begin{aligned}&-\left(1-\tau_{\boldsymbol{\varepsilon}}\right)\int_\Omega \boldsymbol{\gamma}_h : \mathbb{C} : \left(\boldsymbol{\varepsilon}_h - \boldsymbol{\nabla}^s \boldsymbol{u}_h\right) + \\ &\qquad -\tau_u \int_\Omega \left[\boldsymbol{\nabla} \cdot \left(\mathbb{C} : \boldsymbol{\gamma}_h\right)\right] \cdot \left[\boldsymbol{\nabla} \cdot \boldsymbol{\sigma}_h - P_h\left(\boldsymbol{\nabla} \cdot \boldsymbol{\sigma}_h\right)\right] = \boldsymbol{0} \quad \forall \boldsymbol{\gamma}_h \in \mathbb{G}_h \\ &\int_\Omega \boldsymbol{\nabla}^s \boldsymbol{v}_h : \mathbb{C} : \boldsymbol{\varepsilon}_{stab,h} = F(\boldsymbol{v}_h) \quad \forall \boldsymbol{v}_h \in \mathbb{V}_h\end{aligned} \tag{3.44}$$

The set of equations with OSGS stabilization resembles the one for the ASGS, except for the second term in the first equation. In order to compute the projection of stresses $\boldsymbol{\Pi}_{\boldsymbol{\sigma}}$ at each time step, we can recall expression (3.38), and write

$$\int_\Omega \left(\boldsymbol{\Pi}_{\boldsymbol{\sigma}} - \boldsymbol{\nabla} \cdot \boldsymbol{\sigma}_h\right) : \boldsymbol{\eta}_h = 0 \quad \forall \boldsymbol{\eta}_h \in \mathbb{G}_h \tag{3.45}$$

and, with the additional projection equation, it reads:

$$\begin{aligned} &-(1-\tau_{\boldsymbol{\varepsilon}})\int_\Omega \boldsymbol{\gamma}_h : \mathbb{C} : (\boldsymbol{\varepsilon}_h - \boldsymbol{\nabla}^s \boldsymbol{u}_h) \\ &\qquad -\tau_u \int_\Omega [\boldsymbol{\nabla}\cdot(\mathbb{C}:\boldsymbol{\gamma}_h)]\cdot[\boldsymbol{\nabla}\cdot\boldsymbol{\sigma}_h - \boldsymbol{\Pi}_{\boldsymbol{\sigma}}] = \mathbf{0} \quad \forall \boldsymbol{\gamma}_h \in \mathbb{G}_h \\ &\int_\Omega \boldsymbol{\nabla}^s \boldsymbol{v}_h : \mathbb{C} : \boldsymbol{\varepsilon}_{stab,h} = F(\boldsymbol{v}_h) \quad \forall \boldsymbol{v}_h \in \mathbb{V}_h \\ &\int_\Omega (\boldsymbol{\Pi}_{\boldsymbol{\sigma}} - \boldsymbol{\nabla}\cdot\boldsymbol{\sigma}_h) : \boldsymbol{\eta}_h = 0 \quad \forall \boldsymbol{\eta}_h \in \mathbb{G}_h \end{aligned} \tag{3.46}$$

As commented before, the OSGS scheme is less diffusive than the ASGS scheme [202]. However, this comes at the price of solving an additional equation: in the implementation details it is shown how this problem can be circumvented.

3.5 Modified OSGS

The ASGS and OSGS formulations are stable and display optimal order of convergence in space for smooth solutions. However, when dealing with problems in which the solution presents strong gradients, such as the localization problem, a simplified stabilization technique can be devised.

In the first expression of (3.46), the nodal stress $\boldsymbol{\sigma}_h$ and its orthogonal projection are used to provide the displacement subscale term. If $\mathrm{dev}\,(\boldsymbol{\sigma}_h)$ and $\mathrm{vol}\,(\boldsymbol{\sigma}_h) = \frac{1}{3}\mathrm{tr}\,(\boldsymbol{\sigma}_h)$ are respectively the deviatoric and the volumetric part of the stress $\boldsymbol{\sigma}_h$, the stabilization contribution can be written as:

$$\begin{aligned} &\int_\Omega [\boldsymbol{\nabla}\cdot(\mathbb{C}:\boldsymbol{\gamma}_h)]\cdot\left[\boldsymbol{\nabla}\cdot\left(\mathrm{dev}\tilde{P}^{\perp}(\boldsymbol{\sigma}_h) + \mathrm{vol}\tilde{P}^{\perp}(\boldsymbol{\sigma}_h)\right)\right] = \\ &\qquad \int_\Omega [\boldsymbol{\nabla}\cdot(\mathbb{C}:\boldsymbol{\gamma}_h)]\cdot\left[\boldsymbol{\nabla}\cdot\mathrm{dev}\tilde{P}^{\perp}(\boldsymbol{\sigma}_h)\right] + \int_\Omega [\boldsymbol{\nabla}\cdot(\mathbb{C}:\boldsymbol{\gamma}_h)]\cdot\left[\boldsymbol{\nabla}\cdot\mathrm{vol}\tilde{P}^{\perp}(\boldsymbol{\sigma}_h)\right] \end{aligned} \tag{3.47}$$

where, as we defined before for the subscale projection operator, $P^{\perp}(\boldsymbol{\sigma}_h) = \boldsymbol{\sigma}_h - P_h(\boldsymbol{\sigma}_h)$. Taking advantage of the orthogonality between deviatoric and volumetric components of the stress and disregarding the local cross terms in the inner-products, last expression is approximated as:

$$\begin{aligned} &\int_\Omega [\boldsymbol{\nabla}\cdot(\mathbb{C}:\boldsymbol{\gamma}_h)]\cdot\left[\boldsymbol{\nabla}\cdot\mathrm{dev}\tilde{P}^{\perp}(\boldsymbol{\sigma}_h)\right] + \int_\Omega [\boldsymbol{\nabla}\cdot(\mathbb{C}:\boldsymbol{\gamma}_h)]\cdot\left[\boldsymbol{\nabla}\cdot\mathrm{vol}\tilde{P}^{\perp}(\boldsymbol{\sigma}_h)\right] \approx \\ &\int_\Omega \mathrm{dev}\,[\boldsymbol{\nabla}\cdot(\mathbb{C}:\boldsymbol{\gamma}_h)]\cdot\mathrm{dev}\left[\boldsymbol{\nabla}\cdot\tilde{P}^{\perp}(\boldsymbol{\sigma}_h)\right] + \int_\Omega \mathrm{vol}\,[\boldsymbol{\nabla}\cdot(\mathbb{C}:\boldsymbol{\gamma}_h)]\cdot\mathrm{vol}\left[\boldsymbol{\nabla}\cdot\tilde{P}^{\perp}(\boldsymbol{\sigma}_h)\right] \end{aligned} \tag{3.48}$$

This methodology is similar to the term-by-term stabilization presented in the works of Chiumenti et al. [225], for a 3-field mixed finite element formulation, and

Castillo and Codina [226], where it was used for the analysis of viscoelastic fluids. It is noteworthy to remark that this *split OSGS* is not consistent owing to the fact that substituting the continuous solution will not provide a null residual. However, the consistency error remains of optimal order in space and allows to eliminate some problematic cross terms which are not beneficial to convergence in a highly non-linear problem, as pointed out by Castillo and Codina [227].

It has been proven by numerous numerical tests that this approach is frequently more robust than the full consistent counterpart and its use requires a smaller number of projection operations, resulting in a smaller computational stencil. For example, in problems involving localization of strain in J2 plasticity, the incompressibility condition plays a major role. Consequently, a selective stabilization containing only the volumetric terms is chosen and the *split non-residual based OSGS* contribution is:

$$\begin{aligned} \frac{1}{9}\int_\Omega \left[\boldsymbol{\nabla}\mathrm{tr}\left(\mathbb{C}:\boldsymbol{\gamma}_h\right)\right]\cdot\left[\boldsymbol{\nabla}\mathrm{tr}\left(\boldsymbol{\sigma}_h\right)-P_h\left(\boldsymbol{\nabla}\mathrm{tr}\left(\boldsymbol{\sigma}_h\right)\right)\right]= \\ =\frac{1}{3}\int_\Omega \left[\left(\mathbb{C}:\boldsymbol{\nabla}^s\boldsymbol{\gamma}_h\right)\right]\cdot\left[\boldsymbol{\nabla}p_h-P_h\left(\boldsymbol{\nabla}p_h\right)\right] \end{aligned} \tag{3.49}$$

where $p_h=\frac{1}{3}\mathrm{tr}\left(\boldsymbol{\sigma}_h\right)$.

3.6 Additional local stabilization

Mechanical analysis with localization of strain is considered a non-smooth numerical problem, due to the strong gradients of displacements and/or strains that characterize the solution. The VMS method that has been presented is able to provide global stability which implies that the norm of the unknowns are bounded. However, in the vicinity of substantial variations of the field variables, there are local oscillations. In the field of computational mechanics, a discontinuity capturing technique is usually introduced with the objective of selectively provide additional numerical dissipation close to shock fronts.

Likewise, in the problem under consideration, it is possible to modify the parameters $\tau_{\boldsymbol{\varepsilon}}$ and $\tau_{\boldsymbol{u}}$ in a consistent manner, in order to locally increase the weight of the stabilization contribution. If μ_0 is an elastic mechanical parameter and μ is its secant counterpart, then the stabilization parameters in expression (3.31) read:

$$\tau_u=c_u\frac{hL_0}{\mu}\quad\text{and}\quad\tau_{\boldsymbol{\varepsilon}}=c_{\boldsymbol{\varepsilon}}\frac{h}{L_0}\frac{\mu}{\mu_0} \tag{3.50}$$

If softening is considered, with decreasing value of μ, the parameter $\tau_{\boldsymbol{\varepsilon}}$ decreases and, consequently, the blended strain tensor in (3.35) tends to the continuous nodal strain one:

$$\lim_{\tau_{\boldsymbol{\varepsilon}}\to 0}\boldsymbol{\varepsilon}_{stab,h}=\boldsymbol{\varepsilon}_h \tag{3.51}$$

Owing to the fact that this quantity is employed in the computation of the stresses, it means that a smoother field is used for the computation of the equilibrium, even in the vicinity of the localization.

At the same time, $\tau_{\boldsymbol{u}}$ increases with decreasing μ. As a consequence, the first equation in (3.36) or (3.46) shows a predominance of the displacement subscale with respect to the requirements of compatibility of strains. Again, the relative numerical importance of the discontinuous symmetric gradient of displacements is reduced in favor of a smoother solution.

3.7 Compatibility with standard $\boldsymbol{u}$ finite elements

In strong form, the mechanical problem is governed by the equilibrium equation (3.1), the compatibility equation (3.2) and the constitutive equation (3.4). Once the primal unknowns of the problem are chosen, the variational formulation, either mixed or irreducible, is written.

In the mixed $\boldsymbol{\varepsilon} - \boldsymbol{u}$ problem, presented in equation (3.22), $\boldsymbol{\varepsilon}$ and $\boldsymbol{u}$ are main variables. A dual formulation in terms of stresses $\boldsymbol{\sigma}$ and displacements $\boldsymbol{u}$ is also available from the Hellinger-Reissner variational principle in (3.17). Both of them express compatibility and equilibrium in weak form, whereas the constitutive equation is enforced strongly. Finally, selecting the element and, consequently, restricting the functional space of interpolation, the discrete FE form allows the solution of strain and the displacement fields, with $\boldsymbol{\varepsilon}_h$ and $\boldsymbol{u}_h$ as nodal degrees of freedom.

In the standard displacement-based problem, the irreducible strong form is found by substituting equation (3.2) into equation (3.4), and this into equation (3.1):

$$\boldsymbol{\nabla} \cdot [\mathbb{C} : \boldsymbol{\nabla}^s \boldsymbol{u}] + \boldsymbol{f} = 0 \tag{3.52}$$

where the displacement $\boldsymbol{u}$ is the only unknown of the problem. The corresponding variational (weak) form reads:

$$\int_\Omega \boldsymbol{\nabla}^s \boldsymbol{v} : \mathbb{C} : \boldsymbol{\nabla}^s \boldsymbol{u} = F(\boldsymbol{v}) \quad \forall \boldsymbol{v} \in \mathbb{V} \tag{3.53}$$

The irreducible discrete FE form requires solely the interpolation of the displacement field:

$$\boldsymbol{u} \to \boldsymbol{u}_h = \sum_{i=1}^{n_{pts}} \boldsymbol{v}_h^{(i)} \boldsymbol{u}_h^{(i)} \qquad \boldsymbol{v}_h \in \mathbb{V}_h \tag{3.54}$$

with $\boldsymbol{u}_h$ as the nodal degrees of freedom.

Comparing the variational form used in the mixed and the irreducible problem, it is possible to identify some key features. From a computational perspective, the $\boldsymbol{\varepsilon} - \boldsymbol{u}$ finite element presents a larger number of variables to be solved compared to the standard one. For each mesh node of a 3D problem, the vector of unknowns contains

9 scalars, 3 displacements (u_x, u_y, u_z) and 6 strains $(\varepsilon_{xx}, \varepsilon_{yy}, \varepsilon_{zz}, \varepsilon_{xy}, \varepsilon_{xz}, \varepsilon_{yz})$ of the symmetric deformation tensor, in Voigt's notation.

Nevertheless, the same linear triangle or bilinear quadrilateral element can be used to interpolate the strains and the displacements in the (stabilized) mixed elements or the displacements in the standard elements.

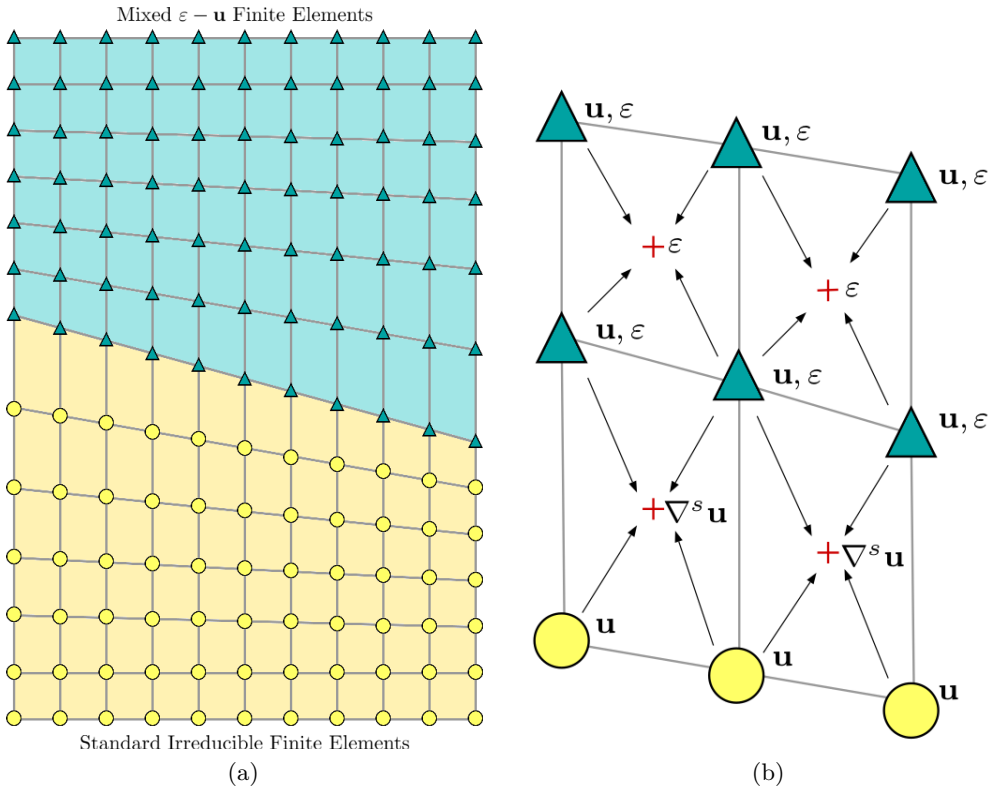

Figure 3.1: FE mesh with combined standard and mixed formulations. Turquoise color represents the mixed $\boldsymbol{\varepsilon} - \boldsymbol{u}$ elements whereas yellow represents the displacement-based ones. The strain tensor at the Gauss points (symbolized with red crosses) is computed with the interpolation of nodal strain in the mixed formulation or the discrete symmetric gradient of displacements in the irreducible one.

Yet, from the equilibrium equation in (3.36) for the ASGS method and (3.46) for the OSGS method, it is apparent that standard finite elements are a particular case of the stable mixed formulation.

On the one hand, if the same interpolation and test functions $\boldsymbol{u}_h$ are selected, the kinematics of the mixed and the irreducible formulations are compatible, i.e. the requirement of inter-elemental continuity is satisfied. A convergent numerical method must be consistent and stable. To prove consistency of the FE form in the classical Rayleigh-Ritz sense it is required to ensure continuity of the interpolation fields across the element edges. Owing to the fact that, in the elastic case, compatibility of strains and symmetric gradient of displacements holds either in weak and strong form, then nodal values of both fields are ensured to coincide at the boundary of

the elements. Therefore, a mesh constructed as in Figure 3.1, where the top part is formed by mixed $\boldsymbol{\varepsilon} - \boldsymbol{u}$ elements while the bottom part is made of standard $\boldsymbol{u}$ ones, is feasible.

Moreover, setting $\tau_{\boldsymbol{\varepsilon}} = 1$ and $\tau_{\boldsymbol{u}} = 0$ in expressions (3.36) or (3.46), the weak compatibility equation becomes an identity and the equilibrium equation reduces to (3.53).

This feature of the proposed method allows to reduce the computational burden by considering a combined standard/mixed FE mesh. Setting the stabilization parameters $\tau_{\boldsymbol{\varepsilon}} = 1$ and $\tau_{\boldsymbol{u}} = 0$ where possible and skipping the corresponding elemental computations leads to substantial savings in the total number of degrees of freedom, global operations and corresponding matrix storage.

This page is left intentionally blank.

Chapter 4

Implementation

4.1 Iterative schemes for non-linear system

In order to calculate the nodal values of strain $\boldsymbol{\varepsilon}_h$ and displacement $\boldsymbol{u}_h$ fields, the set of equations in (3.36) needs to be resolved for the ASGS method or equations in (3.46) for the OSGS method.

In the proposed formulation, an iterative procedure is introduced to take into account the non-linear evolution of the plastic strains $\boldsymbol{\varepsilon}_p$ from the stress $\boldsymbol{\sigma}_h$. The quasi-static mechanical problem is discretized in time with a Backward Euler approximation resulting in an implicit solution scheme. The Picard or Newton-Raphson methods are implemented for the numerical solution. Both methods are discussed in the following and their advantages, drawbacks and trade-offs in the context of the mixed strain-displacement finite element are highlighted.

Consider a nonlinear multidimensional problem expressed by

$$\boldsymbol{R}(\boldsymbol{X}) = \boldsymbol{P}(\boldsymbol{X}) - \boldsymbol{F} = 0 \tag{4.1}$$

In the last expression, $\boldsymbol{X} = [\boldsymbol{\varepsilon}, \boldsymbol{u}]^T$ is the solution vector of the mixed problem; $\boldsymbol{R}$, $\boldsymbol{P}$, $\boldsymbol{F}$ are respectively the residual, internal and external force vectors. For a Backward Euler approximation in time, the same expression at time step $n+1$ reads:

$$\boldsymbol{R}(\boldsymbol{X}_{n+1}) = \boldsymbol{P}(\boldsymbol{X}_{n+1}) - \boldsymbol{F}_{n+1} = 0 \tag{4.2}$$

Let the first order Taylor's approximation of $\boldsymbol{R}(\boldsymbol{X}_{n+1})$ around the solution point $\boldsymbol{X}_{n+1}$ at iteration $i+1$ be

$$\boldsymbol{R}\left(\boldsymbol{X}_{n+1}^{i+1}\right) \simeq \boldsymbol{R}\left(\boldsymbol{X}_{n+1}^{i}\right) + \boldsymbol{J}\left(\boldsymbol{X}_{n+1}^{i}\right)\left(\boldsymbol{X}_{n+1}^{i+1} - \boldsymbol{X}_{n+1}^{i}\right) = \boldsymbol{0} \tag{4.3}$$

where the Jacobian matrix is defined as

$$\boldsymbol{J}\left(\boldsymbol{X}_{n+1}^{i}\right)=\frac{\partial \boldsymbol{R}\left(\boldsymbol{X}_{n+1}^{i}\right)}{\partial \boldsymbol{X}_{n+1}^{i}} \tag{4.4}$$

The difference between the solution vector at iteration $i+1$ and i is the incremental correction:

$$\delta \boldsymbol{X}^{i+1}=\boldsymbol{X}_{n+1}^{i+1}-\boldsymbol{X}_{n+1}^{i} \tag{4.5}$$

It follows that, if the Jacobian matrix $\boldsymbol{J}\left(\boldsymbol{X}_{n+1}^{i}\right)$ is not singular, expression (4.3) can be inverted to compute:

$$\delta \boldsymbol{X}^{i+1}=-\left[\boldsymbol{J}\left(\boldsymbol{X}_{n+1}^{i}\right)\right]^{-1}\boldsymbol{R}\left(\boldsymbol{X}_{n+1}^{i}\right) \tag{4.6}$$

When the linearization is properly performed, quadratic convergence is achieved for an initial guess $\boldsymbol{X}_n$ close to the solution $\boldsymbol{X}_{n+1}$. In some problems, the Jacobian matrix is not defined or non-symmetric or too expensive to compute.

Alternatively, it is possible to solve the nonlinear algebraic problem with Picard's secant method. If the internal forces are written as:

$$\boldsymbol{P}\left(\boldsymbol{X}_{n+1}\right)=\boldsymbol{S}\left(\boldsymbol{X}_{n+1}\right)\boldsymbol{X}_{n+1} \tag{4.7}$$

where $\boldsymbol{S}\left(\boldsymbol{X}_{n+1}\right)$ is the secant matrix, the system of equations for the residual in (4.2) reads:

$$\boldsymbol{R}\left(\boldsymbol{X}_{n+1}\right)=\boldsymbol{S}\left(\boldsymbol{X}_{n+1}\right)\boldsymbol{X}_{n+1}-\boldsymbol{F}_{n+1} \tag{4.8}$$

and, consequently, the value of the iterative correction to the solution vector at iteration $i+1$ is found by inverting:

$$\boldsymbol{S}\left(\boldsymbol{X}_{n+1}^{i}\right)\delta \boldsymbol{X}^{i+1}=-\boldsymbol{R}_{n+1}^{i} \tag{4.9}$$

The secant method presents the advantage of being more robust than the Newton-Rapshon method and it does not require a consistent derivation. Although its definition may not be unique, a symmetric secant matrix may be constructed and, frequently, it is positive definite. This results in a method that shows super-linear rate of convergence.

Finally, by calculating the system matrix at the first iteration and maintaining it constant for the current step

$$\boldsymbol{J}\left(\boldsymbol{X}_{n+1}^{i}\right)=\boldsymbol{J}\left(\boldsymbol{X}_{n+1}^{1}\right)\qquad\text{or}\qquad\boldsymbol{S}\left(\boldsymbol{X}_{n+1}^{i}\right)=\boldsymbol{S}\left(\boldsymbol{X}_{n+1}^{1}\right) \tag{4.10}$$

a further gain in computational cost is feasible, but the convergence rate drops to linear for both methods.

4.2 ASGS implementation

Let us recall the relationship (3.8) for the secant constitutive tensor. Differentiating the algebraic system of nonlinear equations presented in (3.36) with respect to the total strains tensor $\boldsymbol{\varepsilon}_h$ and the displacement vector $\boldsymbol{u}_h$, it reads:

$$\boldsymbol{M}_\tau = -\left(1-\tau_{\boldsymbol{\varepsilon}}\right)\int_\Omega \boldsymbol{N}_{\boldsymbol{\varepsilon}}{}^T \mathbb{C}_0 \boldsymbol{N}_{\boldsymbol{\varepsilon}} - \tau_{\boldsymbol{u}}\int_\Omega \mathbb{C}_0\,\boldsymbol{B}\boldsymbol{B}^T\,\mathbb{C}_0\left(\mathbb{I}-\frac{\partial \boldsymbol{\varepsilon}_p}{\partial \boldsymbol{\varepsilon}_h}\right) \tag{4.11}$$

$$\boldsymbol{G}_\tau = \left(1-\tau_{\boldsymbol{\varepsilon}}\right)\int_\Omega \boldsymbol{N}_{\boldsymbol{\varepsilon}}{}^T \mathbb{C}_0 \boldsymbol{B} + \tau_{\boldsymbol{u}}\int_\Omega \mathbb{C}_0\,\boldsymbol{B}\boldsymbol{B}^T\,\mathbb{C}_0\left(\frac{\partial \boldsymbol{\varepsilon}_p}{\partial \boldsymbol{u}_h}\right) \tag{4.12}$$

$$\boldsymbol{D}_\tau = \left(1-\tau_{\boldsymbol{\varepsilon}}\right)\int_\Omega \boldsymbol{B}^T \mathbb{C}_0 \boldsymbol{N}_{\boldsymbol{u}} - \int_\Omega \boldsymbol{B}^T \mathbb{C}_0\left(\frac{\partial \boldsymbol{\varepsilon}_p}{\partial \boldsymbol{\varepsilon}_h}\right) \tag{4.13}$$

$$\boldsymbol{K}_\tau = \tau_{\boldsymbol{\varepsilon}}\int_\Omega \boldsymbol{B}^T \mathbb{C}_0 \boldsymbol{B} - \int_\Omega \boldsymbol{B}^T \mathbb{C}_0\left(\frac{\partial \boldsymbol{\varepsilon}_p}{\partial \boldsymbol{u}_h}\right) \tag{4.14}$$

which compose the Jacobian or tangent matrix:

$$\boldsymbol{J}^i_{n+1} = \left[\begin{array}{cc} \boldsymbol{M}_\tau & \boldsymbol{G}_\tau \\ \boldsymbol{D}_\tau & \boldsymbol{K}_\tau \end{array}\right]^i_{n+1} \tag{4.15}$$

In the differentiation, $\boldsymbol{N}_{\boldsymbol{\varepsilon}}$ and $\boldsymbol{N}_{\boldsymbol{u}}$ represent the matrices of shape functions respectively for the strains and the displacements whereas $\boldsymbol{B}$ is the matrix of the gradient of such shape functions. The algebraic system of equations reads:

$$\left[\begin{array}{cc} \boldsymbol{M}_\tau & \boldsymbol{G}_\tau \\ \boldsymbol{D}_\tau & \boldsymbol{K}_\tau \end{array}\right]^i_{n+1} \left[\begin{array}{c} \delta\boldsymbol{\varepsilon}_h \\ \delta\boldsymbol{u}_h \end{array}\right]^{i+1}_{n+1} = -\left[\begin{array}{c} R_{1,h} \\ R_{2,h} \end{array}\right]^i_{n+1} \tag{4.16}$$

where $(\delta\boldsymbol{\varepsilon}_h, \delta\boldsymbol{u}_h)$ are the iterative corrections for $(\boldsymbol{\varepsilon}_h, \boldsymbol{u}_h)$ in the Newton-Raphson scheme.

To complete the linearization of the system of equations, the dependence of the plastic strain from the field variables must be made explicit. Being $\boldsymbol{\varepsilon}_p$ computed starting from known trial stresses, it follows:

$$\frac{\partial \boldsymbol{\varepsilon}_p^{n+1}}{\partial \boldsymbol{\varepsilon}_h^{n+1}} = \frac{\partial \boldsymbol{\varepsilon}_p^{n+1}}{\partial \boldsymbol{\sigma}_{trial}}\,\frac{\partial \boldsymbol{\sigma}_{trial}}{\partial \boldsymbol{\varepsilon}_h^{n+1}} \tag{4.17}$$

and

$$\frac{\partial \boldsymbol{\varepsilon}_p^{n+1}}{\partial \boldsymbol{u}_h^{n+1}} = \frac{\partial \boldsymbol{\varepsilon}_p^{n+1}}{\partial \boldsymbol{\sigma}_{trial}}\,\frac{\partial \boldsymbol{\sigma}_{trial}}{\partial \boldsymbol{u}_h^{n+1}} \tag{4.18}$$

Recalling that $\boldsymbol{\sigma}_{trial}$ is computed as:

$$\boldsymbol{\sigma}_{trial} = \mathbb{C}^{n+1}\boldsymbol{\varepsilon}_h^{n+1} = \mathbb{C}_0 : \left(\boldsymbol{\varepsilon}_h^{n+1} - \boldsymbol{\varepsilon}_p^{n}\right) \tag{4.19}$$

it is possible to write the plastic strain differentiation as:

$$\frac{\partial \boldsymbol{\varepsilon}_p^{n+1}}{\partial \boldsymbol{\varepsilon}_h^{n+1}} = \frac{\partial \boldsymbol{\varepsilon}_p^{n+1}}{\partial \boldsymbol{\sigma}_{trial}} \mathbb{C}_0 \qquad \text{and} \qquad \frac{\partial \boldsymbol{\varepsilon}_p^{n+1}}{\partial \boldsymbol{u}_h^{n+1}} = \mathbf{0} \tag{4.20}$$

Recalling the definition of the tangent elasto-plastic constitutive tensor, it is demonstrated that:

$$\frac{\partial \boldsymbol{\varepsilon}_p^{n+1}}{\partial \boldsymbol{\sigma}_{trial}^{n+1}} = \mathbb{C}_0^{-1} : \left[\mathbb{C}_0 - \mathbb{C}_{ep}^{n+1}\right] : \mathbb{C}_0^{-1} \tag{4.21}$$

and, finally

$$\frac{\partial \boldsymbol{\varepsilon}_p^{n+1}}{\partial \boldsymbol{\varepsilon}_h^{n+1}} = \mathbb{C}_0^{-1} : \left[\mathbb{C}_0 - \mathbb{C}_{ep}^{n+1}\right] \tag{4.22}$$

Substituting this result in the previously computed submatrices in (4.15), the Jacobian matrix takes the following form:

$$\boldsymbol{M}_\tau = -\left(1 - \tau_{\boldsymbol{\varepsilon}}\right) \int_\Omega {\boldsymbol{N}_{\boldsymbol{\varepsilon}}}^T \mathbb{C}_0 \boldsymbol{N}_{\boldsymbol{\varepsilon}} - \tau_{\boldsymbol{u}} \int_\Omega \mathbb{C}_0 \, \boldsymbol{B}\boldsymbol{B}^T \, \mathbb{C}_{ep}^{n+1} \tag{4.23}$$

$$\boldsymbol{G}_\tau = \left(1 - \tau_{\boldsymbol{\varepsilon}}\right) \int_\Omega {\boldsymbol{N}_{\boldsymbol{\varepsilon}}}^T \mathbb{C}_0 \boldsymbol{B} \tag{4.24}$$

$$\boldsymbol{D}_\tau = \int_\Omega \boldsymbol{B}^T \left[\mathbb{C}_{ep}^{n+1} - \tau_{\boldsymbol{\varepsilon}} \mathbb{C}_0\right] \boldsymbol{N}_{\boldsymbol{u}} \tag{4.25}$$

$$\boldsymbol{K}_\tau = \tau_{\boldsymbol{\varepsilon}} \int_\Omega \boldsymbol{B}^T \mathbb{C}_0 \boldsymbol{B} \tag{4.26}$$

$\boldsymbol{M}_\tau$ is a mass-like projection matrix, $\boldsymbol{G}_\tau$ is a gradient matrix, $\boldsymbol{D}_\tau$ is a divergence matrix and $\boldsymbol{K}_\tau$ is the stiffness matrix. The subscript τ refers to the fact that those matrices incorporate stabilization terms. With the presented Jacobian matrix, the rate of convergence is quadratic but the algebraic system to be solved is not symmetric due to the dependence of the plastic strain to the total strain tensor $\boldsymbol{\varepsilon}_h^{n+1}$. With this solution scheme symmetry is restored only in the case of elasticity, for which $\mathbb{C}_{ep}^{n+1} = \mathbb{C}_0$. For the secant method, the set of equations is obtained by substituting the constitutive matrices with the ones given in (3.10). Hence, the global stiffness matrix becomes symmetric and results in

$$\boldsymbol{M}_\tau^{sym} = -\left(1 - \tau_{\boldsymbol{\varepsilon}}\right) \int_\Omega {\boldsymbol{N}_{\boldsymbol{\varepsilon}}}^T \mathbb{C}^{n+1} \boldsymbol{N}_{\boldsymbol{\varepsilon}} - \tau_{\boldsymbol{u}} \int_\Omega \mathbb{C}^{n+1} \, \boldsymbol{B}\boldsymbol{B}^T \, \mathbb{C}^{n+1} \tag{4.27}$$

$$\boldsymbol{G}_\tau^{sym} = \left(1 - \tau_{\boldsymbol{\varepsilon}}\right) \int_\Omega {\boldsymbol{N}_{\boldsymbol{\varepsilon}}}^T \mathbb{C}^{n+1} \boldsymbol{B} \tag{4.28}$$

$$\boldsymbol{D}_\tau^{sym} = \left(1 - \tau_{\boldsymbol{\varepsilon}}\right) \int_\Omega \boldsymbol{B}^T \mathbb{C}^{n+1} \boldsymbol{N}_{\boldsymbol{u}} \tag{4.29}$$

$$\boldsymbol{K}_\tau^{sym} = \tau_{\boldsymbol{\varepsilon}} \int_\Omega \boldsymbol{B}^T \mathbb{C}^{n+1} \boldsymbol{B} \tag{4.30}$$

From the given derivation, it is clear that a proper linearization of the non linear equations in the Newton-Raphson method requires a non-symmetric solver. Con-

sequently, the computational gains given by the smaller number of iterations in a quadratic convergence rate can be neutralized by the need of larger factorization time. Indeed, using a direct solver, a complete LU decomposition requires roughly twice the time and the computational resources with respect to a Cholesky one. Additionally, the constitutive tangent matrix for a softening process is not positive definite which implies that global numerical stability can be lost.

Conversely, the use of secant constitutive tensor results in a symmetric global stiffness matrix. This allows the use of faster solution methods, even if the required number of iterations is higher than for the Newton-Raphson case.

4.3 OSGS implementation

The OSGS implementation is similar to the ASGS one, except for the additional projection of the nodal stresses. Differentiation of the residuals with respect to strains and displacements gives identical terms $\boldsymbol{M}_\tau$, $\boldsymbol{G}_\tau$, $\boldsymbol{D}_\tau$ and $\boldsymbol{K}_\tau$.

The projection equation gives some additional terms in the Jacobian matrix when differentiating (3.46), owing to the presence of the additional stress projection variable $\boldsymbol{\Pi}_h$:

$$\begin{bmatrix} \boldsymbol{M}_\tau & \boldsymbol{G}_\tau & \boldsymbol{D}_\Pi^T \\ \boldsymbol{D}_\tau & \boldsymbol{K}_\tau & \boldsymbol{0} \\ \boldsymbol{D}_\Pi & \boldsymbol{0} & \boldsymbol{M}_\Pi \end{bmatrix}_{n+1}^{i} \begin{bmatrix} \delta\boldsymbol{\varepsilon}_h \\ \delta\boldsymbol{u}_h \\ \delta\boldsymbol{\Pi}_h \end{bmatrix}_{n+1}^{i+1} = - \begin{bmatrix} R_{1,h} \\ R_{2,h} \\ R_{3,h} \end{bmatrix}_{n+1}^{i} \tag{4.31}$$

where $(\delta\boldsymbol{\varepsilon}_h, \delta\boldsymbol{u}_h, \delta\boldsymbol{\Pi}_h)$ are the iterative corrections for $(\boldsymbol{\varepsilon}_h, \boldsymbol{u}_h, \boldsymbol{\Pi}_h)$ in the Newton-Raphson scheme. The added projection matrices are computed as:

$$\boldsymbol{M}_{\boldsymbol{\Pi}} = -\int_\Omega {\boldsymbol{N}_\varepsilon}^T \boldsymbol{N}_\varepsilon \tag{4.32}$$

$$\boldsymbol{D}_{\boldsymbol{\Pi}} = \int_\Omega \boldsymbol{B}^T \boldsymbol{N}_\varepsilon \tag{4.33}$$

Alternatively to this procedure, a staggered scheme can be devised. First, the projection of the stresses $\boldsymbol{\Pi}_h$ is computed at the beginning of the time step. Then, $\boldsymbol{\Pi}_h$ is used for the solution of $(\boldsymbol{\varepsilon}_h, \boldsymbol{u}_h)$. With this substitution, the matrix depicted in (4.31) can be *formally* condensed [1] and it becomes:

$$-\begin{bmatrix} \boldsymbol{M}_\tau - \boldsymbol{D}_\Pi^T \boldsymbol{M}_\Pi^{-1} \boldsymbol{D}_\Pi & \boldsymbol{G}_\tau \\ \boldsymbol{D}_\tau & \boldsymbol{K}_\tau \end{bmatrix}_{n+1}^{i} \begin{bmatrix} \delta\boldsymbol{\varepsilon}_h \\ \delta\boldsymbol{u}_h \end{bmatrix}_{n+1}^{i+1} = \begin{bmatrix} R_{1,h} \\ R_{2,h} \end{bmatrix}_{n+1}^{i} \tag{4.34}$$

This scheme is preferred with respect to the monolithic one due to the reduced computation time required. In a similar fashion to the ASGS method, it is possible to symmetrize the global stiffness matrix using the secant constitutive equation (3.4).

This page is left intentionally blank.

Chapter 5

Failure under mode I loading

5.1 Introduction

This chapter deals with the application of the mixed $\boldsymbol{\varepsilon} - \boldsymbol{u}$ strain-displacement finite element method to problems involving failure under mode I loading. In particular, examples of the 2D and 3D pull-out tests on plain concrete specimens are addressed.

Mode I fracture, also known as opening fracture mode, is one the most commonly encountered failure mechanisms in civil engineering materials at their ultimate state. This kind of failure is associated with rock-like and glass-like materials such as concrete, ceramics and Plexiglass, which have a very low resistance to tensile stresses compared to their compression strength. In nature, very porous materials also fail due to crushing of the internal structure under mode I compression: typical examples are ceramics, rocks (sandstones and limestones), human bones and weak layers of snow hoar crystals. Many of the mentioned materials show highly brittle behavior, with abrupt and very little inelastic deformation due to the fact that the dissipated fracture energy is very close to the elastic one.

From an experimental point of view, it is difficult to devise tests that stress a body in such a way that the inelastic branch evolution is linked solely to tensile mode I fracture. The pure uniaxial tensile test can only be performed on specimens that are able to support the clamping force without localized failure. Indeed, various techniques have been developed to measure the tensile strength of a material indirectly. For example, for concrete, the indirect tensile test by Berenbaum and Brodie [228] (also known as "*Brazilian split cylinder test*") is often used; it takes advantage of the tension created by Poisson's effect under radial compression. Alternatively, the wedge splitting test by Brühwiler and Wittmann [229], Trunk [230], Abdalla and Karihaloo [231] considers a volume of concrete with a central cut; each face of the cut is subjected to a force which aims to widen the initial flaw.

Further experimental techniques are the 3-point bending tests, as realized by Mazars et al. [232], Guinea et al. [233], Gálvez et al. [234], and the L-shaped panels,

tested by Winkler et al. [235]. However, all these rely on flexural loading rather than pure uniaxial stretching to characterize the specimen. For homogeneous materials, the correlation of peak force between flexural and uniaxial strengths is straightforward. However, when the experiments are performed on concrete (either reinforced or not) a sensible variation in results is found.

Additionally, it is important to note that the inelastic behavior is the result of the complex interplay of energy dissipation, redistribution of stresses and external forces. When a material is perfectly brittle, fracture appears suddenly after the peak load is reached. In such cases, failure dissipates instantly the elastic energy previous to the fracture. Conversely, for ductile materials, the peak load is followed by a redistribution of the stresses due to the deferred unloading of the specimen as the crack progresses. In these circumstances, the loading mode on the specimen can change substantially. The rotation of principal stress directions or the activation of other resisting mechanisms in the vicinity of the failure affected zone causes a considerable change in the global experimental result. Hence, the study of the inelastic behavior is fundamental for the proper characterization of quasi-brittle materials and it requires a high level of accuracy.

The pull-out test is an experiment commonly used to evaluate the performance of anchorages in concrete structures. In this test, the application of a traction force to a steel bolt embedded in a plain concrete specimen is used for the evaluation of the tensile strength. Also, pull-out tests have been used to determine the ultimate slip force of rebars and adhesive compounds [236, 237].

In this chapter, the works of Dejori [238] and Thenier and Hofstetter [239] are considered for the 2D pull-out test whereas, for the 3D version of the experiment, the contributions by Areias and Belytschko [240], Gasser and Holzapfel [241] and Duan et al. [242] are taken into account. The aim is to demonstrate that the use of an accurate and reliable numerical method for the computation of localization and failure is fundamental for both the study of quasi-brittle materials and the assessment of a correct experimental setup.

5.2 Plasticity in small strains

Before entering in the discussion of Rankine's failure criterion and for sake of completeness, the basic framework for plasticity is presented. Within the framework of infinitesimal deformation, the total strains tensor can be split in the elastic and the plastic contributions as follows:

$$\boldsymbol{\varepsilon} = \boldsymbol{\varepsilon}_e + \boldsymbol{\varepsilon}_p \tag{5.1}$$

Hence, in plasticity, Cauchy's stress tensor is computed as:

$$\boldsymbol{\sigma} = \mathbb{C}_0 : (\boldsymbol{\varepsilon} - \boldsymbol{\varepsilon}_p) \tag{5.2}$$

The elastic space of admissible stress $\mathbb{E}_{\boldsymbol{\sigma}}$ is defined as:

$$\mathbb{E}_{\boldsymbol{\sigma}} = \left\{ \boldsymbol{\sigma} \in \mathbb{R}^{\dim \times \dim} \,|\, f(\boldsymbol{\sigma}) \leq 0 \right\} \tag{5.3}$$

where the scalar function $f(\boldsymbol{\sigma})$ represents the yield surface and, for an admissible stress tensor, its value is less or equal to zero.

The evolution of the yield surface can be accounted for introducing the a set of internal variables. Defining the scalar function q as the isotropic softening stress-like variable, $\mathbb{E}_{\boldsymbol{\sigma}}$ reads:

$$\mathbb{E}_{\boldsymbol{\sigma}} = \left\{ (\boldsymbol{\sigma}, q) \in \mathbb{R}^{\dim \times \dim} \times \mathbb{R} \,|\, f(\boldsymbol{\sigma}, q) \leq 0 \right\} \tag{5.4}$$

The function q depends on the conjugate (strain-like) variable ξ. Frequently, the softening stress-like variable is assumed as linear:

$$q(\xi) = \begin{cases} -H_s \, \xi & 0 \leq \xi < \frac{\sigma_y}{H_s} \\ \\ 0 & \frac{\sigma_y}{H_s} \leq \xi < \infty \end{cases} \tag{5.5}$$

or exponential:

$$q(\xi) = \sigma_y \left(1 - \exp^{-\frac{2H_s}{\sigma_y}\xi} \right) \tag{5.6}$$

where H_s is the parameter that controls the softening behavior and σ_y is the uniaxial stress threshold.

The plastic potential function $g = g(\boldsymbol{\sigma}, q)$ is introduced such that the evolution of the plastic strain tensor $\boldsymbol{\varepsilon}_p$ and of the internal variable ξ is given by:

$$\begin{aligned} \dot{\boldsymbol{\varepsilon}_p} = &\quad \dot{\lambda} \frac{\partial g(\boldsymbol{\sigma}, q)}{\partial \boldsymbol{\sigma}} = \dot{\lambda} \, \boldsymbol{m} \\ \dot{\xi} = &\quad \dot{\lambda} \frac{\partial g(\boldsymbol{\sigma}, q)}{\partial q} \end{aligned} \tag{5.7}$$

where the scalar $\lambda \geq 0$ is the plastic multiplier. This parameter must satisfy the *Kuhn-Tucker complementarity conditions* [53]:

$$\dot{\lambda} \geq 0 \quad f(\boldsymbol{\sigma}, q) \leq 0 \quad \dot{\lambda} \, f(\boldsymbol{\sigma}, q) = 0 \tag{5.8}$$

and the *consistency condition*:

$$\text{if } \; f = 0 \; \text{ and } \; \dot{\lambda} > 0 \quad \Rightarrow \quad \dot{\lambda} \, \dot{f}(\boldsymbol{\sigma}, q) = 0 \quad \Rightarrow \quad \dot{f} = 0 \tag{5.9}$$

Note that expressions (5.8) and (5.9) determine the cases of:

$$\begin{aligned} &\text{Plastic loading} && f = 0,\ \dot{\lambda} > 0 \\ &\text{Neutral loading} && f = 0,\ \dot{\lambda} = 0 \\ &\text{Elastic loading/unloading} && f < 0,\ \dot{\lambda} = 0 \end{aligned} \tag{5.10}$$

The time derivative of the yield surface reads as:

$$\dot{f} = \frac{\partial f}{\partial \boldsymbol{\sigma}} : \dot{\boldsymbol{\sigma}} + \frac{\partial f}{\partial q}\dot{q} = \frac{\partial f}{\partial \boldsymbol{\sigma}} : \mathbb{C}_0 : [\dot{\boldsymbol{\varepsilon}} - \dot{\boldsymbol{\varepsilon}}_p] + \frac{\partial f}{\partial q}\frac{\partial q}{\partial \xi}\dot{\xi} \tag{5.11}$$

Recalling the evolution expressions in (5.7) for the variables $\dot{\boldsymbol{\varepsilon}}_p$ and $\dot{\xi}$, last expression reads:

$$\dot{f} = \frac{\partial f}{\partial \boldsymbol{\sigma}} : \mathbb{C}_0 : \dot{\boldsymbol{\varepsilon}} - \dot{\lambda}\,\frac{\partial f}{\partial \boldsymbol{\sigma}} : \mathbb{C}_0 : \frac{\partial g}{\partial \boldsymbol{\sigma}} + \dot{\lambda}\,\frac{\partial f}{\partial q}\frac{\partial q}{\partial \xi}\frac{\partial g}{\partial q} \tag{5.12}$$

Enforcing the consistency condition $\dot{f} = 0$, the value of the plastic multiplier is calculated as:

$$\dot{\lambda} = \frac{\left\langle \frac{\partial f}{\partial \boldsymbol{\sigma}} : \mathbb{C}_0 : \dot{\boldsymbol{\varepsilon}} \right\rangle}{\frac{\partial f}{\partial \boldsymbol{\sigma}} : \mathbb{C}_0 : \frac{\partial g}{\partial \boldsymbol{\sigma}} - \frac{\partial f}{\partial q}\frac{\partial q}{\partial \xi}\frac{\partial g}{\partial q}} \tag{5.13}$$

where the Macaulay brackets or ramp function $\langle\cdot\rangle$ is required since $\dot{\lambda} > 0$ only under a positive strain increment which satisfies the plastic loading condition. Finally, the evolution of Cauchy's stress tensor reads:

$$\dot{\boldsymbol{\sigma}} = \mathbb{C}_0 : [\dot{\boldsymbol{\varepsilon}} - \dot{\boldsymbol{\varepsilon}}_p] = \mathbb{C}_0 : \dot{\boldsymbol{\varepsilon}} - \dot{\lambda}\,\mathbb{C}_0 : \frac{\partial g}{\partial \boldsymbol{\sigma}} \tag{5.14}$$

and, substituting the expression of $\dot{\lambda}$, it reads:

$$\dot{\boldsymbol{\sigma}} = \mathbb{C}_0 : \dot{\boldsymbol{\varepsilon}} - \frac{\left(\mathbb{C}_0 : \frac{\partial f}{\partial \boldsymbol{\sigma}}\right) \otimes \left(\mathbb{C}_0 : \frac{\partial g}{\partial \boldsymbol{\sigma}}\right)}{\frac{\partial f}{\partial \boldsymbol{\sigma}} : \mathbb{C}_0 : \frac{\partial g}{\partial \boldsymbol{\sigma}} - \frac{\partial f}{\partial q}\frac{\partial q}{\partial \xi}\frac{\partial g}{\partial q}} : \dot{\boldsymbol{\varepsilon}} = \mathbb{C}_{ep} : \dot{\boldsymbol{\varepsilon}} \tag{5.15}$$

Hence, the tangent elasto-plastic constitutive tensor $\mathbb{C}_{ep}$ is defined as:

$$\mathbb{C}_{ep} = \mathbb{C}_0 - \frac{\left(\mathbb{C}_0 : \frac{\partial f}{\partial \boldsymbol{\sigma}}\right) \otimes \left(\mathbb{C}_0 : \frac{\partial g}{\partial \boldsymbol{\sigma}}\right)}{\frac{\partial f}{\partial \boldsymbol{\sigma}} : \mathbb{C}_0 : \frac{\partial g}{\partial \boldsymbol{\sigma}} - \frac{\partial f}{\partial q}\frac{\partial q}{\partial \xi}\frac{\partial g}{\partial q}} \tag{5.16}$$

where $\otimes$ indicates the outer vectorial product. Note that, in general, $\mathbb{C}_{ep}$ is not symmetric.

In the case of associative plasticity, the plastic potential is equal to the yield surface, i.e. $g(\boldsymbol{\sigma}, q) = f(\boldsymbol{\sigma}, q)$ and the evolution equations in (5.7) read

$$\begin{aligned} \dot{\boldsymbol{\varepsilon}}_p = &\quad \dot{\lambda} \frac{\partial f(\boldsymbol{\sigma}, q)}{\partial \boldsymbol{\sigma}} = \dot{\lambda}\, \boldsymbol{n} \\ \dot{\xi} = &\quad \dot{\lambda} \frac{\partial f(\boldsymbol{\sigma}, q)}{\partial q} \end{aligned} \tag{5.17}$$

In such case, the flow of plastic strains $\boldsymbol{m} = \boldsymbol{n}$ is orthogonal to the yield surface and, consequently, the plastic multiplier $\dot{\lambda}$ is computed as:

$$\dot{\lambda} = \frac{\left\langle \frac{\partial f}{\partial \boldsymbol{\sigma}} : \mathbb{C}_0 : \dot{\boldsymbol{\varepsilon}} \right\rangle}{\frac{\partial f}{\partial \boldsymbol{\sigma}} : \mathbb{C}_0 : \frac{\partial f}{\partial \boldsymbol{\sigma}} - \frac{\partial f}{\partial q} \frac{\partial q}{\partial \xi} \frac{\partial f}{\partial q}} \tag{5.18}$$

Finally, the tangent elasto-plastic constitutive tensor becomes symmetric as:

$$\mathbb{C}_{ep} = \mathbb{C}_0 - \frac{\left(\mathbb{C}_0 : \frac{\partial f}{\partial \boldsymbol{\sigma}}\right) \otimes \left(\mathbb{C}_0 : \frac{\partial f}{\partial \boldsymbol{\sigma}}\right)}{\frac{\partial f}{\partial \boldsymbol{\sigma}} : \mathbb{C}_0 : \frac{\partial f}{\partial \boldsymbol{\sigma}} - \frac{\partial f}{\partial q} \frac{\partial q}{\partial \xi} \frac{\partial f}{\partial q}} \tag{5.19}$$

5.3 Rankine's plasticity

In the last decades, concrete has been studied using continuum damage models [137, 243, 244], plasticity [132, 245] or a combination of the two [61, 246, 247].

In order to study Mode I fracture, a plasticity constitutive model based on Rankine's failure criterion is used. It can be written as follows:

$$f_i(\boldsymbol{\sigma}, q) = \sigma_i - r_i(\xi_i) = \sigma_i - (\sigma_y - q_i(\xi_i)) \quad \forall i = 1, 2, 3 \tag{5.20}$$

where all principal stresses must be contained in the elastic admissible space and, for sake of generality, different principal directions can have different hardening/softening functions. Figure 5.1a depicts this failure surface.

A multi-surface failure criterion such as (5.20) introduces additional difficulties that require specific algorithms as shown by Simo et al. [248]. The boundary of the space of admissible stresses $\partial \mathbb{E}_{\boldsymbol{\sigma}}$, where loading conditions are considered, is divided in different zones:

$$\begin{aligned} &\text{Face:} && f_1 = 0 \text{ or } f_2 = 0 \text{ or } f_3 = 0 \\ &\text{Edge:} && f_1 = 0 \wedge f_2 = 0 \text{ or } f_2 = 0 \wedge f_3 = 0 \text{ or } f_3 = 0 \wedge f_1 = 0 \\ &\text{Apex:} && f_1 = 0 \wedge f_2 = 0 \wedge f_3 = 0 \end{aligned} \tag{5.21}$$

For associative plasticity, the gradient of the yield surface (i.e. the vector of plastic

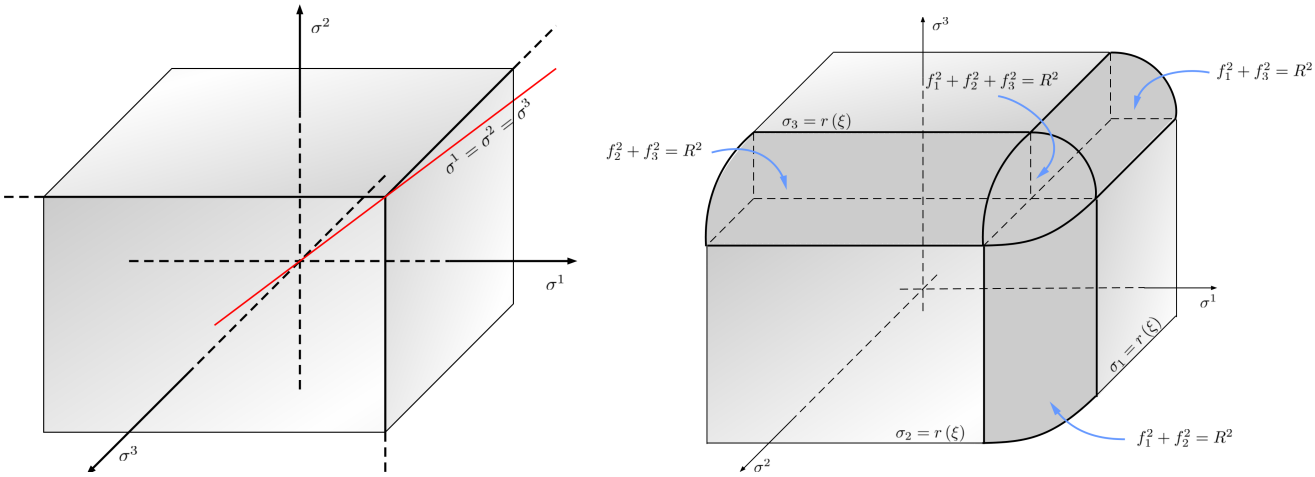

Figure 5.1: Comparison of the (a) original and (b) modified Rankine's yielding surface in the Haigh-Westergaard space. The original criterion can be recovered from the modified one by setting the parameter $c = 0$.

flow) is undefined in the cases of edges and apex. To avoid this issue, it is possible to devise a return mapping strategy that solves a set of equations rather than a scalar condition. Likewise, other typical algorithmic steps, such as computing the evolution equations and updating the failure surfaces, have to be generalized to a multidimensional version which results in a larger database for historical variables. Furthermore, when edges and apex are sharp, the tangent constitutive matrix is frequently ill-conditioned.

To avoid these computational issues, it is possible to regularize the sharp edges of the failure surface with a quarter of cylinder and the apex with an eight of a sphere. Hence, the three failure surfaces are approximated by a continuous and derivable scalar function. Let us consider the curvature radius ρ of these regularization surfaces defined as a fraction $c \in [0, 1]$ of the uniaxial threshold:

$$\rho\left(c, q\left(\xi\right)\right) = c\left(\sigma_y - q\left(\xi\right)\right) \tag{5.22}$$

The modified Rankine yielding criterion is defined as:

$$f\left(c, \boldsymbol{\sigma}, q\left(\xi\right)\right) = \sqrt{\left\langle f_1\left(c, \boldsymbol{\sigma}, q\left(\xi\right)\right)\right\rangle^2 + \left\langle f_2\left(c, \boldsymbol{\sigma}, q\left(\xi\right)\right)\right\rangle^2 + \left\langle f_3\left(c, \boldsymbol{\sigma}, q\left(\xi\right)\right)\right\rangle^2} - \rho\left(c, q\left(\xi\right)\right) \tag{5.23}$$

where $f_i\left(c, \boldsymbol{\sigma}, q\left(\xi\right)\right)$ is the i-th uniaxial yield function defined as:

$$f_i\left(c, \boldsymbol{\sigma}, q\left(\xi\right)\right) = \sigma^i - \left(1 - c\right)\left(\sigma_y - q\left(\xi\right)\right) \tag{5.24}$$

Figure 5.1b shows the proposed modification to the failure surface.

From a computational standpoint, the modified Rankine yield criterion allows to deal with scalar quantities rather than vectorial ones, which increases the efficiency of the return mapping algorithm. Indeed, defining:

$$\bar{f}_i(\boldsymbol{\sigma}, q) = \frac{\langle f_i(\boldsymbol{\sigma}, q)\rangle}{\sqrt{f_1(\boldsymbol{\sigma}, q)^2 + f_2(\boldsymbol{\sigma}, q)^2 + f_3(\boldsymbol{\sigma}, q)^2}} \tag{5.25}$$

the evolution equations for the continuous case can be compactly written as:

$$\begin{cases} \dot{\boldsymbol{\varepsilon}}_p = \dot{\gamma} \sum_{i=1}^{3} \bar{f}_i(\boldsymbol{\sigma}, q) \dfrac{\partial \sigma_i}{\partial \boldsymbol{\sigma}} \\ \\ \dot{\xi} = \dot{\gamma} \left(c + (1-c) \sum_{i=1}^{3} \bar{f}_i(\boldsymbol{\sigma}, q) \right) \end{cases} \tag{5.26}$$

Since $f(c, \boldsymbol{\sigma}, q)$ in (5.23) is continuous and smooth, the gradient of the yield surface is also continuous. Therefore, it is possible to implement a Newton-Raphson scheme in order to have a more efficient numerical computation of the plastic multiplier.

As regards the computation of the elasto-plastic tangent constitutive matrix, the proposed approximation is less convenient than the original version. In the uniaxial case, an analytical form of the elasto-plastic constitutive matrix can be easily computed and it corresponds in both original and modified models. However, when dealing with the multi-surface case, the two algorithms do not coincide anymore in this respect. In the case of the original Rankine model, the multi-surface tangent matrix is a linear combination of the single-surface ones. Contrariwise, in the case of the modified Rankine model, it is necessary to compute explicitly the first and the second order derivatives of the yield surface function in (5.23). Not only the analytical expression is difficult to handle, but also the implementation is very prone to coding errors. Nevertheless, the exact differentiation can be substituted by a finite difference numerical scheme to compute the tangent elasto-plastic constitutive tensor:

$$\mathbb{C}_{ep}\, \hat{\boldsymbol{e}}_i \approx \frac{\boldsymbol{\sigma}(\boldsymbol{\varepsilon} + h\hat{\boldsymbol{e}}_i) - \boldsymbol{\sigma}(\boldsymbol{\varepsilon} - h\hat{\boldsymbol{e}}_i)}{2h} \tag{5.27}$$

where $\hat{\boldsymbol{e}}_i$ is the unit vector of the i-th component of the stress tensor.

Such computation requires the evaluation of multiple return mapping procedures given by the perturbation of each single strain component. However, this method has second order accuracy and converges to the exact differentiation result for small enough perturbations. Moreover, it allows to create a secant-like matrix for stresses in the vicinity of edge or apex zones. In turn, this provides a more robust alternative to a possibly ill-conditioned constitutive tangent matrix.

5.4 Softening behavior

In a softening process, the energy dissipated by the inelastic behavior is linked to the fracture energy G_f [138], defined by unit surface. When using a plastic model defined in terms of stress and strain, the dissipated plastic energy $\mathscr{W}_p$ is defined by unit volume. In the discrete FE setting, these two definitions are related through a characteristic length l_{ch}, which depends on the resolution of the discretization:

$$\mathscr{W}_p = \frac{G_f}{l_{ch}} \tag{5.28}$$

The size of the strain concentration band depends on the finite element technology used, as pointed out by Cervera et al. [5]: irreducible finite elements, due to the discontinuous strain field, provide a concentration band within a single element span whereas in the $\boldsymbol{\varepsilon} - u$ mixed FE formulation, with inter-elemental continuous strain, the slip line spans two elements. Consequently, the characteristic length l_{ch} is taken accordingly. In the plastic model, the uniaxial stress threshold function has been defined as $r(\xi) = \sigma_y - q(\xi)$ from (5.23) and recalling the evolution of the plastic strains (5.26), the rate of plastic work is computed as:

$$\dot{\mathscr{W}}_p = \boldsymbol{\sigma} : \dot{\boldsymbol{\varepsilon}}_p = r(\xi)\,\dot{\xi} \tag{5.29}$$

From the expression of the hardening/softening stress-like function $q(\xi)$, either linear as in (5.5) or exponential as in (5.6), the total plastic work is calculated then as:

$$\mathscr{W}_p = \int_{t=0}^{t=\infty} \dot{\mathscr{W}}_p \,\mathrm{d}t = \int_{\xi=0}^{\xi=\infty} r(\xi)\,\dot{\xi} = \frac{{\sigma_y}^2}{2H_S} \tag{5.30}$$

Now, comparing expressions (5.28) and (5.30), the parameter H_S can be computed as:

$$H_S = \frac{{\sigma_y}^2}{2G_f} l_{ch} = \bar{H}_S l_{ch} \tag{5.31}$$

where the parameter $\bar{H}_S$ depends only on material properties.

5.5 2D pullout tests

In the referenced 2D pull-out tests [238, 239], a T-shaped flange is embedded in a panel of plain concrete (Figure 5.2). The experiment consists in applying a vertical traction to the steel bolt until a fracture is produced and a volume of concrete material is detached. The unreinforced panel is restrained from vertical motion by two pairs of steel rods which are placed in the vicinity of the two ends of the panel. In the experiment, horizontal forces are not expected. Consequently, the movements in the remaining two directions are limited by the friction exerted by the panel on

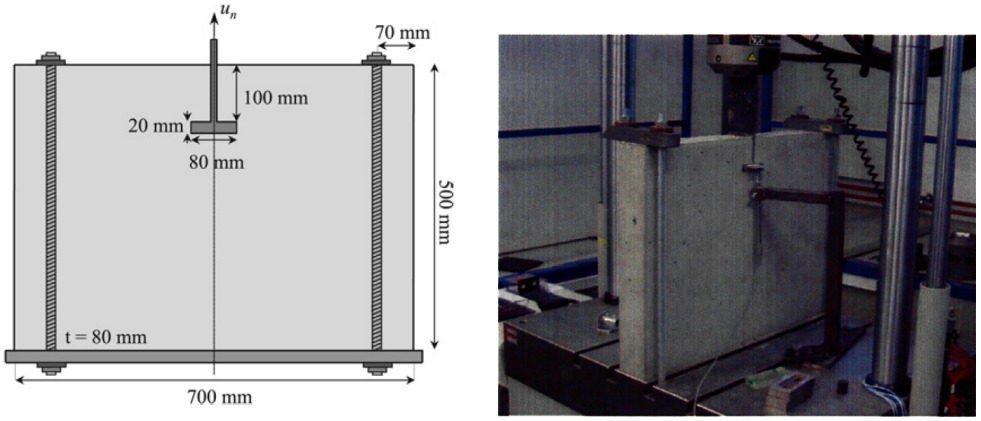

(a) (b)

Figure 5.2: Test setup in [238, 239]: (a) geometry and (b) detail of the experimental stand.

the base of the test apparatus.

Despite a quite simple setup, the experimental results show significant differences across the specimens. In particular, two main families of outcomes are apparent. When the load is perfectly centered, a quasi-symmetric cracking pattern is observed in the vicinity of the flange as presented in Figure 5.3a. The angle of fracture of almost 45 degrees suggests that failure appears due to shear loading on the portion of concrete in contact with the flange. Moreover, due to symmetry, the contact between the top surface of the embedded flange and the concrete does not create any unbalanced horizontal force. Since a small amount of sway in the load as well as slight variations in the concrete strength (either due to quality or aggregates) is expected, the fracture pattern is not exactly symmetric. Moreover, in this case, the solution does not depends on the stiffness of the bracing frame since it will provide centered reaction to the force applied from the flange.

Contrariwise, in the asymmetric case, the experimental outcome shows on one

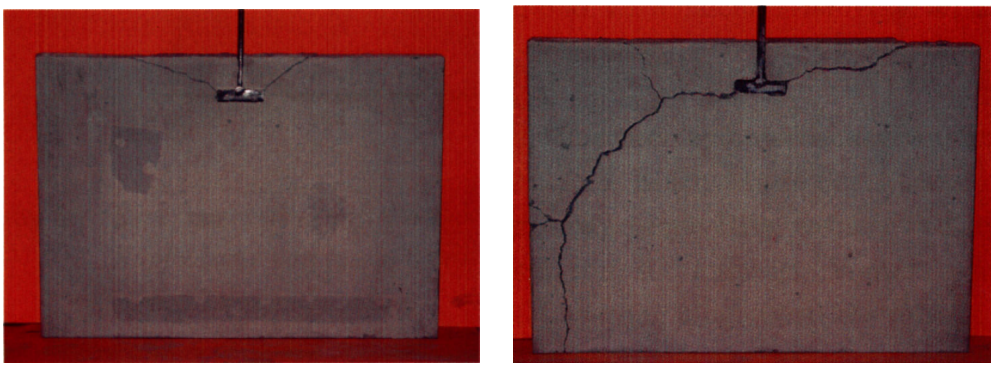

(a) (b)

Figure 5.3: Test results in [238]: (a) symmetric and (b) asymmetric crack patterns.

side a single fracture and on the other side a bifurcating pattern, as reported in Figure 5.3b. It is crucial to characterize the sequence of cracking in a detailed way. Initially, owing to a non centered flange load or considerable heterogeneity in the concrete, the load creates a fracture on one side of the panel. From the experiments, it starts from the contact zone, where significant friction at the interface is expected, and it propagates in a clear direction to the bracing support. This means that, with respect to this side of the specimen, there is a considerable reaction force given by the steel rods on the concrete. Successively, a shift of the applied force to the less damaged part of the specimen is observed for equilibrium reasons and this results in a bending moment applied to the concrete. A horizontal cracking pattern suggests that the stresses in the vicinity of the flange are vertical rather than diagonal, proving that the bracing frame is not exerting any substantial reaction. Finally, the fracture bifurcates in two branches and the extensive cracking concludes the test.

This experimental test has been studied numerically, with the objective of reproducing the experimental outcomes and to compare the performance of the mixed $\boldsymbol{\varepsilon} - \boldsymbol{u}$ with the standard irreducible finite elements.

Firstly, the symmetric test has been modeled. As discussed before, the influence of the bracing stiffness on the resulting 45 degrees fracture is negligible. In addition, the boundary conditions at the point of application of the force of the bolt does not constrain horizontal displacement, in line with the expected symmetric distribution of reaction forces. Consequently, two models are calculated, one with stiff and

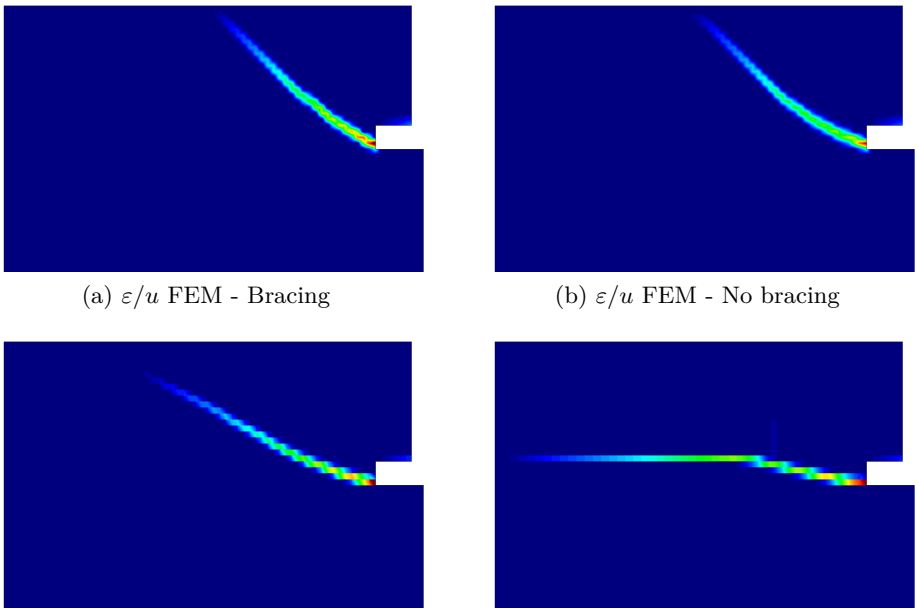

(a) ε/u FEM - Bracing (b) ε/u FEM - No bracing

(c) Std FEM - Bracing (d) Std FEM - No Bracing

Figure 5.4: Equivalent plastic strain contours with mixed (top row) and the standard (bottom row) finite element formulations in the pure shear case.

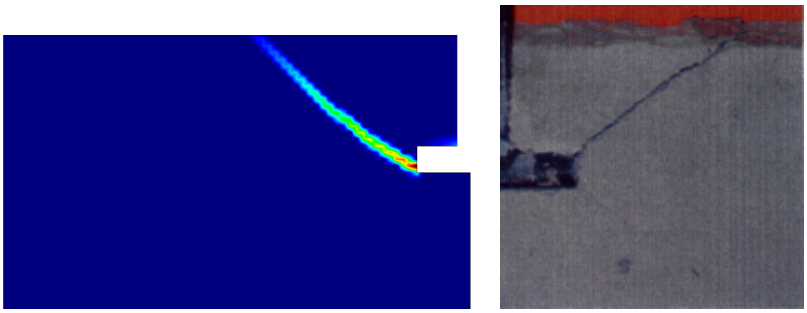

(a) (b)

Figure 5.5: Comparing the symmetric pattern in the case of free horizontal sliding of the steel flange.

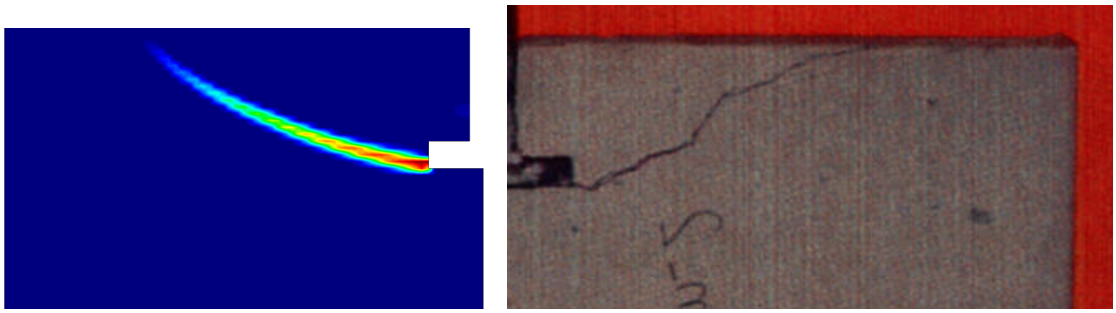

(a) (b)

Figure 5.6: Comparing the symmetric pattern for the case of effective vertical constraint of steel bracing and constrained horizontal motion of the steel flange.

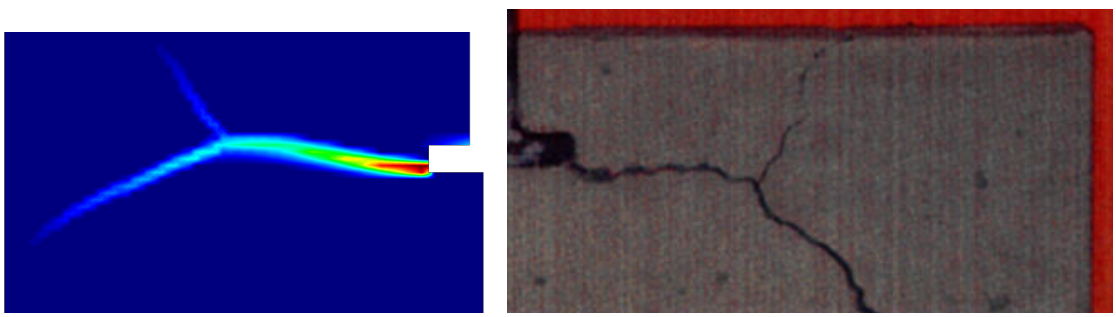

(a) (b)

Figure 5.7: Comparing the bifurcation pattern in the asymmetric case.

another with loose bracing. The objective of this numerical analysis is to study the sensibility of the finite element formulations to the frame stiffness in a problem where the symmetric boundary conditions provide an analytical solution. The comparison of outcomes is reported in Figure 5.4. The results show that the mixed formulation yields similar localization patterns for the two cases. In both models, the localization band is oriented at 45 degrees, confirming insensitivity to frame stiffness and mesh orientation. Instead, the standard displacement-based finite element provides substantially distinct results. In the case of effective bracing, the irreducible formulation shows a fracture oriented in the direction of the constrained zone. Contrariwise, when the bracing is not effective, the computed crack is initially growing diagonally but, shortly after, it follows the mesh orientation.

This numerical example proves that the error introduced by the lack of accuracy in the irreducible method is substantial enough to pollute the solution. The change in numerical results is significant and highlights the intrinsic limitations of the displacement-based finite elements. On the contrary, the mixed $\boldsymbol{\varepsilon} - \boldsymbol{u}$ formulation provides the required numerical capability to solve consistently localization and failure problems.

Next, the mixed strain-displacement formulation is applied to the asymmetric fracture pattern. Figure 5.5 shows the previously studied symmetric solution, whereas Figure 5.6 and Figure 5.7 present the two different outcomes of the asymmetric case compared with the actual tests. The agreement between numerical and experimental results is remarkably good. This is obtained even if the Rankine plasticity criterion does not take into account crushing due to compressive stresses.

When the steel-concrete contact is engaged and the bracing is effective, the fracture shape starts from the flange and grows in the direction of the support as shown in Figure 5.6a. The corresponding experimental result depicts a similar behavior, although the variability of concrete causes a little deviation in the crack path (Figure 5.6b).

In the case of ineffective bracing, the numerical solution suggests an initial horizontal localization followed by a bifurcation as presented in Figure 5.7a. The complex shape of this crack is also found in the experiment (Figure 5.7b). On the one hand, the mixed strain displacements formulation provides a bifurcation pattern without the use of any additional technique. On the other hand, this finite element technology achieves very accurate results, which allow a precise investigation of the experimental tests and their outcome.

5.6 3D pullout tests

The 3D pullout test in analysis has been previously studied numerically by Areias and Belytschko [240], Gasser and Holzapfel [241], Duan et al. [242] and Armero and

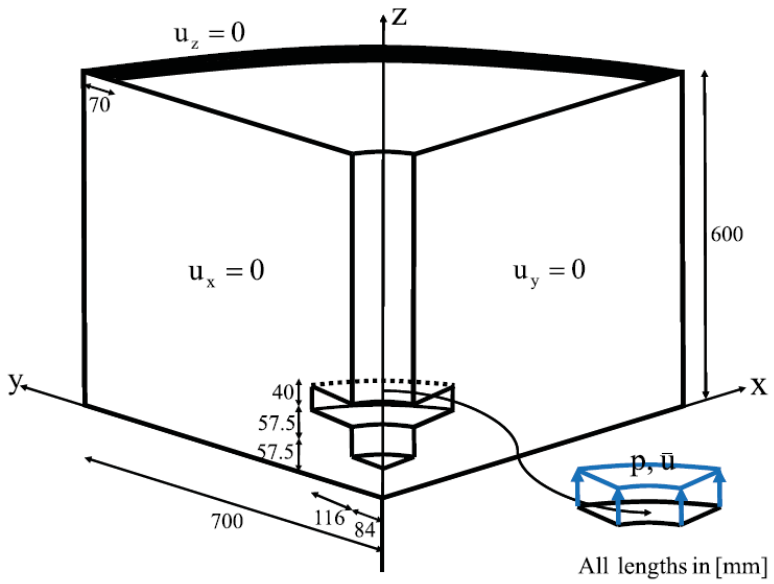

Figure 5.8: Geometry of the 3D pullout test, from Armero and Kim [249].

Kim [249]. It consists in a cylindrical concrete anchorage with an embedded steel bolt as shown in Figure 5.8. The specimen is constrained from movement by a circular steel hoop running around the external circumference of the top face. Due to the axial symmetry, the solution to this mechanical problem is a conical fracture surface which starts in the vicinity of the steel bolt and progresses outward and upward in a diagonal fashion with a circular front.

This example is studied with three different meshes which are characterized by

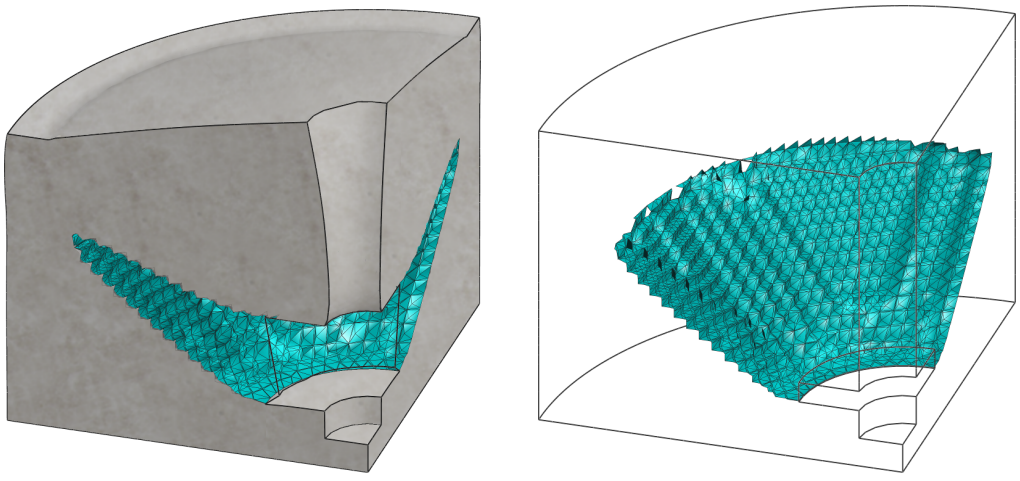

(a) (b)

Figure 5.9: Deformed concrete block with the crack opening (left) and conical crack surface (right) resulting from the mixed formulation analysis.

decreasing element sizes. The objective is to demonstrate the convergence of the mixed strain displacement formulation when reducing the element size and compare the results with the irreducible FE.

In Figure 5.9, the final deformed model and the failure mechanism obtained with the finer mesh are presented. As expected, the crack surface is axisymmetric and the failure propagates from the bolt insert to the points constrained by the steel hoop. A comparison of the irreducible and mixed formulations results across different mesh sizes is presented in 5.10. Two facts are observable:

(a) the mixed formulation provides convergent results; even relatively coarse meshes can produce fairly accurate results, in good agreement with reported numerical simulations [240–242];

(b) the standard formulation is severely affected by the discretization adopted, both qualitatively and quantitatively; the corresponding curves show significant over-dissipation.

Even if the plots of the reaction force may appear very similar, it is clear that a nonlinear mechanical problem which involves localization of strains can be resolved in a more consistent and accurate fashion using a coarse mesh with the mixed displacement-strain formulation rather than a finer mesh but the standard displacement-based one. The $\boldsymbol{\varepsilon} - \boldsymbol{u}$ finite elements captures the correct failure mechanism and the corresponding peak and post-peak behavior with relative coarse meshes. This fact represents a substantial proof of the higher accuracy of the method, and it is an important consideration regarding the computational cost-effectiveness.

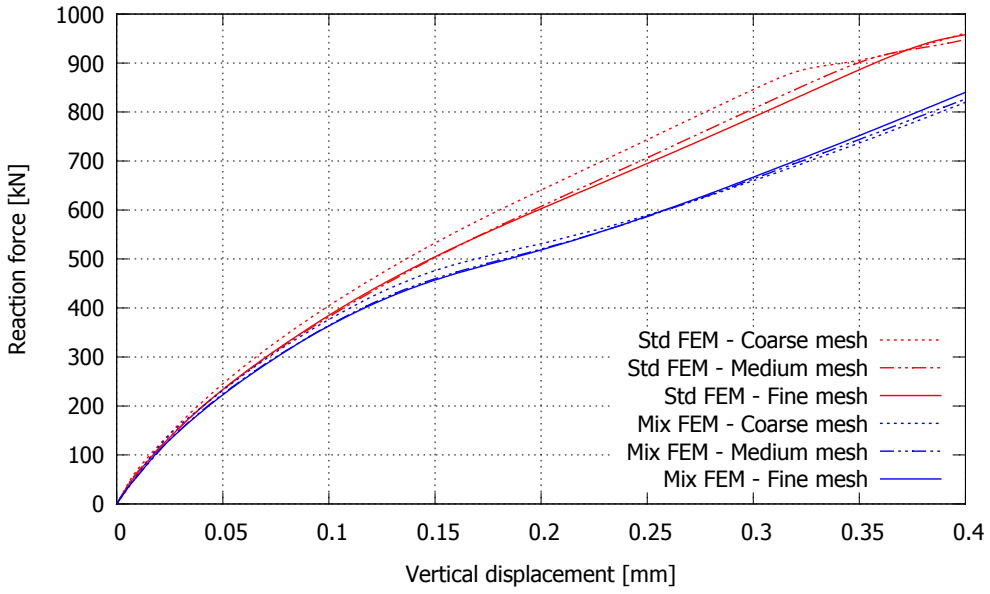

Figure 5.10: Reaction versus displacement curve for the 3D pullout test.

Chapter 6

Failure under mode II loading

6.1 Introduction

This chapter presents a set of numerical benchmarks for compressible and incompressible plasticity employing von Mises and Drucker-Prager yield criteria and associative flow rule. The mixed $\boldsymbol{\varepsilon} - \boldsymbol{u}$ formulation is compared with analytical solutions and with other finite elements technologies, namely the $\boldsymbol{u}$ displacement-based irreducible formulation and mixed $\boldsymbol{u} - \boldsymbol{p}$ displacement-pressure one.

Mode II fracture, or shearing fracture mode, is caused by shear acting in the plane of the strain localization. Under these conditions, the creation of a slip line or surface, is observed.

Rupture of metal is historically linked with mode II fracture. Tresca (1864) and von Mises (1913) developed failure criteria based on the shear stress values for metal tubes under high pressure. A macroscopic phenomenon frequently observed in uniaxial tests of low-carbon steel are Lüders lines [250]. In the inelastic deformation range, a series of diagonal bands, caused by the creation of microscopical sliding planes, appears progressively leading to failure (Figure 6.1).

Likewise, strength of soil and granular materials relies on the friction force exerted between the grains. In turn, this depends on the roughness of the material and on the stress state. When the applied shear reaches the maximum static friction force, these materials have the tendency to show a sudden reduction of strength. An example of

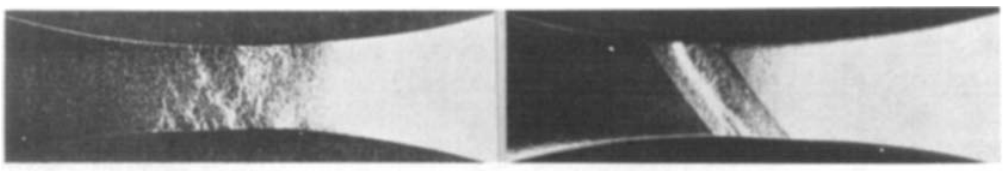

Figure 6.1: Appearance of Lüders bands in steel specimens subjected to uniaxial traction force, from Fujita and Miyazaki [251].

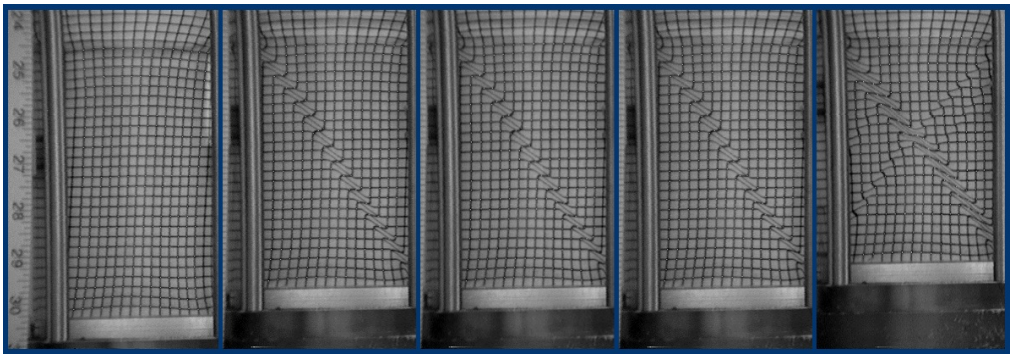

Figure 6.2: Appearance of diagonal shear bands in a sand specimen during a triaxial test, from Alshibli and Sture [252]

shear bands in a sand specimen during a triaxial test is depicted in Figure 6.2.

Failure under mode II loading is also encountered in materials whose volume does not change upon deformation. In elasticity, this condition is characterized by the Poisson's ratio equal to 0.5 and an infinite bulk modulus. In plasticity, the von Mises (J2) failure criterion describes materials which present pure deviatoric inelastic strains.

The strong form of the incompressible problem, whether in solid or fluid mechanics, does not allow an irreducible format of the field equations insomuch as it is not possible to enforce incompressibility solely with the equilibrium equation in terms of displacements. Conversely, it is convenient to split the stress tensor into volumetric and deviatoric contributions. Then, both the balance of momentum and mass conservation equations are modified accordingly. This format is suitable for both compressible and incompressible problems [2].

From a numerical point of view, the standard irreducible finite elements show locking of the pressure in the analysis of quasi incompressible materials. As a result, the mean-stress field is usually characterized by a checkerboard solution with highly oscillating values across the mesh. To solve this issue, a mixed formulation in terms of displacements and pressures is required.

Among the numerous contributions on the topic of isochoric plasticity, Simo [253, 254] showed that the problem can be tackled using a penalty function for the incompressibility constrain. Later, Pastor [220, 221] introduced a mixed finite element formulation in the variables of displacement and pressure for low order elements. In the work published by Chiumenti et al. [222], the mechanical problem in incompressible elasticity was solved using triangular and quadrilateral low-order elements with equal interpolation were chosen for $\boldsymbol{u}$ and $\boldsymbol{p}$. In order to circumvent the *Inf-Sup condition*, Variational Multiscale Stabilization using Orthogonal Subscales[16, 199] was introduced. Then, the method was extended to J2 plasticity in Cervera et al. [1] and Cervera et al. [4] and J2 damage in Cervera et al. [3].

In this work it is shown that the displacement-pressure finite elements show a good performance when dealing with problems involving isochoric deformation. However, the $\boldsymbol{u}-\boldsymbol{p}$ FE has the same accuracy as the irreducible formulation in compressible situations. In fact, the displacement-pressure elements compute the deviatoric strains by discrete differentiation of the displacement vector. Consequently, lack of precision in localization problems and mesh biased solutions are to be expected.

The mixed $\boldsymbol{\varepsilon}-\boldsymbol{u}$ strain-displacement finite element computes the strains in weak form. Therefore, it provides enhanced kinematics and improved accuracy, both in elasticity and plasticity. Indeed, the proposed formulation allows substantial improvements in the analysis of localization of strains and failure of solids. The 2-field formulation can also be expanded to a mixed 3-field $\boldsymbol{s}-\boldsymbol{u}-\boldsymbol{p}$ formulation [225] in terms of deviatoric stress, displacement and pressure, to be able to reach the incompressible limit.

6.2 Drucker-Prager's plasticity

The Drucker-Prager failure criterion may be constructed as a linear combination of a J2 von Mises and a Pure Pressure criterion. The von Mises yield criterion states that a material reaches the elastic limit when the equivalent octaedral stress equals the uniaxial admissible threshold, whereas the pure pressure yield criterion relates the hydrostatic pressure with an admissible pressure. The linear combination of the two criteria is done by introducing the tangent of the friction angle ϕ:

$$f\left(\boldsymbol{\sigma},q\right)=\left[\sqrt{3J_2(\boldsymbol{\sigma})}-r^d\left(\xi\right)\right]+a\left[\frac{1}{3}I_1(\boldsymbol{\sigma})-r^p\left(\xi\right)\right]\tan\phi=0 \tag{6.1}$$

where a determines the orientation of the failure surface, $r^d\left(\xi\right)$ and $r^p\left(\xi\right)$ are the shear and pressure threshold values respectively which, in turn, depend on the stress-like hardening/softening function $q\left(\xi\right)$. In the space of principal stresses, the Drucker-Prager failure surface is a cone which symmetry axis is the hydrostatic one (Figure 6.3a). On the (p,J_2) plane, it is a line with a slope equal to $\tan\phi$ (Figure 6.3b). The point $(p_{min},0)$ is the vertex of the cone, the state of minimum allowed mean stress. For the geotechnical engineering applications addressed in the following, the orientation of the Drucker-Prager cone is set to be open for triaxial compression ($a=1$) and crushing-like failures are not considered ($r^p=0$).

Defining the interpolation coefficient $\rho=1/(1+\tan\phi)$ and the shear stress threshold as $r^d\left(\xi\right)=\sigma_y-q(\xi)$, the failure surface reads:

$$f\left(\boldsymbol{\sigma},q\right)=\rho\left(\sqrt{\frac{3}{2}}\left\|\mathrm{dev}\boldsymbol{\sigma}\right\|-\left(\sigma_y-q\left(\xi\right)\right)\right)+a\left(1-\rho\right)\frac{1}{3}\operatorname{tr}\boldsymbol{\sigma}=0 \tag{6.2}$$

For associative plasticity, the plastic potential coincides with the yield surface

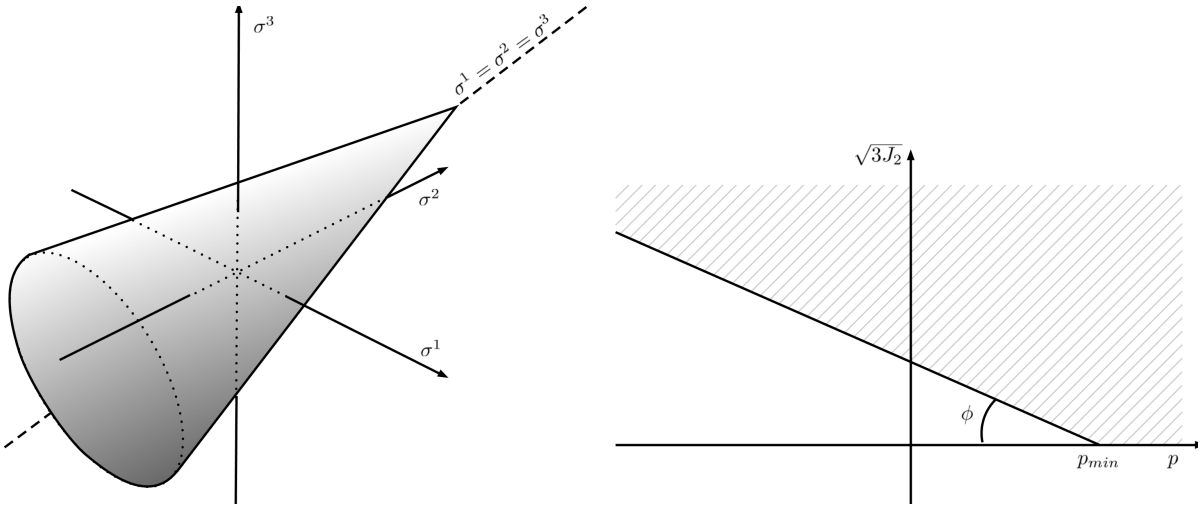

(a) (b)

Figure 6.3: Drucker-Prager elastic domain in (a) the Haigh-Westergaard principal stress space and (b) in the (p, J_2) plane

$f(\boldsymbol{\sigma}, q)$ as shown in expression (5.17) and the evolution equations for the plastic variables read:

$$\begin{aligned} \dot{\boldsymbol{\varepsilon}}_p &= \dot{\lambda} \frac{\partial f(\boldsymbol{\sigma}, q)}{\partial \boldsymbol{\sigma}} = \dot{\lambda} \left[\rho \sqrt{\frac{3}{2}} \frac{\mathrm{dev}\boldsymbol{\sigma}}{\|\mathrm{dev}\boldsymbol{\sigma}\|} + \frac{a(1-\rho)}{3} \mathbf{1} \right] \\ \dot{\xi} &= \dot{\lambda} \frac{\partial f(\boldsymbol{\sigma}, q)}{\partial q} = \dot{\lambda} \rho \end{aligned} \tag{6.3}$$

where $\dot{\lambda}$ is the plastic multiplier or plastic consistency parameter. Note that the flow of plastic strains is the sum of a volumetric and deviatoric part. Owing to the orthogonality between these two tensors, it is possible to perform the computation of the plastic multiplier and, consequently, of the other quantities involved in the return mapping algorithm by decomposing and computing separately the deviatoric or the volumetric parts.

As result of the volumetric-deviatoric decomposition, the tangent elasto-plastic constitutive tensor is written as:

$$\mathbb{C}_{ep} = \mathbb{C}_0 - \frac{\left[\rho 2G \sqrt{\frac{3}{2}} \mathbf{n}_d + a(1-\rho) K \mathbf{1} \right] \otimes \left[\rho 2G \sqrt{\frac{3}{2}} \mathbf{n}_d + a(1-\rho) K \mathbf{1} \right]}{\mathscr{D}} \tag{6.4}$$

where K and G are the bulk and shear elastic moduli, $\mathscr{D}$ is:

$$\mathscr{D} = \left[(1-\rho)^2 K + \rho^2 3G \right] - \rho^3 \frac{\mathrm{d}q(\xi)}{\mathrm{d}\xi} \tag{6.5}$$

and $\mathbf{n}_d$ is the unit vector in the deviatoric component of the stress:

$$\mathbf{n}_d = \frac{\text{dev}\boldsymbol{\sigma}}{\|\text{dev}\boldsymbol{\sigma}\|} \tag{6.6}$$

The deviatoric and volumetric contributions in the constitutive tensor are easy to identify. The coefficient ρ combines linearly the shear and the pressure components of the plastic flow.

6.2.1 Apex return mapping treatment

The apex of the cone represents the maximum admissible pressure and it is the only singular point in the Drucker-Prager plasticity surface. The part located outside the admissible stress space can be divided in two zones by considering the orthogonal plane to the yielding surface passing through the apex. When the failure criterion is smooth and continuously differentiable, the plastic flow is well defined. However, at the apex, the flow vector is not uniquely defined and, as it was presented for the Rankine plasticity model, the singular point case requires a special treatment. Thanks to the orthogonality between the deviatoric and volumetric parts, it is possible to identify the "apex" cases by checking when the condition $p = p_{min}$ is satisfied.

6.2.2 Softening behavior

As it was discussed for the Rankine model, the softening behavior has to be related to the characteristic length l_{ch} (connected to the mesh resolution) to be consistent energy-wise. Once again, the dissipated plastic energy per unit volume reads:

$$\mathscr{W}_p = \frac{G_f}{l_{ch}} \tag{6.7}$$

In the plastic model, the rate of plastic work is computed as:

$$\dot{\mathscr{W}}_p = \boldsymbol{\sigma} : \dot{\boldsymbol{\varepsilon}}_p = \bar{\sigma}\, \dot{\bar{\varepsilon}}_p = \alpha\, r\,(\xi)\, \dot{\xi} \tag{6.8}$$

where $\bar{\sigma}$ is the equivalent Drucker-Prager stress:

$$\bar{\sigma} = \rho\sqrt{\frac{3}{2}}\, \|\text{dev}\boldsymbol{\sigma}\| + (1-\rho)\, a \frac{1}{3}\, \text{tr}\, \boldsymbol{\sigma}\, \tan(\phi) = \rho\,(\sigma_y - q) = r\,(\xi) \tag{6.9}$$

and $\dot{\bar{\varepsilon}}_p$ is the rate of equivalent plastic strain:

$$\dot{\bar{\varepsilon}}_p = \|\dot{\boldsymbol{\varepsilon}}_p\| = \dot{\lambda} \left[\rho\sqrt{\frac{3}{2}} + a\,(1-\rho) \right] \tag{6.10}$$

With respect to the Rankine failure criteria, in the Drucker-Prager model the additional scaling factor α appears and it depends on the friction angle,

$$\alpha = \sqrt{\frac{3}{2}} + \frac{1-\rho}{\rho} \tag{6.11}$$

Similarly to expression (5.30), the total plastic work reads:

$$\mathscr{W}_p = \int_{t=0}^{t=\infty} \dot{\mathscr{W}}_p \, \mathrm{d}t = \int_{\xi=0}^{\xi=\infty} \alpha \, r\left(\xi\right) \dot{\xi} = \alpha \frac{{\sigma_y}^2}{2H_S} \tag{6.12}$$

and the parameter H_S reads:

$$H_S = \alpha \frac{{\sigma_y}^2}{2G_f} l_{ch} = \bar{H}_S l_{ch} \tag{6.13}$$

Once again, the parameter $\bar{H}_S$ depends only on material properties, whereas l_{ch} depends on the resolution of the discretization. Note that, with respect to the softening parameter in (5.31), the only modification is given by the scalar factor α.

6.3 Prandtl's punch test

In the first numerical example, the irreducible standard-based, the mixed diplacement pressure $\boldsymbol{u}-\boldsymbol{p}$ and the mixed strain-displacement $\boldsymbol{\varepsilon}-\boldsymbol{u}$ finite elements are compared in Prandtl's punch test. Let us consider a rigid shallow foundation with uniform downward displacement into a soil in undrained conditions. Thanks to the symmetry of the problem, the numerical model consists of half of the domain. Therefore, possible asymmetric solutions of the problem are not accounted for.

The problem has a known analytical solution for the case of rigid-plastic soil, with a friction angle of ϕ, which is reported in Figure 6.4 [255]. Three different zones can be defined in the solution. Below the foundation, a first zone consists of a triangular wedge, with an angle of $45+\phi/2$ degrees with respect to the horizontal line of the shallow foundation. Its response is elastic while sliding along the interface with the second zone. The second wedge is defined by the previous interface and a slip line which is orthogonal to the first one. The lower boundary of the second zone is given by a logarithmic spiral shaped slip line. This zone is characterized by a rotation movement around point A. Finally, the third zone is a symmetric triangular wedge which slides along a line inclined at $45-\phi/2$ degrees.

Firstly, the problem is studied for the case of friction angle $\phi = 0$. With respect to the theoretical solution, the numerical analysis considers elasto-plastic behavior instead of rigid-plastic. The mesh is composed by linear triangular elements orientated mostly in the -60/0/+60 degrees directions. The resulting displacement and equivalent plastic strain fields are presented in Figure 6.5. The irreducible

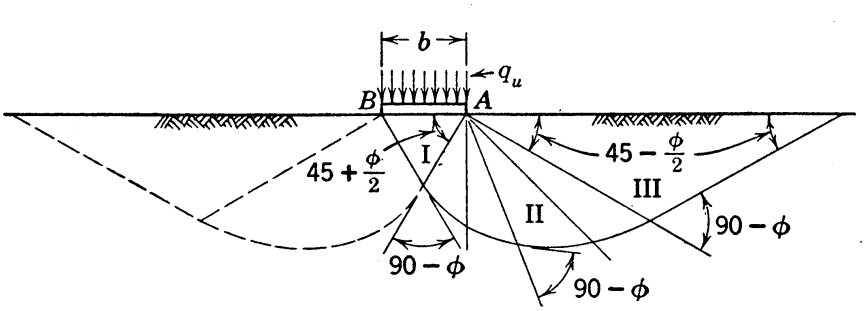

Figure 6.4: Prandtl's punch theoretical solution from Taylor [255]

formulation shows strongly mesh-biased localization, with the direction of the slip lines orientated with the mesh. The incompressible nature of plasticity causes the locking of the pressure and, at the same time, the lack of accuracy is given by the discontinuous deviatoric strain field computed from the nodal displacements.

The mixed displacement-pressure $\boldsymbol{u}-\boldsymbol{p}$ finite element presents a better solution than the irreducible formulation, with the displacement field substantially identical to the theoretical one. The localization depicted in the equivalent plastic strains plot presents a slip band that is one element thick, with a sharp jump in value. Still, a slight mesh dependence is observed in the localization band.

Finally, the mixed strain-displacement $\boldsymbol{\varepsilon}-\boldsymbol{u}$ provides a good solution in terms of displacements, whereas the equivalent plastic strain field is continuous rather than discontinuous. In particular, the localization band shows a linear variation spanning across a two elements band. The mesh objectivity of the result is appreciable, with the localization band crossing elements irrespectively of their orientation.

Secondly, the cases of $\phi = 0, 15, 30$ degrees are analyzed with the mixed strain-displacement formulation. The objective is to assess the Drucker-Prager constitutive model with respect to the analytical solution given in Figure 6.4. In this analysis a uniform mesh of square elements is used.

The first case, for $\phi = 0°$, is computed in order to verify the previous result with respect to two different meshes. As it is possible to see in Figure 6.6a, the localization band calculated from the quadrilateral mesh coincides with that of the triangular one. The angle of the localization band which defines zone I is clearly at 45° as expected from the analytical solution. However, the wedges corresponding to zones II and III are not identified due to the elastic components.

In the case of $\phi = 15°$ (Figure 6.6c), the region involved in the localization process becomes larger, with a higher angle of the slip line for the elastic wedge and for the sliding zone III, as expected. An almost vertical failure line appears starting from the edge of the shallow foundation to the lowest point of the main slip line.

Finally, the case for $\phi = 30°$ is shown in Figure 6.6c. The solution is characterized by a clear definition of the three wedges. The elastic zone is half of an equilateral

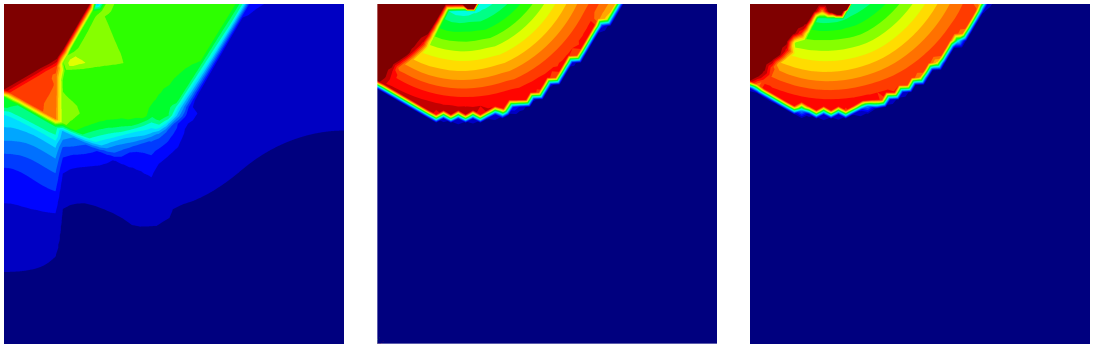

(a) Irreducible - Displacements (b) Mixed $\boldsymbol{u}-\boldsymbol{p}$ - Displacements (c) Mixed $\boldsymbol{\varepsilon}-\boldsymbol{u}$ - Displacements

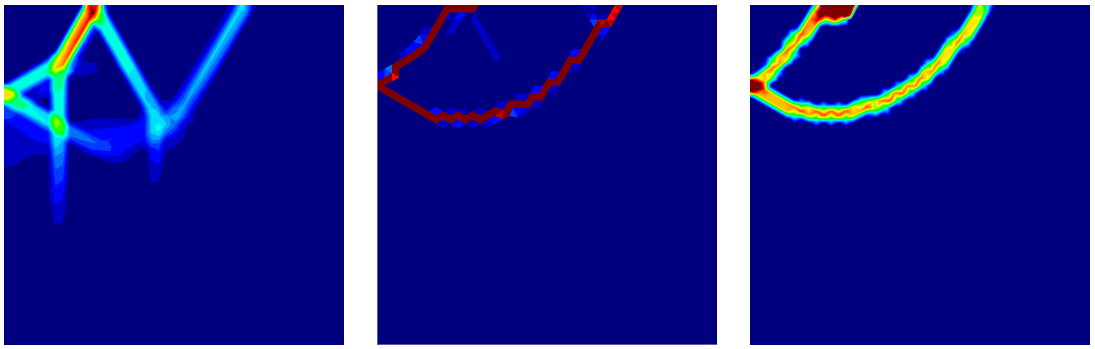

(d) Irreducible - Plastic strains (e) Mixed $\boldsymbol{u}-\boldsymbol{p}$ - Plastic strains (f) Mixed $\boldsymbol{\varepsilon}-\boldsymbol{u}$ - Plastic strains

Figure 6.5: Solution of Prandtl's punch test

triangle as it shows a localization angle of $45° + \phi/2 = 60°$. Then, the rotation wedge has a spiral-like slip line, spanning approximately 90°. Finally, the third zone is a triangular wedge with linear slip lines.

It is shown that the mixed $\boldsymbol{\varepsilon}-\boldsymbol{u}$ is able to provide accurate and rather complex failure mechanisms. The agreement with the theoretical solution is remarkable and it shows a significant mesh objectivity. In addition, the method is able to handle multiple localization lines at the same time. This capability is difficult to achieve with numerical techniques such as crack tracking. Nevertheless, with the proposed formulation, this is achieved without the need of additional modifications.

(a) $\phi = 0°$

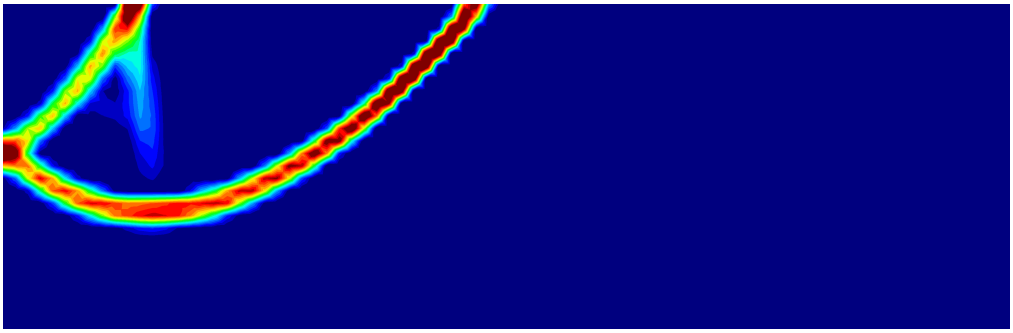

(c) $\phi = 15°$

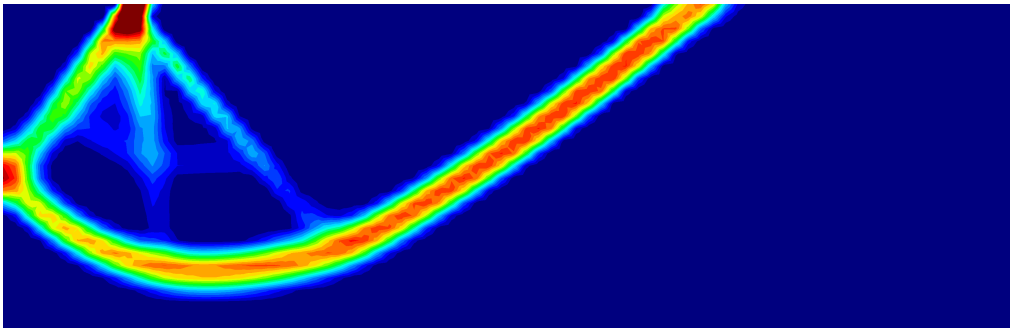

(d) $\phi = 30°$

Figure 6.6: Prandtl's punch problem with Drucker-Prager plasticity: equivalent plastic strain for an internal friction angle $\phi = 0°, 15°, 30°$

6.4 Hollow plate test under tension

The second example consists of a hollow steel plate under tension. In Figure 6.7, the geometry of the problem is presented and, for the case in analysis, the parameter $r = 1$. The single hole is centered so that only a quarter of the domain is discretized. Owing to its double symmetry, the left and bottom contours are constrained respectively in the horizontal and vertical displacements. A vertical displacement u_0 is imposed on the top of the plate.

The constitutive model is Drucker-Prager with four different friction angles: 0°, 15°, 30° and 45°. The solution of the problem is a single slip line starting from the

side of the hole and moving diagonally to the unconstrained side of the specimen. An analytical expression for the localization angle is obtained from Cervera et al. [155] and Wu and Cervera [256].

The results in terms of equivalent plastic strain field are given in Figure 6.8 whereas the computed localization angles are presented in Table 6.1. Remarkable good agreement with the analytical results is observed. The slight variation in their values is due to the resolution of the discretization and to boundary effects.

Plane strain	Analytical [155, 256]	Numerical
$\phi = 0$	$\theta_{loc} = 45.00°$	$\theta_{loc} = 44.32°$
$\phi = 15$	$\theta_{loc} = 40.53°$	$\theta_{loc} = 39.30°$
$\phi = 30$	$\theta_{loc} = 35.07°$	$\theta_{loc} = 33.90°$
$\phi = 45$	$\theta_{loc} = 26.12°$	$\theta_{loc} = 26.90°$

Table 6.1: Results for a the hollow strip under tension: comparison of the analytical localization angles and numerical ones computed with the $\boldsymbol{\varepsilon} - \boldsymbol{u}$ formulation.

Figure 6.9 presents the force-displacement curves for each studied friction angle. The steepness of the response after the peak load depends on the friction angle: the lower the value of ϕ, the faster the softening. Note that, in the proposed Drucker-Prager constitutive law, the softening effects are applied directly to the deviatoric part and, for this reason, higher angles of friction have a less steep inelastic branch.

Finally, Figure 6.10 presents a comparison of the numerical results obtained in the case of mixed displacement-pressure and mixed strain-displacement formulations. Results for the mesh sizes $h = 0.25$ and $h = 0.15$ are given and the dissipated energy for the complete J2 ($\phi = 0$) plastic process is compared.

The theoretical solution suggests a perfectly straight localization band orientated at 45°. The energy dissipated by such solution is 5091 J. By integrating the area under the reaction-displacement curve for the $\boldsymbol{\varepsilon} - \boldsymbol{u}$ formulation, the work done by the external forces is 5210 J. Performing the same computation for the $\boldsymbol{u} - \boldsymbol{p}$ analysis, the total work equals 6723 J. Even if the solution is similar in terms of failure mechanism and localization angle, the displacement-pressure formulation is sensibly more dissipative than the theoretical solution (32.02% difference). Contrariwise, the mixed strain-displacement finite element solution is very close to the analytical value, with just a difference of 2.33%. The enhancement in global post-peak behavior is given by the higher accuracy in the computation of the strains.

It was observed in the previous chapter that the proposed formulation has a convergence rate with respect to the mesh size to a continuum solution which is sensibly faster than the irreducible method. In this example, similar conclusions apply with respect to the $\boldsymbol{u} - \boldsymbol{p}$ formulation.

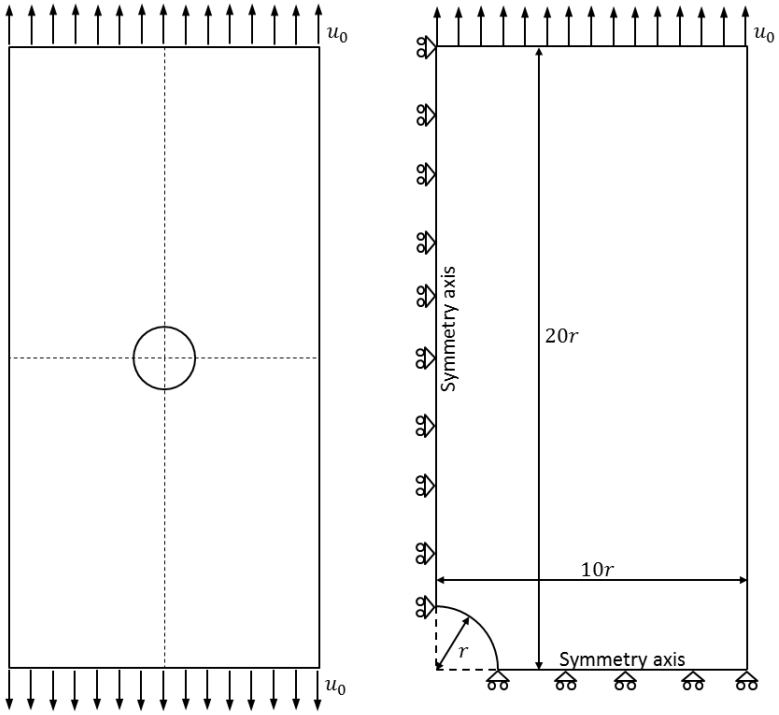

Figure 6.7: Geometry of the steel hollow plate under tension. In this case, the parameter $r = 1$.

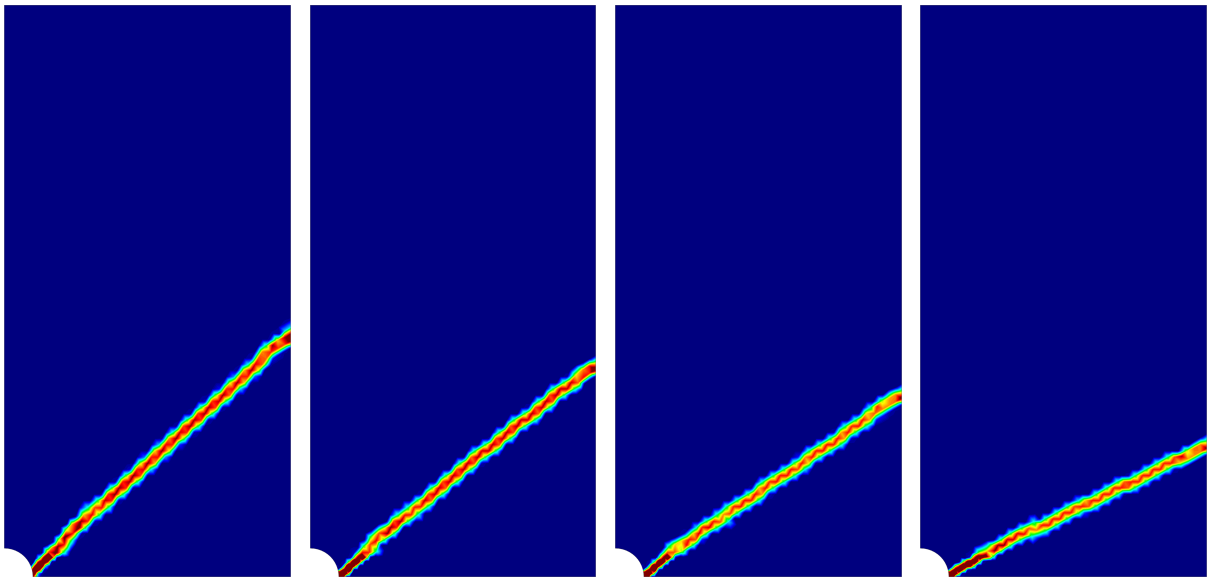

(a) (b) (c) (d)

Figure 6.8: Localization of strain in a hollow strip under tension with $\phi = 0°, 15°, 30°, 45°$.

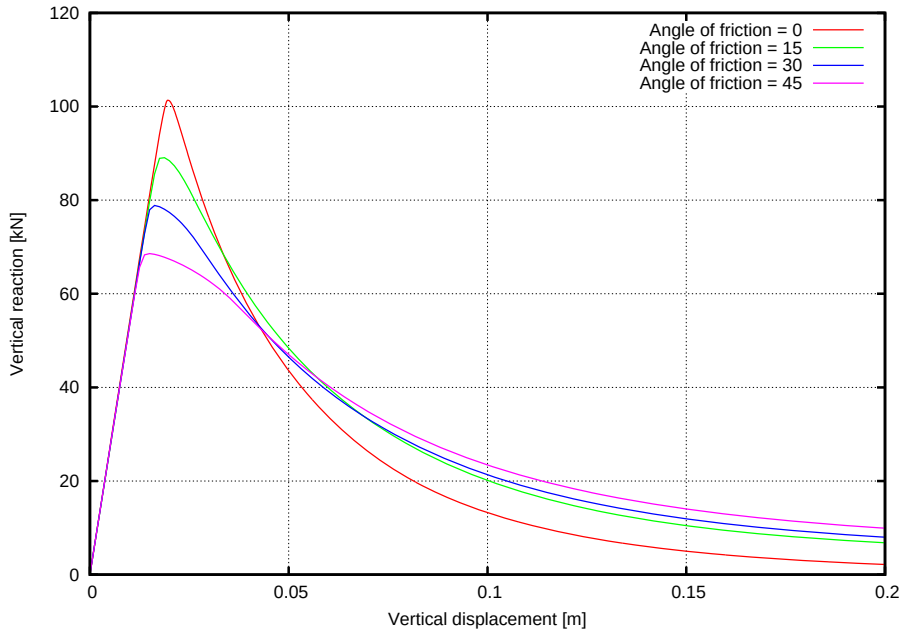

Figure 6.9: Force-displacement curves for the singly perforated strip under tension

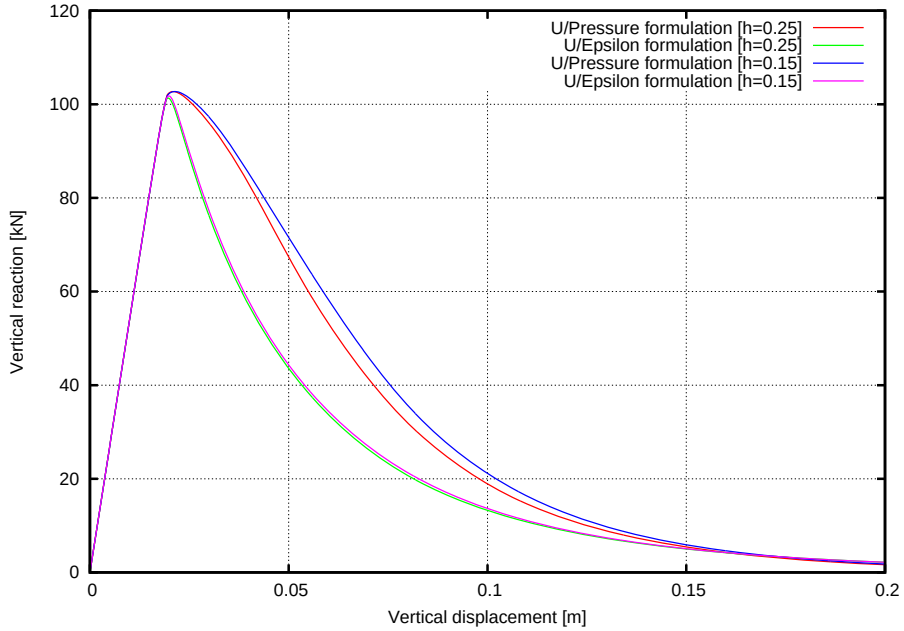

Figure 6.10: Force-displacement curves for the hollow strip under tension with the $\boldsymbol{u} - \boldsymbol{p}$ and $\boldsymbol{\varepsilon} - \boldsymbol{u}$ mixed formulations.

6.5 3D cylinder test under tension

The following example consists in a 3D thin-walled cylinder with a small hole in the front under tension (Figure 6.11). The cylinder is stretched from the top with an imposed displacement u_0. Once again, because of double symmetry, the modeled domain is one quarter of the complete cylinder. The thin walled cylinder is in a state of uniaxial tension, since no hoop or radial stresses appear. The post-peak behavior of the material is described by J2 plasticity ($\phi = 0°$).

The numerical analysis has been performed with the mixed $\boldsymbol{\varepsilon}-\boldsymbol{u}$ strain-displacement and mixed $\boldsymbol{u}-\boldsymbol{p}$ displacement-pressure finite element formulations, using the iterative Newton-Raphson scheme and the same convergence criteria on a mesh of triangular prisms. The cylinder is discretized with a single element in the radial direction. The results in terms of total displacements, equivalent plastic strain, pressure and principal strain vectors are presented in Figure 6.13 whereas the global force-displacement curve is shown in Figure 6.12.

Although both numerical methods predict correctly the global failure mechanism with a helicoidal slip line at about 35°, typical of a plane stress problem, the local solutions are considerably different. In the case of the $\boldsymbol{\varepsilon} - \boldsymbol{u}$ elements, a single localization line appears, with a clear concentration of strains in the slip band. The pressure field is also homogeneous. On the contrary, the solution given by the $\boldsymbol{u} - \boldsymbol{p}$ method shows a spurious stepped localization. This result is due to the

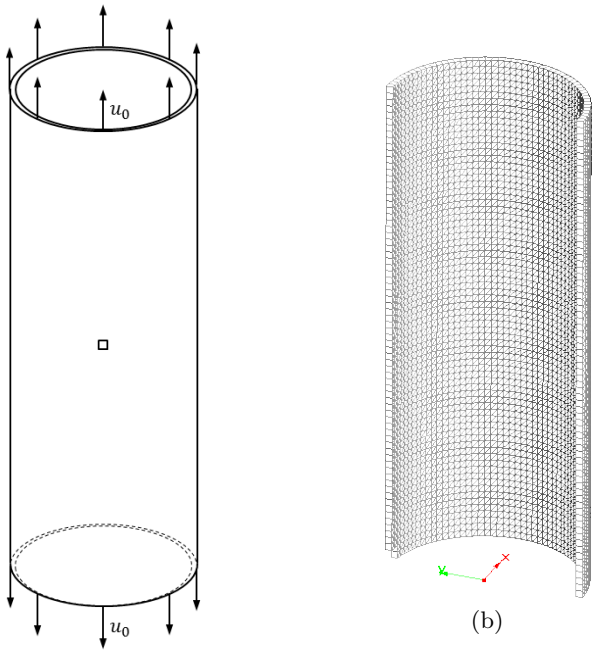

Figure 6.11: Geometry and computational mesh for the 3D cylinder test under tension

discontinuous approximation of the deviatoric strains, that results in a physically unrealistic numerical solution. Note that this outcome cannot be improved by refining the mesh since the error norm of the local stress in the displacement-pressure formulation does not depend on the element size (see [5, 6]).

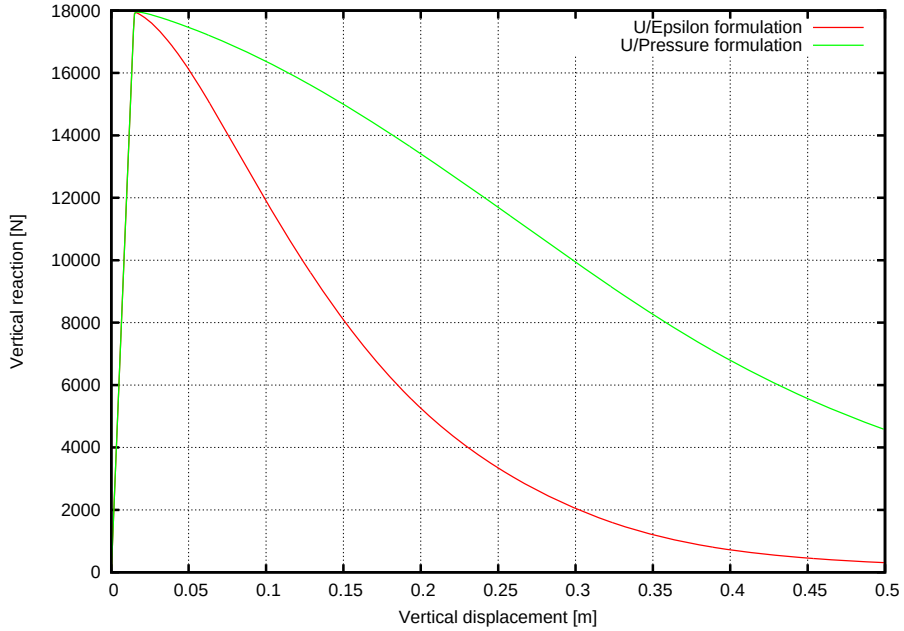

Figure 6.12: Comparison of force-displacement curves for the $\boldsymbol{u} - \boldsymbol{p}$ and the $\boldsymbol{\varepsilon} - \boldsymbol{u}$ mixed formulations.

In the force-displacement curves of Figure 6.12, the overly dissipative behavior of the $\boldsymbol{u} - \boldsymbol{p}$ method with respect to the $\boldsymbol{\varepsilon} - \boldsymbol{u}$ finite elements is clearly exhibited. The higher accuracy of the proposed mixed formulation is due to two correlated facts: (i) the independent solution of the strain field allows the stresses to have at least a linear order of convergence with respect to mesh refinement; (ii) the continuity of the strains enforces the continuity of the localization band, which, in turn, precludes the appearance of spurious discontinuous solutions.

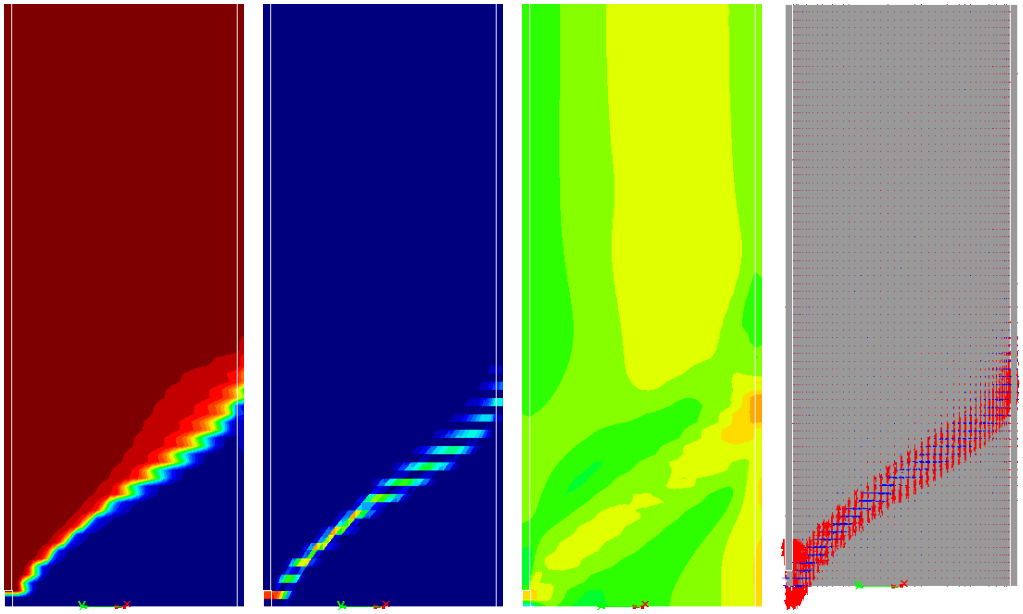

(a) (b) (c) (d)

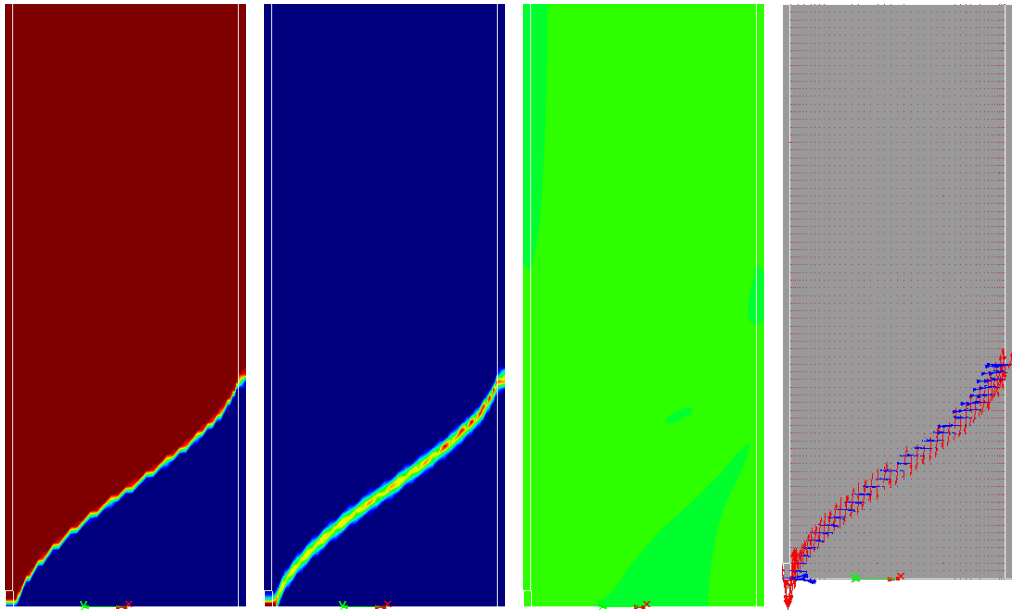

(e) (f) (g) (h)

Figure 6.13: Comparison of solutions of the 3D cylinder under tension with the $\boldsymbol{u}-\boldsymbol{p}$ and the $\boldsymbol{\varepsilon}-\boldsymbol{u}$ formulations. Mixed displacement-pressure solution for (a) vertical displacements, (b) deviatoric plastic strains, (c) pressure and (d) principal strain vectors. Mixed strain-displacement solution for (e) vertical displacements, (f) deviatoric plastic strains, (g) pressure and (h) principal strain vectors.

This page is left intentionally blank.

Chapter 7

Failure under mode III and mixed mode loading

7.1 Introduction

This chapter is dedicated to the application of the proposed $\boldsymbol{\varepsilon} - \boldsymbol{u}$ strain-displacement formulation to problems involving failure under mode III and mixed mode loading in quasi-brittle materials.

Mode III fracture is also known as tearing mode. With respect to the crack path, mode I is characterized by orthogonal separation whereas mode II by the sliding of the two crack surfaces. In turn, mode III is given by the relative rotation of said surfaces. A shear force acting parallel to the plane of the crack but orthogonal to the crack propagation direction results in shear stresses arising parallel to the crack front. This loading condition causes a mode III failure mechanism. Tearing is also known as out-of-plane shear loading.

Mode III loading occurs in non-uniform torsion and asymmetrical bending, where shear stresses appear orthogonal to the plane of the applied forces. However, having experimental tests which consist of pure mode III loading is not straightforward.

In cementicious materials (such as concrete) subjected to pure shear, aggregate interlock and other friction effects occur in the planes subjected to shear, bringing about a significant shear strength. Contrariwise, planes at 45° with respect to the shear stress are subjected to (pure) tension. As the aggregate-cement paste interface and the paste itself are characterized by a low tensile strength, failure in Mode I along this plane is far easier than in Mode II by sliding or Mode III by tearing. Consequently, even in the case of Mode II or III loading, it is common to have failure in Mode I.

Moreover, due to the eventual different orientation of the load with respect to the fracture, a rotation of the stress field from mode II/III to mode I can be observed. The simultaneous application of various loading modes is called mixed mode loading.

Likewise, the onset of fracture due to the combined effect of shear (mode II/III) and tension (mode I) is called mixed mode fracture.

There is a vast literature regarding mode III and mixed mode testing of quasi brittle materials [257–261] and the corresponding theoretical treatment [262–265]. Although the use of Linear Fracture Mechanics in such cases effectively provides useful quantitative assessment of the stress intensity factor and the strain energy near the tip of an evolving crack, it has limitations when dealing with elaborated geometries and it does not provide either the crack shape or the global force-displacement behavior. Hence, a numerical method such as the Finite Element Method is required to model a complex 3D problem with cracks exhibiting twisting rotation.

In the following, the behavior of quasi-brittle materials under mixed mode loading conditions is studied using Rankine's and Drucker-Prager's failure criteria, implemented in both plasticity and isotropic continuum damage format. As it was presented in the previous chapters, Rankine's surface is used to model crack formation due to tensile stresses whereas Drucker-Prager's one is used for materials whose maximum shear stress is pressure dependent. In this way, the transition from mode III to mode I fracture can be studied by means of Rankine's failure criterion, whereas Drucker-Prager's constitutive law allows the study of the transition to mode II. Rankine's model was presented in Section 5.3 and depicted in Figure 5.1 while Drucker-Prager's one was discussed in Section 6.2 and sketched in Figure 6.3.

The plasticity framework provides directional inelastic behavior, with the associative plastic flow which is orthogonal to Rankine's and Drucker-Prager's failure surface. Instead, the isotropic continuum damage model provide a reduction of the carrying capability without the dilatancy effect of associative plasticity. A summary of the constitutive models used is presented in Table 7.1.

In the next sections, three example tests on beams with a 45° skew notch at the midspan are presented: (a) a three point bending test of a PolyMethyl MethaAcrylate

	Associative plasticity model	Isotropic continuum damage model
Constitutive equation	$\boldsymbol{\sigma} = \mathbb{C} : (\boldsymbol{\varepsilon} - \boldsymbol{\varepsilon}_p)$	$\boldsymbol{\sigma} = (1-d)\,\mathbb{C} : \boldsymbol{\varepsilon}$
Softening function	$q = q(\xi)$	
Inelastic criterion	$f(\boldsymbol{\sigma}, q) = \tau(\boldsymbol{\sigma}) - (\sigma_y - q)$	
Internal variables evolution	$\dot{\xi} = \dot{\lambda},\ \dot{\boldsymbol{\varepsilon}}_p = \dot{\lambda}\frac{\partial f}{\partial \boldsymbol{\sigma}}$	$\dot{\xi} = \dot{\lambda},\ d(\xi) = 1 - \frac{q}{\xi}$
Loading-unloading conditions	$\dot{\lambda} \geq 0,\ f(\boldsymbol{\sigma}, q) \leq 0,\ \dot{\lambda} f(\boldsymbol{\sigma}, q) = 0$	

Table 7.1: Summary of associative plasticity and isotropic continuum damage models.

(or Plexiglas) beam, (b) torsion test of a prismatic beam with square base made of plain concrete, (c) a cylindrical beam under torsion as well.

7.2 Three point bending test

A PolyMethyl MethaAcrylate beam with a 45° skew notch at the midspan undergoes a three point bending test [260, 266]. The geometry of the test is shown in Figure 7.1. The initial diagonal flaw is responsible of asymmetric bending which results in mode III loading. However, since the Plexiglas tends to fracture due to tensile stresses, the characteristic behavior found in the test is a transition from mode III to mode I. As the experiment progresses, a rotation of the crack front is appreciable and the resulting failure surface aligns with the midspan plane of the beam (Figure 7.2).

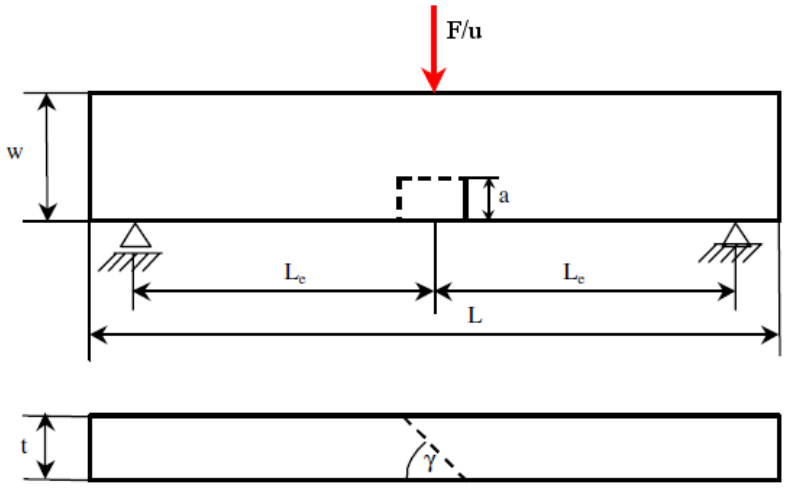

Figure 7.1: Geometry of the three point bending test on a skew-notched beam.

The numerical analysis aims to compare the results from the mixed strain-displacement $\boldsymbol{\varepsilon} - \boldsymbol{u}$ and the $\boldsymbol{u}$ standard irreducible finite elements. In order to take into account the nonlinear mechanical behavior, Rankine's failure criterion is implemented in both plasticity and isotropic continuum damage formats. It is interesting to test the two constitutive model on the same numerical example since, due to the nature of the experiment, a similar crack surface due to mode I fracture is expected to appear independently from the two methods.

Plotting the computed isosurface corresponding to the crack surface, the closeness of the experimental and the mixed formulation results are evident (Figure 7.2). The crack front starts from opposing corners of the initial notch. Then, it rotates and finally aligns with the vertical plane of the midspan of the beam.

Figure 7.3 presents a detail of the mesh used in the vicinity of the initial notch and the resulting failure mechanism prediction of both the mixed and the irreducible finite elements. As anticipated, the $\boldsymbol{\varepsilon} - \boldsymbol{u}$ provides a similar solution for both the

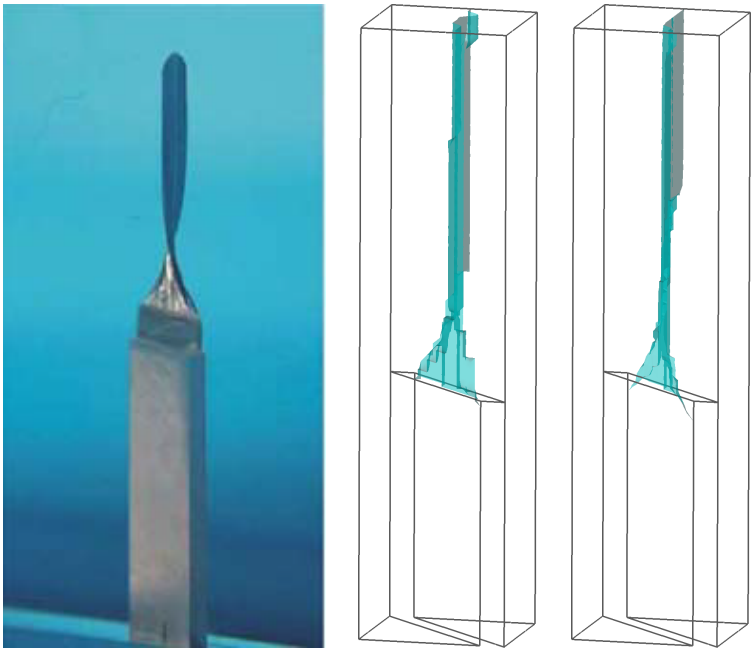

(a) Experiment (b) IsoDamage (c) Plasticity

Figure 7.2: Experimental [265] and numerical ($\boldsymbol{\varepsilon} - \boldsymbol{u}$ formulation) crack surface of the three point bending test on PMMA.

plasticity and the isotropic continuum damage cases. Contrariwise, the displacement based FE formulation yields a significantly mesh-biased solution. In the case of isotropic continuum damage, a single localization band appears from the notch and propagates along the vertical direction of the mesh. However, the twisting rotation of the crack surface is very small. Furthermore, in the case of plasticity, multiple fracture surfaces appear and almost no rotation of the failure surface is observed. The slight asymmetry in the localization band is due, on the one hand, to the orientation of the structured mesh and, on the other hand, to the use of a pure tensile failure criterion, which does not allow the crack surface to cross the compression head at the top of the beam.

Finally, the experimental crack shape is depicted in Figure 7.4, to be compared with the numerically computed ones. Firstly, it is possible to notice that the limited number of elements in the direction of the crack path causes the failure surface profile to be defined piecewise. Nevertheless, the difference between mixed and irreducible formulations is obvious. All the cases show a crack propagating in a diagonal fashion in the vicinity of the notch. However, as the crack grows, the displacement-based finite elements are suddenly locked to the vertical direction as the solution is strongly mesh biased. Contrariwise, the $\boldsymbol{\varepsilon} - \boldsymbol{u}$ elements predict the crack to gradually align with the vertical direction, agreeing with the experimental tests. Consequently, the improved kinematic capabilities of the mixed formulation allow

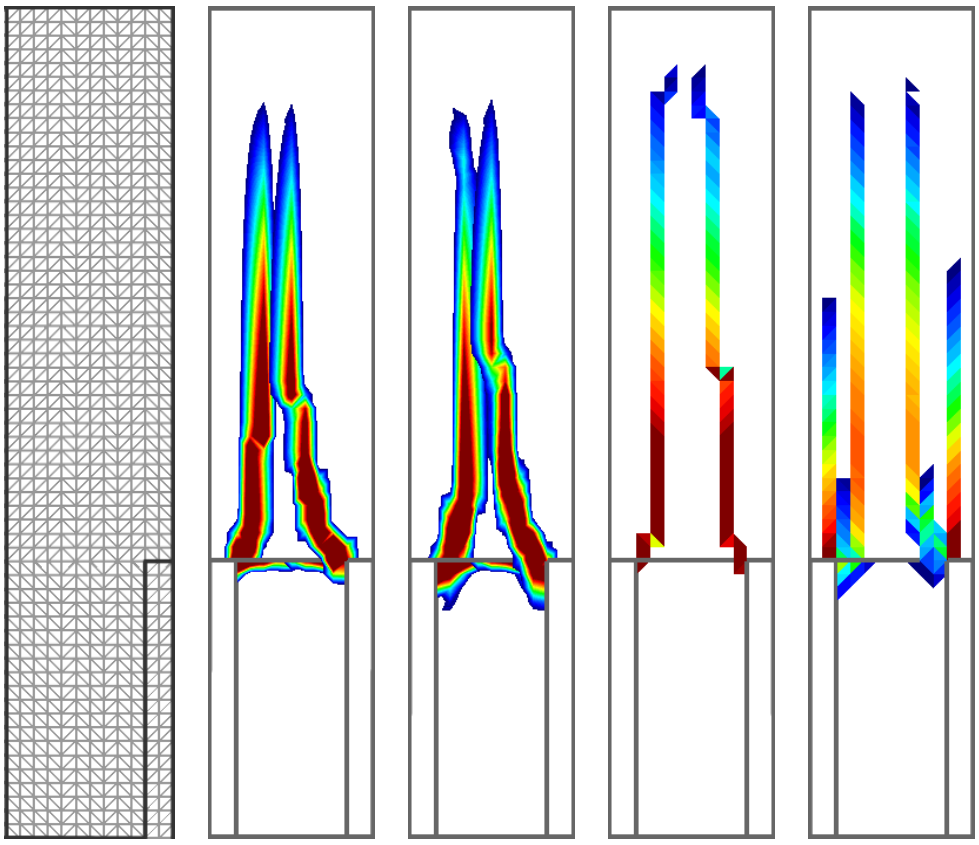

(a) Detail of the structured mesh in the middle region

(b) $\boldsymbol{u} - \boldsymbol{\varepsilon}$ with IsoDamage

(c) $\boldsymbol{u} - \boldsymbol{\varepsilon}$ with Plasticity

(d) $\boldsymbol{u}$ with IsoDamage

(e) $\boldsymbol{u}$ with Plasticity

Figure 7.3: Contour fills of major principal total strain at the front and back faces of the beam under three point bending test.

to compute consistently the complex evolution of the failure surface without being distinctly affected by the relatively coarse computational grid and, in particular, by the alignment of the elements.

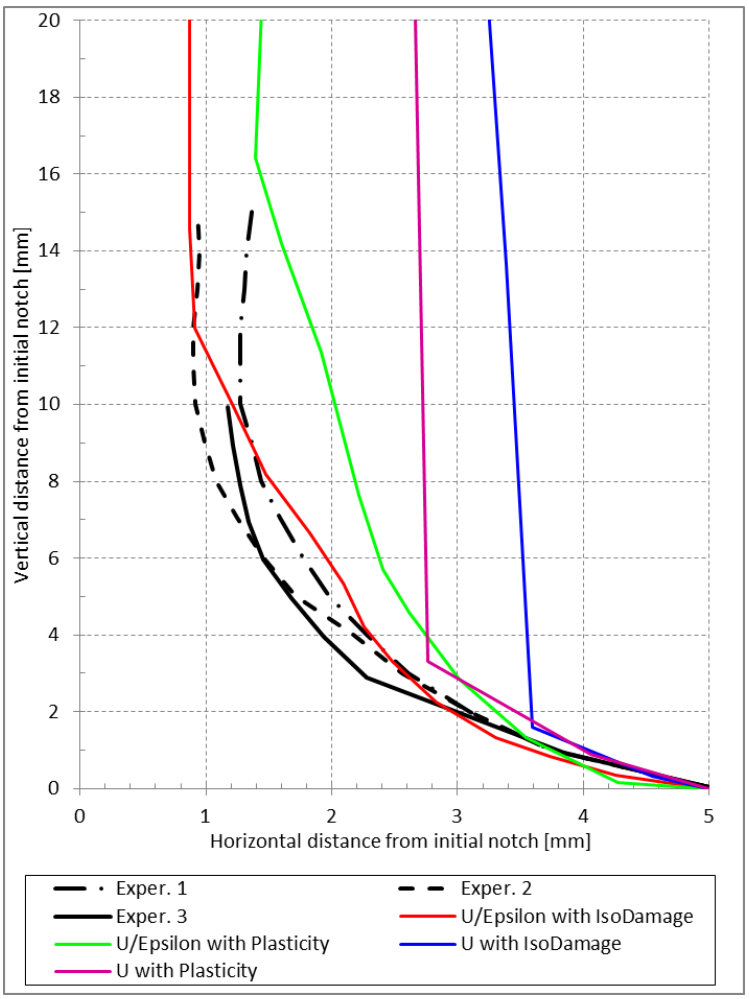

Figure 7.4: Plot of the computed crack path with respect to the experimental data from Citarella and Buchholz [267].

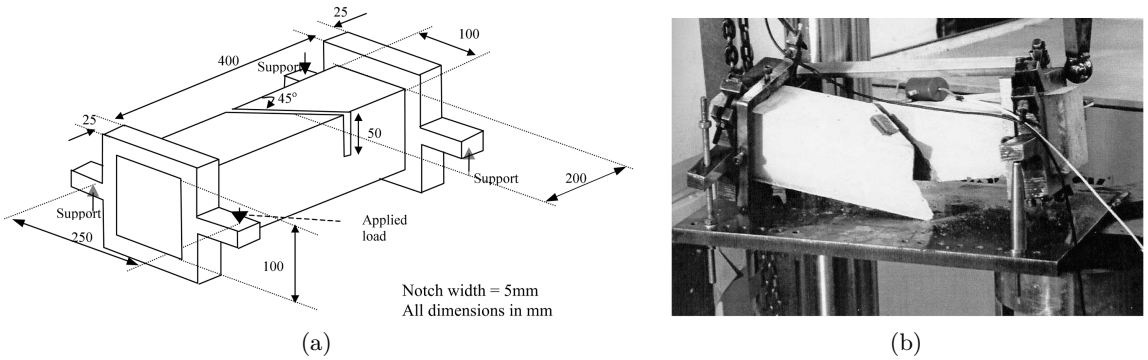

(a) (b)

Figure 7.5: Geometry and experimental setup of the tests on prismatic beam under torsion with square cross section, from Jefferson et al. [268].

7.3 Torsion test of a prismatic beam with square base

The following example consists in a prismatic beam with a 45° slanted notch which is subjected to torsional loading. The test setup is illustrated in Figure 7.5. The test is performed to evaluate the tensile strength and the post-peak behavior of unreinforced concrete specimens. The external force is exerted by a steel frame with four appendages. On three of these, minimal boundary conditions to avoid rigid movements are applied. The fourth one is loaded with an imposed displacement which provide the desired torsional force on the specimen.

It is worth noting how the slanted notch causes the specimen to be in a state of non-uniform torsion. The sudden change in cross-section creates a concentration of shear stresses in the vicinity of the cut. Considering tensile fracture as the main cause for the crack appearance in the unreinforced concrete, it is possible to numerically model this experiment with a Rankine failure criterion. In particular, it is interesting to study the difference of results that the plasticity and the isotropic continuum damage provide in this experimental setting. All numerical tests are performed with the mixed strain displacement finite element method. The FE mesh has been divided in three separate zones. Exploiting the compatibility condition, the center part is discretized with mixed elements whereas the lateral parts and the frames consists of standard displacement-based elements in order to significantly reduce the computational time.

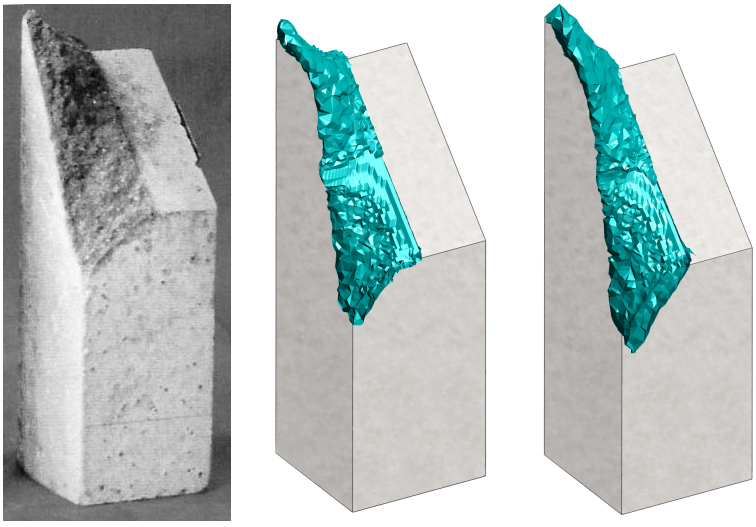

(a) (b) (c)

Figure 7.6: Comparison of (a) the experimental outcome with the computed crack surfaces in the case of (b) isotropic damage and (c) plasticity for the prismatic beam with square cross section.

As it possible to see in Figure 7.6, the crack surface provided with the plasticity and damage settings are comparable. Owing to the fact that the problem is skew-

symmetric with regard both the mid-span and the mid-longitudinal planes of the beam, the predicted crack surface is skew-symmetric as well. The crack starts at the diagonal notch and propagates to the bottom of the beam. With respect to the experimental outcome, both constitutive models predict the failure mechanism accurately. A slight difference in the solution is given by a more curved surface in the isotropic continuum damage with respect to the plasticity one.

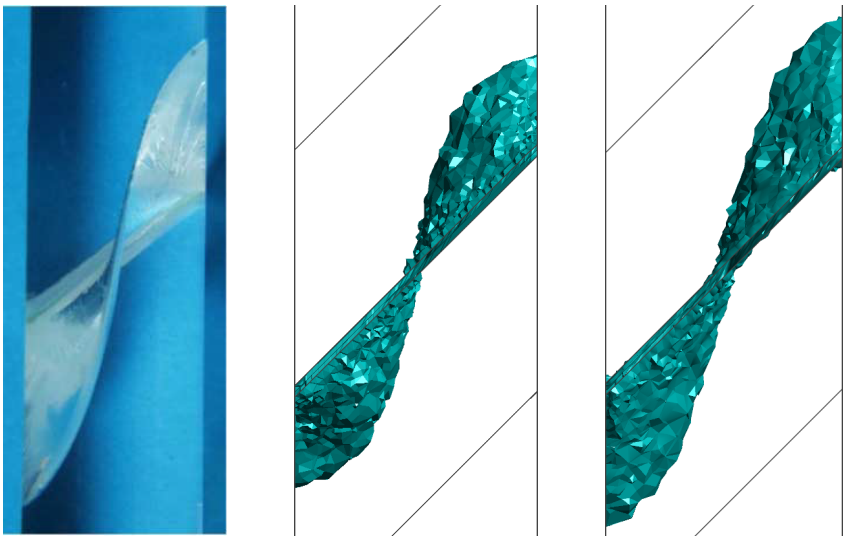

(a) (b) (c)

Figure 7.7: Top views of the crack surface from (a) tests on PMMA [269], (b) isotropic damage and (c) plasticity.

Figure 7.7 shows the computed crack shape from a top perspective. The crack surface is clearly skew-symmetric and it is characterized by two features. The central part is planar and it crosses the geometrical middle point of the specimen. As the crack nears the border, its bottom profile turns, intersecting at a certain angle the external surface of the beam. This evidences that, even if the failure is due to pure tensile stress, there is a substantial rotation in the principal strains, typical of a mixed mode loading condition. Moreover, skew-symmetry is kept at all times.

Although the plasticity and the isotropic damage models appear to yield almost identical results, there is a key difference in their numerical solutions. Figure 7.8 shows the plot of the force applied to the free appendage of the steel frame with respect to the crack mouth open displacements (CMOD) in the orthogonal and parallel directions to the notch.

The analysis characterized by the isotropic continuum damage model presents a very good capture of the peak load value. The subsequent inelastic branch is characterized by a strain softening in good agreement with the experimental values. In fact, the structure of this constitutive model implies a uniform reduction of the all principal stresses, both tensile and compressive, upon damage.

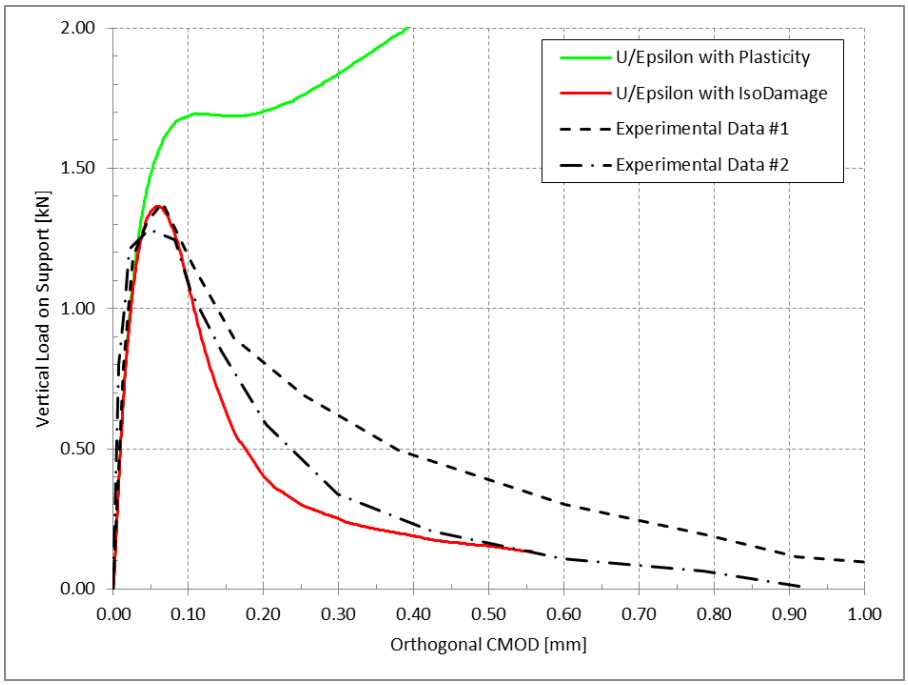

(a)

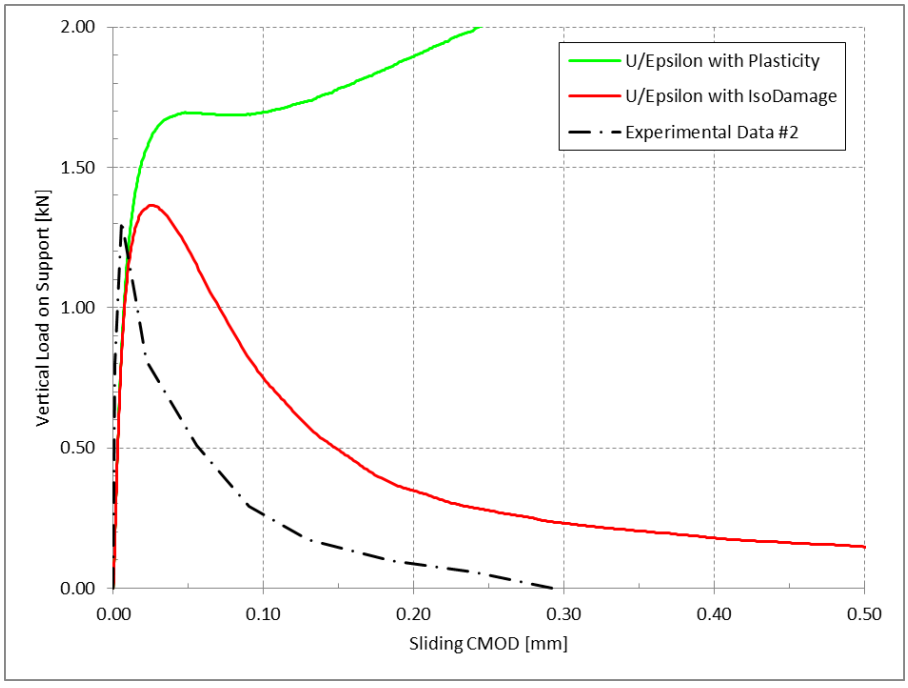

(b)

Figure 7.8: Plots of vertical force versus (a) orthogonal CMOD and (b) sliding CMOD

Contrariwise, the numerical results given by the plasticity case show an initial stress plateau followed by a nonlinear behavior marked by an increase of the applied force. In plasticity, the inelastic deformation grows in the direction given by the gradient of the plastic potential which, in the case of associativity, is represented by the failure surface itself. The corresponding reduction of the stresses depends on the Poisson's ratio of the material. For null Poisson's ratio, the reduction of stresses is oriented as the plastic strain flow, but when it is not null, significant changes occur in the stresses in the orthogonal directions. As this orthotropic behavior emerges during the softening process, the reduction of forces is not necessarily ensured. In the numerical analysis of the skew notched prismatic beam under torsion, the Poisson's effect generates residual compressive stresses around the crack, as it can be observed in Figure 7.9. As the boundary conditions do not allow the specimen to extend, an increase of the longitudinal compressive force is observed as result of the cracking.

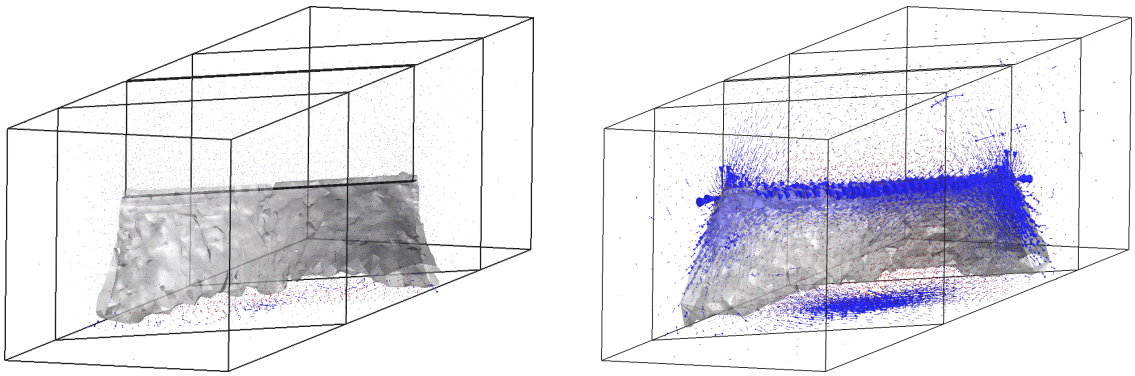

(a) (b)

Figure 7.9: Residual principal stresses in the (a) isotropic damage and (b) plasticity cases. Blue vectors represents compressive stress, red vectors represents tensile stress.

7.4 Torsion test of a cylindrical beam

Similarly to the previous case, this experiment consists in testing the resistance of a cylindrical specimen with a 45° skew notch at midspan. The details of the test geometry are presented in Figure 7.10. Although the material is plain concrete, the experimental results in [268] report that the second batch of plain concrete for the cylindrical beams has not been tested for Young's elastic modulus or fracture energy. Likewise, the loading process is performed using an equivalent steel frame with four appendages.

Non-uniform torsion is expected to appear in this test as well. However, it is important to notice that, if the specimen was unnotched, an imposed external torsion would result in a uniform stress without any warping involved, due to the circular

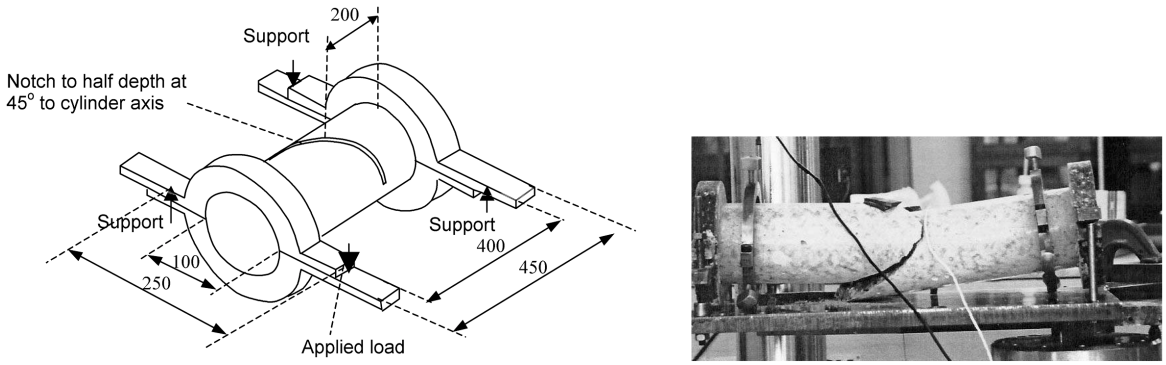

Figure 7.10: Geometry and experimental setup of the tests on cylindrical beam under torsion, from Jefferson et al. [268].

geometry of the bases. For this reason, the stress field in the concrete can differ from the previous tests on prismatic beams.

Initially, the problem is studied with the Rankine failure criterion as in the previous example. The final shape of the fracture surface for the isotropic continuum damage and plasticity models is presented in Figures 7.11a and 7.11b, respectively. The crack is very similar to the previous case, with a skew-symmetric form. However, due to the curved geometry of the cylinder, the slip line on the external surface tends to twist more than in the respective prismatic beam test. In Figure 7.12, the global response of the cylinder with respect to the orthogonal and parallel CMOD. Once again, the plasticity model shows an increasing reaction force in the inelastic range, whereas the isotropic continuum damage shows a consistent softening behavior. However, in this case, the Rankine failure criterion results in a higher peak load than the experimental value.

The test of concrete beams under torsional load shows a mode III stress state, with high values of shear around the skewed notch. Since concrete fails primarily under tension, the failure mode shows a change from mode III to mode I.

In the dedicated literature, it is known that similar experiments can involve also shear stresses under certain conditions (e.g. [262, 265]). In particular, in the work of Yates and Mohammed [261], it is stated that the geometrical features of the initial notch, such as orientation, depth or inclination, cause different failure modes in the specimen. In particular, it is possible to have a stress state typical of mixed I+II+III modes.

Next, the Drucker-Prager failure surface with $\phi = 45°$ friction angle is introduced to test if the interdependence between shear and pressure is significant. Figure's 7.11c and 7.11d present the failure surfaces provided by the isotropic continuum damage and plasticity models, respectively. The predicted failure surface for Drucker-Prager is significantly less rounded than for the Rankine criterion. However, the "S" shape

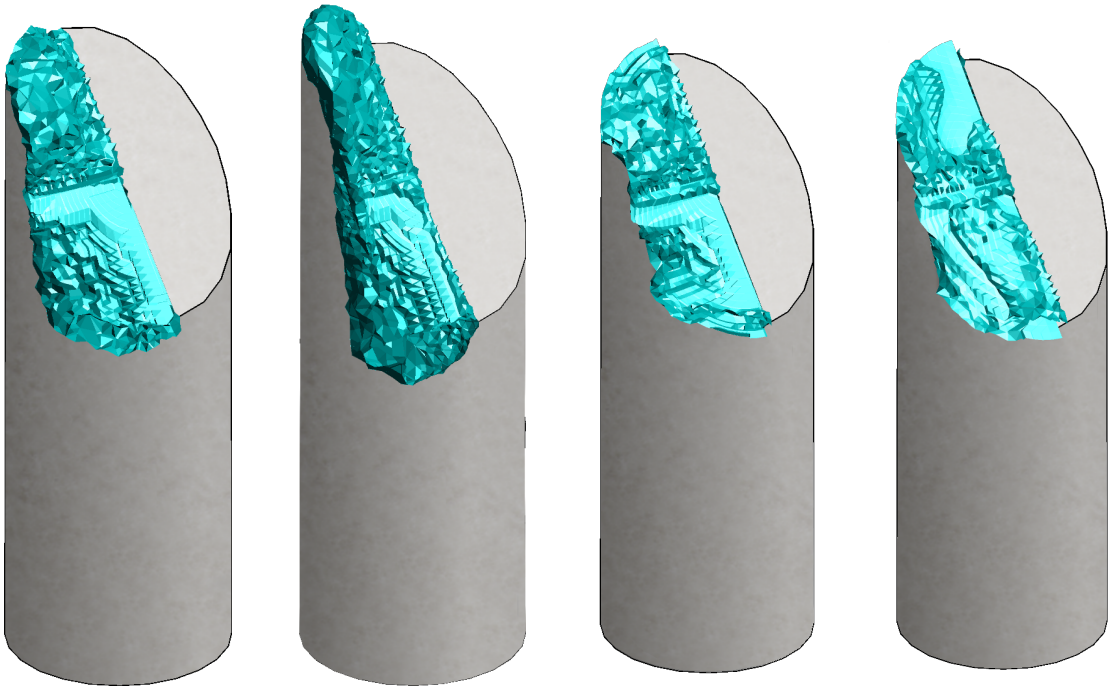

(a) (b) (c) (d)

Figure 7.11: View of the crack surface at the end of the analysis from (a) Rankine's isotropic damage, (b) Rankine's plasticity, (c) Drucker-Prager's isotropic damage and (d) Drucker-Prager's plasticity solutions.

as well as the skew-symmetry are maintained.

In Figure 7.13, the applied force is plotted against orthogonal and parallel CMODs. Both plasticity and isotropic continuum damage formats provide a monotonic reduction of carrying capability of the specimen. There is a slight difference in the stiffness of the reported experimental curve with respect to the numerical one. However, the mechanical properties of the concrete were not directly evaluated for the test of cylindrical beams and, in the proposed numerical simulations, the same values as for the prismatic beam are used. The peak load is found to agree with the experiments, especially using the isotropic continuum damage model. The softening branches are similar in the numerical analysis and the tests.

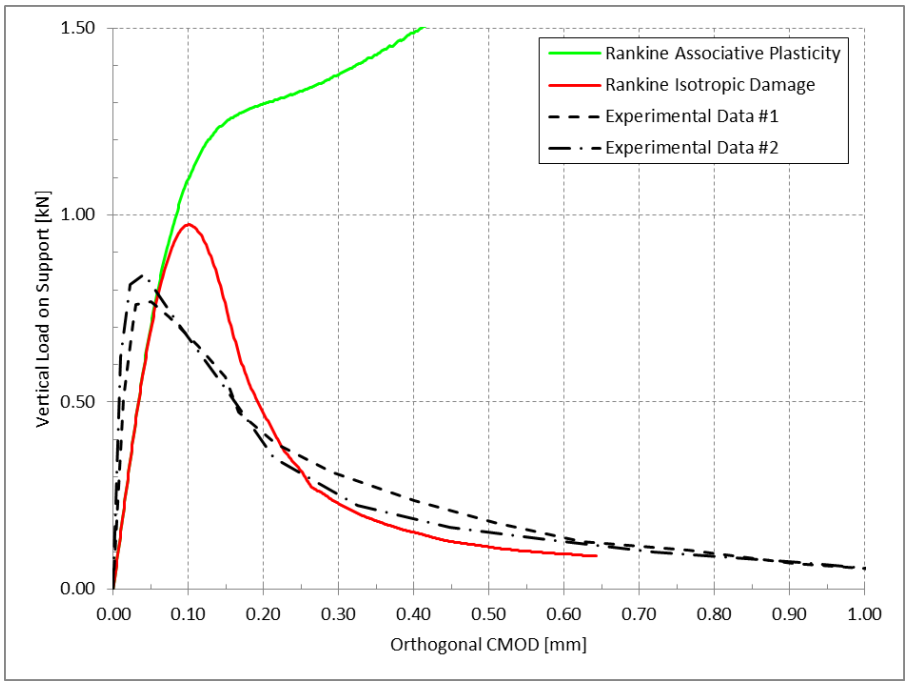

(a)

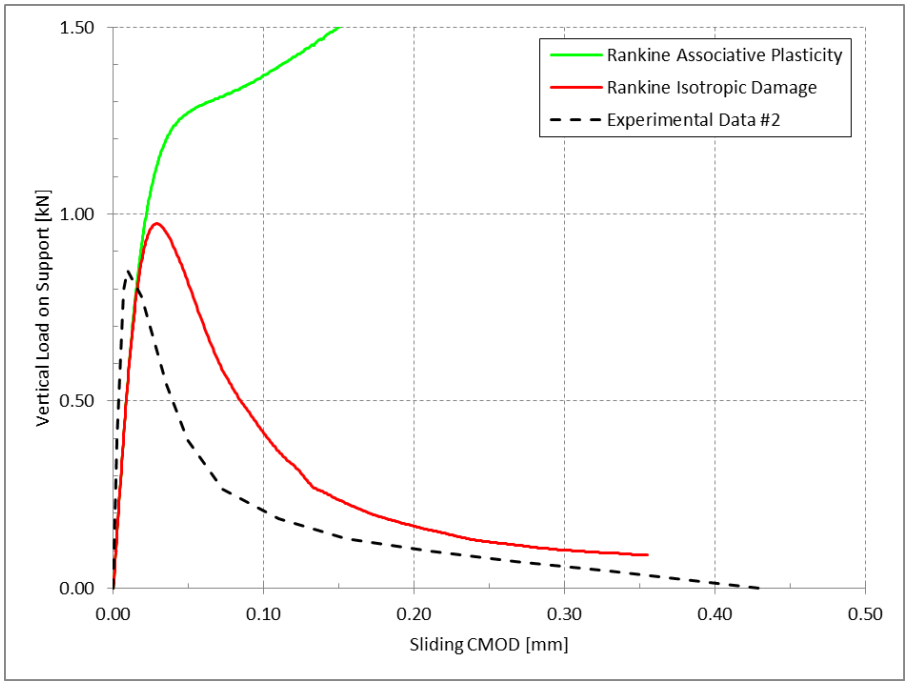

(b)

Figure 7.12: Plots of vertical force versus (a) orthogonal CMOD and (b) sliding CMOD using Rankine's failure criterion

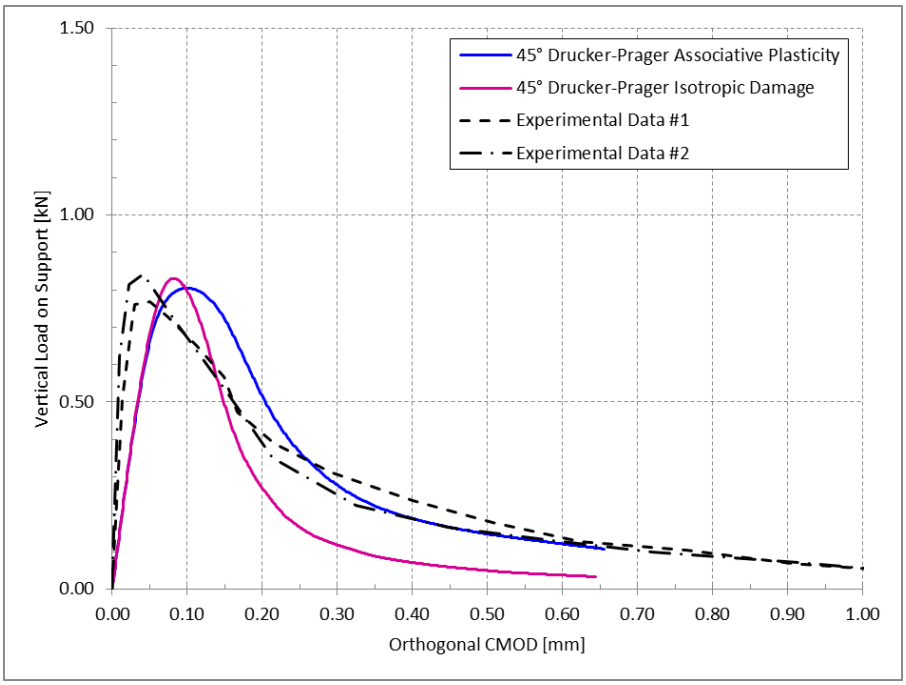

(a)

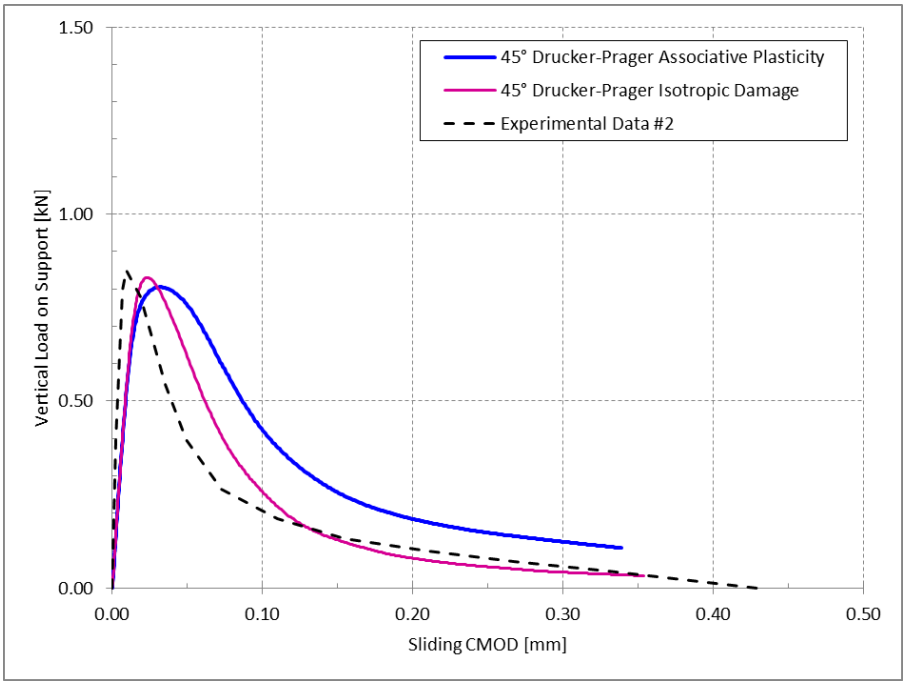

(b)

Figure 7.13: Plots of vertical force versus (a) orthogonal CMOD and (b) sliding CMOD using Drucker-Prager failure criterion with 45° friction angle

7.5 Computational pay-off of kinematic compatibility and iterative procedure

The computational time and memory requirements for the last two examples are presented in the following tables. Three different finite element technologies are considered: full mixed $\boldsymbol{\varepsilon}-\boldsymbol{u}$, combined kinematically compatible mixed and irreducible FE and full displacement-based standard $\boldsymbol{u}$ formulations. In the first one, the whole mesh consists of mixed elements and, for this reason, it is the most demanding from the computational point of view. The second one combines compatible elements in the same mesh; its performance pay-off will be benchmarked. Finally, the third one, with the standard irreducible only, is the less demanding.

These numerical analysis are run on a desktop computer with 8 GB of RAM and a dual core CPU clocking at 2.83 GHz.

The prismatic skew notched concrete beam under torsion is calculated with a mesh of 67,038 elements. When the combined formulation is used, the computational grid is composed of 9,783 irreducible and 57,255 mixed finite elements. Table 7.2 shows a substantial reduction in computational time for the proposed methodology. Similarly, the RAM usage is slightly reduced. The irreducible formulation is added for reference, as the corresponding results are generally deficient.

Formulation	Solver	t_{fact}	n_{iter}	t_{iter}	t_{step}	RAM
Full mixed $\boldsymbol{\varepsilon}-\boldsymbol{u}$ formulation (67,038 elements)	Newton-Raphson	71	3	71	213	5660
	Secant scheme	55	10	2	75	2833
Mixed $\boldsymbol{\varepsilon}-\boldsymbol{u}$ and irreducible $\boldsymbol{u}$ (57,255 + 9,783 elements)	Newton-Raphson	61	3	61	183	4129
	Secant scheme	51	10	2	71	2065
Irreducible $\boldsymbol{u}$ (67,038 elements)	Newton-Raphson	7	3	7	21	683
	Secant scheme	6	10	2	26	369

Table 7.2: CPU time (in seconds) and RAM memory requirements (in MB) in the prismatic skew notched concrete beam under torsion. The proposed method is compared with the full mixed and full irreducible formulations. Likewise, the Newton-Raphson and Secant schemes are compared per first iteration factorization time, number of iterations and step average time.

The cylindrical skew notched concrete beam under torsion is modeled with 62,309 elements. In the case of combination of kinematically compatible FE, the mesh is subdivided in 53,876 mixed and 8,433 irreducible elements. CPU time gains are similar to the ones observed for the prismatic beam case.

Note that using the irreducible formulation in only 14 % of the total number of elements translates directly in a 14 % pay-off of CPU time per step in the Newton-Raphson, and 5.6 % in the Secant method. In analyses where the ratio of irreducible to mixed elements can be greater, the gain increases correspondingly.

Moreover, for each case, the performance of the Newton-Raphson solver is

Formulation	Solver	t_{fact}	n_{iter}	t_{iter}	t_{step}	RAM
Full mixed $\boldsymbol{\varepsilon} - \boldsymbol{u}$ formulation (62,309 elements)	Newton-Raphson	65	3	65	195	4459
	Secant scheme	50	8	2	66	2232
Mixed $\boldsymbol{\varepsilon} - \boldsymbol{u}$ and Irreducible $\boldsymbol{u}$ (53,876 + 8,433 elements)	Newton-Raphson	54	3	54	162	3334
	Secant scheme	45	8	2	61	1668
Irreducible $\boldsymbol{u}$ (62,309 elements)	Newton-Raphson	6	3	6	18	546
	Secant scheme	6	8	2	22	299

Table 7.3: CPU time (in seconds) and RAM memory requirements (in MB) in the skew-notched cylindrical beam under torsion. The proposed method is compared with the full mixed and full irreducible formulations. Likewise, the Newton-Raphson and Secant schemes are compared per first iteration factorization time, number of iterations and step average time.

compared with the Secant scheme. The first one requires a lower number of iterations per step thanks to the quadratic convergence given by the consistently linearized global matrix. Nevertheless, each iteration requires the solution of the full updated algebraic system which, as in this case, can not be symmetric.

Contrarily, the modified Secant scheme updates the global matrix only at the beginning of each step and then it iterates using the already factorized system. Although the rate of convergence is linear and more iterations are needed, it results in a faster procedure. In both of the proposed examples, the computational time for the secant solver is less than half of the Newton-Raphson for the same convergence tolerance, which is set to 10^{-3} with respect to the residual forces. Moreover, the symmetry of the matrix reduces the required memory to almost half.

Chapter 8

Fracture and crack propagation in snowpack layers

8.1 Introduction

In this chapter, the link between the work done at the Technical University of Catalonia (UPC), in partnership with the International Center for Numerical Method in Engineering (CIMNE) in Barcelona (Spain), and the research performed in the Federal Research and Training Centre for Forests, Natural Hazards and Landscape BFW in Innsbruck (Austria), in the framework of the MUMOLADE project is presented. The objective of the stay at BFW has been the analytical and numerical study of the crack propagation in weak snowpack layers. In particular, the Propagation Saw Test has been taken as study case. An analytical model has been developed and compared with the numerical analyses based on the mixed $\boldsymbol{\varepsilon} - \boldsymbol{u}$ finite element method.

(a) (b)

Figure 8.1: Destructive effects of snow avalanches.(a) The aftermath of the 1999 snow avalanche in Galtur (Tyrol, Austria). (b) The results of the recent snow avalanche in Farindola (Abruzzo, Italy) in 2017.

(a) (b) (c)

Figure 8.2: Example of (a) loose snow avalanche, (b) slab avalanche and (c) glide avalanche, from EAW [274].

Snow avalanches are one of the most catastrophic natural events to be found in alpine zones [270, 271]. They initiate when large volumes of snow detach from the surrounding snowpack due to natural or artificial causes. The weight of the snow layers is usually sustained by the cohesive and the frictional forces exerted between the snow crystals and the terrain below. As soon as the equilibrium is lost due to the increase of the load or a reduction of resisting forces, snow starts to move downhill. During the descent, it accelerates and, if the kinetic energy is enough, it is able of eroding other layers, increasing momentum, and even tearing off most of the structures or trees encountered in the path.

Depending on the type of snow and on the environmental conditions, multiple types of avalanches develop [272]. The initial release type of an avalanche is defined as “loose snow” if it occur at a single point (Figure 8.2a) or “snow slab” when it interests a larger zone with blocks of cohesive snow sliding on a bed surface (Figure 8.2b). The bed surface is usually well consolidated and it presents on top a layer of crystals which is significantly weaker than the adjacent ones. In addition, glide (wet) snow avalanches release can appear during the spring season and it is caused by rain or relatively intense heat affecting the resistance of the snowpack [273]. During such events, free water starts to percolate through the porous matrix of the snow. This flow is capable of reducing the strength or even modifying the structure of the layers. If a sliding plane is created, a glide avalanche can occur. It is common to find such slip line located in the vicinity of the interface between the snowpack and the vegetation (Figure 8.2c).

Once the mass of snow starts to accelerate due to gravity, various flow conditions are observed. Powder snow avalanches are characterized by a large volume of material which, after detachment, is suspended by turbulent currents [275]. Under the white cloud, a viscous flow of dense snow can be observed as well. This kind of avalanches is very destructive due to the large mass of snow moving at high speeds (sometimes in excess of 150 km/h) and, consequently, having the ability of traveling large distances (Figure 8.3a). Contrariwise, dense snow avalanches are created when the failure

(a) (b)

Figure 8.3: Example of snow avalanches characterized by (a) powder or (b) dense snow flow, from EAW [274].

of the snowpack leads to a viscous flow, which, even at lower speeds, represents a substantial threat.

Slab avalanches (whether resulting in powder or dense flow) are by far the most exacting, accounting for the 90 % of skier-related fatalities due to the large volume of snow suddenly released (Figure 8.2b).

8.2 Snow formation and metamorphosis

To fully understand which are the mechanisms that bring a volume of layered snow to failure, it is central to understand its production and continuous evolution.

Snow is a natural material found seasonally on alpine zones. It is created by the nucleation and subsequent freezing of water vapor around particles suspended in clouds. When supersaturated air meets with low temperatures, diffuse humidity solidifies in crystals which grow until the weight is high enough to precipitate. The psychrometric conditions of the air masses involved in the process is crucial for the type of resulting snow crystals. As "*there are not two snowflakes alike*", fresh snow precipitates under one of the multiple possible structures depending on temperature and humidity (see Figure 8.4). Studies on formation and growth of snow crystals in the atmosphere started with the works of Schaefer [276] and Nakaya [277]. A recent review on the topic has been written by Libbrecht [278].

It is well known that the snow cover is very variable. Morphology, orientation and vegetation of the terrain interact with the wind direction during a snow fall to provide a particularly uneven layer. As reported by Kronholm et al. [279], even in a small slope of 20 meters by 20 meters it is possible to find changes in layers strength in the range of 25 %. Immediately after deposition, snow starts an unceasing process of modification, being subjected to an extensive number of environmental and mechanical variables.

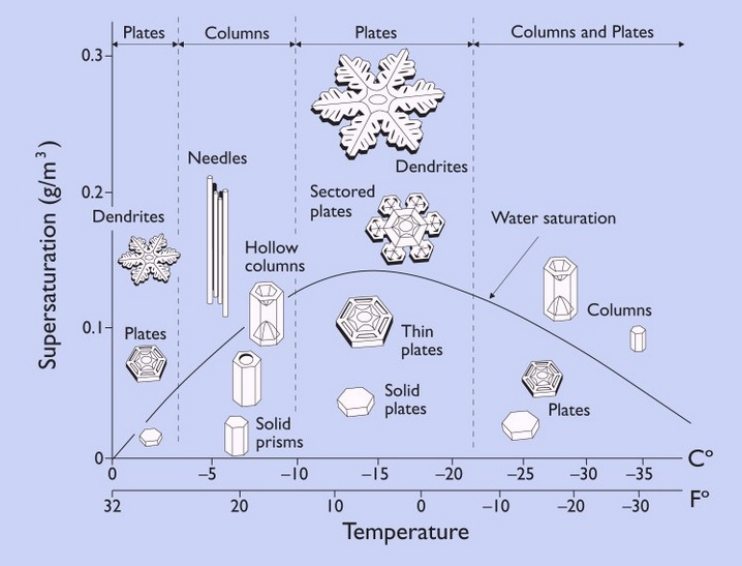

Figure 8.4: Structures of fresh snow crystals depending on temperature and water vapor supersaturation, from Libbrecht [278].

Fresh snow behaves similarly to virgin soil. It creates a porous structure with interconnected grains and, as soon as it is deposited, a process of consolidation starts, as reported by Feldt and Ballard [280], Bradley and Bowles [281] and Kojima [282]. As a result, the density can increase from 70 kg/m^3 of fresh snow up to 300 kg/m^3 of well bonded snow. The snowpack is also characterized by viscosity effects, which is the prevalent form of deformation for an undisturbed cover on a inclined slope [283–285]. Finally, on the top surface, wind drift lifts and redistributes part of the loose snowpack, eventually exposing icy lower slabs [286–288].

In addition to the mechanical consolidation, a metamorphic process is also present. Initial work on the topic was made by Colbeck [289, 290] but recently micro-tomographic scans were used by Pinzer and Schneebeli [291], Pinzer et al. [292] to understand the process at a crystal scale. While, in general terms, consolidation reduces the air volume among the grains, metamorphosis moves the water content through the porous structure. In the winter period, the atmospheric air is capable of reaching very low temperatures, even lower than −30°C during some nights, whereas the vegetated ground maintains a temperature slightly above 0°C. This is due to the fact that porous snow is a very good insulator. Heat is also exchanged between snow and the above air through radiation. Short waves are usually reflected, owing to the fact that the snowpack has a reflection coefficient of 0.8-0.9. Contrariwise, long waves are usually adsorbed during the day and expelled again as thermal radiation during the night, being the snow behaving as a black body and releasing more heat to cold air.

Consequently, an inverted temperature gradient is often observed in the snowpack.

When multiple layers are deposited at different times of the season, the temperature gradient is very non-linear, the conductivity varying extensively from fresh to old snow (see Sturm et al. [293], Schneebeli and Sokratov [294]). The soil at the ground level is usually humid, thanks to the presence of vegetation. The available water vapor moves in the porous structure of the snow following the convective force due to the temperature gradient and, therefore, moving mass upwards. During this transport process, the internal matrix structure of the snowpack is continuously changing.

The available water vapor promotes sintering, a process that creates and strengthen the ice bridges between grains. At the same time, the transport of water vapor results in a change of crystal structure. In fact, when the snow crystals are formed, water suddenly freezes around grains and this fact causes the creation of the classical dendritic form, characterized by high surface energy. Naturally, the crystals tend to reach a configuration at which the surface energy is in a lower state. When the temperature gradient is small (less than 1°C over 1 centimeter), grains tend to round their shape and this is called equilibrium metamorphism. Contrariwise, when the temperature gradient is high (more than 1°C over 1 centimeter), grains shape becomes more faceted and this is called kinematic metamorphism. If the conductivity of the layers is homogeneous, then the water vapor is able to reach the atmosphere and the sudden refreezing causes the creation of surface hoar (Figure 8.5). This is a phenomenon frequently encountered after a large snowfall followed by very cold nights of clear sky as discussed by Birkeland [295]. It is possible that the surface hoar is buried by a subsequent snowfall as well. Otherwise, especially in snowpacks that present a sharp change in conductivity properties, a weak layer can be created in the interface between the layers. These cases are typically found when the snowpack consists of multiple snowfalls with different degrees of compaction.

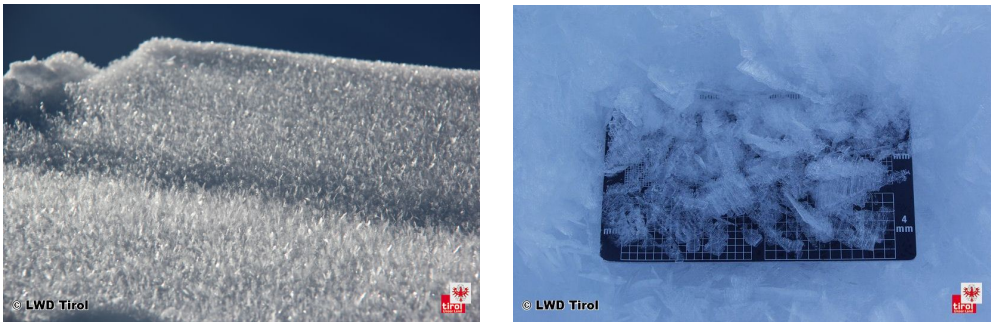

(a) (b)

Figure 8.5: Surface hoar crystals formation, from EAWS [274]

Finally, in the spring period, the high temperatures of the top surface (close to the melting point) during daytime creates free water which re-freezes for the low

temperatures at night. The melt-freeze metamorphism creates the so-called *corn* grains, with high water content (see Wakahama [296]).

Faceted and corn structures have a fundamental role in triggering avalanches. Their appearance creates the weak layer, a part of the snowpack that is characterized by extremely poor bonding and limited mechanical properties. After being buried under successive snowfalls, this crystal structure is subjected to the gravitational load of upper layers. Additional loading, such the weight of a skier, can trigger a fracture in the weak layer. The subsequent crack propagation along this failure surface provokes the release of the cohesive slabs above and, consequently, the creation of an avalanche.

The mechanical characteristics of the snow varies extensively among all different types of crystal structures and environmental conditions. The history of previous matrix transformations crucially determines the current mechanical state of the snowpack. Nevertheless, depending on small changes of characteristics such as density, crystal shapes, intergranular bridges, temperature and water content it is possible to observe a variation of strength, elastic and viscous moduli of snow that can span many orders of magnitude. These variations have been observed in the field in a very short time span (1-2 hours) which immediately affect the snow specimen characteristics and the outcomes of the experiments. Izumi [297] showed this phenomenon in controlled laboratory tests.

This implies that, in order to have practical information on the stability of the snowpack, a large quantity of precise data is required. On the one hand, weather information and short-term predictions are fundamental to evaluate which are the environmental factors that constitute the boundary conditions to be found in the field, as done with numerical models such as *SNOWPACK* [298]. On the other hand, in-situ experimental testing is, still to the present day, the only effective way to have direct information on the mechanical state of the snow and the avalanche release hazard since it is not possible to replicate the exact field state and variability in the laboratory.

8.3 Mechanics of release of a dry snow avalanche

Dry snow slab avalanches are initiated by the local failure of a weak snow layer, buried under a slab of cohesive snow. The initial crack is due to gravity or external forces overcoming the resistance of the crystals in the weak layer. McClung [299] first described the process of "*shear fracture precipitated by strain softening*" in the snowpack (see also [300] for a geotechnical related discussion). Further studies by Schweizer [301], Chiaia et al. [302] and Reiweger et al. [303] confirmed the shear failure but also identified the dependence of the weak layer strength from the pressure, typical of Mohr-Coulomb like materials. The initial collapse is followed by a rapid

propagation of the crack which can extend to a wide area of release. Consequently, the upper slab is progressively bent during propagation and not supported anymore (Figure 8.6).

Frequently, it is possible to identify such weak layers by direct inspection of the crystals but, since the weak layer is located several centimeters under the surface, having a direct indication of the location of the initial failure is a daunting task. In addition, the crack in the weak layer propagates suddenly, even for long distances without any visible change. Then, the upper cohesive slab fractures and a large volume of snow starts to slide. For this reason, snow avalanches represent an elusive threat. The substantial difference in mechanical behavior between well consolidated and fragile layers represents a highly nonlinear problem, which depends from a large number of environmental conditions.

Nevertheless, dry snow avalanches (both powder and dense ones) leave a similar evidence in the form of the release zone (Figure 8.7). After the initial localized failure and propagation in the weak layer, if the snowpack is not capable of redistributing the subsequent additional stresses, this volume of cohesive snow appears to be suspended since there are no other resisting forces beside static friction. The dead weight of the upper slab is then redistributed on the adjacent snow. On the top, a slope orthogonal crack surface, the crown, is created by the fracture of the cohesive layer under tensile force. This failure is characterized by a clean separation of the snow slab. Sometimes, tensile fractures appear as a warning sign of an incipient avalanche release. On the sides of the hanging volume, the cohesive snow is resisting a shear force. Upon fracture a jagged surface called flank is created. The irregularity is given by the competitive mechanism of shear and tensile failure in a non-homogeneous and mostly anisotropic material such as snow. Finally, a compressive zone appears at the bottom of the hanging volume. Triaxial tests [305, 306] show that cohesive

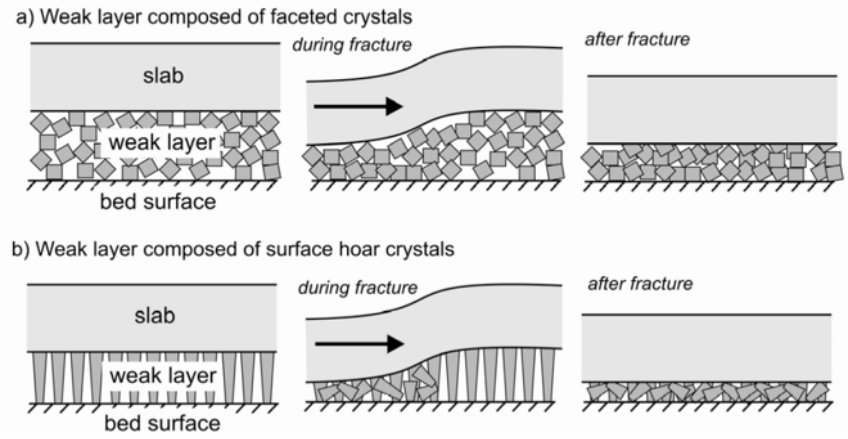

Figure 8.6: Propagation of crack in the weak layer for the faceted or hoar crystals, from Heierli [304]

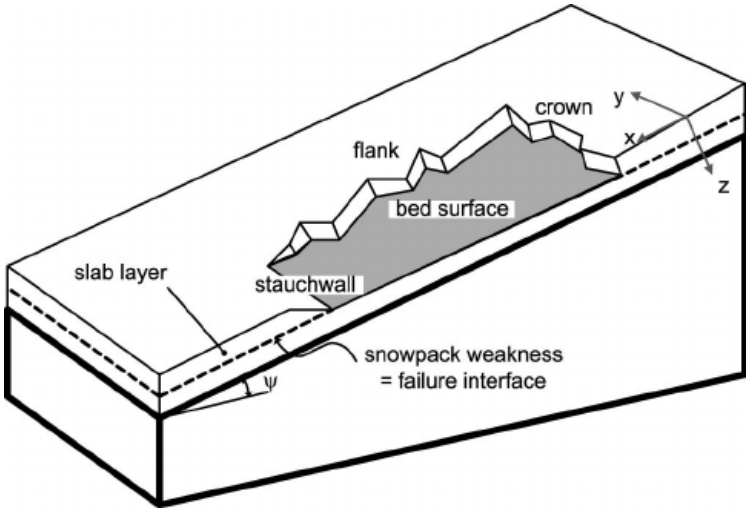

Figure 8.7: Scheme of the detachment location of a dry snow avalanche, taken from Schweizer et al. [272]

snow consolidates and hardens under compression and, then, fails due to shear on a oblique plane. Likewise, due to sustained compression, the volume of detached snow creates a diagonal slip line to overcome the zone of firm slab. The resulting plane of failure is called *stauchwall*.

The complexity inherent to this failure mechanism is obvious. As a matter of fact, in-situ experimental tests are devised in order to reproduce single aspects of the problem in an isolated fashion. Instead of studying the complete phenomena of failure initiation, crack propagation and upper slab release on a generic alpine slope, it is more effective to analyze simpler tests which are repeatable and performed in a more controlled environment.

8.4 Experimental testing of snow

In order to evaluate the stability of the snowpack in-situ, numerous experimental techniques have been developed. Generally, their objective is to stress the weak layer by applying a load on the upper cohesive slab. As result, the test provides a stability index or, equivalently, a threshold value for the ultimate load.

Unfortunately, many avalanche events take place on slopes which are difficult to access and dangerous for the alpine guides to stop and perform direct experiments. Indeed, avalanches are most common on slopes of inclination between 30° and 40°, with a north facing aspect. In order to avoid hazardous sites, testing zones are selected in equivalent but safer locations, where the snowpack is undisturbed and the characteristics of the layers can be related directly to the zone of interest. After digging a pit of the required dimensions, the usual procedure is to measure the thickness, temperature and hardness of the layers and identify the type of crystals. If

weak layers are found, further stability tests are required to evaluate their mechanical characteristics and the stress state given the gravitational load.

(a) Compression test

(b) Extended column test

(c) Rutsch-block test

(d) Shear frame test

Figure 8.8: In-situ tests for the evaluation of the strength, the stability and the propagation characteristics of the snowpack, from Schweizer and Jamieson [307].

Among the numerous available in-situ experimental procedures, the following ones are the most indicative and frequently used by practitioners:

- The compression test (CT) [308] is performed by considering an isolated column with a 30 cm by 30 cm base. A shovel is placed on top and the practitioner hits it with increasing force for 30 times. If separation of the column is observed at the weak layer level, then the stability index is inversely proportional to the number of hits. This test aims at identifying the weak layer and evaluating its limit shear strength indirectly.

- The extended column test (ECT) [309] is similar to the previous one, but a larger width of the specimen is considered (90 cm by 30 cm base). The shovel is placed at the border of the volume of snow and a sequence of 30 hits with increasing force is applied. In this case, the tester is interested in observing the local failure followed by the horizontal propagation of the crack onset.

- The *rutsch-block* test (literally the "sliding block" test) [310] is performed by isolating a volume of 2 m by 1.5 m and loading the top surface with a sequences of movements by a skier. The test considers first the simple weight of the skier followed by 3 dynamic knee bending, followed by 3 final jumps. A score is given based on the kind of observed failure and propagation type. This experiment has the objective to test directly the snowpack with a realistic loading case.

- The shear-frame test [311] measures the resistance of the weak layer by applying a sliding force to the cohesive snow through an ad-hoc steel frame. Usually, the test takes place as close as possible to the interface with the layer of interest, in order to avoid bending-like loads.

These tests are depicted in Figure 8.8, taken from the work of Schweizer and Jamieson [307]. In this chapter, attention is focused on the Propagation Saw Test, a promising novel in-situ technique to evaluate initiation and propagation of cracks in weak layers buried under cohesive snow slabs.

8.5 The Propagation Saw Test

In the last decade, the Propagation Saw Test (PST) [312, 313] has emerged as one of the most indicative tests to evaluate stability and crack propagation propensity of the snowpack.

When snow samples are available in the laboratory, the effects of different kinds of loads are accurately evaluated. Theories on the mechanics of snow are predominantly based on such measurements, being performed in a controlled environment. As it was mentioned before, snow is a very complex material and slight variations in the external actions can result in profound changes in the outcome. Nevertheless, in the classical tests presented previously, the loads applied to the snowpack are hardly well measured. Even worse, many tests rely on approximative procedural guidelines as well as are affected by in-situ variables such as uneven layers distribution, rocks or vegetation.

In the compression test and its extended counterpart, the experiment procedure requires the experimentalist to hit the column of snow with a gradual increase in the hitting force. Instead, in the rutsch-block test, the skier movements represent a typical loading pattern applied to the snowpack.

As a matter of fact, expert alpine guides are able to flawlessly distinguish various test outcomes and properly interpret them, even when they are confusingly similar [314]. However, when the in-situ results must be transmitted to the weather forecast stations, a clear scale for comparison is missing. It is stressed that this problem has profound consequences in the prediction of snow avalanches. If the tests are similarly

executed but applied loads differ among the cases, then it is difficult to have a clear idea of what conditions are actually present in the field.

In recent years, a strong push has been made to find a unified way to quantify and share the results of many of the in-situ experiments, in order to create a reference database. However, few tests are able to give a precise quantitative evaluation of the outcome.

The propagation saw test is performed by isolating a conventional volume of snow of width 30 cm and length 2 m in the downslope direction. Once the weak layer of interest has been identified in the stratigraphy from manual snow profiling, a saw is used to cut through it progressively (Figure 8.10). This technique aims at slowly reducing the resisting cross section of the weak layer.

If the saw cut reaches a critical crack length for the fracture to occur, three outcomes are possible, depending on snow properties. In the first case, defined as *full propagation* or *END case*, a crack in the weak layer propagates from the saw cut to the end of the specimen releasing the whole cohesive volume of snow. An alternative outcome, defined as *slab fracture after propagation* or *SFa*, consists in the initial propagation of the crack in the weak layer followed by a detachment of the upper slab before the end of the specimen. Finally, if the upper slab fails before any crack propagation in the weak layer crack, then the case is identified as *slab fracture before propagation* or *SFb*. In the PST, the critical saw cut length is accurately measured, since the experiment is stopped as soon as failure is initiated and the saw remains stuck in the middle of the layers. In the same way, the propagation length can be properly measured when the upper cohesive snow slab clearly separates (see Figure 8.9). More recently, the PST has been studied using high-speed cameras and particle tracking velocimetry by van Herwijnen and Jamieson [316], van Herwijnen et al. [317].

Numerous statistical studies have validated the consistency of the test and

Figure 8.9: A typical weak layer composed by hoar crystals buried under a cohesive snow slab (from Jamieson and Schweizer [315]). Note the collapsed crystal structure and the detachment of the upper layer.

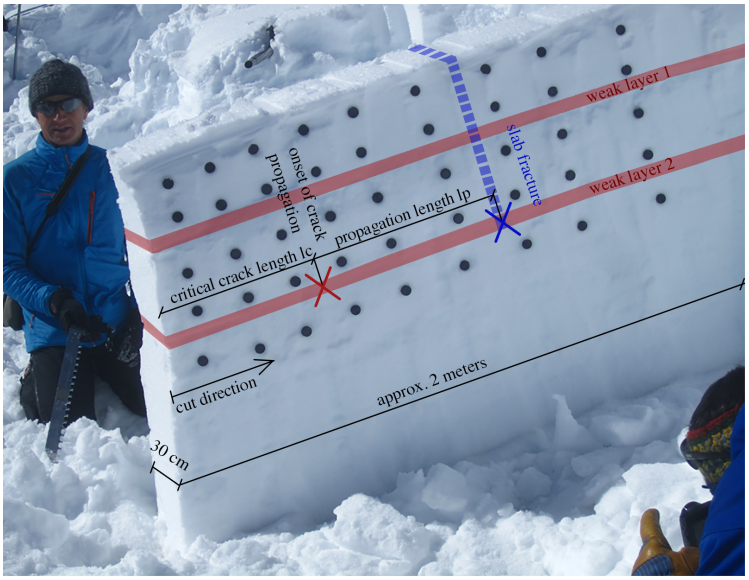

Figure 8.10: Setup of the Propagation Saw Test. The black dots have been placed to follow the test via high-speed cameras.

confirmed the good correlation between test results and likelihood of avalanche release [318–323] but little work has been realized to analytically describe the test evolution and outcome.

Consequently, a detailed analytical model of the Propagation Saw Test is developed by means of well known mathematical models in the field of continuum mechanics. A snowpack consisting of three ideal layers is considered, as presented in Figure 8.11. The top layer is a cohesive upper slab which is supported by a weak layer. In turn, the weak layer rests above a lower bed that is considered ideally rigid.

Initially, the sequence of events that take place in a Propagation Saw Test due to the increasing gravitational load are studied. At the beginning of the test, increasing the cut length l creates a volume of cohesive snow, clamped on one side and hanging freely on the other one (Figure 8.12(a)) whereas the weak layer reduces its resisting area. The upper layer is displaced both vertically and horizontally under its own weight until it touches the lower bed (Figure 8.12(b)). The cut length l at which this

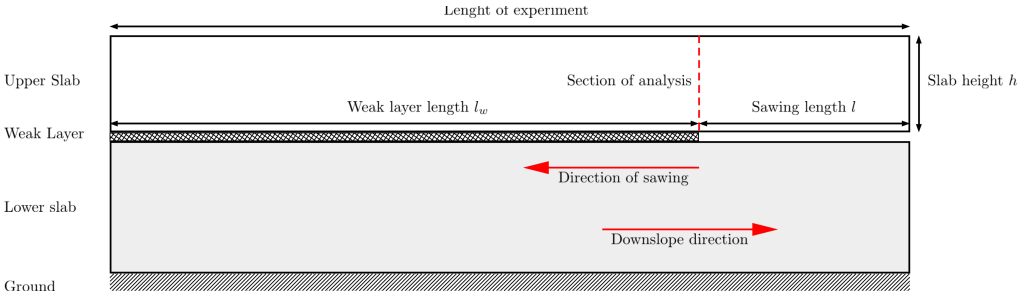

Figure 8.11: Side view sketch of the modeled Propagation Saw Test

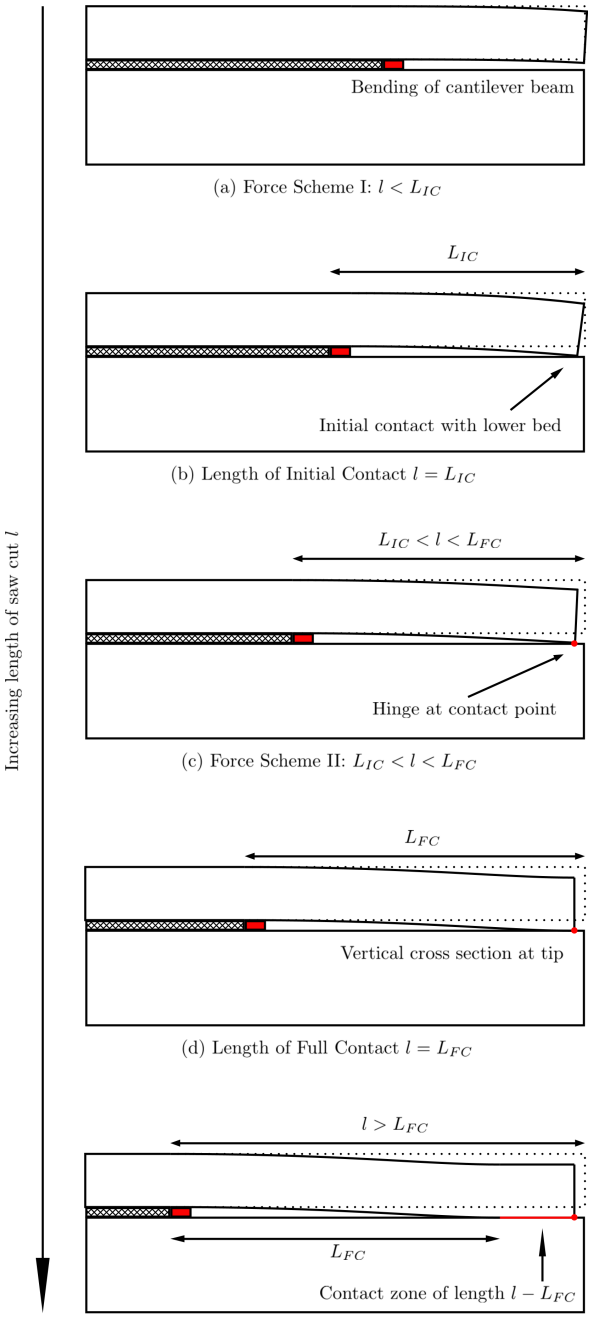

(a) Force Scheme I: $l < L_{IC}$

(b) Length of Initial Contact $l = L_{IC}$

(c) Force Scheme II: $L_{IC} < l < L_{FC}$

(d) Length of Full Contact $l = L_{FC}$

(e) Force Scheme III: $l > L_{FC}$

Figure 8.12: Stages of the Propagation Saw Test: after initial bending (a), first contact of upper slab and lower bed is reached at cut length $l = L_{IC}$ (b). Following the sawing (c), the full contact length is achieved for $l = L_{FC}$ (d), at which point the cross section has rotated back to orthogonal to the lower bed. Successively, the length of the beam under bending is kept constant at L_{FC} for $l > L_{FC}$, while the contact zone is increasing as the saw progresses further (e).

initial contact (IC) is observed is identified with $l = L_{IC}$. At first, only the tip of the cantilever rests on the lower slab: the resulting effect is a hinged restrain, where the beam does not displace vertically anymore but it has freedom to rotate (Figure 8.12(c)). Then, following the increase of l, the slab bends back due to its own weight and rests with vertical cross section with respect to the lower bed. At this point, not only the vertical movement is constrained, but also the rotation of the beam is fixed. The cut length l, required for this condition to happen, is called length of full contact (FC) and it is denoted by L_{FC} (Figure 8.12(d)). If the sawing continues, the contact zone of the two slabs increases. However, the length between the saw and the first touching point remains constant, being equal to the full contact length L_{FC} (Figure 8.12(e)) due to equilibrium requirements. Hence, the beam is now behaving as a double clamped beam, with a fixed length of L_{FC}, and, consequently, with a linear bending moment and constant shear resultants along the beam. Moreover, at the specific cross section in correspondence of the sawing, the bending moment and the shear will not further increase.

Introducing an Euler-Bernoulli beam model, the evolution of the stresses in the upper slab and the weak layer is computed with respect to the length of sawing. The two layers are studied independently, assuming an interface which transfers perfectly the applied forces. It is found that the stresses in the two studied layers are strictly depending on the length of initial contact L_{IC} and full adherence L_{FC}. The stress in the upper slab at the cross section in correspondence of sawing is initially varying quadratically and, upon contact with the rigid bed, the stress evolution shows linear variation (see Figure 8.13(a) and 8.13(b)). Contrariwise, the stresses in the weak layer have an exponential increase, both in the compressive and shear components.

In order to take into account the creation of cracks in upper slab and weak layer, a purely brittle constitutive law is used. In the upper slab, since tensile and bending forces are expected, the stress on the top fiber is compared with the tensile threshold of cohesive snow. In the proposed constitutive law, after reaching the threshold stress value, fracture appears immediately, with null dissipated energy and immediate separation of the volume of snow. The critical saw cut length that provokes detachment of the upper slab is denoted with l_c^s. Likewise, in the weak layer, compression and shear are present. They are considered separately and compared with their respective maximum admissible value. The minimum value of critical saw cut length that causes failure (either in shear or in compression) is given by l_c^w.

The gravitational load on the weak layer also depends, besides the geometrical quantities, on the upper slab weight. In turn, it is known that Young's elastic modulus and the tensile strength of cohesive snow are directly related to the density of the slab. Then, by considering different density values of the cohesive snow slab, the different outcomes of the propagation saw test are recovered using the proposed model.

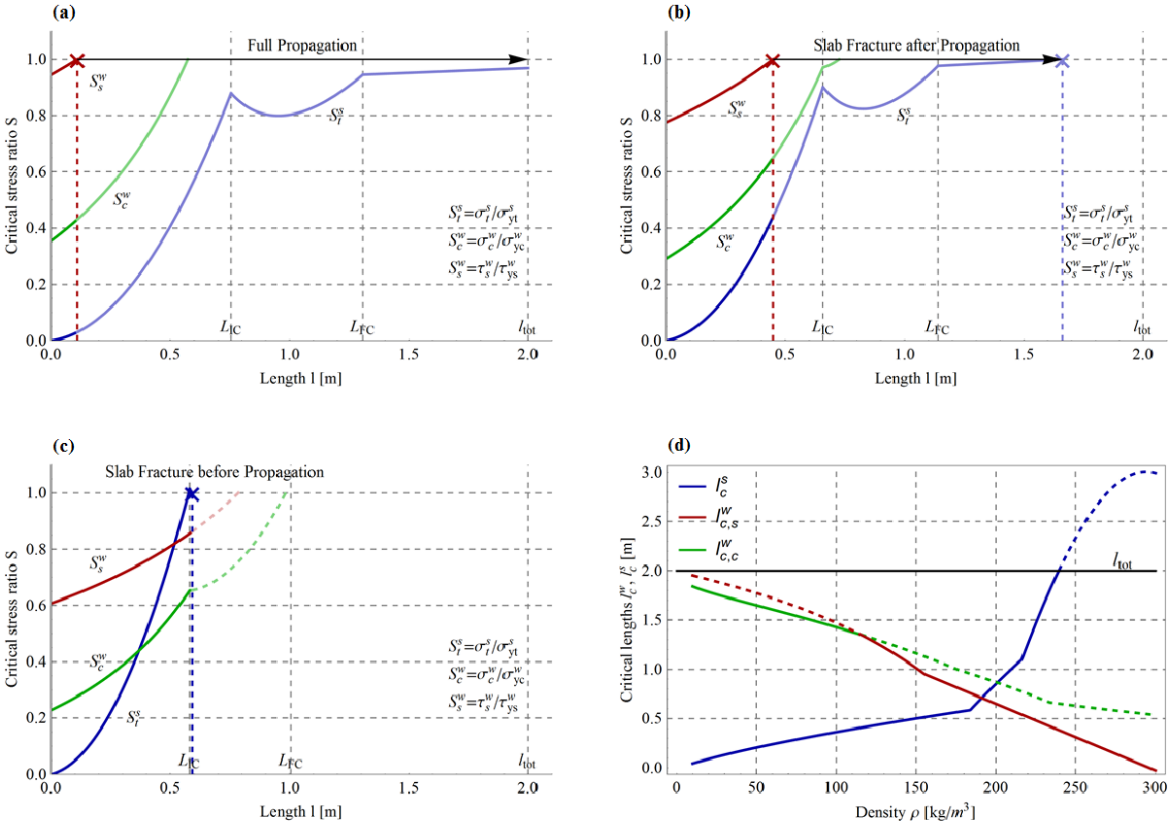

Figure 8.13: Model application results for a specimen composed of a $0.3 \times 0.3 \times 2$ m^3 upper slab and a weak layer of thickness $h_w = 2$ mm. The slope is inclined at 35°. (a) Full propagation (END) case for (density of 280 kg/m^3). (b) Slab Fracture after propagation (SFa) (density of 230 kg/m^3). (c) (density of 180 kg/m^3). (d) Critical crack length with respect to the upper slab density.

In Figure 8.13, a simple example setup of a $0.3 \times 0.3 \times 2$ m^3 upper slab and a weak layer of thickness $h_w = 2$ mm on a 35° slope is presented. S_t^s is the ratio of the stress of the combined bending and tensile load due to gravity and the tensile threshold in the upper slab. S_c^w and S_s^w are respectively the ratio of the compressive and shear stresses due to the upper slab weight and their threshold counterparts in the weak layer.

Figure 8.13(a) shows the Full propagation (END) case for a cohesive snow density of 280 kg/m^3. Failure is initiated by the shear load in the weak layer which propagates to the end of the specimen. Then, Figure 8.13(b) shows the Slab Fracture after propagation (SFa) case, given by an upper slab density of 230 kg/m^3. A crack is initially created in the weak layer and then propagated. Then the upper slab fracture follows. Finally, Figure 8.13(c) shows the slab fracture before crack propagation (SFb) case for a density of 180 kg/m^3. Since the tensile failure in the upper slab appears before any weak layer fracture, no propagation is observed.

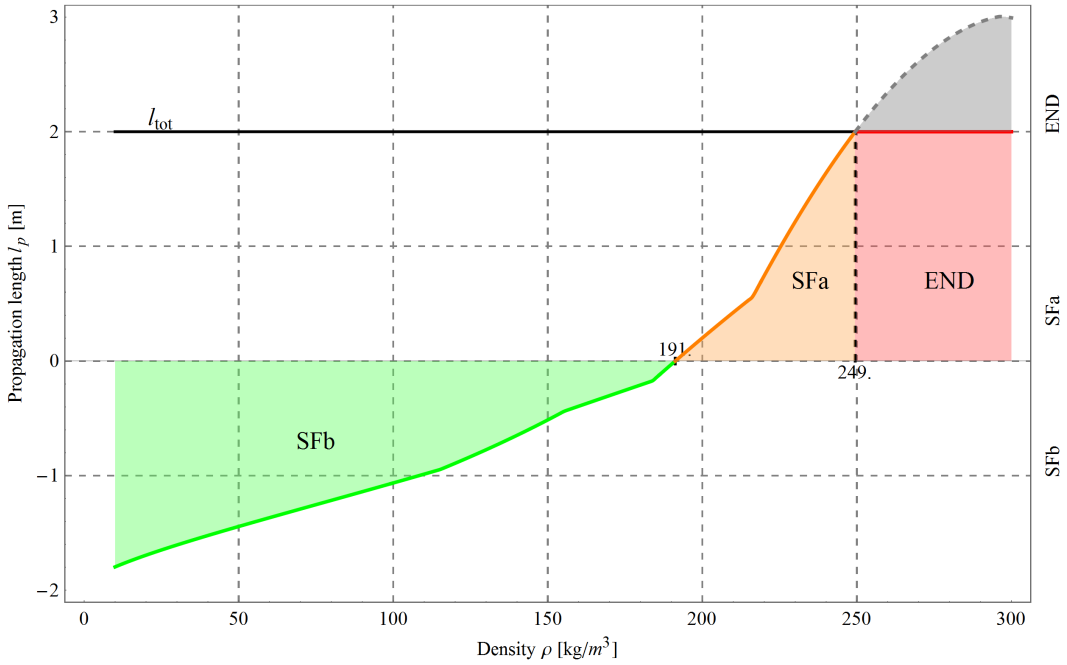

Figure 8.14: Signed propagation length with respect to the upper slab density for a $0.3 \times 0.3 \times 2$ m^3 specimen on a 35° slope. The different test outcomes full propagation (END), slab fracture after propagation (SFa) and slab fracture before propagation (SFb) are highlighted on the plot with the respective limit values of density.

Figure 8.13(d) shows the critical crack length with respect to the upper slab density. l_c^s is the critical saw length for the tensile fracture in the upper slab. Similarly, $l_{c,c}^w$ and $l_{c,s}^w$ represent, respectively, the critical crack length for shear and compression stresses in the weak layer.

Furthermore, the *signed* propagation length is computed by subtracting the upper slab critical length l_c^s from the weak layer one l_c^w (as minimum value between $l_{c,c}^w$ and $l_{c,s}^w$). Plotting the dependence of the propagation length with respect to the density of the upper slab, a map of all possible outcomes is developed as presented in Figure 8.14. Very good agreement with previous field experimental data is found [324, 325].

Certainly, it is possible to refine the mathematical model to take into account additional mechanical details. For example, more complex constitutive models are required for the interdependence of pressure and shear in the cohesive snow failure criterion. Similarly, modeling the weak layer and upper slab as connected, rather than independent, is necessary to consider the effect of relative deformation observed during in-situ Propagation Saw Tests. However, the complexity and non-linearity of the analytical solution grows significantly with each model refinement and a numerical analysis of the mechanics connected with the experimental tests of the snowpack is preferred.

8.6 Numerical analysis

In the previous chapters, accurate numerical analyses of localization and propagation of cracks has been presented employing the mixed $\boldsymbol{\varepsilon} - \boldsymbol{u}$ finite element formulation. Now, the objective is to reproduce the outcomes of the Propagation Saw Test. The experiment is modeled as a 2D problem, in a consistent fashion with the analytical model presented in Figure 8.13. The model is 2 m long and 0.3 m wide. The upper slab has a thickness of 0.3 m and it is supported by a weak layer of 2 mm. The lower bed is added to the model but it is assumed to remain elastic. The gravitational load is rotated 35° with respect to the vertical direction due to the inclination of the slope.

As done in the previous analytical analysis, most properties are computed using derived formulas extracted from reliable experimental tests. With regards to the upper slab, the elastic Young's modulus is computed as in the work of Scapozza and Bartelt [306]:

$$E(\rho) = 1.873 \cdot 10^5 \exp^{0.0149\rho} \quad [\text{Pa}] \tag{8.1}$$

where ρ is the density in kg/m^3. The Poisson's ratio for cohesive snow is usually equal to 0.1.

Since the upper slab is subjected to bending and tensile loading, an isotropic continuum damage model based on Rankine tensile failure criterion is assumed. In particular, the maximum admissible tensile stress is recovered from Jamieson and Johnston [326]:

$$\sigma_{yt}^s = 2.4 \cdot 10^5 \left(\frac{\rho}{917}\right)^{2.44} \quad [\text{Pa}] \tag{8.2}$$

In the field, the weak layer is usually found to contain numerous voids, as it is possible to see in Figure 8.9. Owing to the high porosity, density of the weak layer is assumed to be 50 kg/m^3. Likewise, the elastic modulus for the weak layer is equal to one fifth of the upper slab one, in line with the values reported by Sigrist and Schweizer [327]. Following the work of Reiweger et al. [303], the weak layer fails under shear, with a pressure dependent behavior. Consequently, it is reasonable to use the Drucker-Prager plasticity model. For this case, the friction angle is 20° and the cohesion (i.e. shear strength at zero applied pressure) is 0.5 kPa.

It is well known that snow and, in particular, weak layer crystals have a very brittle behavior. Nevertheless, the fracture energy has been experimentally evaluated in multiple occasions. Numerous experimental techniques have been studied to find fracture energy starting from snow density. As discussed in the work of Schweizer et al. [328] and van Herwijnen et al. [329] the fracture energy of the weak layer is found to be approximately 1 J/m^2. In the upper slab, owing to the well bonded and sintered microstructure, it is plausible to assume an order of magnitude higher, so the fracture energy is set as 10 J/m^2.

In order to simulate the cut provided by the advancing saw, it is necessary to progressively remove the elements of the weak layer and release the vertical constraint of the upper slab. Chiumenti et al. [330] proposed a technique of element activation for the analysis of metal deposition in a manufacturing process. In this case, instead of activating parts of the model, the weak layer elements are turned off at the rate of cut speed. From an implementation point of view, this technique removes the elements from the computational procedure and it allows to simulate the progressive increase of gravitational load on both upper slab and weak layer.

When the displacement of the upper slab is equal to the weak layer thickness h_w, contact with the lower bed is expected. This is a key feature of the proposed analytical model, since it motivates the various conditions that discriminate a full propagation of the crack in the weak layer or an arrest of crack propagation due to slab failure. From the FEM standpoint, a robust contact algorithm with frictional interfaces is required to model such behavior. Unfortunately, this goes beyond the purpose of this work and it has not been studied nor implemented for the mixed strain-displacement finite element. Nevertheless, it is possible to simulate the full propagation (END) and the slab fracture before propagation (SFb) outcomes being the limit cases of the analytical model. In addition, the numerical model takes into account the different rigidities of the snowpack and, then, it is able to compute the relative deformation of the layers. The effect of such phenomena is key for describing accurately the PST but it cannot be observed in the simplified analytical model.

In the introduced non-linear constitutive model, the fracture of the weak layer is described using the discrete weak discontinuities approach, with a localization of the inelastic strains inside a finite dimensional band. In reality, each material presents a limit deformation that represents the instant at which physical separation is observed. Camponovo and Schweizer [331] showed that the initial proportional behavior of cohesive snow specimens stops at a total strain of 0.1. Then, after the total strain value of 0.2, a sudden increase of strain rate is observed due to the lost of all carrying capabilities. In the numerical test, failure of the weak layer is conventionally defined when all points inside a slip band reach the inelastic strain value of 0.1.

Firstly, as done when presenting the analytical model, a very stiff upper slab is considered setting the density at 280 kg/m^3. Then, Young's elastic modulus is 12.15 MPa and the maximum tensile strength is 13.28 kPa. The results of this numerical analysis are presented in Figure 8.15. Complete failure due to shear (Mode II) fracture entailing the whole weak layer is observed, as this case corresponds to the full propagation (END) case. From the plot of displacement in the slope direction, it is possible to observe a clear jump in the computed field. The inelastic strains are concentrated in the weak layer and, from the plot of principal strain vectors, the failure is induced mostly due to shear forces.

The analytical model computes the critical length of sawing at 11 cm. In this

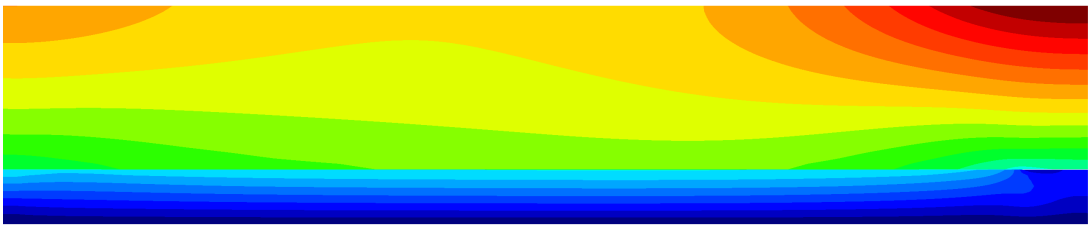

(a) Displacement in the slope direction

(b) Norm of inelastic strains

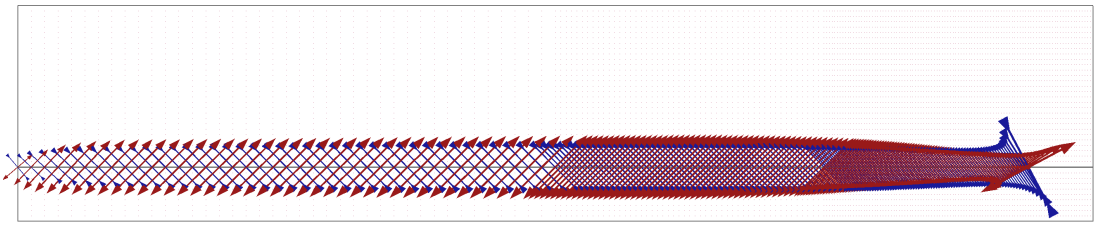

(c) Vectors of inelastic strain

Figure 8.15: Numerical analysis for the full propagation (END) case with a density of 280kg/m^3

case, the numerical solution of the critical crack length, which corresponds to the length of deactivated elements before all weak layer is characterized by the limit strain, is 13 cm.

It can be noticed that the missing numerical description of the contact causes an increase of the pressure in the weak layer. As it was discussed before, the weak layer is modeled with a Drucker-Prager failure criterion, where the resistance to shear forces is linearly dependent from the vertical compression and the friction angle. In particular, as the vertical loading increases, the constitutive model predicts a higher admissible shear stress. If contact was considered, the vertical force would be distributed between the rigid bed and the weak layer. In that case, the compressive force from gravitational load would be smaller, resulting in a lower shear strength and, consequently, in a reduced value of critical length. A rotation of principal axis due to pressure effects is more visible in the vicinity of the crack tip, where the highest compression is found. Indeed, a change in the principal strain directions is visible in the plot (Figure 8.15(c)).

The numerical solution depicts correctly the failure mechanism and it calculates

a critical length value in agreement with the analytical model that, due to the assumptions of pure brittleness and rigid interfaces between the layers, represents a lower bound case.

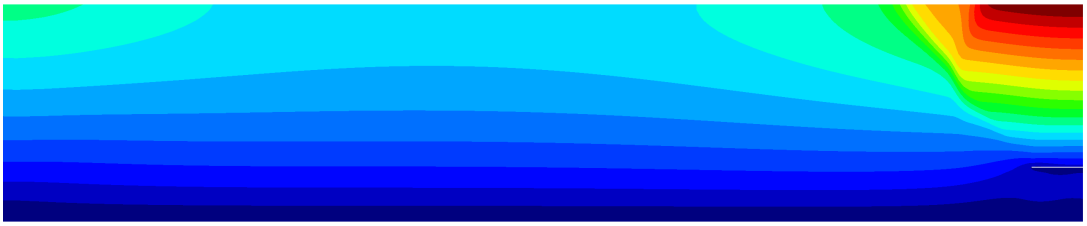

(a) Displacement in the slope direction

(b) Norm of inelastic strains

(c) Vectors of inelastic strain

Figure 8.16: Numerical analysis for the slab fracture before propagation (SFb) case with a density of 180kg/m^3

In a second numerical simulation, an upper slab density of 180 kg/m^3 is considered. Young's elastic modulus is 2.74 MPa and the threshold value for the tensile stress is 4.52 kPa. Figure 8.16 shows the resulting displacements in the slope direction, the norm of inelastic strains and principal strain vectors. In this case, a branched slip line appears in the upper slab due to bending and traction in the slope direction. The localization starts in the top fiber of cohesive snow and moves diagonally in the direction of the saw cut. This case represents a slab fracture before propagation (SFb). The plot of principal inelastic strain vectors shows that the main cause of failure is opening (Mode I). It is noteworthy that the presented solution corresponds to the last converged step, before an equilibrated numerical solution is not available. In fact, this model has been solved within a quasi-static analysis. If a part of the upper slab has separated from the rest of the model, then static equilibrium conditions are not met anymore.

The slab failure is inclined, at an angle approximately close to the slope angle. This is mostly due to the Rankine criterion as the failure appears for the maximum combined bending and tensile stress, that is dependent on the slope inclination. The length at which failure appears is 33 cm whereas the analytical model suggests 59 cm.

In the FEM model, the relative deformation of the each layer is taken into account. This assumption is crucial in the solution because stress at the interface between upper slab and weak layer have a different distribution than in the analytical model. In particular, if this case is interpreted as a beam on elastic soil, a concentration of stresses is expected at the saw point. Moreover, the numerical solution does not consider that the vertical displacement of the upper slab limited by the contact with the lower bed which, for a deformable weak layer, appears before than the rigid interface case. In turn, this results in a increment of tensile stress higher than expected. For these two reasons, the critical cut is sensibly reduced with respect to the analytical model.

It is clear that the physical limitations of the real experiment are fundamental for a correct numerical simulation. Even if beyond the scope of this work, a proper representation of phenomena such as frictional contact and dynamic effects would definitely enhance the modeling of the Propagation Saw Test.

Nonetheless, even simplified numerical analyses require a high degree of accuracy and the possibility of taking into account the various material non-linearities. While many in-situ experiments are made and interpreted through the experienced eyes of snow scientists, frequently, loading and environmental conditions are rather complex and require a reliable tool to provide a quantitative and qualitative validation of findings.

In this practical example, mixed strain-displacement finite elements show good capabilities of computing failure mechanisms as well as the different studied behavior with respect to density. Even if multiple physical phenomena are not implemented and the failure mechanisms in snow is still an open question, it is possible to evaluate failure lengths close to the analytical solutions. In turn, these analytical solutions are shown to be quite close to field data, as in Gaume et al. [324] and Gaume et al. [325]. Moreover, such an accurate numerical tool opens the possibility of consistently computing the mechanical state of snow cover over larger regions, in order to provide detailed information for avalanche hazard predictions.

This page is left intentionally blank.

Chapter 9

Conclusions

In this work, a novel mixed $\boldsymbol{\varepsilon} - \boldsymbol{u}$ finite element method for strain localization and failure in plasticity is presented. The proposed formulation proves significant advantages when dealing with non-linear mechanical behavior of solids. In particular, with respect to the initial objectives, the mixed $\boldsymbol{\varepsilon} - \boldsymbol{u}$ finite element method:

- is able to tackle effectively localization and failure problems, without the need of any auxiliary technique such as tracking;
- it is a general purpose FEM, being applicable to both plasticity and damage constitutive laws;
- it provides accurate solutions in terms of displacements and strains;
- it can be used with low order elements with equal interpolation in strain and displacements, which allows a direct extension to 3D cases;
- it employs without hindrance triangular, quadrilateral, tetrahedral, hexahedral and prismatic elements;
- it is virtually mesh independent and energy consistent;
- it represents a key enhancement in the kinematics of standard finite elements.

Many of the advancements in the topic of localization of strains and failure have been developed over the last three decades and this field has reached a substantial maturity in the academic research. With these stable theoretical foundations, it was possible to devise the proposed mixed formulation which satisfies the requirements of consistency and stability, ensuring a convergent numerical solution. Hence, it does not suffer from the known limitations found in the standard displacement-based irreducible formulation.

The modeling of fracture in Mode I, Mode II, Mode III and Mixed Mode can be correctly performed with the smeared crack approach using local constitutive

laws. The simultaneous continuity of strains and displacements ensures the local convergence of strains/stresses and this is the crucial factor for improving the numerical analysis of strain localization in solids.

The mixed $\boldsymbol{\varepsilon} - \boldsymbol{u}$ formulation is capable to encompass a wide range of engineering problems and it represents a reliable solution of the problem of material non-linearity. While it provides accurate results, the method has a relatively simple mathematical structure. Indeed, this makes the proposed formulation very appealing for the engineering practice.

9.1 Contributions

The mixed $\boldsymbol{\varepsilon} - \boldsymbol{u}$ finite element method consists of the following features:

- **Mixed weak formulation for plasticity.** The mixed $\boldsymbol{\varepsilon}-\boldsymbol{u}$ strain-displacement finite element method has been developed for the strain localization in plasticity starting from the compatibility and equilibrium equations in weak form.

- **Choice of interpolation spaces.** With the objective of maintaining a general approach and easy extension to the 3D case, equal shape functions interpolation are selected for the discrete weak version of the proposed formulation. In particular, the cases of linear triangles, linear tetrahedra, bi-linear quadrilateral, tri-linear hexahedra and prismatic elements are considered.

- **Stabilization of the discrete weak form.** Equal interpolation of variables in a mixed formulation does not satisfy the *Inf-Sup condition*. To circumvent it, the Variational Multiscale Stabilization is introduced and the problem is stabilized by approximating the subscale variables through projection operators. Besides the ASGS and the OSGS methods, a non-residual based stabilization has been proposed for quasi-incompressible situations.

- **Solution of the algebraic system.** Initially, the Newton-Raphson method is studied. Exact linearization of the system of equations provides quadratically convergent iterations, although the resulting global stiffness matrix is non-symmetric. Alternatively, using the secant-based Picard's method, symmetry is restored and it allows the use of a faster solver.

- **Compatibility with standard FEM.** In the $\boldsymbol{\varepsilon}-\boldsymbol{u}$ elements, the compatibility condition is enforced weakly, whereas, in the irreducible formulation, it is assumed to hold in the strong form. However, the displacement interpolation space is the same. For this reason, the two methods can coexist in the same computational mesh and it is possible to reduce considerably the required computational resources.

The proposed mixed strain displacement finite element method is applied to several practical examples and benchmarks. The following study cases are discussed:

- **Mode I (opening) loading.** 2D and 3D pullout tests are studied using a modified Rankine's failure criterion, developed to cope with non-differentiable locations in the standard failure surface. With the enhanced accuracy of the proposed formulation, it is possible to recover both the symmetric and asymmetric solutions found in the experimental 2D pullout test and link the characteristic cracking pattern to the effect of boundary conditions. Moreover, in the 3D pullout case, the mixed $\boldsymbol{\varepsilon} - \boldsymbol{u}$ finite element is able to converge faster to the continuous solution in term of stresses with respect to the irreducible formulation as the computational grid refines.

- **Mode II (shearing) loading.** A Drucker-Prager plasticity model is written as linear combination of the J2 von Mises and the pure pressure failure criteria through the tangent of the friction angle. In the Prandtl punch test, while the irreducible formulation is not able of providing satisfactory results, the $\boldsymbol{\varepsilon} - \boldsymbol{u}$ formulation is consistent with the solution given by the displacement-pressure elements. Then the cases for 0°, 15° and 30° friction angles are simulated and the results agree with the rigid-plastic analytical solution.
  In the uniaxially stretched hollow plate the angle of localization with the proposed formulation are calculated and in good agreement with the analytical values for the Drucker-Prager plasticity. Moreover, the dissipation energy for the pure isochoric plasticity case is computed and only a 2.33 % deviation from the theoretical result is found.
  Finally, the strain-displacement and the displacement-pressure finite elements are studied in a 3D perforated thin walled cylinder subjected to a vertical imposed displacement.
  The enhanced kinematics of the method results in an accurate solution, whereas the $\boldsymbol{u} - \boldsymbol{p}$ FEM fails to do so, owing to the fact that the deviatoric strains are computed from the discrete symmetric gradient of the interpolated displacements in strong form.

- **Mode III (tearing) or Mixed Mode loading.** Thanks to the high fidelity of the mixed $\boldsymbol{\varepsilon} - \boldsymbol{u}$ finite elements, it is possible to study the differences in results between the isotropic continuum damage and the plasticity model. Then, a series of three point bending tests and torsion experiments on skew notched beams are modeled. The failure mechanisms are pinpointed and the global structural behavior observed in the experiments is reproduced as well.

Finally, in collaboration with the Federal Research Center BFW, Innsbruck, the proposed formulation has been applied to problems involving crack propagation in

snow avalanche release. An analytical model is developed to link the experimental outcomes of the Propagation Saw Test to the mechanical and quantitative description of the test. Critical crack length and propagation length are computed and the findings are in very good agreement with the in-situ values. Then, these results are compared with the ones calculated with the proposed mixed $\boldsymbol{\varepsilon} - \boldsymbol{u}$ finite element method.

9.2 Future work

The mixed $\boldsymbol{\varepsilon} - \boldsymbol{u}$ finite element method shows to be a promising leap in the solution of non-linear mechanical problems in solids. Therefore, further investigation in the following topics is suggested:

- **Crack opening-reclosure behavior.** The case studies in this work are subjected to monotonic loading. However, in many practical cases the crack surfaces can interact after fracture. This can happen due to cyclic reclosure (Mode I) or cyclic frictional contact (Mode II and Mode III).
- **Dynamics.** The extension of the proposed finite element to dynamics is a natural continuation of the present work and will allow the accurate study of structures under seismic events.
- **Large strains.** In the presented work, infinitesimal strains were assumed in the strong form of the mechanical problem. Further research is required in order to include finite deformation effects, which are crucial for the description of many real-life case studies.
- **Higher order elements.** The interpolation used in the case studies consisted of linear shape functions. Higher order elements were not studied and this will provide more insights in the proposed FE technology.

9.3 Publications

The work presented in this thesis resulted in the following peer-reviewed journal publications:

1. Cervera, M., Chiumenti, M., Benedetti, L. and Codina, R. **Mixed stabilized finite element methods in nonlinear solid mechanics. Part III: Compressible and incompressible plasticity**. *Computer Methods in Applied Mechanics and Engineering*, 285, 752-775, (2015).
2. Benedetti, L., Cervera, M. and Chiumenti, M. **Stress-accurate Mixed FEM for soil failure under shallow foundations involving strain localization in plasticity**. *Computers and Geotechnics*, 64, 32-47, (2015).

3. Benedetti, L., Cervera, M. and Chiumenti, M. **High-fidelity prediction of crack formation in 2D and 3D pullout tests**. *Computers & Structures*, 172, 93-109, (2016).

4. Benedetti, L., Cervera, M. and Chiumenti, M. **3D numerical modelling of twisting cracks under bending and torsion of skew notched beams**. Submitted to *Engineering Fracture Mechanics*, (2017).

5. Benedetti, L., Gaume, J. and Fischer, J.-T. **A mechanically-based model of snow slab and weak layer fracture in the Propagation Saw Test**. Submitted to *International Journal of Solids and Structures*, (2017).

These contributions are attached in the following pages.

This page is left intentionally blank.

Simplicity is the final achievement.
After one has played a vast quantity of notes and more notes,
it is simplicity that emerges as the crowning reward of art.

Frédéric Chopin

This page is left intentionally blank.

Bibliography

[1] M. Cervera, M. Chiumenti, Q. Valverde, and C. Agelet De Saracibar. Mixed linear/linear simplicial elements for incompressible elasticity and plasticity. *Computer Methods in Applied Mechanics and Engineering*, 192(49):5249–5263, 2003.

[2] M. Chiumenti, Q. Valverde, C. Agelet De Saracibar, and M. Cervera. A stabilized formulation for incompressible plasticity using linear triangles and tetrahedra. *International Journal of Plasticity*, 20(8):1487–1504, 2004.

[3] M. Cervera, M. Chiumenti, and C. Agelet de Saracibar. Shear band localization via local J2 continuum damage mechanics. *Computer Methods in Applied Mechanics and Engineering*, 193(9-11):849–880, March 2004.

[4] M. Cervera, M. Chiumenti, and C. Agelet de Saracibar. Softening, localization and stabilization: capture of discontinuous solutions in J2 plasticity. *International Journal for Numerical and Analytical Methods in Geomechanics*, 28(5): 373–393, 2004.

[5] M. Cervera, M. Chiumenti, and R. Codina. Mixed stabilized finite element methods in nonlinear solid mechanics: Part I: Formulation. *Computer Methods in Applied Mechanics and Engineering*, 199(37):2559–2570, 2010.

[6] M. Cervera, M. Chiumenti, and R. Codina. Mixed stabilized finite element methods in nonlinear solid mechanics: Part II: Strain localization. *Computer Methods in Applied Mechanics and Engineering*, 199(37):2571–2589, 2010.

[7] M. Cervera, M. Chiumenti, and R. Codina. Mesh objective modeling of cracks using continuous linear strain and displacement interpolations. *International Journal for Numerical Methods in Engineering*, 87(10):962–987, 2011.

[8] J. Hansen, A. Lacis, D. Rind, G. Russell, P. Stone, I. Fung, R. F. Ruedy, and J. Lerner. Climate sensitivity: Analysis of feedback mechanisms. *Geophysical Monograph Series*, 29:130–163, 1984.

[9] European Economic and Social Committee and the Committee of the Regions. Communication from the Commission to the Council - Thematic Strategy for Soil Protection [SEC(2006)620] [SEC(2006)1165]. Technical Report COM/2006/0231 final, European Parliament, 2006.

[10] H.-J. Etter, R. Meister, and D. Atkins. Icar and its importance in avalanche rescue. In *Proceedings ISSW*, pages 360–369, 2004.

[11] C. Wilhelm, T. Wiesinger, M. Bründl, and W. J. Ammann. The avalanche winter 1999 in Switzerland-an overview. In *Proceedings International Snow Science Workshop, Big Sky, Montana, USA, 1-6 October 2000*, pages 487–494, 2001.

[12] C. A. Felippa. Course notes on Introduction to Finite Element Methods. URL `http://www.colorado.edu/engineering/Aerospace/CAS/courses.d/IFEM.d`.

[13] G. Strang and G. J. Fix. *An analysis of the finite element method*, volume 212. Prentice-hall Englewood Cliffs, NJ, 1973.

[14] T. J. R. Hughes, L. P. Franca, and M. Balestra. A new finite element formulation for computational fluid dynamics: V. Circumventing the Babuška-Brezzi condition: A stable Petrov-Galerkin formulation of the Stokes problem accommodating equal-order interpolations. *Computer Methods in Applied Mechanics and Engineering*, 59(1):85–99, 1986.

[15] T. J. R. Hughes, L. P. Franca, and G. M. Hulbert. A new finite element formulation for computational fluid dynamics: Viii. the galerkin/least-squares method for advective-diffusive equations. *Computer Methods in Applied Mechanics and Engineering*, 73(2):173–189, 1989.

[16] R. Codina. Stabilization of incompressibility and convection through orthogonal sub-scales in finite element methods. *Computer Methods in Applied Mechanics and Engineering*, 190:1579–1599, 2000.

[17] R. Codina. Stabilized finite element approximation of transient incompressible flows using orthogonal subscales. *Computer Methods in Applied Mechanics and Engineering*, 191(39):4295–4321, 2002.

[18] S.P. Timoshenko and J.N. Goodier. *Theory of elasticity*. Mac Graw-Hill, 1951. ISBN 978-0070701229.

[19] C. Truesdell and W. Noll. *The Non-Linear Field Theories of Mechanics*. Springer Berlin Heidelberg, 1965. ISBN 978-3662103883.

[20] J. E. Marsden and T. J. R. Hughes. *Mathematical Foundations of Elasticity*. Courier Dover Publications, 1994. ISBN 978-0486678658.

[21] G. I. Taylor. Plastic Strain in Metals. *Journal of the Institute of Metals*, 62: 307–324, 1938.

[22] J. F. W. Bishop and R. Hill. XLVI. a theory of the plastic distortion of a polycrystalline aggregate under combined stresses. *The London, Edinburgh,*

and Dublin Philosophical Magazine and Journal of Science, 42(327):414–427, 1951.

[23] J. F. W. Bishop and R. Hill. CXXVIII. a theoretical derivation of the plastic properties of a polycrystalline face-centred metal. *The London, Edinburgh, and Dublin Philosophical Magazine and Journal of Science*, 42(334):1298–1307, 1951.

[24] T. H. Lin. Analysis of elastic and plastic strains of a face-centred cubic crystal. *Journal of the Mechanics and Physics of Solids*, 5(2):143–149, 1957.

[25] J. W. Hutchinson. Elastic-plastic behaviour of polycrystalline metals and composites. *Proceedings of the Royal Society of London A: Mathematical, Physical and Engineering Sciences*, 319(1537):247–272, 1970.

[26] L. M. Kachanov. Time of the rupture process under creep conditions. *Isv. Akad. Nauk. SSR. Otd Tekh. Nauk.*, 8:26–31, 1958.

[27] J. Lemaitre. A continuous damage mechanics model for ductile fracture. *Journal of engineering materials and technology*, 107(1):83–89, 1985.

[28] J. Lemaitre and J. Dufailly. Damage measurements. *Engineering Fracture Mechanics*, 28(5):643–661, 1987.

[29] J. L. Chaboche. Continuum Damage Mechanics: Part I — General Concepts. *Journal of Applied Mechanics*, 55(1):59–64, 1988.

[30] J. L. Chaboche. Continuum damage mechanics: Part II — Damage growth, crack initiation, and crack growth. *Journal of applied mechanics*, 55(1):65–72, 1988.

[31] D. Krajcinovic. Damage mechanics. *Mechanics of Materials*, 8(2):117 – 197, 1989.

[32] V. Tvergaard and A. Needleman. Analysis of the cup-cone fracture in a round tensile bar. *Acta Metallurgica*, 32(1):157 – 169, 1984. ISSN 0001-6160.

[33] A. Needleman and V. Tvergaard. An analysis of ductile rupture in notched bars. *Journal of the Mechanics and Physics of Solids*, 32(6):461 – 490, 1984.

[34] J. Koplik and A. Needleman. Void growth and coalescence in porous plastic solids. *International Journal of Solids and Structures*, 24(8):835 – 853, 1988.

[35] R. Becker, A. Needleman, O. Richmond, and V. Tvergaard. Void growth and failure in notched bars. *Journal of the Mechanics and Physics of Solids*, 36(3): 317 – 351, 1988.

[36] V. Tvergaard. Material failure by void growth to coalescence. 27:83 – 151, 1989. ISSN 0065-2156.

[37] A. C. Fischer-Cripps. *Introduction to contact mechanics*. Springer, 2000.

[38] M. M. Carroll and A. C. Holt. Static and dynamic pore-collapse relations for ductile porous materials. *Journal of Applied Physics*, 43(4):1626–1636, 1972.

[39] E. Klein, P. Baud, T. Reuschlé, and T. F. Wong. Mechanical behaviour and failure mode of bentheim sandstone under triaxial compression. *Physics and Chemistry of the Earth, Part A: Solid Earth and Geodesy*, 26(1-2):21–25, 2001.

[40] T.-F. Wong, P. Baud, and E. Klein. Localized failure modes in a compactant porous rock. *Geophysical Research Letters*, 28(13):2521–2524, 2001.

[41] J. Heierli, P. Gumbsch, and M. Zaiser. Anticrack nucleation as triggering mechanism for snow slab avalanches. *Science*, 321(5886):240–243, 2008.

[42] L. P. Pook. Five decades of crack path research. *Engineering Fracture Mechanics*, 77(11):1619–1630, 2010.

[43] C. A. de Coulomb. *Essai sur une application des règles de maximis et de minimis à quelques problèmes de Statique relatifs à l'Architecture*. 1773.

[44] H. Tresca. *Mémoire sur l'ecoulement des corps solides.*, volume 18 of *Mémoires présentés par divers savants á l'Institut impérial de France*. 1868.

[45] W. J. M. Rankine. *Manual of Applied Mechanics*. Griffin, London, 1868.

[46] M. Lévy. Mémoire sur les équations générales des mouvements intérieurs des corps solides ductiles au delà des limites où l'élasticité pourrait les ramener à leur premier état. *Comptes Rendus de l'Académie des Sciences, Paris*, 70 (1323), 1870.

[47] R. von Mises. Mechanik der festen Körper im plastisch-deformablen Zustand. *Nachrichten von der Gesellschaft der Wissenschaften zu Göttingen, Mathematisch-Physikalische Klasse*, 1913:582–592, 1913.

[48] L. Prandtl. Über die härte plastischer körper. *Nachrichten von der Gesellschaft der Wissenschaften zu Göttingen, Mathematisch-Physikalische Klasse*, 1920: 74–85, 1920.

[49] H. Hencky. Über einige statisch bestimmte fälle des gleichgewichts in plastischen körpern. *ZAMM-Journal of Applied Mathematics and Mechanics/Zeitschrift für Angewandte Mathematik und Mechanik*, 3(4):241–251, 1923.

[50] A. Reuss. Berücksichtigung der elastischen Formänderung in der Plastizitätstheorie. *ZAMM-Journal of Applied Mathematics and Mechanics/Zeitschrift für Angewandte Mathematik und Mechanik*, 10(3):266–274, 1930.

[51] A. Nadai. *Plasticity, a mechanics of the plastic state of matter.* McGraw-Hill, 1931.

[52] R. Hill. *The Mathematical Theory of Plasticity.* Oxford classic texts in the physical sciences. Clarendon Press, 1950.

[53] H. W. Kuhn and A. W. Tucker. Nonlinear programming. In *Second Berkeley Symposium on Mathematical Statistics and Probability*, volume 1, pages 481–492, 1951.

[54] J. Mazars and J. Lemaitre. Application of continuous damage mechanics to strain and fracture behavior of concrete. In *Application of Fracture Mechanics to Cementitious Composites*, pages 507–520. Springer, 1985.

[55] J. C. Simo and J. W. Ju. Strain-and stress-based continuum damage models — I. Formulation. *International Journal of Solids and Structures*, 23(7):821–840, 1987.

[56] J. C. Simo and J. W. Ju. Strain-and stress-based continuum damage models — II. Computational aspects. *International journal of solids and structures*, 23 (7):841–869, 1987.

[57] J. P. Cordebois and F. Sidoroff. Damage induced elastic anisotropy. In *Mechanical Behavior of Anisotropic Solids/Comportment Méchanique des Solides Anisotropes*, pages 761–774. Springer, 1982.

[58] G. Z. Voyiadjis and P. Kattan. A comparative study of damage variables in continuum damage mechanics. *International Journal of Damage Mechanics*, 2008.

[59] C. L. Chow and J. Wang. An anisotropic theory of elasticity for continuum damage mechanics. *International Journal of Fracture*, 33(1):3–16, 1987.

[60] C. L. Chow and J. Wang. An anisotropic theory of continuum damage mechanics for ductile fracture. *Engineering Fracture Mechanics*, 27(5):547–558, 1987.

[61] J. Lubliner, J. Oliver, S. Oller, and E. Oñate. A plastic-damage model for concrete. *International Journal of solids and structures*, 25(3):299–326, 1989.

[62] E. G. Kirsch. Die theorie der elastizität und die bedürfnisse der festigkeitslehre. *Zeitschrift des Vereines deutscher Ingenieure*, 42:797–807, 1898.

[63] C. E. Inglis. Stresses in a plate due to the presence of cracks and sharp corners. *Transactions of the Institute of Naval Architects*, 55:219–241, 1913.

[64] A. A. Griffith. The phenomena of rupture and flow in solids. *Philosophical Transactions of the Royal Society of London A: Mathematical, Physical and Engineering Sciences*, 221(582-593):163–198, 1921.

[65] G. R. Irwin. Analysis of stresses and strains near the end of a crack traversing a plate. *Journal of Applied Mechanics*, 24(57):361–364, 1957.

[66] G. I. Banreblatt. Equilibrium cracks formed during brittle fracture. *Prikl. Mat. Mech*, 23, 1959.

[67] D. S. Dugdale. Yielding of steel sheets containing slits. *Journal of the Mechanics and Physics of Solids*, 8(2):100 – 104, 1960. ISSN 0022-5096.

[68] G. I. Barenblatt. The mathematical theory of equilibrium cracks in brittle fracture. volume 7 of *Advances in Applied Mechanics*, pages 55 – 129. Elsevier, 1962.

[69] Z. P. Bazant and J. Planas. *Fracture and size effect in concrete and other quasibrittle materials*, volume 16. CRC press, 1997.

[70] A. Carpinteri. *Size-scale effects in the failure mechanisms of materials and structures*. CRC Press, 2002.

[71] M. Cervera and M. Chiumenti. Size effect and localization in J2 plasticity. *International Journal of Solids and Structures*, 46(17):3301–3312, 2009.

[72] J. H. Argyris and H. Kelsey. Energy theorems and structural analysis. *Aircraft Engineering*, 26, Oct-Nov 1954.

[73] M. J. Turner, R. W. Clough, H. C. Martin, and L. J. Topp. Stiffness and deflection analysis of complex structures. *Journal of the Aeronautical Sciences*, 23:805–824, 1956.

[74] M. J. Turner. The direct stiffness method of structural analysis. *Paper presented at a meeting of the Structures & Materials Panel, AGARD, at the Technische Hockschule, Aachen, Germany*, 1959.

[75] M. J. Turner, E. H. Dill, H. C. Martin, and R. J. Melosh. Large deflections of structures subjected to heating and external loads. *Journal of the Aerospace Sciences*, 27(2):97–106, 1960.

[76] R. W. Clough. The finite element method in plane stress analysis. In *Proc. 2nd ASCE Conf. on Electronic Computation*, 1960.

[77] R. W. Clough. The stress distribution of norfolk dam. *Structures and Materials Research*, 100(19), 1962.

[78] R. J. Melosh. Basis for derivation of matrices for the direct stiffness method. *AIAA Journal*, 1(7):1631–1637, 1963.

[79] E. L. Wilson. Structural analysis of axisymmetric solids. *AIAA Journal*, 3(12): 2269–2274, 1965.

[80] B. M. Irons and J. Barlow. Comment on "Basis for derivation of matrices for the direct stiffness method". *AIAA Journal*, 2(2):403–404, 1964.

[81] B. M. Irons and K. J. Draper. Inadequacy of nodal connections in a stiffness solution for plate bending. *AIAA Journal*, 3(5):961–961, 1965.

[82] B. M. Irons. Engineering applications of numerical integration in stiffness methods. *AIAA journal*, 4(11):2035–2037, 1966.

[83] O. C. Zienkiewicz and Y. K. Cheung. Finite elements in the solution of field problems. *The Engineer*, page 507–510, 1965.

[84] H. C. Martin and G. F. Carey. *Introduction to finite element analysis: Theory and application*. McGraw-Hill College, 1973.

[85] O. C. Zienkiewicz and R. L. Taylor. *The finite element method in Engineering Science*. McGraw-Hill, London, 1967.

[86] C. A. Felippa. A historical outline of matrix structural analysis: a play in three acts. *Computers & Structures*, 79(14):1313–1324, 2001.

[87] T. Y. Thomas. *Plastic Flow and Fracture in Solids*. Elsevier, 1961.

[88] R. W. Clough. The stress distribution of norfork dam. Technical Report 19, Department of Civil Engineering, University of California, Berkley, California, USA, 1962.

[89] D. Ngo and A. C. Scordelis. Finite element analysis of reinforced concrete beams. *ACI Journal*, 64(3):152–163, 1967.

[90] A. H. Nilson. Nonlinear analysis of reinforced concrete by the finite element method. 65(9):757–766, 1968.

[91] M. S. Shephard, N. A. B. Yehia, G. S. Burd, and T. J. Weidner. Automatic crack propagation tracking. *Computers & Structures*, 20(1-3):211–223, 1985.

[92] P. A. Wawrzynek and A. R. Ingraffea. An interactive approach to local remeshing around a propagating crack. *Finite Elements in Analysis and Design*, 5(1):87–96, 1989.

[93] T. N. Bittencourt, P. A. Wawrzynek, A. R. Ingraffea, and J. L. Sousa. Quasi-automatic simulation of crack propagation for 2d lefm problems. *Engineering Fracture Mechanics*, 55(2):321–334, 1996.

[94] A. Trädegård, F. Nilsson, and S. Östlund. Fem-remeshing technique applied to crack growth problems. *Computer Methods in Applied Mechanics and Engineering*, 160(1-2):115–131, 1998.

[95] P.-O. Bouchard, F. Bay, Y. Chastel, and I. Tovena. Crack propagation modelling using an advanced remeshing technique. *Computer methods in applied mechanics and engineering*, 189(3):723–742, 2000.

[96] P.-O. Bouchard, F. Bay, and Y. Chastel. Numerical modelling of crack propagation: automatic remeshing and comparison of different criteria. *Computer methods in applied mechanics and engineering*, 192(35):3887–3908, 2003.

[97] M. Cervera. An orthotropic mesh corrected crack model. *Computer Methods in Applied Mechanics and Engineering*, 197(17):1603–1619, 2008.

[98] M. Ortiz, Y. Leroy, and A. Needleman. A finite element method for localized failure analysis. *Computer Methods in Applied Mechanics and Engineering*, 61 (2):189–214, 1987.

[99] T. Belytschko, J. Fish, and B. E. Engelmann. A finite element with embedded localization zones. *Computer Methods in Applied Mechanics and Engineering*, 70(1):59 – 89, 1988.

[100] T. Belytschko and T. Black. Elastic crack growth in finite elements with minimal remeshing. *International journal for numerical methods in engineering*, 45(5): 601–620, 1999.

[101] J. Dolbow and T. Belytschko. A finite element method for crack growth without remeshing. *International journal for numerical methods in engineering*, 46(1): 131–150, 1999.

[102] N. Sukumar, N. Moës, B. Moran, and T. Belytschko. Extended finite element method for three-dimensional crack modelling. *International Journal for Numerical Methods in Engineering*, 48(11):1549–1570, 2000.

[103] N. Sukumar, D. L. Chopp, N. Moës, and T. Belytschko. Modeling holes and inclusions by level sets in the extended finite-element method. *Computer methods in applied mechanics and engineering*, 190(46):6183–6200, 2001.

[104] N. Moës and T. Belytschko. Extended finite element method for cohesive crack growth. *Engineering fracture mechanics*, 69(7):813–833, 2002.

[105] J. M. Melenk and I. Babuška. The partition of unity finite element method: basic theory and applications. *Computer methods in applied mechanics and engineering*, 139(1-4):289–314, 1996.

[106] M. Griebel and M. A. Schweitzer. A particle-partition of unity method for the solution of elliptic, parabolic, and hyperbolic pdes. *SIAM Journal on Scientific Computing*, 22(3):853–890, 2000.

[107] T. Strouboulis, I. Babuška, and K. Copps. The design and analysis of the generalized finite element method. *Computer methods in applied mechanics and engineering*, 181(1):43–69, 2000.

[108] C. A. Duarte, O. N. Hamzeh, T. J. Liszka, and W. W. Tworzydlo. A generalized finite element method for the simulation of three-dimensional dynamic crack propagation. *Computer Methods in Applied Mechanics and Engineering*, 190 (15):2227–2262, 2001.

[109] T.-P. Fries and T. Belytschko. The extended/generalized finite element method: an overview of the method and its applications. *International Journal for Numerical Methods in Engineering*, 84(3):253–304, 2010.

[110] J. C. Simo, J. Oliver, and F. Armero. An analysis of strong discontinuities induced by strain-softening in rate-independent inelastic solids. *Computational mechanics*, 12(5):277–296, 1993.

[111] J. Oliver. Modelling strong discontinuities in solid mechanics via strain softening constitutive equations. Part 1: Fundamentals. *International journal for numerical methods in engineering*, 39(21):3575–3600, 1996.

[112] J. Oliver. Modelling strong discontinuities in solid mechanics via strain softening constitutive equations. Part 2: Numerical simulation. *International journal for numerical methods in engineering*, 39(21):3601–3623, 1996.

[113] J. Oliver, M. Cervera, and O. Manzoli. Strong discontinuities and continuum plasticity models: the strong discontinuity approach. *International Journal of Plasticity*, 15(3):319 – 351, 1999.

[114] F. Armero and K. Garikipati. An analysis of strong discontinuities in multiplicative finite strain plasticity and their relation with the numerical simulation of strain localization in solids. *International Journal of Solids and Structures*, 33(20):2863–2885, 1996.

[115] C. Linder and F. Armero. Finite elements with embedded strong discontinuities for the modeling of failure in solids. *International Journal for Numerical Methods in Engineering*, 72(12):1391–1433, 2007.

[116] F. Armero and C. Linder. New finite elements with embedded strong discontinuities in the finite deformation range. *Computer Methods in Applied Mechanics and Engineering*, 197(33):3138–3170, 2008.

[117] R. A. Regueiro and R. I. Borja. A finite element model of localized deformation in frictional materials taking a strong discontinuity approach. *Finite Elements in Analysis and Design*, 33(4):283 – 315, 1999.

[118] R. I. Borja. A finite element model for strain localization analysis of strongly discontinuous fields based on standard galerkin approximation. *Computer Methods in Applied Mechanics and Engineering*, 190(11–12):1529 – 1549, 2000.

[119] R. I. Borja and R. A. Regueiro. Strain localization in frictional materials exhibiting displacement jumps. *Computer Methods in Applied Mechanics and Engineering*, 190(20–21):2555 – 2580, 2001.

[120] C. D. Foster, R. I. Borja, and R. A. Regueiro. Embedded strong discontinuity finite elements for fractured geomaterials with variable friction. *International Journal for Numerical Methods in Engineering*, 72(5):549–581, 2007.

[121] J. Chessa, H. Wang, and T. Belytschko. On the construction of blending elements for local partition of unity enriched finite elements. *International Journal for Numerical Methods in Engineering*, 57(7):1015–1038, 2003.

[122] T.-P. Fries. A corrected xfem approximation without problems in blending elements. *International Journal for Numerical Methods in Engineering*, 75(5): 503–532, 2008.

[123] J. E. Tarancón, A. Vercher, E. Giner, and F. J. Fuenmayor. Enhanced blending elements for xfem applied to linear elastic fracture mechanics. *International Journal for Numerical Methods in Engineering*, 77(1):126–148, 2009.

[124] T. C. Gasser and G. A. Holzapfel. 3d crack propagation in unreinforced concrete.: A two-step algorithm for tracking 3d crack paths. *Computer Methods in Applied Mechanics and Engineering*, 195(37):5198–5219, 2006.

[125] J. M. Sancho, J. Planas, D. A. Cendón, E. Reyes, and J. C. Gálvez. An embedded crack model for finite element analysis of concrete fracture. *Engineering Fracture Mechanics*, 74(1):75–86, 2007.

[126] P. Jäger, P. Steinmann, and E. Kuhl. Modeling three-dimensional crack propagation—a comparison of crack path tracking strategies. *International Journal for Numerical Methods in Engineering*, 76(9):1328–1352, 2008.

[127] M. Cervera and M. Chiumenti. Mesh objective tensile cracking via a local continuum damage model and a crack tracking technique. *Computer methods in applied mechanics and engineering*, 196(1):304–320, 2006.

[128] Y. R. Rashid. Ultimate strength analysis of prestressed concrete pressure vessels. *Nuclear Engineering and Design*, 7(4):334–344, 1968.

[129] Z. P. Bažant and L. Cedolin. Blunt crack band propagation in finite element analysis. *Journal of the Engineering Mechanics Division*, 105(2):297–315, 1979.

[130] Z. P. Bažant and L. Cedolin. Finite element modeling of crack band propagation. *Journal of Structural Engineering*, 109(1):69–92, 1983.

[131] J. G. Rots, P. Nauta, G. M. A. Kuster, and J. Blaauwendraad. Smeared crack approach and fracture localization in concrete. *HERON, 30 (1), 1985*, 1985.

[132] P. H. Feenstra and R. De Borst. A plasticity model and algorithm for mode-I cracking in concrete. *International Journal for Numerical Methods in Engineering*, 38:2509–2529, 1995.

[133] A. R. Ingraffea and M. J. Panthaki. Analysis of shear fracture tests of concrete beams. In *Finite element analysis of reinforced concrete structures*, pages 151–173. ASCE, 1985.

[134] Z. P. Bažant and P. A. Pfeiffer. Shear fracture tests of concrete. *Materials and Structures*, 19(2):111–121, 1986.

[135] J. G. Rots and R. De Borst. Analysis of mixed-mode fracture in concrete. *Journal of Engineering Mechanics*, 113(11):1739–1758, 1987.

[136] M. Cervera, J. Oliver, E. Herrero, and E. Oñate. A computational model for progressive cracking in large dams due to the swelling of concrete. *Engineering Fracture Mechanics*, 35(1):573–585, 1990.

[137] M. Cervera, J. Oliver, and R. Faria. Seismic evaluation of concrete dams via continuum damage models. *Earthquake Engineering and Structural Dynamics*, 24(9):1225–1246, 1995.

[138] S. T. Pietruszczak and Z. Mroz. Finite element analysis of deformation of strain-softening materials. *International Journal for Numerical Methods in Engineering*, 17(3):327–334, 1981.

[139] Z. P. Bažant and B. H. Oh. Crack band theory for fracture of concrete. *Matériaux et construction*, 16(3):155–177, 1983.

[140] M. Cervera and J.-Y. Wu. On the conformity of strong, regularized, embedded and smeared discontinuity approaches for the modeling of localized failure in solids. *International Journal of Solids and Structures*, 71:19–38, 2015.

[141] G. Pijaudier-Cabot and Z. P. Bazant. Nonlocal damage theory. *Journal of engineering mechanics*, 113(10):1512–1533, 1987.

[142] M. Jirasek. Nonlocal models for damage and fracture: comparison of approaches. *International Journal of Solids and Structures*, 35(31):4133–4145, 1998.

[143] Z. P. Bazant and M. Jirásek. Nonlocal integral formulations of plasticity and damage: survey of progress. *Journal of Engineering Mechanics*, 128(11): 1119–1149, 2002.

[144] I. Vardoulakis and E. C. Aifantis. A gradient flow theory of plasticity for granular materials. *Acta Mechanica*, 87(3-4):197–217, 1991.

[145] R. De Borst and H.-B. Mühlhaus. Gradient-dependent plasticity: Formulation and algorithmic aspects. *International Journal for Numerical Methods in Engineering*, 35(3):521–539, 1992.

[146] R. H. J. Peerlings, R. De Borst, W. A. M. Brekelmans, and M. G. D. Geers. Gradient-enhanced damage modelling of concrete fracture. *Mechanics of Cohesive-frictional Materials*, 3(4):323–342, 1998.

[147] E. C. Aifantis. On the microstructural origin of certain inelastic models. *Journal of Engineering Materials and technology*, 106(4):326–330, 1984.

[148] R. De Borst. Simulation of strain localization: a reappraisal of the Cosserat continuum. *Engineering computations*, 8(4):317–332, 1991.

[149] P. Steinmann and K. Willam. Localization within the framework of micropolar elasto-plasticity. In *Advances in continuum mechanics*, pages 296–313. Springer, 1991.

[150] C. Miehe, F. Welschinger, and M. Hofacker. Thermodynamically consistent phase-field models of fracture: Variational principles and multi-field FE implementations. *International Journal for Numerical Methods in Engineering*, 83 (10):1273–1311, 2010.

[151] C. Kuhn and R. Müller. A continuum phase field model for fracture. *Engineering Fracture Mechanics*, 77(18):3625–3634, 2010.

[152] J. Vignollet, S. May, R. De Borst, and C. V. Verhoosel. Phase-field models for brittle and cohesive fracture. *Meccanica*, 49(11):2587–2601, 2014.

[153] M. Ambati, T. Gerasimov, and L. De Lorenzis. A review on phase-field models of brittle fracture and a new fast hybrid formulation. *Computational Mechanics*, 55(2):383–405, 2015.

[154] S. May, J. Vignollet, and R. De Borst. A numerical assessment of phase-field models for brittle and cohesive fracture: γ-convergence and stress oscillations. *European Journal of Mechanics-A/Solids*, 52:72–84, 2015.

[155] M. Cervera, M. Chiumenti, and D. Di Capua. Benchmarking on bifurcation and localization in J2 plasticity for plane stress and plane strain conditions. *Computer Methods in Applied Mechanics and Engineering*, 241-244:206–224, oct 2012.

[156] O. C. Zienkiewicz, M. Pastor, and M. Huang. Softening, localisation and adaptive remeshing. Capture of discontinuous solutions. *Computational mechanics*, 17(1-2):98–106, 1995.

[157] O. C. Zienkiewicz, M. Huang, and M. Pastor. Localization problems in plasticity using finite elements with adaptive remeshing. *International Journal for Numerical and Analytical Methods in Geomechanics*, 19(2):127–148, 1995.

[158] J. C. Simo and M. S. Rifai. A class of mixed assumed strain methods and the method of incompatible modes. *International journal for numerical methods in engineering*, 29(8):1595–1638, 1990.

[159] J. C. Simo and F. Armero. Geometrically non-linear enhanced strain mixed methods and the method of incompatible modes. *International Journal for Numerical Methods in Engineering*, 33(7):1413–1449, 1992.

[160] J. C. Simo, J. Oliver, and F. Armero. An analysis of strong discontinuities induced by strain-softening in rate-independent inelastic solids. *Computational mechanics*, 12(5):277–296, 1993.

[161] M. Cervera. A smeared-embedded mesh-corrected damage model for tensile cracking. *International journal for numerical methods in engineering*, 76(12): 1930, 2008.

[162] E. Hinton and J. S. Campbell. Local and global smoothing of discontinuous finite element functions using a least squares method. *International Journal for Numerical Methods in Engineering*, 8(3):461–480, 1974.

[163] O. C. Zienkiewicz and J. Z. Zhu. The superconvergent patch recovery and a posteriori error estimates. part 1: The recovery technique. *International Journal for Numerical Methods in Engineering*, 33(7):1331–1364, 1992.

[164] O. C. Zienkiewicz and J. Z. Zhu. The superconvergent patch recovery and a posteriori error estimates. part 2: Error estimates and adaptivity. *International Journal for Numerical Methods in Engineering*, 33(7):1365–1382, 1992.

[165] D. J. Payen and K.-J. Bathe. The use of nodal point forces to improve element stresses. *Computers & Structures*, 89(5):485–495, 2011.

[166] D. J. Payen and K.-J. Bathe. A stress improvement procedure. *Computers & Structures*, 112:311–326, 2012.

[167] T. H. H. Pian. Derivation of element stiffness matrices by assumed stress distributions. *AIAA journal*, 2(7):1333–1336, 1964.

[168] R. H. MacNeal. Derivation of element stiffness matrices by assumed strain distributions. *Nuclear Engineering and Design*, 70(1):3–12, 1982.

[169] J. C. Simo and T. J. R. Hughes. On the variational foundations of assumed strain methods. *Journal of Applied Mechanics*, 53(1):51–54, 1986.

[170] B. Fraeijs De Veubeke. Displacement and equilibrium models in the finite element method. *Stress analysis*, 9:145–197, 1965.

[171] L. R. Herrmann. Elasticity equations for incompressible and nearly incompressible materials by a variational theorem. *AIAA journal*, 3(10):1896–1900, 1965.

[172] R. L. Taylor, K. S. Pister, and L. R. Herrmann. On a variational theorem for incompressible and nearly-incompressible orthotropic elasticity. *International Journal of Solids and Structures*, 4(9):875–883, 1968.

[173] K. Washizu. On the variational principles of elasticity and plasticity. Technical report, DTIC Document, 1955.

[174] K. Washizu. *Variational methods in elasticity and plasticity*. Pergamon press, 1975.

[175] M. Crouzeix and P.-A. Raviart. Conforming and nonconforming finite element methods for solving the stationary stokes equations i. *Revue française d'automatique, informatique, recherche opérationnelle. Mathématique*, 7(3): 33–75, 1973.

[176] P.-A. Raviart and J.-M. Thomas. A mixed finite element method for 2-nd order elliptic problems. In *Mathematical aspects of finite element methods*, pages 292–315. Springer, 1977.

[177] T. H. H. Pian and K. Sumihara. Rational approach for assumed stress finite elements. *International Journal for Numerical Methods in Engineering*, 20(9): 1685–1695, 1984.

[178] D. Boffi, F. Brezzi, and M. Fortin. *Mixed Finite Element Methods and Applications*. Springer, 2013.

[179] V. Girault and P.-A. Raviart. *Finite element methods for Navier-Stokes equations: theory and algorithms*, volume 5. Springer Science & Business Media, 1986.

[180] A. J. Chorin. Numerical solution of the Navier-Stokes equations. *Mathematics of computation*, 22(104):745–762, 1968.

[181] R. Temam. Sur l'approximation de la solution des équations de Navier-Stokes par la méthode des pas fractionnaires (I). *Archive for Rational Mechanics and Analysis*, 32(2):135–153, 1969.

[182] J. Donea, S. Giuliani, H. Laval, and L. Quartapelle. Finite element solution of the unsteady Navier-Stokes equations by a fractional step method. *Computer Methods in Applied Mechanics and Engineering*, 30(1):53–73, 1982.

[183] O. C. Zienkiewicz, P. Nithiarasu, R. Codina, M. Vazquez, and P. Ortiz. The characteristic-based-split procedure: an efficient and accurate algorithm for fluid problems. *International Journal for Numerical Methods in Fluids*, 31(1): 359–392, 1999.

[184] R. Codina. Pressure stability in fractional step finite element methods for incompressible flows. *Journal of Computational Physics*, 170(1):112–140, 2001.

[185] O. A. Ladyzhenskaya. Solution "in the large" to the boundary value problem for the navier-stokes equations in two space variables. In *Sovjet Physics Dokl*, volume 123, pages 1128–1131, 1958.

[186] I. Babuška. The finite element method with lagrangian multipliers. *Numerische Mathematik*, 20(3):179–192, 1973.

[187] F. Brezzi. On the existence, uniqueness and approximation of saddle-point problems arising from lagrangian multipliers. *Revue française d'automatique, informatique, recherche opérationnelle. Analyse numérique*, 8(2):129–151, 1974.

[188] C. Johnson and J. Pitkäranta. Analysis of some mixed finite element methods related to reduced integration. *Mathematics of Computation*, 38(158):375–400, 1982.

[189] D. J. Silvester and N. Kechkar. Stabilised bilinear-constant velocity-pressure finite elements for the conjugate gradient solution of the stokes problem. *Computer Methods in Applied Mechanics and Engineering*, 79(1):71–86, 1990.

[190] M. Bercovier. Perturbation of mixed variational problems. application to mixed finite element methods. *RAIRO-Analyse numérique*, 12(3):211–236, 1978.

[191] D. J. Silvester. Optimal low order finite element methods for incompressible flow. *Computer methods in applied mechanics and engineering*, 111(3-4):357–368, 1994.

[192] C. Taylor and P. Hood. A numerical solution of the Navier-Stokes equations using the finite element technique. *Computers & Fluids*, 1(1):73–100, 1973.

[193] F. Brezzi and R. S. Falk. Stability of higher-order Hood-Taylor methods. *SIAM Journal on Numerical Analysis*, 28(3):581–590, 1991.

[194] D. Mijuca. On hexahedral finite element hc8/27 in elasticity. *Computational mechanics*, 33(6):466–480, 2004.

[195] D. N. Arnold, F. Brezzi, and M. Fortin. A stable finite element for the stokes equations. *Calcolo*, 21(4):337–344, 1984.

[196] L. P. Franca and T. J. R. Hughes. Two classes of mixed finite element methods. *Computer Methods in Applied Mechanics and Engineering*, 69(1):89 – 129, 1988. ISSN 0045-7825.

[197] D. S. Malkus and T. J. R. Hughes. Mixed finite element methods—reduced and selective integration techniques: a unification of concepts. *Computer Methods in Applied Mechanics and Engineering*, 15(1):63–81, 1978.

[198] A. N. Brooks and T. J. R. Hughes. Streamline upwind/Petrov-Galerkin formulations for convection dominated flows with particular emphasis on the incompressible Navier-Stokes equations. *Computer methods in applied mechanics and engineering*, 32(1):199–259, 1982.

[199] T. J. R. Hughes. Multiscale phenomena: Green's functions, the Dirichlet-to-Neumann formulation, subgrid scale models, bubbles and the origins of stabilized methods. *Computer methods in applied mechanics and engineering*, 127(1):387–401, 1995.

[200] T. J. R. Hughes, G. R. Feijóo, L. Mazzei, and J.-B. Quincy. The variational multiscale method—a paradigm for computational mechanics. *Computer Methods in Applied Mechanics and Engineering*, 166(1):3 – 24, 1998. ISSN 0045-7825.

[201] R. Codina. A stabilized finite element method for generalized stationary incompressible flows. *Computer Methods in Applied Mechanics and Engineering*, 190:2681–2706, 2001.

[202] R. Codina. Analysis of a stabilized finite element approximation of the oseen equations using orthogonal subscales. *Applied Numerical Mathematics*, 58(3): 264 – 283, 2008.

[203] R. Codina. Finite element approximation of the three-field formulation of the Stokes problem using arbitrary interpolations. *SIAM Journal on Numerical Analysis*, 47(1):699–718, 2009.

[204] S. Badia and R. Codina. Unified stabilized finite element formulations for the Stokes and the Darcy problems. *SIAM Journal on Numerical Analysis*, 47(3): 1971–2000, 2009.

[205] S. Badia and R. Codina. Stabilized continuous and discontinuous Galerkin techniques for Darcy flow. *Computer Methods in Applied Mechanics and Engineering*, 199:1654–1667, 2010.

[206] T. J. R. Hughes and L. P. Franca. A new finite element formulation for computational fluid dynamics: VII. The Stokes problem with various well-posed boundary conditions: symmetric formulations that converge for all velocity/pressure spaces. *Computer Methods in Applied Mechanics and Engineering*, 65(1):85–96, 1987.

[207] L. P. Franca, T. J. R. Hughes, A. F. D. Loula, and I. Miranda. A new family of stable elements for nearly incompressible elasticity based on a mixed Petrov-Galerkin finite element formulation. *Numerische Mathematik*, 53(1-2):123–141, 1988.

[208] J. Bonet and A. J. Burton. A simple average nodal pressure tetrahedral element for incompressible and nearly incompressible dynamic explicit applications. *International Journal for Numerical Methods in Biomedical Engineering*, 14(5): 437–449, 1998.

[209] J. Bonet, H. Marriott, and O. Hassan. An averaged nodal deformation gradient linear tetrahedral element for large strain explicit dynamic applications. *International Journal for Numerical Methods in Biomedical Engineering*, 17(8): 551–561, 2001.

[210] A. M. Maniatty, Y. Liu, O. Klaas, and M. S. Shephard. Stabilized finite element method for viscoplastic flow: formulation and a simple progressive solution strategy. *Computer methods in applied mechanics and engineering*, 190(35): 4609–4625, 2001.

[211] A. M. Maniatty, Y. Liu, O. Klaas, and M. S. Shephard. Higher order stabilized finite element method for hyperelastic finite deformation. *Computer methods in applied mechanics and engineering*, 191(13):1491–1503, 2002.

[212] J. K. Djoko, B. P. Lamichhane, B. D. Reddy, and B. I. Wohlmuth. Conditions for equivalence between the hu–washizu and related formulations, and computational behavior in the incompressible limit. *Computer methods in applied mechanics and engineering*, 195(33):4161–4178, 2006.

[213] J. K. Djoko and B. D. Reddy. An extended hu–washizu formulation for elasticity. *Computer methods in applied mechanics and engineering*, 195(44):6330–6346, 2006.

[214] J. N. Reddy and J. T. Oden. Mixed finite-element approximations of linear boundary-value problems. *Quarterly of Applied Mathematics*, 33(3):255–280, 1975.

[215] J. N. Reddy. On penalty function methods in the finite-element analysis of flow problems. *International Journal for Numerical Methods in Fluids*, 2(2), 1982. ISSN 1097-0363.

[216] E. A. de Souza Neto, D. Perić, G. C. Huang, and D. R. J. Owen. Remarks on the stability of enhanced strain elements in finite elasticity and elastoplasticity. *Communications in Numerical Methods in Engineering*, 11(11):951–961, 1995.

[217] E. A. de Souza Neto, D. Perić, M. Dutko, and D. R. J. Owen. Design of simple low order finite elements for large strain analysis of nearly incompressible solids. *International Journal of Solids and Structures*, 33(20):3277–3296, 1996.

[218] E. P. Kasper and R. L. Taylor. A mixed-enhanced strain method: Part I: Geometrically linear problems. *Computers & Structures*, 75(3):237–250, 2000.

[219] E. P. Kasper and R. L. Taylor. A mixed-enhanced strain method: Part II: Geometrically nonlinear problems. *Computers & Structures*, 75(3):251–260, 2000.

[220] M. Pastor, M. Quecedo, and O. C. Zienkiewicz. A mixed displacement-pressure formulation for numerical analysis of plastic failure. *Computers & structures*, 62(1):13–23, 1997.

[221] M. Pastor, O. C. Zienkiewicz, T. Li, L. Xiaoqing, and M. Huang. Stabilized finite elements with equal order of interpolation for soil dynamics problems. *Archives of Computational Methods in Engineering*, 6(1):3–33, 1999.

[222] M. Chiumenti, Q. Valverde, C. Agelet De Saracibar, and M. Cervera. A stabilized formulation for incompressible elasticity using linear displacement and pressure interpolations. *Computer methods in applied mechanics and engineering*, 191(46):5253–5264, 2002.

[223] J. C. Simo and T. J. R. Hughes. *Computational inelasticity*, volume 7 of *Interdisciplinary Applied Mathematics*. Springer-Verlag, Berlin, 1998.

[224] R. Codina, J. Principe, and J. Baiges. Subscales on the element boundaries in the variational two-scale finite element method. *Computer Methods in Applied Mechanics and Engineering*, 198(5):838–852, 2009.

[225] M. Chiumenti, M. Cervera, and R. Codina. A mixed three-field FE formulation for stress accurate analysis including the incompressible limit. *Computer Methods in Applied Mechanics and Engineering*, 283:1095–1116, 2015.

[226] E. Castillo and R. Codina. Variational multi-scale stabilized formulations for the stationary three-field incompressible viscoelastic flow problem. *Computer Methods in Applied Mechanics and Engineering*, 279:579–605, 2014.

[227] E. Castillo and R. Codina. First, second and third order fractional step methods for the three-field viscoelastic flow problem. *Journal of Computational Physics*, 296:113–137, 2015.

[228] R. Berenbaum and I. Brodie. Measurement of the tensile strength of brittle materials. *British Journal of Applied Physics*, 10(6):281, 1959.

[229] E. Brühwiler and F. H. Wittmann. The wedge splitting test, a new method of performing stable fracture mechanics tests. *Engineering Fracture Mechanics*, 35(1):117–125, 1990.

[230] B. G. Trunk. *Einfluß der Bauteilgröße auf die Bruchenergie von Beton*. Ph.D. thesis, ETH - Eidgenössischen Technischen Hochschule Zürich, 1999.

[231] H. M. Abdalla and B. L. Karihaloo. Determination of size-independent specific fracture energy of concrete from three-point bend and wedge splitting tests. *Magazine of Concrete Research*, 55(2):133–142, 2003.

[232] J. Mazars, D. J. Boerman, and G. Piatti. Mechanical damage and fracture of concrete structures. In *ICF5, Cannes (France) 1981*, 1981.

[233] G. V. Guinea, J. Planas, and M. Elices. Measurement of the fracture energy using three-point bend tests: Part 1 - Influence of experimental procedures. *Materials and Structures*, 25(4):212–218, 1992.

[234] J. C. Gálvez, M. Elices, G. V. Guinea, and J. Planas. Mixed mode fracture of concrete under proportional and nonproportional loading. *International Journal of Fracture*, 94(3):267–284, 1998.

[235] B. Winkler, G. Hofstetter, and G. Niederwanger. Experimental verification of a constitutive model for concrete cracking. *Proceedings of the Institution of Mechanical Engineers, Part L: Journal of Material Design and Applications*, 215:75–86, 2001.

[236] M. Baena, L. Torres, A. Turon, and C. Barris. Experimental study of bond behaviour between concrete and FRP bars using a pull-out test. *Composites Part B: Engineering*, 40(8):784–797, 2009.

[237] T. Lecompte, A. Perrot, A. Subrianto, A. Le Duigou, and G. Ausias. A novel pull-out device used to study the influence of pressure during processing of cement-based material reinforced with coir. *Construction and Building Materials*, 78:224–233, 2015.

[238] M. Dejori. *Experimentelle und numerische Traglastanalysen von axial beanspruchten Kopfbolzen beim Versagensmechanismus Betonausbruch.* Diplomarbeit (Master thesis), University of Innsbruck, 2006.

[239] Y. Thenier and G. Hofstetter. Numerical prediction of crack propagation and crack widths in concrete structure. *Engineering Structures*, 31:1832–1840, 2009.

[240] P. M. A. Areias and T. Belytschko. Analysis of three-dimensional crack initiation and propagation using the extended finite element method. *International journal for numerical methods in engineering*, 63:760–788, 2005.

[241] T. C. Gasser and G. A. Holzapfel. Modeling 3D crack propagation in unreinforced concrete using PUFEM. *Computer methods in applied mechanics and engineering*, 194:2859–2896, 2005.

[242] Q. Duan, J.-H. Song, T. Menouillard, and T. Belytschko. Element-local level set method for three-dimensional dynamic crack growth. *International journal for numerical methdod in engineering*, 80:1520–1543, 2009.

[243] J. Mazars and G. Pijaudier-Cabot. Continuum damage theory. Application to concrete. *ASCE Journal of Engineering Mechanics*, 115(2):345–365, 1989.

[244] R. de Borst. Fracture in quasi-brittle materials: a review of damage-based approaches. *Engineering Fracture Mechanics*, 69:95–112, 2002.

[245] B. Winkler, G. Hofstetter, and H. Lehar. Application of a constitutive model for concrete to the analysis of a precast segmental tunnel lining. *International*

Journal for Numerical and Analytical Methods in Geomechanics, 28:797–819, 2004.

[246] R. Faria, J. Oliver, and M. Cervera. A strain-based plastic viscous damage model for massive concrete structures. *International Journal of Solids and Structures*, 35(14):1533–1558, 1998.

[247] G. Meschke, R. Lackner, and H. A. Mang. An anisotropic elastoplastic-damage model for plain concrete. *International Journal for Numerical Methods in Engineering*, 42(4):703–727, 1998.

[248] J. C. Simo, J. G. Kennedy, and S. Govindjee. Non-smooth multisurface plasticity and viscoplasticity. loading/unloading conditions and numerical algorithms. *International Journal for Numerical Methods in Engineering*, 26(10):2161–2185, 1988.

[249] F. Armero and J. Kim. Three-dimensional finite elements with embedded strong discontinuities to model material failure in the infinitesimal range. *International Journal for Numerical Methods in Engineering*, 91(12):1291–1330, 2012.

[250] R. Hutanu, L. Clapham, and R. B. Rogge. Intergranular strain and texture in steel luders bands. *Acta materialia*, 53(12):3517–3524, 2005.

[251] H. Fujita and S. Miyazaki. Lüders deformation in polycrystalline iron. *Acta Metallurgica*, 26(8):1273–1281, 1978.

[252] K. A. Alshibli and S. Sture. Shear band formation in plane strain experiments of sand. *Journal of Geotechnical and Geoenvironmental Engineering*, 126(6): 495–503, 2000.

[253] J. C. Simo and R. L. Taylor. Penalty function formulations for incompressible nonlinear elastostatics. *Computer Methods in Applied Mechanics and Engineering*, 35(1):107–118, 1982.

[254] J. C. Simo, R. L. Taylor, and K. S. Pister. Variational and projection methods for the volume constraint in finite deformation elasto-plasticity. *Computer Methods in Applied Mechanics and Engineering*, 51(1-3):177–208, 1985.

[255] Donald W Taylor. *Fundamentals of soil mechanics*. J. Wiley & Sons; London: Chapman & Hall, 1956.

[256] J.-Y. Wu and M. Cervera. A thermodynamically consistent plastic-damage framework for localized failure in quasi-brittle solids: Material model and strain localization analysis. *International Journal of Solids and Structures*, 88: 227–247, 2016.

[257] L. P. Pook. The effect of crack angle on fracture toughness. *Engineering Fracture Mechanics*, 3(3):205 – 218, 1971.

[258] L. P. Pook. The fatigue crack direction and threshold behaviour of mild steel under mixed mode I and III loading. *International Journal of Fatigue*, 7(1): 21–30, 1985.

[259] L. P. Pook. On fatigue crack paths. *International Journal of Fatigue*, 17(1): 5–13, 1995.

[260] M. L. Cooke and D. D. Pollard. Fracture propagation paths under mixed mode loading within rectangular blocks of polymethyl methacrylate. *Journal of Geophysical Research: Solid Earth*, 101(B2):3387–3400, 1996.

[261] J. R. Yates and R. A. Mohammed. Crack propagation under mixed mode (I+ III) loading. *Fatigue & Fracture of Engineering Materials & Structures*, 19(10): 1285–1290, 1996.

[262] V. Lazarus and J.-B. Leblond. Crack paths under mixed mode (I+III) or (I+II+III) loadings. *Comptes Rendus de l'Academie des Sciences Series IIB Mechanics Physics Chemistry Astronomy*, 326(3):171–177, 1998.

[263] V. Lazarus, J.-B. Leblond, and S.-E. Mouchrif. Crack front rotation and segmentation in mixed mode I+III or I+II+III. Part I: Calculation of stress intensity factors. *Journal of the Mechanics and Physics of Solids*, 49(7):1399–1420, 2001.

[264] V. Lazarus, J.-B. Leblond, and S.-E. Mouchrif. Crack front rotation and segmentation in mixed mode I+III or I+II+III. Part II: Comparison with experiments. *Journal of the Mechanics and Physics of Solids*, 49(7):1421–1443, 2001.

[265] V. Lazarus, F.-G. Buchholz, M. Fulland, and J. Wiebesiek. Comparison of predictions by mode II or mode III criteria on crack front twisting in three or four point bending experiments. *International Journal of Fracture*, 153(2): 141–151, 2008.

[266] F.-G. Buchholz, A. Chergui, and H. A. Richard. Fracture analyses and experimental results of crack growth under general mixed mode loading conditions. *Engineering Fracture Mechanics*, 71(4):455–468, 2004.

[267] R. Citarella and F.-G. Buchholz. Comparison of crack growth simulation by DBEM and FEM for SEN-specimens undergoing torsion or bending loading. *Engineering Fracture Mechanics*, 75(3):489–509, 2008.

[268] A. D. Jefferson, B. I. G. Barr, T. Bennett, and S. C. Hee. Three dimensional finite element simulations of fracture tests using the Craft concrete model. *Computers and Concrete*, 1(3):261–284, 2004.

[269] F.-G. Buchholz, V. Just, and H. A. Richard. Computational simulation and experimental findings of three-dimensional fatigue crack growth in a single-edge notched specimen under torsion loading. *Fatigue & Fracture of Engineering Materials & Structures*, 28(1-2):127–134, 2005.

[270] C. Ancey. Snow avalanches. In *Geomorphological Fluid Mechanics*, pages 319–338. Springer, 2001.

[271] D. McClung and P. A. Schaerer. *The avalanche handbook*. The Mountaineers Books, 2006.

[272] J. Schweizer, J. B. Jamieson, and M. Schneebeli. Snow avalanche formation. *Reviews of Geophysics*, 41(4), 2003.

[273] A. Jones. Review of glide processes and glide avalanche release. *Avalanche News*, 69(7):53–60, 2004.

[274] European Avalanche Warning System (EAWS) Glossary. URL `http://www.avalanches.org/eaws/en/includes/glossary/glossary_en_all.html`.

[275] E. J. Hopfinger. Snow avalanche motion and related phenomena. *Annual review of fluid mechanics*, 15(1):47–76, 1983.

[276] V. J. Schaefer. The production of ice crystals in a cloud of supercooled water droplets. *Science*, 104(2707):457–459, 1946.

[277] U. Nakaya. The formation of ice crystals. In *Compendium of Meteorology*, pages 207–220. Springer, 1951.

[278] K. G. Libbrecht. The physics of snow crystals. *Reports on progress in physics*, 68(4):855, 2005.

[279] K. Kronholm, M. Schneebeli, and J. Schweizer. Spatial variability of micropenetration resistance in snow layers on a small slope. *Annals of Glaciology*, 38(1): 202–208, 2004.

[280] E. D. Feldt and G. E. H. Ballard. A theory of the consolidation of snow. *Journal of Glaciology*, 6(43):145–157, 1966.

[281] C. C. Bradley and D. Bowles. Strength-load ratio an index of deep slab avalanche. *Geophys. Res*, 70:3903–39Q7, 1967.

[282] K. Kojima. Densification of seasonal snow cover. *Physics of Snow and Ice: proceedings*, 1(2):929–952, 1967.

[283] M. Mellor. A review of basic snow mechanics. In *International Symposium on Snow Mechanics. International Association of Hydrological Sciences, Grindewald*, pages 251–291, 1975.

[284] L. H. Shapiro, J. B. Johnson, M. Sturm, and G. L. Blaisdell. Snow mechanics: review of the state of knowledge and applications. Technical report, DTIC Document, 1997.

[285] P. Bartelt and M. von Moos. Triaxial tests to determine a microstructure-based snow viscosity law. *Annals of Glaciology*, 31(1):457–462, 2000.

[286] M. Takeuchi. Vertical profile and horizontal increase of drift snow transport. *Journal of the Faculty of Science, Hokkaido University. Series 7, Geophysics*, 6 (1):143–156, 1980.

[287] R. A. Schmidt. Vertical profiles of wind speed, snow concentration, and humidity in blowing snow. *Boundary-Layer Meteorology*, 23(2):223–246, 1982.

[288] R. A. Schmidt. Transport rate of drifting snow and the mean wind speed profile. *Boundary-Layer Meteorology*, 34(3):213–241, 1986.

[289] S. C. Colbeck. An overview of seasonal snow metamorphism. *Reviews of Geophysics*, 20(1):45–61, 1982.

[290] S. C. Colbeck. Theory of metamorphism of dry snow. *Journal of Geophysical Research: Oceans*, 88(C9):5475–5482, 1983.

[291] B. R. Pinzer and M. Schneebeli. Snow metamorphism under alternating temperature gradients: Morphology and recrystallization in surface snow. *Geophysical research letters*, 36(23), 2009.

[292] B. R. Pinzer, M. Schneebeli, and T. U. Kaempfer. Vapor flux and recrystallization during dry snow metamorphism under a steady temperature gradient as observed by time-lapse micro-tomography. *The Cryosphere*, 6(5):1141, 2012.

[293] M. Sturm, J. Holmgren, M. König, and K. Morris. The thermal conductivity of seasonal snow. *Journal of Glaciology*, 43(143):26–41, 1997.

[294] M. Schneebeli and S. A. Sokratov. Tomography of temperature gradient metamorphism of snow and associated changes in heat conductivity. *Hydrological Processes*, 18(18):3655–3665, 2004.

[295] K. W. Birkeland. Terminology and predominant processes associated with the formation of weak layers of near-surface faceted crystals in the mountain snowpack. *Arctic and Alpine Research*, pages 193–199, 1998.

[296] G. Wakahama. The role of meltwater in densification processes of snow and firn. In *Snow Mechanics Symposium; Proceedings of the Grindelwald Symposium, Grindelwald, Bernese Oberland (Switzerland)*, volume 114, 1974.

[297] K. Izumi. Effects of solar radiation on the formation of weak wet snow. *Annals of Glaciology*, 13:120–123, 1989.

[298] M. Lehning, P. Bartelt, B. Brown, T. Russi, U. Stöckli, and M. Zimmerli. Snowpack model calculations for avalanche warning based upon a new network of weather and snow stations. *Cold Regions Science and Technology*, 30(1): 145–157, 1999.

[299] D. M. McClung. Shear fracture precipitated by strain softening as a mechanism of dry slab avalanche release. *Journal of Geophysical Research: Solid Earth*, 84 (B7):3519–3526, 1979.

[300] D. M. McClung. Mechanics of snow slab failure from a geotechnical perspective. In *Avalanche Formation, Movement and Effects (Proceedings of the Davos Symposium, September 1986)*, volume 162. IAHS Publ., 1986.

[301] J. Schweizer. Laboratory experiments on shear failure of snow. *Annals of Glaciology*, 26(1):97–102, 1998.

[302] B. M. Chiaia, P. Cornetti, and B. Frigo. Triggering of dry snow slab avalanches: stress versus fracture mechanical approach. *Cold Regions Science and Technology*, 53(2):170–178, 2008.

[303] I. Reiweger, J. Gaume, and J. Schweizer. A new mixed-mode failure criterion for weak snowpack layers. *Geophysical Research Letters*, 42(5):1427–1432, 2015.

[304] J. Heierli. *Anticrack model for slab avalanche release.* PhD thesis, Karlsruhe Univiversity, 2008.

[305] M. von Moos, P. Bartelt, A. Zweidler, and E. Bleiker. Triaxial tests on snow at low strain rate. Part I. Experimental device. *Journal of Glaciology*, 49(164): 81–90, 2003.

[306] C. Scapozza and P. Bartelt. Triaxial tests on snow at low strain rate. Part II. Constitutive behaviour. *Journal of Glaciology*, 49(164):91–101, 2003.

[307] J. Schweizer and J. B. Jamieson. Snowpack tests for assessing snow-slope instability. *Annals of Glaciology*, 51(54):187–194, 2010.

[308] J. B. Jamieson. The compression test-after 25 years. *The Avalanche Review*, 18(1):10–12, 1999.

[309] R. Simenhois and K. W. Birkeland. The extended column test: a field test for fracture initiation and propagation. In *Proceedings ISSW*, pages 79–85, 2006.

[310] P. M. B. Föhn. The rutschblock as a practical tool for slope stability evaluation. *IAHS publication*, 162:223–228, 1987.

[311] B. Jamieson and C. D. Johnston. Evaluation of the shear frame test for weak snowpack layers. *Annals of Glaciology*, 32(1):59–69, 2001.

[312] C. Sigrist. *Measurement of Fracture Mechanical Properties of Snow and Application to Dry Snow Slab Avalanche Release*. Ph.d. thesis, ETH Zurich, 2006.

[313] D. Gauthier and J. B. Jamieson. Evaluation of a prototype field test for fracture and failure propagation propensity in weak snowpack layers. *Cold Regions Science and Technology*, 51(2):87–97, 2008.

[314] K. Winkler and J. Schweizer. Comparison of snow stability tests: Extended column test, rutschblock test and compression test. *Cold Regions Science and Technology*, 59(2):217–226, 2009.

[315] J. B. Jamieson and J. Schweizer. Texture and strength changes of buried surface-hoar layers with implications for dry snow-slab avalanche release. *Journal of Glaciology*, 46(152):151–160, 2000.

[316] A. van Herwijnen and B. Jamieson. High-speed photography of fractures in weak snowpack layers. *Cold Regions Science and Technology*, 43(1):71–82, 2005.

[317] A. van Herwijnen, J. Schweizer, and J. Heierli. Measurement of the deformation field associated with fracture propagation in weak snowpack layers. *Journal of Geophysical Research: Earth Surface (2003–2012)*, 115(F3), 2010.

[318] D. Gauthier and B. Jamieson. Fracture propagation propensity in relation to snow slab avalanche release: Validating the propagation saw test. *Geophysical Research Letters*, 35(13), 2008.

[319] D. Gauthier and B. Jamieson. Predictions of the propagation saw test: comparisons with other instability tests at skier tested slopes. *Proceedings of the 2008 International Snow Science Workshop, Whistler, BC*, pages 21–27, 2008.

[320] D. Gauthier, C. Ross, and B. Jamieson. Validation of the propagation saw test near whumpfs and avalanches. *Proceedings of the 2008 International Snow Science Workshop, Whistler, BC*, pages 16–21, 2008.

[321] E. H. Bair, R. Simenhois, K. Birkeland, and J. Dozier. A field study on failure of storm snow slab avalanches. *Cold Regions Science and Technology*, 79:20–28, 2012.

[322] B. Reuter, J. Schweizer, and A. van Herwijnen. A process-based approach to estimate point snow instability. *The Cryosphere*, 9(3):837–847, 2015.

[323] F. Monti, J. Gaume, A. van Herwijnen, and J. Schweizer. Snow instability evaluation: calculating the skier-induced stress in a multi-layered snowpack. *Natural Hazards and Earth System Sciences*, 16(3):775–788, 2016.

[324] J. Gaume, A. van Herwijnen, J. Schweizer, G. Chambon, and K. Birkeland. Discrete element modeling of crack propagation in weak snowpack layers. In *Proceedings of the International Snow Science Workshop, Banff, Canada*, 2014.

[325] J. Gaume, A. van Herwijnen, G. Chambon, K. Birkeland, and J. Schweizer. Modeling of crack propagation in weak snowpack layers using the discrete element method. *Cryosphere*, 9(5):1915–1932, 2015.

[326] J. B. Jamieson and C. D. Johnston. In-situ tensile tests of snow-pack layers. *Journal of Glaciology*, 36(122):102–106, 1990.

[327] C. Sigrist and J. Schweizer. Critical energy release rates of weak snowpack layers determined in field experiments. *Geophysical Research Letters*, 34(3), 2007.

[328] J. Schweizer, A. van Herwijnen, and B. Reuter. Measurements of weak layer fracture energy. *Cold Regions Science and Technology*, 69(2):139–144, 2011.

[329] A. van Herwijnen, J. Gaume, E. H. Bair, B. Reuter, K. W. Birkeland, and J. Schweizer. Estimating the effective elastic modulus and specific fracture energy of snowpack layers from field experiments. *Journal of Glaciology*, pages 1–11, 2016.

[330] M. Chiumenti, M. Cervera, A. Salmi, C. Agelet De Saracibar, N. Dialami, and K. Matsui. Finite element modeling of multi-pass welding and shaped metal deposition processes. *Computer methods in applied mechanics and engineering*, 199(37):2343–2359, 2010.

[331] C. Camponovo and J. Schweizer. Rheological measurements of the viscoelastic properties of snow. *Annals of Glaciology*, 32(1):44–50, 2001.

This page is left intentionally blank.

Mixed stabilized finite element methods in nonlinear solid mechanics. Part III: Compressible and incompressible plasticity

M. Cervera, M. Chiumenti, L. Benedetti and R. Codina

Computer Methods and Applied Mechanics in Engineering,
Vol. 285, pp. 752-775, (2015)
http://dx.doi.org/10.1016/j.cma.2014.11.040

This page is left intentionally blank.

Mixed Stabilized Finite Element Methods in Nonlinear Solid Mechanics. Part III: Compressible and incompressible plasticity

M. Cervera, M. Chiumenti, L. Benedetti and R. Codina
International Center for Numerical Methods in Engineering (CIMNE)
Technical University of Catalonia (UPC)
Edificio C1, Campus Norte, Jordi Girona 1-3, 08034 Barcelona, Spain.

KEYWORDS: mixed finite elements, stabilization, strain softening, strain localization, local damage models, mesh dependence.

Abstract

This paper presents the application of a stabilized mixed strain/displacement finite element formulation for the solution nonlinear solid mechanics problems involving compressible and incompressible plasticity. The variational multiscale stabilization introduced allows the use of equal order interpolations in a consistent way. Such formulation presents two advantages when compared to the standard, displacement based, irreducible formulation: (a) it provides enhanced rate of convergence for the strain (and stress) field and (b) it is able to deal with incompressible situations. The first advantage also applies to the comparison with the mixed pressure/displacement formulation. The paper investigates the effect of the improved strain and stress fields in problems involving strain softening and localization leading to failure, using low order finite elements with continuous strain and displacement fields ($P1P1$ triangles or tetrahedra and $Q1Q1$ quadrilaterals, hexahedra, and triangular prisms) in conjunction with an associative frictional Drucker-Prager plastic model. The performance of the strain/displacement formulation under compressive and nearly incompressible deformation patterns is assessed and compared to a previously proposed pressure/displacement formulation. Benchmark numerical examples show the capacity of the mixed formulation to predict correctly failure mechanisms with localized patterns of strain, virtually free from any dependence of the mesh directional bias. No auxiliary crack tracking technique is necessary.

1 Introduction

In previous works [7, 8], the authors have formulated stable mixed stress/displacement and strain/displacement finite elements with equal order interpolation for the solution of nonlinear problems in solid mechanics. The proposed formulation uses the sub-grid scale approach to circumvent the restrictiveness of the inf-sup compatibility conditions on the choice of the interpolation spaces. The objective of such formulation is to achieve a discrete scheme with enhanced stress accuracy. This means that the mixed formulation displays a global rate of convergence on stresses higher than the corresponding irreducible formulation. Such improvement of the convergence estimates also applies at local level. And this characteristic proves to be crucial in strain localization problems involving softening materials.

Strain localization inevitably occurs in softening materials subjected to monotonic straining. Once the peak stress is reached, and upon continuing straining, the stress decreases and strains concentrate inside a narrow band of material while the material outside the band unloads elastically. As the localization progresses, the width of the localization band diminishes and, unless there is a microstructural limitation, it tends to zero. The particular components of the strain tensor that localize during this process depend on the specific constitutive behavior of the material. In Rankine-type materials, only normal elongations localize, eventually forming tensile cracks; if the nonlinear behavior is incompressible, shear strains concentrate, leading to slip surfaces.

Quasi-singular strain or stress states occur at the vicinity of the propagating cracks or slip lines. For linear elements and even in elastic behavior, it is well known that the standard irreducible formulation fails to provide guarantee of local convergence of stress values in such situations, such as the tip of a notch or a propagating crack. And this lack of local convergence leads to the spurious mesh bias dependence often displayed by standard finite elements when using local softening constitutive models. Contrariwise, the proposed mixed formulations do provide the necessary guarantee of convergence for local stress convergence. This characteristic proves to be sufficient to avoid mesh bias dependence of the numerically computed failure mechanisms and responses.

In reference [8], the mixed strain/displacement formulation was applied in conjunction with an isotropic Rankine damage model, formulated in secant form, to model problems of tensile cracking propagation and failure. It was observed there that: (a) the resulting discrete FE model is well posed and stable, (b) the formulation is convergent and, on mesh refinement, it approaches the original continuum problem, and (c) the results obtained are not spuriously dependent of the finite element mesh used; they depend only on the actual material model (damage criterion in this case) adopted. This represented a significant advancement in the solution of such problems, particularly considering two noteworthy features of the approach. On one hand, it is of general application, in 2D and 3D problems, to structured and unstructured meshes and to simplicial or non simplicial elements. On the other hand, no "ad hoc" auxiliary crack tracking technique is necessary. However, the application of the proposed formulation to problems involving local softening plasticity models remained open.

In previous works, the authors have applied stabilized mixed displacement-pressure methods ([1, 2, 3, 4, 5] and [6]) to the solution of J_2 elasto-plastic problems with simplicial elements. In J_2 dependent problems, the plastic flow is isochoric and the main challenge for the discrete formulation is the incompressibility constraint. Unless this is properly dealt with, spurious pressure oscillations appear and the discrete solution is totally polluted. A stabilized mixed formulation

provides a discrete problem which is fully stable, even for problems involving localization of shear strains and the formation of slip lines. The results obtained, both in terms of collapse mechanism and global load-deflection response, compare very favorably with those obtained with the standard irreducible formulation, which almost inevitably shows an unacceptable mesh dependence. Nevertheless, regarding the computation of the deviatoric stresses, the stabilized mixed pressure-displacement formulation has the same convergence behavior than the irreducible formulation. This is because, in both formulations, the discrete deviatoric strains are computed by direct differentiation of the discrete displacement field. This means that the corresponding convergence rate is necessarily one order less than that of the displacements. When using linear interpolation for the displacements and in quasi-singular situations, this may prove to be insufficient. The remedy is to use an independent interpolation, linear at least, not only for the volumetric part of the strain (or stress) tensor, but for all of its components.

Therefore, the objectives of this paper are five: (1) to extend the stabilized mixed strain/displacement formulation to plasticity problems, (2) to investigate the effect of the improved strain and stress fields in problems involving strain softening and localization leading to failure, (3) to assess the performance of the formulation under nearly incompressible deformation patterns, (4) to compare the performance of the proposed formulation with the previously proposed pressure/displacement formulation and (5) to show that the formulation is applicable in 2D and 3D, to structured or unstructured meshes of triangles, quadrilaterals, tetrahedra, hexahedra or prisms. Both pressure sensitive and incompressible plasticity models are contemplated. To achieve this, the Drucker-Prager plasticity model is selected as target model, as it may incorporate pressure sensitivity through the friction angle of the material, as well as reduce to a pure cohesional behavior when null friction is assumed.

Inelastic plastic flow is a directional phenomenon. In the stress space, assuming associative plasticity, it occurs in the direction normal to the yield surface; in non-associative plasticity, the directionality of the flow is established from a plastic potential, different from the yield criterion. In any case, plasticity does not occur isotropically. This is an additional objective of this work: to investigate the performance of the proposed mixed formulation in strain localization situations substantially different to those studied in previous works. Satisfactory performance under directional inelastic behavior, without spurious stress locking and without the need of auxiliary discontinuity tracking procedures, would reopen the path to the use of orthogonal and anisotropic constitutive models than cannot be used today in practical applications.

The outline of the paper is as follows. In Section 2, the stabilized mixed strain/displacement formulation for the solution of nonlinear solid mechanics problems is applied in conjunction with a small strain plasticity model. The continuum problem and the corresponding discrete formulation are introduced. Following the ideas in [7] and [8], stabilization of the latter is achieved by considering a residual-based subscale approach. Both algebraic and orthogonal subgrid scales are considered. Section 3 describes the implementation details for both stabilization procedures. Section 4 describes the Drucker-Prager plasticity model. Details on the return mapping, consistent tangent constitutive tensor and the consideration of the singular case of the apex of the yield surface are discussed. Section 5 presents selected numerical examples involving unstructured and structured low order finite elements meshes (triangles in 2D and triangular prisms in 3D) with continuous linear strain and displacement fields to assess the generality and robustness of the proposed formulation.

2 Stabilized mixed strain/displacement formulation for plasticity

2.1 Mixed ε/u formulation for plasticity

The strong form of the continuous quasi-static solid mechanics problem can be stated as: given the prescribed body forces $\mathbf{f}$, find the displacement field $\mathbf{u}$ and the stress field $\boldsymbol{\sigma}$ such that:

$$-\mathbf{C}^{-1} : \boldsymbol{\sigma} + \nabla^s \mathbf{u} = \mathbf{0} \quad \text{in } \Omega \tag{1a}$$

$$\nabla \cdot \boldsymbol{\sigma} + \mathbf{f} = \mathbf{0} \quad \text{in } \Omega \tag{1b}$$

where Ω is the open and bounded domain of $\mathbb{R}^{\text{dim}}$ occupied by the solid in a space of dim dimensions. The symbol $\boldsymbol{\nabla}^s(\cdot)$ is used to denote the symmetric gradient, whereas $\boldsymbol{\nabla} \cdot (\cdot)$ refers to the divergence operator. Eq. (1a) enforces both the geometric equation for linear kinematics and the non-linear constitutive relationship $\boldsymbol{\sigma} = \mathbf{C} : \boldsymbol{\varepsilon}$, with $\mathbf{C} = \mathbf{C}(\boldsymbol{\sigma})$ being the (secant) nonlinear constitutive tensor; Eq. (1b) is the balance of momentum Cauchy equation.

Equations (1a)-(1b) are subjected to appropriate Dirichlet and Neumann boundary conditions. In the following, we will assume these in the form of prescribed displacements $\mathbf{u} = \mathbf{0}$ on $\partial\Omega_u$, and prescribed tractions $\overline{\mathbf{t}}$ on $\partial\Omega_t$, respectively, being $\partial\Omega_u$ and $\partial\Omega_t$ a partition of $\partial\Omega$.

This mixed formulation in terms of the stress and displacement fields, $\boldsymbol{\sigma}/\mathbf{u}$, is classical and it has been used many times in the context of linear elasticity, where the constitutive tensor $\mathbf{C} = \mathbf{C_o}$ is constant. However, this is not the most convenient format for the nonlinear problem. The reason for this is that most of the algorithms used for nonlinear constitutive equations in solid mechanics have been derived for the irreducible formulation. Thus, these procedures are usually strain driven, and they have a format in which the stress $\boldsymbol{\sigma}$ is computed in terms of the strain $\boldsymbol{\varepsilon}$, with $\boldsymbol{\varepsilon} = \nabla^s \mathbf{u}$ for linear kinematics.

Because of this, the strong form of the continuum problem can be alternatively stated as: find the displacement field $\mathbf{u}$ and the strain field $\boldsymbol{\varepsilon}$, for given prescribed body forces $\mathbf{f}$, such that:

$$-\mathbf{C} : \boldsymbol{\varepsilon} + \mathbf{C} : \nabla^s \mathbf{u} = \mathbf{0} \quad \text{in } \Omega \tag{2a}$$

$$\nabla \cdot [\mathbf{C} : \boldsymbol{\varepsilon}] + \mathbf{f} = \mathbf{0} \quad \text{in } \Omega \tag{2b}$$

In small strain plasticity, the strain tensor $\boldsymbol{\varepsilon}$ is decomposed additively as

$$\boldsymbol{\varepsilon} = \boldsymbol{\varepsilon}_e + \boldsymbol{\varepsilon}_p \tag{3}$$

with $\boldsymbol{\varepsilon}_e$ the elastic strain tensor and $\boldsymbol{\varepsilon}_p$ the plastic strain tensor. The plasticity model is defined by appropriate evolution laws for the plastic strain. The constitutive equation is usually stated as

$$\boldsymbol{\sigma} = \mathbf{C}_o : \boldsymbol{\varepsilon}_e = \mathbf{C}_o : (\boldsymbol{\varepsilon} - \boldsymbol{\varepsilon}_p) \tag{4}$$

The problem is closed once the expression of $\boldsymbol{\varepsilon}_p$ is provided. In practice, an evolution law $\dot{\boldsymbol{\varepsilon}}_p = \dot{\boldsymbol{\varepsilon}}_p(\boldsymbol{\sigma})$ is formulated, the dot standing for the time derivative.

Using this constitutive equation, rather the secant one, the strong form of the plasticity problem may be written as

$$-\mathbf{C}_o : \boldsymbol{\varepsilon} + \mathbf{C_o} : \nabla^s \mathbf{u} = \mathbf{0} \quad \text{in } \Omega \tag{5a}$$

$$\nabla \cdot [\mathbf{C}_o : (\boldsymbol{\varepsilon} - \boldsymbol{\varepsilon}_p)] + \mathbf{f} = \mathbf{0} \quad \text{in } \Omega \tag{5b}$$

Let $\mathcal{V}$ and $\mathcal{G}$ be the appropriate functional spaces where $\mathbf{u}$ and $\boldsymbol{\varepsilon}$ are sought, respectively. Multiplying by appropriate test functions and integrating by parts the second equation, the associated weak form of the mixed problem can be stated as:

$$\begin{aligned} -(\boldsymbol{\gamma}, \mathbf{C}_o : \boldsymbol{\varepsilon}) + (\boldsymbol{\gamma}, \mathbf{C}_o : \nabla^s \mathbf{u}) &= 0 \qquad \forall \boldsymbol{\gamma} \qquad (6a) \\ (\nabla^s \mathbf{v}, \mathbf{C}_o : (\boldsymbol{\varepsilon} - \boldsymbol{\varepsilon}_p)) &= (\mathbf{v}, \mathbf{f}) + \left(\mathbf{v}, \bar{\mathbf{t}}\right)_{\partial\Omega_t} \qquad \forall \mathbf{v} \qquad (6b) \end{aligned}$$

where $\mathbf{v} \in \mathcal{V}$ and $\boldsymbol{\gamma} \in \mathcal{G}$ are the variations of the displacements and strain fields, respectively, with $\mathcal{V} \subset H^1(\Omega)^{\dim}$, this being the space of square integrable vector functions $\mathbf{v}$ which are at least square integrable and have square integrable first derivative, and $\mathcal{G} \subset L^2(\Omega)^{\dim \times \dim}_{\text{sym}}$, this being the space of square integrable symmetric tensors $\boldsymbol{\gamma}$. The inclusions $\mathcal{V} \subset H^1(\Omega)^{\dim}$ and $\mathcal{G} \subset L^2(\Omega)^{\dim \times \dim}_{\text{sym}}$ are required because functions in $\mathcal{V}$ must vanish on $\partial\Omega_u$ and because more regularity might be needed for the evolution law $\dot{\boldsymbol{\varepsilon}}_p = \dot{\boldsymbol{\varepsilon}}_p(\boldsymbol{\sigma})$ to make sense. Parenthesis $(\cdot, \cdot)$ denotes the inner product in $L^2(\Omega)$, and $(\mathbf{v}, \bar{\mathbf{t}})_{\partial\Omega_t}$ denotes the integral of the product of $\mathbf{v}$ and $\bar{\mathbf{t}}$ over $\partial\Omega_t$.

Let us consider a finite element partition of the domain Ω from which we can construct finite element spaces $\mathcal{V}_h \subset \mathcal{V}$ and $\mathcal{G}_h \subset \mathcal{G}$ in the usual manner. A generic element size of this partition will be denoted by h, and this subscript will be used to refer to finite element functions. The discrete Galerkin finite element counterpart problem is defined as:

$$\begin{aligned} -(\boldsymbol{\gamma}_h, \mathbf{C}_o : \boldsymbol{\varepsilon}_h) + (\boldsymbol{\gamma}_h, \mathbf{C}_o : \nabla^s \mathbf{u}_h) &= 0 \qquad \forall \boldsymbol{\gamma}_h \qquad (7a) \\ (\nabla^s \mathbf{v}_h, \mathbf{C}_o : (\boldsymbol{\varepsilon}_h - \boldsymbol{\varepsilon}_p)) &= F(\mathbf{v}_h) \qquad \forall \mathbf{v}_h \qquad (7b) \end{aligned}$$

where $\mathbf{u}_h$, $\mathbf{v}_h \in \mathcal{V}_h$ and $\boldsymbol{\varepsilon}_h$, $\boldsymbol{\gamma}_h \in \mathcal{G}_h$ are the discrete displacement and strain fields and their variations, and $F(\mathbf{v}_h) = (\mathbf{v}_h, \mathbf{f}) + \left(\mathbf{v}_h, \bar{\mathbf{t}}\right)_{\partial\Omega_t}$. It is understood that $\boldsymbol{\varepsilon}_p$ is now computed in terms of the finite element unknowns.

Remark The strong form (5a)-(5b), as well as the corresponding discrete weak form (7a)-(7b), are not symmetric, because of the functional dependence of the plastic strain on the primary variables of the problem. This can be remedied in two ways.

The constitutive equation (4) can be equivalently expressed, for example, as

$$\boldsymbol{\sigma} = \left[\mathbf{C}_o - \frac{(\mathbf{C}_o : \boldsymbol{\varepsilon}_p) \otimes (\mathbf{C}_o : \boldsymbol{\varepsilon}_p)}{\boldsymbol{\varepsilon} : \mathbf{C}_o : \boldsymbol{\varepsilon}_p} \right] : \boldsymbol{\varepsilon} = \mathbf{C} : \boldsymbol{\varepsilon} \qquad (8)$$

where the (secant) nonlinear constitutive tensor $\mathbf{C}$ is symmetric by construction. The form (8) can be fitted directly in the strong form (2a)-(2b) to provide the corresponding symmetric discrete weak form:

$$\begin{aligned} -(\boldsymbol{\gamma}_h, \mathbf{C} : \boldsymbol{\varepsilon}_h) + (\boldsymbol{\gamma}_h, \mathbf{C} : \nabla^s \mathbf{u}_h) &= 0 \qquad \forall \boldsymbol{\gamma}_h \qquad (9a) \\ (\nabla^s \mathbf{v}_h, \mathbf{C} : \boldsymbol{\varepsilon}_h) &= F(\mathbf{v}_h) \qquad \forall \mathbf{v}_h \qquad (9b) \end{aligned}$$

This form is identical to the discrete form obtained in references [7] and [8].

The second alternative is as follows. The constitutive equation (4) may be expressed in rate form as

$$\dot{\boldsymbol{\sigma}} = \mathbf{C}_{ep} : \dot{\boldsymbol{\varepsilon}} \qquad (10)$$

where $\mathbf{C}_{ep}$ is the (tangent) elasto-plastic constitutive tensor, symmetric for associative plasticity (see Subsection 4.3).

Making use of this, and stating all the governing equations in rate form, the strong form of the problem can be written as

$$-\mathbf{C}_{ep} : \dot{\boldsymbol{\varepsilon}} + \mathbf{C}_{ep}{:}\nabla^s \dot{\mathbf{u}} = \mathbf{0} \quad \text{in } \Omega \tag{11a}$$

$$\nabla \cdot [\mathbf{C}_{ep} : \dot{\boldsymbol{\varepsilon}}] + \dot{\mathbf{f}} = \mathbf{0} \quad \text{in } \Omega \tag{11b}$$

This form is symmetric and leads to the symmetric discrete weak form:

$$-\left(\boldsymbol{\gamma}_h, \mathbf{C}_{ep}{:}\, \dot{\boldsymbol{\varepsilon}}_h\right) + \left(\boldsymbol{\gamma}_h, \mathbf{C}_{ep}{:}\nabla^s \dot{\mathbf{u}}_h\right) = 0 \qquad \forall \boldsymbol{\gamma}_h \tag{12a}$$

$$\left(\nabla^s \mathbf{v}_h, \mathbf{C}_{ep}{:}\, \dot{\boldsymbol{\varepsilon}}_h\right) = \dot{F}(\mathbf{v}_h) \qquad \forall \mathbf{v}_h \tag{12b}$$

where $\dot{F}(\mathbf{v}_h)$ is the counterpart of $F(\mathbf{v}_h)$ when loads are expressed in rate form.

2.2 Variational Multiscale Stabilization

The *inf-sup* condition [20] establishes that the stability of the discrete formulation depends on the appropriate choice of the finite element spaces $\mathcal{V}_h$ and $\mathcal{G}_h$. Even for linear elasticity, standard Galerkin mixed elements with continuous equal order $P1P1$ (linear/linear) and $Q1Q1$ (bilinear/bilinear) interpolation for both fields do not satisfy the condition and, therefore, are not stable. For the $\boldsymbol{\varepsilon}/\mathbf{u}$ (or the $\boldsymbol{\sigma}/\mathbf{u}$) problem, lack of stability manifests as spurious oscillations in the displacement field that pollute the solution. A satisfactory way of circumventing the inf-sup condition is to modify the discrete variational form, introducing numerical stabilization techniques that can provide the necessary stability without affecting the consistent formulation of the discrete problem nor degrading its convergence rate. Such techniques can be sustained from the so-call Variational Multiscale Stabilization (VMS).

VMS was developed in first instance by [21] and then generalized in [22]. This technique modifies appropriately the variational form of the problem in order to provide the required numerical stability. The corresponding modified *inf-sup* condition is milder than the original one and it holds for most common equal order finite element spaces [23].

The multiscale procedure decomposes the solution $(\boldsymbol{\varepsilon}, \mathbf{u})$ into a resolvable finite element scale $(\boldsymbol{\varepsilon}_h, \mathbf{u}_h)$ and an unresolvable subscale $(\tilde{\boldsymbol{\varepsilon}}, \tilde{\mathbf{u}})$, so that:

$$\boldsymbol{\varepsilon} = \boldsymbol{\varepsilon}_h + \tilde{\boldsymbol{\varepsilon}} \tag{13a}$$

$$\mathbf{u} = \mathbf{u}_h + \tilde{\mathbf{u}} \tag{13b}$$

This extends the solution spaces for the displacements and the strains to $\mathcal{V} \simeq \mathcal{V}_h \oplus \widetilde{\mathcal{V}}$ and $\mathcal{G} \simeq \mathcal{G}_h \oplus \widetilde{\mathcal{G}}$, where $\widetilde{\mathcal{V}}$ and $\widetilde{\mathcal{G}}$ are the functional spaces for the subscale variables $(\tilde{\boldsymbol{\varepsilon}}, \tilde{\mathbf{u}})$ and their test functions $(\tilde{\boldsymbol{\gamma}}, \tilde{\mathbf{v}})$. It can also be assumed that $\tilde{\boldsymbol{\varepsilon}}$ and $\tilde{\boldsymbol{\gamma}}$ vanish on the boundary $\partial\Omega$.

The plastic strain $\boldsymbol{\varepsilon}_p$ is non-linearly dependent on the stress field, this in turn being dependent on the strain field through the constitutive equation. Since the strain field $\boldsymbol{\varepsilon}$ includes a subscale contribution, then also the plastic strain tensor $\boldsymbol{\varepsilon}_p$ could present a corresponding subscale part. However, since the subscale contribution is assumed to be small with respect the resolvable scale, the plastic strain will be approximated as:

$$\boldsymbol{\varepsilon}_p = \boldsymbol{\varepsilon}_p(\boldsymbol{\sigma}) \approx \boldsymbol{\varepsilon}_p(\boldsymbol{\sigma}_h) \tag{14}$$

This implies that the constitutive model is evaluated only with the resolvable part of the strain:

$$\boldsymbol{\sigma}_h = \mathbf{C}_o : [\boldsymbol{\varepsilon}_h - \boldsymbol{\varepsilon}_p(\boldsymbol{\sigma}_h)] \tag{15}$$

It would be possible however to account for the effect of the subscales in this expression, at the expense of increasing the non-linearity of the problem.

Considering the scale splitting, the discrete problem corresponding to Eqs. (6a)-(6b) is now:

$$\begin{aligned}
-(\boldsymbol{\gamma}_h, \mathbf{C}_o : [\boldsymbol{\varepsilon}_h + \widetilde{\boldsymbol{\varepsilon}}]) + (\boldsymbol{\gamma}_h, \mathbf{C}_o : \nabla^s(\mathbf{u}_h + \widetilde{\mathbf{u}})) &= 0 \qquad \forall \boldsymbol{\gamma}_h && \text{(16a)}\\
(\nabla^s \mathbf{v}_h, \mathbf{C}_o : [\boldsymbol{\varepsilon}_h + \widetilde{\boldsymbol{\varepsilon}} - \boldsymbol{\varepsilon}_p]) &= F(\mathbf{v}_h) \qquad \forall \mathbf{v}_h && \text{(16b)}\\
-(\widetilde{\boldsymbol{\gamma}}, \mathbf{C}_o : [\boldsymbol{\varepsilon}_h + \widetilde{\boldsymbol{\varepsilon}}]) + (\widetilde{\boldsymbol{\gamma}}, \mathbf{C}_o : \nabla^s(\mathbf{u}_h + \widetilde{\mathbf{u}})) &= 0 \qquad \forall \widetilde{\boldsymbol{\gamma}} && \text{(16c)}\\
-(\nabla^s \widetilde{\mathbf{v}}, \boldsymbol{\nabla} \cdot \mathbf{C}_o : [\boldsymbol{\varepsilon}_h + \widetilde{\boldsymbol{\varepsilon}} - \boldsymbol{\varepsilon}_p]) + (\widetilde{\mathbf{v}}, \mathbf{f}) &= 0 \qquad \forall \widetilde{\mathbf{v}} && \text{(16d)}
\end{aligned}$$

where due to linear independence, each of the equations in (6a) and (6b) unfolds into two equations, one related to each scale considered.

Rewriting the third and fourth equations, tested against the subscale test functions, and assuming that the subscale $(\tilde{\boldsymbol{\varepsilon}}, \tilde{\mathbf{u}})$ vanishes on the boundary, it follows that

$$\begin{aligned}
-(\widetilde{\boldsymbol{\gamma}},\ \mathbf{C}_o : \widetilde{\boldsymbol{\varepsilon}})_h + (\widetilde{\boldsymbol{\gamma}}, \mathbf{C}_o : \nabla^s \widetilde{\mathbf{u}})_h &= -\left(\widetilde{\boldsymbol{\gamma}},\ \mathbf{r}_{1,h}\right)_h \qquad \forall \widetilde{\boldsymbol{\gamma}} && \text{(17a)}\\
(\nabla^s \widetilde{\mathbf{v}}, \boldsymbol{\nabla} \cdot \mathbf{C}_o : \widetilde{\boldsymbol{\varepsilon}})_h &= -\left(\widetilde{\mathbf{v}},\ \mathbf{r}_{2,h}\right)_h \qquad \forall \widetilde{\mathbf{v}} && \text{(17b)}
\end{aligned}$$

where subscript h refers now to the fact the integrals are evaluated element-wise and where the residuals of the first and second equations, in the finite element scale, are:

$$\begin{aligned}
\mathbf{r}_{1,h} &= \mathbf{C}_o : (\nabla^s \mathbf{u}_h - \boldsymbol{\varepsilon}_h) && \text{(18a)}\\
\mathbf{r}_{2,h} &= \boldsymbol{\nabla} \cdot \boldsymbol{\sigma}_h + \mathbf{f} && \text{(18b)}
\end{aligned}$$

where the definition of the stress in expression (15) has been used.

This last system of equations shows that the solution of the subscale variables depends on the residuals upon substitution of the resolvable FE solution in the strong form of the problem. Therefore, following the work of [24], the *residual based* subscales strain can be localized within each finite element and expressed as

$$\begin{aligned}
\widetilde{\boldsymbol{\varepsilon}} &= \tau_\varepsilon\, \mathbf{C}_o^{-1} : P(\mathbf{r}_{1,h}) = \tau_\varepsilon\, P(\nabla^s \mathbf{u}_h - \boldsymbol{\varepsilon}_h) && \text{(19a)}\\
\tilde{\mathbf{u}} &= \tau_u\, P(\mathbf{r}_{2,h}) = \tau_u\, P(\boldsymbol{\nabla} \cdot \boldsymbol{\sigma}_h + \mathbf{f}) && \text{(19b)}
\end{aligned}$$

where $P(\cdot)$ represents an appropriate projection operator onto the space of subscales and τ_ε, τ_u are computed as

$$\tau_\varepsilon = c_\varepsilon \frac{h}{L} \frac{\mu}{\mu_o} \quad \text{and} \quad \tau_u = c_u \frac{hL}{\mu} \tag{20}$$

where c_ε and c_u are positive constants, μ is a mechanical parameter of the problem, usually chosen as the ratio between the norms of the deviatoric stress and total strain tensors, $\mu = \|\text{dev}\ \boldsymbol{\sigma}\| \,/\, \|\text{dev}\ \boldsymbol{\varepsilon}\|$, μ_o being its initial elastic value. For nonlinear constitutive models, this ratio is non-constant and it varies along the deformation process. Dimension h is the size of the finite element and L is a characteristic length of the problem. The expression given by (20) has been chosen according

to the optimal convergence results obtained for equal interpolation in [24], since in the following we precisely assume equal continuous interpolation for displacements and strains. For the sake of clarity, h will be assumed constant for all elements, even if in practice expressions (20) are evaluated element-wise.

To complete the stabilization method, an appropriate projection operator has to be selected in order to be able to compute the subscale variables.

2.2.1 ASGS

In the Algebraic Subgrid Scale Stabilization [22], the projection operator is taken as the identity when applied to finite element residuals, that is, $P(\mathbf{r}) = \mathbf{r}$, and, therefore, the subscales read:

$$\widetilde{\boldsymbol{\varepsilon}} = \tau_\varepsilon \left(\nabla^s \mathbf{u}_h - \boldsymbol{\varepsilon}_h\right) \tag{21a}$$

$$\tilde{\mathbf{u}} = \tau_u \left(\boldsymbol{\nabla} \cdot \boldsymbol{\sigma}_h + \mathbf{f}\right) \tag{21b}$$

Introducing these strain and displacement subscales in Eqs. (16a) and (16c), integrating by parts the last term in the first equation and recalling that the subscales vanish on the boundary, the mixed discrete system of equations can be written as

$$-\left(1 - \tau_\varepsilon\right)\left(\boldsymbol{\gamma}_h, \mathbf{C}_o : [\boldsymbol{\varepsilon}_h - \nabla^s \mathbf{u}_h]\right)_h + \tau_u \left(\boldsymbol{\nabla} \cdot \left(\mathbf{C}_o : \boldsymbol{\gamma}_h\right), \boldsymbol{\nabla} \cdot \boldsymbol{\sigma}_h + \mathbf{f}\right)_h = 0 \quad \forall \boldsymbol{\gamma}_h \tag{22a}$$

$$\left(\nabla^s \mathbf{v}_h, \mathbf{C}_o : [\boldsymbol{\varepsilon}_{\text{stab}} - \boldsymbol{\varepsilon}_p]\right)_h = F(\mathbf{v}_h) \quad \forall \mathbf{v}_h \tag{22b}$$

where

$$\boldsymbol{\varepsilon}_{\text{stab}} = \left(1 - \tau_\varepsilon\right)\boldsymbol{\varepsilon}_h + \tau_\varepsilon \nabla^s \mathbf{u}_h \tag{23}$$

2.2.2 OSGS

In the Orthogonal Subgrid Scale Stabilization [22], the projection operator is the orthogonal projector, $P(\mathbf{r}) = P_h^\perp(\mathbf{r}) = \mathbf{r} - P_h(\mathbf{r})$, where P_h represents the projection on the appropriate finite element space. It is performed taking advantage of the orthogonality condition

$$\left(\boldsymbol{\eta}_h, \boldsymbol{\Pi}_{\mathbf{r}} - \mathbf{r}\right) = 0 \quad \forall \boldsymbol{\eta}_h \tag{24}$$

where $\boldsymbol{\Pi}_{\mathbf{r}}$ is the projected value of $\mathbf{r}$ on the finite element space and $\boldsymbol{\eta}_h$ belongs either to $\mathcal{V}_h$ or $\mathcal{G}_h$.

According to this, the subscale variables $\tilde{\mathbf{u}}$ and $\tilde{\boldsymbol{\varepsilon}}$ are approximated as:

$$\widetilde{\boldsymbol{\varepsilon}} = \tau_\varepsilon \left(\nabla^s \mathbf{u}_h - P_h\left(\boldsymbol{\nabla}^s \mathbf{u}_h\right)\right) \tag{25a}$$

$$\tilde{\mathbf{u}} = \tau_u \left(\boldsymbol{\nabla} \cdot \boldsymbol{\sigma}_h - P_h\left(\boldsymbol{\nabla} \cdot \boldsymbol{\sigma}_h\right)\right) \tag{25b}$$

where it has been assumed that $P_h(\mathbf{f}) = \mathbf{f}$.

Back-substituting in the set of equations of the problem, the problem to be solved is

$$-\left(\boldsymbol{\gamma}_h, \mathbf{C}_o : \boldsymbol{\varepsilon}_h\right) - \tau_\varepsilon(\boldsymbol{\gamma}_h, \mathbf{C}_o : [\nabla^s \mathbf{u}_h - P_h(\nabla^s \mathbf{u}_h)])_h + \left(\boldsymbol{\gamma}_h, \mathbf{C}_o : \nabla^s \mathbf{u}_h\right) - \tau_u(\nabla \cdot \mathbf{C}_o : \boldsymbol{\gamma}_h, \nabla \cdot \boldsymbol{\sigma}_h - P_h(\nabla \cdot \boldsymbol{\sigma}_h))_h = 0 \quad \forall \boldsymbol{\gamma}_h \tag{26a}$$

$$\left(\nabla^s \mathbf{v}_h, \mathbf{C}_o : (\boldsymbol{\varepsilon}_h - \boldsymbol{\varepsilon}_p) + \tau_\varepsilon(\nabla^s \mathbf{v}_h, \mathbf{C}_o : (\nabla^s \mathbf{u}_h - P_h(\nabla^s \mathbf{u}_h)))_h = F(\mathbf{v}_h) \quad \forall \mathbf{v}_h \tag{26b}$$

2.2.3 Modified OSGS

The formulation given by (26a)-(26b) has a numerical performance very similar to the ASGS method given by (21a)-(21b). However, when localization occurs the formulation that has been found most robust, and that has been used in the numerical examples, is the modification of (26a)-(26b) described next.

First, it may be assumed that

$$P_h(\nabla^s \mathbf{u}_h) \approx \boldsymbol{\varepsilon}_h \tag{27}$$

which essentially means that the strain subscale is assumed to be given by the ASGS formulation rather than by the OSGS one. This avoids the need to compute the projection $P_h(\nabla^s \mathbf{u}_h)$, but it is not crucial at all, neither for stability nor for accuracy.

The second modification is the important one. If $\mathrm{dev}(\mathbf{a})$ and $\frac{1}{3}\mathrm{tr}(\mathbf{a})\mathbf{1}$, with $\mathbf{1}$ the second order identity tensor, are respectively the deviatoric and volumetric components of a tensor $\mathbf{a}$, and $P_h^\perp = I - P_h$ is the projection orthogonal to the appropriate finite element space, the last term in (26a) may be writen as

$$\begin{aligned} & (\nabla \cdot \mathbf{C}_o : \boldsymbol{\gamma}_h, \nabla \cdot \boldsymbol{\sigma}_h - P_h(\nabla \cdot \boldsymbol{\sigma}_h))_h \\ = \; & \Big(P_h^\perp(\nabla \cdot \mathrm{dev}(\mathbf{C}_o : \boldsymbol{\gamma}_h)) + \frac{1}{3} P_h^\perp(\nabla \mathrm{tr}(\mathbf{C}_o : \boldsymbol{\gamma}_h)), P_h^\perp(\nabla \cdot \mathrm{dev}(\boldsymbol{\sigma}_h)) + \frac{1}{3} P_h^\perp(\nabla \mathrm{tr}(\boldsymbol{\sigma}_h)) \Big)_h \end{aligned} \tag{28}$$

For any function f smooth enough, $P_h^\perp(f) = f - P_h(f)$ goes to zero as $h \to 0$ at the optimal rate allowed by the finite element interpolation. Therefore, any term in this last expression may be deleted without upsetting the accuracy of the formulation (see [10] for the analysis of the Oseen problem and a discussion about this point).

The critical point is that we have observed that in cases in which there are strong gradients of the solution the cross-products deviatoric-volumetric terms in (28) cause a numerical misbehavior, that manifests in the plasticity problem as a (small) volumetric locking. A similar situation was found in [11] for the viscoelastic flow problem in the presence of high stress gradients. Note that when the solution is smooth, formulation (26a)-(26b) yields accurate and stable numerical approximations. Moreover, the deviatoric-deviatoric product in (28) leads to a positive-definite term and in principle should enhance stability, but we have found no instability problems when it is omitted.

In view of these observations, only the volumetric-volumetric term is kept in (28), i.e.,

$$(\nabla \cdot \mathbf{C}_o : \boldsymbol{\gamma}_h, \nabla \cdot \boldsymbol{\sigma}_h - P_h(\nabla \cdot \boldsymbol{\sigma}_h))_h \approx \frac{1}{9}(\nabla \mathrm{tr}(\mathbf{C}_o : \boldsymbol{\gamma}_h), \nabla \mathrm{tr}(\boldsymbol{\sigma}_h) - P_h(\nabla \mathrm{tr}(\boldsymbol{\sigma}_h)))_h \tag{29}$$

This, together with (27), leads to the modified OSGS formulation:

$$-(1-\tau_\varepsilon)\,(\boldsymbol{\gamma}_h, \mathbf{C}_o : [\boldsymbol{\varepsilon}_h - \nabla^s \mathbf{u}_h]) + \tau_u \frac{1}{9}(\nabla \mathrm{tr}(\mathbf{C}_o : \boldsymbol{\gamma}_h), \nabla \mathrm{tr}(\boldsymbol{\sigma}_h) - P_h(\nabla \mathrm{tr}(\boldsymbol{\sigma}_h))) = 0 \quad \forall \boldsymbol{\gamma}_h \tag{30a}$$

$$(\nabla^s \mathbf{v}_h, \mathbf{C}_o : [\boldsymbol{\varepsilon}_{\mathrm{stab}} - \boldsymbol{\varepsilon}_p])_h = F(\mathbf{v}_h) \quad \forall \mathbf{v}_h \tag{30b}$$

with $\boldsymbol{\varepsilon}_{\mathrm{stab}}$ given by (23). As mentioned above, this is the numerical formulation used in the numerical examples.

3 Implementation and computational aspects

In the presented mixed formulation, the presence of the non-linear plastic strains requires an iterative procedure to deal with the nonlinearity of the problem. Iterative solution schemes, such as Picard or Newton-Raphson methods, need to be introduced. Constitutive laws involving plasticity are usually written in terms of rate equations and, consequently, the matrices involved in the resulting algebraic set of equations are tangent to the strain-stress path. Hence, the use of the Newton-Raphson scheme will be considered in the following. The advantage of such method is a quadratic convergence rate in the iteration at each time step. Its use requires the computation of the Jacobian matrix of the system of equation at each iteration of every time step.

3.1 ASGS

In the case of the ASGS scheme, differentiating the system of equations (22a)-(22b) at iteration i of time step $n+1$, the Jacobian matrix presents the structure:

$$\boldsymbol{J}^{(i,n+1)} = \left[\begin{array}{cc} \boldsymbol{M}_\tau & \boldsymbol{G}_\tau \\ \boldsymbol{D}_\tau & \boldsymbol{K}_\tau \end{array} \right]^{(i,n+1)} \tag{31}$$

where $\boldsymbol{M}$ is a projection mass-like matrix, $\boldsymbol{G}$ is a gradient matrix, $\boldsymbol{D}$ is a divergence matrix and $\boldsymbol{K}$ is the stiffness matrix. The subscript τ refers to the fact that those matrices incorporates stabilization terms. Differentiating Eqs. (22a)-(22b), with the hypothesis introduced in Eqs. (14)-(15) that the plastic strain depends only on $\boldsymbol{\varepsilon}_h$, and after some manipulation, the previous matrices read:

$$\boldsymbol{M}_\tau = -\left(1 - \tau_\varepsilon\right) \int_\Omega {\mathbf{N}_\varepsilon}^T \mathbf{C}_o \, \mathbf{N}_\varepsilon - \tau_u \int_\Omega \mathbf{C}_o \, \mathbf{B}^T \mathbf{B} \, \mathbf{C}_{ep} \tag{32}$$

$$\boldsymbol{G}_\tau = \left(1 - \tau_\varepsilon\right) \int_\Omega {\mathbf{N}_\varepsilon}^T \mathbf{C}_o \, \mathbf{B} \tag{33}$$

$$\boldsymbol{D}_\tau = \int_\Omega \mathbf{B}^T \left[\mathbf{C}_{ep} - \tau_\varepsilon \, \mathbf{C}_o\right] \mathbf{N}_u \tag{34}$$

$$\boldsymbol{K}_\tau = \tau_\varepsilon \int_\Omega \mathbf{B}^T \mathbf{C}_o \mathbf{B} \tag{35}$$

where $\mathbf{N}_\varepsilon$ and $\mathbf{N}_u$ are the matrices of shape functions of the respective strain and displacement fields and $\mathbf{B}$ is the matrix of the gradient of those shape functions. The resulting algebraic system of equations is, in general, not symmetric. Note that disregarding the terms due to plasticity, the system matrix is symmetric and it coincides with the one presented in [7], [8]. In the general elasto-plastic case, matrix $\mathbf{C}_{ep}$ is tangent to the stress-strain path. In Subsection 4.3 we introduce it and describe how to compute it so that it is tangent to the time-discrete stress-strain path.

3.2 Modified OSGS

The modified OSGS implementation is identical to the ASGS implementation, except for the additional projection of the gradient of the trace of the nodal stresses and the second term in (32), which in this case only contains the volumetric components of $\mathbf{C}_o$ and $\mathbf{B}$.

Concerning the additional equation due to the projection, it has the structure

$$\boldsymbol{M}_{\boldsymbol{\Pi}}\boldsymbol{\Pi} + \boldsymbol{D}_{\boldsymbol{\Pi}}\boldsymbol{\Sigma} = \mathbf{0} \tag{36}$$

where $\boldsymbol{\Pi}$ are the nodal values of the projected variable (gradient of the trace of the stress) and $\boldsymbol{\Sigma}$ of the stresses, and where

$$\boldsymbol{M}_{\boldsymbol{\Pi}} = -\int_{\Omega} \mathbf{N}_u{}^T \mathbf{N}_u$$

The Jacobian in (31) has to be completed with the last row corresponding to (36) and the columns accounting for the effect of $\boldsymbol{\Pi}$ in the first equation. Alternatively to this procedure, a staggered scheme can be devised. First, the projection of the stresses $\boldsymbol{\Pi}^{(0,n+1)}$ is computed at the beginning of the time step. Then, the approximation $\boldsymbol{\Pi}^{(i,n+1)} \approx \boldsymbol{\Pi}^{(0,n+1)}$ is used for the solution of $(\boldsymbol{\varepsilon}_h, \mathbf{u}_h)$. This scheme is preferred with respect to the monolithic one due to the reduced computation time required, almost identical to that of the ASGS scheme.

4 Pressure dependent plasticity. The Drucker-Prager model

4.1 Yield criterion

The Drucker-Prager plasticity model may be constructed as a linear combination of a pure isochoric plasticity model and a pure pressure plasticity model, in the form:

$$f\left(\boldsymbol{\sigma}, q\right) = \left[\sqrt{\frac{3}{2}}\left\|\text{dev }\boldsymbol{\sigma}\right\| - r^d\left(q\right)\right] + a\tan\phi\left[\frac{1}{3}\text{tr }\boldsymbol{\sigma} - r^p\left(q\right)\right] = 0 \tag{37}$$

where the angle of friction ϕ is introduced to relate the admissible deviatoric stresses to the pressure. Here, $r^d = r^d\left(q\right)$ and $r^p = r^p\left(q\right)$ are the admissible stresses of the deviatoric and volumetric parts of the model, respectively, and q is a stress-like internal variable that controls the hardening/softening of the model. In this work, the pressure threshold is taken as $r^p = 0$ to allow a direct comparison between J2 incompressible plasticity and Drucker-Prager plasticity.

In the principal stress Haig-Westergaard space, the Drucker-Prager yield surface appears as a symmetric cone with the axis coinciding with the hydrostatic pressure and a circular trace on the octahedral plane (see Figure 1). The parameter $a = \pm 1$ controls the sign of the pressure part and the orientation of the cone. For $a = 1$, the cone is open in the triaxial compression end, while for $a = -1$, it is open for triaxial tension.

The deviatoric stress threshold is expressed as:

$$r^d\left(q\right) = \sigma_y - q(\xi) \tag{38}$$

where ξ is an internal strain-like parameter and $q(\xi)$ is the hardening/softening function:

$$q\left(\xi\right) = \begin{cases} H\ \xi & \text{for} \quad 0 \leq \xi \leq \frac{\sigma_y}{H} \\ 0 & \text{for} \quad \frac{\sigma_y}{H} \leq \xi \leq \infty \end{cases} \tag{39}$$

for linear softening, whereas, in the case of exponential softening, it takes the form:

$$q\left(\xi\right) = \sigma_y\left(1 - \exp\left(\frac{-2H}{\sigma_y}\xi\right)\right) \qquad \text{for} \quad 0 \leq \xi \leq \infty \tag{40}$$

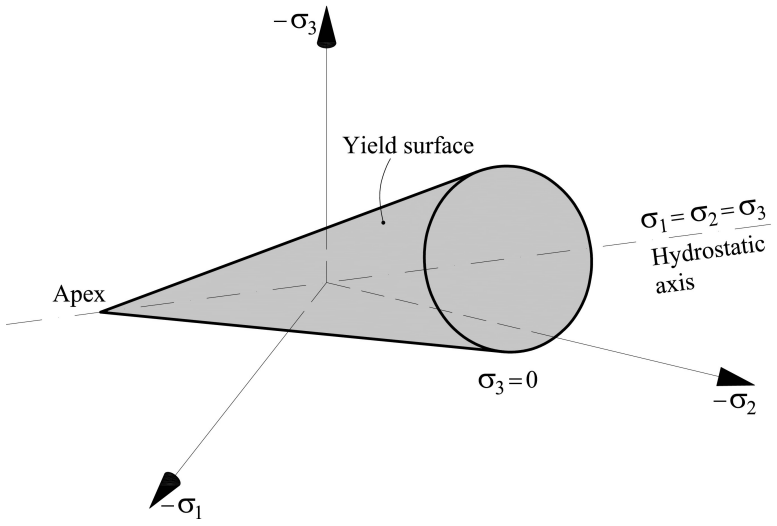

Figure 1: Yield surface for Drucker-Prager plasticity model in the stress space ($a = 1$)

where σ_y is the initial deviatoric threshold and H is the softening parameter.

Making $\rho = 1/(1 + \tan\phi)$, the yield surface may be rewritten as:

$$f(\boldsymbol{\sigma}, q) = \rho \left(\sqrt{\frac{3}{2}} \|\text{dev } \boldsymbol{\sigma}\| - (\sigma_y - q(\xi)) \right) + a(1-\rho)\frac{1}{3}\text{tr } \boldsymbol{\sigma} = 0 \tag{41}$$

In the following, linear isotropic elasticity is assumed, with the elastic constitutive tensor given by:

$$\mathbf{C}_o = K\ \mathbf{1} \otimes \mathbf{1} + 2G \left(\mathbf{I} - \frac{1}{3}\mathbf{1} \otimes \mathbf{1} \right) \tag{42}$$

where K is the bulk modulus, G is the shear modulus and $\mathbf{1}$ and $\mathbf{I}$ are the second and fourth order identity tensors, respectively.

4.2 Return mapping algorithm

Assuming associative plasticity and the existence of a plastic potential that coincides with the definition of the admissible stress surface $f(\boldsymbol{\sigma}, q)$, the evolution equations for the plastic variables read:

$$\begin{aligned} \dot{\boldsymbol{\varepsilon}}_p &= \dot{\gamma}\, \partial_{\boldsymbol{\sigma}} f(\boldsymbol{\sigma}, q) \\ \dot{\xi} &= \dot{\gamma}\, \partial_q f(\boldsymbol{\sigma}, q) \end{aligned} \tag{43}$$

where $\dot{\gamma}$ is the plastic multiplier or plastic consistency parameter.

Additionally, given the Karush-Kuhn-Tucker and consistency conditions:

$$\gamma \geq 0, \qquad f(\boldsymbol{\sigma}, q) \leq 0, \qquad \gamma f(\boldsymbol{\sigma}, q) = 0 \tag{44}$$

$$\text{if} \qquad f(\boldsymbol{\sigma}, q) = 0 \qquad \Rightarrow \qquad \dot{\gamma} \geq 0, \quad \dot{f}(\boldsymbol{\sigma}, q) \leq 0 \quad \text{and} \quad \dot{\gamma}\dot{f}(\boldsymbol{\sigma}, q) = 0 \tag{45}$$

Substituting the definition of the failure surface and differentiating, the plastic multiplier $\dot{\gamma}$ is computed as [26]:

$$\dot{\gamma} = \frac{1}{D}\ \partial_{\boldsymbol{\sigma}} f : \mathbf{C}_o : \dot{\boldsymbol{\varepsilon}} \tag{46}$$

with

$$D = \left\langle \partial_{\boldsymbol{\sigma}} f : \mathbf{C}_o : \partial_{\boldsymbol{\sigma}} f + \partial_q f\ \frac{dq}{d\xi}\ \partial_q f \right\rangle \tag{47}$$

The time derivative of the evolution equations of the plastic variables can be approximated introducing a Backward-Euler scheme with time steps of length Δt. Let us consider the time span $[t_n, t_{n+1}]$, with $t_{n+1} = t_n + \Delta t$, where variables are known at step (n) and must be computed at step $(n+1)$. Then, the discrete-in-time version of (43) reads:

$$\begin{array}{rcl} \dot{\boldsymbol{\varepsilon}}_p \approx \frac{\boldsymbol{\varepsilon}_p^{(n+1)} - \boldsymbol{\varepsilon}_p^{(n)}}{\Delta t} & = & \frac{\gamma^{(n+1)} - \gamma^{(n)}}{\Delta t} \left[\rho \sqrt{\frac{3}{2}} \frac{\text{dev}\ \boldsymbol{\sigma}^{(n+1)}}{\left\| \text{dev}\ \boldsymbol{\sigma}^{(n+1)} \right\|} + \frac{a(1-\rho)}{3} \mathbf{1} \right] \\ \dot{\xi} \approx \frac{\xi^{(n+1)} - \xi^{(n)}}{\Delta t} & = & \rho \frac{\gamma^{(n+1)} - \gamma^{(n)}}{\Delta t} \end{array} \tag{48}$$

The trial state is defined at step $n+1$ with the plasticity variables $\boldsymbol{\varepsilon}_p$ and ξ frozen at step n. Therefore, the trial stresses are:

$$\begin{array}{rcl} \boldsymbol{\sigma}_{trial}^{(n+1)} & = & \mathbf{C}_o \colon \left(\boldsymbol{\varepsilon}^{(n+1)} - \boldsymbol{\varepsilon}_p^{(n)} \right) \\ q_{trial}^{(n+1)} & = & q^{(n)} \end{array} \tag{49}$$

The trial yielding function is:

$$f_{trial}^{(n+1)} = \rho \left(\sqrt{\frac{3}{2}} \left\| \text{dev}\ \boldsymbol{\sigma}_{trial}^{(n+1)} \right\| - \left(\sigma_y - q_{trial}^{(n+1)} \right) \right) + a\,(1-\rho) \left(\frac{1}{3} \text{tr}\ \boldsymbol{\sigma}_{trial}^{(n+1)} \right) \tag{50}$$

Plasticity occurs if $f_{\text{trial}}^{(n+1)} \geq 0$. The update of the stress is then

$$\boldsymbol{\sigma}^{(n+1)} = \boldsymbol{\sigma}_{trial}^{(n+1)} - \Delta\gamma^{(n+1)}\ \mathbf{C}_o : \partial_{\boldsymbol{\sigma}} f \tag{51}$$

which can be particularized for the Drucker-Prager criterion as:

$$\boldsymbol{\sigma}^{(n+1)} = \boldsymbol{\sigma}_{trial}^{(n+1)} - \Delta\gamma^{(n+1)} \left[a\,(1-\rho)\,K\mathbf{1} + 2G\rho \sqrt{\frac{3}{2}} \frac{\text{dev}\ \boldsymbol{\sigma}_{trial}^{(n+1)}}{\left\| \text{dev}\ \boldsymbol{\sigma}_{trial}^{(n+1)} \right\|} \right] \tag{52}$$

The change of plastic multiplier $\Delta\gamma^{(n+1)} = \gamma^{(n+1)} - \gamma^{(n)}$ is computed with the discrete counterpart of (46) as:

$$\Delta\gamma^{(n+1)} = \frac{f_{trial}^{(n+1)}}{(1-\rho)^2\,K + 3G\rho^2 + \rho^2\ \frac{dq}{d\xi}\Big|^{(n+1)}} \tag{53}$$

4.3 Constitutive Elasto-Plastic Tangent operator

On one hand, the constitutive elasto-plastic tensor in continuous form is [26]:

$$\mathbf{C}_{ep} = \mathbf{C}_o - \mathbf{C}_p = \mathbf{C}_o - \frac{1}{D}\left(\mathbf{C}_o : \partial_{\boldsymbol{\sigma}} f\right) \otimes \left(\mathbf{C}_o : \partial_{\boldsymbol{\sigma}} f\right) \tag{54}$$

On the other hand, considering the discrete Backward Euler time integration, the *algorithmic consistent* constitutive elasto-plastic tensor [27] can be computed as:

$$\mathbf{C}_{ep}^{(n+1)} = \frac{\Delta\boldsymbol{\sigma}^{(n+1)}}{\Delta\boldsymbol{\varepsilon}^{(n+1)}} \tag{55}$$

Carrying out the differentiation, it yields:

$$\begin{aligned}
\mathbf{C}_{ep}^{(n+1)} \;=\; & \mathbf{C}_o \\
& - \tfrac{1}{D^{(n+1)}} \left[\rho 2G\sqrt{\tfrac{3}{2}}\mathbf{n}_{d,trial}^{(n+1)} + a\left(1-\rho\right)K\ \mathbf{1}\right] \otimes \left[\rho 2G\sqrt{\tfrac{3}{2}}\mathbf{n}_{d,trial}^{(n+1)} + a\left(1-\rho\right)K\ \mathbf{1}\right] \\
& - \Delta\gamma^{(n+1)}(2G)^2\rho\sqrt{\tfrac{3}{2}}\tfrac{1}{\left\|\text{dev }\boldsymbol{\sigma}_{trial}^{(n+1)}\right\|}\left[\left(\mathbf{I} - \tfrac{1}{3}\mathbf{1}\otimes\mathbf{1}\right) - \mathbf{n}_{d,trial}^{(n+1)} \otimes \mathbf{n}_{d,trial}^{(n+1)}\right]
\end{aligned} \tag{56}$$

where $D^{(n+1)}$ is the discrete counterpart of (47):

$$D^{(n+1)} = \left[\left(1-\rho\right)^2 K + \rho^2 3G\right] - \rho^3 \frac{dq\left(\xi^{(n)} + \rho\Delta\gamma^{(n+1)}\right)}{d\xi} \tag{57}$$

and $\mathbf{n}_{d,\text{trial}}^{(n+1)}$ is the unit vector in the trial deviatoric stress direction:

$$\mathbf{n}_{d,trial}^{(n+1)} = \frac{\text{dev }\boldsymbol{\sigma}_{trial}^{(n+1)}}{\left\|\text{dev }\boldsymbol{\sigma}_{trial}^{(n+1)}\right\|} \tag{58}$$

4.4 Apex return mapping

The apex of the Drucker-Prager cone is a singular point in the yield surface. This means that the cases when the return mapping is to the apex, rather than to the regular lateral surface of the cone, have to be identified and an "ad-hoc" procedure is necessary [28, 29, 30]. In the standard return mapping algorithm, Eq. (52), considering the deviatoric part and taking norms, it is:

$$\left\|\text{dev }\boldsymbol{\sigma}^{(n+1)}\right\| = \left\|\text{dev }\boldsymbol{\sigma}_{trial}^{(n+1)}\right\| - \Delta\gamma^{(n+1)}\rho 2G\sqrt{\frac{3}{2}} \tag{59}$$

which requires that that:

$$\Delta\gamma^{(n+1)} \leq \frac{\left\|\text{dev }\boldsymbol{\sigma}_{trial}^{(n+1)}\right\|}{\rho 2G\sqrt{\frac{3}{2}}} \tag{60}$$

If this condition is verified, then the return mapping is made through the standard procedure described previously. Otherwise, the return mapping will be made to the apex of the Drucker-Prager cone.

The stress at the apex point is:

$$\boldsymbol{\sigma}_{apex} = p_{min}\ \mathbf{1} = a\frac{\rho}{(1-\rho)}\left(\sigma_y - q\right)\ \mathbf{1} \tag{61}$$

And, given that

$$\boldsymbol{\sigma}_{apex} = \boldsymbol{\sigma}_{trial}^{(n+1)} - \mathbf{C}_o\colon \Delta\boldsymbol{\varepsilon}_p^{(n+1)} \tag{62}$$

the discrete increment of plastic strain is:

$$\Delta\boldsymbol{\varepsilon}_p^{(n+1)} = \mathbf{C}_o^{-1}\colon\left(\boldsymbol{\sigma}_{trial}^{(n+1)} - \boldsymbol{\sigma}_{apex}\right) \tag{63a}$$

$$= \frac{a}{3K}\left(p_{trial}^{(n+1)} - p_{min}\right)\mathbf{1} + \frac{1}{2G}\text{dev}\ \boldsymbol{\sigma}_{trial}^{(n+1)} \tag{63b}$$

Notice that the value of $p_{\min}$ depends on the value of the isotropic hardening $q = q(\xi)$. Consequently, an iterative procedure is necessary in order to evaluate correctly the plastic multiplier.

Once the stress state arrives at the vertex of the cone, it will remain at the apex unless unloading or neutral loading occurs. This means that once the apex is reached, the consistent constitutive tensor is the null fourth order tensor.

4.5 Softening behavior

Physically, the energy dissipated during the formation of a slip surface is linked with the fracture energy G_f, defined by unit surface. When using a plastic model defined in terms of stress and strain to represent the behavior of the (regularized) slip surface, the dissipated plastic energy W_p is defined by unit volume. In the discrete FE setting, these two definitions are related through a characteristic length l_{ch}, connected to the mesh resolution:

$$W_p = \frac{G_f}{l_{ch}} \tag{64}$$

In the plastic model, the rate of plastic work is computed as:

$$\dot{W}_p = \boldsymbol{\sigma} : \dot{\boldsymbol{\varepsilon}}_p = \bar{\sigma}\ \dot{\bar{\varepsilon}}_p \tag{65}$$

where $\bar{\sigma}$ is the equivalent Drucker-Prager stress:

$$\bar{\sigma} = \rho\ \left(\boldsymbol{\sigma}_y - q\left(\xi\right)\right) \tag{66}$$

and $\dot{\bar{\varepsilon}}_p$ is the rate of equivalent plastic strain:

$$\dot{\bar{\varepsilon}}_p = \sqrt{\frac{2}{3}}\left\|\dot{\boldsymbol{\varepsilon}}_p\right\| = \left[\rho + a\sqrt{\frac{2}{3}}\left(1-\rho\right)\right]\ \dot{\xi} = \frac{\alpha}{\rho}\ \dot{\xi} \tag{67}$$

where $\alpha \geq 1$ depends only on the friction angle. In both the linear and exponential softening cases, where $q(\xi)$ is defined by (39) and (40), respectively, the total plastic work is integrated to be:

$$W_p = \int_0^\infty \dot{W}_p \, dt = \int_0^\infty \bar{\sigma} \, \dot{\bar{\varepsilon}}_p \, dt = \alpha \, \frac{{\sigma_y}^2}{2H} \tag{68}$$

From expressions (64) and (68), the parameter H can be computed as:

$$H = \alpha \, \frac{{\sigma_y}^2}{2G_f} l_{ch} = \bar{H} \, l_{ch} \tag{69}$$

The parameter $\bar{H}$ depends only on material properties, whereas l_{ch} depends on the resolution of the discretization. As pointed out by [8], the size of the strain concentration band depends on the finite element technology. For instance, irreducible finite elements provide a concentration band within a single element span, due to the discontinuous strain field. On the contrary, in the $\boldsymbol{\varepsilon}/u$ mixed FE formulation, with inter-elemental continuous strain, the slip line spans two elements. The characteristic length l_{ch} is taken accordingly.

4.6 Orientation of the shear band discontinuities

Several authors [12, 13, 14, 15, 16, 17, 18] have found analytical and geometrical solutions for the orientation of the discontinuity bands resulting from elasto-plastic models using different strategies. All of them seek their solutions after the so-called *localization condition,* which implies the *loss of material ellipticity* of the constitutive relation and is shown to be a necessary condition for the appearance of *weak discontinuities* and *localized failure* to take place.

In this work, a different approach is adopted to find analytical expressions for the orientation of localization bands for the Drucker-Prager model, both under plane strain and plane stress conditions. This procedure, proposed in reference [19], produces far more realistic results than those used beforehand. It makes use of the *stress boundedness* and *decohesion conditions,* which, combined, can be shown to be also necessary conditions for the shear band to form, but more constrictive than the before mentioned *localization condition.* In fact, they can be shown to be necessary conditions for the occurrence of bifurcation and localization of the strain field, with bounded stresses and decohesion in the limit case along a localization band (or a regularized strong discontinuity). This is why the term *strong discontinuity condition* was used in reference [18] for it. However, it applies to localization bands (limited by weak discontinuities) and strong discontinuities alike.

The physical interpretation of this condition is simple: all of the difference in the strain field between the interior and the exterior points of the localization band, that is, the strain "jump", must be inelastic (plastic in this case). For a given plastic flow tensor, the condition may be used to determine the orientation of the discontinuity.

A remarkable difference between this approach and those other mentioned (based on the acoustic tensor) is that the orientation of the discontinuity does not depend on the elastic properties. It depends only on the plastic yield surface adopted and the stress state of interest.

In the next Section it is shown that this strategy predicts analytically orientations for the shear bands that are almost in perfect agreement with the ones computed numerically using the proposed stabilized mixed $\boldsymbol{\varepsilon}/\mathbf{u}$ formulation.

5 Numerical examples

The formulation presented in the preceding sections is illustrated below in a number of benchmark problems. Performance of the proposed stabilized mixed formulations is tested considering both 2D and 3D examples to demonstrate the generality of the formulation and its independence from the type of finite elements utilized. In 2D, plane-strain 3-noded linear triangular unstructured meshes are used. In 3D, structured meshes of regular triangular prisms are employed. The examples involve both compressible and incompressible plasticity using the Drucker-Prager model with exponential softening. Results obtained for the incompressible cases are compared with those obtained with the previously developed stabilized mixed pressure/displacement formulation ([1, 2, 3, 4, 5] and [6]).

The following material properties are assumed: Young's modulus $E = 10$ MPa, Poisson's ratio $\nu = 0.3$, deviatoric stress threshold $\sigma_y = 10$ KPa and fracture energy $G_f = 400$ J/m^2. For the Drucker-Prager model $a = 1$, the cone is open in the triaxial compression end. Values $c_\varepsilon = 0.01$ and $c_u = 1.0$ and $L = 1$ m are taken for the evaluation of the stabilization parameters.

The Newton-Raphson method is used to solve the non-linear system of equations arising from the spatial and temporal discretization of the weak form of the stabilized problem. In all cases 200 equal time steps are performed to complete the analyses. Convergence of a step is attained when the ratio between the norms of the iterative residual forces and the incremental total forces is lower than 10^{-5}. Calculations are performed with an enhanced version of the finite element program COMET [31, 32], developed by the authors at the International Center for Numerical Methods in Engineering (CIMNE). Pre and post-processing is done with GiD, also developed at CIMNE [33].

5.1 Singly perforated strip

The first example is a plane-strain singly perforated strip subjected to axial imposed straining. Because of the double symmetry of the domain and boundary conditions, only one quarter of the

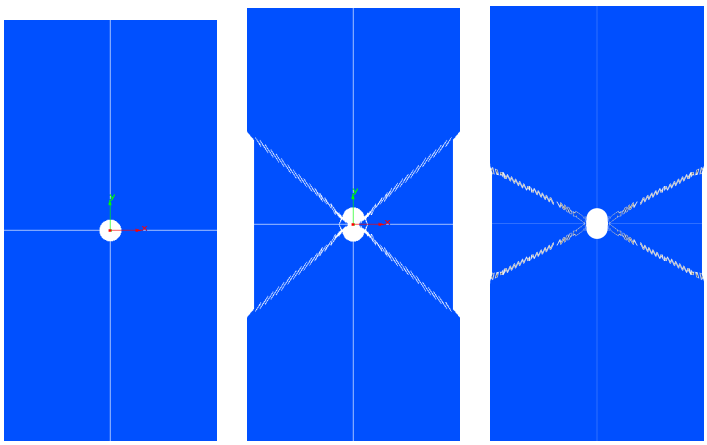

(a) (b) (c)

Figure 2: Geometries for the singly perforated strip: (a) undeformed, (b) deformed (x 5) $\phi = 0^o$, (c) deformed (x 5) $\phi = 45^o$

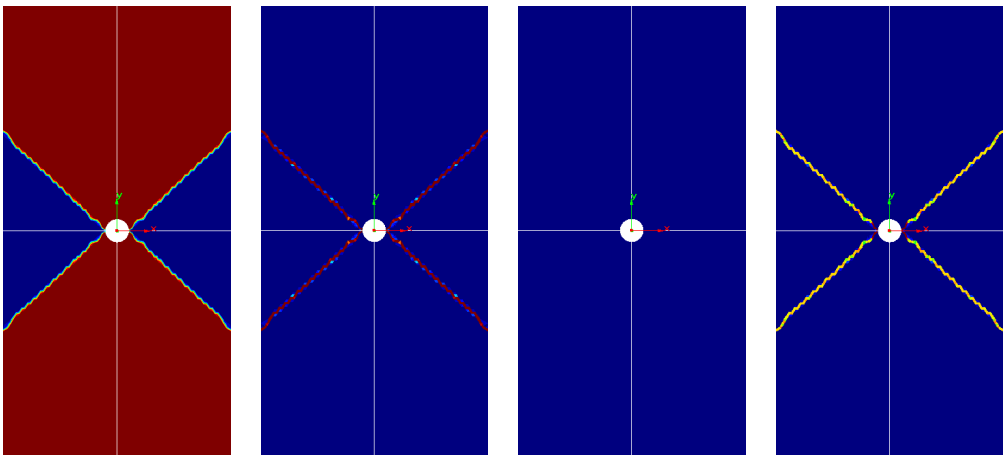

(a) (b) (c) (d)

Figure 3: Results for singly perforated strip using the mixed $\mathbf{u}/p$ formulation; incompressible case $\phi = 0^o$. Contours for: (a) vertical displacement, (b) equivalent plastic strain, (c) volumetric plastic strain and (d) deviatoric plastic strain

domain (the top right quarter) needs to be discretized. Figure 2a depicts the original geometry of the problem; dimensions are 20 × 40 m × m (width × height) and the radius of the perforation is $r = 1$ m. Thickness is 1 m. A uniform upward vertical displacement is imposed at the top boundary.

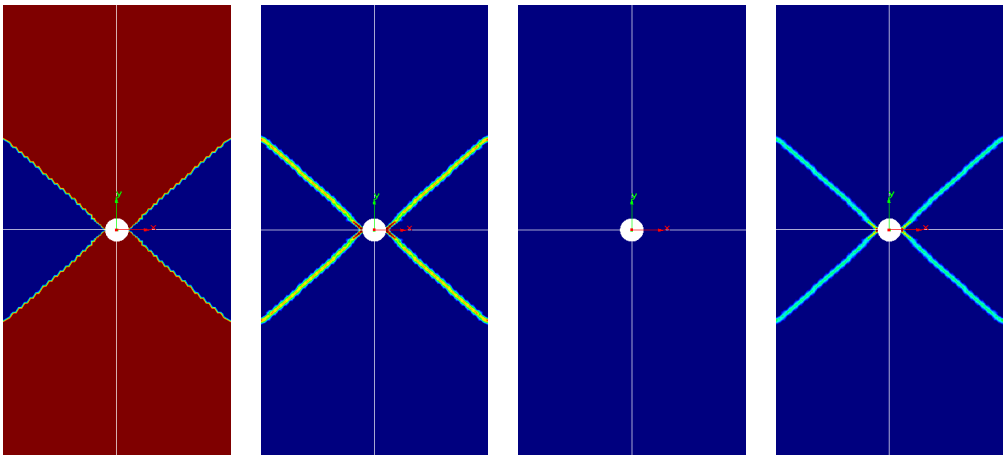

(a) (b) (c) (d)

Figure 4: Results for singly perforated strip with the mixed $\boldsymbol{\varepsilon}/\mathbf{u}$ formulation; incompressible case $\phi = 0^o$. Contours for: (a) vertical displacement, (b) equivalent plastic strain, (c) volumetric plastic strain and (d) deviatoric plastic strain

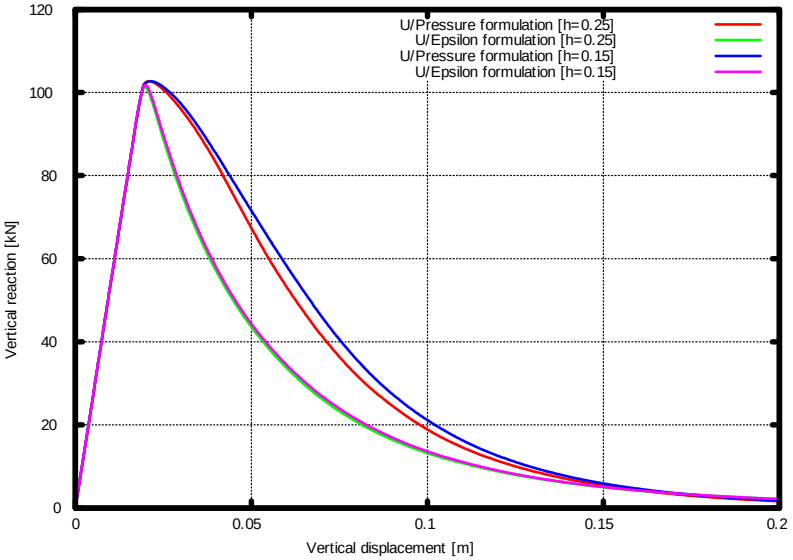

(a)

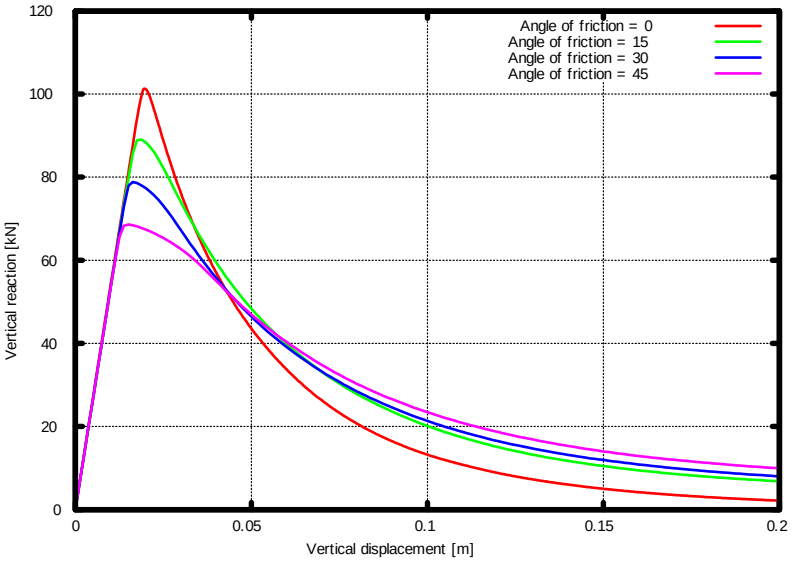

(b)

Figure 5: Results for singly perforated strip. (a) Comparison between the mixed $\mathbf{u}/p$ and $\boldsymbol{\varepsilon}/\mathbf{u}$ formulations for the incompresible case. Effect of mesh refinement. (b) Comparison for the $\boldsymbol{\varepsilon}/\mathbf{u}$ formulation for different friction angles.

The computational domain is divided into an unstructured uniform mesh of 7,202 linear triangles (3,721 nodes) with an average mesh size of $h = 0.25$ m, not shown. The pre-processor used tends to introduce patches of equilateral triangles with predominant directions at -30^o, $+30^o$ and $+90^o$ with the horizontal axis.

First, the incompressible case, with friction angle $\phi = 0^o$ is investigated.

Figure 3 shows the results obtained using the stabilized mixed $\mathbf{u}/p$ formulation, once the shear bands are fully developed and the collapse mechanism can be appreciated ((half)-imposed vertical upward displacement $\delta = 0.20$ m). The failure mechanism is correctly predicted, with X-shaped shear bands forming at 45^o. No mesh-bias dependency is observed. The resolution of the shear bands is optimal for the mesh used, as shown by the displacement and equivalent plastic strain plots. Discontinuity of the displacement tangential to the slip line and localization of the deviatoric strain occurs across one single element. The isochoric nature of the deformation pattern is demonstrated by the absence of volumetric plastic strains. No indication of overshoots or undershoots of any magnitude is observed at either side of the discontinuity lines. Control on the pressure is completely attained, and no spurious oscillations are observed anywhere in the domain.

Figure 4 shows the results obtained using the proposed stabilized mixed $\boldsymbol{\varepsilon}/\mathbf{u}$ formulation, also for a (half)-imposed vertical displacement $\delta = 0.20$ m. Results are very similar to those obtained with the $\mathbf{u}/p$ formulation. The failure mechanism is correctly predicted and no mesh-bias dependency is observed. The resolution of the shear bands is also optimal for the mesh used. Now localization of the deviatoric strain occurs across two elements, because of inter-element strain continuity. Volumetric plastic strains are negligible. No spurious oscillation of any variable is observed. The deformed shape of the strip (with an amplification factor of 5) is shown in Figure 2.

Figure 5a compares (half)-load vs (half)-imposed vertical displacement curves (recall 1 m thickness is assumed) obtained with the two stabilized mixed formulations: $\mathbf{u}/p$ and $\boldsymbol{\varepsilon}/\mathbf{u}$. Both mixed

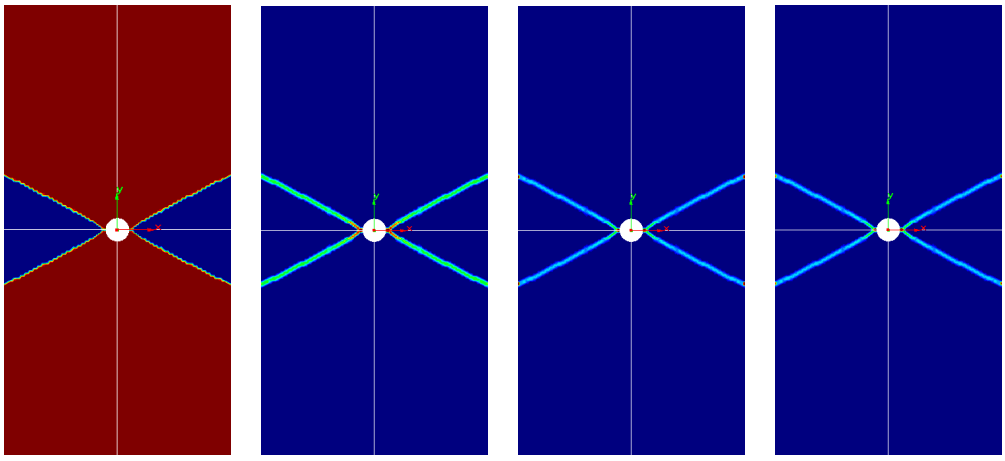

(a) (b) (c) (d)

Figure 6: Results for singly perforated strip with the mixed $\boldsymbol{\varepsilon}/\mathbf{u}$ formulation; compressible case $\phi = 45^o$. Contours for: (a) vertical displacement, (b) equivalent plastic strain, (c) volumetric plastic strain and (d) deviatoric plastic strain

formulations capture adequately the peak load and the softening branch of the curve, but the response obtained with the newly proposed formulation is less dissipative. The reason for this is that this formulation is locally more accurate and it reduces the stress locking induced by the isochoric deformation behavior inside the shear bands.

The total dissipated energy required to create a perfectly straight shear band branch at 45^o, similar to those shown in Figures 3 and 4, but without any boundary effect, is $W_{dis} = G_f \cdot A = 400 \cdot 9\sqrt{2} \cdot 1 = 5091$ J. The work spent by the external forces in the $\boldsymbol{\varepsilon}/\mathbf{u}$ formulation (area under the curve in Figure 5a) is $W_{dis}^{\boldsymbol{\varepsilon}/\mathbf{u}} = 5210$ J (2.33 % difference with respect the idealized solution), while the work spent by the $\mathbf{u}/p$ formulation is $W_{dis}^{\mathbf{u}/p} = 6723$ J (32.02 % difference). The accuracy of the proposed formulation is remarkable.

Figure 5a also shows the (half)-load vs (half)-imposed vertical displacement curves obtained with the two stabilized mixed formulations, $\mathbf{u}/p$ and $\boldsymbol{\varepsilon}/\mathbf{u}$, on a refined unstructured uniform mesh of 20,255 linear triangles (10,342 nodes) with an average mesh size of $h = 0.15$ m. These show that the solution obtained with $\boldsymbol{\varepsilon}/\mathbf{u}$ formulation is independent of the mesh size and bias. Contrarily, the solution of the $\mathbf{u}/p$ formulation converges to an over-dissipative solution. This is due to the stress-locking induced by the poor kinematics of the elements used under localized shear. The problem is much alleviated in the $\boldsymbol{\varepsilon}/\mathbf{u}$ formulation (see reference [8]).

Next, compressible cases, with increasing friction angles $\phi = 15^o$, $30^o, 45^o$ are investigated.

Figure 5b shows (half)-load vs (half)-imposed vertical displacement curves obtained with the $\boldsymbol{\varepsilon}/\mathbf{u}$ formulation for these cases. The limit load reduces as the friction angle increases, due to the orientation of the cone ($a = 1$). Even if the dissipated energy per unit area remains constant, and equal for the fracture energy of the material, the total dissipated energy decreases as the friction angle increases, because the length of the shear band diminishes.

Table 1 shows the comparison between the analytical localization angles computed for uniaxial tension in plane strain conditions and the ones obtained numerically. The analytical values are obtained with the procedure presented in reference [19]. The remarkable agreement between the analytical and the numerical values validates both the analytical and the numerical approaches.

Figure 6 shows the results obtained using the proposed stabilized mixed $\boldsymbol{\varepsilon}/\mathbf{u}$ formulation, friction angle $\phi = 45^o$, and a (half)-imposed vertical displacement $\delta = 0.20$ m. The failure mechanism is correctly predicted, with shear band now forming an angle of 26.90^o with the horizontal axis (being 26.11^o the analytical value), completely independent of the mesh-bias. The resolution of the shear bands is also optimal for the mesh used. Volumetric plastic strains are of the same order than the deviatoric plastic strains. The deformed shape (x 5) of the strip is shown in Figure 2c.

Plane strain	**Analytical** [19]	**Numerical**
$\phi = 0^o$	$\theta_{loc} = 45.00^o$	$\theta_{loc} = 44.32^o$
$\phi = 15^o$	$\theta_{loc} = 40.53^o$	$\theta_{loc} = 39.30^o$
$\phi = 30^o$	$\theta_{loc} = 35.07^o$	$\theta_{loc} = 33.90^o$
$\phi = 45^o$	$\theta_{loc} = 26.12^o$	$\theta_{loc} = 26.90^o$

Table 1: Results for singly perforated strip with the mixed $\boldsymbol{\varepsilon}/\mathbf{u}$ formulation. Comparison between the analytical localization angles for uniaxial tension in *plane strain* conditions and the ones obtained numerically

5.2 Circular rigid inclusion

The second example is a plane-strain circular rigid inclusion subjected to an imposed vertical downward imposed displacement. Perfect stick conditions are assumed between the inclusion and the surrounding medium; thus, the vertical displacement is imposed directly to the interface. Figure 7a depicts the original geometry of the problem; dimensions are 20 × 20 m × m (width × height) and the radius of the inclusion is $r = 1$ m. Thickness is 1 m.

This example is interesting because the symmetric collapse mechanism consists of two almost circular curved shear bands that intersect each other. Therefore, it is an adequate test to assess the ability of the different formulations to deal with such a complex situation in a given mesh.

Because of the symmetry of the domain and boundary conditions with respect the central vertical axis, only one half of the domain (the right half) needs to be discretized. The computational domain is divided into an unstructured non-uniform mesh of 13,750 linear triangles (7,006 nodes) with smaller elements near the circular inclusion, not shown.

The incompressible case, with friction angle $\phi = 0^o$ is investigated.

Figure 8 shows the results obtained using the stabilized mixed $\mathbf{u}/p$ formulation, once the collapse mechanism and the shear bands are fully developed. The failure mechanism, which can be appreciated in Figure 8a, displaying the contour fills for the norm of the displacements, and Figure 8b, displaying the contour fills for the norm of the equivalent plastic strain, is correctly predicted. Because of the formulation used, discontinuity of the displacements across the slip lines and localization of the plastic strain occurs across one single element. The attained resolution is optimal for the mesh used. Figure 8c shows pressure contours. Not only there is no evidence of pressure oscillations, but the pressure field is completely undisturbed by the presence of the shear bands. An almost perfectly skew-symmetric pressure distribution is attained. Finally, Figure 8d shows the principal strain vectors at failure. Strain localization is clear, and the direction of the computed vectors is affected by the mesh alignment, although this is not evident because the mesh is unstructured. The deformed shape of the problem (with a displacement amplification factor of 5) is shown in Figure 7.

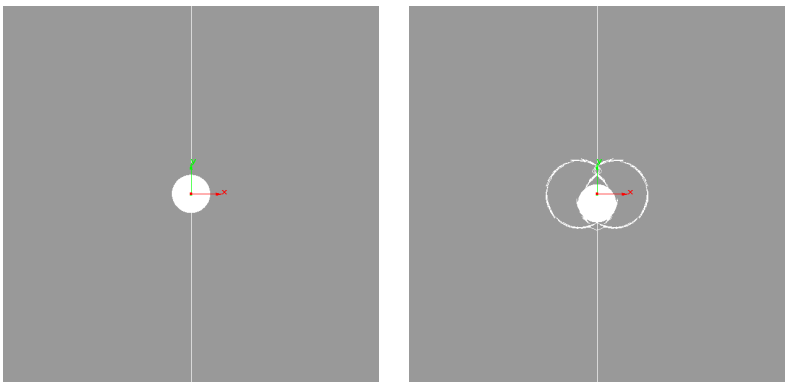

(a) (b)

Figure 7: Original and deformed (x 5) geometries for circular rigid inclusion

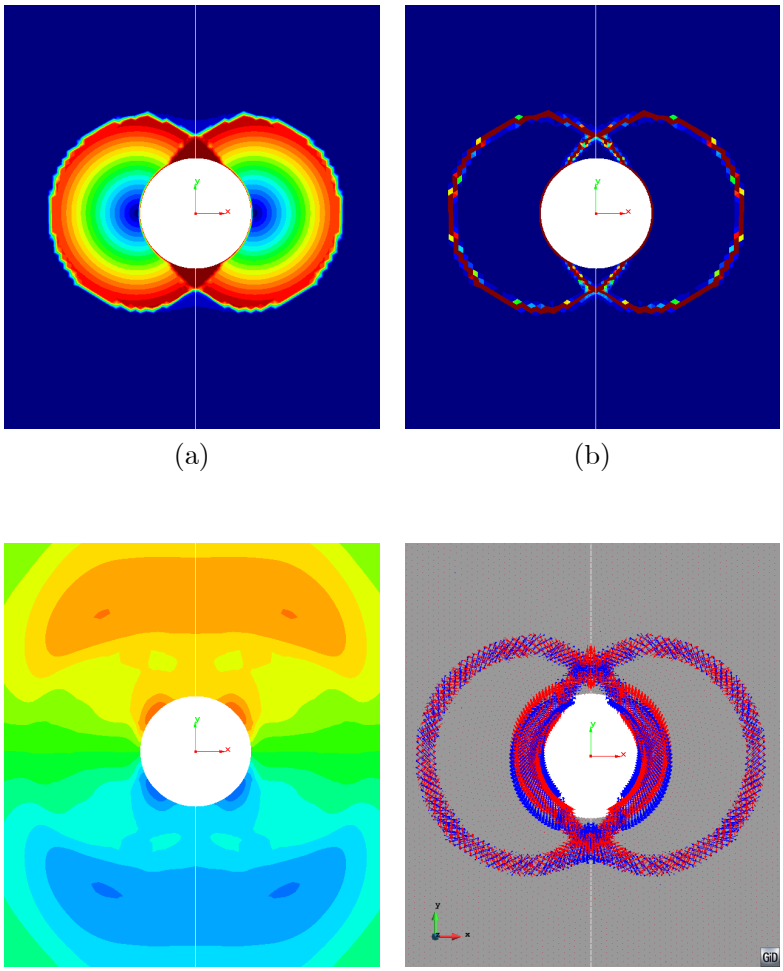

(a) (b)

(c) (d)

Figure 8: Results for circular rigid inclusion using the mixed $\mathbf{u}/p$ formulation. Incompressible plasticity, $\phi = 0^o$. Contours for: (a) displacement, (b) equivalent plastic strain, (c) pressure and (d) principal strain vectors

Figure 9 shows the corresponding results obtained using the proposed stabilized mixed $\boldsymbol{\varepsilon}/\mathbf{u}$ formulation. As in the previous example, results are qualitatively very similar to those obtained with the $\mathbf{u}/p$ formulation. The failure mechanism is obviously the same and no mesh-bias dependency is observed. Contour plots for the displacement and the pressure fields, Figures 9a and 9c are almost identical to those in 8a and 8c, because in both formulations these fields are linearly interpolated. A clear difference can be observed in the contour plot of the plastic strain, Figure 9b, which can be considered as the smoothing of the piece-wise discontinuous field of Figure 8c. The inter-element continuity of the plastic strain is clear in the picture. Figure 9d shows the principal strain vectors at failure. In this case, the direction of the computed vectors is much less affected by the mesh alignment than in Figure 8d.

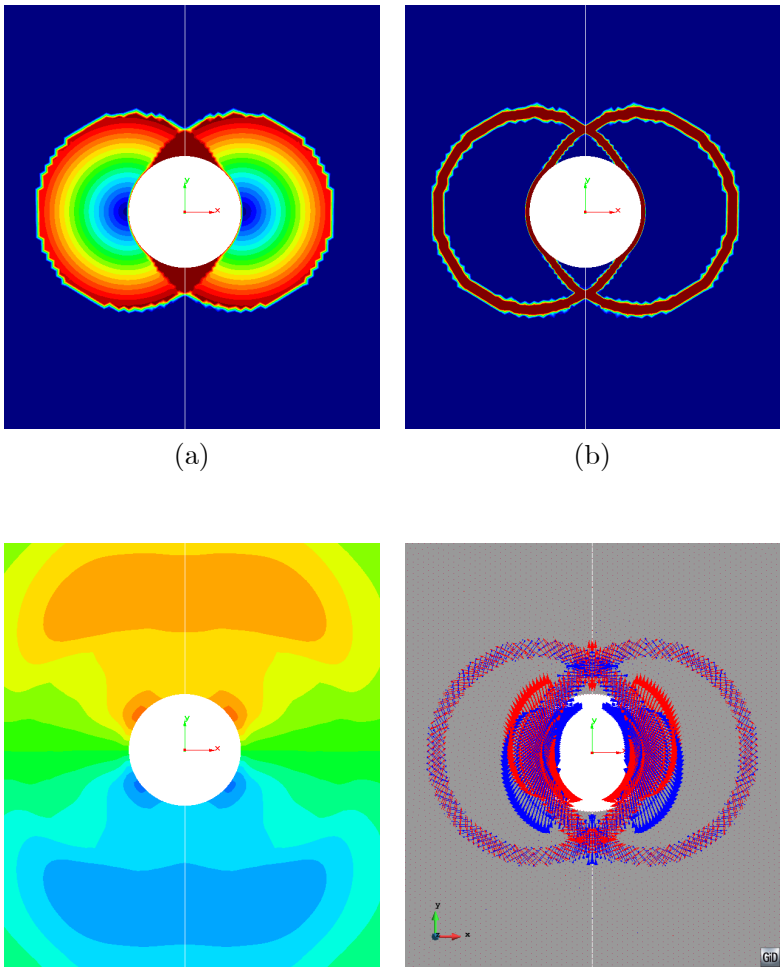

Figure 9: Results for circular rigid inclusion using the mixed $\boldsymbol{\varepsilon}/\mathbf{u}$ formulation. Incompressible plasticity, $\phi = 0^o$. Contours for: (a) displacement, (b) equivalent plastic strain, (c) pressure and (d) principal strain vectors

Figure 10 compares (half)-load vs imposed vertical displacement curves obtained with the two stabilized mixed formulations: $\boldsymbol{u}/p$ and $\boldsymbol{\varepsilon}/\mathbf{u}$. As in the previous example, both mixed formulations capture well the limit load and the general softening trend of the curve, but the response obtained with the newly proposed formulation is more accurate and less dissipative.

5.3 Simply perforated thin-walled cylinder

The last example is a simply perforated thin-walled cylinder subjected to axial imposed straining. Dimensions of the cylinder are: height 30 m, outer radius 6 m, inner radius 5.8 m, thickness 0.2 m. The perforation is a square indentation of trace 0.4×0.4 m^2. Because of the double symmetry

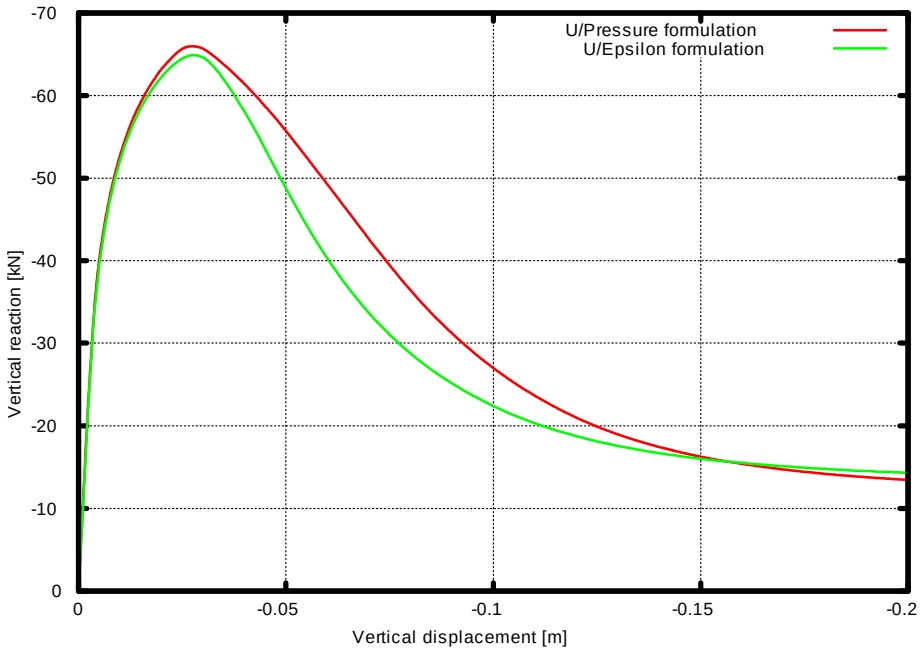

Figure 10: Force vs. displacement plot for circular rigid inclusion. Comparison between the $\mathbf{u}/p$ and the $\boldsymbol{\varepsilon}/\mathbf{u}$ formulations

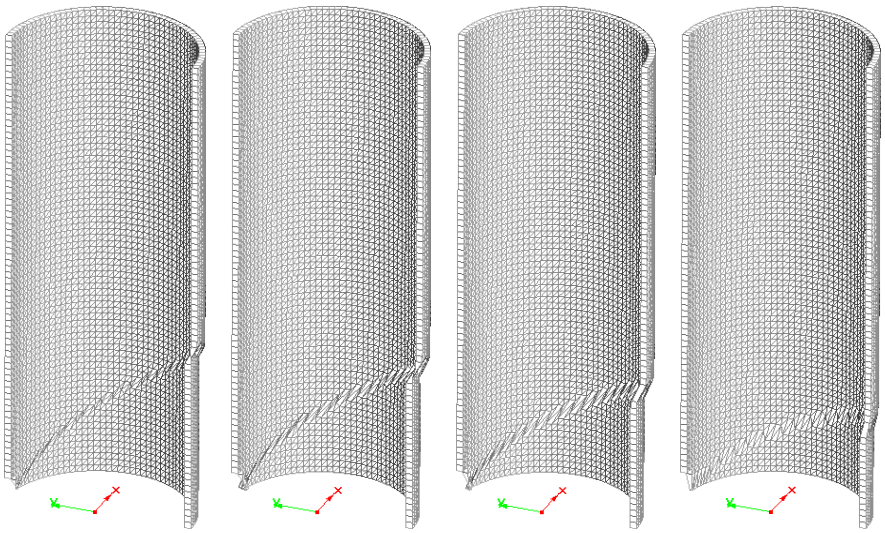

(a) (b) (c) (d)

Figure 11: Deformed (x 5) geometries for singly perforated thin-walled cylinder for different friction angles: (a) 0^o, (b) 15^o, (c) 30^o, (d) 45^o

of the domain and boundary conditions, only one quarter of the cylinder is discretized. A uniform upward vertical displacement is imposed at the top boundary. Because the cylinder is thin-walled and there is no restriction to deformation in the radial and hoop directions, the normal stresses in the radial and hoop directions are null, so that the cylinder is subjected to a state of uniaxial vertical stress. Therefore, the angles of the localized shear bands can be analytically obtained under plane stress conditions.

The computational domain is divided into a structured uniform mesh of 3,749 triangular prisms (7,750 nodes) with a mesh size of $h = 0.2$ m, half the size of the indentation and equal to the thickness of the cylinder.

Incompressible and compressible cases, with increasing friction angles $\phi = 0^o, 15^o, 30^o, 45^o$ are investigated using the stabilized mixed $\boldsymbol{\varepsilon}/\mathbf{u}$ formulation. The deformed shapes obtained are shown in Figure 11 (amplification factor 5). The failure mechanisms are correctly predicted in all cases, with X-shaped helicoidal shear bands forming at different orientations, independently of the marked alignment of the structured mesh, and without the use of any auxiliary tracking technique. It can be observed that, as in the first example, the angle that the shear band forms with the horizontal plane decreases as the angle of friction of the material increases.

Table 2 shows the comparison between the analytical localization angles computed for uniaxial tension in plane stress conditions and the ones obtained numerically. The analytical values are obtained with the procedure presented in reference [19]. Note that the localization angles are different in plane stress situations than under plane strain conditions. As in the first example, the agreement between the analytical and the numerical values is remarkable, and validates both the analytical and the numerical approaches.

This example provides a case to illustrate not only the quantitative, but the qualitative difference between the $\boldsymbol{u}/p$ and $\boldsymbol{\varepsilon}/\mathbf{u}$ formulation. Figure 12 shows the results obtained for the incompressible case ($\phi = 0^o$), with the $\boldsymbol{\varepsilon}/\mathbf{u}$ formulation. As can be noted, the computed failure mechanism is correct, as all plots, vertical displacement, equivalent plastic strain, pressure and principal strain vectors, corroborate. Figure 13 shows the results obtained with the $\boldsymbol{u}/p$ formulation. It can be appreciated that the solution obtained with this formulation is not realistic. Figure 13c shows that in this case the obtained plastic strain localizes in a layered pattern which is discontinuous from one horizontal layer of elements to the ones above or below. This spurious type of stepped localization is possible with the $\boldsymbol{u}/p$ discrete formulation, where the deviatoric strains are discontinuous, but cannot occur with the $\boldsymbol{\varepsilon}/\mathbf{u}$ discrete formulation, where all strains are continuous.

Figure 14 compares (half)-load vs (half)-imposed vertical displacement curves obtained with

Plane stress	**Analytical** [19]	**Numerical**
$\phi = 0^o$	$\theta_{loc} = 35.26^o$	$\theta_{loc} = 34.04^o$
$\phi = 15^o$	$\theta_{loc} = 31.55^o$	$\theta_{loc} = 31.20^o$
$\phi = 30^o$	$\theta_{loc} = 26.92^o$	$\theta_{loc} = 26.07^o$
$\phi = 45^o$	$\theta_{loc} = 19.47^o$	$\theta_{loc} = 20.44^o$

Table 2: Results for simply perforated thin-walled cylinder with the mixed $\boldsymbol{\varepsilon}/\mathbf{u}$ formulation. Comparison between the analytical localization angles for uniaxial tension in *plane stress* conditions and the ones obtained numerically

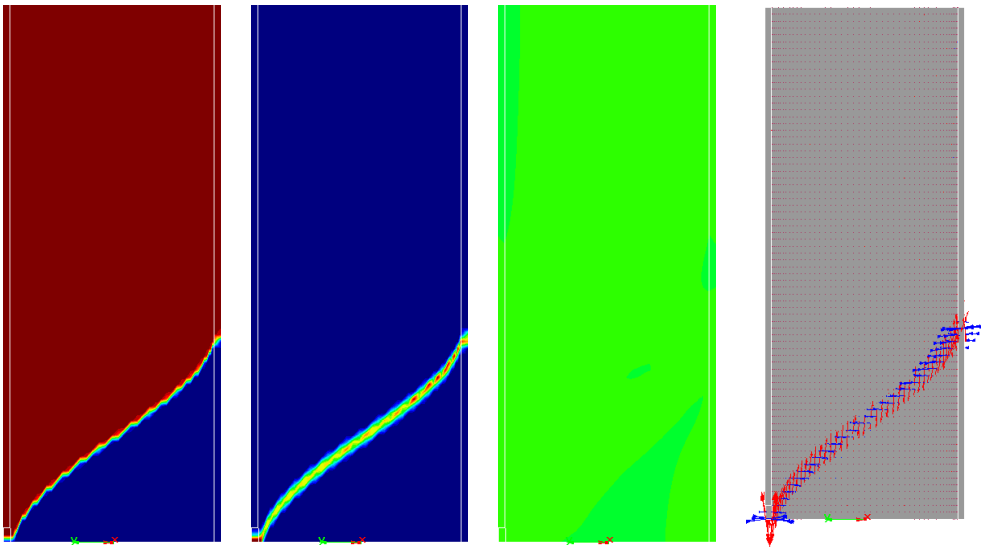

(a) (b) (c) (d)

Figure 12: Results for simply perforated thin-walled cylinder with the mixed $\boldsymbol{\varepsilon}/\mathbf{u}$ formulation. Contours for: (a) vertical displacement, (b) equivalent plastic strain, (c) pressure and (d) principal strain vectors

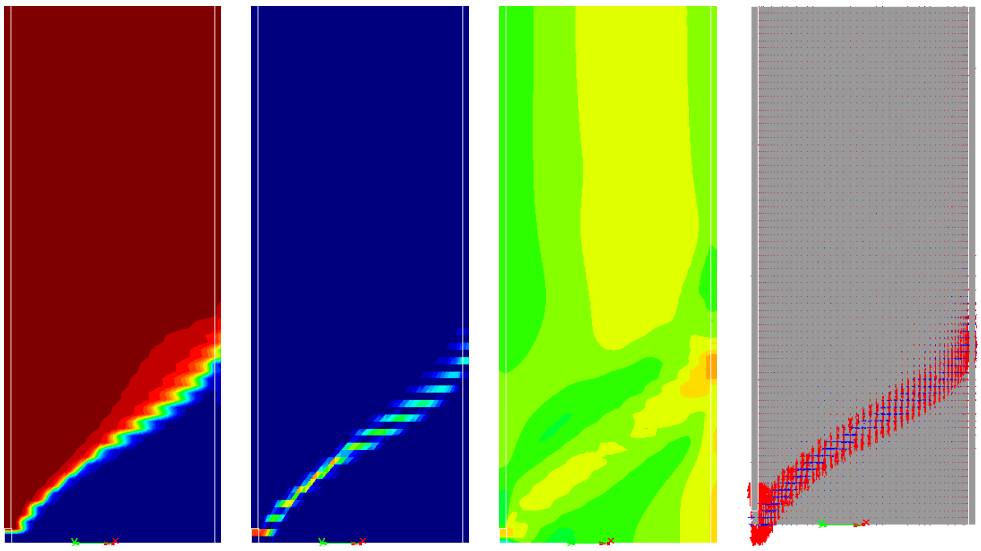

(a) (b) (c) (d)

Figure 13: Results for simply perforated thin-walled cylinder with the mixed $\mathbf{u}/p$ formulation. Contours for: (a) vertical displacement, (b) equivalent plastic strain, (c) pressure and (d) principal strain vectors

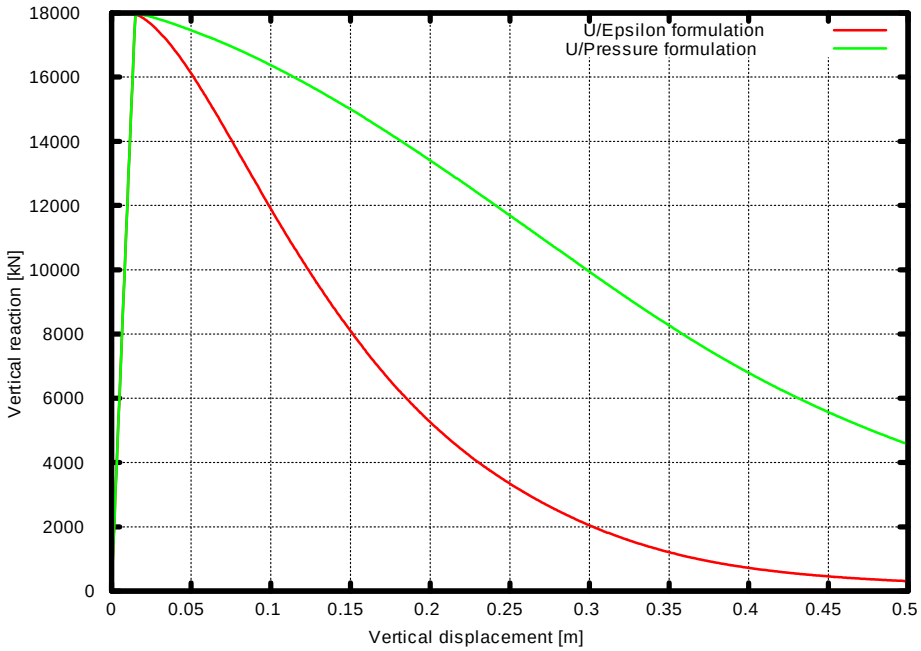

Figure 14: Force vs. displacement plot for simply perforated thin-walled cylinder. Comparison between the $\mathbf{u}/p$ and the $\boldsymbol{\varepsilon}/\mathbf{u}$ formulations

the two stabilized mixed formulations: $\boldsymbol{u}/p$ and $\boldsymbol{\varepsilon}/\mathbf{u}$. Here, the incorrect prediction of the failure mechanism when using the mixed $\boldsymbol{u}/p$ formulation shows in the over prediction of the dissipated energy spent during the failure process.

6 Conclusions

This paper presents the application of a stabilized mixed strain/displacement finite element formulation for the solution nonlinear solid mechanics problems involving compressible and incompressible plasticity. Such formulation presents two advantages when compared to the standard, displacement based, irreducible formulation: (a) it provides enhanced strain (and stress) rate of convergence and (b) it is able to deal with incompressible situations. The first advantage applies also to the mixed pressure/displacement formulation.

The variational multiscale stabilization introduced allows the use of equal order interpolations in a consistent way. Consequently, low order finite elements with continuous strain and displacement fields are used in conjunction with an associative frictional Drucker-Prager plastic model to model strain localization and failure. The derived model yields a general and robust scheme, suitable for engineering applications. Its application translates in the achievement of the goals:

1. the resulting discrete FE model is well posed and stable,

2. the formulation is able to tackle compressible and incompressible inelastic behavior, without indications of pressure oscillations in the latter case,

3. the formulation is able to tackle directional inelastic behavior, and

4. the results are convergent and not spuriously dependent of the finite element mesh used.

Benchmark numerical examples (using triangles in 2D and triangular prisms in 3D) show the substantial advantage of the mixed formulation over the irreducible and the mixed pressure/displacement one to predict correct failure mechanisms with localized patterns of strain, virtually free from any dependence of the mesh directional bias.

The proposed formulation has two salient features. On one side, it is of general application, in 2D and 3D problem, to structured and unstructured meshes and to simplicial or non simplicial elements. On the other side, no "ad hoc" auxiliary crack tracking technique is necessary.

Acknowledgments

Financial support from the EC 7th Framework Programme under the MuMoLaDe project - Multiscale Modelling of Landslides and Debris Flows - within the framework of Marie Curie ITN (Initial Training Networks) and the Spanish Ministry of Economy and Competitivity under the EACY project - Enhanced accuracy computational and experimental framework for strain localization and failure mechanisms- within the "Excellency" Programme for Knowledge Generation is gratefully acknowledged.

References

[1] Cervera, M., Chiumenti, M., Valverde, Q. and Agelet de Saracibar, C. (2003). Mixed Linear/linear Simplicial Elements for Incompressible Elasticity and Plasticity. Comp. Meth. in Appl. Mech. and Eng., 192, 5249-5263.

[2] Cervera, M., Chiumenti, M. and Agelet de Saracibar, C. (2004). Softening, localization and stabilization: capture of discontinuous solutions in J2 plasticity. Int. J. for Num. and Anal. Meth. in Geomechanics, 28, 373-393.

[3] Cervera, M., Chiumenti, M. and Agelet de Saracibar, C. (2004). Shear band localization via local J_2 continuum damage mechanics. Comp. Meth. in Appl. Mech. and Eng., 193, 849-880.

[4] Chiumenti, M., Valverde, Q., Agelet de Saracibar, C. and Cervera, M., (2004). A stabilized formulation for incompressible plasticity using linear triangles and tetrahedra, Int. J. of Plasticity, 20, 1487-1504.

[5] Agelet de Saracibar C., Chiumenti M., Valverde Q., and Cervera M. (2006). On the Orthogonal Subgrid Scale Pressure stabilization of Small and Finite deformation J2 Plasticity, Computer Methods in Applied Mechanics and Engineering, 195, 1224-1251.

[6] Cervera, M. and Chiumenti, M. (2009). Size effect and localization in J_2 plasticity, International Journal of Solids and Structures 46, 3301-3312.

[7] Cervera, M., Chiumenti, M. and Codina, R. (2010). Mixed stabilized finite element methods in nonlinear solid mechanics. Part I: Formulation, Comp. Meth. in Appl. Mech. and Eng., 199, 2559-2570.

[8] Cervera, M., Chiumenti, M. and Codina, R. (2010). Mixed stabilized finite element methods in nonlinear solid mechanics. Part II: Strain localization, Comp. Meth. in Appl. Mech. and Eng., 199, 2571-2589.

[9] Cervera, M., Chiumenti, M. and Codina, R. (2011). Mesh objective modelling of cracks using continuous linear strain and displacement interpolations, Int. J. for Numerical Methods in Eng., 87, 962-987.

[10] Codina, R. (2008). Analysis of a stabilized finite element approximation of the Oseen equations using orthogonal subscales, Applied Numerical Mathematics, 58, 264-283.

[11] Castillo, E. and Codina, R. (2014). Variational multi-scale stabilized formulations for the stationary three-field incompressible viscoelastic flow problem, Comp. Meth. in Appl. Mech. and Eng., in press.

[12] Ottosen, N. and Runesson, K. (1991). Properties of discontinuous bifurcation solutions in elasto-plasticity. Int. J. Solids and Structures 27(4), 401-421.

[13] Runesson, K., Ottosen, N.S., and Peric, D. (1991). Discontinuous bifurcations of elastic-plastic solutions at phase stress and plane strain. Int. J. of Plasticity 7, 99-121.

[14] Steinmann, P. and Willam, K. (1994). Finite element analysis of elastoplastic discontinuities. Journal of Engineering Mechanics 120, 2428-2442.

[15] Iordache, M. M. (1996). Failure analysis of classical and micropolar elastoplastic materials. report CU/SR-96/2. Department of Civil, Enviromental and Archetectural Engineering, University of Colorado.

[16] Iordache, M.M. and Willam, K. (1998). Localized failure analysis in elastoplastic Cosserat continua. Comp. Meth. Appl. Mech. Engrg. 151, 559-586.

[17] Oliver, J., Cervera, M. and Manzoli, O. (1998). On the use of strain-softening models for the simulation of strong discontinuities in solids. Material instabilities in solids, 107-123, Wiley.

[18] Oliver, J., Cervera, M. and Manzoli, O. (1999). Strong discontinuities and continuum plasticity models: the strong discontinuity approach. Int. J. of Plasticity, 15, 319-351.

[19] Cervera, M., Chiumenti, M., Di Capua, D. (2012). Benchmarking on bifurcation and localization in J2 plasticity for plane stress and plane strain conditions. Computer Methods in Applied Mechanics and Engineering, 241-244, 206-224.

[20] Brezzi, F. and Fortin, M. (1991) Mixed and Hybrid Finite Element Methods, Spinger.

[21] Hughes, T.J.R., Feijoó, G.R., Mazzei. L., Quincy, J.B. (1998) . The variational multiscale method-a paradigm for computational mechanics, Comp. Meth. in Appl. Mech. and Eng. 166, 3-28.

[22] Codina, R. (2000) . Stabilization of incompressibility and convection through orthogonal subscales in finite element methods, Comp. Meth. in Appl. Mech. and Eng. 190, 1579-1599.

[23] Codina, R. and Blasco, J. (1997) . A finite element method for the Stokes problem allowing equal velocity-pressure interpolations, Comp. Meth. in Appl. Mech. and Eng. 143, 373-391.

[24] Badia, S. and Codina, R. (2009) . Unified stabilized finite element formulations for the Stokes and the Darcy problems, SIAM Journal on Numerical Analysis 17, 309-330.

[25] Codina, R. (2002). Stabilized finite element approximation of transient incompressible flows using orthogonal subscales, Comp. Meth. in Appl. Mech. and Eng.191, 4295-4321.

[26] Simo, J.C. and Hughes, T.J.R. (1998). Computacional Inelasticity. Interdisciplinary Applied Mathematics. Vol. 7. Springer.

[27] Simo, J. C. and Taylor, R. L. (1985). Consistent tangent operators for rate-independent elastoplasticity, Comp. Meth. in Appl. Mech. and Eng. 48, 101-118.

[28] deBorst, R. (1987). Integration of plasticity equations for singular yield functions, Computers & Structures 26, 823 - 829.

[29] Crisfield, M. (1997). Non-linear Finite Element Analysis of Solids and Structures. II: Advanced topics. Wiley.

[30] Peric, D. and de Souza Neto, E. A. (1999). A new computational model for Tresca plasticity at finite strains with an optimal parametrization in the principal space, Comp. Meth. in Appl. Mech. and Eng. 171, 463 - 489.

[31] Cervera, M., Agelet de Saracibar, C. and Chiumenti, M. (2002). COMET: COupled MEchanical and Thermal analysis. Data Input Manual, Version 5.0, Technical report IT-308. Available from: <http://www.cimne.upc.es>.

[32] COMET: Coupled Mechanical and Thermal analysis (2013). <http://www.cimne.com/comet/>.

[33] GiD: The Personal Pre and Post Processor (2009). <http://www.gidhome.com>.

This page is left intentionally blank.

Stress-accurate mixed FEM for soil failure under shallow foundations involving strain localization in plasticity

L. Benedetti, M. Cervera and M. Chiumenti

Computers and Geotechnics,
Vol. 64, pp. 32-47, (2015)
http://dx.doi.org/10.1016/j.compgeo.2014.10.004

This page is left intentionally blank.

Stress-accurate Mixed FEM for soil failure under shallow foundations involving strain localization in plasticity

Lorenzo Benedetti, Miguel Cervera, Michele Chiumenti
International Center for Numerical Methods in Engineering (CIMNE),
Technical University of Catalonia (UPC), Edificio C1, Campus Norte,
Jordi Girona 1-3, 08034 Barcelona, Spain
Corresponding author: lbenedetti@cimne.upc.edu

Abstract

The development of slip lines, due to strain localization, is a common cause for failure of soil in many circumstances investigated in geotechnical engineering. Through the use of numerical methods -like finite elements- many practitioners are able to take into account complex geometrical and physical conditions in their analyses. However, when dealing with shear bands, standard finite elements display lack of precision, mesh dependency and locking. This paper introduces a (stabilized) mixed finite element formulation with continuous linear strain and displacement interpolations. Von Mises and Drucker-Prager local plasticity models with strain softening are considered as constitutive law. This innovative formulation succeeds in overcoming the limitations of the standard formulation and provides accurate results within the vicinity of the shear bands, specifically without suffering from mesh dependency. Finally, 2D and 3D numerical examples demonstrate the accuracy and robustness in the computation of localization bands, without the introduction of additional tracking techniques as usually required by other methods.

1 Introduction

The stability analysis of a slope, both in the small scale of a road embankment and in the larger one of a mountain slope, is a very frequent example of geotechnical engineering. The prevention of failure shear bands is a fundamental requirement to ensure the safety of a volume of soil. In the geotechnical practice, standard design procedures require the computation of a safety factor. This is usually done by comparing the value of the acting forces to the value of the resisting ones through simplified methods. The first recorded case of stability analysis was performed by S. Hultin and K. Pettersson in 1916 (documented only in 1955), for the Stigberg Quay in Gothenburg (Sweden), where the slip surface was taken to be circular and the sliding mass was divided into slices. In the same period, the first major result was the Bishop method, proposed by Prof. A. Bishop as an extension of the "*Swedish Slip Circle Method*" [1]. Although these methods are very useful as preliminary evaluation tool, the validity of the approach is strongly limited when simplified assumptions on soil mechanical constitutive law, geometry and slip lines shape are required a priori. The introduction of the Finite Elements Method represented a sound alternative to tackle detailed problems of geotechnical nature, thanks to their potential versatility and vast application. FEM makes possible the study of materials failure and its complex coupling with environmental actions such as seepage flow.

In the last three decades, the scientific community invested a considerable effort seeking a consistent description of failure modes through the use of numerical methods. A slip line is a physical discontinuity created by a localization of strains, as it is depicted in part *b* of Figure 1 reported from Cervera et al. [2]. From a mathematical stand point, the numerical discontinuity in the field variables can be treated in various ways. In the approach adopted in this work the strain localization is assumed to occur in a band of finite width where the displacements are continuous and the strains are discontinuous but bounded [3]. Actually, this is a regularization of the discontinuity over a finite length, as it is possible to see in part *a* of Figure 1.

It is well known that this kind of "smeared" approach poses some challenges. The standard irreducible formulation of FEM is known to be heavily affected by spurious mesh dependence when softening behavior occurs and, consequently, slip lines evolution is biased by the orientation of the mesh [4]. Moreover, in the case of isochoric behavior, unbounded pressure oscillations arise and the consequent locking of the stresses pollutes the numerical solution. Both problems can be shown not to be related to the mathematical statement of the continuous problem but instead to its discrete (FEM) counterpart [5, 6].

Mixed formulations in terms of both the pressure and the flow velocity are classical in the numerical solution of Darcy's equation [7, 8, 9, 10, 11, 12], where the focus is placed in achieving enhanced accuracy in the velocity. The mathematical structure of Darcy's and Cauchy's problems is analogous, with the pressure and velocity fields in the first one corresponding to the displacement and stress fields in the second one. Therefore, similar mixed methods can be applied to both problems.

In the last decade, the use of mixed finite elements for the description of failure mechanics has proved to be extremely useful. Initially, a stabilized displacement-pressure ($\boldsymbol{u}/p$) formulation was introduced to address the problem of incompressibility in elasto-plasticity [13]. Later, it was shown that a continuum isotropic damage constitutive law can be fitted in such formulation [14]. Recently, Badia and Codina [7], for the Stokes-Darcy problem, and then Cervera et al. [15], for the linear and nonlinear mechanical problem, discussed the local convergence properties of mixed formulations. From these, it follows that the reliability in the prediction of strain concentration bands depends directly on the capability of the method to converge to a meaningful solution. In nearly singular situations, such as when a slip line forms, the $\boldsymbol{u}/p$ formulation presents satisfactory global convergence in the interpolated variables, but it lacks of local convergence in the stress

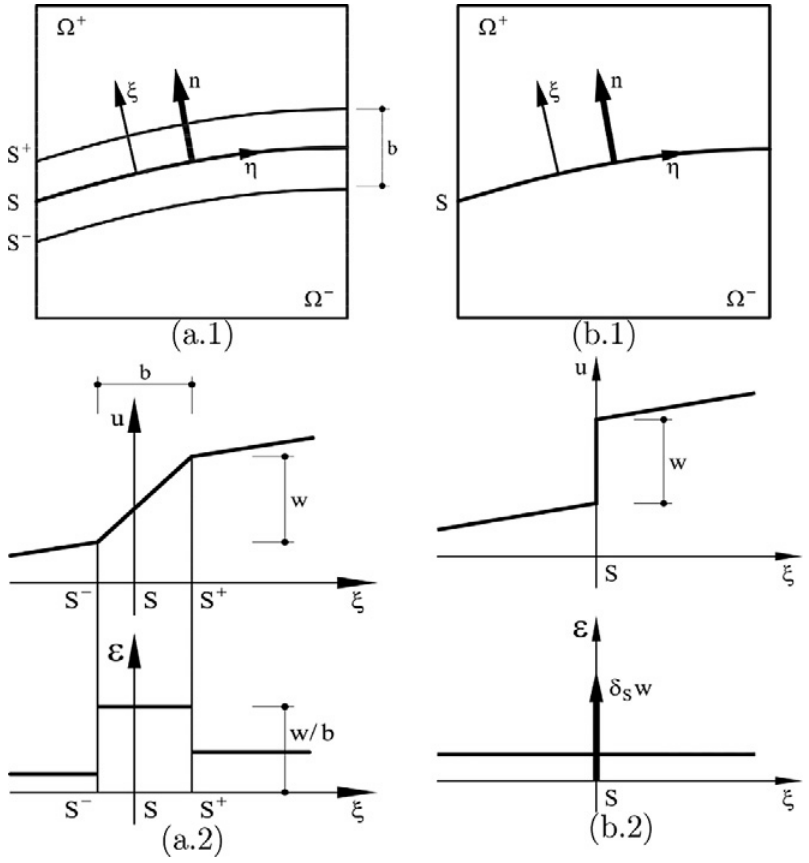

Figure 1: Localized failure: strong (right) and smeared (left) discontinuities

field, although a large number of tests showed a well behaved solution in many cases [16].

In order to achieve local convergence of stresses, and, in turn, objectivity of results with respect of the mesh alignment, a stabilized mixed strain-displacement ($\boldsymbol{\varepsilon}/\boldsymbol{u}$) formulation was developed by Cervera et al. [17, 18] and applied to problems involving softening isotropic damage materials. In these references, it is shown that the enhancement of accuracy attained by the use of mixed strain-displacement ($\boldsymbol{\varepsilon}/\boldsymbol{u}$) formulation overcomes the spurious mesh-bias dependency observed when using the standard irreducible FEM formulation.

In this work, the strain-displacement mixed formulation is extended for the purpose of solving problem involving compressible and incompressible plasticity. The effectiveness of the formulation, outperforming both the standard irreducible and the mixed displacement-pressure ($\boldsymbol{u}/p$) approaches, is demonstrated in examples involving failure and strain concentration bands.

The paper is organized as follows. First, the mixed finite element method is derived and the mathematical basis are presented. Then, the Drucker-Prager constitutive model is introduced as a pressure-dependent generalization of the incompressible Von Mises model. Finally, numerical examples are reported in order to demonstrate the robustness and the accuracy of the proposed mixed finite elements.

2 $\boldsymbol{\varepsilon} - \boldsymbol{u}$ mixed finite elements

2.1 Strong form

Consider a body occupying the space domain Ω, its boundary being $\partial\Omega$. The field of total strain has be compatible with the displacement field, so that

$$-\boldsymbol{\varepsilon} + \boldsymbol{\nabla}^s \boldsymbol{u} = \boldsymbol{0} \tag{1}$$

where $\boldsymbol{u}$ is the field of displacements and $\boldsymbol{\varepsilon}$ is the field of infinitesimal strains. The equilibrium of the body in a (quasi-)static mechanical problem is described by the following equation:

$$\boldsymbol{\nabla} \cdot \boldsymbol{\sigma} + \boldsymbol{f} = \boldsymbol{0} \tag{2}$$

where $\boldsymbol{\sigma}$ is the Cauchy stress tensor and $\boldsymbol{f}$ are the external forces applied to the body. The symbol $\boldsymbol{\nabla} \cdot (\cdot)$ refers to the divergence operator whereas $\boldsymbol{\nabla}^s(\cdot)$ is used to denote the symmetric gradient. In small strain plasticity the strain tensor is decomposed additively as

$$\boldsymbol{\varepsilon} = \boldsymbol{\varepsilon}_e + \boldsymbol{\varepsilon}_p \tag{3}$$

with $\boldsymbol{\varepsilon}_e$ the elastic strain tensor and $\boldsymbol{\varepsilon}_p$ the plastic strain tensor. The constitutive equation can be written as

$$\boldsymbol{\sigma} = \mathbb{C} : \boldsymbol{\varepsilon}_e = \mathbb{C} : (\boldsymbol{\varepsilon} - \boldsymbol{\varepsilon}_p) \tag{4}$$

where $\mathbb{C}$ is the fourth order elastic constitutive tensor. Now, substituting (4) in (2), the problem reads

$$\begin{aligned} -\boldsymbol{\varepsilon} + \boldsymbol{\nabla}^s \boldsymbol{u} &= \boldsymbol{0} \\ \boldsymbol{\nabla} \cdot [\mathbb{C} : (\boldsymbol{\varepsilon} - \boldsymbol{\varepsilon}_p)] + \boldsymbol{f} &= \boldsymbol{0} \end{aligned} \tag{5}$$

In order to obtain a symmetric system, the first equation is pre-multiplied by the elastic constitutive tensor $\mathbb{C}$:

$$\begin{aligned} -\mathbb{C} : \boldsymbol{\varepsilon} + \mathbb{C} : \boldsymbol{\nabla}^s \boldsymbol{u} &= \boldsymbol{0} \\ \boldsymbol{\nabla} \cdot [\mathbb{C} : (\boldsymbol{\varepsilon} - \boldsymbol{\varepsilon}_p)] + \boldsymbol{f} &= \boldsymbol{0} \end{aligned} \tag{6}$$

Hence, (6) is the final system of partial differential equations in strong form in terms of the total strains $\boldsymbol{\varepsilon}$ and displacements $\boldsymbol{u}$ for the mechanical problem involving plasticity. The mixed problem is solved for both unknown fields $[\boldsymbol{u}, \boldsymbol{\varepsilon}]$ introducing appropriate boundary conditions and evolution laws for the plastic strain field [19]. For the sake of shortness and recalling (4), it can be written:

$$\begin{aligned} -\mathbb{C} : \boldsymbol{\varepsilon} + \mathbb{C} : \boldsymbol{\nabla}^s \boldsymbol{u} &= \boldsymbol{0} \\ \boldsymbol{\nabla} \cdot \boldsymbol{\sigma} + \boldsymbol{f} &= \boldsymbol{0} \end{aligned} \tag{7}$$

2.2 Weak form

The weak form of the set of equations presented in (6) is:

$$\begin{aligned} -\int_\Omega \boldsymbol{\gamma} : \mathbb{C} : \boldsymbol{\varepsilon} + \int_\Omega \boldsymbol{\gamma} : \mathbb{C} : \boldsymbol{\nabla}^s \boldsymbol{u} = 0 \quad & \forall \boldsymbol{\gamma} \in \mathbb{G} \\ \int_\Omega \boldsymbol{v} : (\boldsymbol{\nabla} \cdot \boldsymbol{\sigma}) + \int_\Omega \boldsymbol{v} : \boldsymbol{f} = 0 \quad & \forall \boldsymbol{v} \in \mathbb{V} \end{aligned} \tag{8}$$

The functional space $\mathbb{V}$ represents the set of test functions $\boldsymbol{v}$ for the displacement field $\boldsymbol{u}$, whereas $\mathbb{G}$ is the set of test function tensors for the strain $\boldsymbol{\varepsilon}$. Integrating by parts the second equation, it can be written:

$$\begin{aligned} -\int_\Omega \boldsymbol{\gamma} : \mathbb{C} : \boldsymbol{\varepsilon} + \int_\Omega \boldsymbol{\gamma} : \mathbb{C} : \boldsymbol{\nabla}^s \boldsymbol{u} = 0 \quad & \forall \boldsymbol{\gamma} \in \mathbb{G} \\ \int_\Omega \boldsymbol{\nabla}^{\boldsymbol{s}} \boldsymbol{v} : \boldsymbol{\sigma} = F(\boldsymbol{v}) \qquad & \forall \boldsymbol{v} \in \mathbb{V} \end{aligned} \tag{9}$$

where the boundary terms accounting for stresses on the boundary and body forces f are collected in the term

$$F(\boldsymbol{v}) = \int_{\partial\Omega} \boldsymbol{v} : (\boldsymbol{\sigma} \cdot \hat{\boldsymbol{n}}) + \int_\Omega \boldsymbol{v} : \boldsymbol{f} \tag{10}$$

in which $\hat{\boldsymbol{n}}$ represents the outward normal vector with respect to the boundary $\partial\Omega$. From the mathematical requirements of the problem in (9), $\mathbb{V}$ will be in the space of square integrable functions $\boldsymbol{v}$ which are at least square integrable and have square integrable first derivative, whereas $\mathbb{G}$ will belong to the set of square integrable symmetric tensors $\boldsymbol{\gamma}$.

2.3 Discrete Galerkin formulation

The discretized version of the continuous weak form is obtained considering a finite set of interpolating functions for both the solution and the test function. For this reason the discrete functional spaces are a subset of their continuous version:

$$\mathbb{G}_h \subset \mathbb{G} \subseteq L^2(\Omega)^{dim \times dim} \text{ and } \mathbb{V}_h \subset \mathbb{V} \subseteq H^1(\Omega)^{dim} \tag{11}$$

where dim is the number of the dimensions of the domain of the problem. Now, the strain tensor $\boldsymbol{\varepsilon}$ and the displacement field $\boldsymbol{u}$ are approximated as

$$\begin{aligned} \boldsymbol{\varepsilon} \to \boldsymbol{\varepsilon}_h = \sum_{i=1}^{n_{pts}} \boldsymbol{\gamma}_h^{(i)} \boldsymbol{\varepsilon}_h^{(i)} \quad & \boldsymbol{\gamma}_h \in \mathbb{G}_h \\ \boldsymbol{u} \to \boldsymbol{u}_h = \sum_{i=1}^{n_{pts}} \boldsymbol{v}_h^{(i)} \boldsymbol{u}_h^{(i)} \quad & \boldsymbol{v}_h \in \mathbb{V}_h \end{aligned} \tag{12}$$

The system of equations (9), in its discrete form, reads

$$\begin{aligned} -\int_\Omega \boldsymbol{\gamma}_h : \mathbb{C} : \boldsymbol{\varepsilon}_h + \int_\Omega \boldsymbol{\gamma}_h : \mathbb{C} : \boldsymbol{\nabla}^s \boldsymbol{u}_h = 0 \quad & \forall \boldsymbol{\gamma}_h \in \mathbb{G}_h \\ \int_\Omega \boldsymbol{\nabla}^s \boldsymbol{v}_h : \boldsymbol{\sigma} = F(\boldsymbol{v}_h) \quad & \forall \boldsymbol{v}_h \in \mathbb{V}_h \end{aligned} \tag{13}$$

In the following, we will introduce equal interpolation finite element spaces for displacements and strains. Particularly interesting will be the case of linear and bilinear interpolations, i.e. P1P1 and Q1Q1 elements. However, it is well known that the stability of a discrete mixed formulation depends from the choice of the finite element spaces $\mathbb{G}_h$ and $\mathbb{V}_h$ as stated by the *Inf-Sup condition* [20]. Using equal order of interpolation does not satisfy the previous condition; consequently, a Variational Multiscale Stabilization procedure is now introduced.

2.4 Variational Multiscale Stabilization

The Variational Multiscale Stabilization was developed in first instance by Hughes et al. [21] and then generalized by Codina [22]. This technique modifies appropriately the variational form of the problem in order to provide the required numerical stability. The corresponding modified *Inf-Sup condition* is milder than the original one and it holds for most common equal order finite element spaces [23].

The stabilization procedure supposes that the solution of variables $(\boldsymbol{\varepsilon}, u)$ is given by a resolvable scale $(\boldsymbol{\varepsilon}_h, \boldsymbol{u}_h)$, calculated on the FEM mesh, and an irresolvable one $(\tilde{\boldsymbol{\varepsilon}}, \tilde{\boldsymbol{u}})$, called subscale solution:

$$\begin{aligned} \boldsymbol{\varepsilon} &= \boldsymbol{\varepsilon}_h + \tilde{\boldsymbol{\varepsilon}} \\ \boldsymbol{u} &= \boldsymbol{u}_h + \tilde{\boldsymbol{u}} \end{aligned} \tag{14}$$

The subscale variables and their test functions pertain to their respective functional spaces $\tilde{\mathbb{G}}$ for the strain subscale and $\tilde{\mathbb{V}}$ for the displacement subscale. This initial hypothesis allows us to consider extended solution spaces given by $\mathbb{G} \approx \mathbb{G}_h \oplus \tilde{\mathbb{G}}$ and $\mathbb{V} \approx \mathbb{V}_h \oplus \tilde{\mathbb{V}}$. The subscale part $(\tilde{\boldsymbol{\varepsilon}}, \tilde{\boldsymbol{u}})$ can be thought as a high frequency solution that cannot be captured with the coarse FEM mesh.

The plastic strains $\boldsymbol{\varepsilon}_p$ are computed by the return mapping algorithm, given the stress tensor $\boldsymbol{\sigma} = \mathbb{C} : (\boldsymbol{\varepsilon} - \boldsymbol{\varepsilon}_p)$ as input data. Since the total strain field $\boldsymbol{\varepsilon}$ has both coarse and subscale contribution, then also the plastic strain tensor $\boldsymbol{\varepsilon}_p$ could present a corresponding subscale part. However, since the subscale contribution is assumed to be small, the plastic strain will be approximated as:

$$\boldsymbol{\varepsilon}_p = \boldsymbol{\varepsilon}_p(\boldsymbol{\sigma}) \approx \boldsymbol{\varepsilon}_p(\boldsymbol{\sigma}_h) \tag{15}$$

with

$$\boldsymbol{\sigma}_h = \mathbb{C} : [\boldsymbol{\varepsilon}_h - \boldsymbol{\varepsilon}_p(\boldsymbol{\sigma}_h)] \tag{16}$$

Within this enhanced functional setting, the set of equations can be written as:

$$\begin{aligned} -\int_\Omega \boldsymbol{\gamma}_h : \mathbb{C} : (\boldsymbol{\varepsilon}_h + \tilde{\boldsymbol{\varepsilon}}) + \int_\Omega \boldsymbol{\gamma}_h : \mathbb{C} : \boldsymbol{\nabla}^s (\boldsymbol{u}_h + \tilde{\boldsymbol{u}}) &= 0 \qquad \forall \boldsymbol{\gamma}_h \in \mathbb{G}_h \\ \int_\Omega \boldsymbol{\nabla}^s \boldsymbol{v}_h : [\mathbb{C} : (\boldsymbol{\varepsilon}_h + \tilde{\boldsymbol{\varepsilon}} - \boldsymbol{\varepsilon}_p)] &= F(\boldsymbol{v}_h) \quad \forall \boldsymbol{v_h} \in \mathbb{V}_h \\ -\int_\Omega \tilde{\boldsymbol{\gamma}} : \mathbb{C} : (\boldsymbol{\varepsilon}_h + \tilde{\boldsymbol{\varepsilon}}) + \int_\Omega \tilde{\boldsymbol{\gamma}} : \mathbb{C} : \boldsymbol{\nabla}^s (\boldsymbol{u}_h + \tilde{\boldsymbol{u}}) &= 0 \qquad \forall \tilde{\boldsymbol{\gamma}} \in \tilde{\mathbb{G}} \\ \int_\Omega \tilde{\boldsymbol{v}} : (\boldsymbol{\nabla} \cdot [\mathbb{C} : (\boldsymbol{\varepsilon}_h + \tilde{\boldsymbol{\varepsilon}} - \boldsymbol{\varepsilon}_p)]) + \int_\Omega \tilde{\boldsymbol{v}} : \boldsymbol{f} &= 0 \qquad \forall \tilde{\boldsymbol{v}} \in \tilde{\mathbb{V}} \end{aligned} \tag{17}$$

Rewriting the second group of equations, tested against the subscale test functions, and assuming that the subscale $(\tilde{\boldsymbol{\varepsilon}}, \tilde{\boldsymbol{u}})$ vanishes on the boundary, it follows

$$\begin{aligned} -\int_\Omega \tilde{\boldsymbol{\gamma}} : \mathbb{C} : \tilde{\boldsymbol{\varepsilon}} + \int_\Omega \tilde{\boldsymbol{\gamma}} : \mathbb{C} : \boldsymbol{\nabla}^s \tilde{\boldsymbol{u}} &= \int_\Omega \tilde{\boldsymbol{\gamma}} : \mathbb{C} : [\boldsymbol{\varepsilon}_h - \boldsymbol{\nabla}^s \boldsymbol{u}_h] \quad \tilde{\boldsymbol{\gamma}} \in \tilde{\mathbb{G}} \\ \int_\Omega \boldsymbol{\nabla}^s \tilde{\boldsymbol{v}} : \mathbb{C} : \tilde{\boldsymbol{\varepsilon}} &= -\int_\Omega \tilde{\boldsymbol{v}} : [\boldsymbol{\nabla} \cdot \boldsymbol{\sigma}_h + \boldsymbol{f}] \quad \tilde{\boldsymbol{v}} \in \tilde{\mathbb{V}} \end{aligned} \tag{18}$$

The last system of equations shows that the solution of the subscale variables depends on the residuals of the strong form of the equations upon substitution of the FEM solution. Defining $\boldsymbol{R}_{1,h}$ and $\boldsymbol{R}_{2,h}$ as the residuals of the equations defined as:

$$\begin{aligned} \boldsymbol{R}_{1,h} &= -\mathbb{C} : \boldsymbol{\varepsilon}_h + \mathbb{C} : \boldsymbol{\nabla}^s \boldsymbol{u}_h \\ \boldsymbol{R}_{2,h} &= \boldsymbol{\nabla} \cdot \boldsymbol{\sigma}_h + \boldsymbol{f} \end{aligned} \tag{19}$$

equations (18) represent the projection of the residuals on the subscale grid. They can be rewritten as:

$$\begin{aligned}\tilde{P}_1\left(-\mathbb{C}:\tilde{\boldsymbol{\varepsilon}}+\mathbb{C}:\boldsymbol{\nabla}^s\tilde{\boldsymbol{u}}\right)&=\tilde{P}_1\left(\mathbb{C}:\boldsymbol{\varepsilon}_h-\mathbb{C}:\boldsymbol{\nabla}^s\boldsymbol{u}_h\right)=-\tilde{P}_1\left(\boldsymbol{R}_{1,h}\right)\\ \tilde{P}_2\left(\boldsymbol{\nabla}^s\tilde{\boldsymbol{v}}:\mathbb{C}:\tilde{\boldsymbol{\varepsilon}}\right)&=-\tilde{P}_2\left(\boldsymbol{\nabla}\cdot\boldsymbol{\sigma}_h+\boldsymbol{f}\right)=-\tilde{P}_2\left(\boldsymbol{R}_{2,h}\right)\end{aligned}\tag{20}$$

Following the work of Codina [22], it is possible to approximate the subscale variables within each element as:

$$\begin{aligned}\tilde{\boldsymbol{\varepsilon}}&=\tau_{\boldsymbol{\varepsilon}}\,\mathbb{C}^{-1}:\tilde{P}_1\left(\boldsymbol{R}_{1,h}\right)\\ \tilde{\boldsymbol{u}}&=\tau_u\,\tilde{P}_2\left(\boldsymbol{R}_{2,h}\right)\end{aligned}\tag{21}$$

where τ_u and $\tau_{\boldsymbol{\varepsilon}}$ are the stabilization parameters that, for this problem, will be computed as:

$$\tau_u=c_u\frac{hL_0}{\mu}\quad\text{and}\quad\tau_{\boldsymbol{\varepsilon}}=c_{\boldsymbol{\varepsilon}}\frac{h}{L_0}\tag{22}$$

In the last expression, c_u and $c_{\boldsymbol{\varepsilon}}$ are arbitrary positive numbers; μ is a mechanical parameter of the problem, usually chosen as twice the shear modulus of the material G; h is the representative size of the finite element mesh and L_0 is a characteristic length of the problem. To complete the stabilization method, an appropriate projection operator has to be selected in order to be able to compute the subscale variables.

2.4.1 ASGS

In the Algebraic Subgrid Scale Stabilization method [7], the projection operator is taken as the identity, that is:

$$\tilde{P}=I\quad\Rightarrow\quad\begin{aligned}\tilde{\boldsymbol{\varepsilon}}&=\tau_{\boldsymbol{\varepsilon}}\left(-\boldsymbol{\varepsilon}_h+\boldsymbol{\nabla}^s\boldsymbol{u}_h\right)\\ \tilde{\boldsymbol{u}}&=\tau_u\left(\boldsymbol{\nabla}\cdot\boldsymbol{\sigma}_h+\boldsymbol{f}\right)\end{aligned}\tag{23}$$

Back-substituting in the system of equations tested against the finite element functions and rearranging:

$$\begin{aligned}&-\left(1-\tau_{\boldsymbol{\varepsilon}}\right)\int_\Omega\boldsymbol{\gamma}_h:\mathbb{C}:\boldsymbol{\varepsilon}_h+\left(1-\tau_{\boldsymbol{\varepsilon}}\right)\int_\Omega\boldsymbol{\gamma}_h:\mathbb{C}:\boldsymbol{\nabla}^s\boldsymbol{u}_h\\ &\qquad+\tau_u\int_\Omega\boldsymbol{\gamma}_h:\mathbb{C}:\boldsymbol{\nabla}^s\left(\boldsymbol{\nabla}\cdot\boldsymbol{\sigma}_h+\boldsymbol{f}\right)=0\quad\forall\boldsymbol{\gamma}_h\in\mathbb{G}_h\\ &\int_\Omega\boldsymbol{\nabla}^s\boldsymbol{v}_h:\left[\mathbb{C}:\left(\left(1-\tau_{\boldsymbol{\varepsilon}}\right)\boldsymbol{\varepsilon}_h+\tau_{\boldsymbol{\varepsilon}}\boldsymbol{\nabla}^s\boldsymbol{u}_h-\boldsymbol{\varepsilon}_p\right)\right]=F(\boldsymbol{v}_h)\quad\forall\boldsymbol{v}_h\in\mathbb{V}_h\end{aligned}\tag{24}$$

Now, integrating again by parts in the first equation and taking $\boldsymbol{\gamma}_h=0$ on $\partial\Omega$, the final system of equations reads:

$$\begin{aligned}&-\left(1-\tau_{\boldsymbol{\varepsilon}}\right)\int_\Omega\boldsymbol{\gamma}_h:\mathbb{C}:\left(\boldsymbol{\varepsilon}_h-\boldsymbol{\nabla}^s\boldsymbol{u}_h\right)\\ &\qquad-\tau_u\int_\Omega\left[\boldsymbol{\nabla}\cdot\left(\mathbb{C}:\boldsymbol{\gamma}_h\right)\right]\cdot\left[\boldsymbol{\nabla}\cdot\boldsymbol{\sigma}_h+f\right]=0\quad\forall\boldsymbol{\gamma}_h\in\mathbb{G}_h\\ &\int_\Omega\boldsymbol{\nabla}^s\boldsymbol{v}_h:\mathbb{C}:\left[\left(1-\tau_{\boldsymbol{\varepsilon}}\right)\boldsymbol{\varepsilon}_h+\tau_{\boldsymbol{\varepsilon}}\boldsymbol{\nabla}^s\boldsymbol{u}_h-\boldsymbol{\varepsilon}_p\right]=F(v_h)\quad\forall v_h\in\mathbb{V}_h\end{aligned}\tag{25}$$

The first term in the first equation represents a projection (smoothing) of the strain field obtained by differentiation of the discrete displacement field. The second additional

term is given by the displacement subscale that, in turn, depends on the residual of the strong form of the equilibrium equation. The second equation is related to the balance of momentum. Defining the stabilized total strain field as:

$$\boldsymbol{\varepsilon}_{stab} = (1 - \tau_{\boldsymbol{\varepsilon}})\, \boldsymbol{\varepsilon}_h + \tau_{\boldsymbol{\varepsilon}} \boldsymbol{\nabla}^s \boldsymbol{u}_h \tag{26}$$

the system of equations (25) reads:

$$\begin{aligned} &-(1 - \tau_{\boldsymbol{\varepsilon}}) \int_\Omega \boldsymbol{\gamma}_h : \mathbb{C} : (\boldsymbol{\varepsilon}_h - \boldsymbol{\nabla}^s \boldsymbol{u}_h) \\ &\qquad -\tau_u \int_\Omega [\boldsymbol{\nabla} \cdot (\mathbb{C} : \boldsymbol{\gamma}_h)] \cdot [\boldsymbol{\nabla} \cdot \boldsymbol{\sigma}_h + \boldsymbol{f}] = \boldsymbol{0} \quad \forall \boldsymbol{\gamma}_h \in \mathbb{G}_h \\ &\int_\Omega \boldsymbol{\nabla}^s \boldsymbol{v}_h : \mathbb{C} : (\boldsymbol{\varepsilon}_{stab} - \boldsymbol{\varepsilon}_p) = F(\boldsymbol{v}_h) \quad \forall \boldsymbol{v}_h \in \mathbb{V}_h \end{aligned} \tag{27}$$

2.4.2 OSGS

In the Orthogonal Subgrid Scale Stabilization [7], the projection operator selected to solve the unresolvable scale variables is the orthogonal projector

$$\tilde{P}_h^{\perp}(\boldsymbol{X}) = I(\boldsymbol{X}) - P_h(\boldsymbol{X}) \tag{28}$$

where P_h represents the projection over the finite element mesh. It represents the L^2 projection of $\boldsymbol{X}$, or *least square fitting*, on the finite element space [13]. It is performed taking advantage of the orthogonality condition

$$\int_\Omega (\boldsymbol{X}_\Pi - \boldsymbol{X}) : \eta_h = 0 \quad \forall \eta_h \in \mathbb{V}_h \text{ or } \mathbb{G}_h \tag{29}$$

where $\boldsymbol{X}_\Pi$ is the projected value of $\boldsymbol{X}$ on the mesh nodes. Substituting in (21), the subscale variables $\tilde{\boldsymbol{u}}$ and $\tilde{\boldsymbol{\varepsilon}}$ can be approximated as:

$$\begin{aligned} \tilde{\boldsymbol{\varepsilon}} &= \tau_{\boldsymbol{\varepsilon}}\, \mathbb{C}^{-1} : [\boldsymbol{R}_{1,h} - P_h(\boldsymbol{R}_{1,h})] \\ \tilde{\boldsymbol{u}} &= \tau_u\, [\boldsymbol{R}_{2,h} - P_h(\boldsymbol{R}_{2,h})] \end{aligned} \tag{30}$$

with the residuals $\boldsymbol{R}_{1,h}, \boldsymbol{R}_{2,h}$ defined in (19). First of all, as $P_h(\boldsymbol{\varepsilon}_h) = \boldsymbol{\varepsilon}_h$, the strain subscale is given by

$$\tilde{\boldsymbol{\varepsilon}} = \tau_{\boldsymbol{\varepsilon}} [(-\boldsymbol{\varepsilon}_h + \boldsymbol{\nabla}^s \boldsymbol{u}_h) - P_h(-\boldsymbol{\varepsilon}_h + \boldsymbol{\nabla}^s \boldsymbol{u}_h)] = \tau_{\boldsymbol{\varepsilon}} [\boldsymbol{\nabla}^s \boldsymbol{u}_h - P_h(\boldsymbol{\nabla}^s \boldsymbol{u}_h)] \tag{31}$$

Now, comparing the equations (13) and (29), the following substitution is done:

$$\int_\Omega \boldsymbol{\gamma}_h : \mathbb{C} : P_h(\boldsymbol{\nabla}^s \boldsymbol{u}_h) = \int_\Omega \boldsymbol{\gamma}_h : \mathbb{C} : \boldsymbol{\varepsilon}_h \tag{32}$$

For the displacement subscale, assuming that $P_h(\boldsymbol{f}) = \boldsymbol{f}$, it can be written:

$$\tilde{\boldsymbol{u}} = \tau_u [\boldsymbol{\nabla} \cdot \boldsymbol{\sigma}_h - P_h(\boldsymbol{\nabla} \cdot \boldsymbol{\sigma}_h)] \tag{33}$$

Back-substituting in the set of equations of the problem, it reads:

$$\begin{aligned} &-(1 - \tau_{\boldsymbol{\varepsilon}}) \int_\Omega \boldsymbol{\gamma}_h : \mathbb{C} : (\boldsymbol{\varepsilon}_h - \boldsymbol{\nabla}^s \boldsymbol{u}_h) + \\ &\qquad +\tau_u \int_\Omega \boldsymbol{\gamma}_h : \mathbb{C} : \nabla^s [\boldsymbol{\nabla} \cdot \boldsymbol{\sigma}_h - P_h(\boldsymbol{\nabla} \cdot \boldsymbol{\sigma}_h)] = \boldsymbol{0} \quad \forall \boldsymbol{\gamma}_h \in \mathbb{G}_h \\ &\int_\Omega \boldsymbol{\nabla}^s \boldsymbol{v}_h : \mathbb{C} : [(1 - \tau_{\boldsymbol{\varepsilon}})\, \boldsymbol{\varepsilon}_h + \tau_{\boldsymbol{\varepsilon}} \boldsymbol{\nabla}^s \boldsymbol{u}_h - \boldsymbol{\varepsilon}_p] = F(\boldsymbol{v}_h) \quad \forall \boldsymbol{v}_h \in \mathbb{V}_h \end{aligned} \tag{34}$$

Integrating by parts the second equation and rearranging, the final set of equations is:

$$\begin{aligned} -(1-\tau_{\boldsymbol{\varepsilon}}) \int_\Omega \boldsymbol{\gamma}_h : \mathbb{C} : (\boldsymbol{\varepsilon}_h - \boldsymbol{\nabla}^s \boldsymbol{u}_h) + \\ -\tau_u \int_\Omega [\boldsymbol{\nabla} \cdot (\mathbb{C} : \boldsymbol{\gamma}_h)] \cdot [\boldsymbol{\nabla} \cdot \boldsymbol{\sigma}_h - P_h (\boldsymbol{\nabla} \cdot \boldsymbol{\sigma}_h)] = \mathbf{0} \quad \forall \boldsymbol{\gamma}_h \in \mathbb{G}_h \\ \int_\Omega \boldsymbol{\nabla}^s \boldsymbol{v}_h : \mathbb{C} : (\boldsymbol{\varepsilon}_{stab} - \boldsymbol{\varepsilon}_p) = F(\boldsymbol{v}_h) \quad \forall \boldsymbol{v}_h \in \mathbb{V}_h \end{aligned} \tag{35}$$

The set of equations with OSGS stabilization resembles the one for the ASGS, except for the second term in the first equation. In order to compute the projection of stresses at each time step, we can recall expression (29), and write

$$\int_\Omega (\boldsymbol{\Pi}_{\boldsymbol{\sigma}} - \boldsymbol{\nabla} \cdot \boldsymbol{\sigma}_h) : \boldsymbol{\eta}_h = 0 \quad \forall \boldsymbol{\eta}_h \in \mathbb{G}_h \tag{36}$$

and, with the additional projection equation, it reads:

$$\begin{aligned} -(1-\tau_{\boldsymbol{\varepsilon}}) \int_\Omega \boldsymbol{\gamma}_h : \mathbb{C} : (\boldsymbol{\varepsilon}_h - \boldsymbol{\nabla}^s \boldsymbol{u}_h) \\ -\tau_u \int_\Omega [\boldsymbol{\nabla} \cdot (\mathbb{C} : \boldsymbol{\gamma}_h)] \cdot [\boldsymbol{\nabla} \cdot \boldsymbol{\sigma}_h - \boldsymbol{\Pi}_{\boldsymbol{\sigma}}] = \mathbf{0} \quad \forall \boldsymbol{\gamma}_h \in \mathbb{G}_h \\ \int_\Omega \boldsymbol{\nabla}^s \boldsymbol{v}_h : \mathbb{C} : [\boldsymbol{\varepsilon}_{stab} - \boldsymbol{\varepsilon}_p] = F(\boldsymbol{v}_h) \quad \forall \boldsymbol{v}_h \in \mathbb{V}_h \\ \int_\Omega (\boldsymbol{\Pi}_{\boldsymbol{\sigma}} - \boldsymbol{\nabla} \cdot \boldsymbol{\sigma}_h) : \boldsymbol{\eta}_h = 0 \quad \forall \boldsymbol{\eta}_h \in \mathbb{G}_h \end{aligned} \tag{37}$$

The OSGS scheme is less diffusive than the ASGS scheme [24]. However, this comes at the price of solving an additional equation: in the implementation details it is shown how this problem can be circumvented.

3 Implementation details

In the presented formulation, the presence of the non-linear plastic strains $\boldsymbol{\varepsilon}_p = \boldsymbol{\varepsilon}_p(\sigma)$ requires an iterative procedure to deal with the nonlinearity of the system. Iterative solution schemes, such as Picard or Newton-Raphson methods, need to be introduced. Constitutive laws involving plasticity are usually written in terms of rate equations and, consequently, the matrices involved in the resulting algebraic set of equations are tangent. Hence, the use of the Newton-Raphson scheme will be considered in the following.

Consider the nonlinear multidimensional-multivariable problem

$$\boldsymbol{F}(\boldsymbol{X}) = 0 \tag{38}$$

where $\boldsymbol{X} = [\boldsymbol{\varepsilon}, \boldsymbol{u}]^T$ is the unknown vector. Such problem can be solved starting from a Taylor approximation around the solution point at iteration $i+1$ in a particular time step $n+1$:

$$\boldsymbol{F}_{n+1}^{i+1} \approx \boldsymbol{F}_{n+1}^{i} + \boldsymbol{J}_{n+1}^{i} \, \delta \boldsymbol{X}^{i+1} \tag{39}$$

where the Jacobian matrix $\boldsymbol{J}$ is defined as

$$\boldsymbol{J} = \frac{\partial \boldsymbol{F}}{\partial \boldsymbol{X}} \tag{40}$$

Assuming that $\boldsymbol{F}_{n+1}^{i+1} = 0$, an iterative correction is computed as

$$\delta \boldsymbol{X}^{i+1} = - \left[\boldsymbol{J}_{n+1}^{i} \right]^{-1} \boldsymbol{F}_{n+1}^{i} \tag{41}$$

and the solution vector is updated as

$$\boldsymbol{X}^{i+1} = \boldsymbol{X}^{i} + \delta \boldsymbol{X}^{i+1} \tag{42}$$

The Jacobian matrix can be found by differentiating the set of equation with respect to the unknowns variables $\boldsymbol{X} = [\boldsymbol{\varepsilon}, \boldsymbol{u}]^T$ at iteration i. The advantage of such method is a quadratic convergence rate in the iteration at each time step.

3.1 ASGS implementation

In the case of the ASGS scheme, differentiating the system of equations at iteration i of time step $n+1$, the Jacobian matrix presents the mathematical structure:

$$\boldsymbol{J}_{n+1}^{i} = \left[\begin{array}{cc} \boldsymbol{M}_{\tau} & \boldsymbol{G}_{\tau} \\ \boldsymbol{D}_{\tau} & \boldsymbol{K}_{\tau} \end{array} \right]_{n+1}^{i} \tag{43}$$

where $\boldsymbol{M}$ is a mass-like projection matrix, $\boldsymbol{G}$ is a gradient matrix, $\boldsymbol{D}$ is a divergence matrix and $\boldsymbol{K}$ is the stiffness matrix. The subscript τ refers to the fact that those matrices incorporate stabilization terms. Differentiating (25), within the hypothesis introduced in equation (15) that the plastic strain depends only on $\boldsymbol{\varepsilon}_h$, the previous matrices read:

$$\boldsymbol{M}_{\tau} = - \left(1 - \tau_{\boldsymbol{\varepsilon}}\right) \int_{\Omega} \boldsymbol{N}_{\boldsymbol{\varepsilon}}{}^{T} \mathbb{C} \, \boldsymbol{N}_{\boldsymbol{\varepsilon}} - \tau_u \int_{\Omega} \mathbb{C} \, \boldsymbol{B} \boldsymbol{B}^{T} \, \mathbb{C}_{ep}^{n+1} \tag{44}$$

$$\boldsymbol{G}_{\tau} = \left(1 - \tau_{\boldsymbol{\varepsilon}}\right) \int_{\Omega} \boldsymbol{N}_{\boldsymbol{\varepsilon}}{}^{T} \mathbb{C} \, \boldsymbol{B} \tag{45}$$

$$\boldsymbol{D}_{\tau} = \int_{\Omega} \boldsymbol{B}^{T} \left[\mathbb{C}_{ep}^{n+1} - \tau_{\boldsymbol{\varepsilon}} \mathbb{C} \right] \boldsymbol{N}_{\boldsymbol{u}} \tag{46}$$

$$\boldsymbol{K}_{\tau} = \tau_{\boldsymbol{\varepsilon}} \int_{\Omega} \boldsymbol{B}^{T} \mathbb{C} \, \boldsymbol{B} \tag{47}$$

where $\boldsymbol{N}_{\boldsymbol{\varepsilon}}$ and $\boldsymbol{N}_{\boldsymbol{u}}$ are the matrices of shape functions of the respective strain and displacement fields and $\boldsymbol{B}$ is the matrix of the gradient of those shape functions. The resulting algebraic system of equations is, in general, not symmetric. Note that disregarding the terms due to plasticity, the system matrix is symmetric and it coincides with the one presented in Cervera et al. [17, 18]. Details on the differentiation of the plastic strain tensor $\boldsymbol{\varepsilon}_p$ with respect to the problem unknown $\boldsymbol{\varepsilon}_h$ are given in the Appendix A.

3.2 OSS implementation

The OSS implementation is identical to the ASGS implementation, except for the additional projection of the nodal stresses. The projection equation gives some additional terms in the Jacobian matrix when differentiating (37):

$$- \left[\begin{array}{ccc} \boldsymbol{M}_{\tau} & \boldsymbol{G}_{\tau} & \boldsymbol{D}_{\Pi}^{T} \\ \boldsymbol{D}_{\tau} & \boldsymbol{K}_{\tau} & \boldsymbol{0} \\ \boldsymbol{D}_{\Pi} & \boldsymbol{0} & \boldsymbol{M}_{\Pi} \end{array} \right]_{n+1}^{i} \left[\begin{array}{c} \delta \boldsymbol{\varepsilon}_h \\ \delta \boldsymbol{u}_h \\ \delta \boldsymbol{\Pi}_h \end{array} \right]_{n+1}^{i+1} = \left[\begin{array}{c} R_{1,h} \\ R_{2,h} \\ R_{3,h} \end{array} \right]_{n+1}^{i} \tag{48}$$

where $(\delta \boldsymbol{\varepsilon}_h, \delta \boldsymbol{u}_h, \delta \boldsymbol{\Pi}_h)$ are the iterative corrections for $(\boldsymbol{\varepsilon}_h, \boldsymbol{u}_h, \boldsymbol{\Pi}_h)$ in the Newton-Raphson scheme. The added projection matrices are computed as:

$$\boldsymbol{M}_{\boldsymbol{\Pi}} = - \int_{\Omega} \boldsymbol{N}_{\boldsymbol{\varepsilon}}{}^{T} \boldsymbol{N}_{\boldsymbol{\varepsilon}} \tag{49}$$

$$\boldsymbol{D}_{\boldsymbol{\Pi}} = \int_{\Omega} \boldsymbol{B}^T \boldsymbol{N}_{\boldsymbol{\varepsilon}} \tag{50}$$

Alternatively to this procedure, a staggered scheme can be devised. First, the projection of the stresses $\boldsymbol{\Pi}_h$ is computed at the beginning of the time step. Then, $\boldsymbol{\Pi}_h$ is used for the solution of $(\boldsymbol{\varepsilon}_h, \boldsymbol{u}_h)$. With this substitution, the matrix depicted in (48) can be *formally* condensed [13] and it becomes:

$$-\left[\begin{array}{cc} \boldsymbol{M}_\tau - \boldsymbol{D}_\Pi^T \boldsymbol{M}_\Pi^{-1} \boldsymbol{D}_\Pi & \boldsymbol{G}_\tau \\ \boldsymbol{D}_\tau & \boldsymbol{K}_\tau \end{array}\right]_{n+1}^{i} \left[\begin{array}{c} \delta\boldsymbol{\varepsilon}_h \\ \delta\boldsymbol{u}_h \end{array}\right]_{n+1}^{i+1} = \left[\begin{array}{c} R_{1,h} \\ R_{2,h} \end{array}\right]_{n+1}^{i} \tag{51}$$

This scheme is preferred with respect to the monolithic one due to the reduced computation time required.

4 Drucker-Prager Plasticity Model

The Drucker-Prager model is a pressure dependent plasticity model frequently used in geomechanics. It has a singular point in correspondence of the maximum allowed mean stress. In the following sections, this particular model is introduced and details on the return mapping are given.

4.1 Definition of the space of admissible stresses

The Drucker-Prager plasticity model may be constructed as a linear combination of a J2 Von Mises plasticity model and a Pure Pressure plasticity model. The Von Mises yield criterion states that a material reaches the elastic limit when the equivalent octaedral stress is equal to a known uniaxial maximum admissible threshold:

$$f\left(\boldsymbol{\sigma}, q\right) = \sqrt{3J_2(\boldsymbol{\sigma})} - r^d\left(q\right) = 0 \tag{52}$$

where q is a stress-like hardening/softening variable. The value $r^d\left(q\right)$ represents a limit in the admissible stress with respect to the second invariant of the deviatoric tensor $J_2(\boldsymbol{\sigma})$. The Pure Pressure yield criterion relates the hydrostatic pressure with a maximum admissible threshold:

$$f\left(\boldsymbol{\sigma}, q\right) = \frac{1}{3} I_1(\boldsymbol{\sigma}) - r^p\left(q\right) = p - r^p\left(q\right) = 0 \tag{53}$$

where the value $r^p\left(q\right)$ represents a limit in the admissible pressure. In the Drucker-Prager model, the angle of friction ϕ is introduced to relate the admissible deviatoric stresses to the pressure as:

$$f\left(\boldsymbol{\sigma}, q\right) = \left[\sqrt{3J_2(\boldsymbol{\sigma})} - r^d\left(q\right)\right] + a\left[\frac{1}{3} I_1(\boldsymbol{\sigma}) - r^p\left(q\right)\right] \tan(\phi) = 0 \tag{54}$$

Plotting this yielding sufrace on the (p, J_2) plane, the result is a line with a slope equal to $\tan(\phi)$ (Figure 2). In the principal stress Haig-Westergaard space, the Drucker-Prager yield surface appears as a symmetric cone with the axis coinciding with the hydrostatic pressure and a circular trace on the octahedral plane (Figure 3). The parameter $a = \pm 1$ controls the sign of the pressure part and the orientation of the admissible plane of stresses. This means that the material may fail due to high tension states ($a = 1$) or due to high compression states ($a = -1$). The point $(p_{min}, 0)$ in Figure 2 represents the vertex of the cone, the minimum allowed mean stress state. In geotechnical engineering, the value of $a = 1$ is usually assumed. Taking advantage of some trigonometric identities, it is possible to rewrite the surface of failure explicitly as:

$$f\left(\boldsymbol{\sigma}, q\right) = \rho\left(\sqrt{3J_2(\boldsymbol{\sigma})} - r^d\left(q\right)\right) + a\left(1 - \rho\right)\left(\frac{1}{3} I_1(\boldsymbol{\sigma}) - r^p\left(q\right)\right) = 0 \tag{55}$$

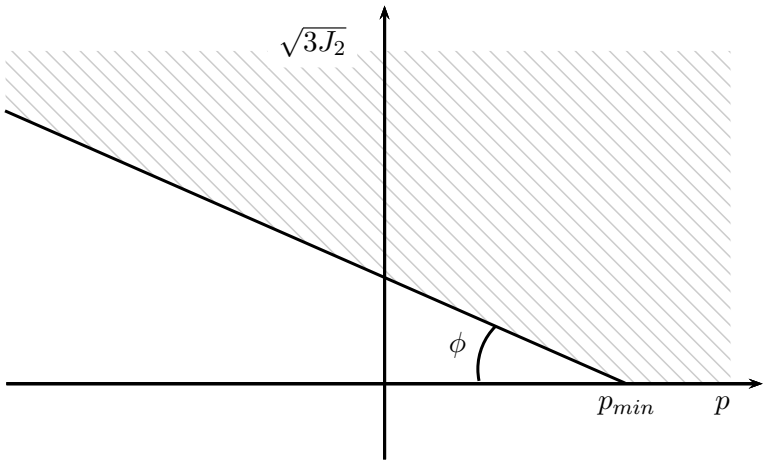

Figure 2: Drucker-Prager elastic domain in the (p, J_2) plane

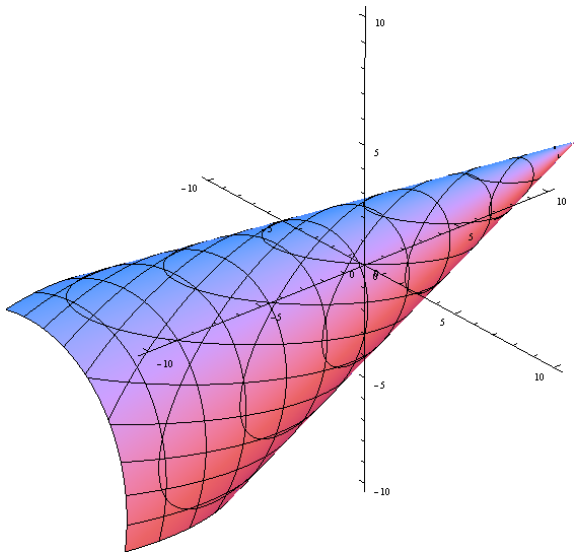

Figure 3: Drucker-Prager elastic domain in the principal stress Haig-Westergaard space

where $\rho = 1/(1 + \tan(\phi))$. In this work, the pressure threshold is taken as $r^p = 0$ to allow a direct comparison between J2 incompressible plasticity and Drucker-Prager plasticity. On the other side, the deviatoric stress threshold reads:

$$r^d(q) = \sigma_y - q(\xi) \tag{56}$$

where $q(\xi)$ is the hardening/softening function and ξ is an internal strain-like parameter. The function $q(\xi)$ controls the value of the intersection between the yielding surface and the deviatoric axis in Figure 2. In the linear softening case, the function $r^d(\xi)$ is:

$$r^d(\xi) = \begin{cases} \sigma_y \left(1 - \frac{H_S}{\sigma_y}\xi\right) & \text{for} \quad 0 \leq \xi \leq \frac{\sigma_y}{H_S} \\ 0 & \text{for} \quad \frac{\sigma_y}{H_S} \leq \xi \leq \infty \end{cases} \tag{57}$$

whereas, in the case of exponential softening, $r^d(\xi)$ assumes the form:

$$r^d(\xi) = \sigma_y \exp\left(\frac{-2H_S}{\sigma_y}\xi\right) \qquad \text{for} \quad 0 \leq \xi \leq \infty \tag{58}$$

Rewriting the invariants $J_2(\boldsymbol{\sigma}) = \frac{1}{2}\|\text{dev}\boldsymbol{\sigma}\|$ and $I_1(\boldsymbol{\sigma}) = \frac{1}{3}\,\text{tr}\,\boldsymbol{\sigma}$, the failure criteria takes the form:

$$f(\boldsymbol{\sigma}, q) = \rho\left(\sqrt{\frac{3}{2}}\|\text{dev}\boldsymbol{\sigma}\| - (\sigma_y - q(\xi))\right) + a(1-\rho)\frac{1}{3}\,\text{tr}\,\boldsymbol{\sigma} = 0 \tag{59}$$

4.2 Return mapping algorithm

Assuming associative plasticity and the existence of a plastic potential that coincides with the definition of the admissible stress surface $f(\boldsymbol{\sigma}, q)$, the evolution equations for the plastic variables read:

$$\begin{aligned} \dot{\boldsymbol{\varepsilon}}_p &= \dot{\gamma}\frac{\partial f(\boldsymbol{\sigma}, q)}{\partial \boldsymbol{\sigma}} \\ \dot{\xi} &= \dot{\gamma}\frac{\partial f(\boldsymbol{\sigma}, q)}{\partial q} \end{aligned} \tag{60}$$

where $\dot{\gamma}$ is the plastic multiplier or plastic consistency parameter. Substituting the definition of the failure surface and differentiating:

$$\begin{aligned} \dot{\boldsymbol{\varepsilon}}_p &= \dot{\gamma}\,\partial_{\boldsymbol{\sigma}} f(\boldsymbol{\sigma}, q) = \dot{\gamma}\left[\rho\sqrt{\frac{3}{2}}\frac{\text{dev}\boldsymbol{\sigma}}{\|\text{dev}\boldsymbol{\sigma}\|} + \frac{a(1-\rho)}{3}\mathbf{1}\right] \\ \dot{\xi} &= \dot{\gamma}\,\partial_q f(\boldsymbol{\sigma}, q) = \dot{\gamma}\rho \end{aligned} \tag{61}$$

Additionally, the Karush-Kuhn-Tucker and consistency conditions hold:

$$\gamma \geq 0, \qquad f(\boldsymbol{\sigma}, q) \leq 0, \qquad \gamma f(\boldsymbol{\sigma}, q) = 0 \tag{62}$$

$$\text{if} \qquad f(\boldsymbol{\sigma}, q) = 0 \qquad \Rightarrow \qquad \dot{\gamma} \geq 0, \quad \dot{f}(\boldsymbol{\sigma}, q) \leq 0 \quad \text{and} \quad \dot{\gamma}\dot{f}(\boldsymbol{\sigma}, q) = 0 \tag{63}$$

Given the last set of conditions, $\dot{\gamma}$ is computed as [19]:

$$\dot{\gamma} = \frac{\langle \partial_{\boldsymbol{\sigma}} f : \mathbb{C} : \dot{\boldsymbol{\varepsilon}} \rangle}{\dfrac{\partial f}{\partial \boldsymbol{\sigma}} : \mathbb{C} : \dfrac{\partial f}{\partial \boldsymbol{\sigma}} + \dfrac{\partial f}{\partial q}\dfrac{\mathrm{d}q}{\mathrm{d}\xi}\dfrac{\partial f}{\partial q}} \tag{64}$$

The time derivative of the evolution equations of the plastic variables can be approximated introducing a Backward-Euler scheme with time steps of length Δt, considering the $[t_n, t_{n+1}]$ span. Then, the discrete-in-time version of (61) reads:

$$\begin{aligned} \dot{\boldsymbol{\varepsilon}}_p \approx \frac{\boldsymbol{\varepsilon}_p^{(n+1)} - \boldsymbol{\varepsilon}_p^{(n)}}{\Delta t} &= \frac{\gamma^{(n+1)} - \gamma^{(n)}}{\Delta t}\left[\rho\sqrt{\frac{3}{2}}\frac{\text{dev}\boldsymbol{\sigma}^{(n+1)}}{\left\|\text{dev}\boldsymbol{\sigma}^{(n+1)}\right\|} + \frac{a(1-\rho)}{3}\mathbf{1}\right] \\ \dot{\xi} \approx \frac{\xi^{(n+1)} - \xi^{(n)}}{\Delta t} &= \rho\frac{\gamma^{(n+1)} - \gamma^{(n)}}{\Delta t} \end{aligned} \tag{65}$$

The trial state is defined at step $n+1$ with the plasticity variables frozen at step n:

$$\begin{aligned} \boldsymbol{\varepsilon}_{p,trial}^{(n+1)} &= \boldsymbol{\varepsilon}_p^{(n)} \\ \xi_{trial}^{(n+1)} &= \xi^{(n)} \end{aligned} \tag{66}$$

Therefore, the trial stresses are:

$$\begin{aligned} \boldsymbol{\sigma}_{trial}^{(n+1)} &= \mathbb{C} : \left(\boldsymbol{\varepsilon}^{(n+1)} - \boldsymbol{\varepsilon}_p^{(n)}\right) \\ q_{trial}^{(n+1)} &= q^{(n)} \end{aligned} \tag{67}$$

Plasticity occurs if $f_{trial}^{(n+1)} \geq 0$. The trial yielding function is:

$$f_{trial}^{(n+1)} = \rho \left(\sqrt{\frac{3}{2}} \left\| \text{dev}\boldsymbol{\sigma}_{trial}^{(n+1)} \right\| - \left(\boldsymbol{\sigma}_y^d - q_{trial}^{(n+1)} \right) \right) + a\,(1-\rho) \left(\frac{1}{3} \,\text{tr}\, \boldsymbol{\sigma}_{trial}^{(n+1)} \right) \tag{68}$$

The change of plastic multiplier $\Delta\gamma^{(n+1)} = \gamma^{(n+1)} - \gamma^{(n)}$ is computed with the discrete counterpart of (64) as:

$$\Delta\gamma^{(n+1)} = \frac{\left\langle f_{trial}^{(n+1)} \right\rangle}{(1-\rho)^2 K + 3G\rho^2 + \rho^2 \frac{\mathrm{d}q}{\mathrm{d}\xi}^{(n+1)}} \tag{69}$$

where K is the bulk modulus and G is the shear modulus of the material. Notice that $q\left(\xi^{(n+1)}\right)$ implicitly depends on the value of $\Delta\gamma^{(n+1)}$ as shown in (65).

4.3 Constitutive Elasto-Plastic Tangent operator

The constitutive elasto-plastic tangent fourth order tensor can be written as a function of $\dot{\gamma}$. Defining:

$$\mathscr{D} = \frac{\partial f}{\partial \boldsymbol{\sigma}} : \mathbb{C} : \frac{\partial f}{\partial \boldsymbol{\sigma}} + \frac{\partial f}{\partial q} \frac{\mathrm{d}q}{\mathrm{d}\xi} \frac{\partial f}{\partial q} \tag{70}$$

On one hand, the constitutive elastoplastic tensor in continuous form is [25]:

$$\mathbb{C}_{ep} = \mathbb{C} - \frac{\left(\mathbb{C} : \frac{\partial f}{\partial \boldsymbol{\sigma}} \right) \otimes \left(\mathbb{C} : \frac{\partial f}{\partial \boldsymbol{\sigma}} \right)}{\mathscr{D}} \tag{71}$$

On the other hand, considering the discrete Backward Euler time integration, the *algorithmic consistent* constitutive elasto-plastic tensor can be computed as:

$$\mathbb{C}_{ep}^{(n+1)} = \frac{\mathrm{d}\boldsymbol{\sigma}^{(n+1)}}{\mathrm{d}\boldsymbol{\varepsilon}^{(n+1)}} \tag{72}$$

Carrying out the differentiation, it yields:

$$\begin{aligned} \mathbb{C}_{ep}^{(n+1)} \;=\; & \mathbb{C} \\ & - \frac{\left[\rho 2G \sqrt{\frac{3}{2}} \mathbf{n}_{d,trial}^{(n+1)} + a\,(1-\rho)\,K\mathbf{1} \right] \otimes \left[\rho 2G \sqrt{\frac{3}{2}} \mathbf{n}_{d,trial}^{(n+1)} + a\,(1-\rho)\,K\mathbf{1} \right]}{\mathscr{D}^{(n+1)}} \\ & - \Delta\gamma^{(n+1)} (2G)^2 \rho \sqrt{\frac{3}{2}} \frac{\left[\left(\mathbb{I} - \frac{1}{3}\mathbf{1} \otimes \mathbf{1} \right) - \mathbf{n}_{d,trial}^{(n+1)} \otimes \mathbf{n}_{d,trial}^{(n+1)} \right]}{\left\| \text{dev}\boldsymbol{\sigma}_{trial}^{(n+1)} \right\|} \end{aligned} \tag{73}$$

where $\mathscr{D}^{(n+1)}$ is the discrete counterpart of (70):

$$\mathscr{D}^{(n+1)} = \left[(1-\rho)^2 K + \rho^2 3G \right] - \rho^3 \frac{\mathrm{d}q\left(\xi^{(n)} + \rho\Delta\gamma^{(n+1)} \right)}{\mathrm{d}\xi} \tag{74}$$

and $\mathbf{n}_{d,trial}^{(n+1)}$ is the unit vector in the deviatoric stress direction:

$$\mathbf{n}_{d,trial}^{(n+1)} = \frac{\text{dev}\boldsymbol{\sigma}_{trial}^{(n+1)}}{\left\| \text{dev}\boldsymbol{\sigma}_{trial}^{(n+1)} \right\|} \tag{75}$$

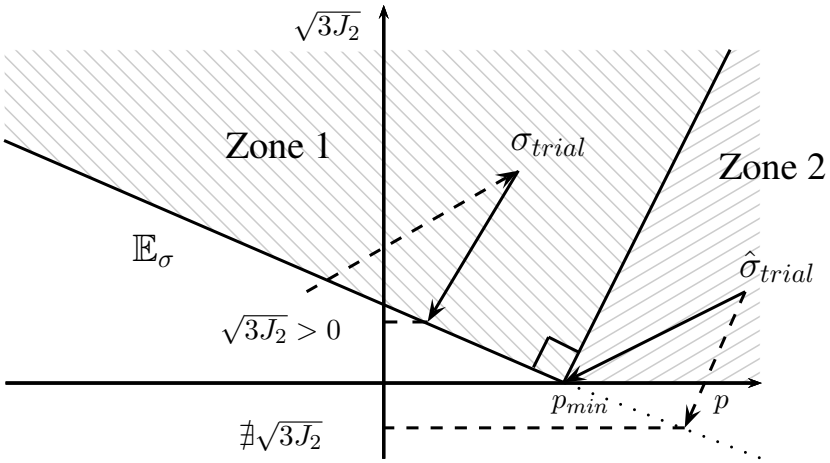

Figure 4: Drucker-Prager domain in the (J_2, p) plane with return mapping zones

4.4 Apex return mapping

The Drucker-Prager model presents a singular point in the yielding surface: the apex of the cone. For the return mapping in those cases when this point is involved, an "ad-hoc" procedure is necessary. In the literature, deBorst [26] and Perić and de Souza Neto [27] proposed some general methods to tackle this problem. In this case, a particular return mapping algorithm is devised in order to have a scalar condition on the components of Cauchy stress tensor.

Consider the yielding surface function in equation (59). The minimum value of the admissible pressure defines the apex of the cone in Figure 4 and its value is:

$$p_{min} = \frac{\rho\,(\boldsymbol{\sigma}_y - q)}{a\,(1-\rho)} \tag{76}$$

The part located outside the admissible stress space can be divided in two zones by considering the orthogonal line to the yielding surface passing through the apex (Figure 4). The standard return mapping, described in the previous section, is used in the cases where the trial stress state falls in the "Zone 1" domain. When the trial stress is in the complementary "Zone 2" of the cone, the differentiation of the yielding surface cannot be performed since the normal vector to the yielding surface does not have a unique definition. However, a family of sub-differentials of the yielding surface exists and the return mapping can be performed, for example, by considering the principal components pressure p and deviatoric stress $\mathrm{dev}\boldsymbol{\sigma}$ to satisfy some particular conditions.

In order to find the condition to discriminate the two situations, consider the return mapping for the deviatoric components, i.e. along the vertical axis of Figure 4. Once the variation of the plastic multiplier is known, the deviatoric components of the stress tensor are updated with the new plastic strains as:

$$\left\|\mathrm{dev}\boldsymbol{\sigma}^{(n+1)}\right\| = \left\|\mathrm{dev}\boldsymbol{\sigma}^{(n+1)}_{trial}\right\| - \Delta\gamma^{(n+1)}\rho\sqrt{\frac{3}{2}}\,2G \tag{77}$$

As the norms are positive definite, it follows that:

$$\Delta\gamma^{(n+1)} \leq \frac{\left\|\mathrm{dev}\boldsymbol{\sigma}^{(n+1)}_{trial}\right\|}{\rho\sqrt{\frac{3}{2}}\,2G} \tag{78}$$

If this condition is verified, then the return mapping is made through the standard procedure described in the previous section. Otherwise, the return mapping will be made to the apex of the Drucker-Prager cone.

The stress at the apex point is:

$$f(\boldsymbol{\sigma}, q) = 0 \quad \text{and} \quad p = p_{min} \quad \Rightarrow \quad \|\text{dev}\boldsymbol{\sigma}\| = 0 \tag{79}$$

Calling $\mathbf{n}_{trial} = \mathbf{n}_{apex}$ the unit vector that points from $\boldsymbol{\sigma}_{trial}$ to the vertex of the cone $(p_{min}, 0)$, the plastic flow is:

$$\dot{\boldsymbol{\varepsilon}}_p = \dot{\gamma}\mathbf{n}_{apex} \tag{80}$$

and in discrete form

$$\boldsymbol{\varepsilon}_p^{(n+1)} = \boldsymbol{\varepsilon}_p^{(n)} + \Delta\gamma^{(n+1)}\mathbf{n}_{apex}^{(n+1)} \tag{81}$$

The trial stress is

$$\boldsymbol{\sigma}_{trial}^{(n+1)} = \text{dev}\boldsymbol{\sigma}_{trial}^{(n+1)} + p_{trial}^{(n+1)}\mathbf{1} \tag{82}$$

and the stress after the return mapping reads:

$$\boldsymbol{\sigma}^{(n+1)} = p_{min}\mathbf{1} \tag{83}$$

Therefore:

$$\boldsymbol{\varepsilon}_p^{(n+1)} = \boldsymbol{\varepsilon}_p^{(n)} + \left[a\frac{p_{trial}^{(n+1)} - p_{min}}{3K}\mathbf{1} + \frac{\text{dev}\boldsymbol{\sigma}_{trial}^{(n+1)}}{2G}\right] = \boldsymbol{\varepsilon}_p^{(n)} + \Delta\boldsymbol{\varepsilon}_p^{(n+1)} \tag{84}$$

Notice that the value of p_{min} depends on the value of the isotropic hardening $q = q(\xi)$. Consequently, an iterative procedure is necessary in order to evaluate correctly the plastic multiplier.

4.5 Apex Consistent Elasto-Plastic Tangent operator

In the case of return mapping to the apex, the consistent constitutive tensor is the null fourth tensor. This means that once the stress state arrives at the vertex of the cone, it will remain at the apex unless unloading or neutral loading occurs.

4.6 Softening behaviour

In a softening process, the energy dissipated by inelastic behaviour is linked with the fracture energy G_f [28], defined by unit surface. When using a plastic model defined in terms of stress and strain, the dissipated plastic energy $\mathscr{W}_p$ is defined by unit volume. In the discrete FE setting, these two definitions are related through a characteristic length l_{ch}, connected to the mesh resolution:

$$\mathscr{W}_p = \frac{G_f}{l_{ch}} \tag{85}$$

In the plastic model, the rate of plastic work is computed as:

$$\dot{\mathscr{W}}_p = \boldsymbol{\sigma} : \dot{\boldsymbol{\varepsilon}}_p = \bar{\sigma}\,\dot{\bar{\varepsilon}}_p = \alpha\, r\,(\xi)\,\dot{\xi} \tag{86}$$

where $\bar{\sigma}$ is the equivalent Drucker-Prager stress:

$$\bar{\sigma} = \rho\sqrt{\frac{3}{2}}\,\|\text{dev}\boldsymbol{\sigma}\| + (1-\rho)\,a\frac{1}{3}\,\text{tr}\,\boldsymbol{\sigma}\,\tan(\phi) = \rho\,(\boldsymbol{\sigma}_y - q) = r\,(\xi) \tag{87}$$

and $\dot{\bar{\varepsilon}}_p$ is the rate of equivalent plastic strain:

$$\dot{\bar{\varepsilon}}_p = \|\dot{\boldsymbol{\varepsilon}}_p\| = \dot{\gamma}\left[\rho\sqrt{\frac{3}{2}} + a\,(1-\rho)\right] \tag{88}$$

and, finally, α is a scaling factor depending on the friction angle,

$$\alpha = \sqrt{\frac{3}{2}} + \frac{1-\rho}{\rho} \tag{89}$$

In both the linear and exponential softening cases, where $r(\xi)$ is defined respectively by (57) and (58), the total plastic work is calculated then as:

$$\mathscr{W}_p = \int_{t=0}^{t=\infty} \dot{\mathscr{W}}_p \, \mathrm{d}t = \int_{\xi=0}^{\xi=\infty} \alpha \, r(\xi) \, \dot{\xi} = \alpha \frac{{\sigma_y}^2}{2H_S} \tag{90}$$

and this represent the area underlying the $r - \xi$ curve. Now, comparing expressions (85) and (90), the parameter H_S can be computed as:

$$H_S = \alpha \frac{{\sigma_y}^2}{2G_f} l_{ch} = \bar{H}_S l_{ch} \tag{91}$$

The parameter $\bar{H}_S$ depends only on material properties, whereas l_{ch} depends on the resolution of the discretization. As pointed out by Cervera et al. [18], the size of the strain concentration band depends on the finite element technology. For instance, irreducible finite elements provide a concentration band within a single element span, due to the discontinuous strain field. On the contrary, in the $\boldsymbol{\varepsilon} - u$ mixed FE formulation, with inter-elemental continuous strain, the slip line spans two elements. The characteristic length l_{ch} is taken accordingly.

4.7 Plastic dissipation rate

The condition of positive rate of dissipation

$$\dot{\mathscr{W}}_p = \boldsymbol{\sigma} : \dot{\boldsymbol{\varepsilon}}_p \geq 0 \qquad \forall \dot{\boldsymbol{\varepsilon}} \tag{92}$$

has to hold in both classical and apex return mappings in order to have a thermodynamically consistent model. In the first case, since $0 \leq \rho \leq 1$ and the initial stress threshold $\sigma_y > 0$, it holds:

$$\dot{\mathscr{W}}_p = \rho \sigma_y \dot{\gamma} \geq 0 \qquad \forall \dot{\boldsymbol{\varepsilon}} \tag{93}$$

In the return of the apex case, a continuous expression is not available, but, using (83) and (84) the incremental dissipation takes the form:

$$\Delta \dot{\mathscr{W}}_p^{(n+1)} = \frac{1}{3K} \left[p_{min}^{(n+1)} \mathbf{1} : p_{min}^{(n+1)} \mathbf{1} \right] \geq 0 \tag{94}$$

which is positive by construction.

5 Numerical Examples

The objective of the following numerical examples is to highlight the benefits of a stress-accurate finite element method, such as the proposed ε/u mixed FEM, in order to capture softening behavior and failure due to the formation of strain localization lines. In all the examples, the convergence tolerance used for the iterative Newton-Raphson procedure is 10^{-5}. Computations have been realized using an enhanced version of COMET-Coupled mechanical and thermal analysis [29], developed by the authors at the International Center of Numerical Methods in Engineering (CIMNE) in Barcelona, Spain. The geometrical models have been created using GiD, a pre and post-processing software, also developed by CIMNE.

5.1 Prandtl's punch problem with J2 plasticity

In this first example, the relative performance of the displacement-pressure formulation u/p and the strain-displacement formulation ε/u in the 2D Prandtl's punch test is assessed. Incompressible J2 plasticity ($\phi = 0°$) is assumed. The problem consists of a foundation loading a semi-infinite soil domain. A portion of 10 by 5 meters of soil is modeled, with a 2 meters wide loading zone. Due to symmetry conditions, only one half of the domain has been meshed. The geometry of the problem is shown in Figure 5. The load is given by an imposed vertical displacement of 0.2 meters in the downward direction. Young's modulus is 10 MPa and Poisson's ratio is 0.4. The maximum tensile strength is 10 kPa, whereas a fracture energy of 200 J/m^2 is considered for the strain softening case. All cases are run with 400 time steps and an unstructured mesh of 4340 triangular P1-P1 elements (typical size of $h = 0.25$).

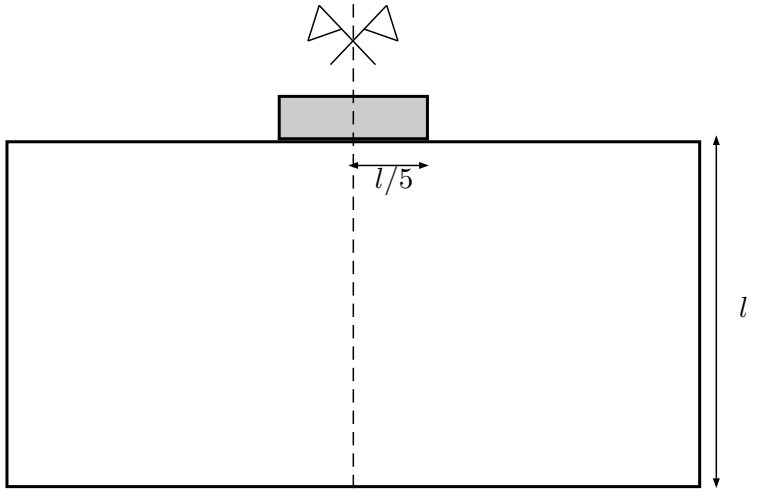

Figure 5: Geometry for Prandtl's punch problem

In Figures 7(a) and 7(b), the norm of displacement field obtained with both formulations at the end of the loading is shown. The results computed with the two formulations are very similar. This is due to the fact that both formulations have the same order of convergence rate in the displacement field. The equivalent plastic strain is presented in Figures 7(d) and 7(e). It can be seen that, even if the displacements do not present substantial difference, the plastic strain field differs for the two formulations, not in the path of the slip line but rather in the quality of the description of the shear band. In fact, the ε/u solution presents a continuous distribution of strains whereas the u/p formulation yields a element-wise constant but inter-element discontinuous field. Principal strain vectors are shown in Figures 7(g) and 7(h). Here, the largest differences between the solution of the two formulations can be observed. In the u/p formulation, the strain tensor is computed summing the volumetric part of the deformation, computed starting from the pressure field, and the deviatoric one, given by differentiation of the displacement field. Clearly, the latter one is mesh dependent across the slip line and this fact biases the orientation of the principal axes of strain. Although the overall behaviour is correct and the solution is the expected one, some sharp changes in the direction of vectors are observed locally in the u/p solution. Contrariwise, in the ε/u solution strain is a continuous variable throughout the domain. This was noted already for the irreducible formulation against the mixed one by Cervera et al. [18]. This discrepancy explains the slightly difference in post peak behaviours of the u/p and ε/u formulations presented in the reaction-displacement plot in Figure 6.

For the sake of comparison, Figures 8(a) and 8(c) show displacement and plastic strain

contours for the same problem, obtained using standard irreducible formulation. The solution is strongly mesh dependent. This is due to two factors. On one hand, the mean stress (the pressure) is completely locked because of the isochoric nature of the plastic flow. On the other hand, the deviatoric part of the strain field fails to converge to the correct, mesh independent, solution of the problem.

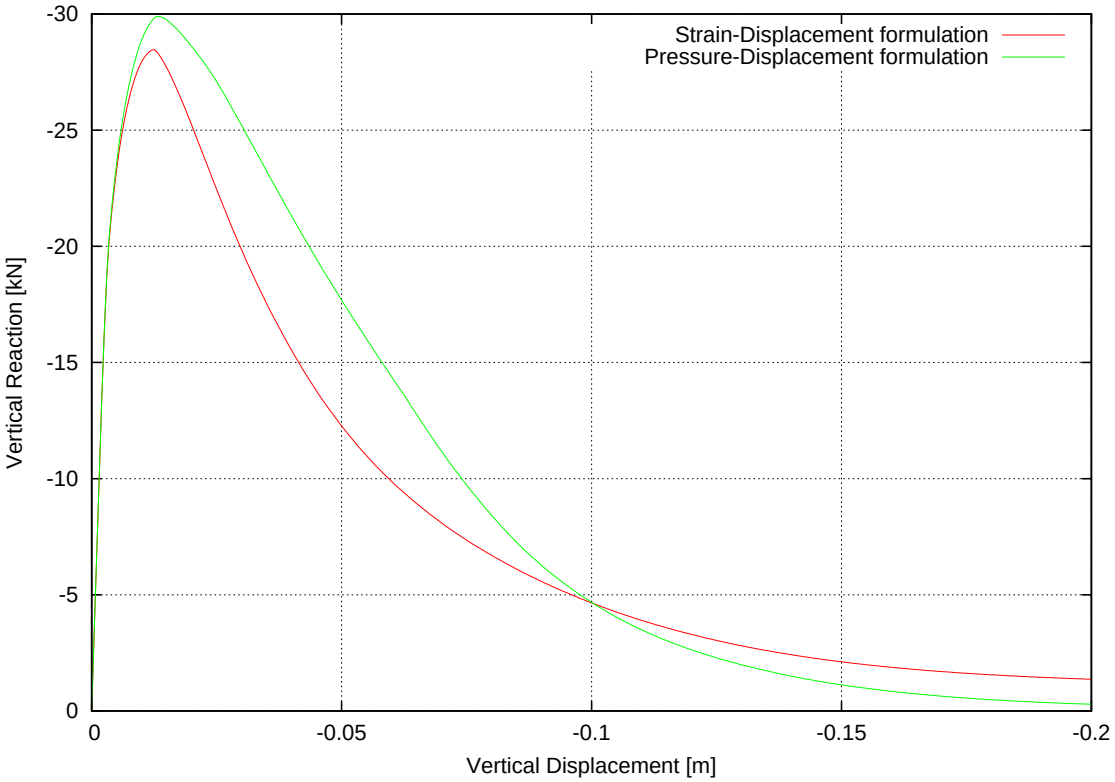

Figure 6: Prandtl's punch problem with J2 plasticity: vertical reaction force vs. imposed vertical displacement of the foundation

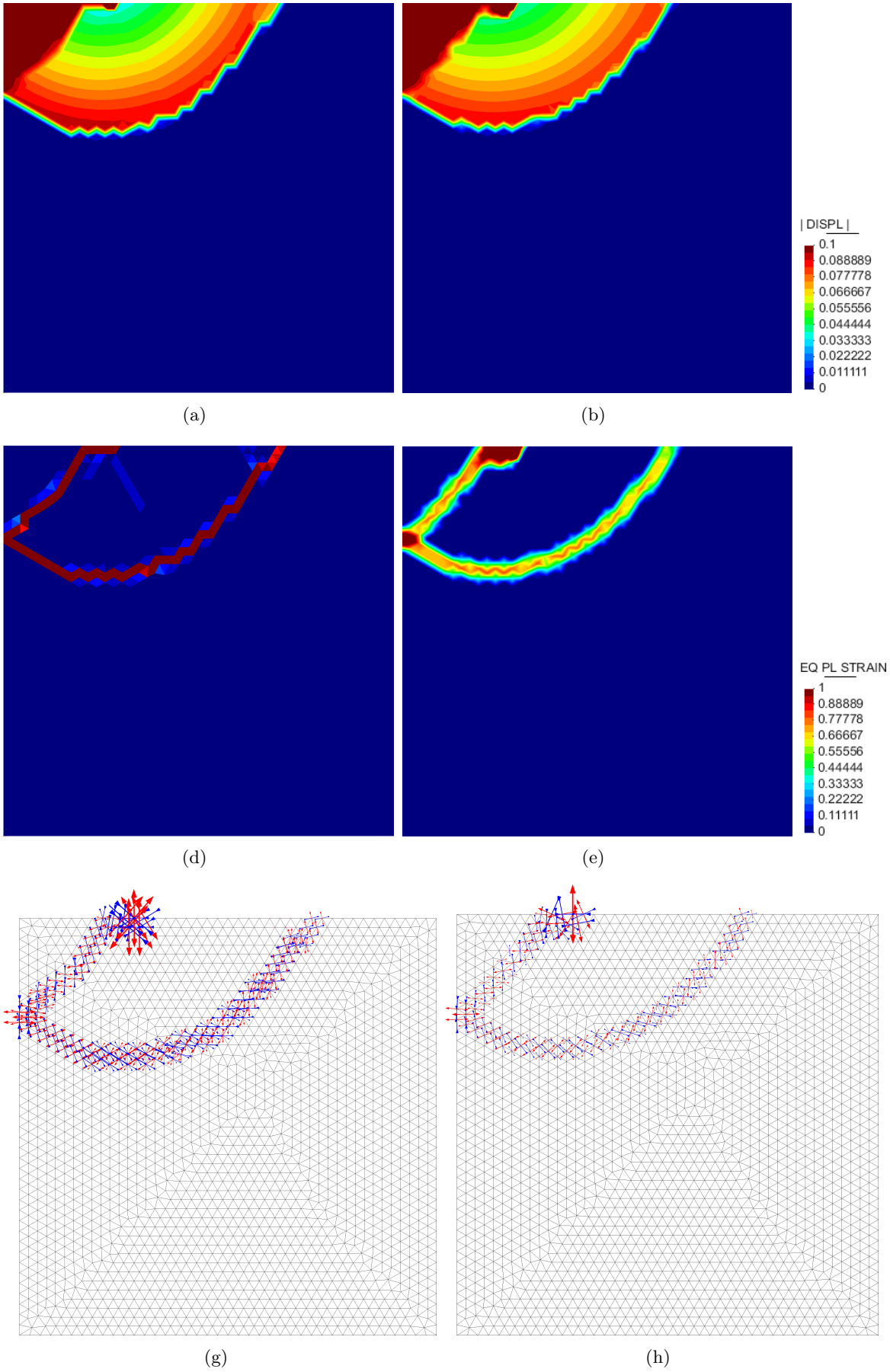

Figure 7: Results for Prandtl's punch problem: u/p (left column) and ε/u (right column). Contours of: total displacements (first row), equivalent plastic strain (second row), vectors of principal strains (third row).

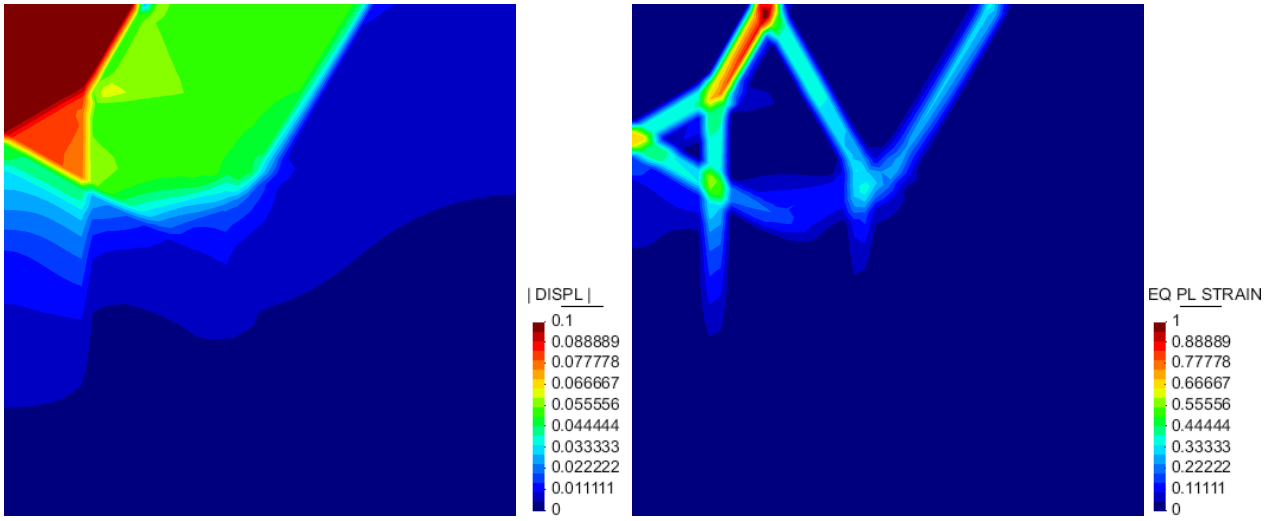

(a) (c)

Figure 8: Results for Prandtl's punch problem in the case of Standard Irreducible finite element formulation

5.2 Prandtl's punch problem with Drucker Prager plasticity

With the geometry and the mechanical properties of the previous example, the Prandtl's punch problem is now analyzed considering the Drucker-Prager plasticity model. The dimensions of the meshed domain have been doubled in order to allow the complete formation of the slip lines and, therefore, to avoid interaction with the boundaries. Again, due to symmetry, the modeled domain is half of the total, 10 by 10 meters with a 1 meter wide footing. The footing applies a downward imposed displacement of 0.2 meters. The mesh is a structured quadrilateral grid with one hundred Q1Q1 elements per side (typical size of $h = 0.1$). The solution is computed for the cases of $\phi = 0, 15, 30$ degrees of internal friction angle. The ε/u formulation is used in all three cases.

In Figure 9, the comparison in the displacement field shows considerable differences in the volume of domain subjected to the effect of the footing. As the angle of friction increases, the affected zone becomes larger, both in the horizontal and vertical directions. In the J2 case, the failure mechanism follows Prandtl's theoretical result for incompressible soils, in which a triangular elastic domain of material, with 45 degrees slip lines, creates a single fan-shaped part sliding along a circular localization zone. Instead, when the angle of friction increases, the shape of the triangular elastic portion under the footing changes and additional fans sliding along the slip line are created. In the equivalent plastic strain plots (Figure 10), the change in the failure mechanism can be clearly appreciated. The ratio of deviatoric and volumetric strain is bigger for higher angles of friction (Figures 11 and 12). Figure 13 shows the resulting reaction force under the footing plotted against the vertical displacement for each one of the considered friction angle. The graph confirms that materials with larger internal friction angle have higher yielding stresses when pressure increases.

(a) $\phi = 0°$

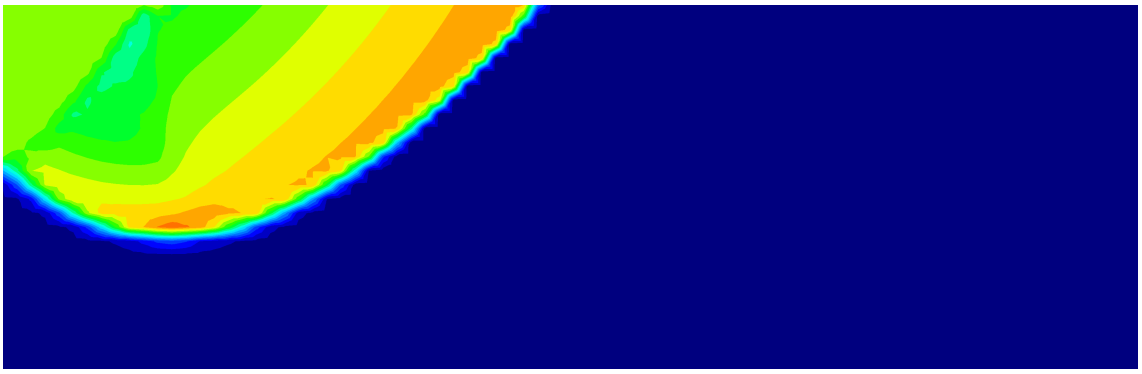

(c) $\phi = 15°$

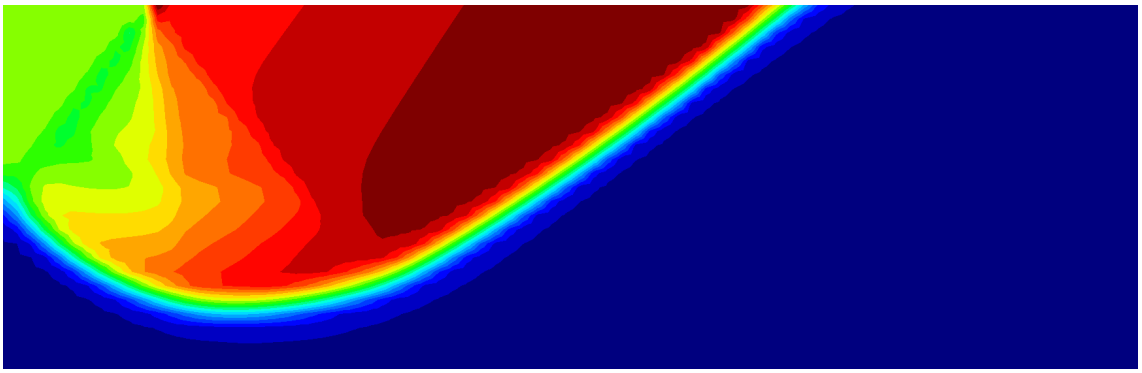

(d) $\phi = 30°$

Figure 9: Prandtl's punch problem with Drucker-Prager plasticity: displacement contour maps for 0, 15 and 30 degrees of internal friction angle

(a) $\phi = 0°$

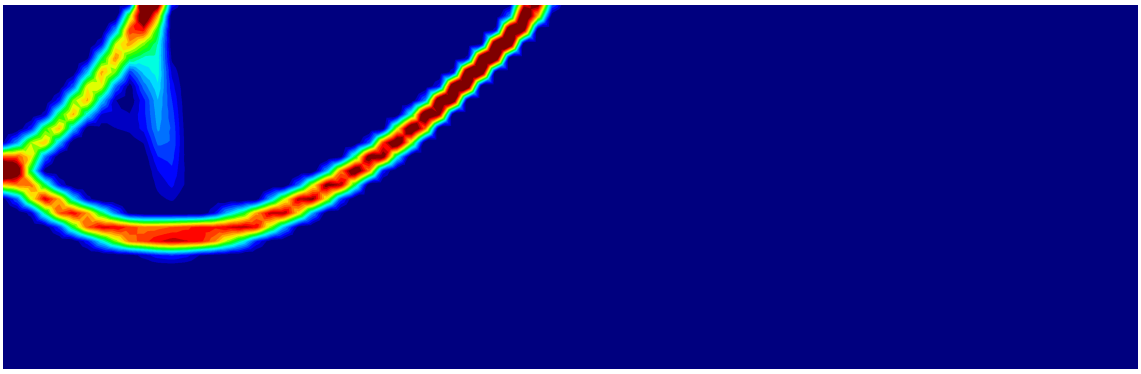

(c) $\phi = 15°$

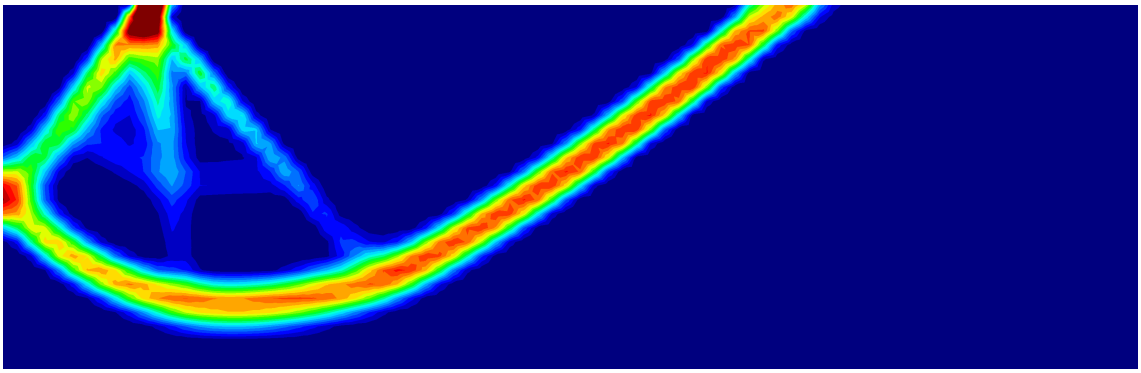

(d) $\phi = 30°$

Figure 10: Prandtl's punch problem with Drucker-Prager plasticity: equivalent plastic strain for 0, 15 and 30 degrees of internal friction angle

(a) $\phi = 0°$

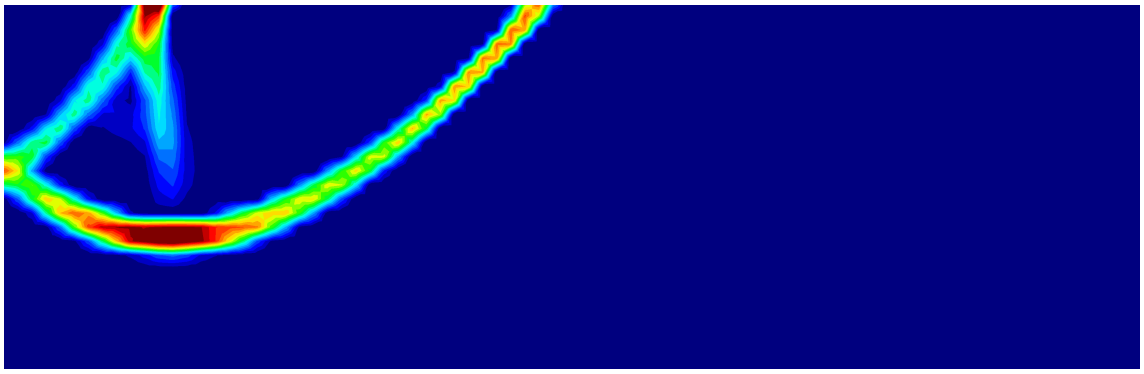

(c) $\phi = 15°$

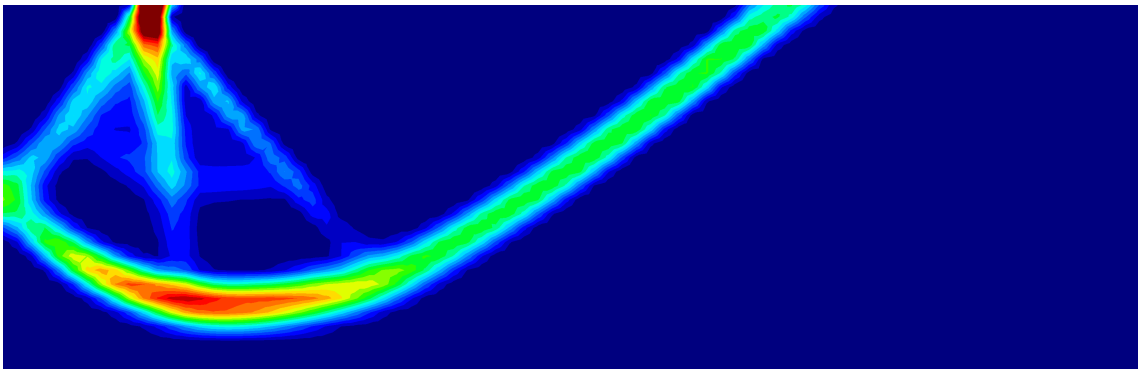

(d) $\phi = 30°$

Figure 11: Prandtl's punch problem with Drucker-Prager plasticity: J2 strain for 0, 15 and 30 degrees of internal friction angle

(a) $\phi = 0°$

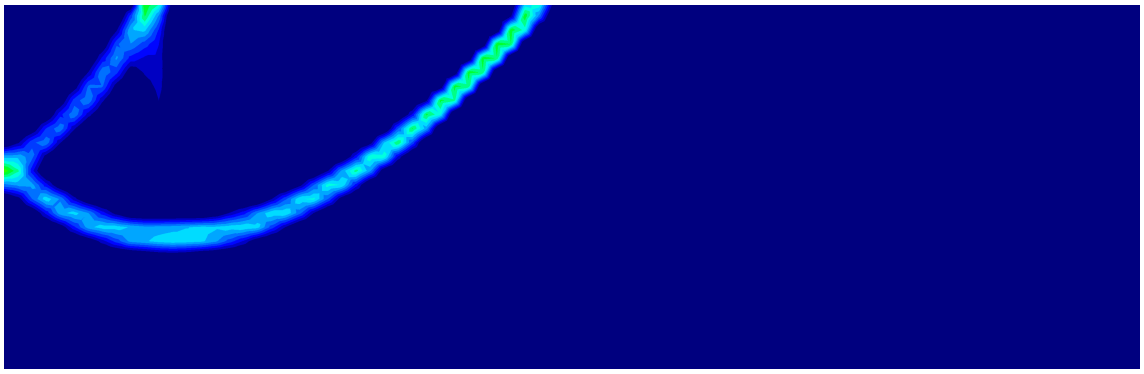

(c) $\phi = 15°$

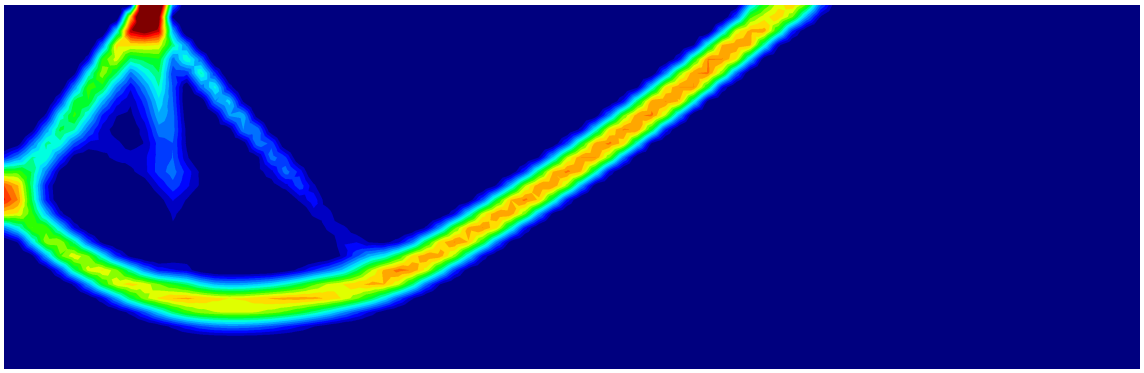

(d) $\phi = 30°$

Figure 12: Prandtl's punch problem with Drucker-Prager plasticity: volumetric strain for 0, 15 and 30 degrees of internal friction angle

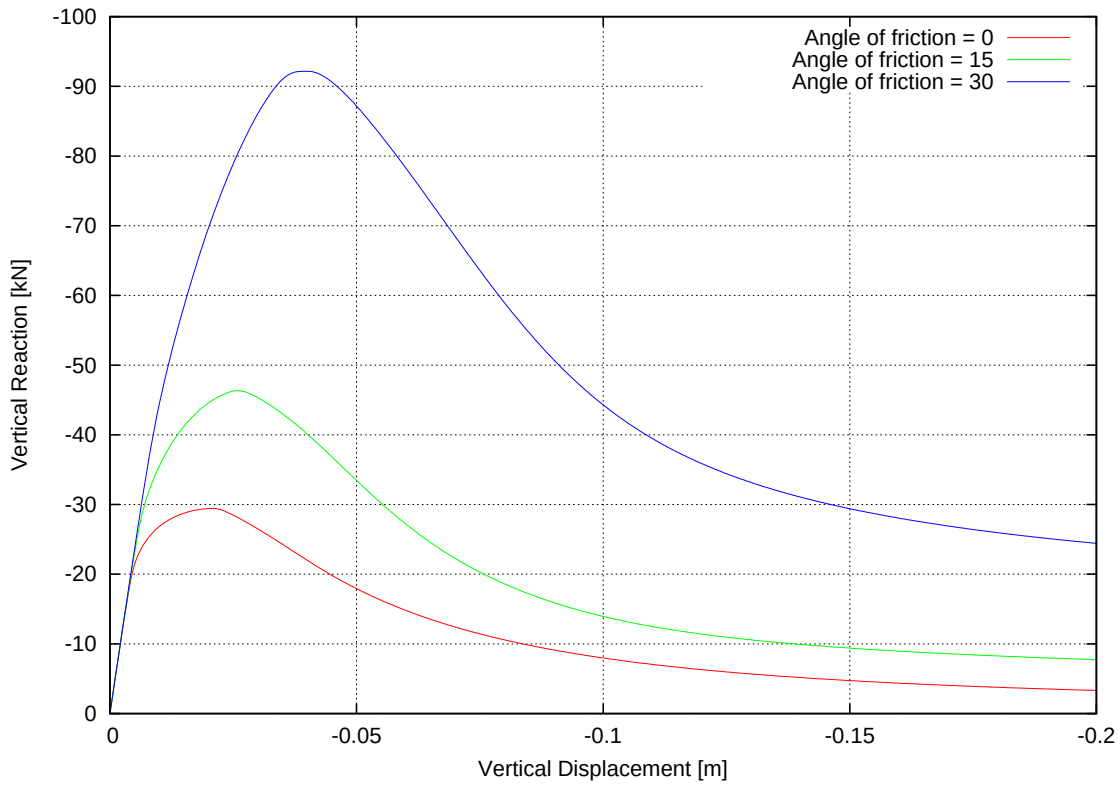

Figure 13: Vertical reaction force vs. vertical displacement for the Prandtl's punch problem with Drucker-Prager plasticity

5.3 Rigid footing on a 3D cube

The final example is a 3D cube of soil with side $l = 2\,m$ with an imposed vertical displacement $\delta = l/10 = 0.2\,m$ in a footprint of $l/2 \times l/2 = 1 \times 1\,m^2$ (Figure 14(a)). The properties of the material are the same as in the previous examples: Young's modulus of 10 MPa, Poisson ratio of 0.4, yielding stress 10 kPa and a fracture energy of 200 J/m^2. The plasticity model is Von Mises ($\phi = 0$). The vertical displacement of 0.2 is applied in 100 time steps. The cube is supported on the three faces that are not adjacent to the footing. The mesh is a structured hexahedral grid with 20 elements per side ($h = 0.1$). This example was solved with the u/p formulation and P1P1 tetrahedral elements in [13].

The computed results show how the cube deforms under the imposed displacement of the rigid foundation (Figure 14(b)): a tetrahedral wedge detaches from the corner of the cube sliding in diagonal along the slip line. Failure is symmetric as expected by the geometry of the problem. Figure 14(c) depicts the computed displacement field, showing an almost rigid motion of the wedge once the failure mechanism is fully developed. Figure 15 confirms that, at the end of the loading process, the reaction force is less than one tenth of the peak value. Figure 14(e) shows the localization of the plastic strains. From the latter two plots it is possible to see that both displacement and plastic strain are continuous across the slip line. The resulting shear band width is, at most, two elements wide. Finally in Figure 15, the vertical reaction force is plotted against the imposed vertical displacement, showing the full development of the resulting softening branch.

6 Conclusion

A mixed strain-displacement finite element formulation has been developed and applied to model the failure due to plastic strain localization of different geotechnical examples.

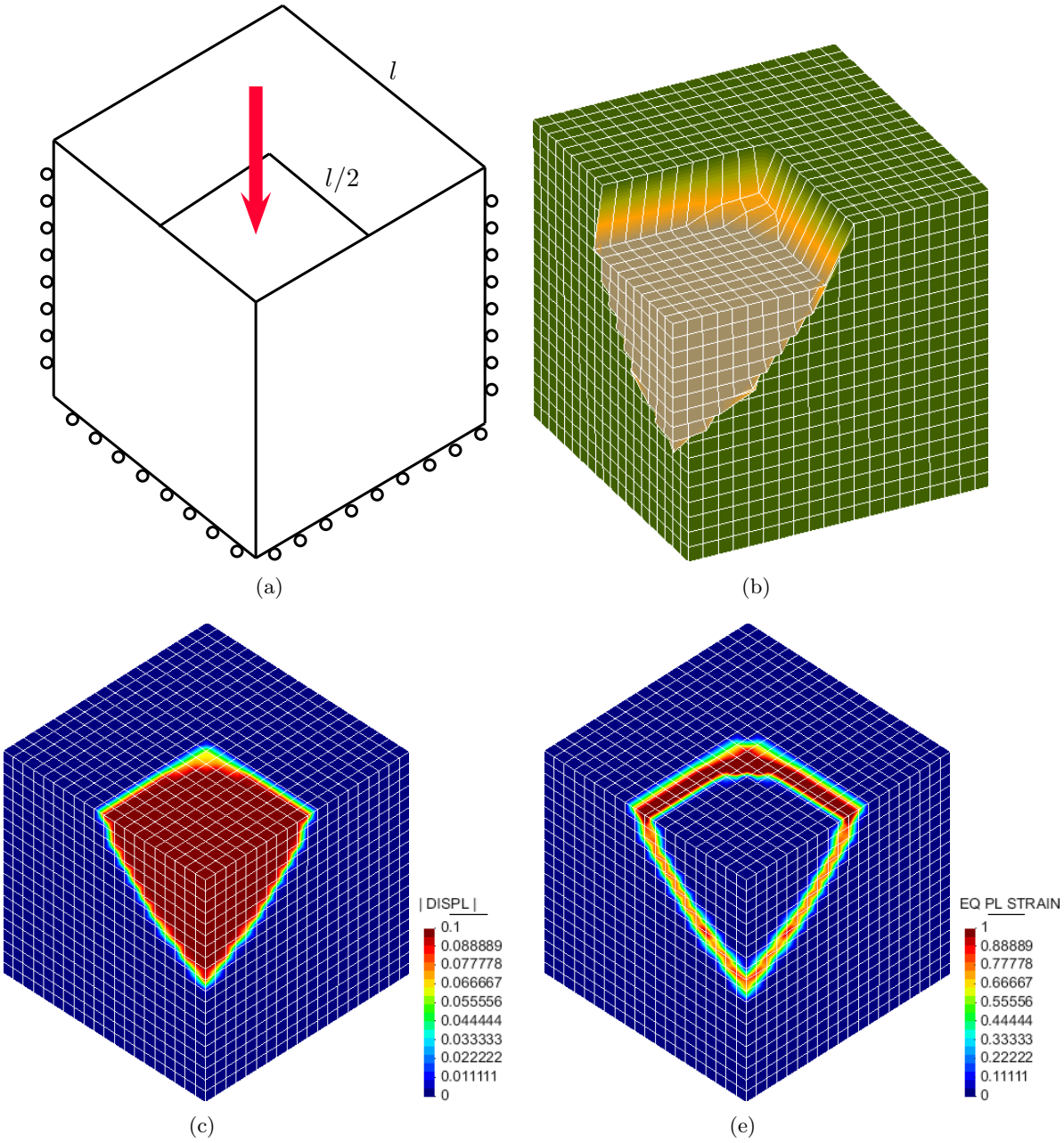

Figure 14: Results for a rigid footing on a 3D cube: (a) geometry of the problem, (b) final deformed mesh, (c) contours of total displacements, (d) equivalent plastic strain

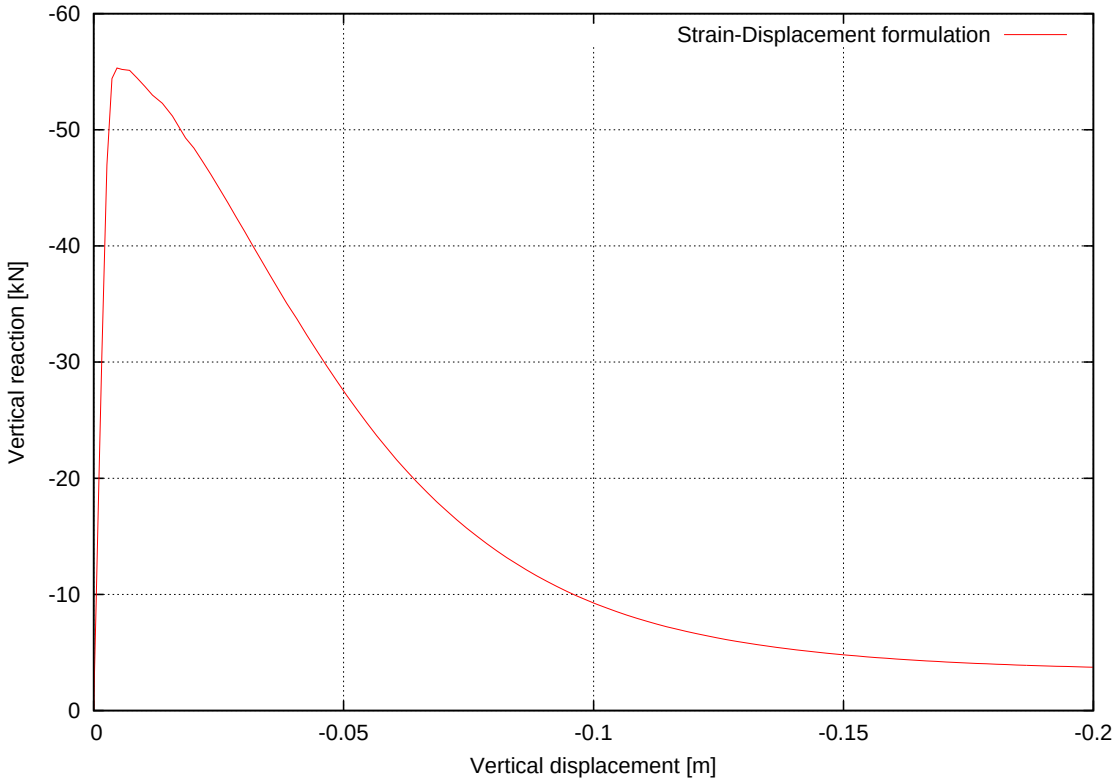

Figure 15: Rigid footing on a 3D cube: vertical reaction vs. imposed displacement

The problem of computation of slip lines has been addressed in pressure dependent as well as incompressible plasticity. The enhanced accuracy in the strain field that this formulation provides, compared to the previously used displacement/pressure formulation, allows a more detailed description of the failure mechanism, peak load and post-peak behaviour. Various examples of 2D and 3D geotechnical problems were solved using triangular, quadrilateral and hexahedral meshes, showing no mesh dependency, theoretical consistency and remarkable robustness.

7 Acknowledgments

Financial support from the EC 7^{th} Framework Programme under the MuMoLaDe project - Multi-scale Modelling of Landslides and Debris Flows - within the framework of Marie Curie ITN (Initial Training Networks) and the Spanish Ministry of Economy and Competitivity under the EACY project - Enhanced accuracy computational and experimental framework for strain localization and failure mechanisms- within the "Excellency" Program for Knowledge Generation is gratefully acknowledged.

Appendix A Differentiation of the plastic strain tensor $\boldsymbol{\varepsilon}_p$

In previous sections, when the linearization of the discrete weak problem was performed, the derivative of the plastic strain tensor was introduced. The plastic strain $\varepsilon_p^{(n+1)}$ depends directly on the trial stress via the return mapping.

Consider the derivative with respect to the nodal strains $\boldsymbol{\varepsilon}_h$. Using the chain rule, it reads:

$$\frac{\partial \boldsymbol{\varepsilon}_p^{(n+1)}}{\partial \boldsymbol{\varepsilon}_h} = \frac{\partial \boldsymbol{\varepsilon}_p^{(n+1)}}{\partial \boldsymbol{\sigma}_{trial}^{(n+1)}} \frac{\partial \boldsymbol{\sigma}_{trial}^{(n+1)}}{\partial \boldsymbol{\varepsilon}_h} \tag{95}$$

The first term on the right hand side represents the variation of the plastic strain with respect to the trial stress at the actual time step. From the discrete evolution equations presented in (65), the plastic strain tensor is updated as:

$$\boldsymbol{\varepsilon}_p^{(n+1)} = \boldsymbol{\varepsilon}_p^{(n)} + \Delta\gamma^{(n+1)}\, \partial_\sigma f\left(\boldsymbol{\sigma}^{(n+1)}, q^{(n+1)}\right) \tag{96}$$

where $\partial_{\boldsymbol{\sigma}} f = \boldsymbol{n}^{(n+1)}$ is the normal to the yield surface. It was shown in equation (61) that, for Drucker-Prager plasticity model, the vector $\boldsymbol{n}^{(n+1)}$ is

$$\boldsymbol{n}^{(n+1)} = \partial_{\boldsymbol{\sigma}} f\left(\boldsymbol{\sigma}, q\right) = \rho\sqrt{\frac{3}{2}}\frac{\mathrm{dev}\boldsymbol{\sigma}}{\|\mathrm{dev}\boldsymbol{\sigma}\|} + \frac{a\left(1-\rho\right)}{3}\mathbf{1} \tag{97}$$

Being $\boldsymbol{\varepsilon}_p^{(n)}$ a constant value, the derivative of $\boldsymbol{\varepsilon}_p^{(n+1)}$ with respect to the trial stresses is:

$$\frac{\partial \boldsymbol{\varepsilon}_p^{(n+1)}}{\partial \boldsymbol{\sigma}_{trial}^{(n+1)}} = \frac{\partial \Delta\gamma^{(n+1)}}{\partial \boldsymbol{\sigma}_{trial}^{(n+1)}} \otimes \boldsymbol{n}^{(n+1)} + \Delta\gamma^{(n+1)}\frac{\partial \boldsymbol{n}^{(n+1)}}{\partial \boldsymbol{\sigma}_{trial}^{(n+1)}} \tag{98}$$

Recall that the tangent consistent elasto-plastic tensor is defined as:

$$\mathbb{C}_{ep}^{(n+1)} = \frac{\partial \boldsymbol{\sigma}^{(n+1)}}{\partial \boldsymbol{\varepsilon}^{(n+1)}} = \mathbb{C} - \mathbb{C}\,\frac{\partial \Delta\gamma^{(n+1)}}{\partial \boldsymbol{\varepsilon}^{(n+1)}} \otimes \boldsymbol{n}^{(n+1)} - \Delta\gamma^{(n+1)}\,\mathbb{C}\frac{\partial \boldsymbol{n}^{(n+1)}}{\partial \boldsymbol{\varepsilon}^{(n+1)}} \tag{99}$$

Comparing (98) and (99), it is possible to write:

$$\frac{\partial \boldsymbol{\varepsilon}_p^{(n+1)}}{\partial \boldsymbol{\sigma}_{trial}^{(n+1)}} = \mathbb{C}^{-1}\left[\mathbb{C} - \mathbb{C}_{ep}^{(n+1)}\right]\mathbb{C}^{-1} \tag{100}$$

The second term on the right hand side of (95) is the derivative of $\sigma_{trial}^{(n+1)}$ with respect to $\varepsilon^{(n+1)}$:

$$\boldsymbol{\sigma}_{trial}^{(n+1)} = \mathbb{C} : \left(\boldsymbol{\varepsilon}^{(n+1)} - \boldsymbol{\varepsilon}_p^{(n)}\right) \quad \Rightarrow \quad \frac{\partial \boldsymbol{\sigma}_{trial}^{(n+1)}}{\partial \boldsymbol{\varepsilon}^{(n+1)}} = \mathbb{C} \tag{101}$$

Finally, the derivative expressed in (95) can be computed as:

$$\frac{\partial \boldsymbol{\varepsilon}_p^{(n+1)}}{\partial \boldsymbol{\varepsilon}_h} = \frac{\partial \boldsymbol{\varepsilon}_p^{(n+1)}}{\partial \boldsymbol{\sigma}_{trial}^{(n+1)}}\frac{\partial \boldsymbol{\sigma}_{trial}^{(n+1)}}{\partial \boldsymbol{\varepsilon}_h} = \mathbb{C}^{-1}\left[\mathbb{C} - \mathbb{C}_{ep}^{(n+1)}\right] \tag{102}$$

which provides the algebraic system matrices in (44), (45), (46) and (47).

References

[1] J. Krahn. The 2001 R . M . Hardy Lecture: The limits of limit. *Canadian Geotechnical Journal*, pages 643–660, 2003.

[2] M. Cervera, M. Chiumenti, and D. Di Capua. Benchmarking on bifurcation and localization in J2 plasticity for plane stress and plane strain conditions. *Computer Methods in Applied Mechanics and Engineering*, 241-244:206–224, October 2012.

[3] Y. R. Rashid. Ultimate strength analysis of prestressed concrete pressure vessels. *Nuclear Engineering and Design*, 7(4):334–344, 1968.

[4] A. Needleman. Material rate dependence and mesh sensitivity in localization problems. *Computer Methods in Applied Mechanics and Engineering*, 67(1):69 – 85, 1988.

[5] M. Ortiz, Y. Leroy, and A. Needleman. A finite element method for localized failure analysis. *Computer Methods in Applied Mechanics and Engineering*, 61(2):189–214, 1987.

[6] D. Bigoni and T. Hueckel. Uniqueness and localization-I. associative and non-associative elastoplasticity. *International Journal of Solids and Structures*, 28(2): 197 – 213, 1991.

[7] S. Badia and R. Codina. Unified stabilized finite element formulations for the Stokes and the Darcy problems. *SIAM Journal on Numerical Analysis*, 47(3):1971–2000, 2009.

[8] S. Badia and R. Codina. Stabilized continuous and discontinuous Galerkin techniques for Darcy flow. *Computer Methods in Applied Mechanics and Engineering*, 199:1654–1667, 2010.

[9] A. Masud and T. J. R. Hughes. A stabilized mixed finite element method for darcy flow. *Computer Methods in Applied Mechanics and Engineering*, 191(39):4341–4370, 2002.

[10] K. A. Mardal, X.-C. Tai, and R. Winther. A robust finite element method for darcy–stokes flow. *SIAM Journal on Numerical Analysis*, 40(5):1605–1631, 2002.

[11] K. B. Nakshatrala, D. Z. Turner, K. D. Hjelmstad, and A. Masud. A stabilized mixed finite element method for darcy flow based on a multiscale decomposition of the solution. *Computer Methods in Applied Mechanics and Engineering*, 195(33): 4036–4049, 2006.

[12] M. R. Correa and A. F. D. Loula. Unconditionally stable mixed finite element methods for darcy flow. *Computer Methods in Applied Mechanics and Engineering*, 197(1718): 1525 – 1540, 2008. ISSN 0045-7825.

[13] M. Cervera, M. Chiumenti, Q. Valverde, and C. Agelet de Saracibar. Mixed linear/linear simplicial elements for incompressible elasticity and plasticity. *Computer Methods in Applied Mechanics and Engineering*, 192(49-50):5249–5263, 12 2003.

[14] M. Cervera, M. Chiumenti, and C. Agelet de Saracibar. Shear band localization via local J2 continuum damage mechanics. *Computer Methods in Applied Mechanics and Engineering*, 193(9-11):849–880, March 2004.

[15] M. Cervera, M. Chiumenti, and R. Codina. Mesh objective modeling of cracks using continuous linear strain and displacement interpolations. *International Journal for Numerical Methods in Engineering*, (February):962–987, 2011.

[16] M. Cervera and M. Chiumenti. Size effect and localization in J2 plasticity. *International Journal of Solids and Structures*, 46(17):3301–3312, August 2009.

[17] M. Cervera, M. Chiumenti, and R. Codina. Mixed stabilized finite element methods in nonlinear solid mechanics. Part I: Formulation. *Computer Methods in Applied Mechanics and Engineering*, 199(37-40):2559–2570, August 2010.

[18] M. Cervera, M. Chiumenti, and R. Codina. Mixed stabilized finite element methods in nonlinear solid mechanics. Part II: Strain localization. *Computer Methods in Applied Mechanics and Engineering*, 199(37-40):2571–2589, August 2010.

[19] J. C. Simo and T. J. R. Hughes. *Computational Inelasticity*. Interdisciplinary applied mathematics: Mechanics and materials. Springer New York, 1998.

[20] D. Boffi, F. Brezzi, and M. Fortin. *Mixed Finite Element Methods and Applications*. Springer, 2013 edition, 7 2013. ISBN 9783642365188.

[21] T. J. R. Hughes, G. R. Feijóo, L. Mazzei, and J. B. Quincy. The variational multiscale methoda paradigm for computational mechanics. *Computer Methods in Applied Mechanics and Engineering*, 7825(98), 1998.

[22] R. Codina. Stabilization of incompressibility and convection through orthogonal subscales in finite element methods. *Computer Methods in Applied Mechanics and Engineering*, 190:1579–1599, 2000.

[23] R. Codina and J. Blasco. A finite element formulation for the stokes problem allowing equal velocity-pressure interpolation. *Computer Methods in Applied Mechanics and Engineering*, 143(34):373 – 391, 1997.

[24] R. Codina. Analysis of a stabilized finite element approximation of the oseen equations using orthogonal subscales. *Applied Numerical Mathematics*, 58(3):264 – 283, 2008.

[25] J. C. Simo and R. L. Taylor. Consistent tangent operators for rate-independent elastoplasticity. *Computer Methods in Applied Mechanics and Engineering*, 48(1):101 – 118, 1985.

[26] R. deBorst. Integration of plasticity equations for singular yield functions. *Computers & Structures*, 26(5):823 – 829, 1987. ISSN 0045-7949.

[27] D. Perić and E. A. de Souza Neto. A new computational model for tresca plasticity at finite strains with an optimal parametrization in the principal space. *Computer Methods in Applied Mechanics and Engineering*, 171(34):463 – 489, 1999. ISSN 0045-7825.

[28] S. Pietruszczak and Z. Mróz. Finite element analysis of deformation of strain-softening materials. *International Journal for Numerical Methods in Engineering*, 17(3):327–334, 1981.

[29] M. Cervera, C. Agelet de Saracibar, and M. Chiumenti. *COMET: Coupled Mechanical and Thermal analysis. Data Input Manual, Version 5.0, Technical Report IT-308*. 2002. URL `http://www.cimne.com/comet/`.

This page is left intentionally blank.

High-fidelity prediction of crack formation in 2D and 3D pullout tests

L. Benedetti, M. Cervera and M. Chiumenti

Computers and Structures,
Vol. 172, pp. 93–109, (2016)
http://dx.doi.org/10.1016/j.compstruc.2016.05.001

This page is left intentionally blank.

High-fidelity prediction of crack formation in 2D and 3D pullout tests

Lorenzo Benedetti, Miguel Cervera, Michele Chiumenti
International Center for Numerical Methods in Engineering (CIMNE),
Technical University of Catalonia (UPC), Edificio C1, Campus Norte,
Jordi Girona 1-3, 08034 Barcelona, Spain
Corresponding author: lbenedetti@cimne.upc.edu

Abstract

This paper presents the 2D and 3D numerical analysis of pullout tests on steel anchorages in concrete blocks using standard and mixed finite elements. A novel (stabilized) mixed formulation in the variables of total strain ε and displacements u is introduced to overcome the intrinsic deficiencies of the standard displacement-based one in the context of localization of strains, such as mesh dependency. The quasi-brittle behaviour of concrete is described through an elastoplastic constitutive law with a local Rankine yielding criterion. The proposed formulation is shown to be a reliable and accurate tool, sensitive to the physical parameters of the pullout tests, but objective with respect to the adopted FE mesh. Furthermore, the mixed ε/u finite element is able to capture the correct failure mechanism with relatively coarse discretizations. At the same time, the spurious behavior of the standard formulation is not alleviated by mesh-refinement.

1 Introduction

Concrete is widely used in the context of civil structures, and yet, it is a rather complex material. Having an inherent internal heterogeneity and reacting to environmental conditions makes the post-peak non-linear behavior and the subsequent failure very difficult to predict, if not impossible. Then, it is clear the key role of experimental tests in the context of concrete structures reliability. Within the extensive literature in the field, one can recall L-shaped panels tests by Winkler et al. [1], wedge splitting by Trunk [2], single edge notched beams by Guinea et al. [3], Gálvez et al. [4], mixed mode fracture tests by Nooru-Mohamed [5], Ballatore et al. [6] and indentation tests by Berenbaum and Brodie [7].

In this work, the pullout test is addressed, being one of the most interesting experimental techniques to evaluate the strength of concrete and the overall behavior of embedded anchorages. First accounts of the pullout test come from Abrams [8] and Slater et al. [9]. Later, Elfgren et al. [10] and Peier [11] introduced numerical modeling as a validation of the experimental procedure. While the laboratory setup can be easily reproduced, the test outcomes are strictly dependent on the choice of various parameters as the mechanical properties of the employed materials, the size of specimens and the anchorage embed depth. The influential works of Eligehausen and Sawade [12], Bažant et al. [13], Ožbolt et al. [14], Karihaloo [15] emphasized the structural size effect on the pullout test and its influence on the energy dissipated in the cracking process. Most recent advances are related to the possibility of testing the coupling between FRP composites and concrete [16, 17]. Hereafter, the attention will be focused on the reported experiments from Dejori [18], Thenier and Hofstetter [19] for the 2D case, whereas the work by Gasser and Holzapfel [20], Areias and Belytschko [21] will be considered for the 3D case.

The methodology used to assess physical properties of specimens during a test is as critical as the details that characterize the particular experiment. Slight changes in the application of a load or in the supporting system can affect severely the results without a clear explanation. Permutating over multiple experimental settings can help to understand better the numerous variables involved, but, in reality, not all combinations are possible, due to limitations in controlling the test bench as well as time and cost restrictions. Hence, it is in this framework that numerical simulations play a fundamental role for the prediction and the possible improvement of experiments.

Recently, the authors presented a general purpose finite element technology for compressible and incompressible plasticity [22], which has successfully tackled geotechnical problems [23]. The proposed mixed strain-displacement (ε/u) formulation has been applied to local constitutive models in plasticity, in the framework of the smeared crack approach [24]. In problems involving strain-localization, standard finite elements present numerous limitations, being affected by spurious mesh-biased dependence and stress locking. In such cases, the sensibility required to evaluate the change of results with respect to diverse boundary conditions can be overshadowed by the lack of precision in the inelastic range of classical displacement-based finite elements. On the contrary, the mixed ε/u finite element formulation is capable to overcome these issues, predicting effectively the peak load, the failure mechanism and the localization bands. The method is also free from any mesh dependence and it does not require any additional tracking technique. This is a substantial clinching feat, as, leaving out theoretical qualms and from the factual point of view, local crack tracking procedures are very difficult to implement in 3D and global methods cannot deal with crack branching.

Taking advantage of its reliability, the proposed method is applied in this work to the pullout problem, using 2D and 3D elements with linear interpolations of both the displacement and total strain fields. In previous works [25, 26, 27], the formulation has been used in the context of isotropic damage models. In this work, though, a plasticity model based on the Rankine failure criterion is used, similarly to those used in references [20, 28, 29, 30, 31]. Furthermore, plasticity with strain softening has been proved to be able to reproduce structural size-effect in a wide range of scales and, particularly, in engineering-size problems [25].

The objective of the paper is proving that the use of an appropriate finite element technology is crucial for the study of the experimental setting and for the assessment of the results, even in the case of a very well known application, as the pullout test is. The outline of the paper is as follows. First,

the displacement-based and the mixed strain-displacement formulations are introduced. Then, the plasticity constitutive model is presented and the Rankine yielding criterion is extended in the case of multi-axial loading condition. A regularization of the singular points, useful to avoid indetermination issues in the return mapping algorithm, is shown. Finally, numerical simulations of 2D and 3D pullout tests are presented: standard and mixed finite element analyses are compared, demonstrating both the sensibility to changes on the boundary conditions and the replication of experiments. The results show that the mixed ε/u finite element provides reliable and high quality outcomes when compared to the standard irreducible formulation.

2 Governing equations

A solid body $\mathscr{B}$ occupying the space domain Ω is described by the position X of each point with respect to a system of coordinates x, y, z.

On the one hand, every point of such domain has a displacement $\boldsymbol{u}$ and a total strain $\boldsymbol{\varepsilon}$. Both displacements and strains are considered small. The compatibility condition relates both fields as:

$$-\boldsymbol{\varepsilon} + \boldsymbol{\nabla}^s \boldsymbol{u} = \boldsymbol{0} \tag{1}$$

where $\boldsymbol{\nabla}^s(\cdot)$ is used to denote the symmetric gradient operator. On the other hand, the equilibrium of forces in (quasi-)static conditions states that:

$$\boldsymbol{\nabla} \cdot \boldsymbol{\sigma} + \boldsymbol{f} = \boldsymbol{0} \tag{2}$$

where $\boldsymbol{\sigma}$ is the Cauchy stress tensor and $\boldsymbol{f}$ are the external forces applied to the body. The symbol $\boldsymbol{\nabla} \cdot (\cdot)$ refers to the divergence operator. The total strain $\boldsymbol{\varepsilon}$ is decomposed additively in the elastic $\boldsymbol{\varepsilon}_e$ and the plastic $\boldsymbol{\varepsilon}_p$ parts. The link between Cauchy's stress and the total strain is given by the constitutive law:

$$\boldsymbol{\sigma} = \mathbb{C} : \boldsymbol{\varepsilon}_e = \mathbb{C} : (\boldsymbol{\varepsilon} - \boldsymbol{\varepsilon}_p) \tag{3}$$

where $\mathbb{C}$ is the fourth order elastic constitutive tensor. Recalling Equations (1) and (2), the problem reads:

$$\begin{aligned} -\boldsymbol{\varepsilon} + \boldsymbol{\nabla}^s \boldsymbol{u} &= \boldsymbol{0} \\ \boldsymbol{\nabla} \cdot [\mathbb{C} : (\boldsymbol{\varepsilon} - \boldsymbol{\varepsilon}_p)] + \boldsymbol{f} &= \boldsymbol{0} \end{aligned} \tag{4}$$

This set of equations represents the strong form for the mixed problem involving the unknown fields of displacements $\boldsymbol{u}$ and total strains $\boldsymbol{\varepsilon}$ in the case of plasticity. In order to obtain a symmetric system, the first equation is pre-multiplied by the elastic constitutive tensor $\mathbb{C}$:

$$\begin{aligned} -\mathbb{C} : \boldsymbol{\varepsilon} + \mathbb{C} : \boldsymbol{\nabla}^s \boldsymbol{u} &= \boldsymbol{0} \\ \boldsymbol{\nabla} \cdot [\mathbb{C} : (\boldsymbol{\varepsilon} - \boldsymbol{\varepsilon}_p)] + \boldsymbol{f} &= \boldsymbol{0} \end{aligned} \tag{5}$$

The irreducible problem, in terms of the displacement field $\boldsymbol{u}$ only, is recovered substituing the first equation into the second, to yield:

$$\boldsymbol{\nabla} \cdot [\mathbb{C} : (\boldsymbol{\nabla}^s \boldsymbol{u} - \boldsymbol{\varepsilon}_p)] + \boldsymbol{f} = \boldsymbol{0} \tag{6}$$

With proper conditions on the boundary $\partial\Omega$ and evolution laws for the plastic strain field [32], both irreducible and mixed formulations provide a well posed boundary value problem.

3 Irreducible finite elements

Recalling the strong form in Equation (6), the corresponding weak problem can be written as:

$$\int_\Omega \boldsymbol{v} \cdot (\boldsymbol{\nabla} \cdot [\mathbb{C} : (\boldsymbol{\nabla}^s \boldsymbol{u} - \boldsymbol{\varepsilon}_p)]) + \int_\Omega \boldsymbol{v} \cdot \boldsymbol{f} = 0 \qquad \forall v \in \mathbb{V} \tag{7}$$

where $\mathbb{V}$ is the space of test functions which are square integrable. Integrating by parts, the forcing terms can be extracted as:

$$\int_\Omega \boldsymbol{\nabla}^s \boldsymbol{v} : \mathbb{C} : (\boldsymbol{\nabla}^s \boldsymbol{u} - \boldsymbol{\varepsilon}_p) = F(\boldsymbol{v}) \tag{8}$$

where the boundary terms accounting for body forces $\boldsymbol{f}$ on Ω and tractions $\boldsymbol{t}$ on the boundary $\partial\Omega$ are collected in the term

$$F(\boldsymbol{v}) = \int_\Omega \boldsymbol{v} \cdot \boldsymbol{f} + \int_{\partial\Omega} \boldsymbol{v} \cdot \boldsymbol{t} \tag{9}$$

The discretized version of Equation (8) is obtained by selecting a finite set of interpolation functions for the displacement field as well as the test function as:

$$\boldsymbol{u} \to \boldsymbol{u}_h = \sum_{i=1}^{n_{pts}} \boldsymbol{v}_h^{(i)} \boldsymbol{u}_h^{(i)} \qquad \boldsymbol{v}_h \in \mathbb{V}_h \tag{10}$$

such that the discrete functional space $\mathbb{V}_h$ is a subset of the continuous version $\mathbb{V} \subseteq H^1(\Omega)^{dim}$. From Equation (8), the final discrete system of equations reads:

$$\int_\Omega \boldsymbol{\nabla}^s \boldsymbol{v}_h : \mathbb{C} : (\boldsymbol{\nabla}^s \boldsymbol{u}_h - \boldsymbol{\varepsilon}_p) = F(\boldsymbol{v}_h) \tag{11}$$

For the standard finite element interpolation, linear triangles P1 and quadrilateral Q1 are considered in this work.

4 Mixed $\boldsymbol{\varepsilon} - \boldsymbol{u}$ finite elements

4.1 Galerkin method

The weak form of the set of equations in (5) is:

$$\begin{aligned} -\int_\Omega \boldsymbol{\gamma} : \mathbb{C} : \boldsymbol{\varepsilon} + \int_\Omega \boldsymbol{\gamma} : \mathbb{C} : \boldsymbol{\nabla}^s \boldsymbol{u} = 0 \quad & \forall \boldsymbol{\gamma} \in \mathbb{G} \\ \int_\Omega \boldsymbol{v} \cdot (\boldsymbol{\nabla} \cdot \boldsymbol{\sigma}) + \int_\Omega \boldsymbol{v} \cdot \boldsymbol{f} = 0 \quad & \forall \boldsymbol{v} \in \mathbb{V} \end{aligned} \tag{12}$$

In this case, besides the functional space $\mathbb{V}$ for the test functions $\boldsymbol{v}$ of the displacement field $\boldsymbol{u}$, it is required to introduce the set of test function tensors for the strain $\boldsymbol{\varepsilon}$ pertaining to $\mathbb{G}$. Integrating by parts the second equation, it can be written:

$$\begin{aligned} -\int_\Omega \boldsymbol{\gamma} : \mathbb{C} : \boldsymbol{\varepsilon} + \int_\Omega \boldsymbol{\gamma} : \mathbb{C} : \boldsymbol{\nabla}^s \boldsymbol{u} = 0 \quad & \forall \boldsymbol{\gamma} \in \mathbb{G} \\ \int_\Omega \boldsymbol{\nabla}^{\boldsymbol{s}} \boldsymbol{v} : \boldsymbol{\sigma} = F(\boldsymbol{v}) \quad & \forall \boldsymbol{v} \in \mathbb{V} \end{aligned} \tag{13}$$

From the mathematical requirements of the problem, $\mathbb{V}$ is in the space of square integrable functions $\boldsymbol{v}$ which are at least square integrable and have square integrable first derivative, whereas $\mathbb{G}$ belongs to the set of square integrable symmetric tensors $\boldsymbol{\gamma}$.

The discretized version of the weak form in Equation (13) is obtained by approximating the strain tensor $\boldsymbol{\varepsilon}$ and the displacement field $\boldsymbol{u}$ as

$$\begin{aligned} \boldsymbol{\varepsilon} \to \boldsymbol{\varepsilon}_h = \sum_{i=1}^{n_{pts}} \boldsymbol{\gamma}_h^{(i)} \boldsymbol{\varepsilon}_h^{(i)} \quad & \boldsymbol{\gamma}_h \in \mathbb{G}_h \\ \boldsymbol{u} \to \boldsymbol{u}_h = \sum_{i=1}^{n_{pts}} \boldsymbol{v}_h^{(i)} \boldsymbol{u}_h^{(i)} \quad & \boldsymbol{v}_h \in \mathbb{V}_h \end{aligned} \tag{14}$$

The system of equations (13), in its discrete form, reads

$$
\begin{aligned}
&-\int_{\Omega} \boldsymbol{\gamma}_h : \mathbb{C} : \boldsymbol{\varepsilon}_h + \int_{\Omega} \boldsymbol{\gamma}_h : \mathbb{C} : \boldsymbol{\nabla}^s \boldsymbol{u}_h = 0 \quad \forall \boldsymbol{\gamma}_h \in \mathbb{G}_h \\
&\int_{\Omega} \boldsymbol{\nabla}^s \boldsymbol{v}_h : \boldsymbol{\sigma} = F(\boldsymbol{v}_h) \quad \forall \boldsymbol{v}_h \in \mathbb{V}_h
\end{aligned}
\tag{15}
$$

For the mixed finite element method, equal interpolation finite element spaces for displacements and strains are considered in this work, and, in particular, the case of linear and bilinear interpolations, i.e. P1P1 and Q1Q1 elements. However, the stability of a discrete mixed formulation derived by the Galerkin method depends from the choice of the finite element spaces $\mathbb{G}_h$ and $\mathbb{V}_h$ as stated by the *Inf-Sup condition* [33]. Using equal order of interpolation does not satisfy the previous condition; consequently, a Variational Multiscale Stabilization procedure is now introduced.

4.2 Variational Multiscale Stabilization

The Variational Multiscale Stabilization was developed in first instance by Hughes et al. [34] and then generalized by Codina [35]. This technique modifies appropriately the variational form of the problem in order to provide the required numerical stability (see Benedetti et al. [23], Cervera et al. [26], Badia and Codina [36], Codina [37] for details).

The stabilization procedure decomposes the solution of fields $(\boldsymbol{\varepsilon}, u)$ into a resolvable scale $(\boldsymbol{\varepsilon}_h, \boldsymbol{u}_h)$, calculated on the FEM mesh, and an irresolvable one $(\tilde{\boldsymbol{\varepsilon}}, \tilde{\boldsymbol{u}})$, proper of a finer scale:

$$
\begin{aligned}
\boldsymbol{\varepsilon} &= \boldsymbol{\varepsilon}_h + \tilde{\boldsymbol{\varepsilon}} \\
\boldsymbol{u} &= \boldsymbol{u}_h + \tilde{\boldsymbol{u}}
\end{aligned}
\tag{16}
$$

The fine scale variables (also known as subscale variables) and their test functions pertain to their respective functional spaces $\tilde{\mathbb{G}}$ for the strain subscale and $\tilde{\mathbb{V}}$ for the displacement subscale. This decomposition allows to consider extended solution spaces given by $\mathbb{G} \approx \mathbb{G}_h \oplus \tilde{\mathbb{G}}$ and $\mathbb{V} \approx \mathbb{V}_h \oplus \tilde{\mathbb{V}}$. The subscale part $(\tilde{\boldsymbol{\varepsilon}}, \tilde{\boldsymbol{u}})$ can be thought as a high frequency solution that cannot be captured by the FEM mesh.

Rewriting the set of equations within this enhanced functional setting, the solution of the subscale variables depends on the residuals of the strong form of the equations upon substitution of the FEM solution. Defining $\boldsymbol{R}_{1,h}$ and $\boldsymbol{R}_{2,h}$ as the residuals of the strong form equations as:

$$
\begin{aligned}
\boldsymbol{R}_{1,h} &= -\mathbb{C} : \boldsymbol{\varepsilon}_h + \mathbb{C} : \boldsymbol{\nabla}^s \boldsymbol{u}_h \\
\boldsymbol{R}_{2,h} &= \boldsymbol{\nabla} \cdot \boldsymbol{\sigma}_h + \boldsymbol{f}
\end{aligned}
\tag{17}
$$

it is possible to approximate the subscale variables within each element as done in the work of Codina [35] with the projection of the residuals on the mesh grid:

$$
\begin{aligned}
\tilde{\boldsymbol{\varepsilon}} &= \tau_{\boldsymbol{\varepsilon}} \, \mathbb{C}^{-1} : \tilde{P}_1 (\boldsymbol{R}_{1,h}) \\
\tilde{\boldsymbol{u}} &= \tau_u \, \tilde{P}_2 (\boldsymbol{R}_{2,h})
\end{aligned}
\tag{18}
$$

where $\tilde{P}_1$ and $\tilde{P}_2$ represent the projection operators. τ_u and $\tau_{\boldsymbol{\varepsilon}}$ are the stabilization parameters computed as:

$$
\tau_u = c_u \frac{h L_0}{E} \quad \text{and} \quad \tau_{\boldsymbol{\varepsilon}} = c_{\boldsymbol{\varepsilon}} \frac{h}{L_0}
\tag{19}
$$

In the last expression, c_u and $c_{\boldsymbol{\varepsilon}}$ are arbitrary positive numbers; E is the Young's modulus, being the mechanical parameter of the problem; h is the representative size of the finite element mesh and L_0 is a characteristic length of the problem. To complete the stabilization method, an appropriate projection operator has to be selected in order to be able to compute the subscale variables.

4.2.1 OSGS stabilization

In the Orthogonal Subgrid Scale stabilization [36], the projection operator selected to solve the unresolvable scale variables is the orthogonal projector

$$\tilde{P}\left(\boldsymbol{X}\right) = \tilde{P}_h^{\perp}\left(\boldsymbol{X}\right) = I\left(\boldsymbol{X}\right) - P_h\left(\boldsymbol{X}\right) \tag{20}$$

where P_h represents the projection over the finite element mesh. It represents the L^2 projection of $\boldsymbol{X}$, or *least square fitting*, on the finite element space [38] and it is performed taking advantage of the orthogonality condition

$$\int_\Omega \boldsymbol{\eta}_h : \left(\boldsymbol{X}_\Pi - \boldsymbol{X}\right) = 0 \quad \forall \boldsymbol{\eta}_h \in \mathbb{V}_h \text{ or } \mathbb{G}_h \tag{21}$$

where $\boldsymbol{X}_\Pi$ is the projected value of $\boldsymbol{X}$ on the mesh nodes. Substituting in (18), the subscale variables $\tilde{\boldsymbol{u}}$ and $\tilde{\boldsymbol{\varepsilon}}$ can be approximated as:

$$\begin{aligned} \tilde{\boldsymbol{\varepsilon}} &= \tau_{\boldsymbol{\varepsilon}}\, \mathbb{C}^{-1} : \left[\boldsymbol{R}_{1,h} - P_h\left(\boldsymbol{R}_{1,h}\right)\right] \\ \tilde{\boldsymbol{u}} &= \tau_u\, \left[\boldsymbol{R}_{2,h} - P_h\left(\boldsymbol{R}_{2,h}\right)\right] \end{aligned} \tag{22}$$

with the residuals $\boldsymbol{R}_{1,h}, \boldsymbol{R}_{2,h}$ defined in (17). Back-substituting in the set of equations of the problem, the final set of equations is:

$$\begin{aligned} &-\left(1-\tau_{\boldsymbol{\varepsilon}}\right)\int_\Omega \boldsymbol{\gamma}_h : \mathbb{C} : \left(\boldsymbol{\varepsilon}_h - \boldsymbol{\nabla}^s \boldsymbol{u}_h\right) + \\ &\qquad -\tau_u \int_\Omega \left[\boldsymbol{\nabla}\cdot\left(\mathbb{C} : \boldsymbol{\gamma}_h\right)\right]\cdot\left[\boldsymbol{\nabla}\cdot\boldsymbol{\sigma}_h - P_h\left(\boldsymbol{\nabla}\cdot\boldsymbol{\sigma}_h\right)\right] = \boldsymbol{0} \quad \forall \boldsymbol{\gamma}_h \in \mathbb{G}_h \\ &\int_\Omega \boldsymbol{\nabla}^s \boldsymbol{v}_h : \mathbb{C} : \left(\boldsymbol{\varepsilon}_{stab} - \boldsymbol{\varepsilon}_p\right) = F(\boldsymbol{v}_h) \quad \forall \boldsymbol{v}_h \in \mathbb{V}_h \end{aligned} \tag{23}$$

In order to compute the projection of stresses at each time step, expression (21) is recalled to write

$$\int_\Omega \boldsymbol{\eta}_h : \left(\boldsymbol{\Pi}_{\boldsymbol{\sigma}} - \boldsymbol{\nabla}\cdot\boldsymbol{\sigma}_h\right) = 0 \quad \forall \boldsymbol{\eta}_h \in \mathbb{G}_h \tag{24}$$

and, with the additional projection equation, it reads:

$$\begin{aligned} &-\left(1-\tau_{\boldsymbol{\varepsilon}}\right)\int_\Omega \boldsymbol{\gamma}_h : \mathbb{C} : \left(\boldsymbol{\varepsilon}_h - \boldsymbol{\nabla}^s \boldsymbol{u}_h\right) \\ &\qquad -\tau_u \int_\Omega \left[\boldsymbol{\nabla}\cdot\left(\mathbb{C} : \boldsymbol{\gamma}_h\right)\right]\cdot\left[\boldsymbol{\nabla}\cdot\boldsymbol{\sigma}_h - \boldsymbol{\Pi}_{\boldsymbol{\sigma}}\right] = \boldsymbol{0} \quad \forall \boldsymbol{\gamma}_h \in \mathbb{G}_h \\ &\int_\Omega \boldsymbol{\nabla}^s \boldsymbol{v}_h : \mathbb{C} : \left[\boldsymbol{\varepsilon}_{stab} - \boldsymbol{\varepsilon}_p\right] = F(\boldsymbol{v}_h) \quad \forall \boldsymbol{v}_h \in \mathbb{V}_h \\ &\int_\Omega \boldsymbol{\eta}_h : \left(\boldsymbol{\Pi}_{\boldsymbol{\sigma}} - \boldsymbol{\nabla}\cdot\boldsymbol{\sigma}_h\right) = 0 \quad \forall \boldsymbol{\eta}_h \in \mathbb{G}_h \end{aligned} \tag{25}$$

4.2.2 ASGS stabilization

In the Algebraic Subgrid Scale stabilization method [36], the projection operator is taken as the identity, that is, $\tilde{P}\left(\boldsymbol{X}\right) = I\left(\boldsymbol{X}\right)$:

$$\begin{aligned} \tilde{\boldsymbol{\varepsilon}} &= \tau_{\boldsymbol{\varepsilon}}\left(-\boldsymbol{\varepsilon}_h + \boldsymbol{\nabla}^s \boldsymbol{u}_h\right) \\ \tilde{\boldsymbol{u}} &= \tau_u\left(\boldsymbol{\nabla}\cdot\boldsymbol{\sigma}_h + \boldsymbol{f}\right) \end{aligned} \tag{26}$$

Substituting in Equation (16) and then in the set of equations (15) and rearranging, the final system of equations reads:

$$\begin{aligned} -\left(1-\tau_{\boldsymbol{\varepsilon}}\right)\int_{\Omega}\boldsymbol{\gamma}_h : \mathbb{C} : \left(\boldsymbol{\varepsilon}_h - \boldsymbol{\nabla}^s \boldsymbol{u}_h\right) \\ -\tau_u \int_{\Omega}\left[\boldsymbol{\nabla}\cdot\left(\mathbb{C}:\boldsymbol{\gamma}_h\right)\right]\cdot\left[\boldsymbol{\nabla}\cdot\boldsymbol{\sigma}_h + f\right] = 0 \quad \forall \boldsymbol{\gamma}_h \in \mathbb{G}_h \\ \int_{\Omega}\boldsymbol{\nabla}^s \boldsymbol{v}_h : \mathbb{C} : \left[\left(1-\tau_{\boldsymbol{\varepsilon}}\right)\boldsymbol{\varepsilon}_h + \tau_{\boldsymbol{\varepsilon}}\boldsymbol{\nabla}^s \boldsymbol{u}_h - \boldsymbol{\varepsilon}_p\right] = F(v_h) \quad \forall v_h \in \mathbb{V}_h \end{aligned} \tag{27}$$

The first term in the first equation represents a projection (smoothing) of the strain field obtained by differentiation of the discrete displacement field. This is exactly the same projection operator presented in Equation (21). The second additional term is given by the displacement subscale that, in turn, depends on the residual of the strong form of the equilibrium equation. The second equation is related to the balance of momentum. The set of equations with OSGS stabilization resembles the one for the ASGS, except for the second term in the first equation: in fact the Orthogonal Subgrid Stabilization scheme is less diffusive than the Algebraic one [39]. However, this comes at the price of solving an additional equation; in the implementation details it is shown how this problem can be circumvented.

5 Implementation

Both in the standard and the mixed formulations, the presence of the non-linear plastic strains $\boldsymbol{\varepsilon}_p = \boldsymbol{\varepsilon}_p\left(\sigma\right)$ requires an iterative procedure to deal with the nonlinearity of the system. One of these schemes is the Newton-Raphson method, which ensures quadratic convergence for convex functions. In addition, constitutive laws involving plasticity are usually written in terms of rate equations and, consequently, the tangent matrices are involved in the resulting algebraic set of equations. Consider the nonlinear multidimensional-multivariable problem

$$\boldsymbol{F}\left(\boldsymbol{X}\right) = 0 \tag{28}$$

where $\boldsymbol{X}$ is the unknown. A non-linear problem of this kind can be solved starting from a Taylor approximation around the solution point at iteration $i+1$ in a particular time step $n+1$:

$$\boldsymbol{F}_{n+1}^{i+1} \approx \boldsymbol{F}_{n+1}^{i} + \boldsymbol{J}_{n+1}^{i}\,\delta\boldsymbol{X}^{i+1} \tag{29}$$

where the Jacobian matrix $\boldsymbol{J}$ is defined as

$$\boldsymbol{J} = \frac{\partial \boldsymbol{F}}{\partial \boldsymbol{X}} \tag{30}$$

Assuming that $\boldsymbol{F}_{n+1}^{i+1} = 0$, an iterative correction is computed as

$$\delta\boldsymbol{X}^{i+1} = -\left[\boldsymbol{J}_{n+1}^{i}\right]^{-1}\boldsymbol{F}_{n+1}^{i} \tag{31}$$

and the solution vector is updated as

$$\boldsymbol{X}^{i+1} = \boldsymbol{X}^{i} + \delta\boldsymbol{X}^{i+1} \tag{32}$$

In the irreducible formulation, the unknown vector $\boldsymbol{X}$ corresponds to the displacement field $\boldsymbol{u}$. The Jacobian matrix can be found by differentiating the set of equation with respect to the unknowns variable $\boldsymbol{u}$ at iteration i. In particular, it is possible to write the algebraic set of equations necessary to find the correction $\delta\boldsymbol{u}$ at the iteration $i+1$ as:

$$\boldsymbol{K}_{t,n+1}^{i}\delta\boldsymbol{u}_{n+1}^{i+1} = \boldsymbol{F}_{n+1}^{i} \tag{33}$$

where $\boldsymbol{F}$ is the residual force and the tangent stiffness matrix $\boldsymbol{K}_t$ is defined as

$$\boldsymbol{K}_t^i = \boldsymbol{B}^T \mathbb{C}_{ep}^i \boldsymbol{B} \tag{34}$$

being $\boldsymbol{B}$ the discrete gradient of shape functions and $\mathbb{C}_{ep}^i$ the algorithmic consistent elastoplastic constitutive tensor at iteration i.

Akin to the irreducible FEM implementation, the mixed finite element problem considers the unknown variable as $\boldsymbol{X} = [\boldsymbol{\varepsilon}, \boldsymbol{u}]^T$. The algebraic system of equations the case of the OSGS implementation is given by

$$-\left[\begin{array}{ccc} \boldsymbol{M}_\tau & \boldsymbol{G}_\tau & \boldsymbol{D}_\Pi^T \\ \boldsymbol{D}_\tau & \boldsymbol{K}_\tau & \boldsymbol{0} \\ \boldsymbol{D}_\Pi & \boldsymbol{0} & \boldsymbol{M}_\Pi \end{array}\right]_{n+1}^{i} \left[\begin{array}{c} \delta\boldsymbol{\varepsilon}_h \\ \delta\boldsymbol{u}_h \\ \delta\boldsymbol{\Pi}_h \end{array}\right]_{n+1}^{i+1} = \left[\begin{array}{c} R_{1,h} \\ R_{2,h} \\ R_{3,h} \end{array}\right]_{n+1}^{i} \tag{35}$$

where $(\delta\boldsymbol{\varepsilon}_h, \delta\boldsymbol{u}_h, \delta\boldsymbol{\Pi}_h)$ are the iterative corrections for $(\boldsymbol{\varepsilon}_h, \boldsymbol{u}_h, \boldsymbol{\Pi}_h)$ in the Newton-Raphson scheme. In the previous expression, $\boldsymbol{M}$ represents a mass-like projection matrix, $\boldsymbol{G}$ a gradient matrix, $\boldsymbol{D}$ a divergence matrix and $\boldsymbol{K}$ a stiffness matrix. The subscript τ refers to the fact that those matrices incorporate stabilization terms. Differentiating (25), within the hypothesis of plastic strain depending only on $\boldsymbol{\varepsilon}_h$, the previous matrices read:

$$\boldsymbol{M}_\tau = -\left(1 - \tau_{\boldsymbol{\varepsilon}}\right) \int_\Omega \boldsymbol{N}_{\boldsymbol{\varepsilon}}{}^T \mathbb{C}\, \boldsymbol{N}_{\boldsymbol{\varepsilon}} - \tau_u \int_\Omega \mathbb{C}\, \boldsymbol{B}\boldsymbol{B}^T\, \mathbb{C}_{ep}^{n+1} \tag{36}$$

$$\boldsymbol{G}_\tau = \left(1 - \tau_{\boldsymbol{\varepsilon}}\right) \int_\Omega \boldsymbol{N}_{\boldsymbol{\varepsilon}}{}^T \mathbb{C}\, \boldsymbol{B} \tag{37}$$

$$\boldsymbol{D}_\tau = \int_\Omega \boldsymbol{B}^T \left[\mathbb{C}_{ep}^{n+1} - \tau_{\boldsymbol{\varepsilon}} \mathbb{C}\right] \boldsymbol{N}_{\boldsymbol{u}} \tag{38}$$

$$\boldsymbol{K}_\tau = \tau_{\boldsymbol{\varepsilon}} \int_\Omega \boldsymbol{B}^T \mathbb{C}\, \boldsymbol{B} \tag{39}$$

where $\boldsymbol{N}_{\boldsymbol{\varepsilon}}$ and $\boldsymbol{N}_{\boldsymbol{u}}$ are the matrices of shape functions of the respective strain and displacement fields and $\boldsymbol{B}$ is the matrix of the gradient of those shape functions. The added projection matrices are computed as:

$$\boldsymbol{M}_{\boldsymbol{\Pi}} = -\int_\Omega \boldsymbol{N}_{\boldsymbol{\varepsilon}}{}^T \boldsymbol{N}_{\boldsymbol{\varepsilon}} \tag{40}$$

$$\boldsymbol{D}_{\boldsymbol{\Pi}} = \int_\Omega \boldsymbol{B}^T \boldsymbol{N}_{\boldsymbol{\varepsilon}} \tag{41}$$

Note that the resulting algebraic system of equations is, in general, not symmetric. However, disregarding the terms due to plasticity, the system matrix is symmetric and it coincides with the one presented in Cervera et al. [26, 40]. In order to reduce computational costs, the following approximation can be considered:

$$\boldsymbol{\Pi}_{\boldsymbol{\sigma}}^{n+1} = P_h^\perp \left(\boldsymbol{\nabla} \cdot \boldsymbol{\sigma}_h^{n+1}\right) \approx P_h^\perp \left(\boldsymbol{\nabla} \cdot \boldsymbol{\sigma}_h^{n}\right) \tag{42}$$

which can be computed at the beginning of time step $n+1$.

Instead, in the case of the ASGS method, the last algebraic equation is automatically verified and the Jacobian matrix presents the mathematical structure:

$$\boldsymbol{J}_{n+1}^i = \left[\begin{array}{cc} \boldsymbol{M}_\tau & \boldsymbol{G}_\tau \\ \boldsymbol{D}_\tau & \boldsymbol{K}_\tau \end{array}\right]_{n+1}^{i} \tag{43}$$

Matrices $\boldsymbol{M}_\tau, \boldsymbol{G}_\tau, \boldsymbol{D}_\tau, \boldsymbol{K}_\tau$ are the same in both the presented methods. Details on the differentiation of the plastic strain tensor $\boldsymbol{\varepsilon}_p$ with respect to the problem unknown $\boldsymbol{\varepsilon}_h$ are given in the work by Benedetti et al. [23].

6 Rankine plasticity model

The Rankine yielding criterion is defined by taking the i-th principal stress, denoted with σ^i, and comparing it to the threshold limit stress $r(\xi)$:

$$f(\boldsymbol{\sigma}, q) = \sigma^i - r(\xi) \tag{44}$$

where $r(\xi)$ is

$$r(\xi) = \sigma_y - q(\xi) \tag{45}$$

being σ_y the uniaxial yielding value of stresses and $q(\xi)$ the hardening/softening function. In plasticity, the Cauchy's stress tensor is defined as:

$$\boldsymbol{\sigma} = \mathbb{C} : \boldsymbol{\varepsilon}_e = \mathbb{C} : (\boldsymbol{\varepsilon} - \boldsymbol{\varepsilon}_p) \tag{46}$$

where the total strain tensor $\boldsymbol{\varepsilon}$ can be split in elastic strain $\boldsymbol{\varepsilon}_e$ and plastic strain $\boldsymbol{\varepsilon}_p$. The plastic strain-like database is composed of the tensor $\boldsymbol{\varepsilon}_p$ and the isotropic hardening strain-like variable ξ. The evolution equations, also known as flow rule, are defined as:

$$\begin{cases} \dot{\boldsymbol{\varepsilon}}_p = \dot{\gamma} \dfrac{\partial g(\boldsymbol{\sigma}, q)}{\partial \boldsymbol{\sigma}} \\ \\ \dot{\xi} = \dot{\gamma} \dfrac{\partial g(\boldsymbol{\sigma}, q)}{\partial q} \end{cases} \tag{47}$$

where $\dot{\gamma}$ is the plastic multiplier and the function $g(\boldsymbol{\sigma}, q)$ represents the plastic potential. In associated plasticity, the plastic potential corresponds with the yielding function $f(\boldsymbol{\sigma}, q)$.

Such definition of the plastic flow gives to the inelastic deformation a directional character by construction. In the case of the Rankine model, the behavior is orthotropic, as the plastic strain depends on the stress eigenvalues. This is in contrast with isotropic continuum damage models, where the effective stress tensor is scaled isotropically, affecting all eigenvalues in the same manner. There exist also orthotropic damage models (see, for instance, Ju [41], Meschke et al. [42], Berto et al. [43], Rizzi and Carol [44], Pelà et al. [45]), closely related to the classical smeared crack models [24, 46, 47, 48, 49] but they are seldom used in practice, being extremely prone to severe stress-locking. In this respect, the mixed formulation can also be used advantageously with these latter models.

In the Haig-Westergaard space, the Rankine criterion appears as the intersection of three planes in the first octant, where $\sigma^1, \sigma^2, \sigma^3$ are positive (Figure 1). The yielding surface loci are also described by the following conditions:

$$\begin{aligned} &\text{Faces: } \sigma^1 = r(\xi) \text{ or } \sigma^2 = r(\xi) \text{ or } \sigma^3 = r(\xi) \\ &\text{Edges: } \sigma^1 = \sigma^2 = r(\xi) \text{ or } \sigma^2 = \sigma^3 = r(\xi) \text{ or } \sigma^1 = \sigma^3 = r(\xi) \\ &\text{Apex: } \sigma^1 = \sigma^2 = \sigma^3 = r(\xi) \end{aligned} \tag{48}$$

The edges and apex are singular cases that require special treatment, to avoid ill-definition of the flow direction in the case of associated plasticity [50]. One possibility to circumvent this problem is to smooth the domain in the vicinity of the corners [51, 52].

The sharp edges are regularized with a quarter of cylindrical surface whereas the apex with an eighth of a sphere. In this way, it is possible to join up the three faces in a unique surface, whose radii are expressed as fraction $c \in [0, 1]$ of the uniaxial threshold:

$$\rho(c, q(\xi)) = c(\sigma_y - q(\xi)) \tag{49}$$

The Extended Rankine yielding criterion is defined as:

$$f(c, \boldsymbol{\sigma}, q(\xi)) = \sqrt{\langle f_1(c, \boldsymbol{\sigma}, q(\xi))\rangle^2 + \langle f_2(c, \boldsymbol{\sigma}, q(\xi))\rangle^2 + \langle f_3(c, \boldsymbol{\sigma}, q(\xi))\rangle^2} - \rho(c, q(\xi)) \tag{50}$$

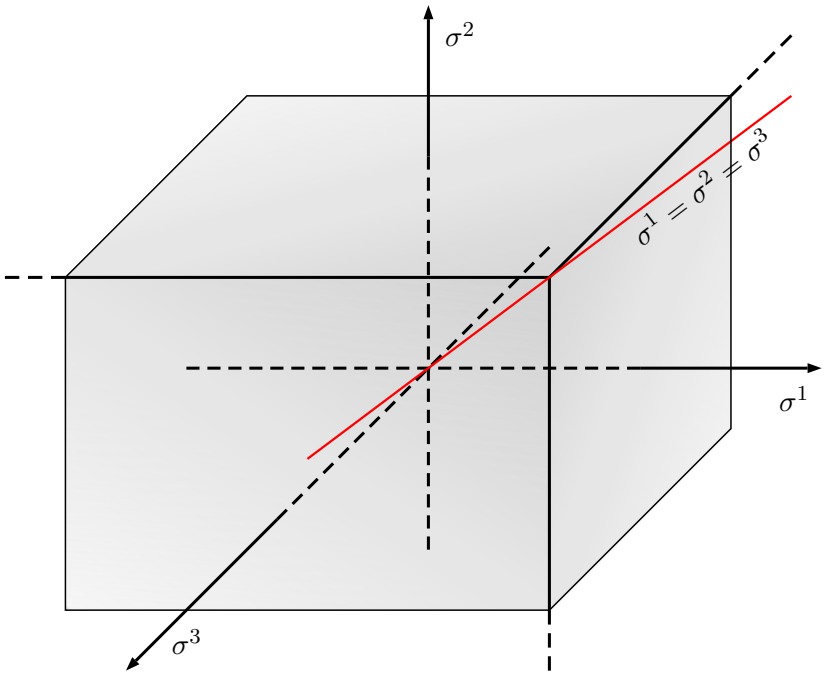

Figure 1: Representation of the yielding surface in the principal stress space $\left(\sigma^1, \sigma^2, \sigma^3\right)$ for $c = 0$. The gray area is the admissible stress domain, while the red line represents the hydrostatic axis.

where $f_i\left(c, \boldsymbol{\sigma}, q\left(\xi\right)\right)$ is the uniaxial yield function defined as:

$$f_i\left(c, \boldsymbol{\sigma}, q\left(\xi\right)\right) = \sigma^i - \left(1 - c\right)\left(\sigma_y - q\left(\xi\right)\right) \tag{51}$$

and $\langle\cdot\rangle$ is the Macaulay brackets, or ramp function. Two important aspects are peculiar of this representation of the yielding function. On the one hand, $f\left(c, \boldsymbol{\sigma}, q\right)$ is the norm of the positive valued uniaxial yielding functions in the three principal directions. In fact, if f_1 is the only non-negative value, the yielding function reduces to the uniaxial original case as in (44):

$$f\left(c, \boldsymbol{\sigma}, q\left(\xi\right)\right) = \sqrt{f_1^2\left(c, \boldsymbol{\sigma}, q\left(\xi\right)\right)} - \rho\left(c, q\left(\xi\right)\right) = \sigma^i - \left(\sigma_y - q\left(\xi\right)\right) \tag{52}$$

On the other hand, the surface is smooth and differentiable at all points. In the case of $c = 0$ the original yielding surface with sharp edges is recovered, whereas, when $c = 1$, the first octant presents a spherical sector.

Defining:

$$\bar{f}_i\left(\boldsymbol{\sigma}, q\right) = \frac{\left\langle f_i\left(\boldsymbol{\sigma}, q\right)\right\rangle}{\sqrt{f_1\left(\boldsymbol{\sigma}, q\right)^2 + f_2\left(\boldsymbol{\sigma}, q\right)^2 + f_3\left(\boldsymbol{\sigma}, q\right)^2}} \tag{53}$$

the evolution equations for the continuous case can be compactly written as:

$$\begin{cases} \dot{\boldsymbol{\varepsilon}}_p = \dot{\gamma} \displaystyle\sum_{i=1}^{3} \bar{f}_i\left(\boldsymbol{\sigma}, q\right) \mathbb{H}^{ii} \\ \dot{\xi} = \dot{\gamma}\left(c + \left(1 - c\right) \displaystyle\sum_{i=1}^{3} \bar{f}_i\left(\boldsymbol{\sigma}, q\right)\right) \end{cases} \tag{54}$$

where the results in Table 1 have been considered. The second order tensor $\mathbb{H}^{ii}$ represents the direction of the plastic flow.

The time variation of the plastic multiplier is computed as [32]:

$$\dot{\gamma} = \frac{\frac{\partial f}{\partial \boldsymbol{\sigma}} : \mathbb{C} : \dot{\boldsymbol{\varepsilon}}}{\frac{\partial f}{\partial \boldsymbol{\sigma}} : \mathbb{C} : \frac{\partial f}{\partial \boldsymbol{\sigma}} - \frac{\partial f}{\partial q}\frac{\partial q}{\partial \xi}\frac{\partial f}{\partial q}} \tag{55}$$

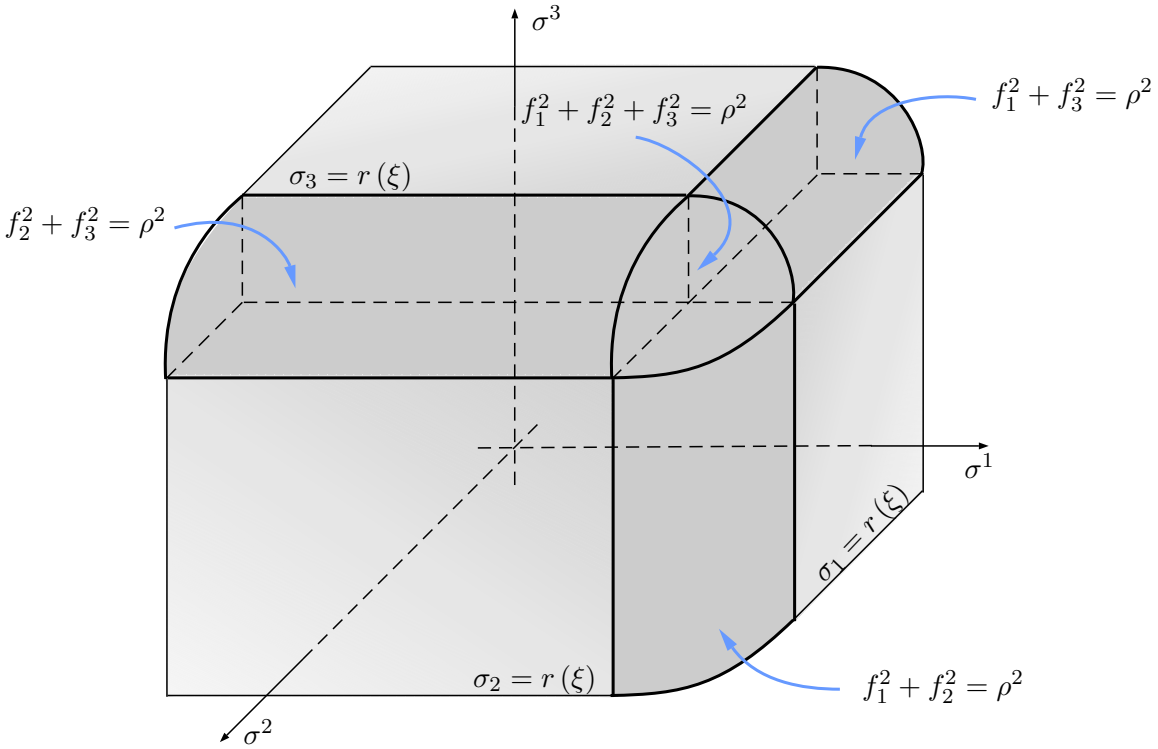

Figure 2: Extended Rankine yield surface: the smoothing of the corners is highlighted and each part presents its own descriptive equation

Principal stress values	$\sigma^i = \hat{e}_i^T \, \hat{\sigma} \, \hat{e}_i = \hat{e}_i^T \, \boldsymbol{\Phi}^T \, \boldsymbol{\sigma} \, \boldsymbol{\Phi} \, \hat{e}_i$
Differential of principal stress values	$\mathrm{d}\sigma^i = \left(\boldsymbol{\phi}^i \otimes \boldsymbol{\phi}^i\right) : \mathrm{d}\boldsymbol{\sigma} = \mathbb{H}^{ij} : \mathrm{d}\boldsymbol{\sigma}$
Differential of principal stress directions	$\mathrm{d}\boldsymbol{\phi}^i = \sum_{j=1}^{n_{dim}} \left(\frac{1}{\sigma^i - \sigma^j} \mathbb{P}^{ij} : \mathrm{d}\boldsymbol{\sigma} \right) \boldsymbol{\phi}^j$
Differential of $\mathbb{H}^{ii}$	$\mathrm{d}\mathbb{H}^{ii} = 2 \sum_{j=1}^{n_{dim}} \left(\frac{\mathbb{P}^{ij} \otimes \mathbb{P}^{ij}}{\sigma^i - \sigma^j} : \mathrm{d}\boldsymbol{\sigma} \right)$

Table 1: Summary of the formulas obtained in Appendix A

The discrete version of Rankine plasticity model follows the closest point projection algorithm, where introducing a Backward Euler time scheme, the plastic multiplier $\Delta\gamma^{n+1}$ is computed by finding the root of the yield function at the step $n+1$:

$$
\begin{aligned}
& f^{n+1}\left(\boldsymbol{\sigma}^{n+1}, q^{n+1}\right)=\sqrt{f_1\left(\boldsymbol{\sigma}^{n+1}, q^{n+1}\right)^2+f_2\left(\boldsymbol{\sigma}^{n+1}, q^{n+1}\right)^2+f_3\left(\boldsymbol{\sigma}^{n+1}, q^{n+1}\right)^2}-\rho\left(q\right)= \\
& =\left[\sum_{i=1}^{n_{ret}}\left(\mathbb{H}^i:\boldsymbol{\sigma}_{trial}-\Delta\gamma^{n+1}\mathbb{H}^i\mathbb{C}\frac{\partial f^{n+1}}{\partial\boldsymbol{\sigma}^{n+1}}-(1-c)\left(\sigma_y-q\left(\xi^n+\Delta\gamma^{n+1}\frac{\partial f^{n+1}}{\partial q^{n+1}}\right)\right)\right)^2\right]^{\frac{1}{2}} \\
& -c\left(\sigma_y-q\left(\xi^n+\Delta\gamma^{n+1}\frac{\partial f^{n+1}}{\partial q^{n+1}}\right)\right)=0
\end{aligned}
\tag{56}
$$

where n_{ret} is the number of principal stresses to be considered in the return mapping. For linear hardening/softening, $q\left(\xi\right)$ reads

$$
q\left(\xi\right)=\begin{cases}\frac{H_S}{\sigma_y}\xi & \text{for} \quad 0\leq\xi\leq\frac{\sigma_y}{H_S} \\ 0 & \text{for} \quad \frac{\sigma_y}{H_S}\leq\xi\leq\infty\end{cases}
\tag{57}
$$

and the value of $\Delta\gamma^{n+1}$ is explicitly computed. For exponential softening, $q\left(\xi\right)$ is

$$
q\left(\xi\right)=\sigma_y\left[1-\exp\left(\frac{-2H_S}{\sigma_y}\xi\right)\right] \qquad \text{for} \quad 0\leq\xi\leq\infty
\tag{58}
$$

and a Newton-Raphson iterative scheme is required. The update of the stress and the hardening function is performed as:

$$
\begin{cases}\boldsymbol{\sigma}^{n+1}=\mathbb{C}:\left[\boldsymbol{\varepsilon}^{n+1}-\boldsymbol{\varepsilon}_p^{n+1}\right]=\boldsymbol{\sigma}_{trial}^{n+1}-\mathbb{C}:\Delta\gamma^{n+1}\dfrac{\partial f^{n+1}}{\partial\boldsymbol{\sigma}^{n+1}} \\ q\left(\xi^{n+1}\right)=q\left(\xi^n+\Delta\gamma^{n+1}\dfrac{\partial f^{n+1}}{\partial q^{n+1}}\right)\end{cases}
\tag{59}
$$

Following standard arguments [32], the continuous elastoplastic constitutive fourth order tensor is:

$$
\mathbb{C}^{ep}=\left[\mathbb{C}-\frac{\left(\mathbb{C}:\frac{\partial f}{\partial\boldsymbol{\sigma}}\right)\otimes\left(\mathbb{C}:\frac{\partial f}{\partial\boldsymbol{\sigma}}\right)}{\frac{\partial f}{\partial\boldsymbol{\sigma}}:\mathbb{C}:\frac{\partial f}{\partial\boldsymbol{\sigma}}-\frac{\partial f}{\partial q}\frac{\partial q}{\partial\xi}\frac{\partial f}{\partial q}}\right]
\tag{60}
$$

In the discrete time setting, an algorithmic tangent operator is used; this is defined by the change of stresses around an admissible equilibrium position (i.e. $\boldsymbol{\sigma}^{n+1}$) due to a small variation in the strain. The i-th column of the approximated constitutive matrix can be computed as:

$$
\mathbb{C}_{ep}^{n+1}\hat{\boldsymbol{e}}_i\approx\left.\frac{\boldsymbol{\sigma}\left(\boldsymbol{\varepsilon}+h\hat{\boldsymbol{e}}_i\right)-\boldsymbol{\sigma}\left(\boldsymbol{\varepsilon}-h\hat{\boldsymbol{e}}_i\right)}{2h}\right|_{n+1}
\tag{61}
$$

where $\hat{\boldsymbol{e}}_i$ is the unit vector of the i-th direction in the reference system. The smaller the perturbation, the closer the approximation tends to the original definition of the elastoplastic tensor. However, it has to be noted that the lower limit of the value of the perturbation is proportional to the machine precision, below which numerical cancellation and instabilities are frequent. Numerical experiments justify a perturbation size of $h=10^{-5}\left\|\boldsymbol{\varepsilon}\right\|$. First, from the value $\boldsymbol{\varepsilon}^{n+1}$, the perturbed strain tensors $\boldsymbol{\varepsilon}+h\hat{\boldsymbol{e}}_i$ and $\boldsymbol{\varepsilon}-h\hat{\boldsymbol{e}}_i$ in the selected direction are computed. Second, the respective stress values are evaluated and the return mapping procedure is applied on both of them. Finally, the i-th column of $\mathbb{C}_{ep}^{n+1}$ can be approximated as in Equation (61). Further details and alternative approximation schemes can be found in the work by Miehe [53], Pérez-Foguet et al. [54], Reps and Rall [55].

6.1 Softening behavior

In a softening process, the energy dissipated by inelastic behavior is linked with the fracture energy G_f [56], defined by unit surface. When using a plastic model defined in terms of stress and strain, the dissipated plastic energy $\mathscr{W}_p$ is defined by unit volume. In the discrete FE setting, these two definitions are related through a characteristic length l_{ch}, connected to the mesh resolution:

$$\mathscr{W}_p = \frac{G_f}{l_{ch}} \tag{62}$$

In the plastic model, recovering Equation (46) and (54), the rate of plastic work is computed as:

$$\dot{\mathscr{W}}_p = \boldsymbol{\sigma} : \dot{\boldsymbol{\varepsilon}}_p = r\left(\xi\right)\dot{\xi} \tag{63}$$

From expressions (57) and (58), in both the linear and exponential softening cases, the total plastic work is calculated then as:

$$\mathscr{W}_p = \int_{t=0}^{t=\infty} \dot{\mathscr{W}}_p \, \mathrm{d}t = \int_{\xi=0}^{\xi=\infty} r\left(\xi\right)\dot{\xi} = \frac{{\sigma_y}^2}{2H_S} \tag{64}$$

and this represent the area underlying the $r-\xi$ curve. Now, comparing expressions (62) and (64), the parameter H_S can be computed as:

$$H_S = \frac{{\sigma_y}^2}{2G_f} l_{ch} = \bar{H}_S l_{ch} \tag{65}$$

The parameter $\bar{H}_S$, depends only on material properties, whereas l_{ch} depends on the resolution of the discretization. In fact, the size of the strain concentration band depends on the finite element technology used, as pointed out by Cervera et al. [26]: irreducible finite elements, due to the discontinuous strain field, provide a concentration band within a single element span whereas in the $\boldsymbol{\varepsilon} - u$ mixed FE formulation, with inter-elemental continuous strain, the slip line spans two elements. Consequently, the characteristic length l_{ch} is taken accordingly.

7 Numerical Simulations

In the present section, the problem of pullout test of a metal anchor in a concrete block is addressed, both in 2D and in 3D. The aim of the pullout test is to evaluate the overall response of embedded steel heads in concrete. On the one hand, the experiment provides valuable data about the fracture pattern and the quality of the anchorage. On the other hand, the maximum tensile strength and the post peak energy dissipation of the concrete can be evaluated with simplified or empiric formulas.

The objective of the following numerical simulations is to demonstrate the advantages of the ε/u mixed FEM with respect to the standard irreducible one. These are assessed in two complementary aspects: (a) convergence to the appropriate solution, without spurious numerical issues, like mesh-size and mesh-bias dependence; (b) enhanced accuracy, able to reproduce optimally the solution for a computational mesh of a chosen degree of refinement. These two facts translate in a high-fidelity simulation of experimental results obtained for the pullout test, in a way that makes it possible to study the sensibility of the data to the variations, desired or not, of the boundary conditions or the bracing system.

Computations have been realized using an enhanced version of COMET-Coupled mechanical and thermal analysis [57], developed by the authors at the International Center of Numerical Methods in Engineering (CIMNE) in Barcelona, Spain. The geometrical models have been created using GiD, a pre and post-processing software, also developed by CIMNE. In all the examples, the convergence tolerance used for the iterative Newton-Raphson procedure is 10^{-4} with respect to the residual forces.

7.1 2D Pullout Test

The 2D pullout test under consideration was performed by Dejori [18], later published by Thenier and Hofstetter [19]. The test consists of a panel of unreinforced concrete of dimensions 700×500 mm^2 in which a T-shaped steel flange is embedded. The latter is 80×20 mm^2 in the horizontal part, whereas the vertical stem has a width of 10 mm (Figure 3).

The experiment, shown in Figure 4(a), is carried out by imposing a vertical displacement to the steel component, which translates in a force applied to the concrete in the surrounding of the horizontal flange. The consequent displacement/reaction plot of the structure is recorded until failure is reached. In order to apply such force to the specimen without suffering of rigid body motions, a bracing system is devised on the sides of the steel flange, as shown in Figure 4(b).

Multiple setups of this experiment are reported, in terms of embedding depth and bracing position. On the one hand, the steel head is positioned at three different positions (60, 80 and 100 mm) from the top surface of the concrete panel. In the present numerical simulations, only the latter case of 100 mm is considered, following the work by Thenier and Hofstetter [19]. On the other hand, the bracing system presents two different dispositions. The first one considers the steel rods centered at a distance of 70 mm from the sides. The rods are then connected with a flange of width of 50 mm in contact with the top of the panel. Instead, the second setup is reported to reduce the distance of between the two bracing systems: "*The distance between the vertical supports has been shortened in order to have the expected fracture growing in the direction of the supports at an average inclination of 30 degrees*" [18]. Despite explicit values are not given, the distance of the bracing system to the symmetry axis can be computed as

$$l_{br} = \frac{w_f}{2} + \frac{\sqrt{3}}{2} h_{ef} \tag{66}$$

where w_f is the flange width equal to 80 mm and h_{ef} is the embedding height. Consequently, l_{br} has a value of about 92, 109, 126 mm with respect to the 60, 80, 100 mm deep setups. Additionally, the 50 mm strip has been substituted by a metal bearing in order to concentrate the load.

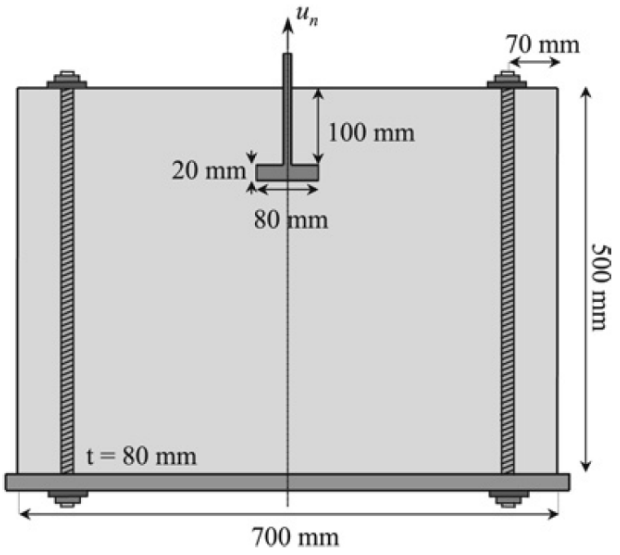

Figure 3: Geometry of the 2D pullout test (from Thenier and Hofstetter [19])

Although the experiment appears to be quite straightforward in its description, significant differences and unexpected results were reported. Almost independently of the flange depth,it is possible to identify two families of failure modes in the experimental series. The first one is quasi-symmetric, which implies that the load has been evenly transferred from the steel flange to the specimen. Surely, a small amount of sway in the fractures is to be expected due to the accidental misalignment of the load, as well as the intrinsic heterogeneity of concrete. The symmetric behaviour, even if it is not the more frequent, happens for all the setup configurations (Figure 5). The second family of failure modes

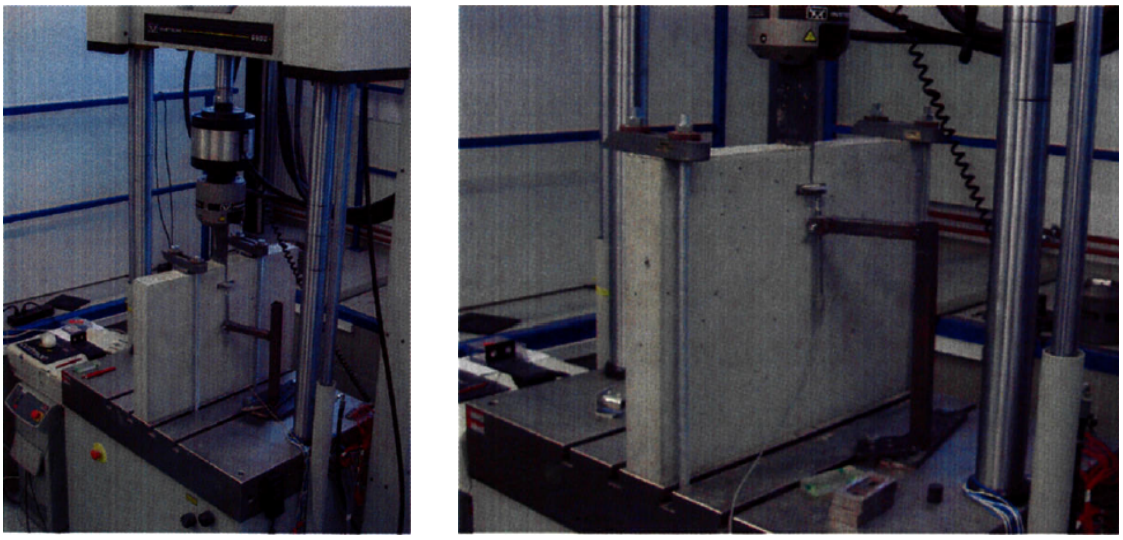

(a) (b)

Figure 4: Detail of the experimental setup and the two different bracing systems used in the 2D pullout test [18]

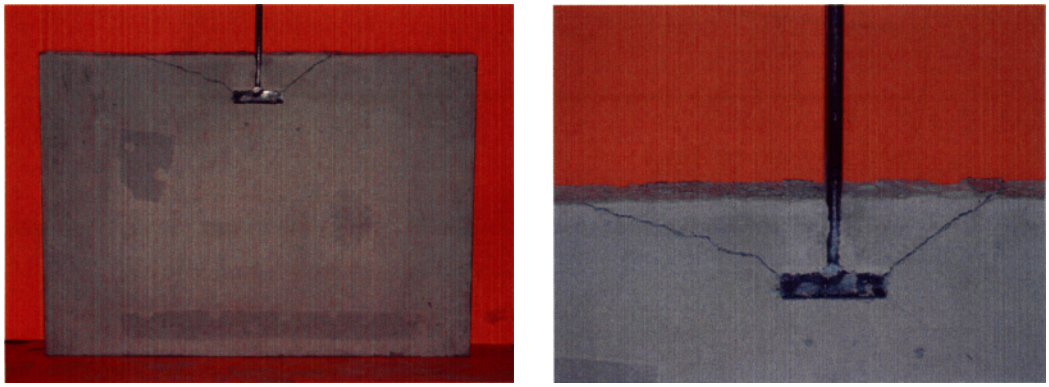

(a) (b)

Figure 5: Detail of the symmetric results for the 2D pullout test in the case of 6 centimeters embed [18]

is clearly asymmetric. Whilst on one side of the specimen a single fracture line forms and progresses upwards to the upper surface (Figure 6 and Figure 7), on the other side a peculiar bifurcation behavior appears, with fracture lines that reach the upper and lower part of the concrete panel. It is unclear from the reported experimental data if the asymmetry is due to different lateral boundary conditions or a sudden change in the force configuration during the test.

The first setup, characterized by spread bracing, results very frequently in the asymmetric mode of failure, with an almost straight crack growing in the direction of the upper bearing whereas the bifurcation appears around the half-height of the panel, independently of the flange depth (Figure 6).

As far as the second setup is concerned, the effect of the closer bracing as well as of concentrating the load with different bearings is evident (Figure 7). The fracture lines form closer to the steel head and show a more symmetrical behavior. Nevertheless, the bifurcation pattern appears again, always on the side with a more curved crack.

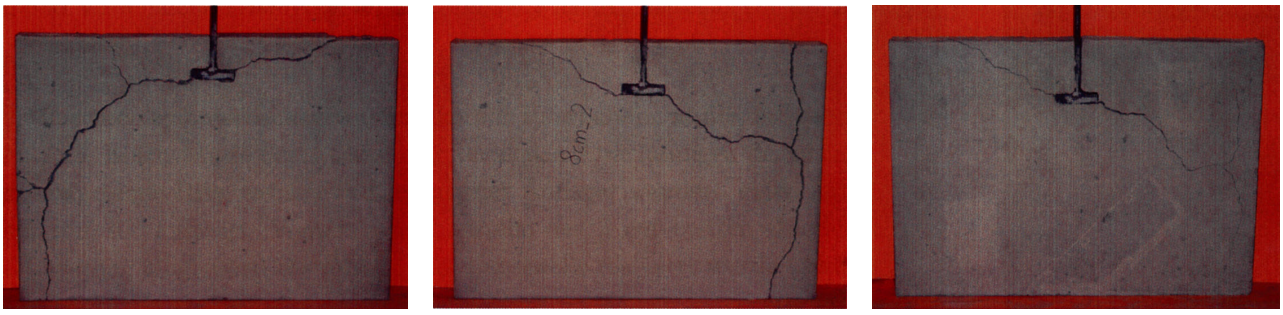

(a) (b) (c)

Figure 6: Asymmetric results for the first experimental setup (distant bracing) [18]

(a) (b) (c)

Figure 7: Asymmetric results for the second experimental setup (close bracing) [18]

It is clear from this that the distance of the bracing frame plays a major role in the outcome of the experiment, as well as the concentration of stresses under the bearings. Not so clear is the dependence of the test results on the mechanical characteristics of the rods of the bracing system, which provide a different stress state for a similar deformation field. With or without little bracing, the concrete panel may be lifted from its base. In addition, little attention has been given to the effect of the sequence of cracking. The delay in the formation of cracks could be the main cause of asymmetry in the experimental outcomes. In fact, if a fracture has already appeared on one side of the panel, the pullout of the anchor provokes a shift of the force scheme resulting in a bending moment in the concrete (Figure 8). This fact would easily explain the onset of horizontal tension which results in vertical cracking.

In the following, two different case studies are presented. The first one is a pure shear case, where a (simplified) analytical solution is compared to the finite element one, to assess the correctness of the numerical results. In the second one, the experimental test cases are addressed and the dependency of the results on the steel bracing constraint is studied.

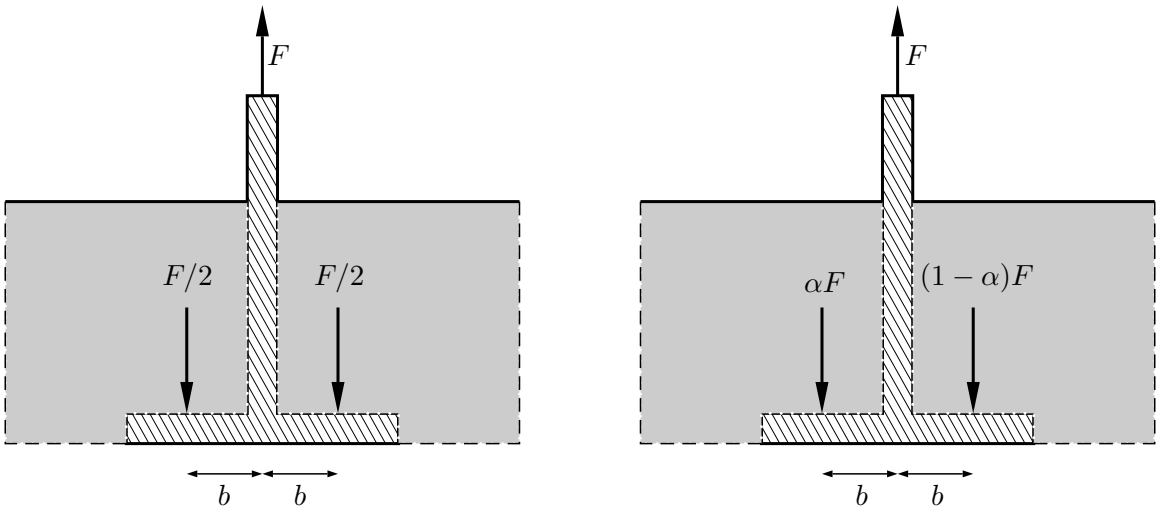

Figure 8: Symmetric and asymmetric force configuration for the pullout test. On the right, the symmetric case due to the initial uncracked state of the concrete. On the left, when one of the sides is cracked, the force shifts to the other side of the specimen and a bending moment equivalent to $(1-\alpha)2Fb$ appears ($\alpha \leq 1/2$).

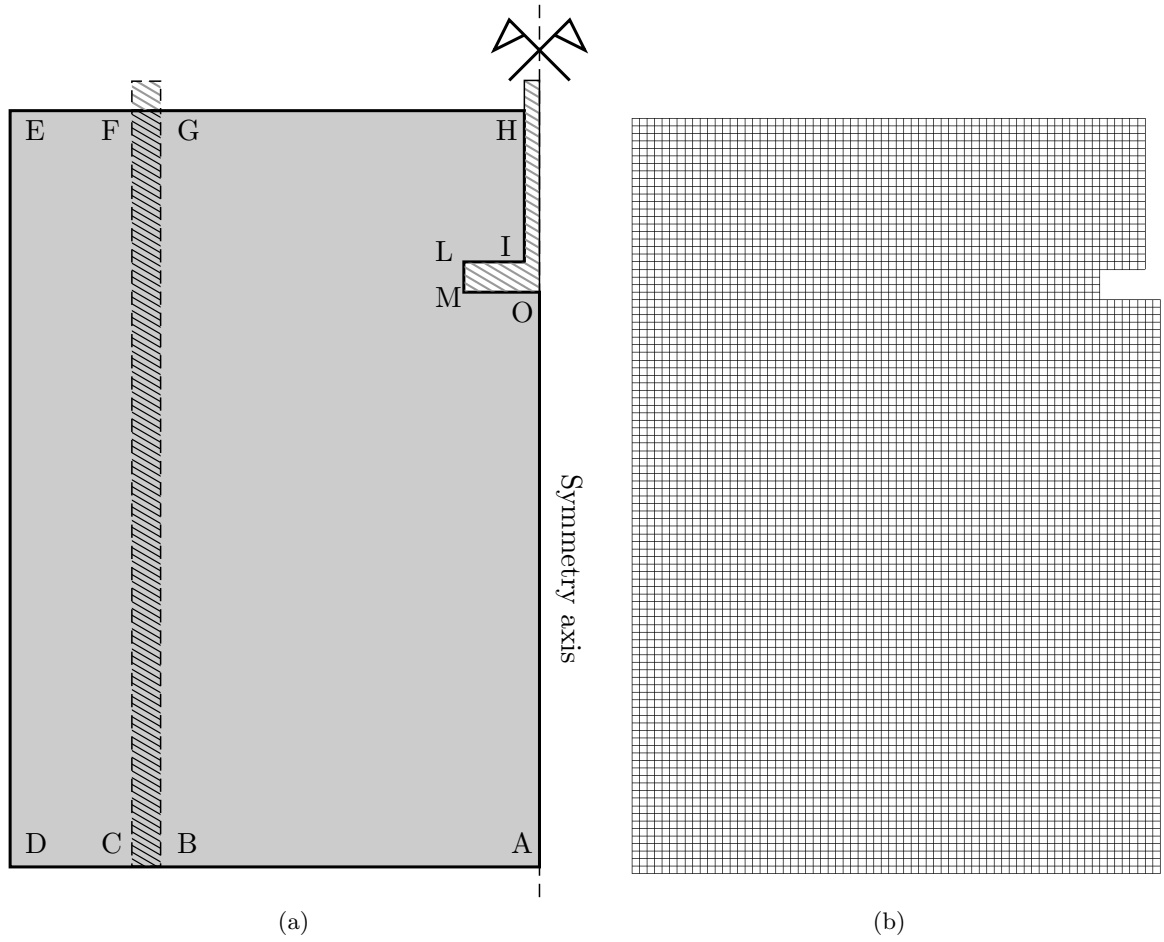

Figure 9: Discretization of the 2D pullout problem: (a) the discretized domain and (b) the structured mesh used in the analysis for the concrete panel.

In all the examples, the discretized domain represents half of the concrete panel, taking advantage of the vertical symmetry line (Figure 9). As shown in the picture, the steel bracing and the top constraint are modeled as a strip of elements which connects line FG in the upper surface to the line CB in the bottom interface. No other connection or friction is simulated between the bracing system and the concrete panel. The thickness of the strip coincides with the resisting area of the metal rods. In this way, it is possible to simulate the presence of a vertical elastic constraint, but allowing horizontal sliding. The pullout of the steel flange is modeled imposing the vertical displacement of the boundary HILM in contact with the head. The complete computational mesh consists of a structured grid with 6936 quadrilateral elements and 7105 nodes. The characteristic size of the concrete element is 5 mm.

The mechanical properties for the concrete are taken from the cited references. Young's modulus $E = 36630$ MPa with a Poisson's ratio $\nu = 0.2$. The tensile strength $\sigma_y = 3780$ kPa and the fracture energy $\mathscr{G}_f = 65$ J/m.

7.1.1 Virtual shear test

In the first example, the boundary HILM, representing the contact with the steel flange, is constrained to move vertically, but no horizontal restriction is set. Considering the upper part of the panel as a semi infinite strip as in Figure 10, the imposed displacement u_0 induces a tensional state of pure shear, with average value along the line LL' $\tau = F/A$. This approximation holds for ML/ML'>> 1. Locally, a concentration of stresses appears close to the imposed boundary condition (Figure 11(a)). The elastic stresses computed in the vicinity of point M are shown in Figure 11(b): the principal directions are at 45° with respect to the horizontal, with equal value and opposite sign of compression and tension. Considering a quasi-brittle material, with a Rankine yielding criterion, the initiation of

Figure 10: Resultant force scheme for initial loading due to the imposed displacement u_0.

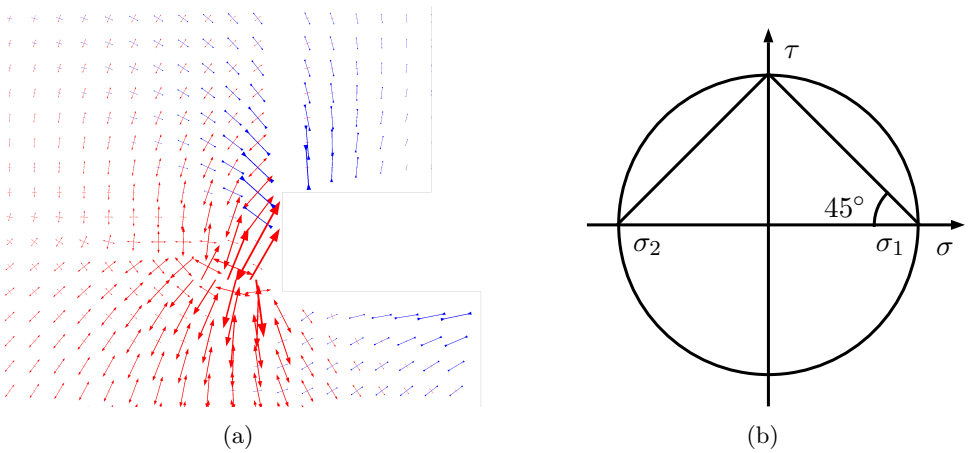

Figure 11: Stress vectors in the elastic case (left) and Mohr's circle at point M (right). The pure shear condition creates a stress state characterized by principal directions inclined at 45° with the horizontal.

the crack follows the direction orthogonal to the maximum tensile stress. Therefore, a crack initiates in M and progresses at 45°. The force scheme changes as depicted in Figure 12. From the global equilibrium of the block M'B'GL', it is possible then to infer that a new shear stress τ', in a similar fashion as before. The crack will consequently follow a 45 degree line.

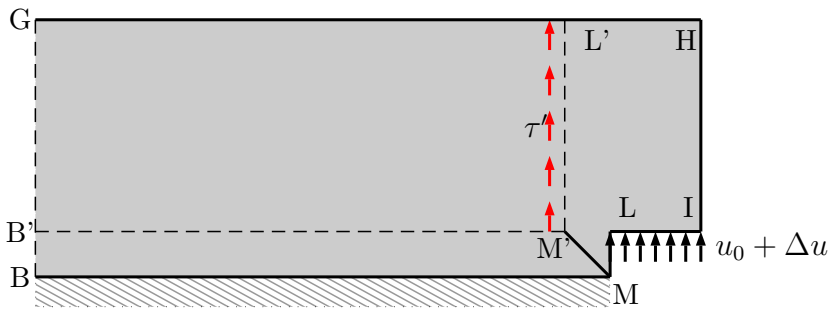

Figure 12: Forces scheme for the initiated crack

This crack pattern is typical of the symmetric solution in the pullout test. In fact, when the imposed displacement is applied in such a way that horizontal forces are very small or lateral reactions are equilibrated, the stress state transferred from the steel head is close to pure shear. Whether the concrete panel is effectively constrained by a steel bar at the line GB, located far from the applied shear, the same solution pattern is expected, with a crack growing diagonally at approximately 45°. Considering Poisson's effect, normal and shear stress-transfer across the fissured crack makes the problem more complex and obtaining an analytical solution is unfeasible. However, the expected solution does not depart significantly from the upward crack at approximately 45°.

Figure 13 and 14 show contours for the equivalent plastic strain and displacements obtained with mixed (top row) and standard (bottom row) finite elements in two situations: with (left) and without (right) steel rod bracing.

All the solutions attempt to reproduce a crack that initiates at point M and progresses upward (Figure 13), inducing the rotation of the detaching part around the tip of the crack (Figure 14). However, the results produced by the mixed and the standard formulations are very different.

On the one hand, the mixed finite elements produce results which are: (a) consistent with those expected from the (simplified) analytical solution; (b) correctly insensitive to the change in the bracing system; (c) correctly insensitive to the mesh alignment.

On the other hand, the standard formulation produces unreliable results that are: (a) not consistent with the expected crack at approximately 45°; (b) spuriously sensitive to the stress state induced by the bracing; (c) spuriously sensitive to the alignment of the mesh.

Figure 15 shows the force F versus the vertical displacement u for the four cases. The mixed formulation produces very consistent results, with very limited effect of the bracing system in the formation of the crack. The standard formulation overestimates the peak load and the energy dissipated in the formation of the crack.

It has to be noted that the reaction force cannot vanish because the compression stresses are not affected by the adopted Rankine criterion. This means that the crack progresses towards the upper surface but it can not reach it.

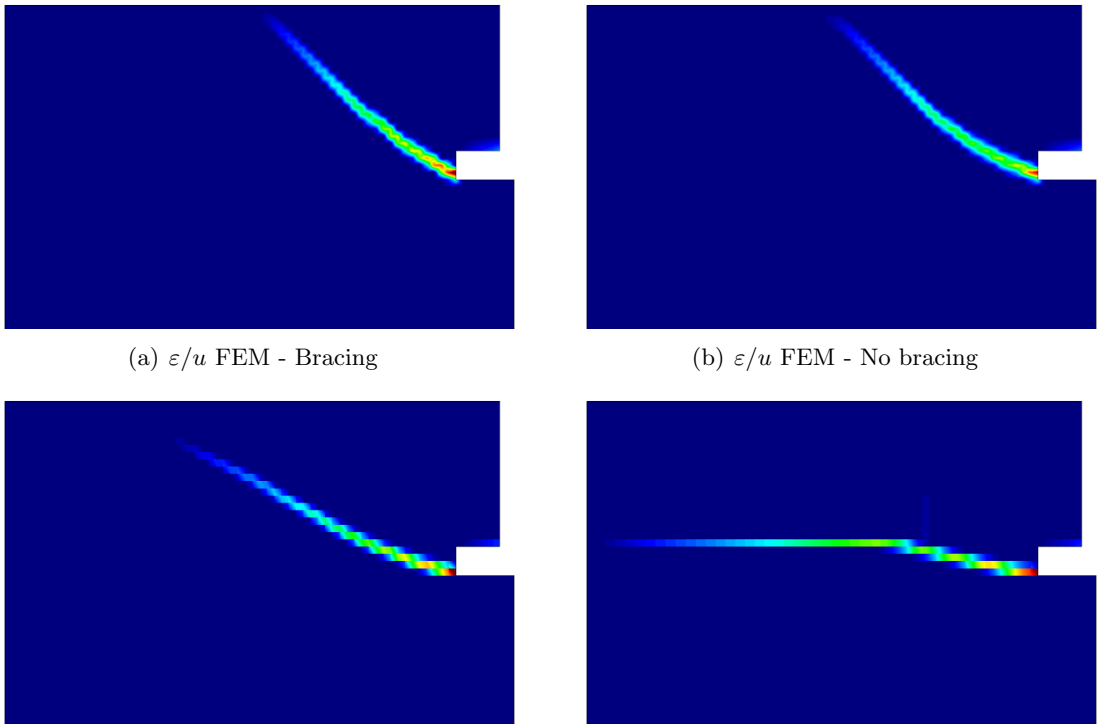

(a) ε/u FEM - Bracing (b) ε/u FEM - No bracing

(c) Std FEM - Bracing (d) Std FEM - No Bracing

Figure 13: Equivalent plastic strain contours with mixed (top row) and the standard (bottom row) finite element formulations in the pure shear case.

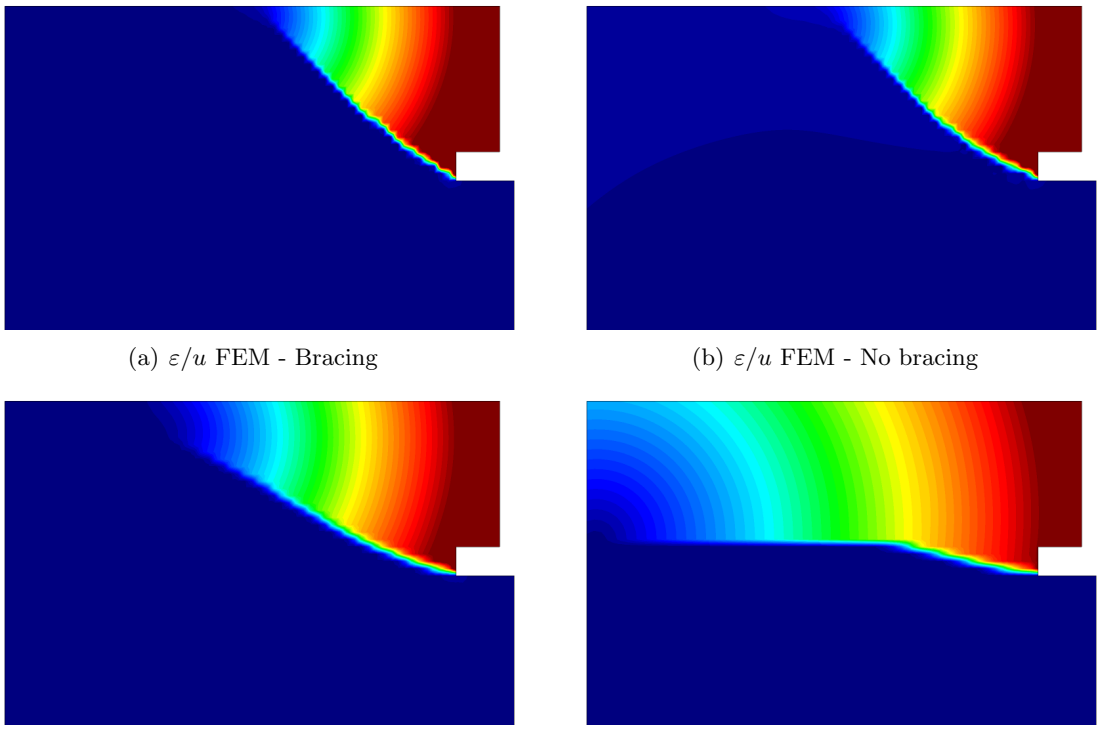

(a) ε/u FEM - Bracing (b) ε/u FEM - No bracing

(c) Std FEM - Bracing (d) Std FEM - No bracing

Figure 14: Displacements contours with mixed (top row) and the standard (bottom row) finite element formulations in the pure shear case.

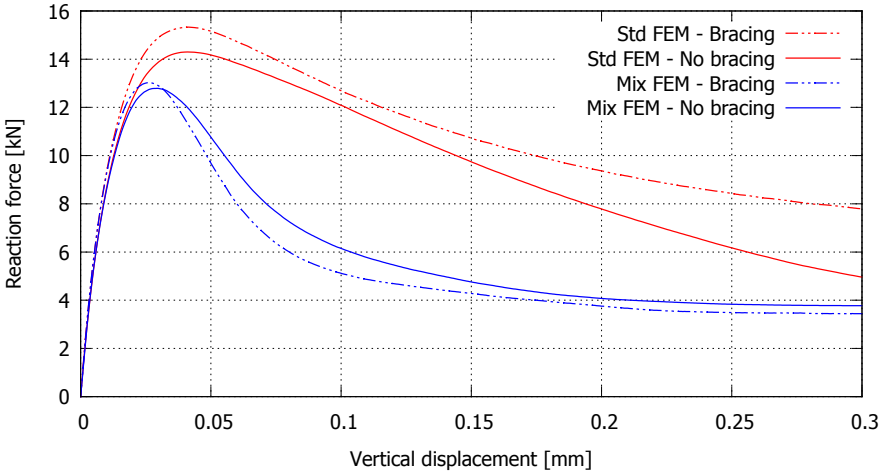

Figure 15: Force versus vertical displacement curves for the pure shear case.

7.1.2 Simulation of the experimental results

In this section, the horizontal displacement of the embedded steel head is restrained, to simulate the high friction between the anchored head and the surrounding concrete. Contrariwise to the cases considered in the previous section, in this situation the steel bracing counterbalances the effect of the applied pullout vertical force, as it supplies an opposed downward concentrated force. This force is proportional to the stiffness of the metal rods and, therefore, the resulting fracture pattern is effectively affected by the rigidity of the bracing system.

Figure 16 and 17 show contours for the equivalent plastic strain and displacements obtained with mixed (top row) and standard (bottom row) finite elements in the two cases given by stiff or loose support frames. For the case for a stiff support, the resulting fracture path is curved, from the base of the bolt to the bearing structure (Figure 16(a) and Figure 16(c)). Both mixed and standard finite elements are able to capture the displacement of the mass of concrete under bending (Figure 17(a) and Figure 17(c)). Even if the two solutions appear similar, it is important to notice two details. First, a clear mesh dependency is visible in the standard solution (Figure 16(c)) while this is not the case in the mixed formulation, with a defined inclination at the crack tip (Figure 16(a)). Second, the proposed formulation produces a crack that turns effectively in the direction of the support, while the curvature given by the standard one is reduced, affected by mesh dependence.

In the case of low rigidity, the solution is qualitatively similar in terms of direction of the crack between the two methods, but it is possible to observe a bifurcation in the crack path for the mixed formulation (Figure 16(b)) which is not captured for the irreducible one (Figure 16(d)). The rotation of the detaching part, due primarily to bending effects, is evident also in this case (Figure 17(b) and Figure 17(d)).

In Figures 18, 19 and 20, the numerical solutions of the more reliable mixed ε/u finite elements are compared with the experimental results. The agreement between numerical solutions and the experimental results is remarkably good. This is achieved even if the adopted constitutive model (Rankine plasticity under tension) does not include phenomena like compressive crushing or friction and dilatation due to grain effects.

In Figure 18, the symmetric pattern (Figure 5) is compared against the solution found in Figure 13(a). With a distant positioning of the bracing and no horizontal restraint, the result is approximately a 45° inclined crack. Note that a shallower embedding of the flange favours less horizontal constraint, being smaller the vertical reaction (and consequently the frictional forces) of the affected concrete.

In Figure 19, the crack formed with the effective restraint of the steel bracing and zero horizontal sliding of the bolt is presented. The numerical simulation, shown in Figure 19(a), considers a homogeneous material whereas the intrinsic heterogeneity of concrete, with an internal distribution of aggregates, affects the direction of the crack observed in Figure 19(b).

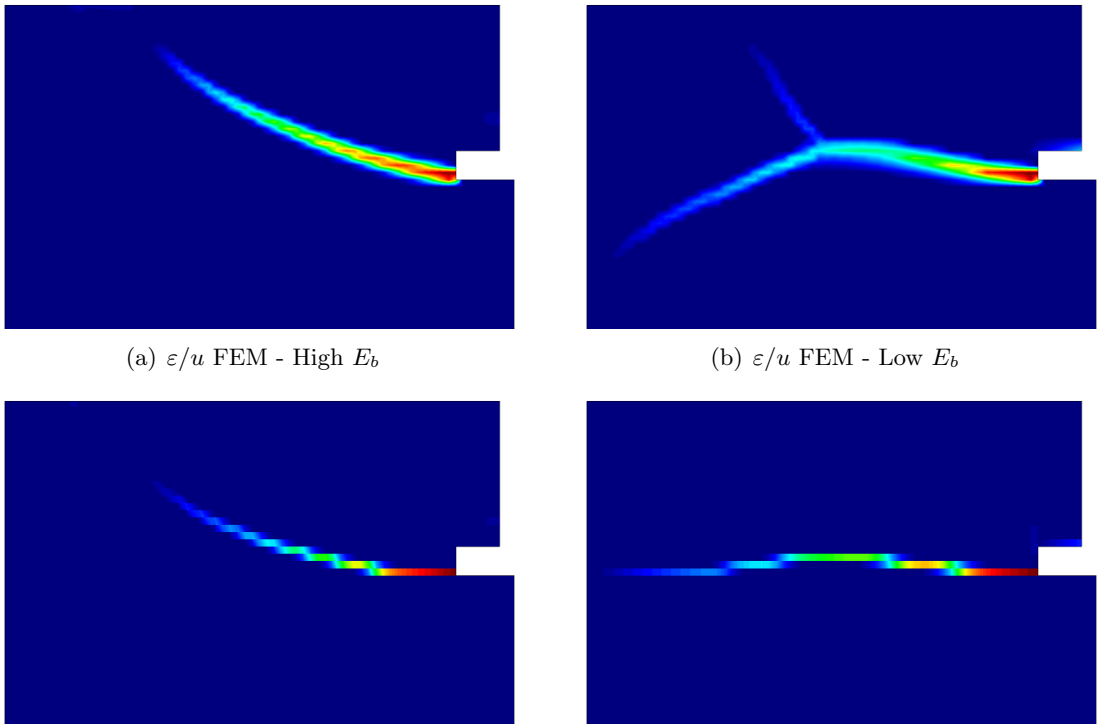

(a) ε/u FEM - High E_b

(b) ε/u FEM - Low E_b

(c) Std FEM - High E_b

(d) Std FEM - Low E_b

Figure 16: Equivalent plastic strain contours with mixed (top row) and the standard (bottom row) finite element formulations in the experimental setup case.

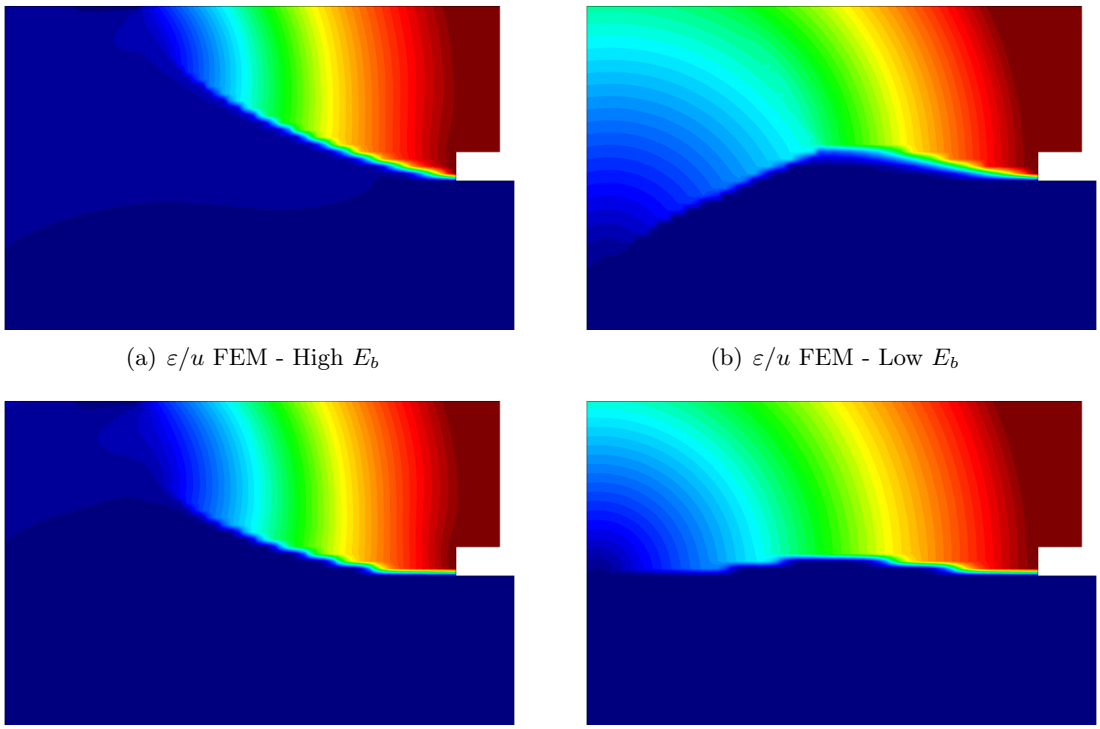

(a) ε/u FEM - High E_b

(b) ε/u FEM - Low E_b

(c) Std FEM - High E_b

(d) Std FEM - Low E_b

Figure 17: Displacements contours with mixed (top row) and the standard (bottom row) finite element formulations in the experimental setup case.

In Figure 20, the bifurcation pattern is shown. This case is due to the low stiffness of the bracing, which implies an initial almost horizontal initiation of the crack, followed by a bifurcation. The longer the horizontal crack path, the bigger the effect of bending is; the slight curvature before the bifurcation point is noticeable. After the bifurcation, the upper part of the crack propagates almost straight to the support bracing. The lower fracture is longer than the upper one in both of the pictures. The agreement between the two results is remarkable.

In Figure 21, the vertical reaction is plotted against the imposed displacement. Two different cases are shown: the first one, corresponding to an effective support action, gives an increasing reaction as the experiment progresses; the second one, corresponding to the bifurcation case, with less stiff bracing, shows a softening behavior. Comparing those results with the ones shown in Figure 15, it is possible to asses the influence of friction and bracing system with respect to the pure shear virtual test. In addition, the peaks load and the dissipated energy fall within the experimental ranges discussed in Dejori [18].

Thanks to the enhanced accuracy provided by the mixed formulation, it is still possible to discuss particular details of the pullout tests, without the need of referring to specific experimental results. For example, the starting point of the crack is determined by the effective contact between the steel flange and the concrete. With reference to Figure 9, in the case of pure vertical motion (i.e. line LI has an imposed displacement, but not LM), the crack starts from point L. Instead, if a slight lateral motion of the head presses on line LM, so that friction makes steel and concrete adherent, then the crack will start from point M. This small horizontal sliding has found to occur frequently for the asymmetric configuration of cracks, where the onset of a first diagonal crack on one side provokes a rotation of the other side. This effect is more visible for larger depth of embedding.

Another key aspect is the sequence of cracking; it is statistically impossible to reach failure at the same time on both sides of the panel due to the natural imperfections in the positioning of the force and in the composition of the concrete. Perturbations largely affect brittle crack propagation and this is reflected by the greater percentage of asymmetric results obtained in the experiments. Nevertheless, a sound hypothesis on the probable sequence of failure can be outlined thanks to the previous examples. The initial cracking is given by a tensile failure as in Figure 18, for the symmetric case, or as in Figure 19, for the asymmetric one. Then, in the latter case, after the first fracture develops, the loading acts unevenly on the two opposite side of the panel and the consequent bifurcating cracks grow in the direction of the steel bracing due to bending-like effects.

7.2 3D Pullout Test

3D pullout tests have been considered in many publications treating numerical methods for crack propagation. Gasser and Holzapfel [20] analyzed it with the partition of the unity method. Later, Areias and Belytschko [21] and Duan et al. [58] studied it using extended finite elements. Recently, Kaczmarczyk et al. [59] solved the problem with a configurational mechanics method, consistent with Griffith's theory.

The problem, shown in Figure 22, is axis-symmetric, so that only a quarter is depicted. A steel bolt with circular head is placed in a cylindrical concrete anchorage and imposes a vertical displacement to the block. To avoid rigid body motion, a metal hoop is placed on top, reacting vertically. In the same picture, the mechanical properties are reported as taken from Areias and Belytschko [21]. Vertical displacement is imposed, whereas no horizontal displacement is allowed at the contact between the bolt and the concrete.

Here, the problem is studied with three different mesh sizes and comparing the results obtained with mixed ε/u and standard formulations. The elements used for the discretization are triangular prisms, so that a semi-structured mesh is easily built. Figure 23 shows the top face of the quarter cylinder composed of triangles, supported by a structured vertical square grid. Table 2 shows the average size of the triangles, the number of nodes and elements in three meshes (coarse, medium and fine) so that the convergence of the solution with respect to the mesh sizes can be assessed.

In Figure 24 it is possible to see the computed deformed shape along the resulting conical crack surface in the case of the mixed finite element with fine meshing. The fields of equivalent plastic strain

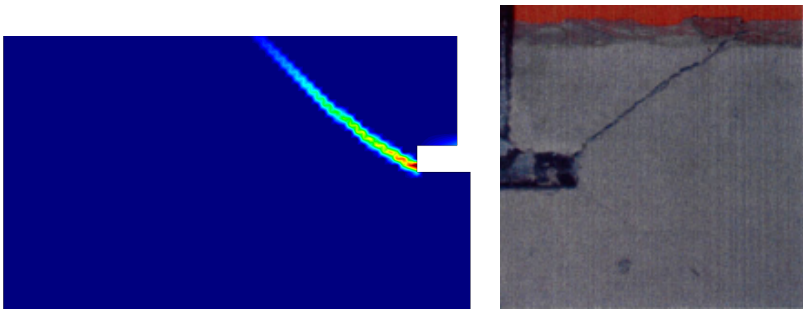

(a) (b)

Figure 18: Comparing the symmetric pattern in the case of free horizontal sliding of the steel flange.

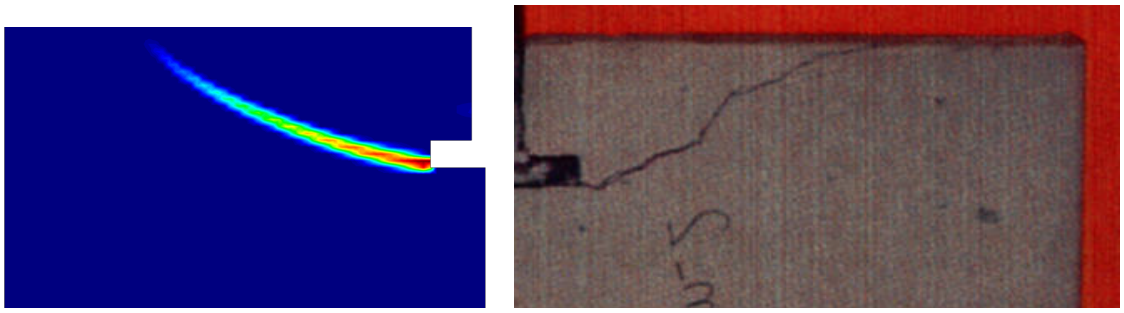

(a) (b)

Figure 19: Comparing the symmetric pattern for the case of effective vertical constraint of steel bracing and constrained horizontal motion of the steel flange.

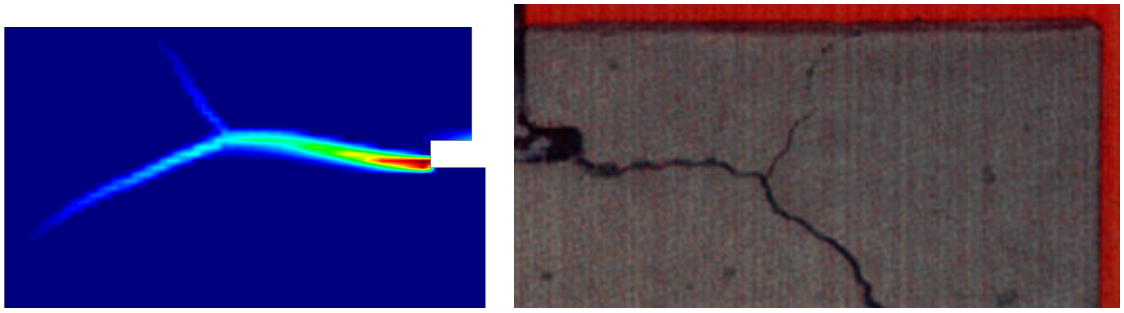

(a) (b)

Figure 20: Comparing the bifurcation pattern in the asymmetric case.

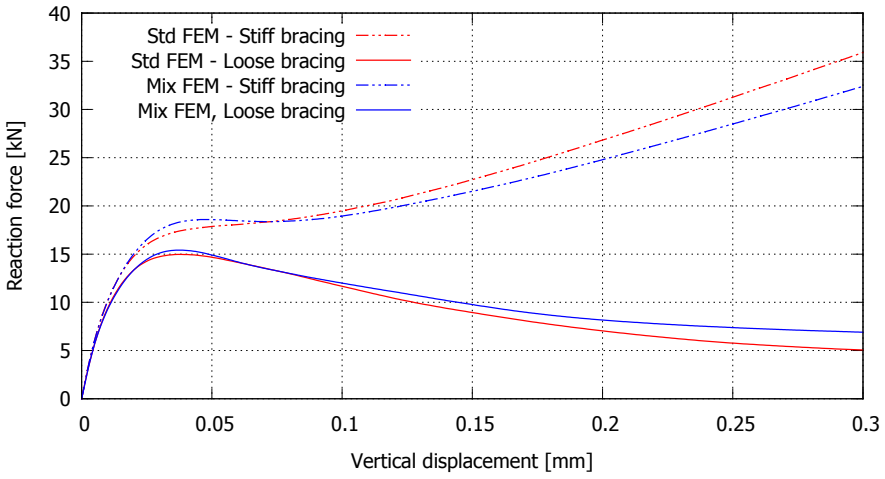

Figure 21: Force versus vertical displacement curves for the experimental case.

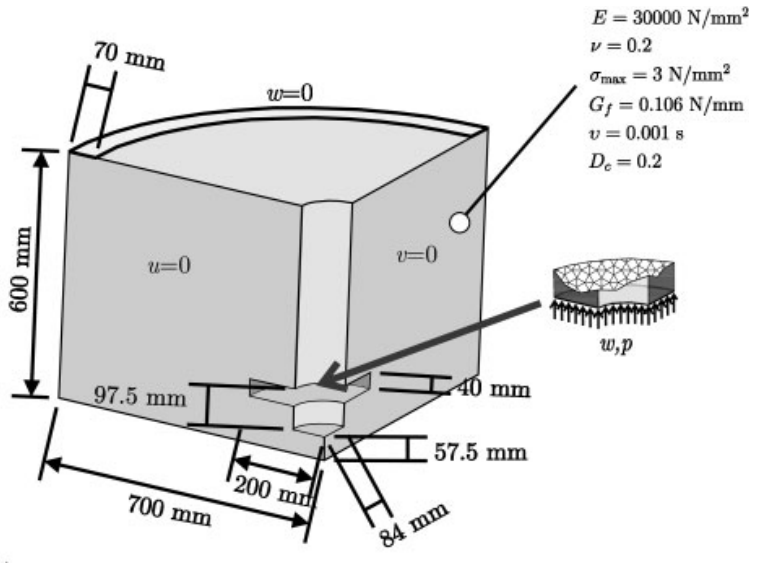

Figure 22: Geometry of the problem and mechanical properties of the concrete (from Areias and Belytschko [21])

Mesh	h	Nodes	Elements
Coarse	40 mm	4664	7742
Medium	30 mm	11555	20166
Fine	25 mm	20672	36985

Table 2: Characteristic mesh sizes, number of nodes and number of elements for the 3D pullout test numerical simulation

for each mesh size are presented in Figure 25. As for the 2D case, the robustness provided by the two methods is very different.

The mixed method yields very consistent results throughout the levels of refinement. For the three meshes, a conical crack starts at the bolt head and progresses towards the steel bracing. The inclination of this crack is defined by the physical geometry of the problem. A secondary, more diffuse, vertical crack appears at the top surface. The standard method produces results which are clearly affected by the bias of the discretization adopted. This is evident for the primary and, even worse, for the secondary cracks.

Figure 26 shows the vertical reaction on the bolt with respect to the imposed displacement. The curves from the three different meshes from both methods are presented. It confirms that:

(a) the mixed formulation provides convergent results; even relatively coarse meshes can produce fairly accurate results, in good agreement with reported numerical simulations;

(b) the standard formulation is severely affected by the discretization adopted, both qualitatively and quantitatively; the corresponding curves show significant over-dissipation.

Finally, it is interesting to observe the similarity in the plots of the reaction forces, between the 2D test (in Figure 21) and 3D test (Figure 26).

8 Conclusion

High-fidelity simulations of 2D and 3D pullout tests on concrete are presented. An elasto-plastic model with Rankine criterion is adopted as constitutive law; details on the formulation and regularization of edge and apex are given.

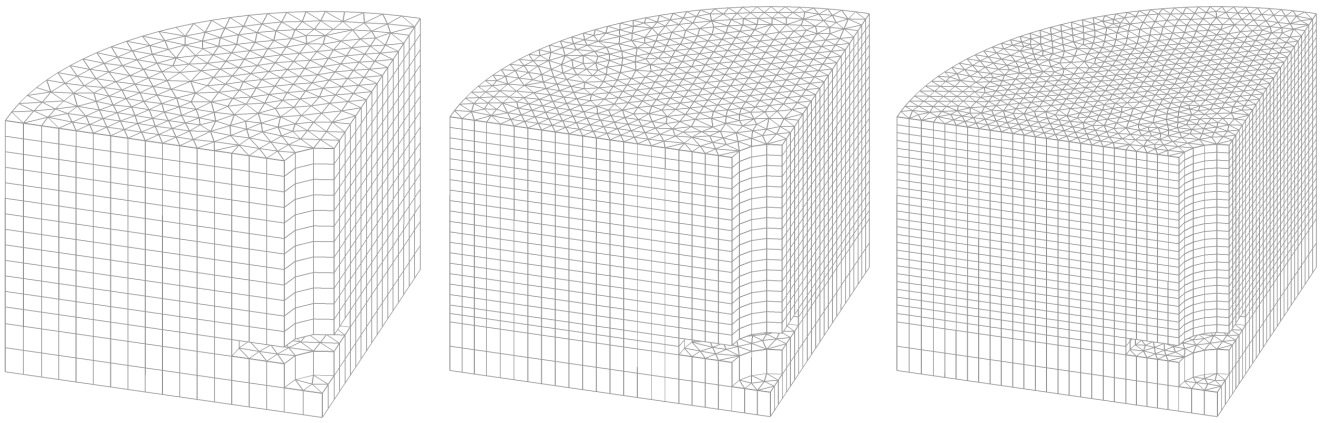

(a) (b) (c)

Figure 23: Discretization meshes for the 3D pullout problem: from left to right, coarse mesh (a), medium mesh (b) and fine mesh (c).

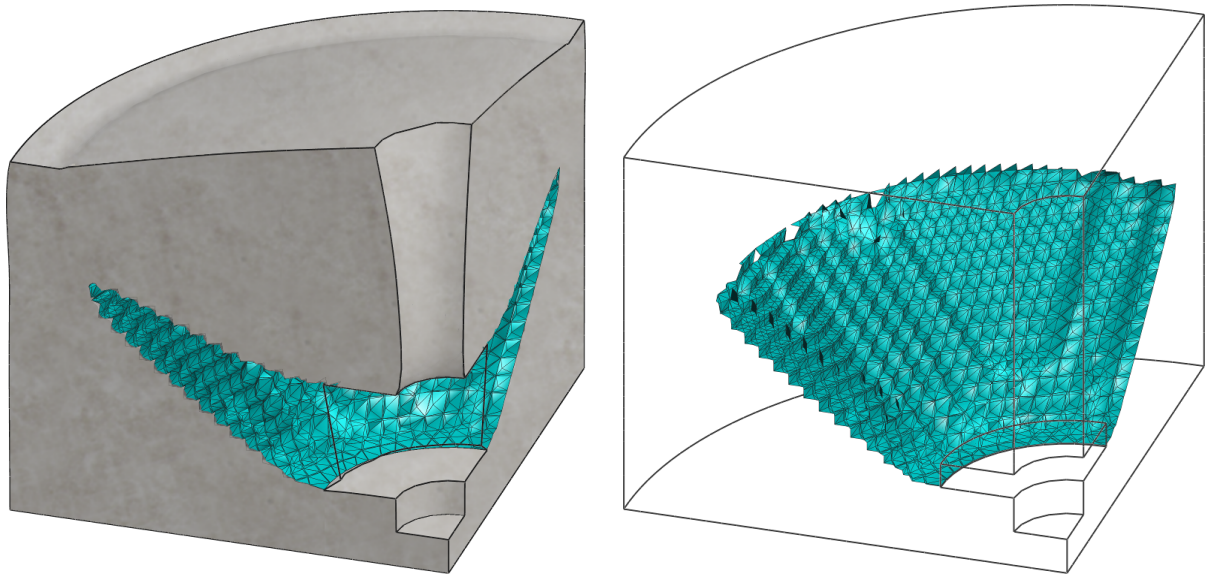

(a) (b)

Figure 24: Deformed concrete block with the crack opening (left) and crack conical surface (right) resulting from the mixed formulation analysis with fine mesh.

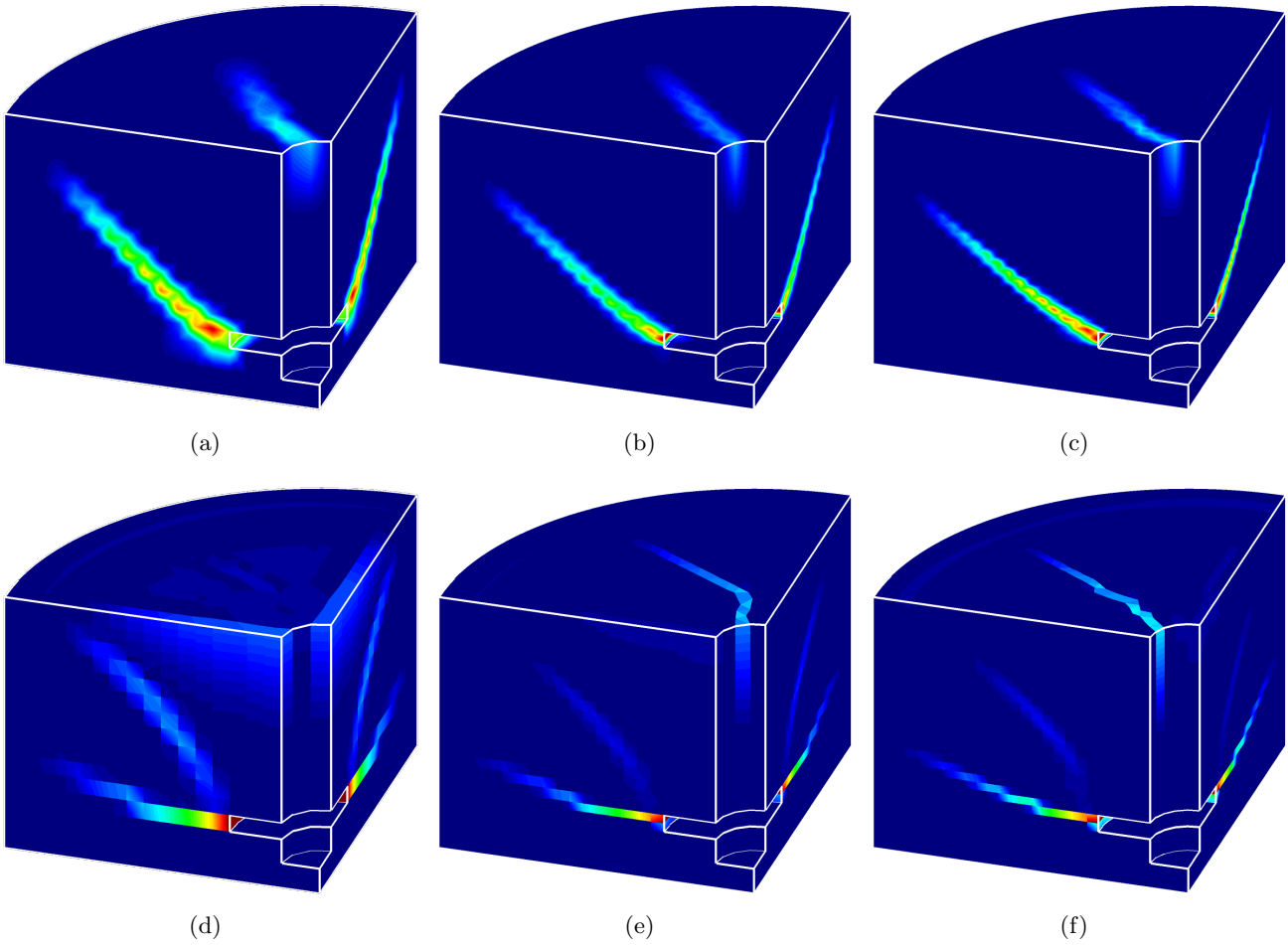

Figure 25: Equivalent plastic strains for the mixed (top) and the standard formulations (bottom).

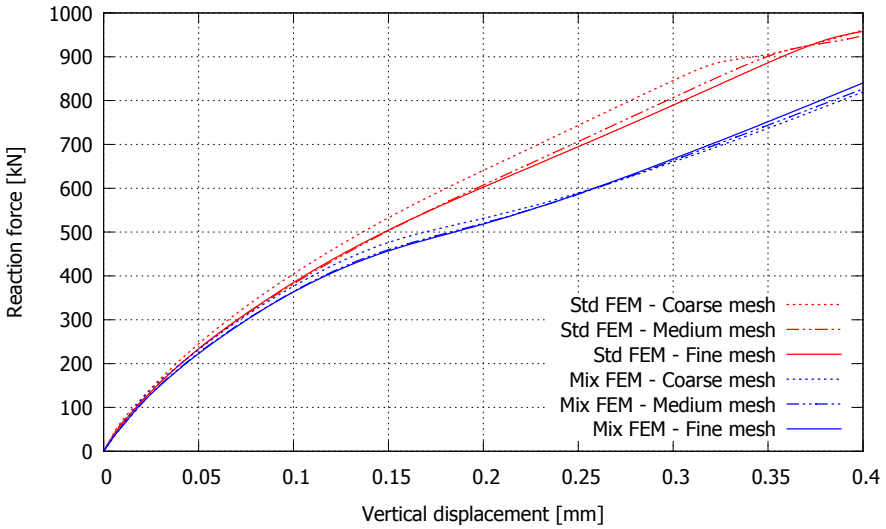

Figure 26: Reaction versus displacement curve for the 3D pullout test.

A novel mixed strain/displacement formulation is used; the necessary stabilization procedure to ensure stability with equal order interpolation spaces is described and implementation issues are covered. The enhanced convergence and accuracy properties of the mixed formulation are demonstrated through the numerical simulation of plane and axis-symmetrical pullout tests. The mixed method yields accurate results, on the one side, showing sensitivity to the physical parameters of the tests, and, on the other side, without spurious sensitivity to the mesh adopted.

In all cases, the expected cracks are predicted as plastic-strain localization bands, without the need of using ad-hoc auxiliar tracking techniques. Crack bifurcation, in accordance with the experimental results, can also be predicted; this is an impossible feat for the local or global tracking algorithm. In addition, the mixed formulation demonstrates ability to capture the correct failure mechanism and the corresponding peak and post-peak behavior with relative coarse meshes. This is an important consideration on the cost-effectiveness of the formulation.

9 Acknowledgments

Financial support from the EC 7^{th} Framework Programme under the MuMoLaDe project - Multiscale Modelling of Landslides and Debris Flows - within the framework of Marie Curie ITN (Initial Training Networks) and the Spanish Ministry of Economy and Competitivity under the EACY project - Enhanced accuracy computational and experimental framework for strain localization and failure mechanisms- within the "Excellency" Program for Knowledge Generation is gratefully acknowledged.

References

[1] B. Winkler, G. Hofstetter, and G. Niederwanger. Experimental verification of a constitutive model for concrete cracking. *Proceedings of the Institution of Mechanical Engineers, Part L: Journal of Material Design and Applications*, 215:75–86, 2001.

[2] B. G. Trunk. *Einfluß der Bauteilgröße auf die Bruchenergie von Beton.* Ph.D. thesis, ETH - Eidgenössischen Technischen Hochschule Zürich, 1999.

[3] G. V. Guinea, J. Planas, and M. Elices. Measurement of the fracture energy using three-point bend tests: Part 1 - Influence of experimental procedures. *Materials and Structures*, 25(4):212–218, 1992.

[4] J. C. Gálvez, M. Elices, G. V. Guinea, and J. Planas. Mixed mode fracture of concrete under proportional and nonproportional loading. *International Journal of Fracture*, 94(3):267–284, 1998.

[5] M. B. Nooru-Mohamed. *Mixed-mode fracture of concrete: an experimental approach.* Ph.D. thesis, TU Delft, Delft University of Technology, 1992.

[6] E. Ballatore, A. Carpinteri, G. Ferrara, and G. Melchiorri. Mixed mode fracture energy of concrete. *Engineering Fracture Mechanics*, 35(13):145 – 157, 1990.

[7] R. Berenbaum and I. Brodie. Measurement of the tensile strength of brittle materials. *British Journal of Applied Physics*, 10(6):281, 1959.

[8] D. A. Abrams. *Tests of bond between concrete and steel.* Number 71. University of Illinois Bulletin edition, 1913.

[9] W. A. Slater, F. E. Richart, and G. G. Scofield. *Tests of bond resistance between concrete and steel.* Number 173. Department of Commerce, Technologic papers of the Bureau of Standards edition, 1920.

[10] L. Elfgren, C. E. Broms, H. Johansson, and A. Rehnstrom. *Anchor Bolts in Reinforced Concrete Foundations: Short Time Tests.* Luleå University of Technology, 1980.

[11] W. H. Peier. Model for pull-out strength of anchors in concrete. *Journal of Structural Engineering*, 109(5):1155–1173, 1983.

[12] R. Eligehausen and G. Sawade. *A fracture mechanics based description of the pull-out behavior of headed studs embedded in concrete.* Universitt Stuttgart, 1989.

[13] Z. P. Bažant, J. Ožbolt, and R. Eligehausen. Fracture size effect: review of evidence for concrete structures. *Journal of structural engineering*, 120(8):2377–2398, 1994.

[14] J. Ožbolt, R. Eligehausen, and H.W. Reinhardt. Size effect on the concrete cone pull-out load. *International Journal of Fracture*, 95(1):391–404, 1999.

[15] B. L. Karihaloo. Pull-out of axisymmetric headed anchors. *Materials and Structures*, 29(3): 152–157, 1996.

[16] M. Baena, L. Torres, A. Turon, and C. Barris. Experimental study of bond behaviour between concrete and FRP bars using a pull-out test. *Composites Part B: Engineering*, 40(8):784–797, 2009.

[17] T. Lecompte, A. Perrot, A. Subrianto, A. Le Duigou, and G. Ausias. A novel pull-out device used to study the influence of pressure during processing of cement-based material reinforced with coir. *Construction and Building Materials*, 78:224–233, 2015.

[18] M. Dejori. *Experimentelle und numerische Traglastanalysen von axial beanspruchten Kopfbolzen beim Versagensmechanismus Betonausbruch.* Diplomarbeit (Master thesis), University of Innsbruck, 2006.

[19] Y. Thenier and G. Hofstetter. Numerical prediction of crack propagation and crack widths in concrete structure. *Engineering Structures*, 31:1832–1840, 2009.

[20] T. C. Gasser and G. A. Holzapfel. Modeling 3D crack propagation in unreinforced concrete using PUFEM. *Computer methods in applied mechanics and engineering*, 194:2859–2896, 2005.

[21] P. M. A. Areias and T. Belytschko. Analysis of three-dimensional crack initiation and propagation using the extended finite element method. *International journal for numerical methods in engineering*, 63:760–788, 2005.

[22] M. Cervera, M. Chiumenti, L. Benedetti, and R. Codina. Mixed stabilized finite element methods in nonlinear solid mechanics. Part III: Compressible and Incompressible Plasticity. *Computer Methods in Applied Mechanics and Engineering*, 285:752–775, 2015.

[23] L. Benedetti, M. Cervera, and M. Chiumenti. Stress-accurate Mixed FEM for soil failure under shallow foundations involving strain localization in plasticity. *Computers and Geotechnics*, 64: 32–47, 2015.

[24] Y. R. Rashid. Ultimate strength analysis of prestressed concrete pressure vessels. *Nuclear Engineering and Design*, 7(4):334–344, 1968.

[25] M. Cervera and M. Chiumenti. Size effect and localization in J2 plasticity. *International Journal of Solids and Structures*, 46(17):3301–3312, August 2009.

[26] M. Cervera, M. Chiumenti, and R. Codina. Mixed stabilized finite element methods in nonlinear solid mechanics. Part II: Strain localization. *Computer Methods in Applied Mechanics and Engineering*, 199(37-40):2571–2589, August 2010.

[27] M. Cervera, M. Chiumenti, and R. Codina. Mesh objective modeling of cracks using continuous linear strain and displacement interpolations. *International Journal for Numerical Methods in Engineering*, (87):962–987, 2011.

[28] R. Faria, J. Oliver, and M. Cervera. A strain-based plastic viscous damage model for massive concrete structures. *International Journal of Solids and Structures*, 35(14):1533–1558, 1998.

[29] C. Feist and G. Hofstetter. An embedded strong discontinuity model for cracking of plain concrete. *Computer Methods in Applied Mechanics and Engineering*, 195(52):7115 – 7138, 2006.

[30] P. H. Feenstra and R. de Borst. A plasticity model and algorithm for mode-I cracking in concrete. *International Journal for Numerical Methods in Engineering*, 38:2509–2529, 1995.

[31] B. Winkler, G. Hofstetter, and H. Lehar. Application of a constitutive model for concrete to the analysis of a precast segmental tunnel lining. *International Journal for Numerical and Analytical Methods in Geomechanics*, 28:797–819, 2004.

[32] J. C. Simo and T. J. R. Hughes. *Computational Inelasticity.* Interdisciplinary applied mathematics: Mechanics and materials. Springer New York, 1998.

[33] D. Boffi, F. Brezzi, and M. Fortin. *Mixed Finite Element Methods and Applications.* Springer, 2013 edition, 7 2013.

[34] T. J. R. Hughes, G. R. Feijóo, L. Mazzei, and J. B. Quincy. The variational multiscale method - A paradigm for computational mechanics. *Computer Methods in Applied Mechanics and Engineering*, 7825(98), 1998.

[35] R. Codina. Stabilization of incompressibility and convection through orthogonal sub-scales in finite element methods. *Computer Methods in Applied Mechanics and Engineering*, 190:1579–1599, 2000.

[36] S. Badia and R. Codina. Unified stabilized finite element formulations for the Stokes and the Darcy problems. *SIAM Journal on Numerical Analysis*, 47(3):1971–2000, 2009.

[37] R. Codina. Finite element approximation of the three-field formulation of the Stokes problem using arbitrary interpolations. *SIAM Journal on Numerical Analysis*, 47(1):699–718, 2009.

[38] M. Cervera, M. Chiumenti, Q. Valverde, and C. Agelet de Saracibar. Mixed linear/linear simplicial elements for incompressible elasticity and plasticity. *Computer Methods in Applied Mechanics and Engineering*, 192(49-50):5249–5263, 12 2003.

[39] R. Codina. Analysis of a stabilized finite element approximation of the Oseen equations using orthogonal subscales. *Applied Numerical Mathematics*, 58(3):264 – 283, 2008.

[40] M. Cervera, M. Chiumenti, and R. Codina. Mixed stabilized finite element methods in nonlinear solid mechanics. Part I: Formulation. *Computer Methods in Applied Mechanics and Engineering*, 199(37-40):2559–2570, August 2010.

[41] J. W. Ju. Isotropic and anisotropic damage variables in continuum damage mechanics. *Journal of Engineering Mechanics*, 116(12):2764–2770, 1990.

[42] G. Meschke, R. Lackner, and H. A. Mang. An anisotropic elastoplastic-damage model for plain concrete. *International Journal for Numerical Methods in Engineering*, 42(4):703–727, 1998.

[43] L. Berto, A. Saetta, R. Scotta, and R. Vitaliani. An orthotropic damage model for masonry structures. *International Journal for Numerical Methods in Engineering*, 55(2):127–157, 2002.

[44] E. Rizzi and I. Carol. Dual orthotropic damageeffect tensors with complementary structures. *International Journal of Engineering Science*, 41(1314):1445 – 1495, 2003.

[45] L. Pelà, M. Cervera, and P. Roca. Continuum damage model for orthotropic materials: Application to masonry. *Computer Methods in Applied Mechanics and Engineering*, 200(9):917–930, 2011.

[46] J. G. Rots, P. Nauta, G. M. A. Kuster, and J. Blaauwendraad. Smeared crack approach and fracture localization in concrete. *HERON, 30 (1), 1985*, 1985.

[47] J. Oliver. A consistent characteristic length for smeared cracking models. *International Journal for Numerical Methods in Engineering*, 28(2):461–474, 1989.

[48] M. Cervera, J. Oliver, and R. Faria. Seismic evaluation of concrete dams via continuum damage models. *Earthquake engineering & structural dynamics*, 24(9):1225–1245, 1995.

[49] R. Faria, J. Oliver, and M. Cervera. A strain-based plastic viscous-damage model for massive concrete structures. *International Journal of Solids and Structures*, 35(14):1533–1558, 1998.

[50] R. de Borst. Integration of plasticity equations for singular yield functions. *Computers and Structures*, 26(5):823 – 829, 1987. ISSN 0045-7949.

[51] H. Matsuoka and T. Nakai. Stress-deformation and strength characteristics of soil under three different principal stresses. *Proc. JSCE*, 232:57–70, 1974.

[52] J. M. Gesto, A. Gens, and J. Vaunat. Smoothing of yield surface and a reformulation of multi-surface plasticity. In E. Oñate, D. R. J. Owen, D. Peric, and B. Suárez, editors, *Proceedings of the XI International Conference on Computational Plasticity. Fundamentals and Applications*. CIMNE - International Center of Numerical Methods in Engineering, 2011.

[53] C. Miehe. Numerical computation of algorithmic (consistent) tangent moduli in large-strain computational inelasticity. *Computer Methods in Applied Mechanics and Engineering*, 134(34): 223–240, 1996.

[54] A. Pérez-Foguet, A. Rodríguez-Ferran, and A. Huerta. Numerical differentiation for local and global tangent operators in computational plasticity. *Computer Methods in Applied Mechanics and Engineering*, 189(1):277–296, 2000.

[55] T. W. Reps and L. B. Rall. Computational divided differencing and divided-difference arithmetics. *Higher-Order and Symbolic Computation*, 16(1-2):93–149, 2003. ISSN 1388-3690.

[56] S. Pietruszczak and Z. Mróz. Finite element analysis of deformation of strain-softening materials. *International Journal for Numerical Methods in Engineering*, 17(3):327–334, 1981.

[57] M. Cervera, C. Agelet de Saracibar, and M. Chiumenti. *COMET: Coupled Mechanical and Thermal analysis. Data Input Manual, Version 5.0, Technical Report IT-308*. 2002. URL `http://www.cimne.com/comet/`.

[58] Q. Duan, J.-H. Song, T. Menouillard, and T. Belytschko. Element-local level set method for three-dimensional dynamic crack growth. *International journal for numerical methdod in engineering*, 80:1520–1543, 2009.

[59] L. Kaczmarczyk, M. M. Nezhad, and C. Pierce. Three dimensional brittle fracture: configurational-force-driven crack propagation. *International Journal for Numerical Methods in Engineering*, 97:531–550, 2014.

3D numerical modelling of twisting cracks under bending and torsion of skew notched beams

L. Benedetti, M. Cervera and M. Chiumenti

Engineering Fracture Mechanics,
In press, (2017)
http://dx.doi.org/10.1016/j.engfracmech.2017.03.025

This page is left intentionally blank.

3D numerical modelling of twisting cracks under bending and torsion of skew notched beams

Lorenzo Benedetti, Miguel Cervera, Michele Chiumenti
International Center for Numerical Methods in Engineering (CIMNE),
Technical University of Catalonia (UPC), Edificio C1, Campus Norte,
Jordi Girona 1-3, 08034 Barcelona, Spain
Corresponding author: lbenedetti@cimne.upc.edu

Abstract

The testing of mode III and mixed mode failure is every so often encountered in the dedicated literature of mechanical characterization of brittle and quasi-brittle materials. In this work, the application of the mixed strain displacement $\boldsymbol{\varepsilon} - \boldsymbol{u}$ finite element formulation to three examples involving skew notched beams is presented. The use of this FE technology is effective in problems involving localization of strains in softening materials.

The objectives of the paper are: (i) to test the mixed formulation in mode III and mixed mode failure and (ii) to present an enhancement in terms of computational time given by the kinematic compatibility between irreducible displacement-based and the mixed strain-displacement elements.

Three tests of skew-notched beams are presented: firstly, a three point bending test of a Poly-Methyl MethaAcrylate beam; secondly, a torsion test of a plain concrete prismatic beam with square base; finally, a torsion test of a cylindrical beam made of plain concrete as well. To describe the mechanical behavior of the material in the inelastic range, Rankine and Drucker-Prager failure criteria are used in both plasticity and isotropic continuum damage formats.

The proposed mixed formulation is capable of yielding results close to the experimental ones in terms of fracture surface, peak load and global loss of carrying capability. In addition, the symmetric secant formulation and the compatibility condition between the standard irreducible method and the strain-displacement one is exploited, resulting in a significant speedup of the computational procedure.

1 Introduction

The experimental testing of brittle and quasi-brittle materials is an exacting and challenging exercise. Three are the failure modes that can be activated: tensile opening, in-plane shearing and out-of-plane shearing. While experimental tests that involve only mode I or mode II are comparatively straightforward to devise, the isolation of mode III represents a challenge. Indeed, this failure type requires the application of a torsion-like load on the specimen but, in reality, it is often impossible to separate mode III from the other two. There is a vast literature that deals specifically with the details of mixed mode tests [1, 2, 3, 4, 5] and their analytical solutions [6, 7, 8, 9, 10]. Quasi brittle materials that fail under tension have the tendency to return to mode I fracture when loaded with a mixed mode stress state. Frequently, this transition takes place because of the curvature of the failure surface and, for this reason, interest is drawn by the shape of the crack propagation.

From the theoretical stand-point, the strength of brittle materials can be predicted by means of Linear Elastic Fracture Mechanics (LEFM), which provides useful quantitative assessment of stress intensity factors and strain energy dissipation near the tip of an evolving crack due to an external load. Nevertheless, LEFM alone is quite limited when addressing elaborated geometries or the progression of the crack tip position. Moreover, it does not provide directly either the shape of the fracture or the global force-displacement behavior. Therefore, the prediction of twisting fracture surfaces in 3D specimens can be only tackled with numerical methods such as the Finite Element Method.

Softening materials exhibiting localization of strains and fracture under external loading are still a strenuous topic in Computational Mechanics. The creation of failure surfaces in a solid body represents, from a mathematical point of view, the inception of a discontinuity in a previously continuous displacement field. Within the FE technology, smearing the localization of strains across a finite length (usually a single element) is an attractive way of avoiding the explicit introduction of discontinuities in the numerical scheme. Once the localization band is smeared across the elements, the dissipation energy becomes dependent on the mesh size and proper energy regularization is necessary for local models to be objective [11, 12]. For that reason, a considerable effort has been focused on reintroducing the missing length scale in the problem. Non-local [13, 14], gradient-enhanced [15, 16] micropolar continua [17, 18] and phase-field [19, 20] are some of the approaches that were proposed in the last three decades. Classically, the problem of mesh size objectivity is overcome by considering explicitly the resolution of the spatial discretization [12, 21]. However, such straight-forward methodology is held back because standard displacement-based finite elements suffer sensibly from mesh bias and stress locking. The first issue causes the solution to be strongly dependent on the orientation of the computational mesh, with the local lack of convergence affecting the results. The second one is linked to the poor kinematics of standard finite elements, similar to the pressure locking in quasi-incompressible situations. These facts are linked with the limitations of the irreducible formulation and, in turn, they crucially affect energy dissipation and global softening behavior. It is clear that the basic FE technology is not able to deal with propagation of 3D twisting cracks, typical of complex mixed load states.

To take into account the limited capability of the irreducible formulation, several alternative technologies were suggested. Initially, local remeshing of the elements in the vicinity of the crack was used [22, 23]. Simo [24, 25] proposed the enhanced strain elements, which take into account a local decomposition of the strains in compatible and incompatible modes. More recently, the XFEM [26, 27] was introduced as an enrichment of finite elements through the notion of partition of unity. Finally, the strong discontinuity approach [28, 29] provides an element formulation that embed the displacement jump in its interior. The implementation of such enrichments requires the use of auxiliary tracking techniques in 2D and 3D.

Recently, the authors have shown that global and local lack of convergence of the standard displacement-based finite element is the reason for FE spurious mesh biased results. Initially, Cervera et al. [30, 31] proved that avoiding global pressure locking in J2 softening material (both with plasticity and isotropic damage constitutive laws) with the introduction of a proper mixed displacement/pressure $\boldsymbol{u}-p$ formulation leads to mesh-bias independent results for quasi-incompressible localization problems. Then, Cervera et al. [32, 33] generalized such concept with the introduction of the strain/displacement

$\boldsymbol{\varepsilon} - \boldsymbol{u}$ formulation. These formulations were capable to cope with strain softening problems involving isotropic damage [34], quasi-brittle tensile cracking [35], J2 [36] and pressure-dependent plasticity [37] without the need of auxiliary techniques.

The mixed $\boldsymbol{\varepsilon} - \boldsymbol{u}$ finite element formulation is very effective for the solution of linear and nonlinear problems, but it comes at some expense. The simultaneous solution of the displacement and the strain unknown requires larger computational resources. However, it is possible to take advantage of the mathematical structure of the proposed formulation to make important savings on this extra cost.

Therefore, the objective of this work is two-fold. On the one hand, to benchmark the mixed strain-displacement $\boldsymbol{\varepsilon} - \boldsymbol{u}$ formulation in problems involving strain localization and crack propagation under mixed mode I, II, III loading. On the other hand, to exploit the kinematic compatibility between the mixed and irreducible FE formulations to reduce the computational time.

The paper initially presents a summary of the mixed (stabilized) strain/displacement finite elements formulation. The implementation of the method is addressed. Firstly, using a secant formulation yields a symmetric algebraic system to be solved. Secondly, the kinematic compatibility between the irreducible and mixed FE enables the use of the two different formulations on the same mesh in order to save on computational resources. The constitutive laws of isotropic continuum damage and associative plasticity are recalled; both Rankine and Drucker-Prager failure criteria are discussed.

Then, three numerical examples are presented. The first example considers the three point bending test of a PolyMethyl MethAcrylate (PMMA) beam with a skewed 45 degree notch located at the midsection. This first analysis is performed with both irreducible and mixed formulations in order to illustrate the relative benefits of the proposed finite elements technology. The second example tackles the torsion test of a skew-notched prismatic beams with square cross section. The specimen is made of plain concrete and has a centered 45° notch as well. The objective of this test is to compare the performance of the isotropic continuum damage model or the associative plasticity one using a mode I failure criterion such as Rankine. The third example is a skew-notched cylindrical beam made of plain concrete under torsional load. This test is identical to the previous one except for the geometry of the specimen. Indeed, the different shapes play a major role in the propagation of the localization and the final crack surface. In this case the Drucker-Prager constitutive law is introduced to study the dependence of the experimental results on shear and, consequently, to evaluate mixed mode loading.

Finally, the simultaneous use of irreducible and mixed formulations is benchmarked in terms of computational time and memory requirements. Results show that the proposed solution scheme is capable of saving substantial computational resources while maintaining the same accuracy.

2 Mixed $\boldsymbol{\varepsilon} - \boldsymbol{u}$ finite elements

The mixed (stabilized) strain displacement $\boldsymbol{\varepsilon} - \boldsymbol{u}$ finite element method was introduced in Cervera et al. [32] for elasticity and it was extended to isotropic damage constitutive models in Cervera et al. [33] and [34]. The extension to plasticity has been recently presented in Cervera et al. [36] and Benedetti et al. [37], where both incompressible and pressure-dependent plasticity models has been considered for shear-softening materials. In the following, the formulation is briefly recalled in a secant format that can accommodate either continuum damage and plasticity constitutive laws.

The mechanical behavior of a solid body $\mathscr{B}$ occupying the space domain Ω is described through the compatibility of deformation and the equilibrium of body forces:

$$-\boldsymbol{\varepsilon} + \boldsymbol{\nabla}^s \boldsymbol{u} = \mathbf{0} \tag{1a}$$

$$\boldsymbol{\nabla} \cdot \boldsymbol{\sigma} + \boldsymbol{f} = \mathbf{0} \tag{1b}$$

where $\boldsymbol{u}$ is the displacement vector, $\boldsymbol{\varepsilon}$ is the strain tensor, $\boldsymbol{\sigma}$ represents the Cauchy stress tensor, $\boldsymbol{\nabla}^s$ and $\boldsymbol{\nabla}\cdot$ are the symmetric gradient and the divergence operators respectively, and $\boldsymbol{f}$ is the vector of body forces. The constitutive equation links the strain and stress fields; in the following, a secant form of the system is assumed

$$\boldsymbol{\sigma} = \mathbb{C}_s \boldsymbol{\varepsilon} \tag{2}$$

where $\mathbb{C}_s$ is the secant constitutive tensor. As the strain and stress tensors are symmetric, thermodynamic considerations imply that the secant constitutive tensor needs be symmetric (see Faria et al. [38] for reference). For the isotropic damage model, the constitutive equation reads:

$$\boldsymbol{\sigma} = (1-d)\,\mathbb{C} : \boldsymbol{\varepsilon} = \mathbb{C}_{s,d} : \boldsymbol{\varepsilon} \tag{3}$$

where d is the damage parameter and $\mathbb{C}$ is the elastic constitutive tensor. The damage secant constitutive tensor can be defined as [36]:

$$\mathbb{C}_{s,d} = (1-d)\,\mathbb{C} \tag{4}$$

In case of plasticity, the constitutive equation reads:

$$\boldsymbol{\sigma} = \mathbb{C} : (\boldsymbol{\varepsilon} - \boldsymbol{\varepsilon}_p) = \mathbb{C}_{s,p} : \boldsymbol{\varepsilon} \tag{5}$$

where $\boldsymbol{\varepsilon}_p$ is the plastic strain tensor. The plastic secant constitutive tensor is defined as:

$$\mathbb{C}_{s,p} = \mathbb{C} - \frac{(\mathbb{C} : \boldsymbol{\varepsilon}_p) \otimes (\mathbb{C} : \boldsymbol{\varepsilon}_p)}{\boldsymbol{\varepsilon} : \mathbb{C} : \boldsymbol{\varepsilon}_p} \tag{6}$$

Note that both secant constitutive tensors, equations (4) and (6), are symmetric.

The strong form of the boundary value problem is completed by imposing proper boundary conditions on $\partial\Omega$ and providing the evolution laws for the plastic strain tensor $\boldsymbol{\varepsilon}_p$ or for the damage variable d.

After symmetrizing the system of equations by pre-multiplication of the secant constitutive tensor $\mathbb{C}_s$, the strong form of the mixed problem in the unknown fields of total strains $\boldsymbol{\varepsilon}$ and displacements $\boldsymbol{u}$ reads:

$$-\mathbb{C}_s : \boldsymbol{\varepsilon} + \mathbb{C}_s : \boldsymbol{\nabla}^s \boldsymbol{u} = \mathbf{0} \tag{7a}$$

$$\boldsymbol{\nabla} \cdot [\mathbb{C}_s : \boldsymbol{\varepsilon}] + \boldsymbol{f} = \mathbf{0} \tag{7b}$$

Now, equation (7a) represents compatibility of deformation and constitutive behavior while equation (7b) represents equilibrium. The corresponding weak form is obtained by introducing the test functions $\boldsymbol{\gamma}$ for strains and $\boldsymbol{v}$ for displacements, respectively, pertaining to the functional spaces $\mathbb{G} \subset L^2(\Omega)^{dim}$ and $\mathbb{V} \subset H^1(\Omega)^{dim}$. Hence, applying Gauss's divergence theorem to the equilibrium equation, the weak form of the mixed problem is:

$$-\int_\Omega \boldsymbol{\gamma} : \mathbb{C}_s : \boldsymbol{\varepsilon} + \int_\Omega \boldsymbol{\gamma} : \mathbb{C}_s : \boldsymbol{\nabla}^s \boldsymbol{u} = 0 \qquad \forall \boldsymbol{\gamma} \in \mathbb{G} \tag{8a}$$

$$\int_\Omega \boldsymbol{\nabla}^{\boldsymbol{s}} \boldsymbol{v} : [\mathbb{C}_s : \boldsymbol{\varepsilon}] = F(\boldsymbol{v}) \qquad \forall \boldsymbol{v} \in \mathbb{V} \tag{8b}$$

where the term $F(\boldsymbol{v})$ represents the work done by tractions on $\partial\Omega$ and body forces in Ω. Note that this continuous weak form is symmetric.

The discrete FE version of the mixed weak form of the problem is found by substituting the unknown fields with their finite element interpolation counterparts:

$$\boldsymbol{\varepsilon} \to \boldsymbol{\varepsilon}_h = \sum_{i=1}^{n_{pts}} \boldsymbol{\gamma}_h^{(i)} \boldsymbol{\varepsilon}_h^{(i)} \qquad \boldsymbol{\gamma}_h \in \mathbb{G}_h \tag{9a}$$

$$\boldsymbol{u} \to \boldsymbol{u}_h = \sum_{i=1}^{n_{pts}} \boldsymbol{v}_h^{(i)} \boldsymbol{u}_h^{(i)} \qquad \boldsymbol{v}_h \in \mathbb{V}_h \tag{9b}$$

where $\boldsymbol{\varepsilon}_h$ and $\boldsymbol{u}_h$ are the nodal degrees of freedom whereas $\boldsymbol{\gamma}_h$ and $\boldsymbol{v}_h$ are the discrete interpolation functions for the strain and the displacement fields pertaining respectively to the spaces $\mathbb{G}_h$ and $\mathbb{V}_h$, the discrete counterparts of $\mathbb{G}$ and $\mathbb{V}$.

The choice of finite elements in the discretization is crucial for the necessary stability of the employed numerical scheme, e.g. [39, 40, 41, 42]. In particular, the *Inf-Sup* condition proves that equal interpolations for strains and displacements (such as P1P1) are bound to be unstable. A stabilization procedure is then required: a modification of the discrete variational form provides the numerical stability, while maintaining consistency. Using the Variational Multiscale Stabilization procedure [43, 44] as presented in [36, 37], the set of equations for the stabilized problem reads:

$$\begin{aligned} -(1-\tau_{\boldsymbol{\varepsilon}})\int_\Omega \boldsymbol{\gamma}_h : \mathbb{C}_s : (\boldsymbol{\varepsilon}_h - \boldsymbol{\nabla}^s \boldsymbol{u}_h) \\ -\tau_u \int_\Omega [\boldsymbol{\nabla}\cdot(\mathbb{C}_s:\boldsymbol{\gamma}_h)]\cdot[\boldsymbol{\nabla}\cdot[\mathbb{C}_s:\boldsymbol{\varepsilon}_h]+f] = 0 \quad \forall \boldsymbol{\gamma}_h \in \mathbb{G}_h \end{aligned} \tag{10a}$$

$$\int_\Omega \boldsymbol{\nabla}^s \boldsymbol{v}_h : \mathbb{C}_s : \boldsymbol{\varepsilon}_h - \tau_{\boldsymbol{\varepsilon}} \int_\Omega \boldsymbol{\nabla}^s \boldsymbol{v}_h : \mathbb{C}_s : [\boldsymbol{\varepsilon}_h - \boldsymbol{\nabla}^s \boldsymbol{u}_h] = F(\boldsymbol{v}_h) \quad \forall \boldsymbol{v}_h \in \mathbb{V}_h \tag{10b}$$

The scalars $\tau_{\boldsymbol{\varepsilon}}$ and $\tau_{\boldsymbol{u}}$ are the stabilization parameter computed as:

$$\tau_{\boldsymbol{\varepsilon}} = c_{\boldsymbol{\varepsilon}} \frac{h}{L_0} \qquad \tau_{\boldsymbol{u}} = c_{\boldsymbol{u}} \frac{hL_0}{E} \tag{11}$$

where $c_{\boldsymbol{u}}$ and $c_{\boldsymbol{\varepsilon}}$ are arbitrary positive numbers, E is the Young's modulus, h is the representative size of the finite element mesh and L_0 is a characteristic length of the problem.

The stabilized formulation is consistent with the original discrete weak form since, with converging values of the unknowns $\boldsymbol{\varepsilon}_h$ and $\boldsymbol{u}_h$, the contribution of the stabilization terms (those multiplied by $\tau_{\boldsymbol{\varepsilon}}$ and $\tau_{\boldsymbol{u}}$) disappears, being dependent on the residuals of the strong form of the problem, respectively (see equations (7a) and (7b)):

$$r_{\boldsymbol{\varepsilon}_h} = \mathbb{C}_s : \boldsymbol{\varepsilon}_h - \mathbb{C}_s : \boldsymbol{\nabla}^s \boldsymbol{u}_h \qquad r_{\boldsymbol{u}_h} = \boldsymbol{\nabla}\cdot[\mathbb{C}_s : \boldsymbol{\varepsilon}_h] + \boldsymbol{f} \tag{12}$$

When dealing with problems that do not involve incompressibility constrains, it is possible to drop the displacement subscale and consider solely the strain one by setting $\tau_{\boldsymbol{u}} = 0$. The final set of equations for the mechanical problem reads:

$$-(1-\tau_{\boldsymbol{\varepsilon}})\int_\Omega \boldsymbol{\gamma}_h : \mathbb{C}_s : (\boldsymbol{\varepsilon}_h - \boldsymbol{\nabla}^s \boldsymbol{u}_h) = 0 \quad \forall \boldsymbol{\gamma}_h \in \mathbb{G}_h \tag{13a}$$

$$\int_\Omega \boldsymbol{\nabla}^s \boldsymbol{v}_h : \mathbb{C}_s : \boldsymbol{\varepsilon}_h - \tau_{\boldsymbol{\varepsilon}} \int_\Omega \boldsymbol{\nabla}^s \boldsymbol{v}_h : \mathbb{C}_s : [\boldsymbol{\varepsilon}_h - \boldsymbol{\nabla}^s \boldsymbol{u}_h] = F(\boldsymbol{v}_h) \quad \forall \boldsymbol{v}_h \in \mathbb{V}_h \tag{13b}$$

Furthermore, expression (13b) can be written as:

$$\int_\Omega \boldsymbol{\nabla}^s \boldsymbol{v}_h : \mathbb{C}_s : \boldsymbol{\varepsilon}_{stab,h} = F(\boldsymbol{v}_h) \quad \forall \boldsymbol{v}_h \in \mathbb{V}_h \tag{14}$$

where the stabilized discrete strain field

$$\boldsymbol{\varepsilon}_{stab,h} = (1-\tau_{\boldsymbol{\varepsilon}})\,\boldsymbol{\varepsilon}_h + \tau_{\boldsymbol{\varepsilon}} \boldsymbol{\nabla}^s \boldsymbol{u}_h \tag{15}$$

is a blending of the continuous ($\boldsymbol{\varepsilon}_h$) and discontinuous ($\boldsymbol{\nabla}^s \boldsymbol{u}_h$) strain fields weighted by the stabilization parameter $\tau_{\boldsymbol{\varepsilon}}$. The discrete stabilized form, equation (13), is symmetric.

3 Compatibility with standard u finite elements

The mechanical problem is governed by the compatibility equation (1a), the equilibrium equation (1b) and the constitutive equation (2), all in strong form. As described above, the variational mixed $\boldsymbol{\varepsilon} - \boldsymbol{u}$ form, in equations (8a)-(8b), takes $\boldsymbol{\varepsilon}$ and $\boldsymbol{u}$ as main variables and considers both compatibility and

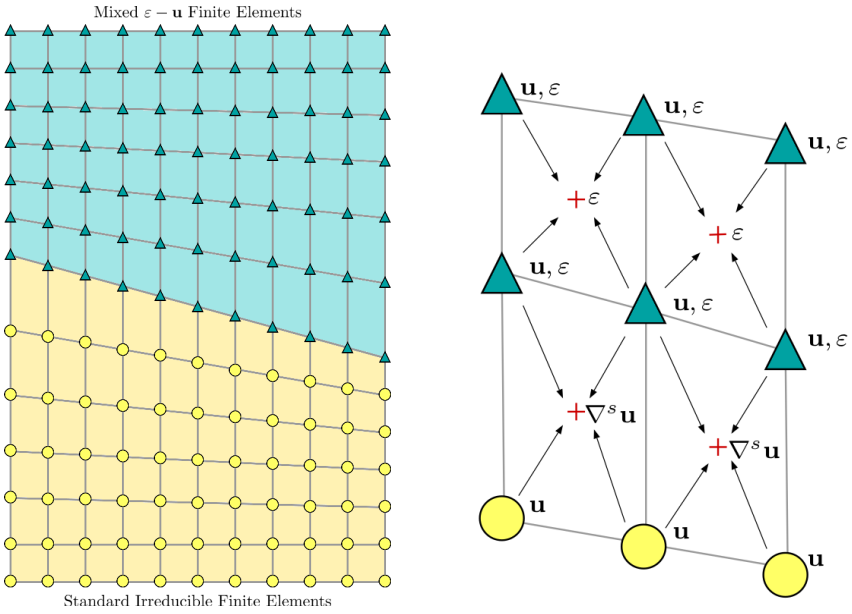

Figure 1: FE mesh with combined standard and mixed formulations. Turquoise color represents the $\boldsymbol{\varepsilon} - \boldsymbol{u}$ elements whereas yellow represents the displacement-based ones. The strain tensor at the Gauss points (symbolized with red crosses) is computed with the interpolation of nodal strain in the mixed formulation or the discrete symmetric gradient of displacements in the irreducible one.

equilibrium in weak form. The corresponding discrete FE form requires the interpolation of both the strain and the displacement fields, with $\boldsymbol{\varepsilon}_h$ and $\boldsymbol{u}_h$ as nodal degrees of freedom.

Alternatively, the more standard irreducible $\boldsymbol{u}$ form takes only the displacement as main variable and considers only equilibrium in weak form. To this end, substituting equation (1a) into equation (2), and this into equation (1b), yields:

$$\boldsymbol{\nabla} \cdot [\mathbb{C}_s : \boldsymbol{\nabla}^s \boldsymbol{u}] + \boldsymbol{f} = 0 \tag{16}$$

with the corresponding variational (weak) form

$$\int_\Omega \boldsymbol{\nabla}^s \boldsymbol{v} : \mathbb{C}_s : \boldsymbol{\nabla}^s \boldsymbol{u} = F(\boldsymbol{v}) \quad \forall \boldsymbol{v} \in \mathbb{V} \tag{17}$$

The irreducible discrete FE form requires solely the interpolation of the displacement field:

$$\boldsymbol{u} \to \boldsymbol{u}_h = \sum_{i=1}^{n_{pts}} \boldsymbol{v}_h^{(i)} \boldsymbol{u}_h^{(i)} \qquad \boldsymbol{v}_h \in \mathbb{V}_h \tag{18}$$

with $\boldsymbol{u}_h$ as the nodal degrees of freedom, which is identical to equation (9b).

From a computational perspective, the $\boldsymbol{\varepsilon} - \boldsymbol{u}$ finite element presents a larger number of variables to be solved compared to the standard one. For each mesh node of a 3D problem, the vector of unknowns contains 9 scalars, 3 displacements (u_x, u_y, u_z) and 6 strains $(\varepsilon_{xx}, \varepsilon_{yy}, \varepsilon_{zz}, \varepsilon_{xy}, \varepsilon_{xz}, \varepsilon_{yz})$ of the symmetric deformation tensor, in Voigt's notation.

Note that, if the same interpolation functions $\boldsymbol{u}_h$ are selected, the kinematics of the mixed and the irreducible formulations are compatible, i.e. the requirement of inter-elemental continuity is satisfied. This is necessary to prove consistency of the FE form in the classical Rayleigh-Ritz sense. Therefore, a mesh constructed as in Figure 1, where the top part is formed by mixed $\boldsymbol{\varepsilon} - \boldsymbol{u}$ elements while the bottom part is made of standard $\boldsymbol{u}$ ones, is feasible.

Indeed, the standard finite elements are a particular case of the stable mixed formulation, see equation (14). Setting $\tau_{\boldsymbol{\varepsilon}} = 1$ in expressions (13), equation (13a) becomes an identity and (13b) reduces to (17).

Therefore, it is possible to reduce the computational burden by considering a combined standard/mixed FE mesh. Setting the stabilization parameter $\tau_{\boldsymbol{\varepsilon}} = 1$ where possible and skipping the corresponding elemental computations leads to substantial savings in the total number of degrees of freedom, global operations and corresponding matrix storage.

4 Algebraic implementation aspects

In previous works [35, 36, 37], the nonlinear algebraic problem in equations (13a)-(13b) was solved in an incremental-iterative manner using the Newton-Raphson method.

Let the algebraic nonlinear problem be written in an incremental-iterative fashion as

$$\boldsymbol{R}\left(\boldsymbol{X}_{n+1}^{i+1}\right) = \boldsymbol{P}\left(\boldsymbol{X}_{n+1}^{i+1}\right) - \boldsymbol{F}_{n+1} = \boldsymbol{0} \tag{19}$$

where n and i are the increment and iteration counters, respectively; $\boldsymbol{X}$ is the solution vector, $\boldsymbol{P}, \boldsymbol{F}$ and $\boldsymbol{R}$ are the internal, external and residual force vectors.

Writing an iterative correction as:

$$\boldsymbol{X}_{n+1}^{i+1} = \boldsymbol{X}_{n+1}^{i} + \delta\boldsymbol{X}^{i+1} \tag{20}$$

and given that a linear Taylor's approximation of the internal forces

$$\boldsymbol{R}\left(\boldsymbol{X}_{n+1}^{i+1}\right) \simeq \boldsymbol{R}\left(\boldsymbol{X}_{n+1}^{i}\right) + \boldsymbol{J}\left(\boldsymbol{X}_{n+1}^{i}\right)\delta\boldsymbol{X}^{i+1} = \boldsymbol{0} \tag{21}$$

where $\boldsymbol{J}\left(\boldsymbol{X}_{n+1}^{i}\right)$ is the jacobian (tangent) matrix. It follows that

$$\boldsymbol{J}\left(\boldsymbol{X}_{n+1}^{i}\right)\delta\boldsymbol{X}^{i+1} = -\boldsymbol{R}\left(\boldsymbol{X}_{n+1}^{i}\right) \tag{22}$$

This is Newton-Raphson's method. On the one hand, this procedure presents asymptotic quadratic convergence when exact tangent matrices are used and the initial approximation is close enough to the solution; on the other hand, this results in a non-symmetric algebraic system to be solved. The reason for the non-symmetry of the rate problem derived from equations (13) are (i) the (possible) lack of symmetry of the constitutive tangent tensor and (ii) the non-symmetric dependence of the discrete stresses on $\boldsymbol{\varepsilon}_h$ and $\boldsymbol{u}_h$.

Alternatively, the nonlinear algebraic problem in equations (13) may be solved using the secant (or Picard's) method.

Let the internal forces be written in secant form as

$$\boldsymbol{P}\left(\boldsymbol{X}_{n+1}^{i+1}\right) = \boldsymbol{S}\left(\boldsymbol{X}_{n+1}^{i+1}\right)\boldsymbol{X}_{n+1}^{i+1} \tag{23}$$

Given that

$$\boldsymbol{R}\left(\boldsymbol{X}_{n+1}^{i}\right) = \boldsymbol{S}\left(\boldsymbol{X}_{n+1}^{i}\right)\boldsymbol{X}_{n+1}^{i} - \boldsymbol{F}_{n+1} \tag{24}$$

it follows that

$$\boldsymbol{S}\left(\boldsymbol{X}_{n+1}^{i}\right)\delta\boldsymbol{X}^{i+1} = -\boldsymbol{R}\left(\boldsymbol{X}_{n+1}^{i}\right) \tag{25}$$

The secant method converges superlinearly, but the need of evaluating consistent derivatives is avoided. Furthermore, in the case under consideration, the secant matrix $\boldsymbol{S}\left(\boldsymbol{X}_{n+1}^{i}\right)$ is symmetric.

Comparing expressions (22) and (25) it is obvious that both methods can be implemented similarly, the only difference being the use of the tangent or secant matrix.

A further approximation can be used in both methods by making $\boldsymbol{J}\left(\boldsymbol{X}_{n+1}^{i}\right) \simeq \boldsymbol{J}\left(\boldsymbol{X}_{n+1}^{1}\right)$ and $\boldsymbol{S}\left(\boldsymbol{X}_{n+1}^{i}\right) \simeq \boldsymbol{S}\left(\boldsymbol{X}_{n+1}^{1}\right)$ with the matrices recomputed only for the first iteration of the increments. These are modified Newton-Raphson's and Picard's schemes. The convergence is linear for both methods.

For the mixed finite element formulation discussed in Section 2, $\boldsymbol{X}_{n+1} = [\boldsymbol{\varepsilon}_h, \boldsymbol{u}_h]^T_{n+1}$. Details on the algebraic tangent system of equations (22) are given in references [37, 36]. The algebraic secant system of equations (25) reads:

$$\left[\begin{array}{cc} \boldsymbol{M}_\tau & \boldsymbol{G}_\tau \\ \boldsymbol{D}_\tau & \boldsymbol{K}_\tau \end{array} \right]^i_n \left[\begin{array}{c} \delta\boldsymbol{\varepsilon}_h \\ \delta\boldsymbol{u}_h \end{array} \right]^{i+1}_{n+1} = - \left[\begin{array}{c} R_{1,h} \\ R_{2,h} \end{array} \right]^i_{n+1} \tag{26}$$

and the submatrices $\boldsymbol{M}_\tau$, $\boldsymbol{G}_\tau$, $\boldsymbol{D}_\tau$ and $\boldsymbol{K}_\tau$ are computed as:

$$\boldsymbol{M}_\tau = -\left(1 - \tau_{\boldsymbol{\varepsilon}}\right) \int_\Omega \boldsymbol{N}_{\boldsymbol{\varepsilon}}{}^T \mathbb{C}_s \, \boldsymbol{N}_{\boldsymbol{\varepsilon}} - \tau_{\boldsymbol{u}} \int_\Omega \mathbb{C}_s \, \boldsymbol{B}\boldsymbol{B}^T \, \mathbb{C}_s \tag{27}$$

$$\boldsymbol{G}_\tau = \left(1 - \tau_{\boldsymbol{\varepsilon}}\right) \int_\Omega \boldsymbol{N}_{\boldsymbol{\varepsilon}}{}^T \mathbb{C}_s \, \boldsymbol{B} \tag{28}$$

$$\boldsymbol{D}_\tau = \left(1 - \tau_{\boldsymbol{\varepsilon}}\right) \int_\Omega \boldsymbol{B}^T \mathbb{C}_s \boldsymbol{N}_{\boldsymbol{u}} \tag{29}$$

$$\boldsymbol{K}_\tau = \tau_{\boldsymbol{\varepsilon}} \int_\Omega \boldsymbol{B}^T \mathbb{C}_s \, \boldsymbol{B} \tag{30}$$

where $\boldsymbol{M}$ is the mass-like projection matrix, $\boldsymbol{G}$ is the discrete gradient matrix, $\boldsymbol{D}$ is the discrete divergence matrix and $\boldsymbol{K}$ is the stiffness matrix.

5 Plasticity and damage models

In this work, both plasticity and damage models are introduced to describe strain localization and failure. Both Rankine and Drucker-Prager failure criteria are used. Figure 2 shows a representation of the corresponding admissible elastic domains in the Haigh-Westergaard space.

In this space of principal stresses, the Rankine criterion appears as the intersection of three mutually orthogonal planes, which are, at the same time, orthogonal to the principal axes. Therefore, it is a triangular pyramid with the apex located on the hydrostatic axis. Contrariwise, the Drucker-Prager criterion appears as a cone with a circular cross-section in the octahedral plane and axisymmetric to the $\sigma^1 = \sigma^2 = \sigma^3$ axis. Both criteria are pressure-dependent, although the Drucker-Prager criterion reduces to the pressure-independent Von Mises one for vanishing friction angle.

In Table 1, a general overview of the implemented constitutive laws is presented. The failure criterion is defined by the scalar function $f\left(\boldsymbol{\sigma}, q\right)$ which depends on the equivalent stress measure

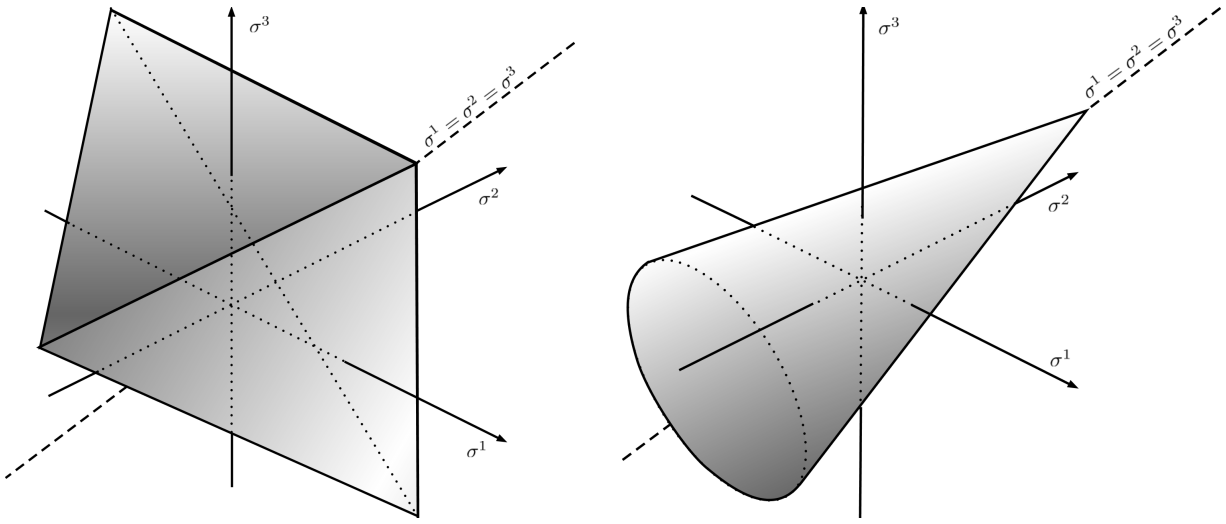

Figure 2: Representation of the Rankine and Drucker-Prager failure criteria in the principal stress space $\left(\sigma^1, \sigma^2, \sigma^3\right)$.

$\tau(\boldsymbol{\sigma})$ and the stress-like isotropic softening function $q(\xi)$; ξ is the strain-like softening variable which controls the evolution of the failure surface.

In the case of the Rankine failure criterion, the equivalent stress is given by the first principal stress value as:

$$\tau(\boldsymbol{\sigma}) = \sigma_1 \tag{31}$$

whereas, in the Drucker-Prager failure criterion, shear stress and pressure are linearly combined through the tangent of the friction angle ϕ:

$$\tau(\boldsymbol{\sigma}) = \sqrt{3J_2(\boldsymbol{\sigma})} + \frac{1}{3} I_1(\boldsymbol{\sigma}) \tan(\phi) \tag{32}$$

being $I_1(\boldsymbol{\sigma})$ the trace of the stress tensor and $J_2(\boldsymbol{\sigma})$ the second invariant of the deviatoric part of $\boldsymbol{\sigma}$.

Despite having identically failure criteria and being their evolution controlled by analogous loading-unloading conditions (Karush-Kuhn-Tucker conditions), the global behavior of the two constitutive models is substantially different. Inelastic flow in plasticity is directional; in particular, in the associative case, it is defined by the normal vector to the yield surface. Therefore, for Rankine-type plastic models, the inelastic flow occurs strictly parallel to one of the principal axes. This does not occur for the Drucker-Prager model, where plastic flow is orthogonal to the cone in Figure 2. In marked contrast, inelastic deformation in the continuum isotropic damage model is not directional, since it affects equally all directions of the Haigh-Westergaard space. As shown later, this has a large influence on strain localization and failure when softening behavior is considered.

In the following, exponential softening is considered for both the plastic and continuum damage models. Note that, in a softening process, the energy dissipated by the inelastic behavior is linked to the fracture energy G_f, defined by unit surface. However, when using a plastic or damage model, the dissipated energy is defined by unit volume. These two definitions are related through a characteristic length l_{ch} in the discrete FE setting, which, in turn, depends on the resolution of the mesh. The size of the strain concentration band depends on the finite element technology, as pointed out by Cervera et al. [33]: irreducible finite elements provide a concentration band within a single element span, having a discontinuos strain field; contrariwise, in the $\boldsymbol{\varepsilon} - \boldsymbol{u}$ mixed FE formulation, the slip line spans two elements due to inter-elemental continuous strain. Consequently, the characteristic length l_{ch} is taken accordingly. Additional details of the models can be found in references [37] for the Drucker-Prager plasticity model, [35] for the Rankine plasticity model and [34, 45, 46] for the Rankine isotropic damage model.

	Associative plasticity model	Isotropic continuum damage model
Constitutive equation	$\boldsymbol{\sigma} = \mathbb{C} : (\boldsymbol{\varepsilon} - \boldsymbol{\varepsilon}_p)$	$\boldsymbol{\sigma} = (1-d)\,\mathbb{C} : \boldsymbol{\varepsilon}$
Softening function	$q = q(\xi)$	
Inelastic criterion	$f(\boldsymbol{\sigma}, q) = \tau(\boldsymbol{\sigma}) - (\sigma_y - q)$	
Internal variables evolution	$\dot{\xi} = \dot{\lambda},\ \dot{\boldsymbol{\varepsilon}}_p = \dot{\lambda}\frac{\partial f}{\partial \boldsymbol{\sigma}}$	$\dot{\xi} = \dot{\lambda},\ d(\xi) = 1 - \frac{q}{\xi}$
Loading-unloading conditions	$\dot{\lambda} \geq 0,\ f(\boldsymbol{\sigma}, q) \leq 0,\ \dot{\lambda} f(\boldsymbol{\sigma}, q) = 0$	

Table 1: Summary of associative plasticity and isotropic continuum damage models. Both Rankine and Drucker-Prager failure criteria are considered.

6 Numerical Simulations

6.1 Three point bending test on skew notched beam

The first example is a three point bending test on a beam with a slanted notch. The slot is vertical, with an inclination of 45° with respect to the longitudinal midplane of the beam. The specimen geometry, represented in Figure 3, has a total length $L = 260$ mm, effectively supported span $L_e = 240$ mm, by a thickness $t = 10$ mm and a total height $w = 60$ mm. The initial notch is $a = 20$ mm high ($a = w/3$), with a constant section width of 2 mm and a slant angle $\gamma = 45°$.

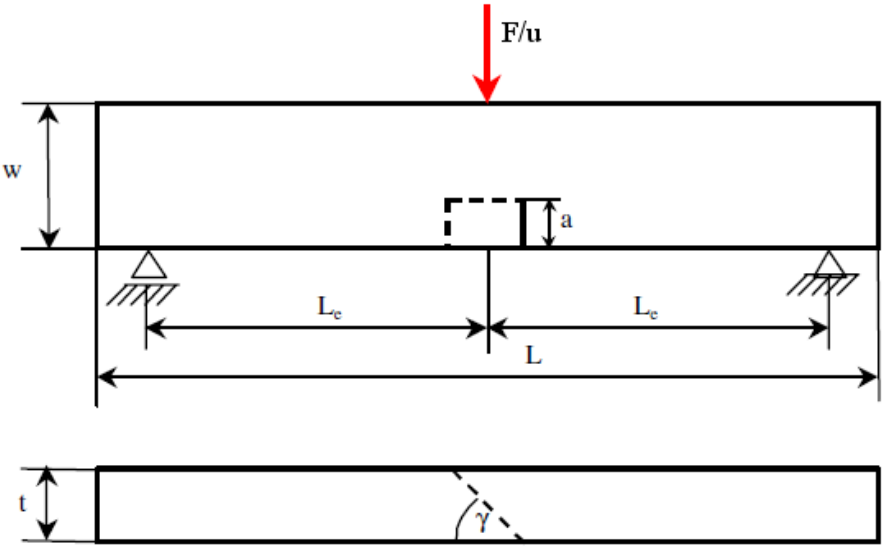

Figure 3: Geometry of the twisted crack 3PB test, taken from Citarella and Buchholz [47]

This test was initially introduced by Pook [1] to study the propagation of the crack front under cyclic loading in steel specimens. More recently, the same tests were recreated by Cooke and Pollard [5], Buchholz et al. [9] using PolyMethyl MethAcrylate (PMMA), also known as Plexiglass, in order to better examine the crack front evolution through its transparency. Lazarus and Leblond [6] and Lazarus et al. [8] studied the same problem in the case of monotonic load. Finally, Citarella and Buchholz [47] and Ferté et al. [48] studied the problem from a computational stand point using the Boundary Elements Method and the X-FEM technology, respectively.

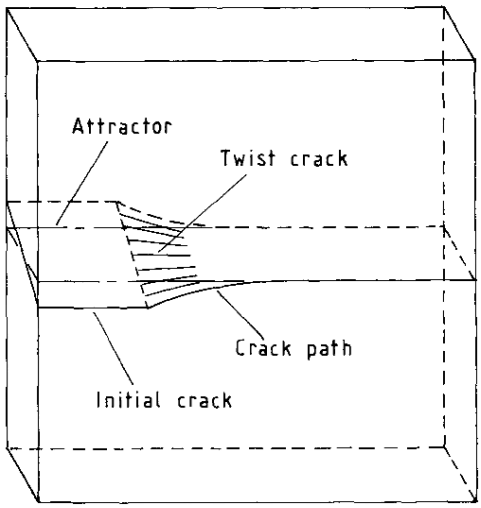

Figure 4: Crack path interpretation from Pook [3]

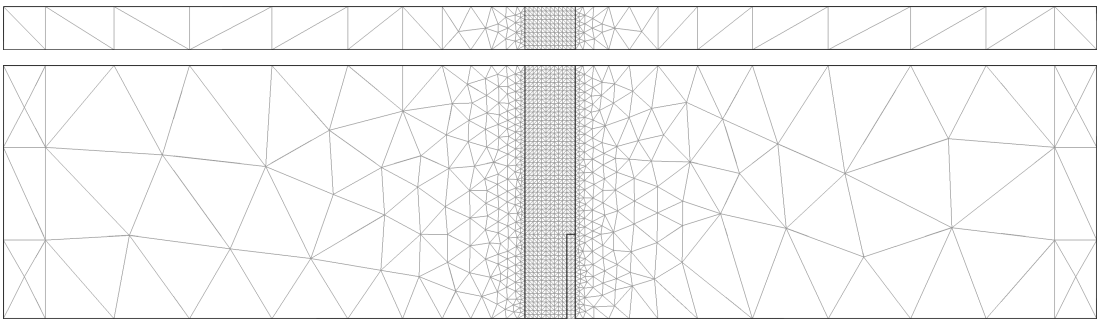

Figure 5: Computational mesh of P1 and P1P1 tetrahedral elements used for the 3 point bending test.

Examining the experimental results (Figure 4), the crack starts from the initial notch and, with increasing applied load, a rotation of the failure surface is observable. Pook [3] and Yates and Mohammed [4] showed that this characteristic behavior is due to the transition from Mode III to Mode I fracture. At the beginning of the test, the stresses in the vicinity of the notch are given by the asymmetrical bending of the specimen, resulting in a diagonal onset of cracking. Then, as the crack progresses, Mode I becomes predominant and the failure surface aligns with the dominant longitudinal normal stresses due to bending. The geometrical symmetry midplane, which coincides with the loading symmetry plane, can be considered as an attractor of the twisting crack.

PolyMethyl MethAcrylate is an amorphous glass polymer which is characterized by homogeneous mechanical properties and brittle failure. The literature previously cited reports a Young's modulus $E = 2800$ MPa, a Poisson's ratio $\nu = 0.38$, an elastic threshold uniaxial stress $\sigma_y = 40$ MPa and fracture energy $G_f = 500$ J/m. Because of the clear role of tensile failure in this problem, it is natural to describe the inelastic processes using constitutive models based on Rankine's criterion.

In the finite element model, the beam is supported by two rollers on the lower surface which sustain only vertical forces (in the Y direction). The centerline on the top surface of the beam not only imposes a vertical displacement of 2 mm, but also provides restraint to the out-of-plane forces (X direction) and horizontal sliding (Z direction). In the numerical analysis, the PMMA beam is subjected to monotonic loading.

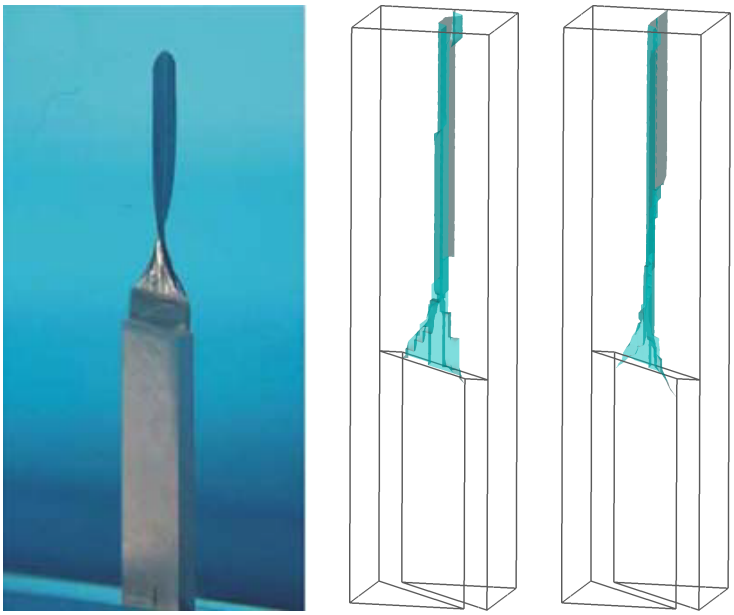

(a) Experiment (b) IsoDamage (c) Plasticity

Figure 6: Experimental [10] and numerical ($\boldsymbol{\varepsilon} - \boldsymbol{u}$ formulation) crack surface of the three point bending test on PMMA.

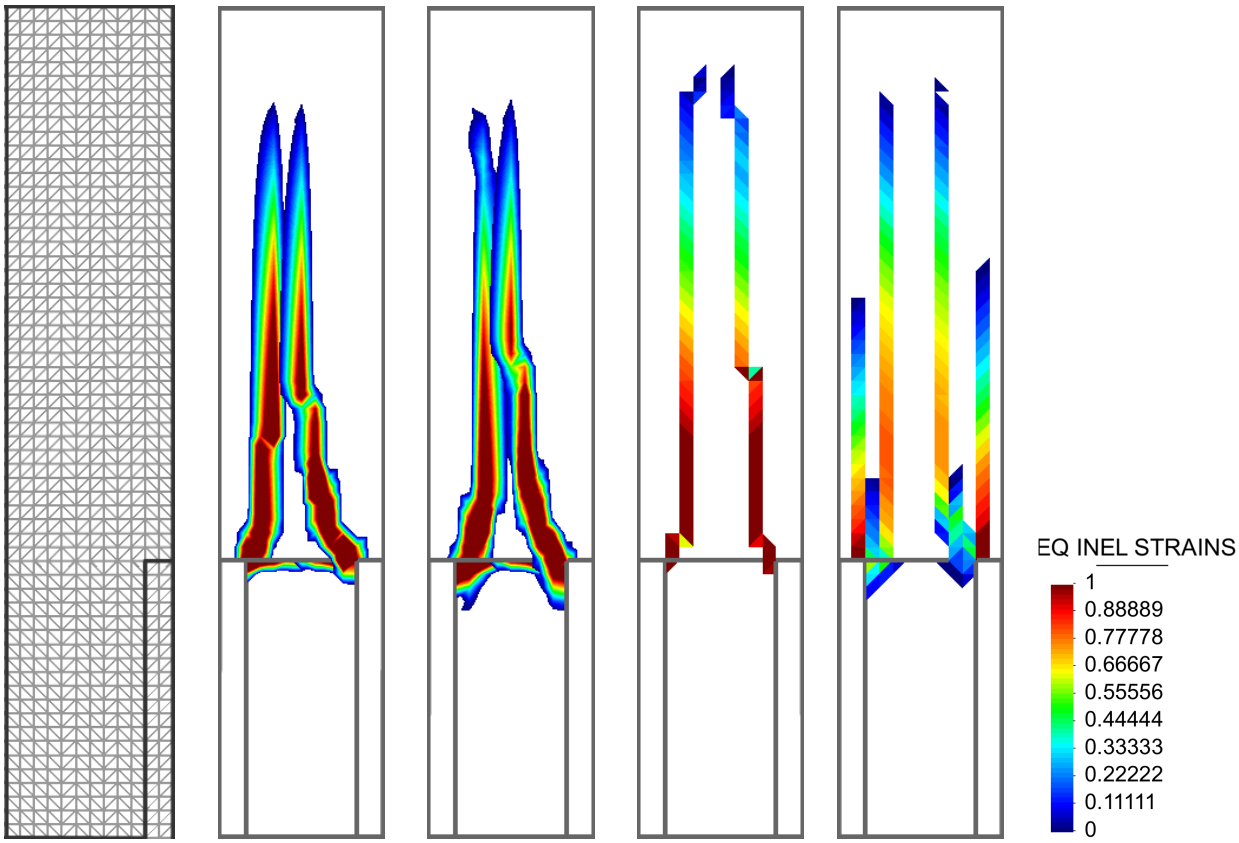

(a) Detail of the structured mesh in the middle region

(b) $\boldsymbol{u} - \boldsymbol{\varepsilon}$ with IsoDamage

(c) $\boldsymbol{u} - \boldsymbol{\varepsilon}$ with Plasticity

(d) $\boldsymbol{u}$ with Iso-Damage

(e) $\boldsymbol{u}$ with Plasticity

(f) Figure legend

Figure 7: Contour fills of major principal total strain in the crack at the front and back faces of the beam under 3 point bending test.

The FE mesh consists of tetrahedral elements (Figure 5 and Figure 7(a) for a detailed view), structured in the vicinity of the slot, where the elements have a characteristic size $h = 1$ mm, and unstructured elsewhere. This allows to model the part subjected to localization with a 12×10 base grid and the notch is two elements wide. The grid of structure elements shows biased planes at $0°, +45°, 90°$ and $-45°$. The final computational mesh is composed by 58,557 tetrahedral elements (11,677 points).

The objective of the numerical analysis is to test the mixed $\boldsymbol{\varepsilon} - \boldsymbol{u}$ formulation in comparison to the standard displacement-based FEM. This benchmark is challenging for two reasons. Firstly, the problem involves strain localization and crack propagation in a rather brittle material, which implies a sudden drop in stresses after cracking. As a consequence, global stability is sharply lost. Secondly, the discretization is rather coarse. In fact, from the notch to the midsection, the mesh presents just 4 elements; that is the available resolution to model the onset of failure propagation and its twisting and alignment with the mid-section.

Both Rankine-like isotropic damage and plasticity models provide similar solutions to this problem: Figure 6 compares the crack surface in the PMMA beam with the crack front propagating from the initial notch to the top surface, obtained with the two constitutive laws using the proposed mixed FE method. The numerical crack surfaces are plotted as the level set of zero horizontal displacements (Z direction), thanks to the symmetry of the problem.

Nevertheless, Figure 7 shows a detail of the mesh grid used for the computations and some substantial differences among the standard and mixed FE formulations in the contour fills of principal total strain in the crack, at the front and the back faces of the beam. Using the $\boldsymbol{\varepsilon} - \boldsymbol{u}$ formulation, the

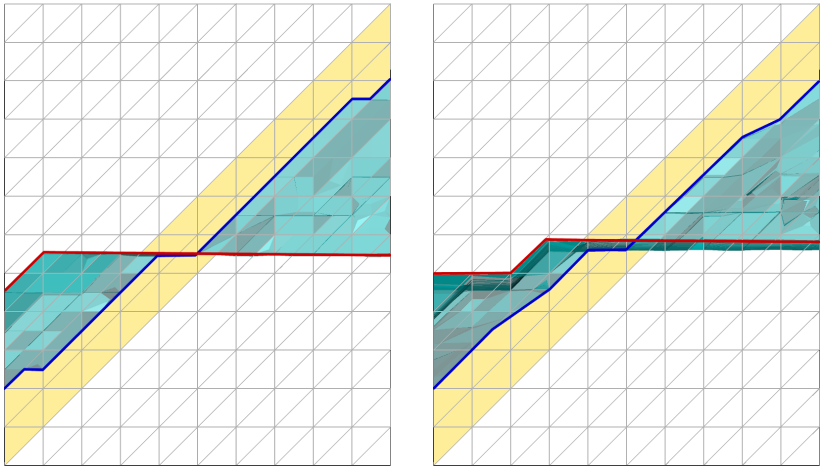

(a) $\boldsymbol{u} - \boldsymbol{\varepsilon}$ with IsoDamage

(b) $\boldsymbol{u} - \boldsymbol{\varepsilon}$ with Plasticity

(c) $\boldsymbol{u}$ with IsoDamage

(d) $\boldsymbol{u}$ with Plasticity

Figure 8: Top view of the crack twist rotation in the 3 point bending test. Light yellow color represents the initial notch. Turquoise color represents the isosurface corresponding to the centerline of the localization band. The bottom crack profile is identified with the blue color while the top crack profile is highlighted in red.

failure surface is very similar with the two constitutive laws (Rankine isotropic damage and directional plasticity), with the strain softening band that initiate from two opposed notch corners and twists to the mid-section of the beam.

The solution given by the irreducible formulation is rather different. A substantially mesh-biased crack surface is obtained for both isotropic damage and plasticity cases: while the first one shows a slight tendency to converge to the center of the specimen, the latter one presents multiple vertical localization bands.

Owing to inter-element continuity of strains, mixed formulations for nonlinear analysis presents an effective localization band that spans two elements. The kinematic enhancement of using a continuous strain field results in a convergent and more accurate outcome than the standard finite elements, which suffer from severe mesh bias dependence.

In order to further compare the two FE technologies, Figure 8 shows the top view of the center line of the localization band, at a position 10 mm below the top surface. As discussed before, the crack starts from the 45° slanted notch and then twists until it aligns with the mid-plane. Figure 8 depicts in yellow the initial notch profile and in turquoise the failure surface. In addition, the bottom crack profile is signaled in blue, whereas the top one is highlighted in red.

The initial profile of the localization band coincides in all four examples: the surface develops from

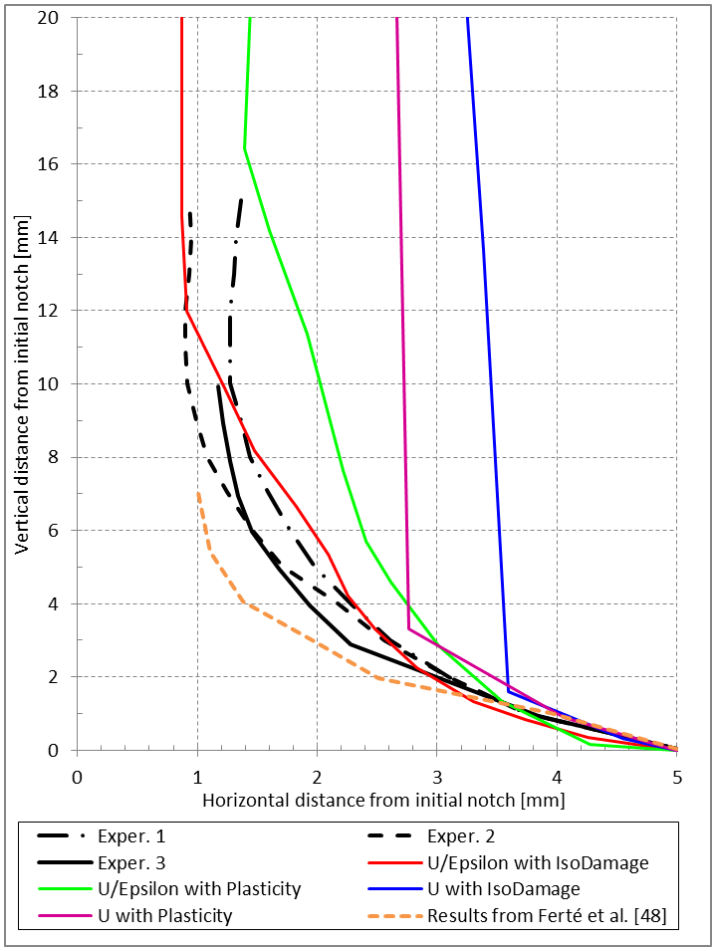

Figure 9: Plot of the computed crack path with respect to the experimental data from Citarella and Buchholz [47] and previous results from Ferté et al. [48].

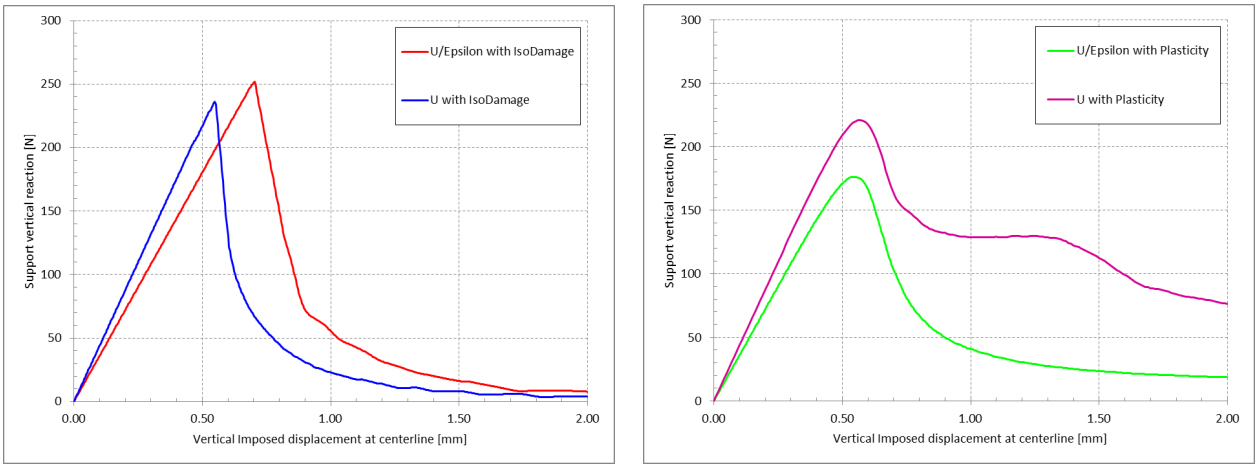

Figure 10: Plot of support reaction force with respect to the imposed vertical displacement.

the two opposite inner corners of the notch and connects (almost) symmetrically at the center of the specimen. The mixed $\boldsymbol{\varepsilon} - \boldsymbol{u}$ formulation shows the expected twist rotation, with the final position of the crack surface close to the central symmetry plane of the beam. The slight asymmetry is due, on the one hand, to the orientation of the structured mesh and, on the other hand, to the use of a pure tensile failure criterion, which does not allow the crack surface to cross the compression head at the top of the beam. Concerning the irreducible formulation, the results shows a clear mesh bias, with a relatively small twisting rotation for the isotropic damage case and almost no twisting at all in the case of plasticity.

Figure 9 depicts the relative position of the computed crack path with respect to the notch location compared to the experimental results reported by Citarella and Buchholz [47] and the XFEM numerical simulation of Ferté et al. [48]. Once again, standard displacement based finite elements are unable to provide a satisfactory result, with the crack having a marked tendency to follow one of the directions of the mesh, independently from the constitutive law. Contrariwise, the mixed formulation achieves rather adequate outcomes. Both the isotropic damage and plasticity models converge at the top of the plot to the experimental range; in fact, the first one computes a crack path which is very close to the experiments. The only substantial differences are attributed to the relatively coarse mesh discretization in the vicinity of the notch.

Finally, the structural softening behavior is studied plotting the support reaction versus the imposed vertical displacement (Figure 10). The reduction of the carrying capacity is visible in all cases. In the elastic range, the standard and mixed finite elements show two different stiffnesses. For a given degree of refinement, the enhanced kinematics of the mixed formulation, with continuous strain fields, results in an accurate, and more flexible, response. Eventually, the two methods will converge to the same result in the elastic case as the mesh is refined.

The isotropic damage solution presents a well defined peak load with a sudden change of global behavior whereas the plastic one has a smoother transition. A similar sharp change in the carrying load was previously studied in PMMA specimens in the work of Cooke and Pollard [5]. The mixed FE is able to reproduce a monotonic softening branch with both constitutive laws. The displacement-based shows excessive energy dissipation in the plasticity case due to the multiple numbers of cracks developed during the inelastic branch of the test, see Figure 7(e).

6.2 Prismatic skew notched concrete beam under torsion

The second example is a prismatic skew edge notched beam under torsional load. This experiment was first performed by Jefferson et al. [49] on plain concrete specimens, but it was conducted on smaller PMMA beams as well by Buchholz et al. [50].

The test setup is shown in Figure 11: a prismatic beam with square base is positioned horizontally, with steel clamps at both ends. These present appendages on both sides which allow to avoid rigid movements and to apply the load. Three of the four steel arms are restrained in the vertical direction,

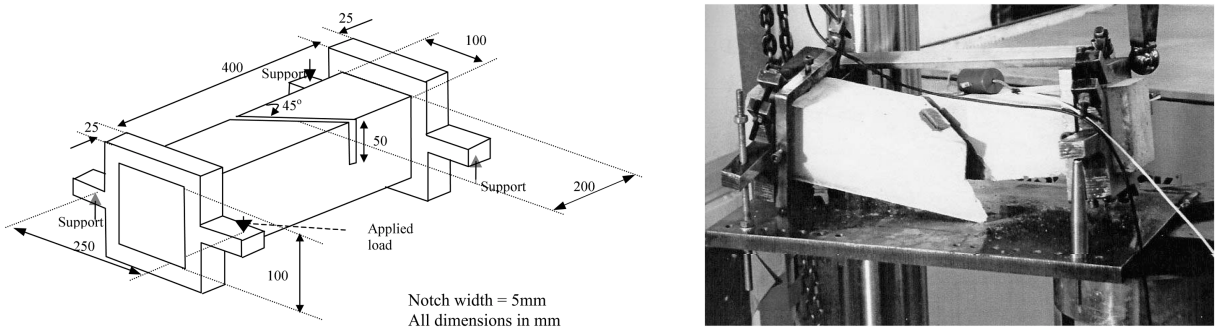

(a) (b)

Figure 11: Geometry and experimental setup of the tests on prismatic beam under torsion with square cross section, from Jefferson et al. [49].

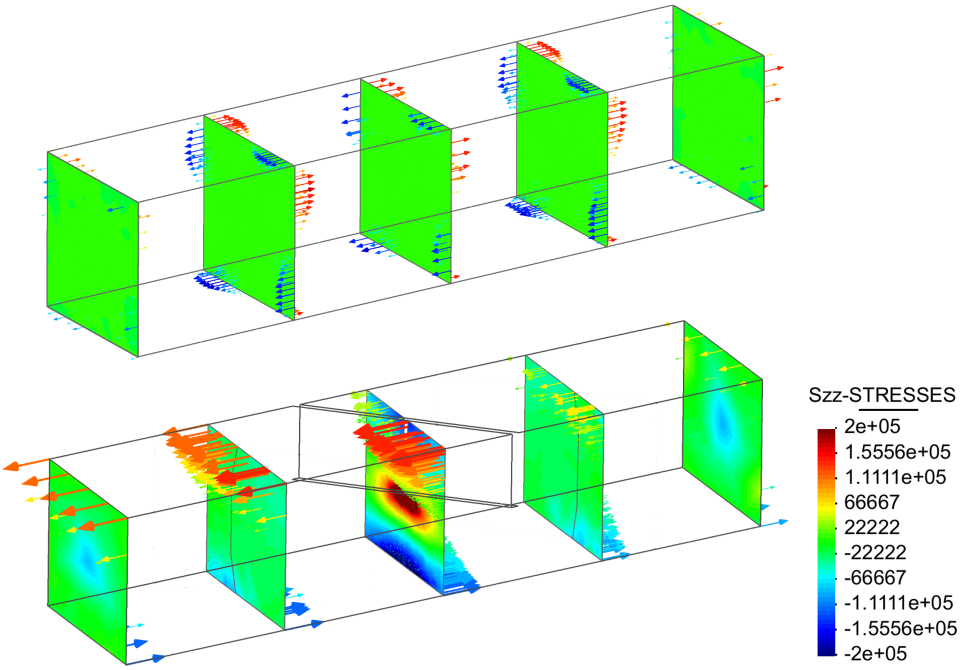

Figure 12: Plot of the contour fill of longitudinal stress distribution and vectors of longitudinal displacements due to uniform and non-uniform torsion on a prismatic square beam. Top figure shows the uniform (Saint Venant's) torsion of the unnotched specimen. Bottom figure shows the case of non uniform torsion of notched specimen.

whereas the last one is subjected to a concentrated load. The clamping frame is assumed to make perfect contact with the concrete specimen and ensure the transferring of the eccentric load to the specimen, resulting in a torsional moment aligned with the axis of the beam. It is also designed not to constrain warping of the end cross-sections.

The objective of this experiment is to test the tensile strength of plain concrete under torsion. The highest stress is located in the vicinity of the notch, with maximum values on the lateral surface of the beam. According to several works in the field [1, 6, 4], the fracture initiation is caused by a mode III loading with transition to mode I brittle failure.

An unnotched specimen would be subjected to uniform (Saint-Venant's) torsion, characterized by a uniform warping of the cross section, unhindered by the design of the clamping frames at both ends. Under uniform torsion, no longitudinal normal stress ($\boldsymbol{\sigma}_{zz}$) would develop.

The slanted notch induces non-uniform torsion. This is shown in Figure 12(b), which overlaps contour fills of the longitudinal normal stresses ($\boldsymbol{\sigma}_{zz}$) and vectors of longitudinal (warping) displacement at five different cross-sections of the beam, in the elastic regime. It is obvious that: (i) the warping displacement is not uniform, being rather distorted by the notch and (ii) the $\boldsymbol{\sigma}_{zz}$ stresses are not zero, particularly in the vicinity of the notch. Note that these non-vanishing normal stresses have null resultant axial force and null resultant bending moments, but they have a resultant warping moment, also known as bimoment. In comparison, Figure 12(a) depicts the case for the unnotched specimen, where uniform displacement and null stress are observed.

Considering tensile fracture as the main cause for cracking of unreinforced concrete, this example investigates the differences between the isotropic damage and plasticity constitutive laws, both based on Rankine's failure criterion with the same mechanical parameters. The material properties are (from [49]): Young's modulus $E = 35$ GPa, Poisson's ratio $\nu = 0.2$, tensile uniaxial strength $\sigma_y = 2.3$ MPa and fracture energy $G_f = 80$ N/m.

The mesh is composed by 67,038 tetrahedral elements (12,729 nodes) subdivided in three regions. The part of the beam around the notch consists of $\boldsymbol{\varepsilon} - \boldsymbol{u}$ mixed finite elements with nonlinear constitutive behavior; outside this, the remaining concrete volume in contact with the clamps and, finally,

the steel frame itself are elastic. In the latter two regions, the FEM formulation is the standard displacement-based, since no cracking is expected there.

The boundary conditions, as demonstrated in [35], are crucial for the correct numerical analysis of the test. In the present case, the model constraints are recovered from photos to be as close as possible to the experimental setup. From Figure 11(b), details of the boundary conditions can be extracted. Three vertical supports consist of steel posts, allowing for free rotation. Two of them (the closest and furthest ones in the photo) restrain the horizontal motion of the beam. Finally, the free appendage is subjected to an imposed vertical displacement.

In the numerical model, the four appendages are restrained vertically in a single point. Taking advantage of the symmetry of the setup, the horizontal motion is limited by constraining the center of the front and rear faces of the beam. Both the geometry and the loading conditions are skew-symmetric, i.e. a 180° rotation of the problem would result in the same test setup. Given the nature of the problem, localization of strains is expected to be skew-symmetric.

The results are presented and discussed next. The displacement solution at the end of the test, with the corresponding deformation, is presented in Figure 13. Here, similar solution fields are captured for the two constitutive laws: the opening of the notch allows for a substantial rotation of one beam end from the other, meaning that localization of strain has occurred.

Figure 14 compares the experimental crack surface with the numerically computed ones, at the end of the analysis. While both plasticity and damage constitutive laws are able to predict correctly the global behavior, it is possible to notice that the latter one provides a more curved profile than the first one. In the case of damage, the crack starts from the notch almost horizontally and, then, rotates to reach the expected angle of 45°. On the contrary, in the case of plasticity, the propagation direction of the crack is constantly orientated at 45°.

The two solutions can be also compared with the top view of the experimental tests on PMMA, as depicted in Figure 15, and a side perspective in Figure 16. In all cases, a skew-symmetric crack is obtained as expected. The top view shows that both material laws, used with the mixed strain-displacement finite elements, are able to describe effectively the complex twisting crack pattern.

The peculiar arch-like shape, observable in the side view, proves that the highest tensile stress is located on the external surface of the beam, as previously discussed. Contrariwise, the central part is under compressive stresses arising from the additional bending. In the numerical analyses, as the failure criterion only involves the major principal tensile stress, the bottom part of the beam remains elastic.

Finally, Figure 17 shows the force-displacement plots. The experimental data is compared with the numerical solution using the $\boldsymbol{\varepsilon} - \boldsymbol{u}$ formulation with isotropic damage and plasticity. There is a

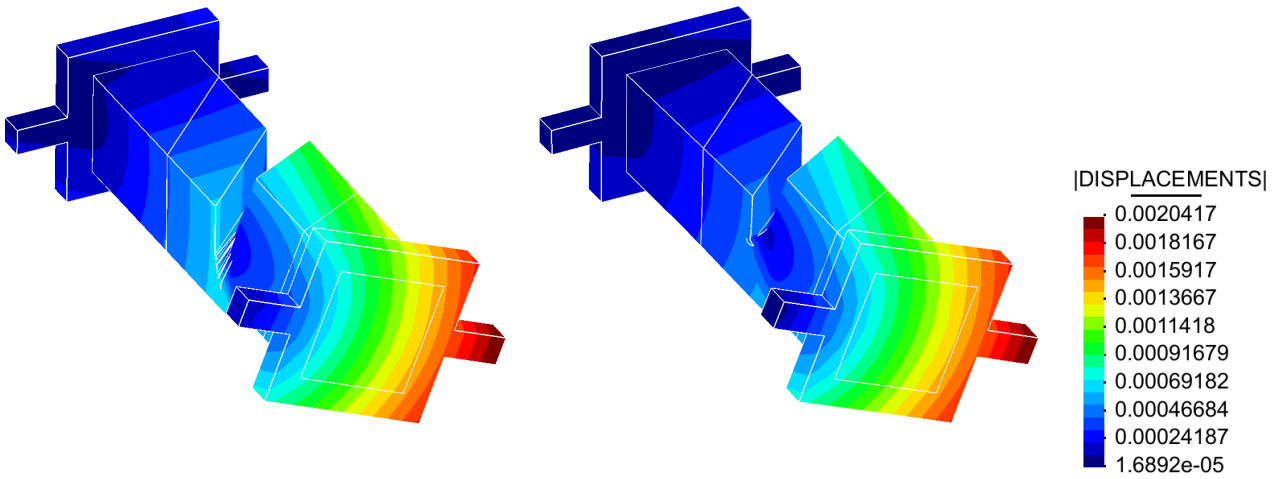

(a) Isodamage (b) Plasticity

Figure 13: Plot of the contour fills of the displacement field superposed on the computed beam deformation at the end of the test. The isotropic damage solution is very similar to the plasticity one.

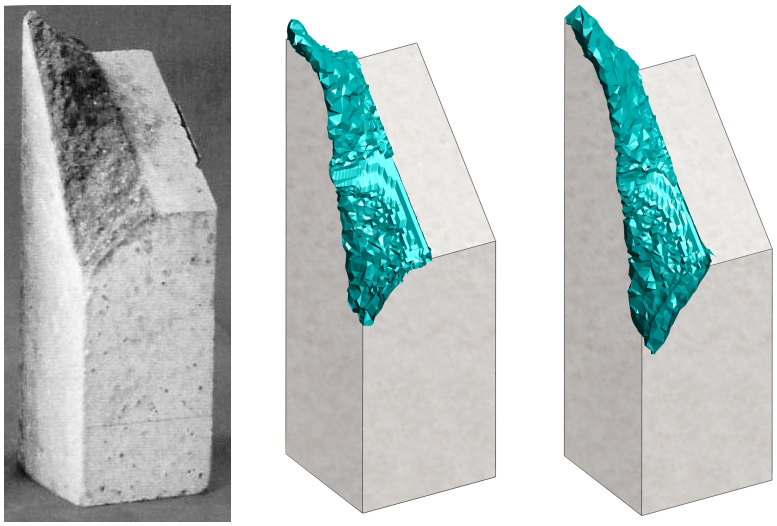

(a) (b) (c)

Figure 14: Comparison of (a) the experimental outcome with the computed crack surfaces in the case of (b) isotropic damage and (c) plasticity for the prismatic beam with square cross section.

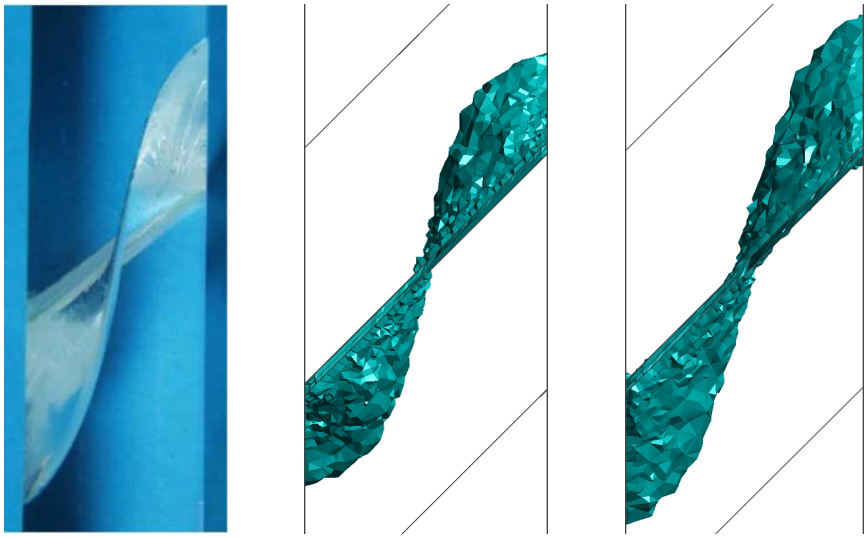

(a) (b) (c)

Figure 15: Top views of the crack surface from (a) tests on PMMA [50], (b) Isotropic Damage and (c) Plasticity.

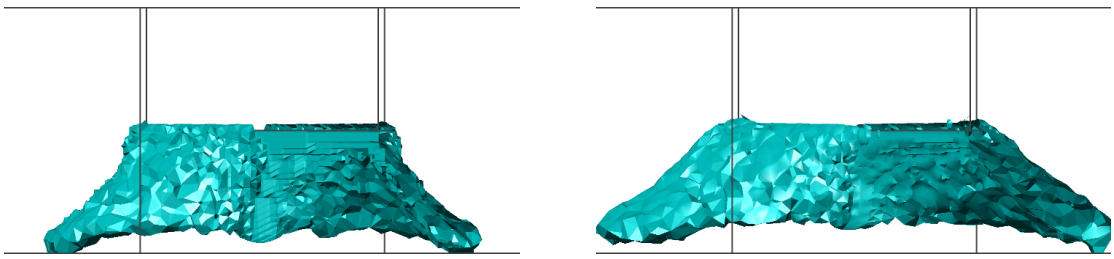

(a) (b)

Figure 16: Side view of the fracture surface: (a) Isotropic Damage and (b) Plasticity.

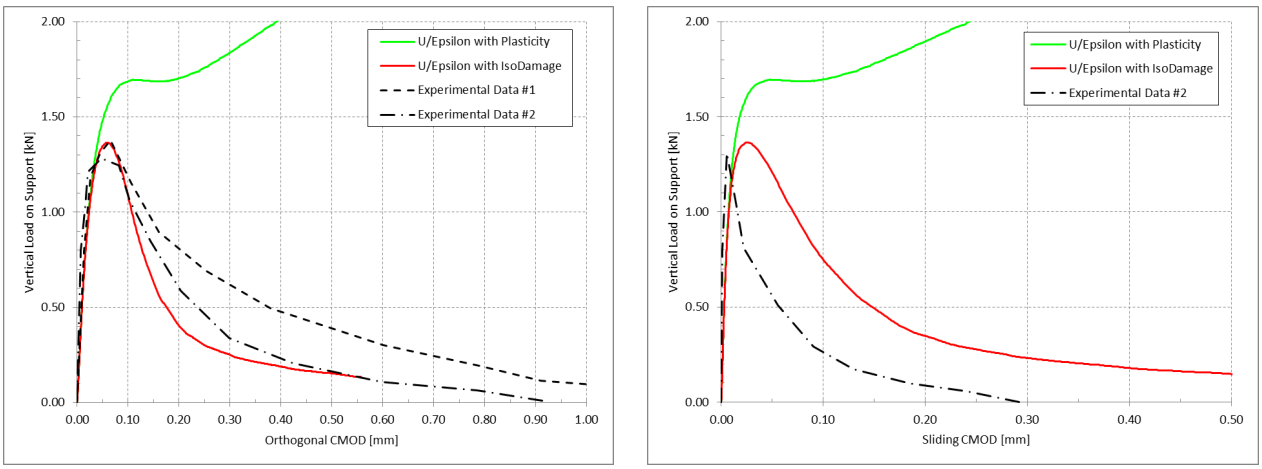

(a) (b)

Figure 17: Plots of vertical force versus (a) orthogonal CMOD and (b) sliding CMOD

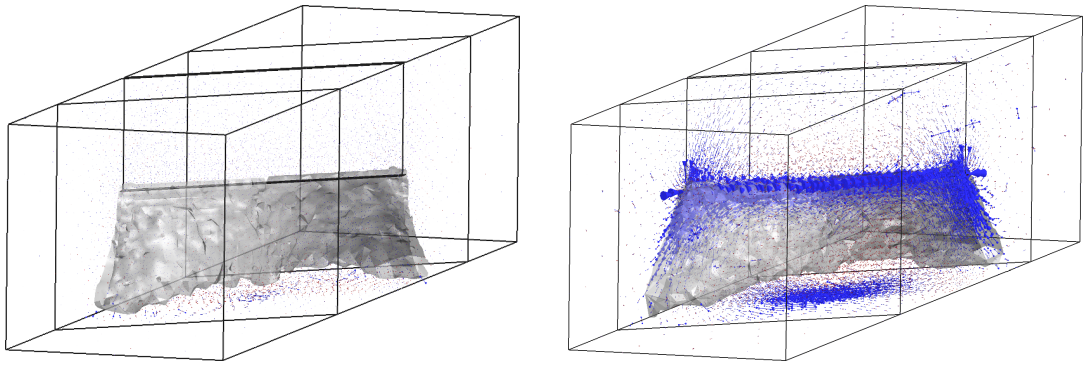

(a) (b)

Figure 18: Residual principal stresses in the (a) isotropic Damage and (b) plasticity cases. Blue vectors represents compressive stress, red vectors represents tensile stress.

major difference in the global behavior: the case involving damage shows an almost complete loss of load carrying capacity due to strain softening whereas the plasticity one does not. Instead, the plastic model reaches a plateau and, then, the load carrying capacity increases again.

Indeed, there is a fundamental difference in the definition of the plastic and damage constitutive laws. Plasticity is based on the definition of plastic flow, which gives a directional character to the inelastic deformation. Moreover, associative plasticity implies that the stress reduction is proportional to the plastic flow, but also to the elastic constitutive tensor; hence, it is affected by the Poisson's effect. Such orthotropic behavior does not ensure a complete stress release even in softening cases. In fact, Poisson's effect generate significant residual compressive stresses around the crack associated to the localization of the opening strains, as it is shown in Figure 18(b). This stress field is restrained by the longitudinal boundary conditions and, consequently, it increases the force required for the progression of the localization.

In contrast, isotropic damage reduces the material stiffness isotropically, resulting in a uniform reduction of all the principal stresses. In Figure 18(a) stresses are almost completely released. The only remaining stresses are the compressive ones due to the non uniform torsion caused by the slanted notch.

6.3 Cylindrical skew notched concrete beam under torsion

In this final example, the test on a skew-notched cylindrical plain concrete beam subjected to torsion is modeled. The experimental setup is quite similar to the previous example. Figure 19(a) shows

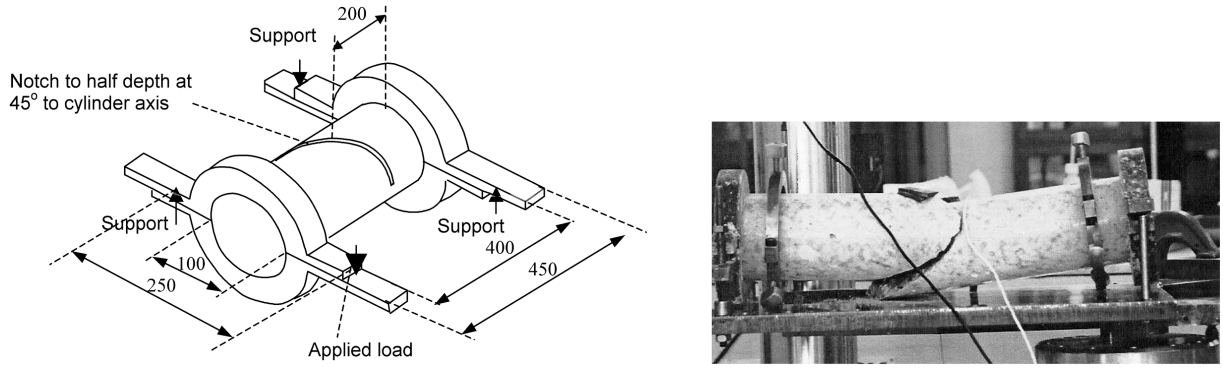

(a) (b)

Figure 19: Geometry and experimental setup of the tests on cylindrical beam under torsion, from Jefferson et al. [49].

the characteristic dimensions of the specimen and of the steel frame. The cylindrical beam has the same length as the prismatic one and also presents a 45° notch located at the center of the specimen. The clamping system is visible in Figure 19(b) and, likewise, it provides the transfer of external vertical imposed displacement to the specimen as a torsion force and ensures proper restraint of rigid movements. Therefore, boundary conditions are identical to the ones used in the previous example.

The material properties are assumed the same as in the last example: Young's modulus $E = 35$ GPa, Poisson's ratio $\nu = 0.2$, tensile uniaxial strength $\sigma_y = 2.3$ MPa and fracture energy $G_f = 80$ N/m. Indeed, the referenced work by Jefferson et al. [49] is followed, although the batch of concrete for the cylindrical beams has not been tested for mechanical parameters. The numerical analysis has been performed considering Rankine's and Drucker-Prager's (with 45° friction angle) failure criteria. In fact, the objective of this example is to assess the influence of the shear stresses in the experimental results and the failure mechanism.

Concrete is frequently thought to fracture in mode I and Rankine based criteria have been widely adopted. However, when dealing with mode III and mixed mode loading, the dependence of shear strength from pressure can play a fundamental role in the prediction of the failure mechanism. Consequently, it is convenient to introduce a pressure dependent model such as Drucker-Prager. Note that, as shown in Saloustros et al. [51], Rankine's criterion is a limit case of a family of pressure dependent constitutive models.

The mesh consists of 62,309 tetrahedral elements (11,892 nodes) which concentrate in the vicinity of the notch. In order to save on computational resources, the central part of the FE mesh is modeled using mixed $\boldsymbol{\varepsilon} - \boldsymbol{u}$ finite elements whereas the two beam ends as well as the steel frame are modeled using irreducible displacement-based elements, since, in these regions, inelastic phenomena do not appear.

An unnotched circular beam, subjected to uniform (Coulomb's) torsion, does not present any warping nor longitudinal stresses. Figure 20(a) shows the null field of $\boldsymbol{\sigma}_{zz}$ and null warping displacements in the elastic range at five different cross sections. As in the case of the square prismatic beam, the slanted notch causes the torsion to be non uniform, resulting in nonzero stresses $\boldsymbol{\sigma}_{zz}$ and longitudinal warping displacements, with the maximum values in the vicinity of the cut (see Figure 20(b)).

Figure 21 compares the final shape of the crack surface for the four analyzed cases. No images of the experimental crack surface are given in [49]. Plasticity and isotropic damage in the case of Rankine's failure criterion show a larger and more complex fracture geometry, whereas the Drucker-Prager's ones are sensibly closer to the notch cross section. The top views of such surfaces are presented on Figure 22 and the side perspectives are depicted in Figure 23. Rankine's cases show a behavior similar to the square prismatic beam, with a typical skew-symmetric curved shape; the circular shape of the specimen causes a more curved bottom profile of the failure surface.

Similarly, the Drucker-Prager criterion shows a curved profile, although rather smaller. The less pronounced crack surface is the direct result of a failure criterion that is based on the interdependence

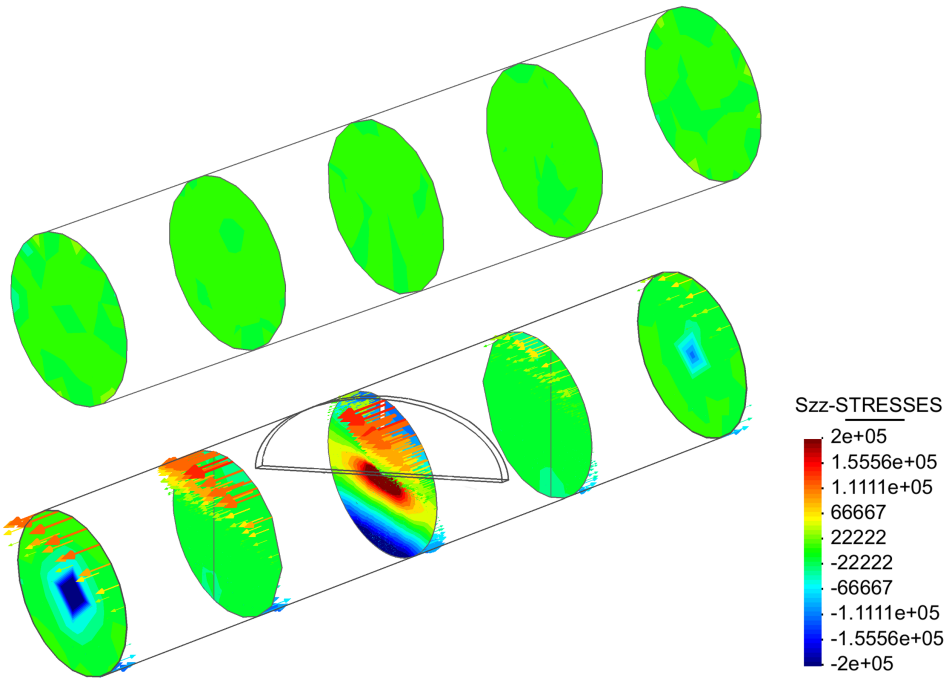

Figure 20: Plot of the contour fill of longitudinal stress distribution and vectors of longitudinal displacements due to uniform and non-uniform torsion on a cylindrical beam. Top figure shows the uniform (Coulombs's) torsion of the unnotched specimen. Bottom figure shows the case of non uniform torsion of notched specimen.

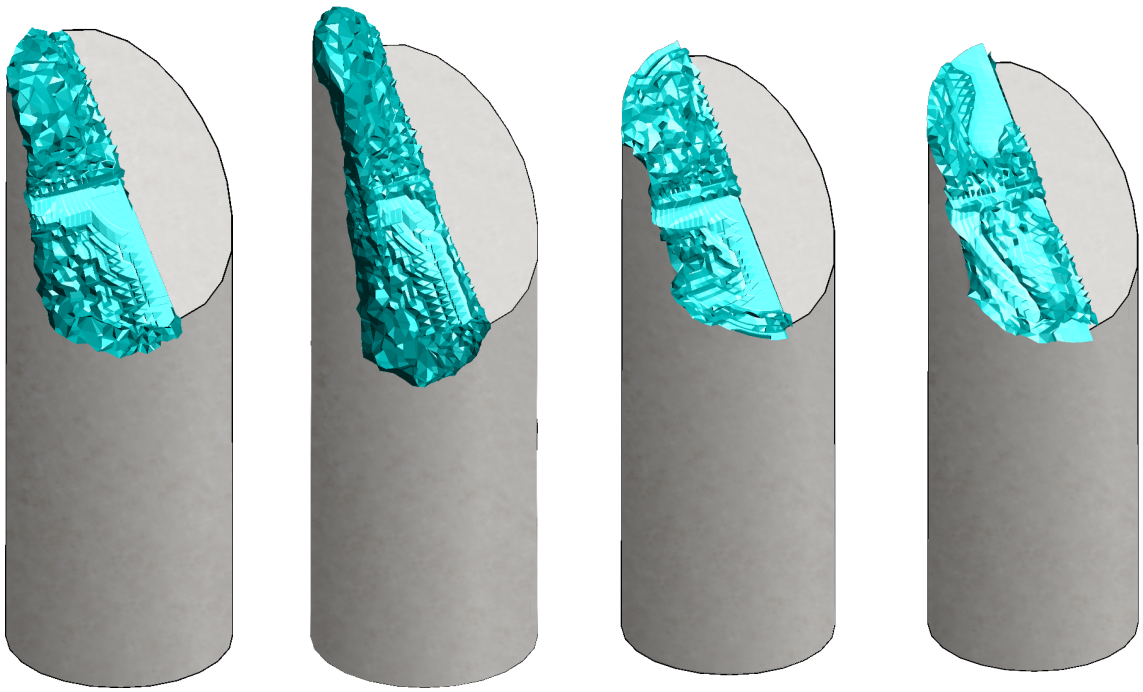

Figure 21: View of the crack surface at the end of the analysis from (a) Rankine Isotropic Damage, (b) Rankine Plasticity, (c) Drucker-Prager isotropic damage and (d) Drucker-Prager plasticity solutions.

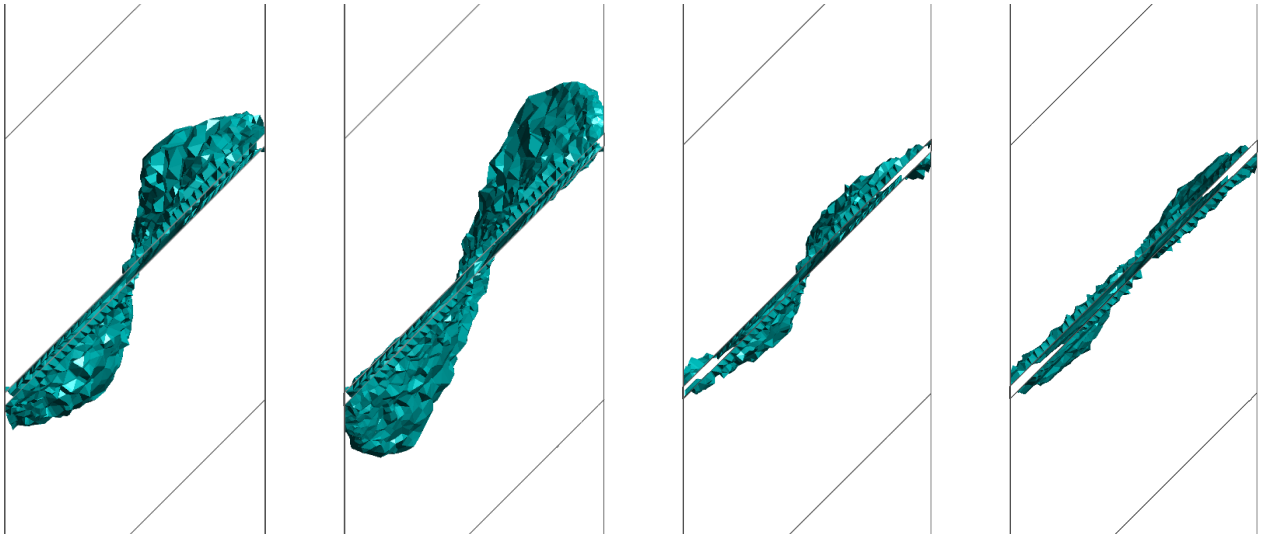

Figure 22: Top view of the crack pattern from (a) Rankine Isotropic Damage, (b) Rankine Plasticity, (c) Drucker-Prager isotropic damage and (d) Drucker-Prager plasticity solutions.

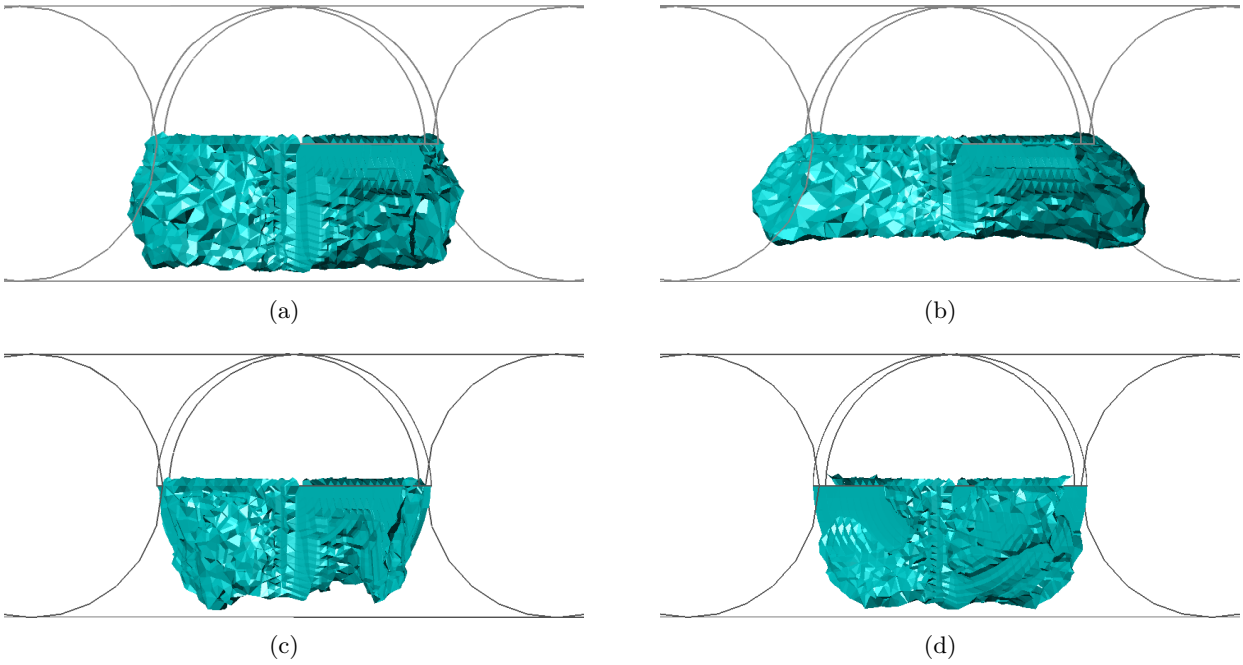

Figure 23: Side view of the crack pattern from (a) Rankine Isotropic Damage, (b) Rankine Plasticity, (c) Drucker-Prager isotropic damage and (d) Drucker-Prager plasticity solutions.

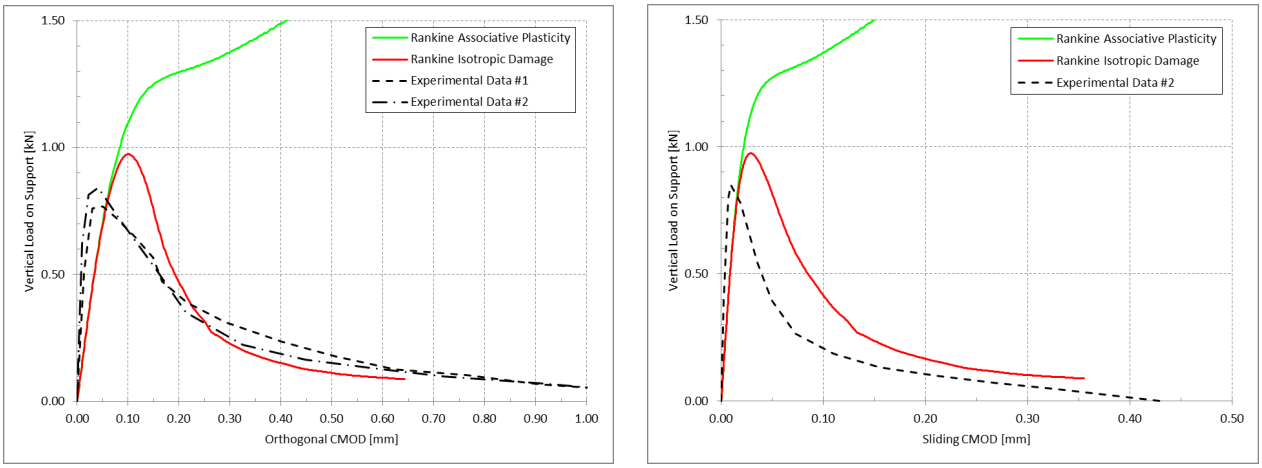

(a) (b)

Figure 24: Plots of vertical force versus (a) orthogonal CMOD and (b) sliding CMOD using Rankine failure criterion

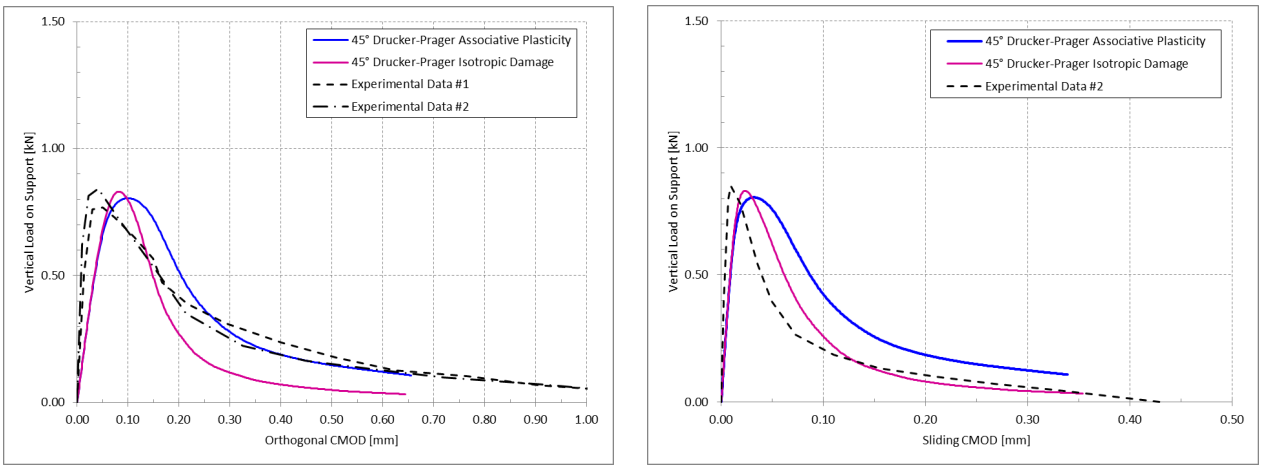

(a) (b)

Figure 25: Plots of vertical force versus (a) orthogonal CMOD and (b) sliding CMOD using Drucker-Prager failure criterion with 45° friction angle

of pressure and shear through the friction angle, in lieu of the major principal stress.

Finally, Figure 24 shows the plot of applied load versus orthogonal and sliding CMOD values with the Rankine constitutive law while Figure 25 shows the same plot for the Drucker-Prager case. Here, the experimental values from [49] are compared with the numerical analyses.

In the first place, it is observed that the stiffness of the experimental specimen differs substantially from that of the numerical analyses. Since it is reported that a different batch was used for the cylinder specimens, it is possible that the concrete mix might have had a higher Young's modulus.

Notwithstanding, the numerical analyses with the Drucker-Prager failure criterion predict the peak load satisfactorily, followed by full reduction of stresses. Contrariwise, the Rankine based models provide different results. As in the previous example, plasticity fails to produce decrease of load-carrying capacity while isotropic damage presents a reduction of the total load, but the peak load value is slightly overestimated.

Hence, the numerical analysis shows that the torsional tests on circular specimens require a detailed description of the mixed mode failure of concrete. On the one hand, the numerically computed fracture surface shows a similar "S" shaped profile in both cases. On the other hand, the softening behavior appears to be properly captured by the $\boldsymbol{\varepsilon}-\boldsymbol{u}$ mixed finite elements when using Drucker-Prager's model with 45° friction angle whereas Rankine's one slightly overestimates the peak load.

7 Computational pay-off of kinematic compatibility and iterative procedure

The computational time and memory requirements for the last two examples are presented in the following tables. Three different finite element technologies are considered: full mixed $\boldsymbol{\varepsilon} - \boldsymbol{u}$, combined kinematically compatible mixed and irreducible FE and full displacement-based standard $\boldsymbol{u}$ formulations. In the first one, the whole mesh consists of mixed elements and, for this reason, it is the most demanding from the computational point of view. The second one combines compatible elements in the same mesh; its performance pay-off will be benchmarked. Finally, the third one, with the standard irreducible only, is the less demanding.

These numerical analysis are run on a desktop computer with 8 GB of RAM and a dual core CPU clocking at 2.83 GHz.

The prismatic skew notched concrete beam under torsion is calculated with a mesh of 67,038 elements. When the combined formulation is used, the computational grid is composed of 9,783 irreducible and 57,255 mixed finite elements. Table 2 shows a substantial reduction in computational time for the proposed methodology. Similarly, the RAM usage is slightly reduced. The irreducible formulation is added for reference, as the corresponding results are generally deficient.

Formulation	Solver	CPU t_{fact} (s)	n_{iter}	CPU t_{iter} (s)	CPU t_{step} (s)	RAM (MB)
Full mixed $\boldsymbol{\varepsilon} - \boldsymbol{u}$ formulation (67,038 elements)	Newton-Raphson	71	3	71	213	5660
	Secant scheme	55	10	2	75	2833
Mixed $\boldsymbol{\varepsilon} - \boldsymbol{u}$ and irreducible $\boldsymbol{u}$ (57,255 + 9,783 elements)	Newton-Raphson	61	3	61	183	4129
	Secant scheme	51	10	2	71	2065
Irreducible $\boldsymbol{u}$ (67,038 elements)	Newton-Raphson	7	3	7	21	683
	Secant scheme	6	10	2	26	369

Table 2: CPU time and RAM memory requirements in the prismatic skew notched concrete beam under torsion. The proposed method is compared with the full mixed and full irreducible formulations. Likewise, the Newton-Raphson and Secant schemes are compared per first iteration factorization time, number of iterations and step average time.

The cylindrical skew notched concrete beam under torsion is modeled with 62,309 elements. In the case of combination of kinematically compatible FE, the mesh is subdivided in 53,876 mixed and 8,433 irreducible elements. CPU time gains are similar to the ones observed for the prismatic beam case.

Note that using the irreducible formulation in only 14 % of the total number of elements translates directly in a 14 % pay-off of CPU time per step in the Newton-Raphson, and 5.6 % in the Secant method. In analyses where the ratio of irreducible to mixed elements can be greater, the gain increases correspondingly.

Moreover, for each case, the performance of the Newton-Raphson solver is compared with the Secant scheme. The first one requires a lower number of iterations per step thanks to the quadratic convergence given by the consistently linearized global matrix. Nevertheless, each iteration requires the solution of the full updated algebraic system which, as in this case, can not be symmetric.

Contrariwise, the modified Secant scheme updates the global matrix only at the beginning of each step and then it iterates using the already factorized system. Although the rate of convergence is linear and more iterations are needed, it results in a faster procedure. In both of the proposed examples, the computational time for the secant solver is less than half of the Newton-Raphson for the same convergence tolerance, which is set to 10^{-3} with respect to the residual forces. Moreover, the symmetry of the matrix reduces the required memory to almost half.

Formulation	Solver	CPU t_{fact} (s)	n_{iter}	CPU t_{iter} (s)	CPU t_{step} (s)	RAM (MB)
Full mixed $\boldsymbol{\varepsilon} - \boldsymbol{u}$ formulation	Newton-Raphson	65	3	65	195	4459
(62,309 elements)	Secant scheme	50	8	2	66	2232
Mixed $\boldsymbol{\varepsilon} - \boldsymbol{u}$ and Irreducible $\boldsymbol{u}$	Newton-Raphson	54	3	54	162	3334
(53,876 + 8,433 elements)	Secant scheme	45	8	2	61	1668
Irreducible $\boldsymbol{u}$	Newton-Raphson	6	3	6	18	546
(62,309 elements)	Secant scheme	6	8	2	22	299

Table 3: CPU time and RAM memory requirements in the skew-notched cylindrical beam under torsion. The proposed method is compared with the full mixed and full irreducible formulations. Likewise, the Newton-Raphson and Secant schemes are compared per first iteration factorization time, number of iterations and step average time.

8 Conclusion

The mixed strain displacement $\boldsymbol{\varepsilon} - \boldsymbol{u}$ finite element method is applied to problems involving mode III and mixed mode failure in quasi-brittle materials. First, the formulation is presented for isotropic continuum damage and plasticity constitutive models. The compatibility between the proposed formulation and the standard irreducible one is established, as a mean to provide a speedup of the computational time. The proposed mixed finite element technology is able to describe effectively failure processes that involve complex crack surfaces.

The three point bending test of a skew notched beam is studied using Rankine's failure criterion. The mixed strain-displacement $\boldsymbol{\varepsilon} - \boldsymbol{u}$ formulation outperforms the standard irreducible one, which shows mesh biased localization and lack of accuracy. The characteristic failure surface twisting rotation is recovered and the numerically computed crack profile is satisfactorily close to the experimental one.

Then, the torsion test of a skew-notched prismatic beam with square cross section is studied. Firstly, using the isotropic damage and the associative plasticity with Rankine's failure criterion, it is possible to properly reproduce the propagation of fracture surface found experimentally. Secondly, the two constitutive laws are compared with the plots of the vertical force versus orthogonal and sliding CMOD. It is determined that, in the mode I failure, the orthotropic nature of plasticity results in a different global behavior than the isotropic damage. The latter one provides good results, with similar values to the experiments.

Using an identical test setup, a skew-notched cylindrical beam under torsion is studied as well. Here, using a Drucker-Prager constitutive model, the influence of shear strength in the experiment is highlighted. By introducing a Drucker-Prager law with friction angle of 45°, the global behavior found in experiments is accurately predicted. This shows that the mode I failure criterion has to be combined with a shear-pressure dependent one, in a mixed mode fracture fashion, to properly compute the cracking of the specimen.

Finally, the kinematic compatibility between the mixed and the standard finite elements is exploited to provide considerable gains in terms of computational time. Moreover, a symmetric scheme, such as the secant one, is demonstrated as a feasible and advantageous alternative to the Newton-Raphson method.

9 Acknowledgments

Financial support from the EC 7^{th} Framework Programme under the MuMoLaDe project - Multiscale Modelling of Landslides and Debris Flows - within the framework of Marie Curie ITN (Initial Training Networks) and the Spanish Ministry of Economy and Competitivity under the EACY project - Enhanced accuracy computational and experimental framework for strain localization and failure mechanisms- within the "Excellency" Program for Knowledge Generation is gratefully acknowledged.

References

[1] L. P. Pook. The effect of crack angle on fracture toughness. *Engineering Fracture Mechanics*, 3 (3):205 – 218, 1971.

[2] L. P. Pook. The fatigue crack direction and threshold behaviour of mild steel under mixed mode I and III loading. *International Journal of Fatigue*, 7(1):21–30, 1985.

[3] L. P. Pook. On fatigue crack paths. *International Journal of Fatigue*, 17(1):5–13, 1995.

[4] J. R. Yates and R. A. Mohammed. Crack propagation under mixed mode (I+ III) loading. *Fatigue & Fracture of Engineering Materials & Structures*, 19(10):1285–1290, 1996.

[5] M. L. Cooke and D. D. Pollard. Fracture propagation paths under mixed mode loading within rectangular blocks of polymethyl methacrylate. *Journal of Geophysical Research: Solid Earth*, 101(B2):3387–3400, 1996.

[6] V. Lazarus and J.-B. Leblond. Crack paths under mixed mode (I+ III) or (I+ II+ III) loadings. *Comptes Rendus de l'Academie des Sciences Series IIB Mechanics Physics Chemistry Astronomy*, 326(3):171–177, 1998.

[7] V. Lazarus, J.-B. Leblond, and S.-E. Mouchrif. Crack front rotation and segmentation in mixed mode I+III or I+II+III. Part I: Calculation of stress intensity factors. *Journal of the Mechanics and Physics of Solids*, 49(7):1399–1420, 2001.

[8] V. Lazarus, J.-B. Leblond, and S.-E. Mouchrif. Crack front rotation and segmentation in mixed mode I+III or I+II+III. Part II: Comparison with experiments. *Journal of the Mechanics and Physics of Solids*, 49(7):1421–1443, 2001.

[9] F.-G. Buchholz, A. Chergui, and H. A. Richard. Fracture analyses and experimental results of crack growth under general mixed mode loading conditions. *Engineering Fracture Mechanics*, 71 (4):455–468, 2004.

[10] V. Lazarus, F.-G. Buchholz, M. Fulland, and J. Wiebesiek. Comparison of predictions by mode II or mode III criteria on crack front twisting in three or four point bending experiments. *International Journal of Fracture*, 153(2):141–151, 2008.

[11] A. Hillerborg, M. Modéer, and P.-E. Petersson. Analysis of crack formation and crack growth in concrete by means of fracture mechanics and finite elements. *Cement and Concrete Research*, 6 (6):773–781, 1976.

[12] Z. P. Bažant and B. H. Oh. Crack band theory for fracture of concrete. *Matériaux et Construction*, 16(3):155–177, 1983.

[13] G. Pijaudier-Cabot and Z. P. Bazant. Nonlocal damage theory. *Journal of engineering mechanics*, 113(10):1512–1533, 1987.

[14] M. Jirasek. Nonlocal models for damage and fracture: comparison of approaches. *International Journal of Solids and Structures*, 35(31):4133–4145, 1998.

[15] R. H. J. Peerlings, R. De Borst, W. A. M. Brekelmans, and M. G. D. Geers. Gradient-enhanced damage modelling of concrete fracture. *Mechanics of Cohesive-frictional Materials*, 3(4):323–342, 1998.

[16] A. Simone, G. N. Wells, and L. J. Sluys. From continuous to discontinuous failure in a gradient-enhanced continuum damage model. *Computer Methods in Applied Mechanics and Engineering*, 192(41):4581–4607, 2003.

[17] P. Steinmann and K. Willam. Localization within the framework of micropolar elasto-plasticity. In *Advances in continuum mechanics*, pages 296–313. Springer, 1991.

[18] H. B. Mühlhaus and I. Vardoulakis. The thickness of shear bands in granular materials. *Geotechnique*, 37(3):271–283, 1987.

[19] C. Miehe, F. Welschinger, and M. Hofacker. Thermodynamically consistent phase-field models of fracture: Variational principles and multi-field fe implementations. *International Journal for Numerical Methods in Engineering*, 83(10):1273–1311, 2010.

[20] J. Vignollet, S. May, R. De Borst, and C. V. Verhoosel. Phase-field models for brittle and cohesive fracture. *Meccanica*, 49(11):2587–2601, 2014.

[21] M. Cervera, E. Hinton, and O. Hassan. Nonlinear analysis of reinforced concrete plate and shell structures using 20-noded isoparametric brick elements. *Computers & structures*, 25(6):845–869, 1987.

[22] D. V. Swenson and A. R. Ingraffea. Modeling mixed-mode dynamic crack propagation nsing finite elements: theory and applications. *Computational Mechanics*, 3(6):381–397, 1988.

[23] T. Belytschko and T. Black. Elastic crack growth in finite elements with minimal remeshing. *International journal for numerical methods in engineering*, 45(5):601–620, 1999.

[24] J. C. Simo and M. S. Rifai. A class of mixed assumed strain methods and the method of incompatible modes. *International journal for numerical methods in engineering*, 29(8):1595–1638, 1990.

[25] J. C. Simo and F. Armero. Geometrically non-linear enhanced strain mixed methods and the method of incompatible modes. *International Journal for Numerical Methods in Engineering*, 33 (7):1413–1449, 1992.

[26] N. Sukumar, D. L. Chopp, N. Moës, and T. Belytschko. Modeling holes and inclusions by level sets in the extended finite-element method. *Computer methods in applied mechanics and engineering*, 190(46):6183–6200, 2001.

[27] N. Moës and T. Belytschko. Extended finite element method for cohesive crack growth. *Engineering fracture mechanics*, 69(7):813–833, 2002.

[28] J. Oliver, M. Cervera, and O. Manzoli. Strong discontinuities and continuum plasticity models: the strong discontinuity approach. *International journal of plasticity*, 15(3):319–351, 1999.

[29] F. Armero and C. Linder. New finite elements with embedded strong discontinuities in the finite deformation range. *Computer Methods in Applied Mechanics and Engineering*, 197(33): 3138–3170, 2008.

[30] M. Cervera, M. Chiumenti, Q. Valverde, and C. Agelet de Saracibar. Mixed linear/linear simplicial elements for incompressible elasticity and plasticity. *Computer Methods in Applied Mechanics and Engineering*, 192(49-50):5249–5263, 12 2003.

[31] M. Cervera, M. Chiumenti, and C. Agelet de Saracibar. Shear band localization via local J2 continuum damage mechanics. *Computer Methods in Applied Mechanics and Engineering*, 193 (9-11):849–880, March 2004.

[32] M. Cervera, M. Chiumenti, and R. Codina. Mixed stabilized finite element methods in nonlinear solid mechanics. Part I: Formulation. *Computer Methods in Applied Mechanics and Engineering*, 199(37-40):2559–2570, August 2010.

[33] M. Cervera, M. Chiumenti, and R. Codina. Mixed stabilized finite element methods in nonlinear solid mechanics. Part II: Strain localization. *Computer Methods in Applied Mechanics and Engineering*, 199(37-40):2571–2589, August 2010.

[34] M. Cervera, M. Chiumenti, and R. Codina. Mesh objective modeling of cracks using continuous linear strain and displacement interpolations. *International Journal for Numerical Methods in Engineering*, 87(10):962–987, 2011.

[35] L. Benedetti, M. Cervera, and M. Chiumenti. High-fidelity prediction of crack formation in 2D and 3D pullout tests. *Computers & Structures*, 172:93 – 109, 2016.

[36] M. Cervera, M. Chiumenti, L. Benedetti, and R. Codina. Mixed stabilized finite element methods in nonlinear solid mechanics. Part III: Compressible and Incompressible Plasticity. *Computer Methods in Applied Mechanics and Engineering*, 285:752–775, 2015.

[37] L. Benedetti, M. Cervera, and M. Chiumenti. Stress-accurate Mixed FEM for soil failure under shallow foundations involving strain localization in plasticity. *Computers and Geotechnics*, 64: 32–47, 2015.

[38] R. Faria, J. Oliver, and M. Cervera. A strain-based plastic viscous-damage model for massive concrete structures. *International Journal of Solids and Structures*, 35(14):1533–1558, 1998.

[39] I. Babuška. Error-bounds for finite element method. *Numerische Mathematik*, 16:322–333, 1971.

[40] F. Brezzi. On the existence, uniqueness and approximation of saddle-point problems arising from lagrangian multipliers. *ESAIM: Mathematical Modelling and Numerical Analysis - Modlisation Mathmatique et Analyse Numrique*, 8(R2):129–151, 1974.

[41] T. J. R. Hughes, L. P. Franca, and M. Balestra. A new finite element formulation for computational fluid dynamics: V. Circumventing the Babuška-Brezzi condition: A stable Petrov-Galerkin formulation of the Stokes problem accommodating equal-order interpolations. *Computer Methods in Applied Mechanics and Engineering*, 59(1):85–99, 1986.

[42] D. Boffi, F. Brezzi, and M. Fortin. *Mixed Finite Element Methods and Applications*. Springer, 2013 edition, 7 2013.

[43] T. J. R. Hughes, G. R. Feijóo, L. Mazzei, and J. B. Quincy. The variational multiscale method - a paradigm for computational mechanics. *Computer Methods in Applied Mechanics and Engineering*, 7825(98), 1998.

[44] R. Codina. Stabilization of incompressibility and convection through orthogonal sub-scales in finite element methods. *Computer Methods in Applied Mechanics and Engineering*, 190:1579–1599, 2000.

[45] M. Cervera, L. Pelà, R. Clemente, and P. Roca. A crack-tracking technique for localized damage in quasi-brittle materials. *Engineering Fracture Mechanics*, 77(13):2431–2450, 2010.

[46] M. Cervera and M. Chiumenti. Mesh objective tensile cracking via a local continuum damage model and a crack tracking technique. *Computer Methods in Applied Mechanics and Engineering*, 196(1):304–320, 2006.

[47] R. Citarella and F.-G. Buchholz. Comparison of crack growth simulation by DBEM and FEM for SEN-specimens undergoing torsion or bending loading. *Engineering Fracture Mechanics*, 75 (3):489–509, 2008.

[48] G. Ferté, P. Massin, and N. Moës. 3D crack propagation with cohesive elements in the extended finite element method. *Computer Methods in Applied Mechanics and Engineering*, 300:347–374, 2016.

[49] A. D. Jefferson, B. I. G. Barr, T. Bennett, and S. C. Hee. Three dimensional finite element simulations of fracture tests using the Craft concrete model. *Computers and Concrete*, 1(3): 261–284, 2004.

[50] F.-G. Buchholz, V. Just, and H. A. Richard. Computational simulation and experimental findings of three-dimensional fatigue crack growth in a single-edge notched specimen under torsion loading. *Fatigue & Fracture of Engineering Materials & Structures*, 28(1-2):127–134, 2005.

[51] S. Saloustros, L. Pelà, and M. Cervera. A crack-tracking technique for localized cohesive–frictional damage. *Engineering Fracture Mechanics*, 150:96–114, 2015.

This page is left intentionally blank.

A mechanically-based model of snow slab and weak layer fracture in the Propagation Saw Test

L. Benedetti, J. Gaume, J.-T. Fischer

Submitted to International Journal of Solids and Structures, (2017)

This page is left intentionally blank.

A mechanically-based model of snow slab and weak layer fracture in the Propagation Saw Test

L. Benedetti[a,b,*], J. Gaume[c,d], J.-T. Fischer[a]

[a] *BFW - Austrian Research Centre for Forests, Department of Natural Hazards, Innsbruck, Austria*
[b] *CIMNE - International Center for Numerical Methods in Engineering, Barcelona, Spain*
[c] *WSL Institute for Snow and Avalanche Research SLF, Davos, Switzerland*
[d] *EPFL - École Politechnique Fédérale de Lausanne, Lausanne, Switzerland*

Abstract

Dry-snow slab avalanche release is the result of failure initiation in a weak snowpack layer buried below a cohesive snow slab followed by rapid crack propagation. The Propagation Saw Test (PST) is a field experiment which allows to evaluate crack propagation propensity in-situ. The critical crack length for the onset of crack propagation and the propagation distance are the two main outcomes of the PST. A consistent number of statistical studies have confirmed a significant correlation between the test result and the likelihood of release of snow slab avalanches. Nevertheless, the results of this field test are hard to interpret in practice because (i) the fracture process in multilayer systems is very complex and only partially explored and (ii) field data is typically insufficient to establish causal links between factors and effects. This study provides a mechanical analysis of the PST based on beam theory with the aim of identifying the influence of snowpack properties on the test results, namely, the critical crack length and propagation distance. An enhanced knowledge of the mechanical processes driving the PST is crucial to interpret snowpack instability and to help to improve avalanche forecasting.

Keywords: mechanical model, Propagation Saw Test

1. Introduction

Dry-snow slab avalanche release is generally caused by failure initiation in a weak snow layer buried below cohesive snow slabs followed by rapid crack propagation (Schweizer et al., 2003). The Propagation Saw Test (PST) is an experimental in-situ technique that has been introduced to assess crack propagation propensity. This test attracted the interest of a large number of practitioners, being relatively easy to perform and providing useful insights for the evaluation of snow instability.

The PST, developed simultaneously by Sigrist and Schweizer (2007) and Gauthier and Jamieson (2008a), is set up which consists in isolating a conventional volume of snow in the downslope direction (Figure 1). Once the weak layer has been identified in the stratigraphy (e.g. from a manual snow profile or a compression test), a saw is used to cut through it progressively. If the length of the saw cut reaches a critical crack length, the onset of crack propagation occurs and depending on snow properties, the crack in the weak layer can initiate the fracture and detachment of the overlying slab.

Statistical studies over a large set of field data confirmed the relevance of the PST, highlighting the positive correlation between test results and the likelihood of avalanche release (Simenhois and Birkeland, 2009; Reuter et al., 2015). The PST has been also extensively tested for different slope angles (Gauthier and Jamieson, 2008b; Bair et al., 2012), compared with Rutschblock and column tests, relevant for skier-triggering events (Gauthier and Jamieson, 2008c; Monti et al., 2016) and peculiar locations like crown fracture lines of previously occurred avalanches or whumps spots (Gauthier et al., 2008).

The analysis of local phenomena that brings the snowpack to failure was initially introduced by McClung (1979), who described the effect of *shear softening* in weak layers and, more recently, size effects (McClung, 2003) and fracture energy dissipation (McClung, 2007) in the case of interfacial weak snow layers by adapting the theory of *Linear Elastic Fracture Mechanics* (LEFM). However, field measurements showed that bending of the upper slab induced by the collapse of the weak layer structure are key elements for the onset of crack propagation (van Herwijnen et al., 2010). Numerous measurements were performed utilizing high speed cameras and particle tracking velocimetry (PTV) by van Herwijnen and Jamieson (2005) revealing key details of the intricate relationship between propagation of weak layer collapse and the upper slab deformation field. Recently, weak layer collapse was taken into account in the anticrack model based on LEFM by Heierli et al. (2008). In addition, experimental studies (Birkeland et al., 2014) and mechanical models (Schweizer et al., 2014) focused on the qualitative description of snowpack properties leading to different failure types, namely full propagation (END) or fracture arrest with or without slab fracture (SF).

Previously, other tests frequently utilized by practitioners

*Corresponding author. Address: BFW - Austrian Research Centre for Forests, Department of Natural Hazards, Rennweg 1, 6020 Innsbruck, Austria
Email addresses: lbenedetti@cimne.upc.edu (L. Benedetti), johan.gaume@slf.ch (J. Gaume), jt.fischer@bfw.gv.at (J.-T. Fischer)

were thoroughly studied as well, both from mechanical and quantitative point of view. For instance, Landry et al. (2001) provided a complete study of the Extended Column Test (ECT). Firstly, they depicted a simplified scheme of the forces acting on the weak layer crystals during the test. Then, comparing field results with the previously developed theories, they were able to assess the dependence from geometrical aspects and mechanical parameters. With regards to the Propagation Saw Test, beside current numerical studies utilizing discrete elements methods (Gaume et al., 2015, 2016), only little attention has been devoted to a detailed analytical description able to give a comprehensive mechanical framework of the sequence of processes involved in the test.

Consequently, this work aims to provide a simple quantitative tool for an exhaustive mechanical interpretation of the PST by means of well known mathematical models in the field of continuum mechanics. The Euler-Bernoulli beam theory is applied to the test setup, allowing an easy description of the snowpack stress state in the quasi-static load regime. We assume the bonded snow in the upper slab as elastic-perfectly brittle whereas the weak layer is considered as a rigid bed of crystals, failing either to compression or shear forces. As a result, the onset of slab and weak layer fracture is described in terms of crack length, slope angle, slab dimensions and the main mechanical parameters such as density, elastic modulus, strength. With the introduction of this approach, it is possible to parametrize the problem, highlighting the dependence of the test outcomes from initial knowledge of the snowpack.

The paper is organized as follows. First, an illustrative discussion of the possible outcome of the test is presented, starting from basic heuristic arguments and field experiences. Therefore, the mechanical problem is set out: the upper cohesive snow slab and the weak layer are analyzed separately, allowing to compute the stresses evolution with respect to the saw cut length. In order to demonstrate the model capabilities, a realistic study case is presented and the outcomes of the test are related directly with a quantitative evaluation. Furthermore, a sensitivity analysis of the parameters is carried out, showing interesting features of this seemingly straightforward but detailed model. Finally, the discussion will layout the advantages and limitations of our approach.

2. Phenomenology of the PST fracture modes

To setup the test, a volume of snow of $b = 30$ cm of width and, at least, 1 meter in length in the downslope direction l_{tot} (Figure 1) is isolated. Although accessing avalanche prone terrain is limited due to safety reasons, the test is usually performed in areas which are representative for the prediction of the prevailing avalanche release conditions.

The case study that we are interested in analyzing is composed of a snow slab overlying a rigid substratum (of total length l_{tot}) with a weak layer in between. Figure 2 shows the side view of the idealized model, where the horizontal is parallel to the slope plane with angle ψ. The slab above the weak layer is characterized by bonded snow, whereas the lower one can be thought as rigid bed and, consequently, it is not included in the analysis.

Once the saw reaches the critical crack length l_c the fracture propagates ahead. The PST results are commonly reported with the following scores (Gauthier and Jamieson, 2008a):

- **Full propagation (END):** the fracture propagates in front of the saw and spans the whole length of the isolated slab.
- **Slab fracture (SF):** the propagation in the weak layer is stopped by a sudden slope-normal fracture in the upper slab; the result of the test is reported as the length of propagation with respect to the total length.
- **Fracture arrest without slab fracture (ARR):** the propagation in the weak layer stops in a point which is hardly identifiable at naked eye.

The first question to address is the sequence of events that could take place in a Propagation Saw Test. Naturally the upper slab introduces a gravitational load on the weak layer. At the beginning of the test, increasing the cut length l creates a volume of cohesive snow, clamped on one side and hanging freely on the other one (Figure 3(a)) whereas the weak layer reduces its resisting area. The upper layer is displaced both vertically and horizontally under its own weight until it touches the lower bed (Figure 3(b)). The cut length l at which this initial contact (IC) is observed is identified with $l = L_{IC}$. At first only the tip of the cantilever rests on the lower slab: the resulting effect is a hinged restrain, where the beam does not displace vertically anymore but it has freedom to rotate (Figure 3(c)). Then, following the increase of l, the slab bends back due to its own weight and rests with vertical cross section with respect to the lower bed. At this point, not only the vertical movement is constrained but also the rotation of the beam is fixed. The cut length l required for this condition to happen is called length of full contact (FC) and it is denoted by L_{FC} (Figure 3(d)). If the sawing continues, the contact zone of the two slabs increases. However, the length between the saw and the first touching point remains constant, being equal to the full contact length L_{FC} (Figure 3(e)) due to equilibrium requirements. Hence the beam is now behaving as a double clamped beam, with a fixed length of L_{FC}, and, consequently, with a constant bending moment and shear on the cross sections.

Then we consider the possible failure modes that can appear during the test. Both upper slab and weak layer are subjected to the same gravitational load and, to analyze all cases in a comprehensive manner, we consider the applied stress on the upper slab σ^s and of the weak layer σ^w with respect to their limit values σ^s_y and σ^w_y, in a generic sense. Considering the ratios $S^s = \sigma^s/\sigma^s_y$ and $S^w = \sigma^w/\sigma^w_y$, it allows us to define different limiting cases. The value of the ratios is limited between zero, representing a stress free situation, and one, corresponding to the failure stress. In fact, it is physically impossible for a material to sustain higher stresses than the admissible one and, consequently, to have a stress ratio larger than 1.0. The variation of S^s and S^w influences the way the upper slab interacts with the weak layer, as well as the the crack propagation process as follows.

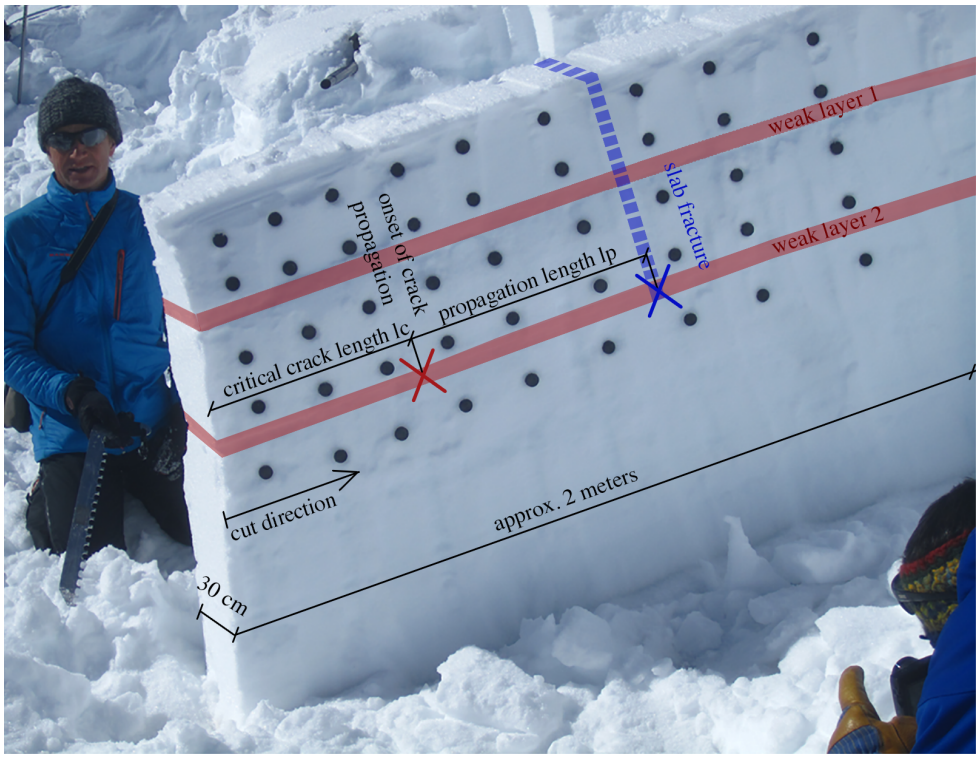

Figure 1: Setup of a typical Propagation Saw Test (photo from the authors).

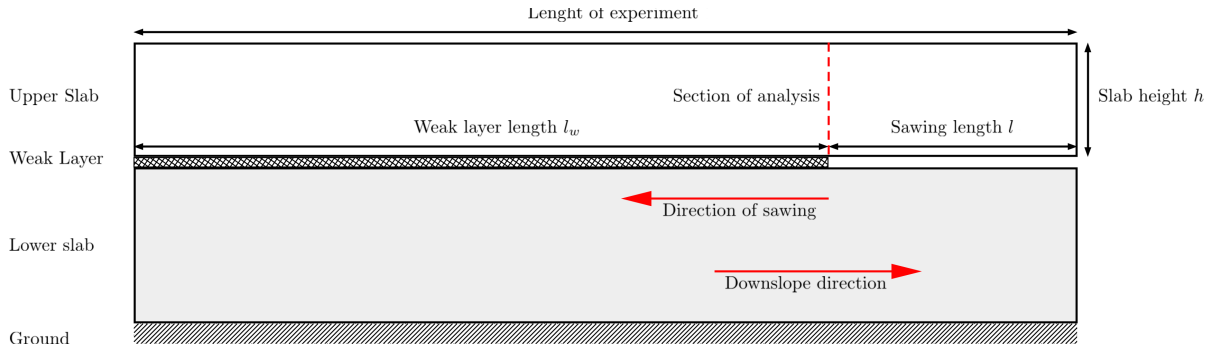

Figure 2: PST side view sketch.

2.1. $S^s \approx 1$ and $S^w << 1$: low strength of upper slab

The first limit case presents a soft upper layer -typical for fresh snowfalls- which did not yet developed enough strength, e.g. due to sintering, settlement or wind. Meanwhile, the weak layer is relatively strong, not having experienced temperature gradient metamorphism or surface hoar formation. Consequently, we formally say $S^s \approx 1$ and $S^w << 1$. In this case, the upper slab material separates in rough wedges as the saw progresses without any creation of a cantilever structure (Figure 4(a) and 4(b)). Shear wedges are common on a flat surface whereas bending and tensile effects are dominant factors for steeper slopes. However, no buildup of stresses on the weak layer is possible, so propagation of the crack in the weak layer is highly unlikely. In this case the critical cut length, initiating crack propagation, tends to infinity ($l_c \rightarrow \infty$), since the saw has to cut the ideally infinite long weak layer to release the entire upper slab.

2.2. $S^s << 1$ and $S^w \approx 1$: low strength of weak layer

When the weak layer shows a very low threshold stress, any perturbation of the equilibrium state would provoke failure and crack propagation. At the same time, assuming a strong upper layer, we can write in a condensed form $S^s << 1$ and $S^w \approx 1$. Given that the buildup load can only increase, the propagation takes place along the whole specimen. Consequently, the critical length of crack propagation tends to zero ($l_c \rightarrow 0$), since very small changes would conclude the test.

2.3. $S^s \approx 1$ and $S^w \approx 1$: Similar strengths in upper slab and weak layer

As the upper and weak layer stresses are comparable with their threshold value, i.e. $S^s \approx 1$ and $S^w \approx 1$, a competitive

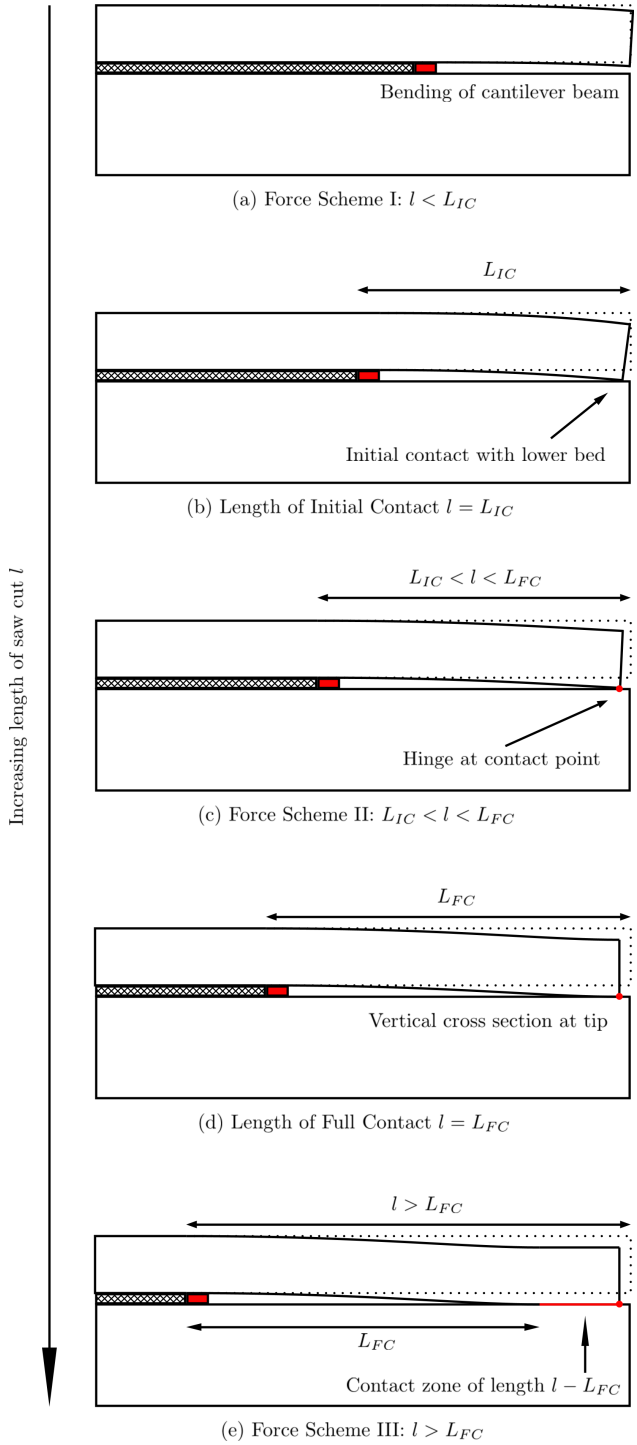

(a) Force Scheme I: $l < L_{IC}$

(b) Length of Initial Contact $l = L_{IC}$

(c) Force Scheme II: $L_{IC} < l < L_{FC}$

(d) Length of Full Contact $l = L_{FC}$

(e) Force Scheme III: $l > L_{FC}$

Figure 3: Stages of the Propagation Saw Test: after initial bending (a), first contact of upper slab and lower bed is reached at cut length $l = L_{IC}$ (b). Following the sawing (c), the full contact length is achieved for $l = L_{FC}$ (d), at which point the cross section has rotated back to normal. Successively, the length of the beam under bending is kept constant at L_{FC} for $l > L_{FC}$, while the contact zone is increasing as the saw progresses further (e).

mechanism of failure between the tensile stress in the upper slab and the compressive or shear force in the weak layer arises. The first one is responsible for the detachment of the cohesive snow slab, whereas the latter corresponds to weak layer failure and the subsequent possible fracture propagation.

If the slab strength is larger relative to the weak layer one ($S^s \leq S^w$), cracks may initiate in the weak layer and propagate upon reaching the peak stress. The upper cohesive snow displaces vertically following the collapse of the lower crystals and, at the same time, the stress state in the slab can increase due to bending and normal tensile force. In this case, propagation may stop when the maximum allowable stress appears in the slab causing a vertical fracture which subsequently releases the gravitational load (Figure 4(c)). Conversely, if the weak layer strength is larger than the upper slab one ($S^s \geq S^w$), the upper slab may fail prior to any propagation of the crack in the rest of the snowpack (Figure 4(d)).

This set of different phenomena shows the importance of analyzing and predicting the characteristic length at which each single mechanism appears. At the same time, scientists are required to identify the correct failure mechanism *in situ* and, without previous knowledge of the complex interplay between slab and weak layer, it represents a challenging problem. Therefore, a detailed analysis of the PST can help to reveal the conditions for a possible failure mechanism to happen.

3. Mechanical model

The objective of this section is to describe analytically a failure criterion for the upper slab and the weak layer. To do so, the evolution of the stresses with respect to the saw-cut length is investigated, taking into account the substantial changes in the force schemes, presented in the previous section.

Snow is assumed to behave like a porous material akin to soil. It is formed by crystals which, through bonds and metamorphism, create a solid-like structure during the sintering process. Similarly, granular particles are linked through bridges like chemical or mechanical bonds in soil. The solid structure of snow changes due to environmental external actions (e.g. consolidation settlement, increase of temperature, change of humidity, etc.) and, then, the mechanical characteristics evolve accordingly. The PST is carried out in a relatively short time with respect to the time required for other natural processes to take place. Consequently, in this study, we consider the solid matrix as fixed, discarding any appreciable influence from the environmental variables.

The isolated volume of snow for the test is presented in Figure 5 in 3D, in order to underline the geometry of the problem. The total length of the specimen is l_{tot}, while l represents the length of snow that has been sawed and, consequently, $l_w = l_{tot} - l$ is the length of the remaining weak layer.

The upper slab is assumed to be a homogeneous cohesive snow beam with constant width b and height h. A coordinate system ξ_s, η_s, ζ_s is placed in the center of mass of the orthogonal cross section at the sawing point. There, we will study the stresses arising in the upper slab. The weak layer, instead,

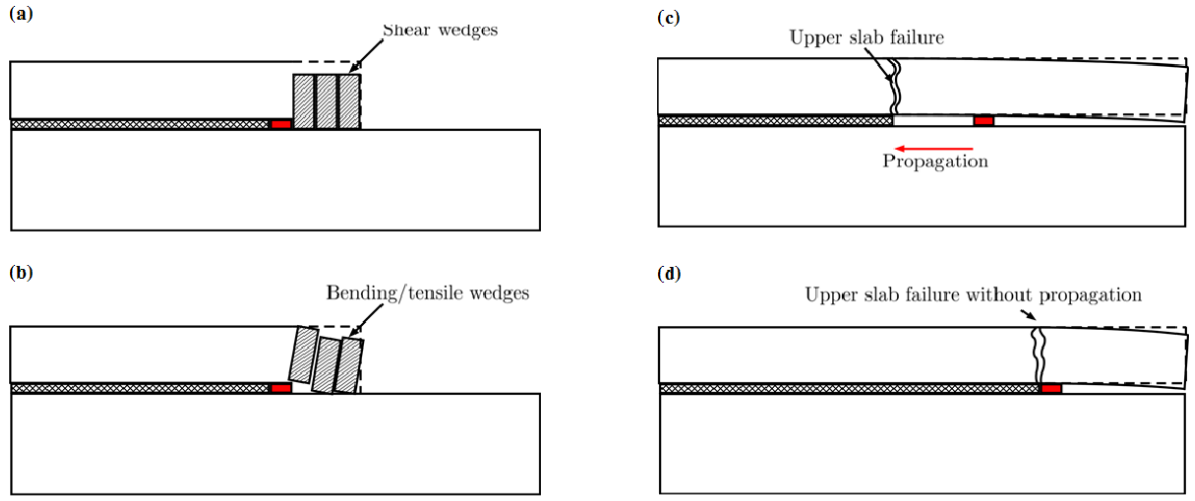

Figure 4: Shear (a) and bending wedges (b) in the limit case of low strength in the upper slab $S^s \approx 1$ and $S^w >> 1$. Example of slab fracture outcome in the PST: (c) propagation in the weak layer followed by a slab failure due to maximum tensile force (SFa); (d) slab fracture due to high bending stresses for the cantilever structure (SFb).

has a thickness h_w and width b. To study the resulting effect of the sawing process, a coordinate system originating from the geometrical center of the upper surface of the weak layer is selected, pointing in upward direction ζ_w. Finally, the lower slab is considered to be rigid and it represents the lower bound of the domain of the test, being not be affected by the saw cut.

Although from the previous considerations, the Propagation Saw Test is a complex 2D problem, in order to easily evaluate the chain of events during the experiment, the different layers in the snowpack are studied separately. In particular, during the analysis of one of the parts, the other ones are considered as rigid bodies. For instance, while studying the forces applied to the weak layer, the upper slab is assumed as a firm volume of material, with uniform displacements and rotations.

For the purposes of the mechanical analysis, the material is considered to be homogeneous and isotropic along each single layer of the snowpack. In the following, we introduce the failure modes of the slab and the weak layer and, consequently, we determine the critical cut length l_c that provokes fracture in either the weak layer (l_c^w) or upper slab (l_c^s). In addition, the crack propagation distance l_p, for which slab fracture occurs leading to fracture arrest, is also computed.

3.1. Failure model of the upper slab

The upper slab is studied as a homogeneous prismatic beam of length l. Gravity represents the only applied load, which is uniformly distributed along its length, with normal and downslope components according to the slope angle ψ, as depicted in Figure 6. Each unitary-length cross section provides a linear distributed load q in the direction of the gravitational force.

The linearly distributed load due to the weight of the slab is:

$$q = \rho\, g\, h\, b \tag{1}$$

where ρ is the density of the upper slab, g is the gravitational acceleration, h is the normal depth of the slab and b is the transversal width. First of all, the gravity load in the slab is projected in its components, in the parallel and the normal direction of the slope:

$$q_h = q \sin\psi \quad q_v = q \cos\psi \tag{2}$$

On the one hand, the load that is parallel to the centerline causes a stretching of the beam along the coordinate ζ_s. On the other hand, the vertical load provokes bending, rotating the cross sections and lowering the tip of the upper slab. In general, these two effects are not independent but, as long as the displacements remain small, the hypothesis of superposition of effects holds. Hence, the beam is studied separately for each load case and, at the end, results are superimposed (Figure 6 (b) and (c)).

To describe the variation of the internal forces with respect to the load and to the geometric characteristics, the Euler-Bernoulli beam theory is employed. A beam that is subjected to the set of forces previously presented usually experiences failure due to bending moment, shear, normal tension or a combination of the previous (Figure 7).

The force that is oriented in the slope downward direction creates a constant tensile stress on the cross section. At the same time, bending is due to the vertical force with respect to the centerline, but it contributes to the normal stresses in the cross section. Along the coordinate η_s, the additional stress due to bending varies linearly from a maximum tensile value on the top surface to the maximum compressive one, located in the lower fiber. Concerning the shear force, a constant vertical stress is created but, for slender beams, the shear stress is smaller than the one of bending and tensile force.

Focusing on cohesive slabs, von Moos et al. (2003) and Scapozza and Bartelt (2003) performed triaxial experiments in which it was possible to describe the mechanical behavior of snow under static loading. In the case of compression, after the initial elastic range, the specimens showed an inelastic branch composed of a hardening part followed by a sudden softening. On the contrary, under tension, snow was characterized by a quasi-brittle fracture with far lower threshold values than com-

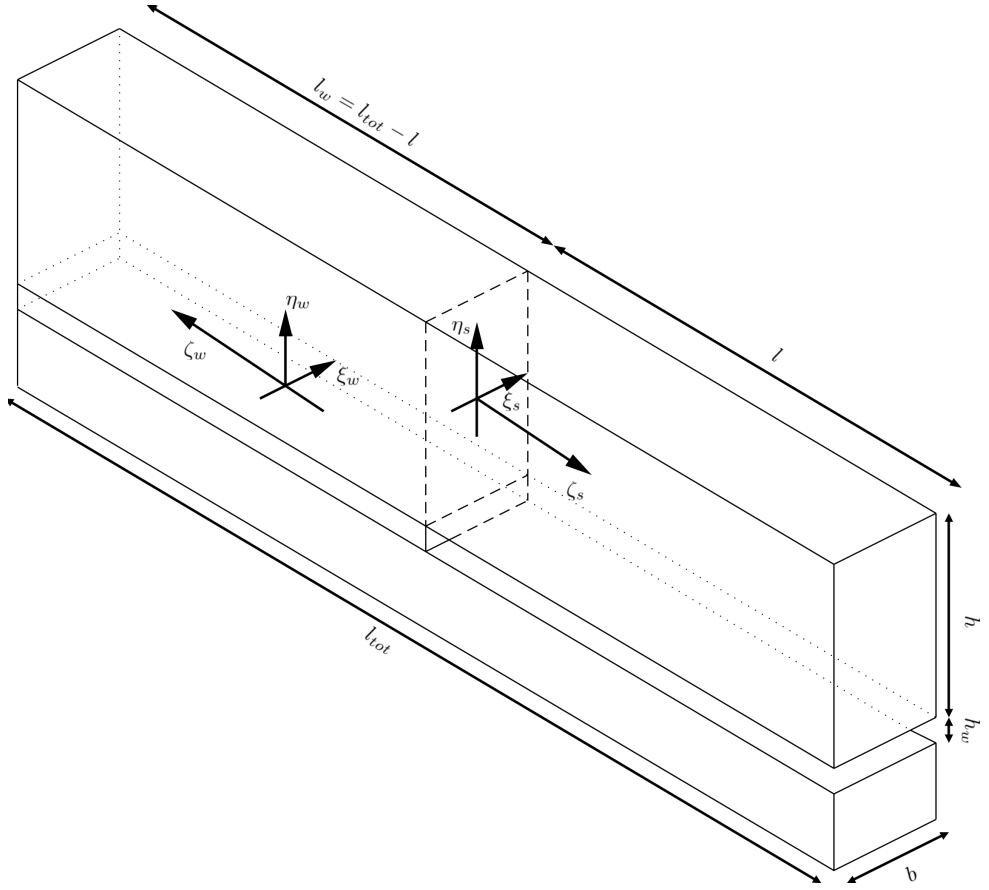

Figure 5: PST model: the resisting cross sections for the upper slab and the weak layer are highlighted by the local coordinate system. In addition, the geometrical dimensions of the specimen are presented.

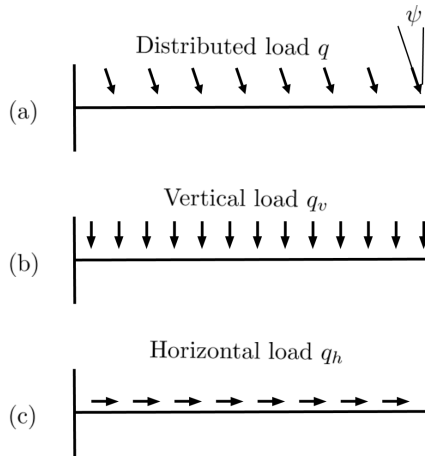

Figure 6: Beam model with distributed load: (a) respect to the slope angle ψ, (b) projected vertically and (c) projected horizontally.

pression. Since, by sawing through the weak layer, the top fiber in the upper slab increases the state of tension, it is reasonable to consider the tensile strength σ^s_{yt} as the limit value of the elastic branch for the cohesive snow. Moreover, assuming pure brittle behavior, this stress state represents the instant at which sudden brittle failure of the upper slab (and its detachment) occurs as well.

3.1.1. Bending stresses

Bending moments are a fundamental component of the study since their evolution is strictly related with the change in the tensile stress in the upper slab. As presented before, different force schemes, depending on the eventual contact with the lower bed, are described by the initial and full contact lengths L_{IC} and L_{FC}. A detailed evaluation of the tensile stress is required to determine the critical cut length l^s_c for a failure to appear in the upper slab.

In the Euler-Bernoulli theory, the behavior of an elastic beam under a distributed weight q_v is given by the following differential equation:

$$\frac{\mathrm{d}^2}{\mathrm{d}x^2}\left[EI\frac{\mathrm{d}^2 v\,(x)}{\mathrm{d}x^2}\right] + q_v = 0 \tag{3}$$

which is the result of considering the relationship equations between vertical displacement v, rotation θ, curvature χ, bending

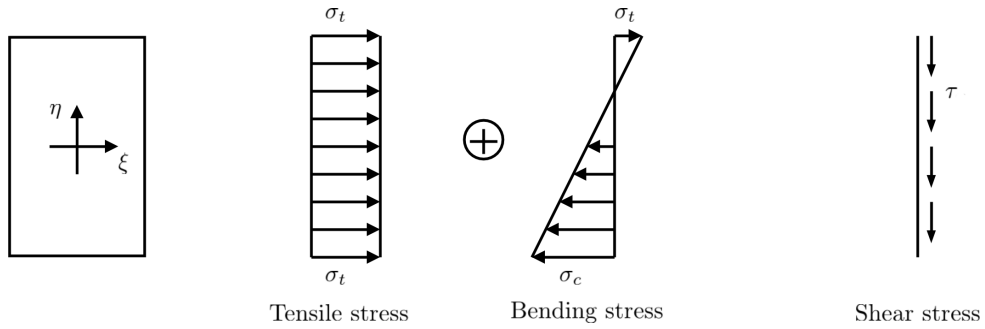

Figure 7: Failure modes for the beam-like cross section: tension combines with bending to give the field of normal stresses whereas shear is in the plane of the section.

moment M and shear force T:

$$\theta = \frac{\mathrm{d}v(x)}{\mathrm{d}x} \tag{4}$$

$$\chi = \frac{\mathrm{d}\theta(x)}{\mathrm{d}x} \tag{5}$$

$$M = -EI\chi \tag{6}$$

$$T = \frac{\mathrm{d}M(x)}{\mathrm{d}x} \tag{7}$$

$$\frac{\mathrm{d}T(x)}{\mathrm{d}x} + q_v(x) = 0 \tag{8}$$

where E is the elastic modulus and I is the second order moment of inertia of the cross section of the beam. Each time that it is required to solve this ordinary differential equation, four boundary conditions have to be set. Two of them are imposed on the cross section at the sawing point where vertical displacement and rotation are null, whereas the other two conditions are obtained by considering the free end of the beam. At the beginning of the PST, the tip is free to rotate (bending moment equal to zero) and displace vertically (shear equal to zero). This situation is denoted bending scheme I and depicted in Figure 8(a).

The solution for the vertical displacement function of the cantilever is:

$$v_I(x) = \frac{-q_v\left(6l^2x^2 - 4lx^3 + x^4\right)}{24E_sI_s} \tag{9}$$

The vertical displacement v of the tip of the cantilever beam at $x = l$ is computed as:

$$v_I = -\frac{q_v l^4}{8E_sI_s} \tag{10}$$

Recalling previous equations, the bending moment $M_I(x)$ for scheme I reads:

$$M_I(x) = \frac{q_v\left(12l^2 - 24lx + 12x^2\right)}{24} \tag{11}$$

and the highest moment is found at the clamped end $x = 0$ (above the sawing point):

$$M_I = \frac{q_v l^2}{2} \tag{12}$$

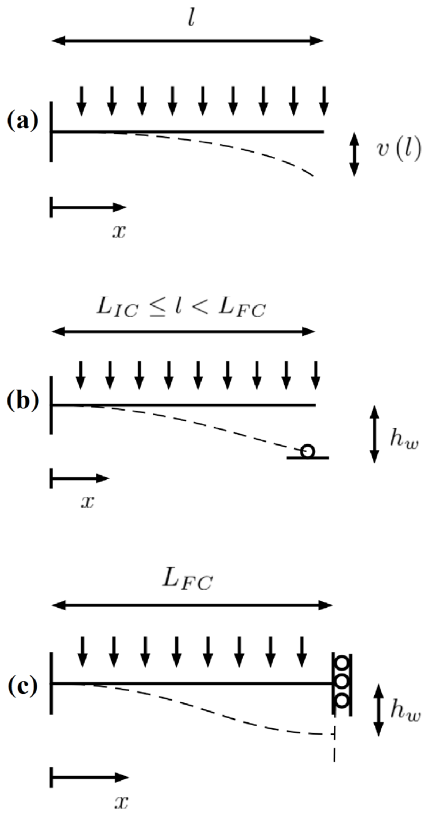

Figure 8: (a) First bending scheme: Cantilever. (b) Second bending scheme: Cantilever with hinge. (c) Third bending scheme: Fixed-Fixed roller.

When the beam tip touches the lower layer at a height $-h_w$, the vertical displacement is restrained and the force scheme is changed. We identify the length L_{IC} at which this happens as:

$$L_{IC} = \sqrt[4]{\frac{8E_sI_sh_w}{q_v}} \tag{13}$$

For $l > L_{IC}$ the cantilever touches the lower slab. This is represented by bending scheme II: left end is fixed and, at the right end, vertical motion is restrained (Figure 8(b)). The small part that is in contact with the lower slab is applying a concentrated vertical reaction F_t on the beam but leaving rotation free.

The resulting vertical displacement function $v(x)$ is ex-

pressed as:

$$v_{II}(x) = -\frac{3h_w x^2}{2l^2} - \frac{q_v l^2 x^2}{16E_s I_s} + \frac{h_w x^3}{2l^3} + \frac{5q_v l x^3}{48E_s I_s} - \frac{q_v x^4}{24E_s I_s} \quad (14)$$

The subsequent bending moment reads:

$$M_{II}(x) = \frac{3E_s I_s h_w}{l^3}(l-x) + \frac{q_v(l-4x)}{8}(l-x) \quad (15)$$

which, taking advantage of the expression (13), reads:

$$M_{II}(x) = \frac{q_v l^2}{8}\left(1 + 3\frac{L_{IC}^4}{l^4} - 4\frac{x}{l}\right) \quad (16)$$

Its maximum value is located again at the clamped end:

$$M_{II}(0) = \frac{q_v l^2}{8}\left(1 + 3\frac{L_{IC}^4}{l^4}\right) \quad (17)$$

Finally, the force F_t is:

$$F_t = T(l) = \frac{3q_v l}{8} - \frac{3E_s I_s h_w}{l^3} = \frac{3q_v l}{8}\left(1 - \frac{L_{IC}^4}{l^4}\right) \quad (18)$$

Going further in the test, with increasing length l, the free end is rotating back to zero due to the gravitational force. Consequently, the bending scheme II is valid until the rotation of at $x = l$ comes back to zero, which, in practice, means that the weight of the snow slab makes the beam to rest on the lower slab. Once the end section is orthogonal to the rigid bed, the full contact length L_{FC} is reached. After that, all slab in excess of this rotation will be supported by the lower surface bed. To find the full contact length L_{FC} we set $\theta(l) = 0$ and get:

$$L_{FC} = \sqrt[4]{\frac{72E_s I_s h_w}{q_v}} = \sqrt{3}L_{IC} \quad (19)$$

which shows that the transition between the latter two schemes is as long as $\sqrt{3} - 1 \approx 0.75$ times longer than the initial touch length L_{IC}.

Increasing the cut length above the full contact one ($l > L_{FC}$), it is possible to notice that both ends of the beam are restrained in rotation, i.e. the beam must be horizontal at boundaries. This is caused by the weight of the touching slab, which makes the cross section orthogonal to the rigid bed itself. We denote this configuration as the bending scheme III. In this scheme two additional effects have to be taken into account: the vertical displacement of the right roller, equal to the weak layer height h_w, and the weight of the upper slab, whose friction will be presented in the following section.

Following the previous reasoning, the boundary conditions on a beam of constant length L_{FC} are:

$$v_{III}|_{x=0} = 0 \qquad v_{III}|_{x=L_{FC}} = -h_w \quad (20)$$

$$v'_{III}\big|_{x=0} = 0 \qquad v'_{III}\big|_{x=L_{FC}} = 0 \quad (21)$$

This yields the vertical displacement function:

$$v_{III}(x) = \frac{h_w}{L_{FC}^3}\left(2x^3 - 3L_{FC}x^2\right) - \frac{q_v x^4}{24E_s I_s}(x - L_{FC})^2 \quad (22)$$

For this scheme, the bending moment $M(x)$ is

$$M_{III}(x) = \frac{E_s I_s h_w}{L_{FC}^3}(6L_{FC} - 12x) + \frac{q_v x^2}{2} - \frac{q_v L_{FC} x}{2} + \frac{q_v L_{FC}^2}{12} \quad (23)$$

which, using expression (19) can be rewritten as:

$$M_{III}(x) = \frac{6q_v x^2 - 8q_v L_{FC} x + 2q_v L_{FC}^2}{12} \quad (24)$$

In the bending scheme III, i.e. for cut lengths $l > L_{FC}$, the maximum moment is located at the sawing point $x = 0$, and reads:

$$M_{III}(0) = \frac{q_v L_{FC}^2}{6} \quad (25)$$

Note that the value of the bending moment will not increase for longer cut lengths l, since the length of the active beam remains constant at the full contact length L_{FC}, while the rest of the upper slab is directly supported by the underlying bed.

3.1.2. Normal stresses

Beside the bending moment, which allows to derive the characteristic lengths L_{IC} and L_{FC}, the upper slab is subjected to a traction force exerted in slope direction. To formally describe the normal force N, two traction schemes are introduced (compare Figure 9):

- **Simply supported:** this case presents the left end as the only constrain to horizontal movement whereas the right end is free to move. The normal force at this point is:

  $$N = q_h(l - x) \quad (26)$$

  This case is linked with the bending schemes I and II, where the tip of the beam is either free or only touches the rigid bed at point, not exerting enough contact force to engage friction.

- **Simply supported with additional frictional resistance:** when the beam is in full contact with the rigid bed, i.e. $l > L_{FC}$, the friction between the two is helping to sustain the longitudinal load. The friction force depends on the weight of the touching part w_{us} and on the static friction coefficient k_f between upper slab and rigid bed. Since w_{us} is assumed to be zero up to the full contact length L_{FC}, the second traction scheme represents the fixed-fixed roller mechanism, corresponding to bending scheme III. Then, it is possible to compute the following reaction force:

  $$N = q(l - x)\sin(\psi) - k_f qbh(l - L_{FC})\cos\psi \quad (27)$$

In a more formal way, one can generalize the normal traction force at the sawing point $x = l$ as:

$$N = \begin{cases} ql\sin(\psi) & \text{for } l < L_{FC} \\ ql\sin(\psi) - k_f q(l - L_{FC})\cos(\psi) & \text{for } l > L_{FC} \end{cases} \quad (28)$$

Typical behavior of the traction force is presented in Figure 10, where is possible to notice the change in behavior due the touching effect.

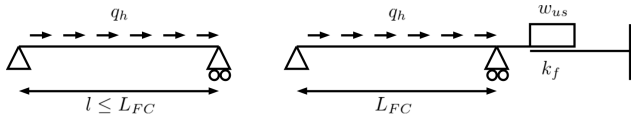

(a) Simply supported (b) Additional frictional effect

Figure 9: Force schemes for the beam under horizontal tensile force.

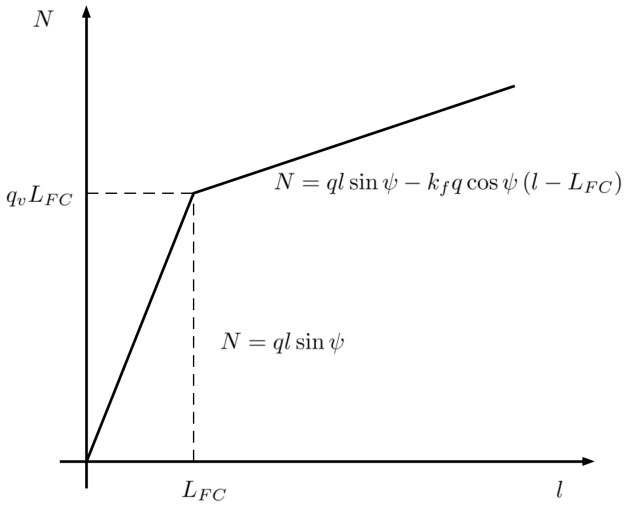

Figure 10: Horizontal tensile force with respect to the length of sawing.

3.1.3. Failure criterion

Now, to determine the failure criterion of the upper slab, the forces computed from the different schemes have to be converted into the corresponding stresses in the resisting cross section. The resisting cross section is defined as area of the beam, orthogonal to the center line, above the sawing point. Namely, in such zone, we observe the highest value of the applied forces that we previously computed. In the elastic range, to evaluate the normal stresses distribution due to bending moment M and normal traction N, it is possible to use Navier's formula:

$$\sigma(\eta_s) = \frac{M}{I}\eta_s + \frac{N}{A} \tag{29}$$

where the second moment of inertia I_s and the area of the section A_s are

$$I_s = \frac{bh^3}{12} \qquad A_s = bh \tag{30}$$

Navier's formula gives a linear distribution of stresses along the height of the beam η_s with values that range from σ_t on the top surface to σ_c on the bottom face. Failure condition is reached when the top fiber registers the maximum admissible stress σ_{yt} due to the pair of actions N, M:

$$\sigma_{yt} = \frac{M}{I_s}\frac{h}{2} + \frac{N}{A_s} \tag{31}$$

After reaching σ_{yt}, the resisting section cannot sustain any additional tension. With the assumption of pure brittle material, snow on the top face gradually starts to detach past this limit point, reducing the resisting area of the beam and, consequently, its bearing capacity. As a result, failure appears as soon as the maximum tension stress is reached, i.e. when the beam experiences $\sigma_t = \sigma_{yt}$. Normal forces (eq. 28) and bending moments (eqn. 12, 17 and 25) were previously derived from the respective force scheme as function of the sawing length and of the linearly distributed weight load:

$$\begin{aligned}
&\text{For } l \leq L_{IC} && M = \tfrac{q_v l^2}{2} \\
&\text{For } L_{IC} < l \leq L_{FC} && M = \tfrac{q_v l^2}{8}\left(1 + 3\tfrac{L_{IC}^4}{l^4}\right) \\
&\text{For } l > L_{FC} && M = \tfrac{q_v L_{IC}^2}{2} = \tfrac{q_v L_{FC}^2}{6}
\end{aligned} \tag{32}$$

$$\begin{aligned}
&\text{For } l \leq L_{FC} && N_u = q_h l \\
&\text{For } l > L_{FC} && N_u = q_h l - k_f q_v\,(l - L_{FC})
\end{aligned} \tag{33}$$

At this point, the tensile stress state for each loading stage can be computed: the resulting expressions are presented in Table 1. These equations can be (numerically) inverted to find the critical length for slab failure l_c^s. In addition, the variation of the stresses versus the sawed length can be studied, as it will be presented in the numerical examples section.

3.2. Failure model of the weak layer

The weak layer is a bed of low strength crystals. There are various types of snow that potentially forms a weak layer. In this study, we consider the weak layer as homogeneous body with a distinct thickness as the only geometrical parameter.

In the PST, the saw cut aims to remove the resisting area of the weak layer, in order to reduce the global vertical and horizontal strength. Simultaneously, the weight of the upper slab loads the weak layer structure in both shear and compression at an angle ψ. When the normal applied force is exceeding the elastic limit, failure can be observed due to crushing of large crystals, with a sudden reduction in volume (Figure 11(a)). On the other hand, the compressive force is beneficial for the friction resistance against shear forces (Figure 11(b)). The two failure modes are potentially possible but, depending on load and strength values, one will be more attainable than the other. Recent studies highlighted the mixed-mode shear-compression failure behavior of the weak snowpack layers (Reiweger et al., 2015; Chandel et al., 2015). However, we assume a simplified failure criterion with constant compressive and shear strength, σ_{yc}^w and τ_{ys}^w respectively, as the only mechanical parameters for the weak layer. This assumption will be discussed in detail in Sec. 6. In addition, we consider that, due to the quasi-brittle nature of the weak layer, the crack onset created by the saw starts to naturally propagate after the failure point.

We are now interested in computing the evolution of the shear and compressive stress in the weak layer with respect to the cut length, in a similar fashion as it was realized for the upper slab. In order to evaluate the stresses applied to the weak layer, we consider the weight of the upper slab as concentrated in its center of gravity. This assumption holds if we consider a rigid

Table 1: Summary of the stress evolution functions applied to the resisting section of the upper slab.

Scheme I: $l \leq L_{IC}$	$\sigma_t = \rho g h \left[\frac{l}{h} \sin(\psi) + 3 \frac{l^2}{h^2} \cos(\psi) \right]$ (34)
Scheme II: $L_{IC} < l \leq L_{FC}$	$\sigma_t = \rho g h \left[\frac{l}{h} \sin(\psi) + \frac{3}{4} \frac{l^2}{h^2} \cos(\psi) \left(1 + 3 \frac{L_{IC}^4}{l^4} \right) \right]$ (35)
Scheme III: $l > L_{FC}$	$\sigma_t = \rho g h \left[\frac{l}{h} \sin(\psi) - k_f \frac{l - L_{FC}}{h} \cos(\psi) + \frac{L_{FC}^2}{h^2} \cos(\psi) \right]$ (36)

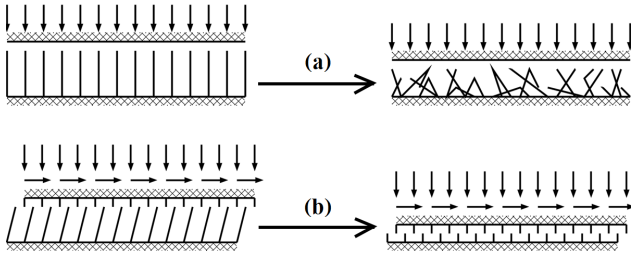

Figure 11: Weak layer failure modes: (a) crushing due to compression and (b) shear failure due to the combined effect of horizontal and vertical load.

interface between the two layers: the upper slab is a rigid solid when the forces on the weak layer are computed. The different load schemes are taken into account also in this case, as done before for the bending and normal force in the upper slab. The distance l_M between the center of gravity and the center of the resisting section, previously identified in Figure 5, is given by geometric construction in Figures 12(a) and 12(b):

$$\begin{aligned} l_M &= \tfrac{l}{2} \qquad \text{for } l < L_{FC} \\ l_M &= \tfrac{L_{FC}}{2} \qquad \text{for } l \geq L_{FC} \end{aligned} \tag{37}$$

Notice that, for $l < L_{IC}$, the vertical force F_t is zero since there is no contact. Instead, when $L_{IC} \leq l < L_{FC}$, the additional normal force F_t applied at the tip of the beam increases with increasing cut length whereas, finally, in case of $l \geq L_{FC}$, F_t is constant because the active beam is always L_{FC} long.

The normal $W_n = q_n l$ and horizontal $W_h = q_h l$ component of the gravitational load result in forces on the weak layer, which are summarized in Table 2. Similarly to the treatment of the upper slab, schemes II and III include the reduced normal weight of the upper slab.

In order to evaluate the stresses applied to the weak layer, Navier's formula and a shear stress approximation are introduced:

$$\sigma(\eta_w) = \frac{N_w}{A_w} + \frac{M_w}{I_w} \eta_w \qquad \tau_s = \frac{T_w}{A_w} \tag{41}$$

where η_w is the coordinate along the longitudinal dimension of the weak layer (Figure 5), I_w and A_w are respectively the second order of inertia and the area of the resisting section:

$$I_w = \frac{b (l_{tot} - l)^3}{12} \qquad A_w = b (l_{tot} - l) \tag{42}$$

The elastic loading branch is limited by the maximum available compression at the sawing point or by the maximum available shear force at the interface between the layers. Then, the maximum compressive stress on the weak layer is computed as:

$$\sigma_c = \sigma \left(-\frac{l_{tot} - l}{2} \right) = \frac{6 M_w}{b (l_{tot} - l)^2} + \frac{N_w}{b (l_{tot} - l)} \tag{43}$$

and the shear stress reads:

$$\tau_s = \frac{T_w}{A_w} = \frac{T_w}{b (l_{tot} - l)} \tag{44}$$

Table 3 summarizes the computed stresses applied to the weak layer. We observe a dependence on the inverse of the quantity $l_{tot} - l$, which results in an increase of stresses which is nonlinear (going to infinity for $l \to l_{tot}$), even when the bending moment is constant for $l \geq L_{FC}$.

The critical crack length l_c^w can be computed here and compared now with the one resulting from the upper slab, in order to evaluate different outcomes of the test.

4. Model Application

In this section, we highlight the features of the presented PST theory. First, we introduce a realistic study case, which is helpful to show how the model can predict the outcomes of the Propagation Saw Test. Then, the sensitivity of the model is tested by varying the numerous parameters. We discuss the dependence of the results on each single quantity as well as their importance on the test outcome.

4.1. Simple study case

A simple PST study case is presented in order to depict, firstly, the stress evolution in the upper slab and in the weak

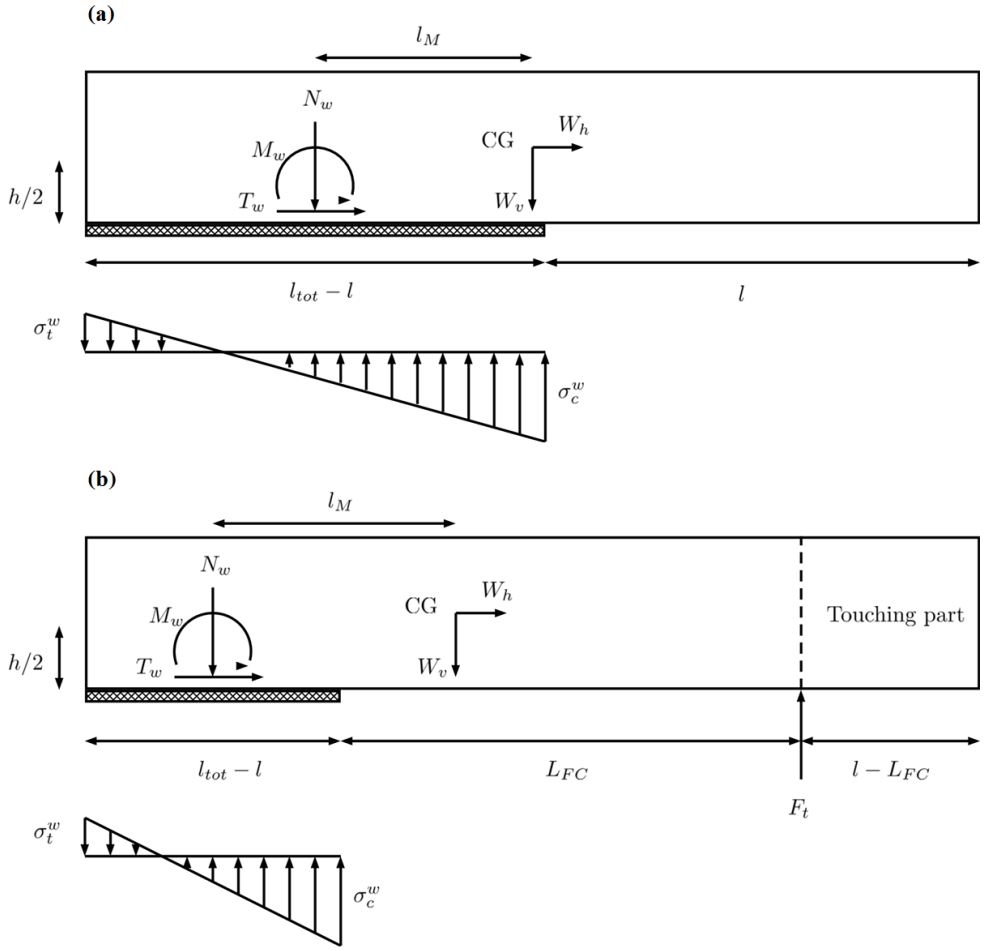

Figure 12: Equilibrium schemes for the computation of stresses in the weak layer: (a) case for $l < L_{FC}$; (b) case for $l \geq L_{FC}$.

layer and, secondly, the link of the quantitative results to the outcomes of the test. In particular, by changing the upper slab density ρ, the cases of full propagation (END) and slab fracture (SF) are recovered. In this study case, the upper slab has a section of width b = 30cm and height h = 30cm. The total length of the specimen is l_{tot} = 2m and the slope angle is 35°. Finally, the thickness of the weak layer is h_w = 1 mm whereas the static friction coefficient between the rigid bed and the upper slab is k_f = 0.5, equivalent to a friction angle of ∼ 27°.

The compressive strength of the weak layer is 2.5kPa whereas shear strength is 0.5kPa, similar values as those reported by Reiweger et al. (2015). For the cohesive snow in the upper slab, the elastic modulus E is a function of the density, as presented by Scapozza and Bartelt (2003):

$$E(\rho) = 1.873 \cdot 10^5 \exp^{0.0149\rho} \tag{48}$$

and the tensile strength is given by Jamieson and Johnston (1990) and Sigrist (2006):

$$\sigma_{yt}^s = 2.4 \times 10^5 \left(\frac{\rho}{\rho_{ice}}\right)^{2.44} \tag{49}$$

where ρ_{ice} = 917kg/m^3. Plotting the tensile stress in the upper slab and the compressive and shear stress in the weak layer, computed by expressions contained in Table 1 and Table 3, it is possible to see the characteristic behavior of each component as the saw cut length increases. In particular, Figure 13 depicts the case for an upper slab density equal to ρ = 230 kg/m^3. As regards the tensile stresses in the upper slab, the initial part of the curve σ_t^s shows a quadratic increase of stress due to growing bending moment. Then, the beam tip comes into contact with the lower bed and between L_{IC} and L_{FC} the stress locally reduces. For cutting lengths greater than the full contact length $l > L_{FC}$, the bending moment is constant but the stress increases linearly: at this point, the normal tensile force in the direction of the slope drives the experiment. Meanwhile, in the weak layer, the compressive σ_c^w and shear stresses τ_s^w have a non-linear increase and the effects of the contact of the slab with the bed are less noticeable.

In Figure 13, failure, i.e. when the stress overcomes the strength, is highlighted with a "X" symbol. However, it is difficult to relate one case to the other due to the sensibly different phenomena in the test. Then, to have a better understanding of the theory developed for Propagation Saw Test, the stresses $\sigma_t^s, \sigma_c^w, \tau_s^w$ are scaled with respect to their admissible stress values $\sigma_{yt}^s, \sigma_{yc}^w, \tau_{ys}^w$ as done in the following paragraph.

Table 2: Summary of the forces acting on the weak layer.

Scheme I: $l \leq L_{IC}$	$N_w = W_n$ $T_w = W_h$ $M_w = W_n \frac{l}{2} + W_h \frac{h}{2}$	(38)
Scheme II: $L_{IC} \leq l < L_{FC}$	$N_w = W_n - F_t$ $T_w = W_h$ $M_w = W_n \frac{l}{2} + W_h \frac{h}{2} - F_t \frac{l_{tot}+l}{2}$	(39)
Scheme III: $l \geq L_{FC}$	$N_w = W_n - q_n (l - L_{FC}) - F_t$ $T_w = W_h - k_f q_n (l - L_{FC})$ $M_w = (W_n - q_n (l - L_{FC})) \frac{L_{FC}}{2} + W_h \frac{h}{2} - F_t \left(L_{FC} + \frac{l_{tot}-l}{2}\right)$	(40)

Table 3: Summary of the stress evolution functions applied to the resisting section of the weak layer.

Scheme I: $l \leq L_{IC}$	$\sigma_c = \rho g h \cos(\psi) \frac{l_{tot}}{(l_{tot}-l)} \left[1 + \frac{3(l+h\tan(\psi))}{(l_{tot}-l)}\right]$ $\tau_s = \rho g h \sin(\psi) \frac{l_{tot}}{(l_{tot}-l)}$	(45)
Scheme II: $L_{IC} < l \leq L_{FC}$	$\sigma_c = \rho g h \cos(\psi) \frac{l_{tot}}{(l_{tot}-l)} \left[1 - \frac{3l}{8l_{tot}} \left(1 - \frac{L_{IC}^4}{l^4}\right) \left(\frac{2l_{tot}+l}{l_{tot}-l}\right) + 3\frac{(l+h\tan(\psi))}{(l_{tot}-l)}\right]$ $\tau_s = \rho g h \sin(\psi) \frac{l_{tot}}{(l_{tot}-l)}$	(46)
Scheme III: $l > L_{FC}$	$\sigma_c = \frac{3}{4}\rho g h \cos(\psi) \frac{L_{FC}}{(l_{tot}-l)} \left(1 + \frac{1}{l_{tot}-l}\left[4h\frac{l_{tot}}{L_{FC}}\tan(\psi) - (l_{tot} - l - 2L_{FC})\right]\right)$ $\tau_s = \rho g h \sin(\psi) \frac{l_{tot}}{(l_{tot}-l)} \left(1 - k_f \frac{l-L_{FC}}{l_{tot}\tan(\psi)}\right)$	(47)

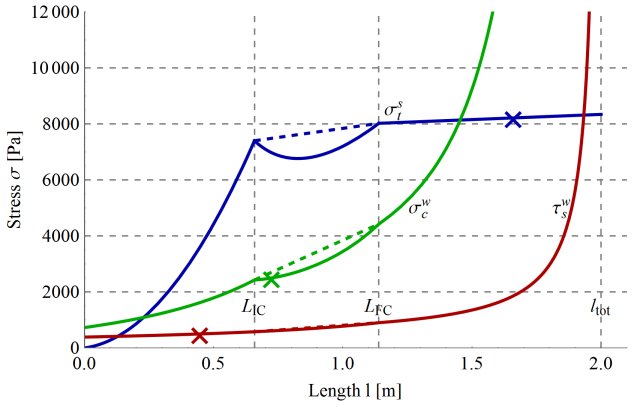

Figure 13: Comparison between the tensile stress in the upper slab and the compressive and shear stresses in the weak layer for $\rho = 230\text{kg/m}^3$.

4.2. Full propagation (END) case

In this first case, the density of the upper slab is $\rho = 280\text{kg/m}^3$, indicative of a stiff slab. First of all, the elastic modulus $E(\rho)$ and the tensile threshold stress are computed as:

$$E\left(280\ \text{kg/m}^3\right) = 12.15\ \text{MPa} \tag{50}$$

$$\sigma_{yt}^s\left(280\ \text{kg/m}^3\right) = 13.28\ \text{kPa} \tag{51}$$

Now, it is possible to retrieve the characteristics lengths L_{IC} and L_{FC} as:

$$L_{IC} = 75\ \text{cm} \qquad \text{L}_{\text{FC}} = \sqrt{3}\text{L}_{\text{IC}} = 131\ \text{cm} \tag{52}$$

Then, the stresses evolution plot is presented in Figure 14(a), after being normalized by their respective limit values. The plot shows that the critical shear stress ratio in the weak layer reaches the unit value, i.e. fracture, for a critical crack length of 11 centimeters. It is important to emphasize that, for the brittle failure criterion we assumed, the fracture is instantaneous and not recoverable unless the stress in the weak layer is suddenly

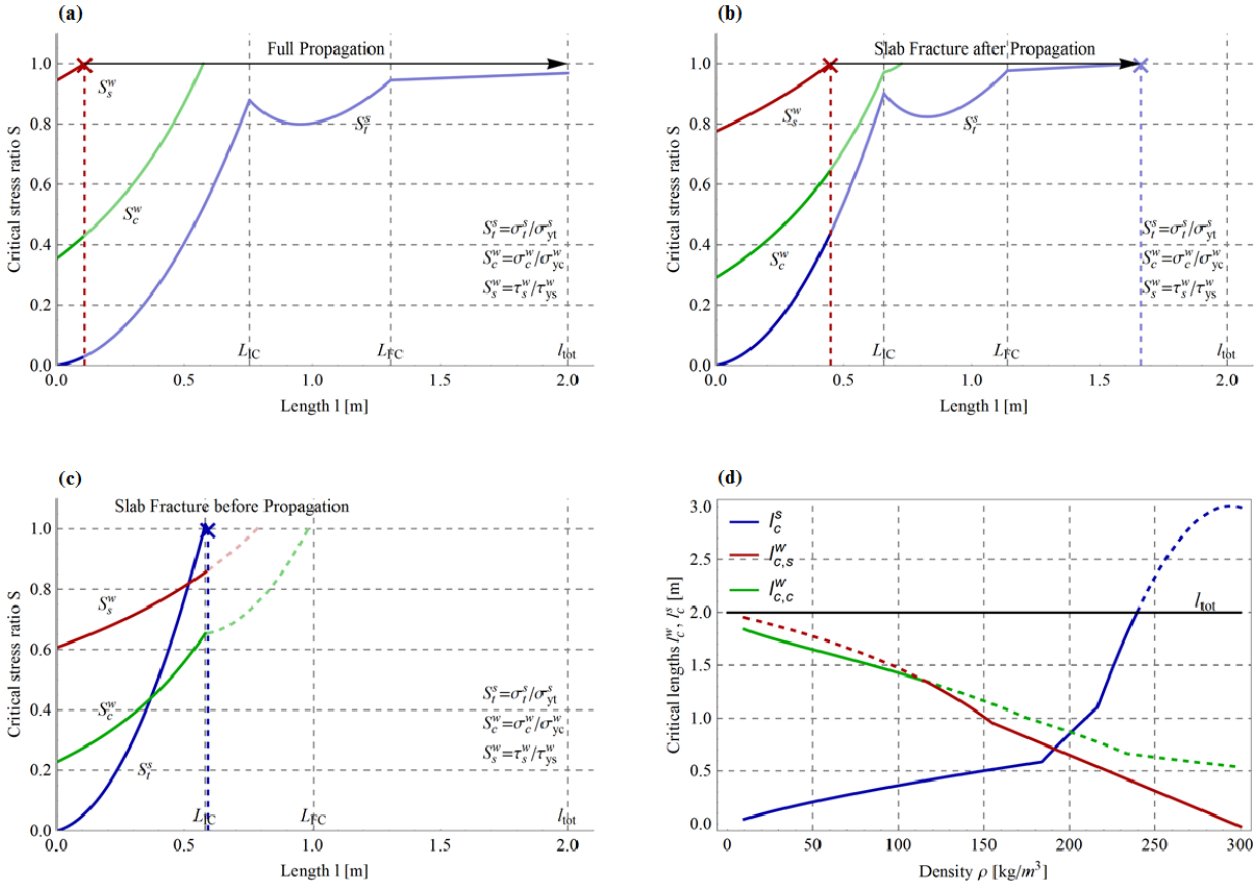

Figure 14: Model application results. Figure (a), Full propagation (END) case: shear failure in the weak layer appears at 11 centimeters and propagates to the end of the specimen. Figure (b), Slab Fracture after propagation (SFa): the initial shear failure in the weak layer at 45 centimeters is followed by the slab fracture at 166 centimeters. Figure (c), Slab fracture before crack propagation (SFb): tensile failure in the upper slab happens at 59 centimeters, before weak layer fracture, which would theoretically appear at 79 centimeters. Figure (d), Critical crack length of failure for the upper slab l_c^s and the weak layer l_c^w. Note that l_c^w is the minimum between the critical crack length for shear $l_{c,s}^w$ and compression $l_{c,c}^w$.

reduced. At this point, crack propagation in the weak layer is engaged and it moves upward from the saw tip thanks to the further increasing load. Conversely, even if the upper slab is subjected to the same increase of load, the critical tensile stress ratio of 1.0 is not reached. Consequently, this case represents the full propagation case (END).

In addition, it is possible to compute the propagation length by subtracting the critical length of the weak layer l_c^w from the upper slab l_c^s. In this case, not having an upper slab failure, the total length of the specimen is considered:

$$l_p = l_c^s - l_c^w = 200 - 11 = 189 \text{ cm} \tag{53}$$

4.3. Slab Fracture after propagation (SFa) case

Consider an upper slab density of $\rho = 230$ kg/m^3. The elastic modulus $E(\rho)$ and the tensile threshold stress are:

$$E\left(230 \text{ kg/m}^3\right) = 5.77 \text{ MPa} \tag{54}$$

$$\sigma_{yt}^s\left(230 \text{ kg/m}^3\right) = 8.22 \text{ kPa} \tag{55}$$

and, consequently, the characteristic lengths of initial L_{IC} and of full contact L_{FC} are:

$$L_{IC} = 66 \text{ cm} \qquad \text{L}_{\text{FC}} = \sqrt{3}\text{L}_{\text{IC}} = 114 \text{ cm} \tag{56}$$

The fracture due to shear is, once again, cause of failure. In Figure 14(b), the evolution of the stresses is plotted. To create the onset of crack propagation, a critical crack length of 45 centimeters is required. Then the weak layer collapses until a length of 166 centimeters, where the increased load induces slab fracture. This case is representative of the slab fracture case after propagation (SFa).

The propagation length is computed by subtracting the critical crack length l_c^w from l_c^s and, in this case, it is:

$$l_p = l_c^s - l_c^w = 121 \text{ cm} \tag{57}$$

4.4. Slab Fracture before propagation (SFb) case

The last case study considers a soft upper slab, with a density of $\rho = 180$ kg/m^3. The elastic modulus $E(\rho)$ and the tensile threshold stress read:

$$E\left(180 \text{ kg/m}^3\right) = 2.74 \text{ MPa} \tag{58}$$

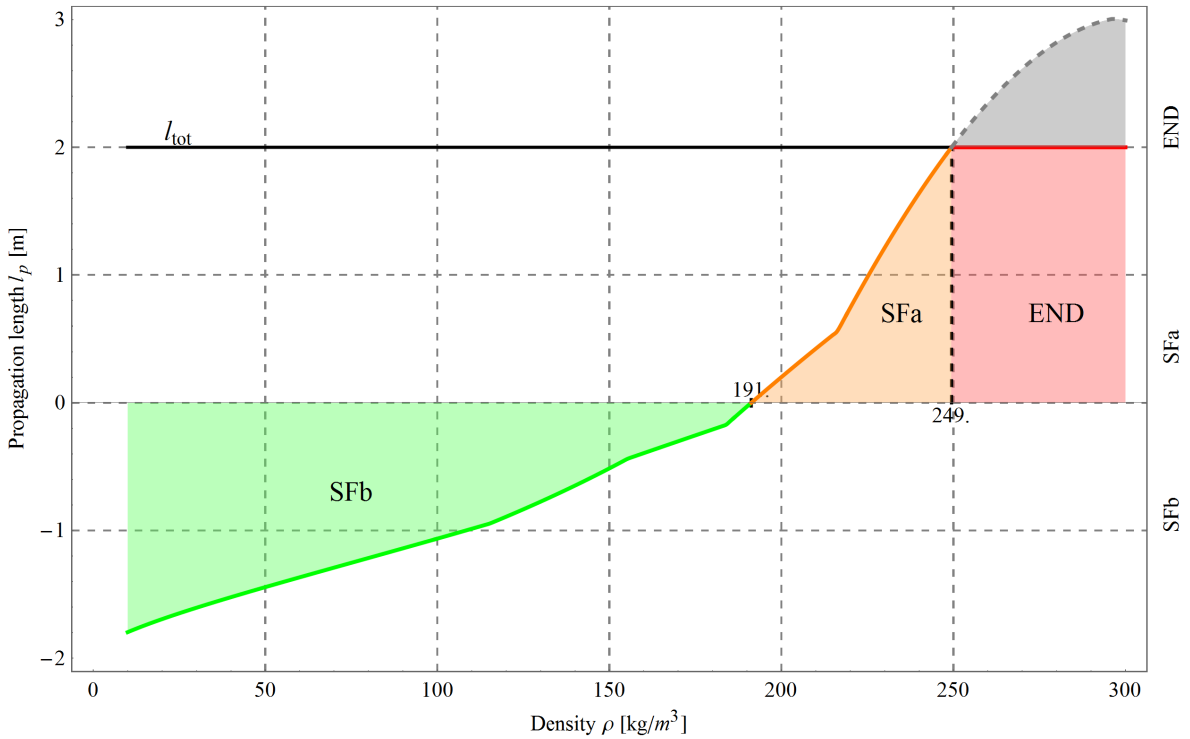

Figure 15: Signed propagation length with respect to the upper slab density for a $0.3 \times 0.3 \times 2$ m^3 specimen on a 35° slope. The different test outcomes full propagation (END), slab fracture after propagation (SFa) and slab fracture before propagation (SFb) are highlighted on the plot with the respective limit value of density.

$$\sigma^s_{yt}\left(180 \text{ kg/m}^3\right) = 4.52 \text{ kPa} \tag{59}$$

The characteristic lengths of initial contact L_{IC} and of full contact L_{FC} are:

$$L_{IC} = 58 \text{ cm} \qquad \text{L}_{\text{FC}} = \sqrt{3}\text{L}_{\text{IC}} = 101 \text{ cm} \tag{60}$$

In Figure 14(c), the tensile stress in the upper slab reaches the unit critical stress ratio (at 59 cm) before the weak layer does, causing the reduction of the load due to the detachment of the volume of the snow. Consequently, the upper slab fractures before any crack propagation is possible in the weak layer. Figure 14(c) shows dashed lines for the shear τ^w_s and the compression σ^w_c stresses after the slab fracture, since the test has already concluded. Instead, if we continue sawing and increasing the cut length, excluding possible spatial variability, the test would be equally repeated.

Finally, the propagation length, following the definition as difference the critical length of the upper slab l^s_c and the weak layer l^w_c one, if failure would happen:

$$l_p = l^s_c - l^w_c = 59 - 79 = -20 \text{ cm} \tag{61}$$

is negative, as indication of slab fracture happening before crack propagation in the weak layer.

4.5. Propagation length with respect to density

Considering the (signed) propagation length with respect to the density variation of the upper slab, it is possible to characterize the Propagation Saw Test setup and its outcomes. First of all, we consider density varying from 50 to 300 kg/m^3, being a typical range found in slab layers (Schweizer, 1999). For each density value, the critical length for the weak layer l^w_c and for the upper slab l^s_c is computed. In order to simplify the computation of propagation length and further analyses, we are replacing the Scheme II curve ($L_{IC} < l < L_{FC}$) with its linear interpolation as pictured in Figure 13 (dashed lines). This is justified by the fact that for the weak layer the linear approximation is close to the actual solution while maintaining easier computations whereas, in the upper slab, the stress at $l = L_{IC}$ is greater than most of the values in the middle range.

In Figure 14(d), the saw cut length which provoke fracture in the upper slab or in the weak layer is plotted against the density variation. The length of slab fracture l^s_c is increasing with the density since the resistance of denser cohesive snow grows faster than the applied load. From 180 kg/m^3, the plot presents a change in the behavior corresponding to the effect of the load reduction due to the contact with the rigid bed ($l > L_{IC}$). After a density of 240 kg/m^3, the critical crack length l^s_c is greater than l_{tot} (dashed line): in the field experiment this is meaningless and we consider the total specimen length instead.

Contrariwise, in the weak layer, the critical length reduces as the load increases. Both compressive and shear failure gives a monotonic descending curve and the critical length l^w_c is given by the minimum of the two values $l^w_{c,c}$ and $l^w_{c,s}$. Compressive failure is predominant at the beginning, for very low values of ρ, whereas, for the rest of the densities, shear plays a major role, reaching zero at 300 kg/m^3. In such situation, shear failure is initiated for any perturbation to the weak layer. The limit point

that represents the change from one type of failure to the other is mainly dependent on the slope angle.

Finally, in order to calculate the length of propagation, we subtract the two latter values l_c^s and l_c^w. Figure 15 shows the resulting plot. Clearly, it is possible to identify the test outcome for each density value. For soft slabs, up to 191 kg/m^3, slab fracture before propagation (SFb) in the weak layer is given. Then, as the upper slab becomes stronger than the weak layer, for densities included in the range 191 – 249 kg/m^3, the model predicts slab fracture after propagation (SFa). Finally, when propagation length becomes bigger than total length of the specimen (i.e. 2 meters), we observe full propagation (END) case, from 249 to 300 kg/m^3.

5. Parameters sensitivity analysis

The objective of this section is to illustrate the outcome dependence from each single variable. The following discussion is a key point in order to determine the relative importance of the parameters in the model. The base experiment in the analysis is the same as the previous sections with an upper slab of section 30×30 cm^2 and a total length of $l_{tot} = 2$ m. Where not specified, the upper slab has a density of 230 kg/m^3. The weak layer thickness is $h_w = 1$ mm and the static friction coefficient between the bed and the upper slab is $k_f = 0.5$. Finally, slope angle is 35°. In every subsection, each parameter of the model is studied in order to evaluate the effects on critical crack lengths and the propagation ones.

5.1. Strength values

In order to test the sensitivity of the results to a variation in the threshold stress, we apply a small perturbation of ±10% and ±5% on the limit values and compute the change in critical crack lengths with respect to the original case.

Firstly, the weak layer strength perturbation is addressed. The resulting failure length for the compressive case is presented in Figure 16(a) while the shear one is depicted in Figure 16(b). In both plots, we observe a moderate variation in the critical length of failure with respect to the variation of strength. In the first case, a maximum change of critical length of about 10 centimeters, corresponding to a 5% of the total length (2 meters), is observed for the 10% compressive strength reduction. Similarly, in the shear one, the maximum change is given by the 10% reduction in shear strength which gives about 38 centimeters less in critical crack length, corresponding to a 19% of the total specimen size (2 meters).

Regarding the upper slab strength, we consider a similar perturbation of the stress threshold value, varying it ±10% and ±5%. The results are presented in Figure 16(c). There, it is clear the major effect induced by a small variation in the upper slab tensile strength. A 10% increase causes a doubling of the slab critical crack length (405 centimeters, corresponding to a 202% difference) whereas a 10% reduction provide a decrease of 104%, corresponding to about 208 centimeters. Note that these values are computed with respect to the analytical curves, focusing on the variation percentage and disregarding the fact that the total length of the specimen is 2 meters.

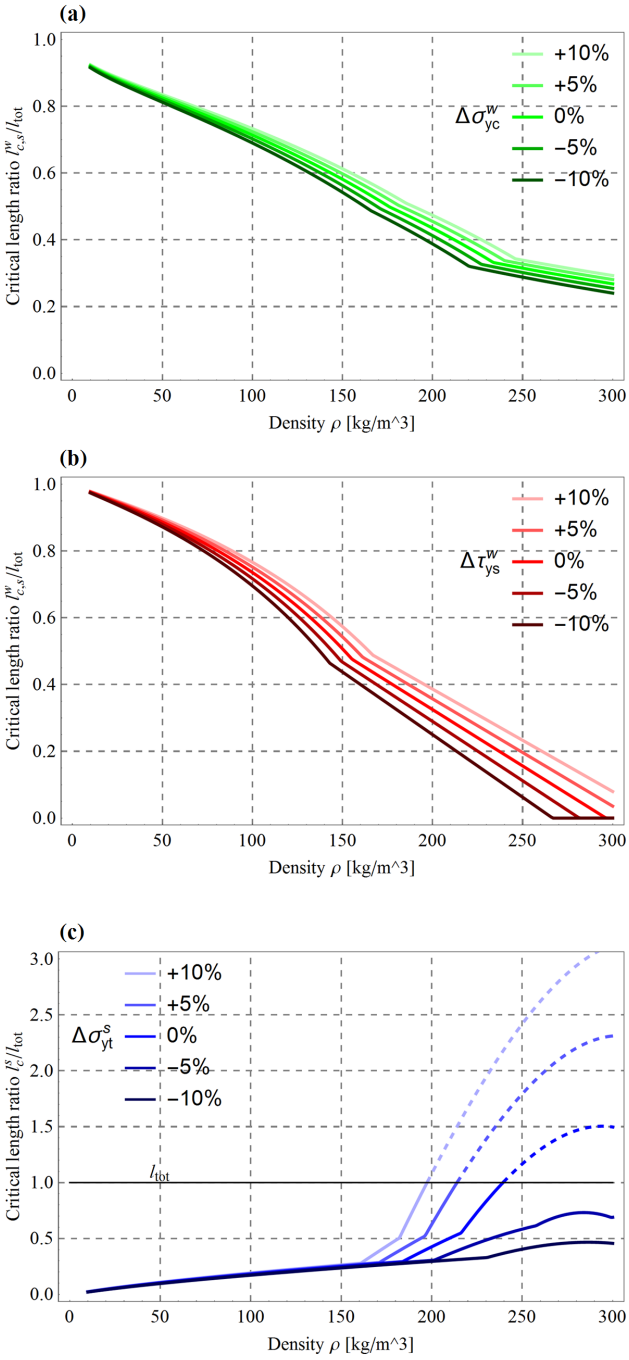

Figure 16: Sensibility analysis of critical crack lengths with respect to a variation in (a) weak layer compressive strength $\Delta\sigma^w_{yc}$, (b) weak layer shear strength $\Delta\tau^w_{ys}$ and (c) upper slab tensile strength $\Delta\sigma^s_{yt}$.

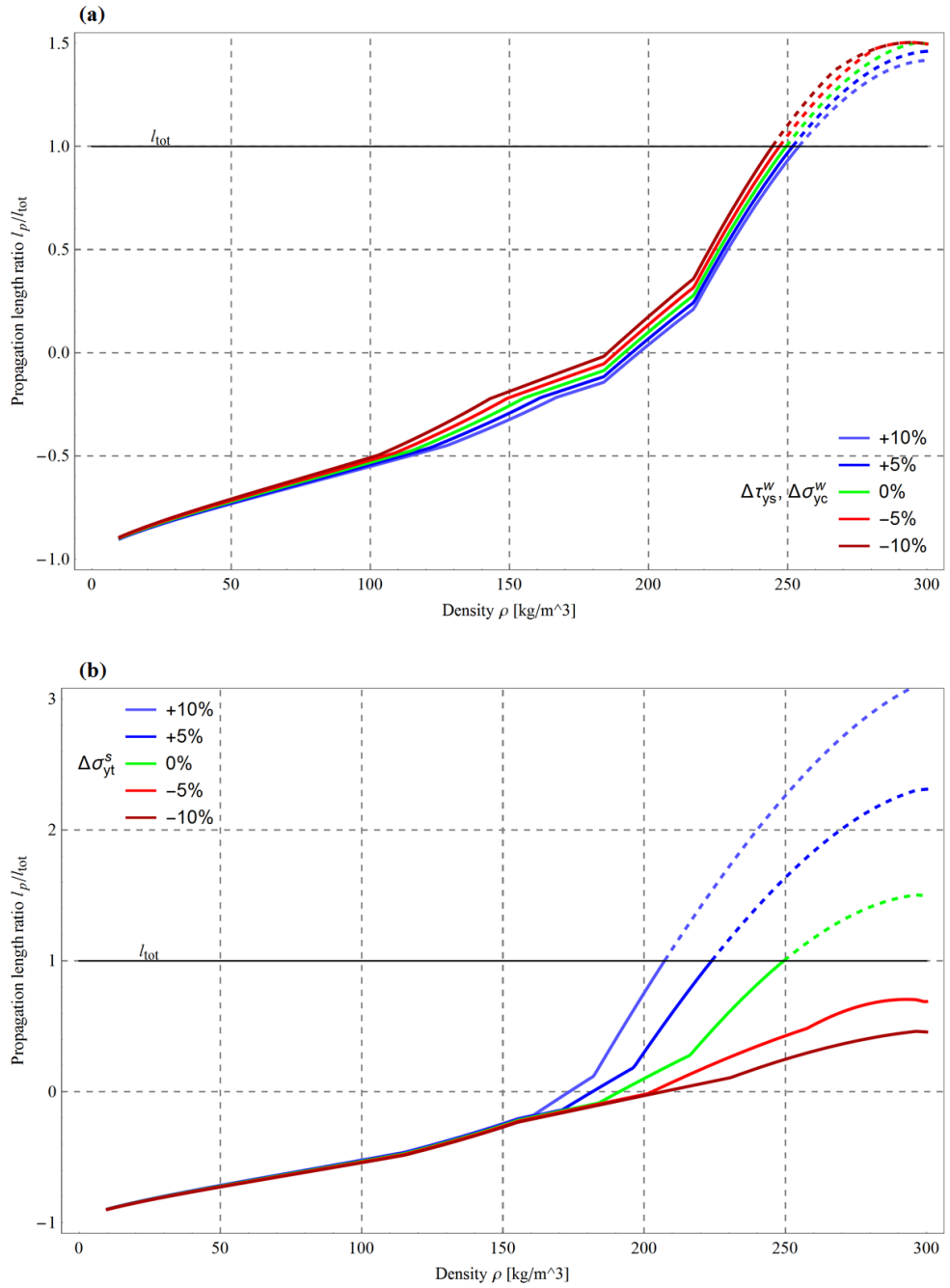

Figure 17: Propagation length with respect to density resulting from the sensibility analysis in the case of variation of (a) weak layer strengths σ^w_{yc}, τ^w_{ys} and (b) upper slab strength σ^s_{yt}. It appears that, for the model previously presented, the change in weak layer resistance has a moderate effect. Vice versa, a small perturbation in the upper slab maximum tensile stress provokes a large variation in the outcomes of the test for the $150 - 300$ kg/m^3 density range. In particular, the propagation length approximately doubles for a change of 10% in the value of σ^s_{yt}.

The changes in failure distances just presented are now reflected in the propagation length plots. Figure 17(a) shows the envelope solution due to the perturbation in of compressive and shear strengths in the weak layer. Again, the moderate deviation from the original case is visible, with a maximum Δl_p of about 20 centimeters (10% of the total specimen length). Instead, Figure 17(b) depicts the substantial change in the propagation length due to upper slab strength variation.

Not only this case provides substantially different values of propagation length, highlighting the considerable sensitivity of the PST to σ^s_{yt}, but also it shows how a $1\% - 2\%$ reduction of the tensile strength would imply a slab fracture outcome (SFa) instead of a full propagation one. On the other hand, it implies that snowpack variability can substantially influence the PST outcome leading to a difficult interpretation of results.

This is a fundamental aspect in the Propagation Saw Test. Not only the test has been developed in order to evaluate the crack propagation propensity in weak layers but also slab fracture. As a matter of fact, the analysis just presented proves the tight dependence of the outcomes from the tensile strength σ^s_{yt}.

5.2. Slope angle

The slope angle is a key factor in avalanche terrain. Here its influence on the critical and propagation length from the flat cases to very steep inclines is investigated. The value of ψ is ranging from 0 to 60°. In Figure 18(a), the critical ratio for the tensile stress in the upper slab is presented. First of all, we notice that the value of the length of initial contact L_{IC} and the length of full contact L_{FC} are not constant: the steeper the slope, the longer cantilever length is required to have contact between the upper slab and the bed. Eventually, the two latter quantities tends to infinity for a 90 degrees inclination, since less and less vertical load will be applied to the slab for increasingly higher angles.

It is noteworthy to highlight the role of the initial contact length in the outcome of the PST. This value represents the change in the regime of stresses in the upper slab from the cantilever (Scheme I) to the hinged (Scheme II) and fixed roller (Scheme III) ones. If there was not a change in the stress evolution, there would not be the possibility to have full propagation cases (END), since the quadratic increase of stress would limit the critical length of failure for the slab.

The tensile stress in the upper slab is the result of the sum of bending and normal force effects. The first one has its maximum value for flat zones, where the arm of the load is the greatest. Instead, the latter one is higher for steeper slope. Consequently, the maximum tensile stress in the upper slab is given for an inclination between 15 and 20 degrees as it is possible to see in Figure 18(a).

The compressive stress in the weak layer is moderately varying along the proposed range of slope angles as we observe in Figure 18(b). All the critical length for this case are concentrated around the 50 centimeters saw cut length and, also in this case, the horizontal case does not represent the worst case scenario. Contrary to this, the shear stress surely depends on the slope angle, as it is depicted in Figure 18(c). In particular, the critical crack length significantly decreases with increasing slope angle. By comparison of the two plots, it is possible to say that, for the an upper slab density of 230 kg/m^3, compressive failure is dominant up to 25 degrees whereas shear stress is the cause of failure for steeper slopes. In the case of 10 degree angle, it is also possible to see the peculiar case in which the friction to the bed absorbs all applied shear stress.

In Figure 18(d), the propagation length is plotted against the density for various slope angles. First, the propagation length increases with increasing slope angle. Second, we observe that, at the selected density 230 kg/m^3, the slab fracture after propagation is predicted for the range of angles from 0 to 30 degrees. In particular, the cases of flat, 10 and 20 degrees presents approximately the same propagation length. The case for 40 degrees is on the limit of the full propagation case, since the upper slab tensile stress provokes failure close to the total length of the specimen. Finally, the model predicts full propagation (END case) for high values of the slope angle, i.e. $\psi > 40°$.

5.3. Slab depth

Now, we analyze the effect of the variation of the upper slab depth on the Propagation Saw Test. On the one hand, the load on the specimen is proportional to the height h, on the other hand, the second order moment of inertia of the cross section of the snow beam increases with the cube of the height. Consequently, this implies that the tensile stresses σ^s_t are limited for very thick slabs, as we can see in Figure 19(a). At the same time, the weak layer is subjected to the equal gravitational load and this proportional increase in stress is visible in Figure 19(b) for the compressive part and in Figure 19(c) for the shear one.

Finally, Figure 19(d) depicts the propagation length against the density values, with respect to different slab heights. For low density of the upper slab, the propagation length increases proportionally to the value of h. On the contrary, starting from about $180 - 200$ kg/m^3, we observe an inversion of the latter case, for which a smaller slab has a larger length of propagation. Moreover, it is possible to notice an asymptotic behavior, with a limit line in the plot for both the lowest and highest values of h.

On the lower end, the asymptote is given by the fact that the plot is approaching the case for zero thickness slab, at which zero load as well as zero resistance are predicted. The strength depends on the cube of the height whereas the bending and tensile load on its square at most. Hence, the predicted stress could grow to infinity. But the maximum threshold stress in the snow limits such value, so the propagation length is limited.

On the higher end of the plot, the solution converges for very thick slabs. Its high stiffness results in very low values of deflection of the tip. At the same time, the larger volume of snow implies a sustained load as bending and tensile stress on the upper slab and compression and shear in the weak layer. These two facts implies that the value of L_{IC} is large. Then, the stress evolution is mainly given by the Scheme I and the critical lengths for both the upper slab and weak layer are limited too. Notice that the effect of friction angle k_f is increasingly less important as the upper slab is thicker, as visible in Figure 19(d) between the 45-50 centimeters and 55-60 centimeters cases, since

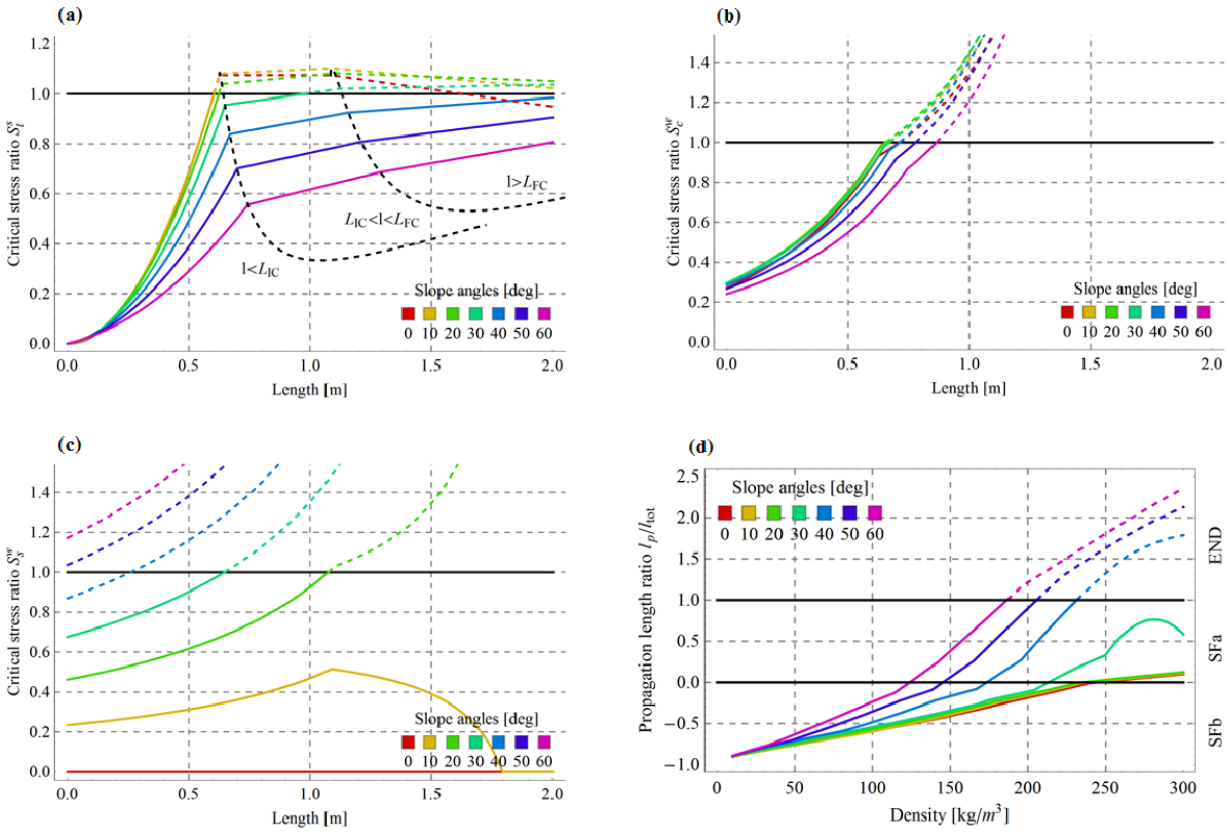

Figure 18: Model dependence to slope angles ψ (from 0° to 60° with 10° steps): Figure (a), (b) and (c) show respectively the tensile stress in the upper slab, the compressive and the shear stresses in the weak layer plotted against length of saw cut; Figure (d) pictures the propagation length with respect to the upper slab density.

no contact with the bed is predicted before slab fracture. This explains the asymptotic value for high values of h.

5.4. Friction

In Figure 20(a), Figure 20(b) and Figure 20(c), the tensile stress in the upper slab and the compressive and shear stresses in the weak layer are presented. While in the weak layer the effect of the friction coefficient k_f is small, in the upper slab, the change in increase of stresses is visible. It is noteworthy to remind that the friction between the bed and the slab is engaged only for the Scheme III, when the saw cut length is bigger than the full contact one L_{FC}. In such case, the weight of the slab is thought to create an additional friction force that counterbalance the tensile force in the slope direction whereas the bending moment is constant.

In Figure 20(d), the propagation length with respect to the density is pictured in the case of friction coefficients k_f varying from 0 to 0.5. First of all, we notice how the effect of this parameter affects only a particular part of the plot. Indeed, this portion is the one that is correspondent with the Scheme III slab fracture.

As counterintuitive as it might be, having higher resisting forces due to friction could represent the worst case scenario, in terms of avalanche size. In fact, although in the case of null k_f the slab has to bear the whole gravitaional load, when friction is present, the total force is reduced. Consequently, this implies that, for the same tensile stress threshold, the diminishing friction case ($k_f = 0$) results in a slab fracture after propagation whereas the high friction one ($k_f = 0.5$) turns out to be a full propagation case. The comparison between these two cases is shown in Figure 21: here, the plot already presented in Figure 15 is compared with the null friction one.

5.5. Weak layer thickness

The thickness h_w is the only geometrical parameter of the weak layer. This value is linked with the definition of the initial contact L_{IC} and full contact length L_{FC}. Consequently, this parameter will have an effect in the separation between the solutions in Scheme I, II and III. In Figure 22(a), the upper slab tensile stress for the h_w variation is presented. As it was expected, the result is a family of parallel shifted curves. All the cases coincide for the initial part, corresponding to the cantilever scheme. If the weak layer is thin enough (in this case up to 1 millimeter), the scheme of forces changes due to contact with the bed before slab fracture takes place. Otherwise, when the weak layer is thicker, the critical length is fixed and independent from h_w.

In Figure 22(b) and Figure 22(c) the compressive and shear stress evolution are depicted. Clearly, the dependence of the stresses on the thickness of the weak layer is marginal.

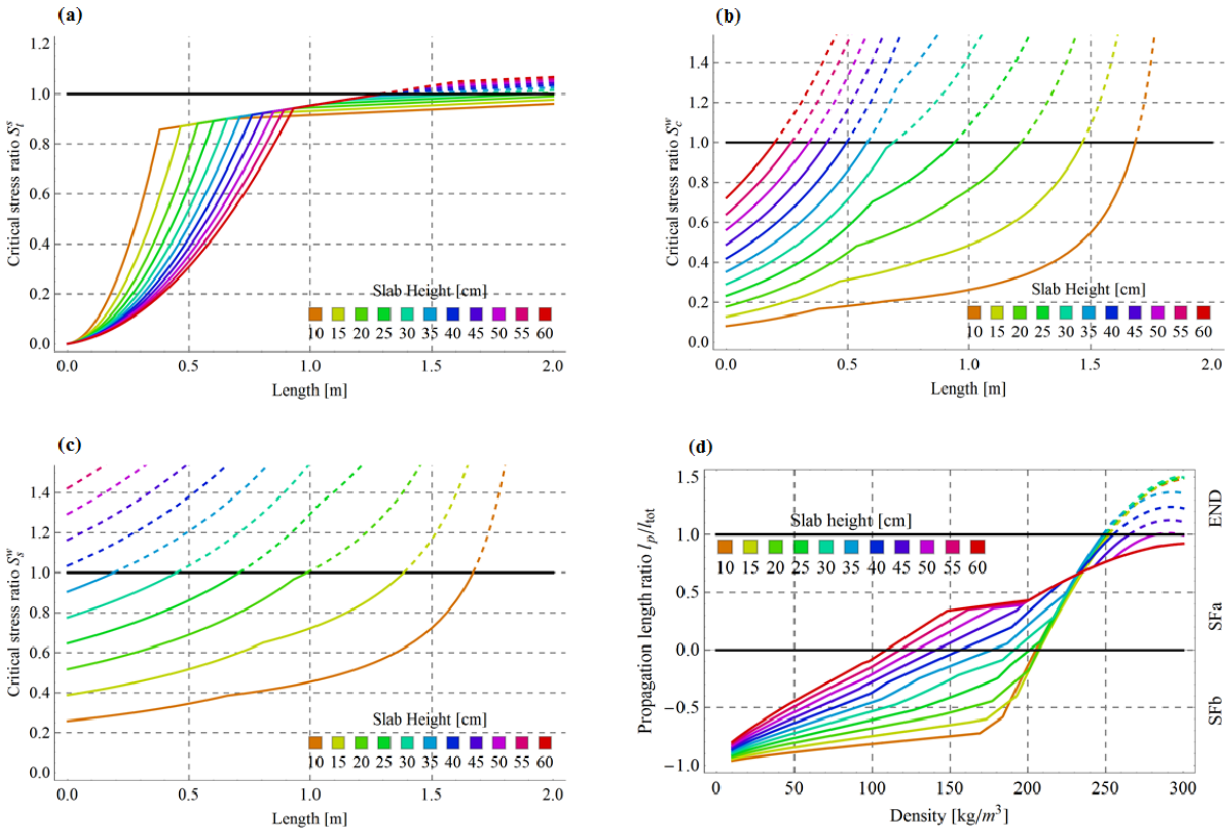

Figure 19: Model dependence to upper slab depth h (from 10 cm to 60 cm with 10 cm steps): Figure (a), (b) and (c) show respectively the tensile stress in the upper slab, the compressive and the shear stresses in the weak layer plotted against length of saw cut; Figure (d) pictures the propagation length with respect to the upper slab density.

Figure 22(d) shows the propagation length plotted against the density for various values of h_w. As we previously stated, for small values of weak layer thickness, contact between the slab and the bed is predicted. As a consequence, the propagation length is large and decreases with increasing values of h_w. This results in a larger range of densities for which it is possible to have full propagation (END) outcome in the PST. On the other hand, for thicker weak layers, the propagation length plot converges asymptotically to a single curve: as clearly visible in the plot, it is a piecewise linear curve which only predicts the case of slab fracture (SFa and SFb).

5.6. Density

Finally, we complement the propagation length plots in Figure 14(d) and Figure 15 with respect to the variation of the density. With increasing values of density, the upper slab increases its weight and, at the same time, its tensile strength. Figure 23(a) shows this competitive mechanism, with the additional curves for the initial and full contact length. For low values of ρ, the tensile strength is not enough to support the stresses applied by the cantilever beam and, then, it results in small critical length of fracture. As observed before, for intermediate values of density, the strength increases to allow suddenly larger values of saw cut lengths. Further increase of density causes a substantial load growth and, again, a reduction of l_c^s. Finally, Figure 23(b) and Figure 23(c) depict the variation of compressive and shear stress in the weak layer with respect to density in the upper slab. In this case, ρ contributes only to the load.

6. Discussion

The proposed analytical model allowed an exhaustive description of the effect of snowpack properties on the outcomes of the Propagation Saw Test (PST). In the previous sections, the sequences of phenomena that take place in the PST were presented in detail, not only from a qualitative point of view, but also from a quantitative one, linking possible scenarios of weak layer and slab fracture (SFb: slab fracture before crack propagation; SFa: slab fracture after crack propagation; END: full propagation) to the stress evolution in upper slab and weak layer. The sensitivity analysis revealed that the critical crack length for the onset of crack propagation in the weak layer l_c^w was decreasing with increasing thickness and density of the slab and with decreasing weak layer strength, a rather intuitive result. In addition, it was shown that the critical crack length l_c^w is decreasing with increasing slope angle in line with the recent results of Gaume et al. (2016) and therefore undermining the anticrack theory (Heierli et al., 2008), although weak layer collapse was accounted for. This trend was also recently suggested by van Herwijnen et al. (2016) who showed using FEM

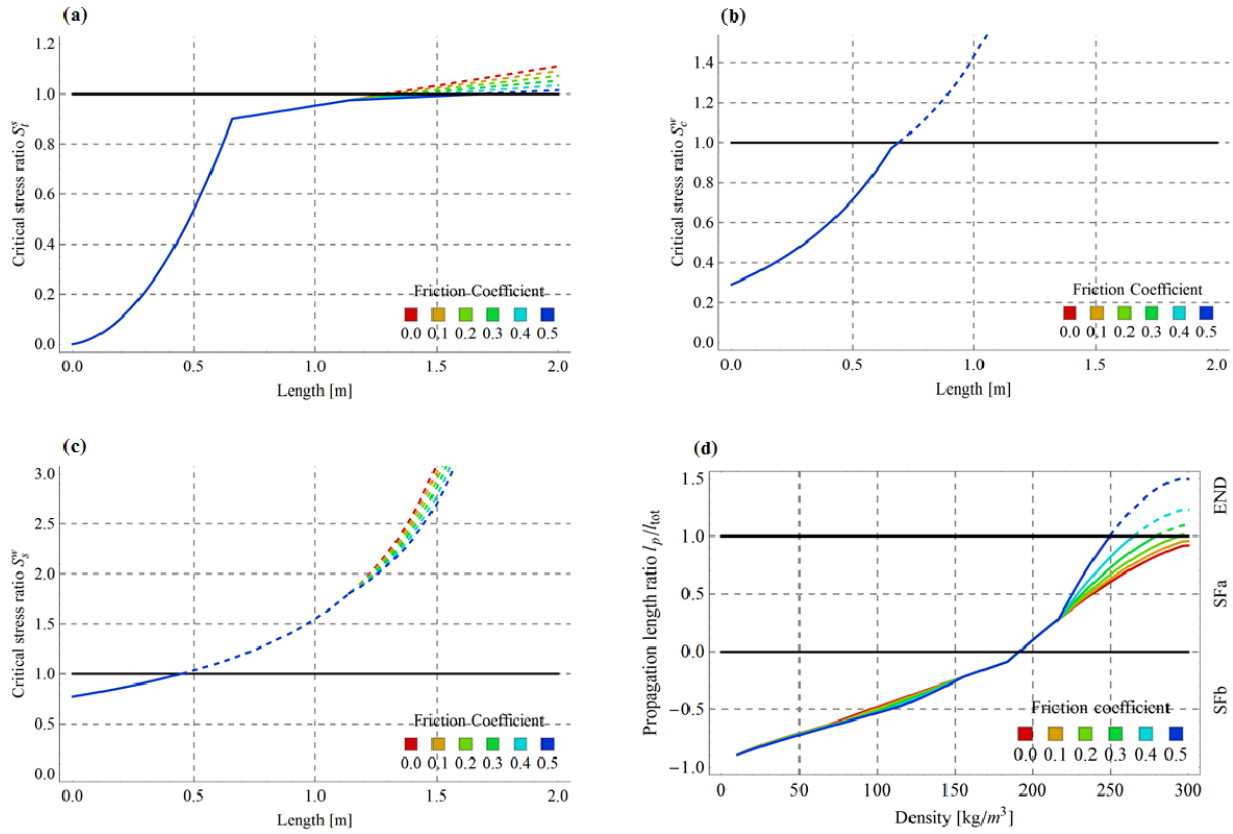

Figure 20: Model dependence to bed friction k_f (from 0.0 to 0.5 with 0.1 steps): Figure (a), (b) and (c) show respectively the tensile stress in the upper slab, the compressive and the shear stresses in the weak layer plotted against length of saw cut; Figure (d) pictures the propagation length with respect to the upper slab density.

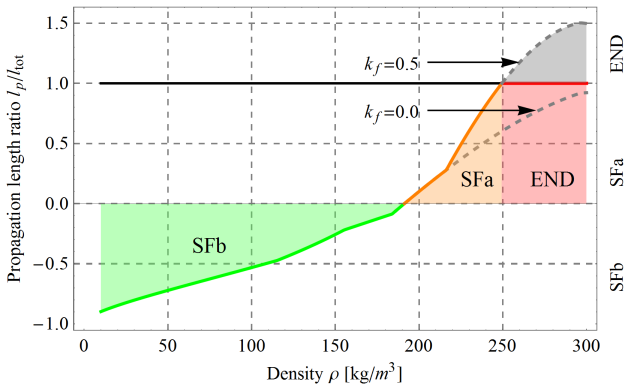

Figure 21: Comparison of propagation length against density in the case of null and $k_f = 0.5$ friction coefficients.

simulations that the mechanical energy provided by the anti-crack model was too low for steep slopes. Hence, as suggested by Gaume et al. (2016), the almost constant trend of the critical crack length with slope angle observed in field studies (Gauthier and Jamieson, 2008a; Bair et al., 2012) is very likely due to changes in the mechanical properties with slope angle (e.g. slab thickness) and geometrical effects.

Concerning slab fracture, the sensitivity analysis showed that the propagation distance significantly influenced by the tensile strength of the slab, the higher the strength the higher the distance, as expected. The propagation distance increases with increasing slope angle and with decreasing weak layer thickness as shown by Gaume et al. (2015) using the discrete element method. For realistic snowpack properties, the propagation distance increases with increasing slab density. As shown in the proposed example, for slab densities below 191 kg/m3, slab fracture occurs before the onset of crack propagation in the weak layer (SFb case). Intermediate densities (191< ρ <249 kg/m3) provide slab fracture after crack propagation in the weak layer (SFa case). Finally, for densities larger than 249, full propagation is predicted to span through the entire weak layer without triggering slab fracture (END case). This result is in line with the discrete element model of Gaume et al. (2016) and the associated field data suggesting that full propagation occurs for densities larger than $\sim$ 280kg/m^3.

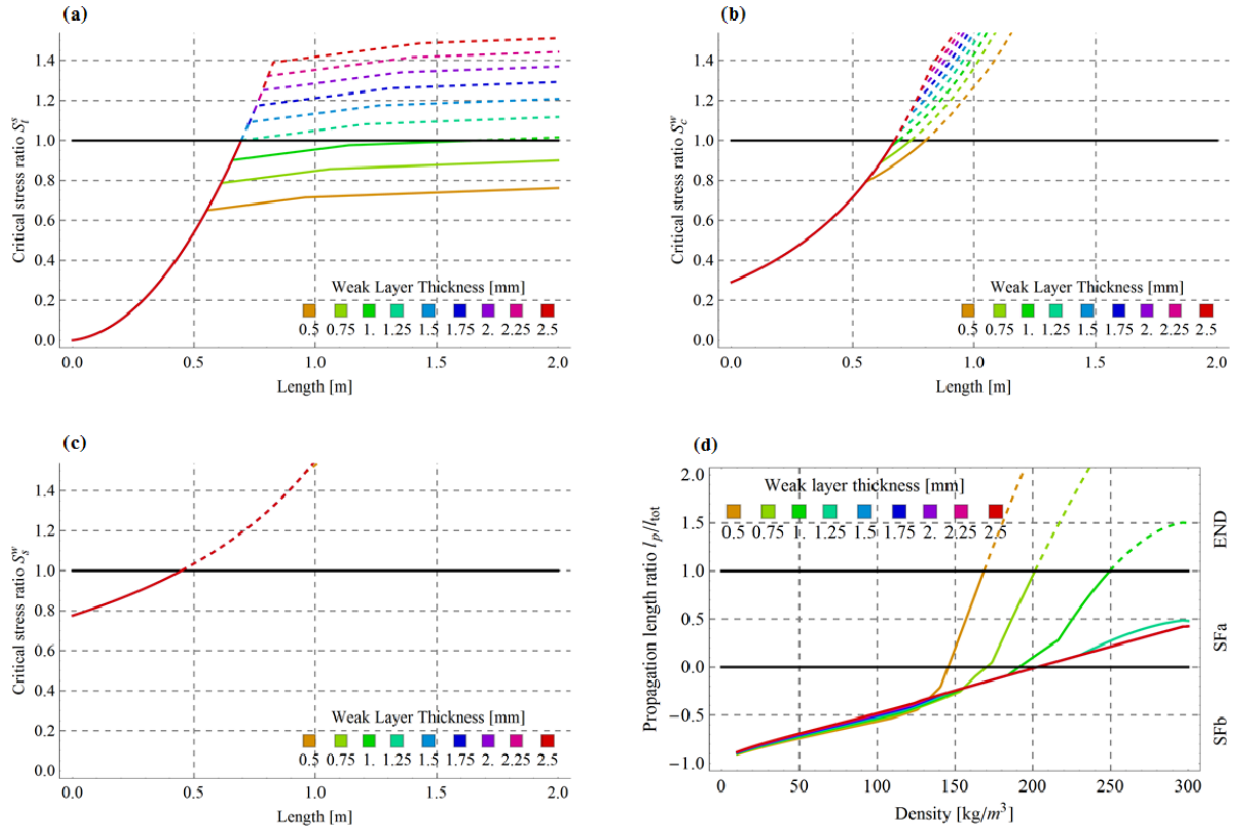

Figure 22: Model dependence to weak layer thickness h_w (from 0.5 mm to 2.5 mm with 0.25 mm steps): Figure (a), (b) and (c) show respectively the tensile stress in the upper slab, the compressive and the shear stresses in the weak layer plotted against length of saw cut; Figure (d) pictures the propagation length with respect to the upper slab density.

Surprisingly, the bed static friction coefficient plays an important but tricky role in the possibility of full propagation of slab fracture. As it was shown, the propagation length generally increases with increasing friction coefficient and its values can change the test outcome in the most sensible range of density, for which SFa and END cases are expected.

However, being based on deterministic assumptions, it is clear that this method is not able to tackle test outcomes, such as "self arrest" or "en-echelon fractures" (van Herwijnen and Jamieson, 2005; van Herwijnen et al., 2010; Gauthier and Jamieson, 2010), since they are related to spatial variability. We have previously analyzed the influence of a small perturbation in the values of the stress thresholds σ_{yt}^s,σ_{yc}^w and τ_{ys}^w, highlighting the key role of these parameters. On the one hand, the PST represents a very good tool for the evaluation of the threshold stress value for the weak layer. On the other hand, the spatial variability of the cohesive snow in the upper slab could profoundly impact the resulting interpretation of the test outcomes. We showed that slab fracture after propagation (SFa) and full propagation (END) cases are the most sensible to small changes in the snowpack. In a practical scenario, sudden changes of mechanical properties in the snow are possible and frequently not measurable without adequate instruments, such as the Snow Micro Pen (Schneebeli et al., 1999; Bellaire et al., 2009; Marshall and Johnson, 2009). As it is well known in the literature (Mellor, 1975; Shapiro et al., 1997), the strength of cohesive snow is not only function of density and grain size, but also highly variable depending on the environmental conditions. The presented model underline the difficulty to evaluate the outcome of the test, without a precise value of the tensile threshold stress in the upper slab. Indeed, the present model assumes homogeneous snow in the isolated volume and consequently gives a result related to the average mechanical characteristics of each snowpack layer.

Furthermore, the presented theory considers a rigid interface between upper slab and weak layer. This assumption was introduced in order to independently analyze the stress evolution using standard Euler-Bernoulli beam theory and taking advantage of the superposition of effects. Additionally, it allows to consider the weight of the upper slab to be concentrated in its center of gravity in the computation of the stresses in the weak layer and, at the same time, perfect boundaries conditions in the upper slab. Although this approach results in a easier analytical description of the model, it does not take into account important effects given by deformation. In reality, the load is supported by the different layers proportionally to their stiffness: the stiffer the layer, the higher load will be applied to it. By considering the interface as rigid, we are assuming infinite stiffness for both the upper slab and the weak layer, resulting in transferring the full load to each part. This assumptions implies an infinite dis-

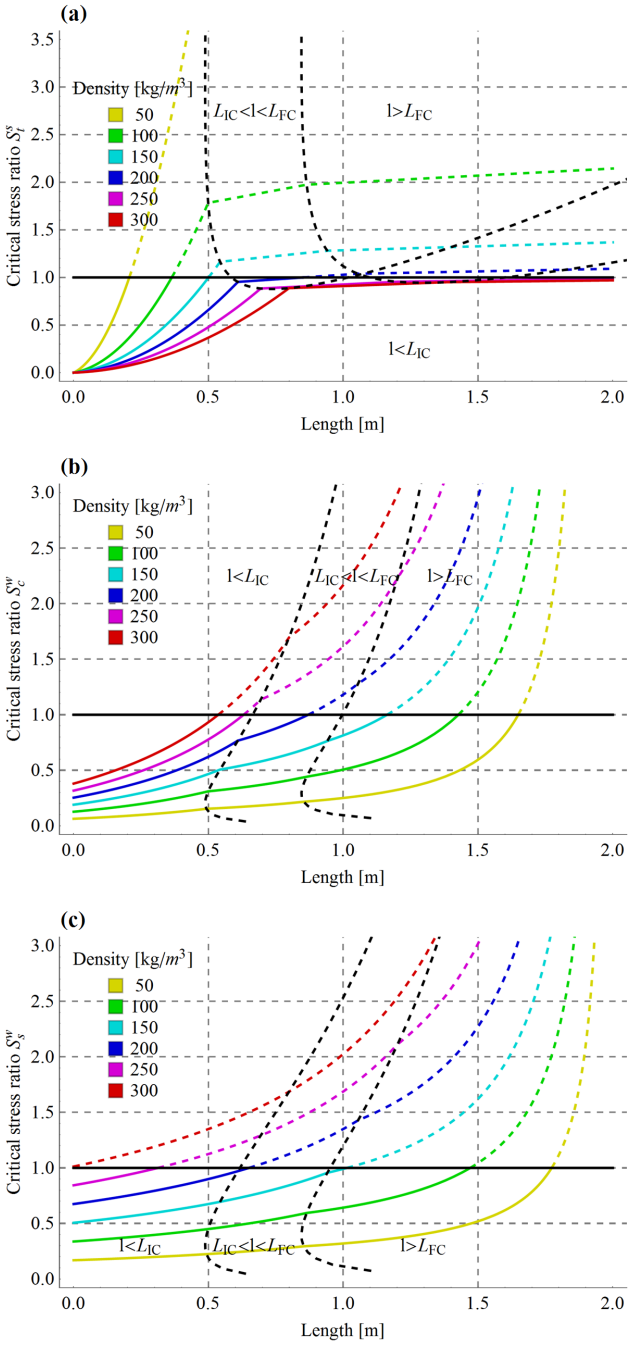

Figure 23: Model dependence to density ρ (from 50 kg/m^3 to 300 kg/m^3 with 50 kg/m^3 steps): Figure (a), (b) and (c) show respectively the tensile stress in the upper slab, the compressive and the shear stresses in the weak layer plotted against length of saw cut.

tribution of stresses for infinite specimen length l_{tot}: this fact has also been proved not to be true in field measurements.

The presented framework is quasi-static, with a pure brittle fracture criterion. It was previously shown by Sigrist and Schweizer (2007) and later by Schweizer et al. (2011) that the weak layer and the upper slab indeed dissipate energy during the fracture process and it can be measured. As a result of these assumptions, we are neglecting dynamic effects during crack propagation. From a theoretical point of view, the lack of dynamic effects implies that the stresses in the slab, computed with our model, are higher than in a dynamic case as shown by Gaume et al. (2015) and that larger values of l_p can be expected.

The failure criterion used is a simplified one in which the single stress component is compared directly with its threshold value. Clearly, in reality this is not the case. For instance, in the case of weak layer, the compressive and the shear fracture modes are related one to the other as it was presented by Reiweger et al. (2015). In Figure 24, the simplified failure criterion used in this work and the correspondent Capped Mohr-Coulomb one are displayed.

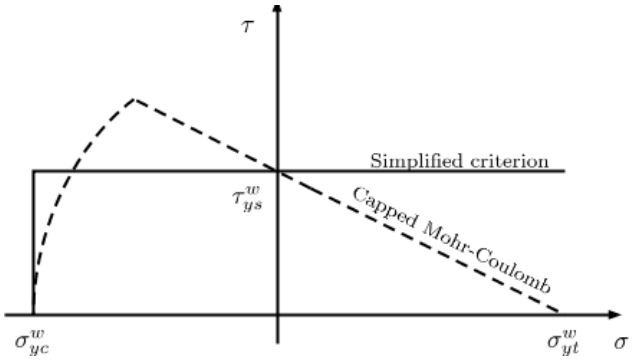

Figure 24: Comparison of the simplified fracture criterion and the corrispondent Capped Mohr-Coulomb model in the weak layer.

For pure compressive and pure shear cases, the two limit values coincides while, for mixed mode fractures, the two models differ significantly. Still, the model is able to provide compressive failure for inclined slopes and shear fracture for avalanche prone terrains, as observed for the weak layer in the field. Similarly, tensile crack in the upper slab is given for bending forces in flat zones and tensile ones at steep angles. However, it was not the purpose of this work to enter in the detail of the specifics of the failure criterion selection, but, rather, to understand the evolution of the stresses in the Propagation Saw Test and its relationship with the physical quantities involved in the experiment. Nevertheless, the presented framework can be extended to any more precise and complex failure criteria.

The developed model is characterized by a clear description of the processes which appear with increasing cut length. The required mechanical quantities in the stress evolution functions are only introduced through the values of L_{IC} and L_{FC}, whereas the stress functions are linearly depending on the distributed load q. In particular, the length of initial contact L_{IC} is a key parameter of the problem because it marks the change of stress evolution in the upper slab, from quadratic to linear increase.

This peculiar fact is the responsible of having full propagation outcomes in the PST, since it suddenly increases the critical length of tensile fracture. In contrary, the weak layer is less affected by this change in force schemes due to the fact that the very nonlinear and steep stress growth (both shear and compressive one) is heavily dependent on the inverse of the quantity $l_{tot} - l$, which is monotonically decreasing.

Finally, after having studied the propagation length with respect to density in various cases, the simplification introduced for the range of saw cut length $L_{IC} < l < L_{FC}$ has a limited effect on the overall precision and detail of results.

7. Conclusions

A new mechanical framework for the analysis of the Propagation Saw Test has been presented: starting from the experimental configurations which are expected during the test, it was possible to recover the stress evolution in the upper slab and in the weak layer. Simple failure criteria were introduced to describe the quasi-brittle nature of snow. Then, by comparing these values with their respective threshold, we have been able to describe the different outcomes of the PST in a simple way. As an additional result of the model, the critical lengths l_c^s, l_c^w and propagation length l_p are available as byproduct of the method.

A thorough analysis of the dependence of each single parameter in the model has been carried out, highlighting the importance and the complex interplay that affect the outcome of the test. The detailed analytical description allowed to quantitatively determine how each single phenomena involved in the test is decisive for the PST.

Further investigation is required to validate the developed model with experimental field data. In fact, although the highly detailed information, the presented theory appears as a first order approximation of a much more complex experiment such as the Propagation Saw Test.

Acknowledgements

L. Benedetti gratefully acknowledges financial support from the BFW - Austrian Research Centre for Forests, Department of Natural Hazards in Innsbruck as partner in the MuMoLaDe project - Multi-scale Modelling of Landslides and Debris Flows - within the framework of Marie Curie ITN (Initial Training Networks) under the EC 7^{th} Framework Programme (Grant Agreement 289911). J. Gaume has been supported by the Ambizione grant of the Swiss National Science Foundation (PZ00P2 161329).

References

Bair, E. H., Simenhois, R., Birkeland, K., Dozier, J., 2012. A field study on failure of storm snow slab avalanches. Cold Regions Science and Technology 79, 20–28.

Bellaire, S., Pielmeier, C., Schneebeli, M., Schweizer, J., 2009. Stability algorithm for snow micro-penetrometer measurements. Journal of Glaciology 55 (193), 805–813.

Birkeland, K. W., van Herwijnen, A., Knoff, E., Staples, M., Bair, E., Simenhois, R., 2014. The role of slabs and weak layers in fracture arrest. Proceedings of international 2014 Snow Science Workshop, Banff, Canada.

Chandel, C., Srivastava, P., Mahajan, P., 2015. Determination of failure envelope for faceted snow through numerical simulations. Cold Regions Science and Technology 116, 56–64.

Gaume, J., van Herwijnen, A., Chambon, G., Birkeland, K. W., Schweizer, J., 2015. Modeling of crack propagation in weak snowpack layers using the discrete element method. The Cryosphere 9, 1915–1932.

Gaume, J., van Herwijnen, A., Chambon, G., Wever, N., Schweizer, J., 2016. Snow fracture in relation to slab avalanche release: critical state for the onset of crack propagation. The Cryosphere Discussions 2016, 1–17.

Gauthier, D., Jamieson, B., 2008a. Evaluation of a prototype field test for fracture and failure propagation propensity in weak snowpack layers. Cold Regions Science and Technology 51 (2), 87–97.

Gauthier, D., Jamieson, B., 2008b. Fracture propagation propensity in relation to snow slab avalanche release: Validating the propagation saw test. Geophysical Research Letters 35 (13).

Gauthier, D., Jamieson, B., 2008c. Predictions of the propagation saw test: comparisons with other instability tests at skier tested slopes. Proceedings of the 2008 International Snow Science Workshop, Whistler, BC, 21–27.

Gauthier, D., Jamieson, B., 2010. On the sustainability and arrest of weak layer fracture in whumpfs and avalanches. Proocedings of the International Snow Science Workshop (ISSW) 2010, 224 – 231.

Gauthier, D., Ross, C., Jamieson, B., 2008. Validation of the propagation saw test near whumpfs and avalanches. Proceedings of the 2008 International Snow Science Workshop, Whistler, BC, 16–21.

Heierli, J., Gumbsch, P., Zaiser, M., 2008. Anticrack nucleation as triggering mechanism for snow avalanches. Science 321, 240–243.

Jamieson, J., Johnston, C., 1990. In-situ tensile tests of snow-pack layers. Journal of Glaciology 36 (122), 102–106.

Landry, C., Borkowski, J., Brown, R., 2001. Quantified loaded column stability test: mechanics, procedure, sample-size selection, and trials. Cold Regions Science and Technology 33 (2), 103–121.

Marshall, H.-P., Johnson, J. B., 2009. Accurate inversion of high-resolution snow penetrometer signals for microstructural and micromechanical properties. Journal of Geophysical Research: Earth Surface 114 (F4).

McClung, D., 1979. Shear fracture precipitated by strain softening as a mechanism of dry slab avalanche release. Journal of Geophysical Research: Solid Earth (1978–2012) 84 (B7), 3519–3526.

McClung, D., 2003. Size scaling for dry snow slab release. Journal of Geophysical Research: Solid Earth (1978–2012) 108 (B10).

McClung, D., 2007. Fracture energy applicable to dry snow slab avalanche release. Geophysical research letters 34 (2).

Mellor, M., 1975. A review of basic snow mechanics. International Symposium on Snow Mechanics. International Association of Hydrological Sciences, Grindewald, 251–291.

Monti, F., Gaume, J., van Herwijnen, A., Schweizer, J., 2016. Snow instability evaluation: calculating the skier-induced stress in a multi-layered snowpack. Natural Hazards and Earth System Sciences 16 (3), 775–788.

Reiweger, I., Gaume, J., Schweizer, J., 2015. A new mixed-mode failure criterion for weak snowpack layers. Geophysical Research Letters 42 (5), 1427–1432.

Reuter, B., Schweizer, J., van Herwijnen, A., 2015. A process-based approach to estimate point snow instability. The Cryosphere 9 (3), 837–847.

Scapozza, C., Bartelt, P., 2003. Triaxial tests on snow at low strain rate. Part II. Constitutive behaviour. Journal of Glaciology 49 (164), 91–101.

Schneebeli, M., Pielmeier, C., Johnson, J. B., 1999. Measuring snow microstructure and hardness using a high resolution penetrometer. Cold Regions Science and Technology 30 (13), 101 – 114.

Schweizer, J., 1999. Review of dry snow slab avalanche release. Cold Regions Science and Technology 30 (1), 43–57.

Schweizer, J., Jamieson, B. J., Schneebeli, M., 2003. Snow avalanche formation. Reviews of Geophysics 41 (4).

Schweizer, J., Reuter, B., van Herwijnen, A., Jamieson, B., Gauthier, D., 2014. On how the tensile strength of the slab affects crack propagation propensity. Proceedings of international 2014 Snow Science Workshop, Banff, Canada, 164–168.

Schweizer, J., van Herwijnen, A., Reuter, B., 2011. Measurements of weak layer fracture energy. Cold Regions Science and Technology 69 (23), 139 – 144.

Shapiro, L. H., Johnson, J. B., Sturm, M., Blaisdell, G. L., 1997. Snow mechanics: review of the state of knowledge and applications. Tech. rep., DTIC Document.

Sigrist, C., 2006. Measurement of fracture mechanical properties of snow and application to dry snow slab avalanche release. Ph.d. thesis, ETH Zurich.

Sigrist, C., Schweizer, J., 2007. Critical energy release rates of weak snowpack layers determined in field experiments. Geophysical Research Letters 34 (3).

Simenhois, R., Birkeland, K., 2009. The extended column test: Test effectiveness, spatial variability, and comparison with the propagation saw test. Cold Regions Science and Technology 59 (23), 210 – 216, international Snow Science Workshop (ISSW) 2008.

van Herwijnen, A., Gaume, J., Bair, E. H., Reuter, B., Birkeland, K. W., Schweizer, J., 2016. Estimating the effective elastic modulus and specific fracture energy of snowpack layers from field experiments. Journal of Glaciology, 1–11.

van Herwijnen, A., Jamieson, B., 2005. High-speed photography of fractures in weak snowpack layers. Cold Regions Science and Technology 43 (1), 71–82.

van Herwijnen, A., Schweizer, J., Heierli, J., 2010. Measurement of the deformation field associated with fracture propagation in weak snowpack layers. Journal of Geophysical Research: Earth Surface (2003–2012) 115 (F3).

von Moos, M., Bartelt, P., Zweidler, A., Bleiker, E., 2003. Triaxial tests on snow at low strain rate. Part I. Experimental device. Journal of Glaciology 49 (164), 81–90.

Thesis submitted in fulfilment of the requirements
for the degree of *Doctor of Philosophy in Structural Analysis*